ARISTOTLE UNIVERSITY OF THESSALONIKI

Simultaneous production of two bosons in the ATLAS experiment at the LHC

by

Eirini Kasimi

A thesis submitted in partial fulfillment for the
Doctor of Philosophy (PhD) degree

Physics Department

Supervising Professor: Chariclia Petridou

June 2023

The world used to be a bigger place…
The world is still the same…
There’s just less in it…

ARISTOTLE UNIVERSITY OF THESSALONIKI

Abstract

Physics Department

Doctor of Philosophy (PhD) Degree

by Eirini Kasimi

This thesis explores diboson and vector boson scattering (VBS) processes, focusing on the simultaneous production of a $W^{\pm}$ and a Z gauge boson from proton-proton collisions at the Large Hadron Collider (LHC) at CERN. For this study, data, which were collected from 2015 to 2018 by the ATLAS experiment and correspond to an integrated luminosity of $140\ fb^{-1}$ at a center-of-mass $13\,TeV$, are used.

These two processes provide the ideal ground for searches for physics beyond the Standard Model (SM) through deviations from the predicted vector boson self-couplings. These deviations could result in additional contributions to triple and quartic gauge couplings.

The way to study such deviations is through an Effective Field Theory (EFT). The use of an EFT allows for systematic exploration of higher-dimensional operators. The relevant operators to our processes are the dimension-6 and dimension-8 operators. The potential effect of various dimension-6 and dimension-8 operators on the $W^{\pm}Z$ diboson and VBS productions are studied. Finally, the 95% Confidence Level (CL) expected and observed limits for the dimension-8 operators that affect the $WZjj$ VBS process, are extracted.

Αριστοτέλειο Πανεπιστήμιο Θεσσαλονίκης

Περίληψη

Τμήμα Φυσικής

Διδακτορικό Δίπλωμα (PhD)

Ειρήνη Κασίμη

Το Καθιερωμένο Πρότυπο (Standard Model, SM) της Σωματιδιακής Φυσικής είναι μια εξαιρετικά επιτυχημένη θεωρία που περιγράφει τη συμπεριφορά των στοιχειωδών σωματιδίων και των αλληλεπιδράσεών τους μέσω των ηλεκτρομαγνητικών, ασθενών και ισχυρών δυνάμεων. Έχει δοκιμαστεί με απίστευτη ακρίβεια σε μια ευρεία γκάμα πειραμάτων και έχει μπορέσει να προβλέψει πολλά νέα φαινόμενα και σωματίδια που στη συνέχεια έχουν ανακαλυφθεί. Ωστόσο, παρά την επιτυχία του, το Καθιερωμένο Πρότυπο έχει ακόμα ορισμένες περιορισμούς που υποδηλώνουν την ύπαρξη νέας φυσικής πέρα από αυτό. Παρά τους περιορισμούς αυτούς, το Καθιερωμένο Πρότυπο παραμένει μία από τις πιο επιτυχημένες θεωρίες στη φυσική και παρέχει ένα ισχυρό πλαίσιο για την κατανόηση της συμπεριφοράς των σωματιδίων και των αλληλεπιδράσεών τους στην υποατομική κλίμακα. Ο Μεγάλος Αδρονικός Επιταχυντής Σωματιδίων (LHC) και ο ανιχνευτής ATLAS έχουν παίξει καθοριστικό ρόλο στον έλεγχο των προβλέψεων του Καθιερωμένου Προτύπου και στην αναζήτηση νέας φυσικής πέρα από αυτό, ανοίγοντας νέες δυνατότητες για ανακαλύψεις στον τομέα της σωματιδιακής φυσικής.

Ο Μεγάλος Αδρονικός Επιταχυντής (LHC) είναι ο μεγαλύτερος και ισχυρότερος επιταχυντής σωματιδίων στον κόσμο, βρίσκεται στο CERN (Ευρωπαϊκός Οργανισμός Πυρηνικής Έρευνας) κοντά στη Γενεύη της Ελβετίας. Ο LHC έχει σχεδιαστεί για να εξερευνά τις ιδιότητες των στοιχειωδών σωματιδίων και των αλληλεπιδράσεών τους, καθώς και για να αναζητά νέα φυσική πέρα από το Καθιερωμένο Πρότυπο. Ένα από τα τέσσερα κύρια πειράματα στο LHC είναι ο ανιχνευτής ATLAS, ο οποίος έχει σχεδιαστεί ως ένας γενικού σκοπού ανιχνευτής, με στόχο να εξερευνήσει την ύπαρξη νέων σωματιδίων μέχρι μάζες που φτάνουν τα TeV και να αναζητήσει νέες αλληλεπιδράσεις πέρα από το Καθιερωμένο Πρότυπο. Η πιο σημαντική συνεισφορά του ανιχνευτή ATLAS είναι η ανακάλυψη του σωματιδίου Higgs το 2012 [1], η οποία επιβεβαίωσε την ύπαρξη του πεδίου Higgs και ολοκλήρωσε το Καθιερωμένο Πρότυπο της Σωματιδιακής Φυσικής.

Γενικά, πριν από την παρατήρηση του μποζονίου Higgs, οι διμποζονικές παραγωγές ήταν ο κύριος τρόπος μελετης του σπασίματος της ηλεκτροασθενούς συμμετρίας. Τα μποζόνια W και Z είναι οι μεταδότες της ασθενούς δύναμης, η οποία είναι υπεύθυνη για ορισμένες θεμελιώδεις διεργασίες, όπως η β-διάσπαση. Η κατανόηση της συμπεριφοράς αυτών

των μποζονίων και των αλληλεπιδράσεών τους ήταν ουσιώδους σημασίας για την αποκρυπτογράφηση των μυστηρίων της σωματιδιακής φυσικής.

Η παρούσα διδακτορική διατριβή επικεντρώνεται στη μελέτη της διμποζονικής παραγωγής ενός $W^{\pm}$ και ενός Z μποζονίου βαθμίδας, όπως επίσης και στην ταυτόχρονη σκέδαση των μποζονίων αυτών (VBS) από τις συγκρούσεις των αρχικών κουάρκ των πρωτονίων στο LHC στο $CERN$. Για τη μελέτη αυτή χρησιμοποιήθηκαν δεδομένα που συλλέχθηκαν από το πείραμα $ATLAS$ κατά την περίοδο 2015-2018 και αντιστοιχούν σε ολοκληρωμένη φωτεινότητα 140 fb^{-1} σε ενέργεια κέντρου μάζας 13 TeV.

Οι παραπάνω διαδικασίες είναι πολύ σπάνιες, με την VBS διαδικασία να είναι η πιο σπάνια, καθώς έχουν πολύ μικρές ενεργές διατομές. Ωστόσο, είναι πολύ μεγάλης σημασίας αφού μπορούν να παράσχουν κρίσιμες πληροφορίες σχετικά με τη φύση του μηχανισμού Higgs ή την πιθανή ύπαρξη νέας φυσικής πέρα από το Καθιερωμένο Πρότυπο.

Στο πλαίσιο της μελέτης αυτών των δύο σημαντικών διαδικασιών, η συγγραφέας συνέβαλε στη λεπτομερή βελτιστοποίηση των κριτηρίων επιλογής των μιονίων, που προέρχονται από τις διασπάσεις των μποζονίων, Η επιλογή των μιονίων είναι ένα κρίσιμο στοιχείο της επιλογής γεγονότων του πειράματος ATLAS, καθώς βοηθά στη μείωση του θορύβου από εσφαλμένα ταυτοποιημένα μιόνια και τη βελτίωση του λόγου σήματος προς θόρυβο.

Οι δύο αυτές διαδικασίες προσφέρουν το ιδανικό έδαφος για την εξερεύνηση φυσικής πέρα από το Καθιερωμένο Πρότυπο, μέσω αποκλείσεων από τις προβλεπόμενες αυτο-συζεύξεις των μποζονίων βαθμίδας. Αυτές οι αποκλίσεις μπορούν να έχουν ως αποτέλεσμα επιπρόσθετες συνεισφορές στις τριπλές και τετραπλές αυτο-συζεύξεις των μποζονίων αυτών.

Η κύρια και πρωτοπόρα συνεισφορά τη συγγραφέως ηταν η μελέτη της ύπαρξης ανώμαλων τριπλών και τετραπλών αυτο-συζεύξεων των μποζονίων $W^{\pm}$ και Z. Ο τρόπος για τη μελέτη τέτοιων αποκλίσεων είναι μέσω μιας Ενεργού Θεωρίας Πεδίου (EFT). Η χρήση μια ενεργούς θεωρίας πεδίου μας επιτρέπει να μελετήσουμε την ύπαρξη τελεστών μεγαλύτερων διαστάσεων. Οι πιο σημαντικοί τελεστές για τις δύο διαδικασίες που μελετάμε είναι οι τελεστές διάστασεων-6 και διαστάσεων-8. Στη διατριβή αυτή μελετάται η επίδραση των τελεστών αυτών στην διμποζονική παραγωγή $W^{\pm}Z$ και στην ταυτόχρονη σκέδαση των δύο μποζονίων σε συνδυασμό με δύο πίδακες σωματιδίων. Τέλος, εξάγονται τα 95% αναμενόμενα και παρατηρήσιμα όρια πιστότητας για τους τελεστές διαστάσεων-8, οι οποίοι επηρεάζουν την ταυτόχρονη σκέδαση των δύο μποζονίων βαθμίδας.

Συνολικά, αυτή η εργασία παρέχει νέες ιδέες σχετικά με τις ιδιότητες των στοιχειωδών σωματιδίων και των αλληλεπιδράσεών τους, και συνεισφέρει στην κατανόηση των θεμελιωδών νόμων της φύσης. Η διατριβή οργανώνεται ως εξής: Το Κεφάλαιο 2 παρέχει μια επισκόπηση του θεωρητικού πλαισίου, ενώ το Κεφάλαιο 3 επικεντρώνεται στα κύρια χαρακτηριστικά του LHC και του πειράματος ATLAS. Στο Κεφάλαιο 4 περιγράφονται οι μηχανισμοί παραγωγήε γεγονότων Monte Carlo και τα δείγματα δεδομένων και προσομοιώσεων που χρησιμοποιήθηκαν στην ανάλυσή μας. Το Κεφάλαιο 5 εξηγεί τις τεχνικές ανακατασκευής αντικειμένων που χρησιμοποιούνται στο ATLAS, ενώ το Κεφάλαιο 6 παρουσιάζει την ανάλυσή μας για την παραγωγή των διμποζονική παραγωγή ενός $W^{\pm}$ και ενός Z μποζονίου βαθμίδας και την μελέτη ανώμαλων τριπλών αυτο-συζεύξεων των μποζονίων αυτών στο πλαίσιο μιας ενεργού θεωρίας πεδίου. Τέλος, το Κεφάλαιο 7 συζητά την ταυτόχρονη σκέδαση των μποζονίων $W^{\pm}$ και Z και την μελέτη ανώμαλων τριπλών και τετραπλών αυτο-συζεύξεων των μποζονίων αυτών στο πλαίσιο μιας ενεργού θεωρίας πεδίου, ενώ στο Κεφάλαιο 8 παρουσιάζεται μια σύνοψη της εργασίας και τα μελλοντικά σχέδιά μας.

Acknowledgements

As this beautiful journey comes to an end I would like to express my gratitude to those who supported, guided and encouraged me. Firstly, words cannot express my gratitude to my supervisor Prof. Chara Petridou for the continuous support and guidance of my Ph.D study and related research, for her patience, motivation, and immense contribution. Her guidance helped me in all the time of research and writing of this thesis. Her pivotal role and in this project made today's dream come true. Her trust and confidence in me made this journey a reality. I could not have imagined having a better supervisor and mentor for my Ph.D study. Also, I am grateful to my Thesis committee, namely Kostantinos Kordas, Dimitrios Sampsonidis, Spyridon Tzamarias, Antonis Leisos, Emmanuel Sauvan and last but not least Iro Koletsou, who all provided their invaluable knowledge, expertise and assistance in support of this endeavour. Major Thanks to my advisor Prof. Spyridon Tzamarias for assisting and providing me with crucial advice and help. His mentoring over these last five years has proven to be of the utmost importance in accomplishing our research goals. I am also grateful to the LAPP Institution and more specifically to my colleagues Emmanuel Sauvan and Iro Koletsou for working together and completing the WZ Run 2 analysis. On a personal level I thank them for welcoming me and making me feel part of the team from day one. It has been a privilege working together. Special thanks to the whole ATLAS Thessaloniki group and and especially to Ioannis Karkanias, Marievi Tsopoulou, Aggelos Tsiamis, Dinos Bachas, Katerina Zachariadou and Alexandros Marantis for their friendship, help and collaboration.

Lastly, I would be remiss in not mentioning my friends and family without whom it would not have been possible to complete this task. Many thanks to my friends Anastasia Mavridou, Nikos Kazos, Savvas Kyriakidis, Chrysoula Betsou and Eleutheria Ioannidou, who stood with me all the way, assisted and supported me in both good and difficult times. Of course I could not have done it without my parents Mary and Stefanos who inspired me to begin this journey and supported me every step of the way. Many thanks to my Aunt Maria for always being like a sister by my side. Also thanks to my parents in law, Kyriaki and Georgios, for their useful advice and support. Finally I find it difficult to express my appreciation to my husband Christoforos who encouraged me all the way, provided moral support and became my most enthusiastic cheerleader.

Contents

List of Figures

List of Tables

To my parents, Mary and Stefanos, my husband, Christoforos and my beloved aunt, Maria

Chapter 1

Introduction

The Standard Model (SM) of Particle Physics is a highly successful theory that describes the behavior of elementary particles and their interactions through the electromagnetic, weak, and strong forces. It has been tested with incredible precision in a wide range of experiments, and has been able to predict many new phenomena and particles that have subsequently been discovered. However, despite its success, the SM still has some limitations that suggest the existence of new physics beyond it. Despite these limitations, the SM remains one of the most successful theories in physics, and provides a powerful framework for understanding the behavior of particles and their interactions at the subatomic scale. The LHC and the ATLAS detector have played a key role in testing the predictions of the SM and searching for new physics beyond it, and have opened up new avenues for discovery in the field of particle physics.

The Large Hadron Collider (LHC) is the world's largest and most powerful particle accelerator, located at CERN (the European Organization for Nuclear Research) near Geneva, Switzerland. The LHC is designed to explore the properties of elementary particles and their interactions, and to search for new physics beyond the Standard Model. One of the four main experiments at the LHC is the ATLAS detector, which is designed to be a general-purpose detector, aimed to explore the existence of new particles up to several TeV masses and search for new interactions beyond the SM. The most important contribution of the ATLAS detector is the discovery of the Higgs boson in 2012 [1], which confirmed the existence of the Higgs field and completed the Standard Model of Particle Physics.

Generally, before the Higgs boson was observed, the diboson productions were the primary way to investigate the electroweak symmetry breaking. The W and Z bosons are the mediators of the weak force, which is responsible for certain fundamental processes such as radioactive decay. Understanding the behavior of these bosons and their interactions was essential for unraveling the mysteries of particle physics.

In this thesis, a study of the $W^{\pm}Z$ inclusive diboson and $W^{\pm}Z$ vector boson scattering (VBS) productions at LHC using data collected by the ATLAS experiment from 2015 to 2018 and correspond to an integrated luminosity of $140\,fb^{-1}$ at a center-of-mass $13\,TeV$, is performed.

WZ diboson production involves the creation of a W and Z boson pair, while $W^{\pm}Z$ VBS productions refers to the scattering of these vector bosons in high-energy collisions. These processes are very rare processes with the VBS process to be the rarest one, as they have very low cross sections. However, they are of great importance due to their sensitivity to the dynamics of electroweak symmetry breaking. Also they can provide crucial information about the nature of the Higgs mechanism or potential new physics beyond the Standard Model.

In the context of the study of these two important processes, the author contributed to the detailed optimization of the muon isolation criteria used in the event selection. Muon isolation is a critical component of the ATLAS trigger and event selection, as it helps to reduce the background mainly from fake muons and improve the signal-to-noise ratio.

In addition to the $W^{\pm}Z$ inclusive diboson and $W^{\pm}Z$ VBS productions, the role of triple gauge couplings (TGCs) and quartic gauge couplings (QGCs) in the production of these processes is investigated. TGCs and QGCs are higher-order interactions between gauge bosons that are predicted by the SM, but they can also be modified in new physics scenarios.

The main and pionnering contribution of the author were the study of the sensitivity of the $W^{\pm}Z$ inclusive diboson and $W^{\pm}Z$ VBS productions to anomalous TGCs (aTGCs) and QGCs (aQGCs), which could provide evidence of new physics effects. An Effective Field Theory (EFT) is used in order to parameterize these anomalous couplings and to search for deviations from the SM predictions. The use of an EFT allows for systematic exploration of higher-dimensional operators. The relevant operators to our processes are the dimension-6 and dimension-8 operators. The potential effect of various dimension-6 and dimension-8 operators on the $W^{\pm}Z$ inclusive diboson and VBS productions as well as the most sensitive kinematical variables for each of these operators, are studied. Finally, the 95% Confidence Level (CL) expected and observed limits for the dimension-8 operators that affect the $WZjj$ VBS process, are extracted.

Overall, this work provides new insights into the properties of elementary particles and their interactions, and contributes to our understanding of the fundamental laws of nature. The thesis is organized as follows: Chapter 2 provides an overview of the theoretical framework, while Chapter 3 focuses on the LHC and the ATLAS experiment. In Chapter 4, the Monte Carlo generators and the MC samples used in our analysis are described. Chapter 5 explains the object reconstruction techniques used in ATLAS, while Chapter 6 presents our analysis of the $W^{\pm}Z$ inclusive diboson production and its EFT re-interpretation. Finally, Chapter 7 discusses the $W^{\pm}Z$ VBS production and its EFT re-interpretation, while in Chapter 8 a conclusion and our future plans are presented.

Chapter 2

Theory Framework

2.1 The Standard Model of Particle Physics

The Standard Model (SM) of particle physics is a widely accepted theory that offers a thorough relativistic quantum field theory description and an incredible explanation of the perceiving world. This section is based on [2] [3] which contain some excellent introductions to the Standard Model (SM) and it summarizes them.

2.1.1 Introduction

The Standard Model is a highly successful theory in particle physics that describes the fundamental particles and their interactions through the fundamental forces. It is a quantum field theory based on the principles of symmetry and gauge invariance and is mathematically formulated using a Lagrangian formalism.

The particle content of the SM consists of two main categories: quarks and leptons, which together called fermions. Both of them are spin-$1/2$ elementary particles. Quarks are particles that come in six different types or flavors: up (u), $down$ (d), $charm$ (c), $strange$ (s), top (t), and $bottom$ (b). These quarks have fractional electric charges, with the up quark carrying $Q = +2/3e$ and the down quark carrying $Q = -1/3e$. On the other hand, leptons also come in six types: $electron (e)$, $electron neutrino (\nu_e)$, $muon (\mu)$, $muon neutrino (\nu_\mu)$, $tau (\tau)$, and $tau\ neutrino$ $(\nu_{\tau)}$. Leptons have integer electric charges, with the electron carrying $-e$, and the neutrinos being neutral. Antiparticles also exist for each elementary particle with opposite charge and the same mass.

The SM incorporates three fundamental forces: electromagnetic, weak, and strong. The electromagnetic force, responsible for interactions between charged particles, is described by

$quantum\ electrodynamics\ (QED)$. It is mediated by massless and chargeless gauge bosons called photons (γ). The weak nuclear force governs certain types of particle decays, such as β-decay and is responsible for the phenomenon of neutrino oscillation. It is described by the electroweak theory and is mediated by the W^+, W^-, and Z bosons. The W^+ and W^- bosons carry a positive and negative charge, respectively, while the Z boson is chargeless. All these gauge bosons are spin-1 elementary particles.

The strong nuclear force is described by $quantum\ chromodynamics\ (QCD)$ and binds quarks together to form composite particles such as protons and neutrons (hadrons). It is mediated by massless gluons (G_a), which are spin-1 elementary particles and carry a color charge associated with the strong force. There are three different color charges (red, green, and blue) and their respective anti-colors. Hadrons can interact through the strong interaction, such as to form nuclei, but only on very short distances on the order of approximately $1\ fm$. The strong force is unique in that it becomes stronger as particles are pulled apart, resulting in the phenomenon of $confinement$, where quarks are always confined within composite particles.

The Higgs mechanism is a crucial component of the SM. It introduces the Higgs field and the associated $Higgs$ boson (H), which is an elementary particle of spin 0 and gives mass to elementary particles. The Higgs field permeates all of space, and particles acquire mass by interacting with it. The discovery of the Higgs boson at the Large Hadron Collider in 2012 [1] confirmed the existence of this field and was a significant validation of the SM.

Table 2.1 provides an overview of the elementary particles in the SM.

The SM uses a Lagrangian to mathematically describe the dynamics and symmetries of fundamental particles and their interactions. The Lagrangian includes terms for the kinetic energies of particles and interaction terms that determine how they interact. It is based on gauge symmetries, which dictate how fields change under specific transformations. By varying the Lagrangian using the principle of least action, the equations of motion for the particles can be derived. In essence, the Lagrangian provides a formal framework for understanding the behavior of particles and the forces between them in the SM.

Despite its successes, the SM has limitations. It does not incorporate gravity, which is described by general relativity. Additionally, it cannot explain phenomena such as dark matter and dark energy, which are significant components of the universe. Therefore, physicists continue to explore extensions to the SM, such as supersymmetry, string theory, and grand unified theories, to address these gaps in our understanding of the universe.

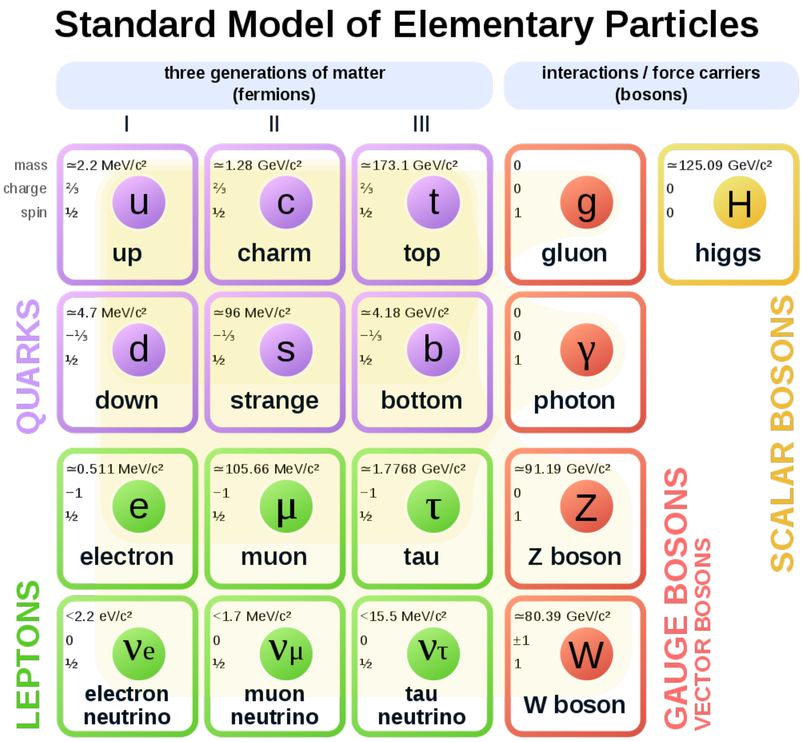

Standard Model of Elementary Particles

	three generations of matter (fermions)			interactions / force carriers (bosons)	
	I	II	III		
mass charge spin					
QUARKS	≃2.2 MeV/c² ⅔ ½ u up	≃1.28 GeV/c² ⅔ ½ c charm	≃173.1 GeV/c² ⅔ ½ t top	0 0 1 g gluon	≃125.09 GeV/c² 0 0 H higgs
	≃4.7 MeV/c² −⅓ ½ d down	≃96 MeV/c² −⅓ ½ s strange	≃4.18 GeV/c² −⅓ ½ b bottom	0 0 1 γ photon	SCALAR BOSONS
LEPTONS	≃0.511 MeV/c² −1 ½ e electron	≃105.66 MeV/c² −1 ½ μ muon	≃1.7768 GeV/c² −1 ½ τ tau	≃91.19 GeV/c² 0 1 Z Z boson	GAUGE BOSONS VECTOR BOSONS
	<2.2 eV/c² 0 ½ νe electron neutrino	<1.7 MeV/c² 0 ½ νμ muon neutrino	<15.5 MeV/c² 0 ½ ντ tau neutrino	≃80.39 GeV/c² ±1 1 W W boson	

TABLE 2.1: Overview of elementary particles in the Standard Model.

2.1.2 Introduction to gauge theories

The Standard Model is a gauge field theory within the framework of relativistic quantum field theory. Symmetry, in classical physics, refers to transformations that preserve observable physical properties.

In this model, particles are described as quantum fields, where their interactions and propagation are described by the Lagrangian formalism. The Euler-Lagrange equations provide a method for deriving the equations of motion for a system based on the given Lagrangian.

The equations of motion for a freely propagating fermion $\psi(\vec{x}, t)$ with mass m applied to a Lagrangian:

$$\mathcal{L}_{\text{Dirac}} = \bar{\psi} \left(i\gamma^\mu \partial_\mu - m \right) \psi \tag{2.1}$$

where γ^μ are the Dirac matrices.

The Lagrangian is invariant under global gauge transformations, of the form $\psi(\vec{x}, t) \rightarrow e^{-i\alpha}\psi$ of the fermion field, where α is a real phase factor. According to Noether's theorem [4], continuous symmetries have corresponding conserved quantities, and vice versa. In the case of a local gauge transformation, the phase factor α is allowed to depend on the spacetime coordinates $x = \vec{x}, t$

$$\psi(\vec{x}, t) \to e^{-i\alpha(\vec{x},t)}\psi(\vec{x}, t). \tag{2.2}$$

In order to maintain the invariance of the Lagrangian given in Equation 2.1 under a local gauge transformation, a gauge field, denoted as A_μ, is introduced

$$A_\mu \to A_\mu + \frac{1}{e}\partial_\mu \alpha \tag{2.3}$$

The A_μ couples to fermionic fields $\psi(\vec{x}, t)$ with strength e. A covariant derivative, which is specific to local gauge transformation, is defined by:

$$D_\mu = -\partial_\mu - ieA_\mu \tag{2.4}$$

The symmetry expressed in Equation 2.2 corresponds to $U(1)$ gauge symmetry, and the gauge field A_μ can be interpreted as the photon field. In order to preserve the gauge invariance of A_μ, a new term is introduced into the Lagrangian

$$\mathcal{L}_{kinetic} = -\frac{1}{4}F_{\mu\nu}F^{\mu\nu} \tag{2.5}$$

where $F^{\mu\nu}$ is the field strength tensor defined as

$$F^{\mu\nu} = \partial^\mu A^\nu - \partial^\nu A^\mu. \tag{2.6}$$

Finally, the Lagrangian in Equation 2.1 becomes

$$\mathcal{L}_{QED} = \bar{\psi}\left(i\gamma^\mu\partial_\mu - m\right)\psi - \frac{1}{4}F_{\mu\nu}F^{\mu\nu} \tag{2.7}$$

This is the Lagrangian of quantum electrodynamics (QED). Similarly, the Lagrangian of quantum chromodynamics (QCD) can be derived by requiring gauge invariance under local $SU(3)_C$ transformations and the Lagrangian of electroweak interaction theory can be obtained by requiring symmetry under local $SU(2)_L \otimes U(1)_Y$ transformations, as it will be explained in the next Sections.

2.1.3 Quantum chromo-dynamics

The theory that describes the interaction between quarks is called quantum chromodynamics (QCD). It is obtained by demanding symmetry under local $SU(3)_C$ gauge transformations on the quark color field q. The Lagrangian for free color fields can be expressed as:

$$\mathcal{L} = \bar{q}_j(i\gamma^\mu\partial_\mu - m)q_j \tag{2.8}$$

where, j ∈(red, green, blue) refers to the colour charge of the quark. The local gauge invariance refers to the transformation

$$q_j \to e^{ia_\alpha(x)\frac{\lambda_a}{2}}q_j \tag{2.9}$$

where λ_α with $a = 1, ...8$ are are the 8 linearly independent, traceless Gell-Mann matrices (Appendix A). The λ_a matrices do not commute with each other

$$[\frac{\lambda_a}{2}, \frac{\lambda_b}{2}] = if_{abc}\frac{\lambda_c}{2} \tag{2.10}$$

where f_{abc} is the structure constant of $SU(3)$. QCD is a non-abelian gauge theory as the generators are non commuting. To make the Lagrangian local gauge invariant, the following covariant derivative is defined

$$D_\mu = \partial_\mu + ig_s\frac{\lambda_a}{2}G^a_\mu \tag{2.11}$$

where G^a_μ are the gluon fields. The introduced covariant derivative couples the quark field and the gluon fields through the generators $\lambda_a/2$, with a coupling strength g_s. There are 8 gluon fields for the phase variation of three quark colour and they transform as

$$G^a_\mu \to G^a_\mu - \frac{1}{g_s}\partial_\mu\alpha_a - f_{abc}\alpha_b bG^c_\mu \tag{2.12}$$

The Lagrangian in Equation 2.8 is modified as

$$\mathcal{L} = \bar{q}_j(i\gamma^\mu\partial_\mu - m)q_j - \frac{1}{4}G^a_{\mu\nu}G^{\mu\nu}_a \tag{2.13}$$

where $G^a_{\mu\nu}$ is the field strength tensor

$$G^a_{\mu\nu} = \partial_\mu G^a_\nu - \partial_\nu G^a_\mu - g_s f_{abc}G^b_\mu G^c_\nu \tag{2.14}$$

Color states can be combined in various ways to create a state that is color-neutral. Hadrons, which are color-neutral bound states of quarks, fall into two primary categories: mesons, which consist of a quark and an antiquark, and baryons, which are composed of three quarks. At high energies, these hadrons reveal a structure involving virtual quark-antiquark pairs arising from vacuum fluctuations. The composition of hadrons can be probabilistically determined based on parton distribution functions (PDF), which summarize the probabilities of finding different types of partons (quarks and gluons) within a hadron.

2.1.4 Electroweak theory

The weak nuclear force plays a crucial role in processes such as radioactive β-decay, where a neutron can transform into a proton by emitting an electron and an electron antineutrino. In the 1930s, quantum mechanics provided a relativistic equation of motion for electrons through the Dirac equation. However, understanding nuclear decay phenomena remained a mystery. Enrico Fermi initially attempted to explain β-decay using quantum physics, proposing a direct contact interaction between the four fermions involved. This idea was motivated by the seemingly extremely short-range nature of the interaction, leading to the term ”weak” interactions. However, Fermi’s model only worked at low energies. Simultaneously, the theory of quantum electrodynamics (QED) was developed, which described the electromagnetic interaction mediated by photons. In 1957, Julian Schwinger proposed the existence of force-mediating gauge bosons for the weak interaction. In 1954, Yang and Mills developed a non-Abelian gauge theory based on the SU(2) symmetry, which formed the foundation for describing the weak interaction. Later, in 1961, Glashow extended the theory to a $SU(2) \otimes U(1)$ group, aiming to incorporate both the electromagnetic and weak interactions.

Experimental observations indicate that the weak interaction specifically affects left-handed fermion fields and right-handed anti-fermion fields. To describe the electromagnetic and weak interactions together, the electroweak theory was developed, which incorporates the $SU(2)_L \otimes U(1)_Y$ gauge symmetry.

The $U(1)_Y$ symmetry is derived based on the principles of electrodynamics, while the $SU(2)_L$ symmetry in weak isospin space is motivated by the characteristics of the weak interaction. This gauge group consists of four massless gauge bosons: W_μ^α ($\alpha = 1, 2, 3$) for the $SU(2)_L$ group and B_μ for the $U(1)_Y$ group. The corresponding gauge coupling constants are denoted as g_1 and g_2.

In the electroweak theory, the fermion fields are represented by left-handed doublets χ_L and right-handed singlets ψ_R.

For the first generation leptons and quarks fields can be expressed as

$$\begin{gathered}\chi_L = \begin{pmatrix} \nu_e \\ e \end{pmatrix}_L \text{ and } \quad \chi_L = \begin{pmatrix} u \\ d \end{pmatrix}_L, \\ \psi_R = e_R \text{ and } \nu_{eR} \text{ and } \quad \psi_R = u_R \text{ and } d_R \end{gathered} \tag{2.15}$$

where the corresponding fermions of the second and third generation follow accordingly. The Lagrangian for these fermion fields is required to be invariant under local gauge transformations corresponding to both the $SU(2)_L$ and $U(1)_Y$ symmetry groups

$$\begin{aligned} \chi_L &\rightarrow e^{i\beta(x)Y + i\alpha_a(x)\tau_a}\chi_L \\ \psi_R &\rightarrow e^{i\beta(x)Y}\psi_R \end{aligned} \tag{2.16}$$

where the $\alpha(x)$ and $\beta(x)$ are the phase transformation factors of the $SU(2)_L$ and $U(1)_Y$ symmetry groups. The Pauli matrices τ_α, $\alpha = 1, 2, 3$ and the weak hypercharge operator Y are the generators of the groups. The gauge invariant Lagrangian for the fermions is

$$\begin{aligned} \mathcal{L}_0 = \bar{\chi}_L \gamma^\mu &\left[i\partial_\mu - g_1 \frac{\tau_a}{2} W_\mu^a + \frac{g_2}{2} B_\mu \right] \chi_L \\ &+ \bar{\psi}_R \gamma^\mu \left[i\partial_\mu + g_2 B_\mu \right] \psi_R \end{aligned} \tag{2.17}$$

The term containing the $SU(2)_L$ matrix gives rise to charged-current interactions with the boson field

$$\begin{aligned} W^+ &= \left(-W^1 + iW^2\right)/\sqrt{2}, \\ W^- &= \left(-W^1 - iW^2\right)/\sqrt{2} \end{aligned} \tag{2.18}$$

and its complex conjugate. The charged current Lagrangian for a single generation of quarks and leptons is expressed as

$$\mathcal{L}_{CC} = \frac{g_1}{2\sqrt{2}} \left\{ W_\mu^\dagger \left[\bar{u}\gamma^\mu \left(1 - \gamma_5\right) d + \bar{\nu}_e \gamma^\mu \left(1 - \gamma_5\right) e \right] + \text{ h.c. } \right\} \tag{2.19}$$

The assumption of gauge symmetry in the Standard Model directly leads to the universality of interactions among quarks and leptons. In Equation 2.17, there are interactions involving the neutral gauge fields W_μ^3 and B_μ. These gauge bosons are identified as the Z boson and the photon (γ), respectively. As both fields are electrically neutral, they can be arbitrary combined as

$$\begin{pmatrix} W_\mu^3 \\ B_\mu \end{pmatrix} \equiv \begin{pmatrix} \cos\theta_W & \sin\theta_W \\ -\sin\theta_W & \cos\theta_W \end{pmatrix} \begin{pmatrix} Z_\mu \\ A_\mu \end{pmatrix} \tag{2.20}$$

The neutral-current Lagrangian is given by

$$\begin{aligned}\mathcal{L}_{NC} = \sum_j \bar{\psi}_j \gamma^\mu \Big\{ A_\mu \Big[g_1 \frac{\tau_3}{2} \sin\theta_W + g_2 Y \cos\theta_W \Big] \\ + Z_\mu \Big[g_1 \frac{\tau_3}{2} \cos\theta_W - g_2 Y \sin\theta_W \Big] \Big\} \psi_j\end{aligned} \tag{2.21}$$

In order to get QED from the A_μ, the following condition needs to be fullfiled

$$g_1 \sin(\theta_W) = g_2 \cos(\theta_W) = e \quad \text{and} \quad Y = Q - T_3 \tag{2.22}$$

where $T_3 = \tau_3/2$ is the weak isospin operator associated to $SU(2)_L$, Q is the electromagnetic charge and Y is the hypercharge associated to $U(1)_Y$. The above Equation relates the $SU(2)_L$ and $U(1)_Y$ couplings to the electromagnetic coupling, providing the unification of the electroweak interactions.

2.1.5 Self-interactions of bosons

The observation of gauge bosons confirmed the most fundamental prediction of the SM as a gauge theory. To fully describe the SM Lagrangian, it is essential to add terms that explain the dynamics of these gauge fields. These terms can be added to the Lagrangian by utilizing generalized field strength tensors.

$$\begin{aligned} B^{\mu\nu} &= \partial^\mu B^\nu - \partial^\nu B^\mu && \text{for } U(1)_Y \\ W_i^{\mu\nu} &= \partial^\mu W_i^\nu - \partial^\nu W_i^\mu + g_2 \epsilon_{ijk} W_j^\mu W_k^\nu && \text{for } SU(2)_L \end{aligned} \tag{2.23}$$

where $i = 1, 2, 3$. The generalization is necessary to account for the non-Abelian nature of $SU(2)$. Since transformations within these groups can be interpreted as higher-dimensional rotations, this property is equivalent to the fact that the order of rotations in multiple dimensions matters.

The bosonic lagrangian can be expressed as

$$\mathcal{L}_{\text{bosons}} = -\frac{1}{4} B^{\mu\nu} B_{\mu\nu} - \frac{1}{4} W_i^{\mu\nu} W_{\mu\nu}^i. \tag{2.24}$$

It can be seen that the field strength tensors enter quadratically in this Lagrangian. Only quadratic terms in the field B^μ or its derivative $\partial^\mu B^\nu$ are included in this Lagrangian for $B^{\mu\nu}$, which describes the dynamics of the B^μ field. Since, W_i^μ contains a term that is already quadratic in the field, the full Lagrangian also includes terms of order three and four in the fields. These terms can be identified as three- and four-point vertices of self-interactions among the gauge bosons.

For this thesis, a more in-depth exploration of the fields W_j^μ is of particular interest. These terms always contain all three components in weak isospin space, namely W_1^μ, W_2^μ, and W_3^μ. W_1^μ and W_2^μ combine to form the physical $W^\pm$ gauge bosons, while the third component has contributions in the physical photon and Z boson. Thus, the resulting three-point interactions described by these terms are interactions between a pair of $W^\pm$ bosons and either a photon or a Z boson, as illustrated in Figure 2.1. Interactions between Z bosons and photons are not part of the Lagrangian and are not included in the SM, although charge conservation allows a three-point interactions between them.

On the other hand, the terms for the four-point interaction exist in all combinations where one of the fields W_i^μ does not contribute, and both other fields are included in quadrature. With the mixing to the physical bosons, the four-particle vertices include either four $W^\pm$ bosons or two $W^\pm$ bosons and two additional bosons, where each can be either a photon or a Z boson, as shown in Figure 2.2. Similar to the three-point interactions, a vertex with four neutral electroweak gauge bosons obeys charge conservation but does not exist in the SM.

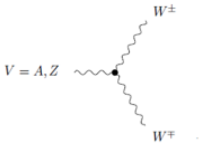

FIGURE 2.1: Feynman diagram of the three-point interaction between the physical gauge fields in the electroweak theory.

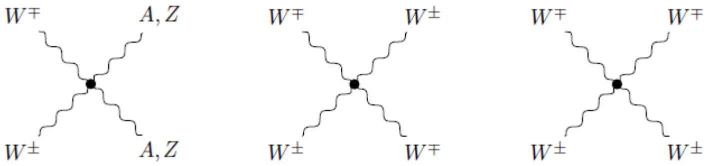

FIGURE 2.2: Feynman diagram of the four-point interaction between the physical gauge fields in the electroweak theory.

A good understanding of the diboson production in high energy experiments is an effective and important way to verify the SM theory, especially its high energy behavior in electroweak interactions and also it is a nice way to search for physics beyond the SM through the potential modification of the vector boson self-interactions.

2.1.6 Masses and the Higgs mechanism

A major challenge faced in the development of the SM was the requirement that all particles in the Lagrangian be massless, as the inclusion of explicit mass terms would violate the $SU(2)$ symmetry or gauge invariance.

However, massless particles appear to be in conflict with observations, where fermions were already known to be massive and the predicted gauge bosons $W^{\pm}$ and Z needed to be massive in order to explain the earlier experimental results.

Spontaneous symmetry breaking

The Brout-Englert-Higgs (BEH) mechanism [5] was developed as a solution to the problem of massless particles in the Standard Model. It involves introducing a new field with an associated potential, which has a non-zero ground state. Although the overall potential and Lagrangian remain gauge invariant, some symmetries are broken in the ground state. Interactions with the field in this state allow particles to acquire mass. This concept is known as spontaneous symmetry breaking.

The BEH mechanism introduces two scalar complex fields ϕ^{+} and ϕ^{0} combined in a $SU(2)_L$ doublet ϕ

$$\phi = \begin{pmatrix} \phi^{+} \\ \phi^{0} \end{pmatrix} \tag{2.25}$$

The SM Lagrangian is extended by the new term

$$\mathcal{L}_{\text{BEH}} = (D_{\mu}\phi)^{\dagger}(D^{\mu}\phi) - V(\phi), \tag{2.26}$$

where the first term describes the kinematic of the new fields and $V(\phi)$ is the new BEH potential expressed as

$$V(\phi) = \mu^{2}\phi^{\dagger}\phi + \lambda(\phi^{\dagger}\phi)^{2}. \tag{2.27}$$

Choosing this extension for the SM Lagrangian, the full Lagrnagian is invariant under the usual gauge tranformations. If the $\mu^2 < 0$ and $\lambda > 0$, the potential has a minimum for

$$\phi^{\dagger}\phi = \frac{-\mu^{2}}{2\lambda} = \frac{\nu^{2}}{2}. \tag{2.28}$$

There are many ways to satisfy this condition. A direction in $SU(2)$ space must be chosen and expand around the minimum. The appropriate choice is the so called "vacuum", ϕ^0

$$\phi_0 = \frac{1}{\sqrt{2}} \begin{pmatrix} 0 \\ \mathrm{v} \end{pmatrix} \tag{2.29}$$

and general expansions around this vacuum state can be transformed to

$$\phi(x) = \frac{1}{\sqrt{2}} \begin{pmatrix} 0 \\ \nu + H(x) \end{pmatrix}. \tag{2.30}$$

The field initially had four degrees of freedom due to the presence of two complex fields. However, the introduction of the new potential led to a reduction in the number of degrees of freedom to one, which corresponds to the expansion around the minimum. The effects of the remaining degrees of freedom can be eliminated using gauge transformations.

The choice of minimum leads to the breaking of some $U(1)_Y$ and $SU(2)_L$ symmetries, and a symmetry group is identified in the expansion around the minimum. This symmetry group is known as the usual phase transformations for QED $U(1)_Q$. According to the Nambu-Goldstone theorem [6, 7], a massless scalar boson exists for each broken symmetry, known as Goldstone boson. The Goldstone bosons correspond to the lost degrees of freedom when choosing a minimum.

Boson masses and interactions

Mass terms for the gauge bosons can be derived by expanding the Lagrangian around the chosen minimum rather that the Higgs field H. The Higgs field is required to be electrically neutral and the choice of $SU(2)_L$ doublet makes the hypercharge of H be $Y_H = 1$. Due to this choice, one can derive the terms

$$\begin{aligned} (D_\mu \phi)^\dagger (D^\mu \phi) &= \frac{1}{8} \left| \begin{pmatrix} g_1 B_\mu + g_2 W_\mu^3 & g_2 \left(W_\mu^1 - i W_\mu^2\right) \\ g_2 \left(W_\mu^1 + i W_\mu^2\right) & g_1 B_\mu - g_2 W_\mu^3 \end{pmatrix} \begin{pmatrix} 0 \\ \nu + H \end{pmatrix} \right|^2 \\ &= \frac{1}{4} (\nu + H)^2 g_2^2 W_\mu^+ W^{-\mu} + \frac{1}{8} \left(g_2^2 + g_1^2\right) (\nu + H)^2 Z_\mu Z^\mu \end{aligned} \tag{2.31}$$

The term of a mass boson in the Lagrangian has the form $c M_\nu^2 V V$, where $c = \frac{1}{2}$ for self-conjugate bosons and $c = 1$ else. So, the mass terms for the $W^\pm$ and Z bosons are

$$
\begin{aligned}
M_W &= g_2 \frac{\nu}{2} \\
M_Z &= \frac{1}{2}\nu\sqrt{g_1^2 + g_2^2}.
\end{aligned}
\tag{2.32}
$$

The mass of photon must be zero since no $A_\mu A^\mu$ term appears.

Thus, a clever approach is developed to provide masses to the mediators of the weak force by incorporating isodoublet complex scalar fields into the Lagrangian of the $SU(2)_L \otimes U(1)_Y$ model. This addition maintains gauge invariance of the total Lagrangian and leads to the phenomenon of spontaneous symmetry breaking. One notable outcome of the BEH mechanism is the prediction of a massive scalar boson, known as the Higgs boson (H), whose mass was initially unknown but subsequently discovered through experimental observations.

Finally, there are terms that describe three-point and four-point interactions between the Higgs field and gauge boson pairs W^+W^- or ZZ. The coupling strength is proportional to the mass of the gauge boson squared, and the Feynman diagrams for these interactions are shown in Figure 2.3.

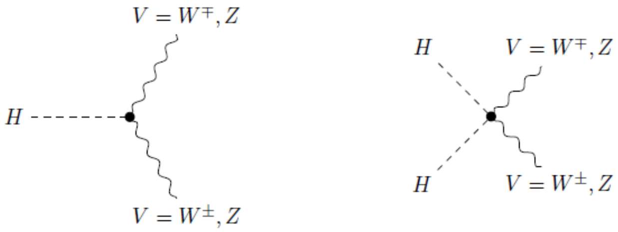

FIGURE 2.3: Feynman diagrams for the three-point (left) and four-point (right) interactions between the physical gauge fields $W^\pm$ and Z and the Higgs field H.

Fermion masses

Now that the Higgs field is available in an $SU(2)$ doublet, it is possible to write an $SU(2)$-invariant interaction of fermions with the Higgs field. To the previous Lagrangian, an interaction term for the leptons can be added

$$
\mathcal{L}_{\text{Yukawa, leptons}} = y_\ell^i \left(\bar{L}^i \phi e_R^i + \phi^\dagger \bar{e}_R^i L^i \right), \tag{2.33}
$$

where $i = 1,\ 2,\ 3$ sums over the generations and with arbitrary couplings y_ℓ^i.

Since this entire term is gauge invariant, the expansion around the minimum can replace the generic BEH field. Due to this expansion, the mass terms for the leptons are

$$
m_l = \frac{y_l \nu}{\sqrt{2}}. \tag{2.34}
$$

By selecting a specific value for the free parameter y_l, mass terms can be added for each lepton to the Lagrangian. Furthermore, the Lagrangian includes an interaction term between the lepton and the Higgs boson with a coupling strength of $\frac{m_l}{\nu}$. However, no terms for neutrino masses are present. For quarks, additional terms are required to generate mass terms for the state with a positive weak isospin

$$\mathcal{L}_{\text{Yukawa, quarks}} = Y_d^{jk}\bar{Q}_L^j\phi d_R^k + Y_u^{jk}\bar{Q}_L^j i\tau_2\phi^* u_R^k + \text{ h.c. }, \tag{2.35}$$

where $j, k = 1, 2, 3$ summing over the generations and the Yukawa matrices Y_d^{jk} and Y_u^{jk} are complex matrices which can be set for each quark to yield the correct mass terms.

The BEH mechanism also introduces additional free parameters, but it also gives a relation between the masses of the vector gauge bosons at tree level. Without higher-order corrections, this relation is given by

$$\frac{M_W}{M_Z} = cos\theta_W. \tag{2.36}$$

The BEH mechanism predicts the existence of a massive scalar boson, namely the Higgs boson H. While the mass of the Higgs boson was a free parameter in the BEH mechanism, once the mass is known, most interactions can be worked out in the theory.

One of the free parameters of the BEH potential can be related to the vacuum expectation value ν of the potential. The value of ν is proportional to the ratio of the $W^{\pm}$ boson mass over the coupling g_2. This ratio can be expressed in terms of the well-known Fermi constant G_F, which has been measured through muon lifetime experiments. Therefore, ν can be determined by

$$\nu = 2\frac{M_W}{g_2} = \frac{1}{\sqrt{\sqrt{2}G_F}} \approx 246\text{GeV} \tag{2.37}$$

The other free parameter λ of the BEH potential can be related to the mass of the Higgs boson M_H, which is

$$M_H = 125.10 \pm 0.14\text{GeV}. \tag{2.38}$$

Finally, the full Standard Model Lagrangian is given by

$$\mathcal{L}_{\text{SM}} = \mathcal{L}_{\text{QED}} + \mathcal{L}_{\text{QCD}} + \mathcal{L}_{\text{boson}} + \mathcal{L}_{\text{BEH}} + \mathcal{L}_{\text{Yukawa}} \tag{2.39}$$

The agreement between the theoretical predictions of the Standard Model and the experimental observations constantly verified to unprecedented precision from the two largest experiments at the Large Hadron Collider at CERN, ATLAS and CMS. The Figure 2.4 shows the summary of several Standard Model total and fiducial production cross-section measurements from Run 2, corrected for branching fractions, compared to the corresponding theoretical expectations. (The cross section of a process is the measure of the probability for a specific process to take place.)

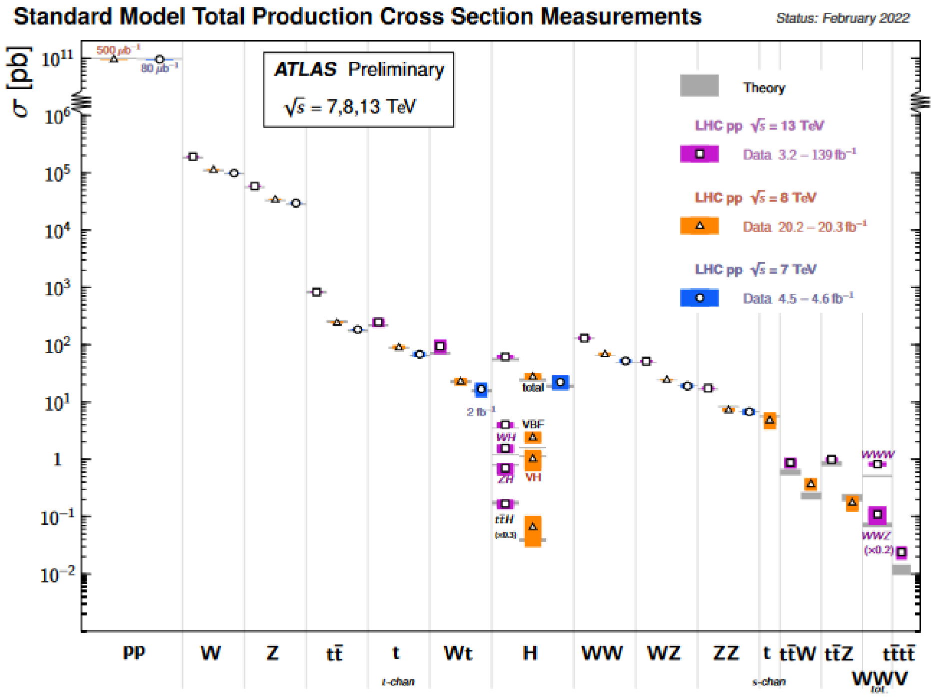

FIGURE 2.4: Summary of several Standard Model total and fiducial production cross-section measurements from Run 2,corrected for branching fractions, compared to the corresponding theoretical expectations.

2.2 Vector Boson Scattering

2.2.1 Overview

The $Vector\ Boson\ Scattering$ (VBS) is a process where two gauge bosons interact with each other in the form $VV \rightarrow VV$, where the V can be any of the electroweak bosons; $V = W^{\pm}, Z, \gamma$ but not every combination of the bosons is allowed.

The VBS process is a very important process because it provides a way to test the quartic gauge couplings. However, the terms that result in the triple gauge couplings, mediated via a gauge boson propagator, must also be present in the Lagrangian with the related terms to be gauge invariant. Thus, it is not viable to separate these diagrams in a gauge-invariant way.

All these diagrams must be taken into account in the calculation of more complete theory predictions. On the other hand, similar diagrams for $V\ V\ \to\ V\ V$ are obtained by coupling massive gauge bosons to the Higgs boson. Finally, Figure 2.5 shows the five Feynman diagrams that contributes to the VBS process at leading order.

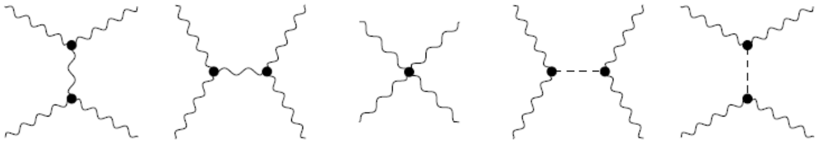

FIGURE 2.5: All leading-order Feynman diagrams where two gauge bosons interact with each other in the form $V\ V\ \to\ V\ V$.

The presence of this scattering process is a direct consequence of the gauge structure of the SM. The non-Abelian structure of the theory implies the existence of direct interactions among the corresponding gauge bosons. The scattering mediated by such couplings is of particular interest in the electroweak $SU(2)_L$ case,due to the masses of the $W^{\pm}$ and Z bosons.

Polarization refers to the projection of the spin of a particle on its momentum. For massless spin-1 particles such as photons and gluons, only two polarization states are allowed, where the spin is parallel or anti-parallel to the momentum. These states are called transversely polarized. However, for massive spin-1 particles, which acquired mass due to the Higgs mechanism, an additional polarization state is allowed, where the spin is perpendicular to the momentum. This state is called longitudinally polarized. As discussed in Section 2.1.6, these states are related to the Goldstone bosons.

The scattering of longitudinally polarized bosons $V_L\ V_L\ \to\ V_L\ V_L$, without the Higgs-mediated contributions, is predicted to increase quadratically with the centre-of-mass energy $\propto\ E^2$. However, this growth breaks unitarity and is unphysical because it implies a scattering probability larger than one for sufficiently high energies. This prediction suggests that the scattering of electroweak gauge bosons cannot be explained consistently in the SM without a Higgs boson. On the other hand, the scattering of gauge bosons with polarization states other than the purely longitudinal does not violate unitarity. The inclusion of the SM Higgs boson, as predicted by the BEH mechanism, cancels out the increase in the cross section, as the Higgs boson couples to the electroweak gauge bosons, as shown in Figure 2.3. This cancellation avoids the violation of unitarity and produces physically meaningful predictions.

The VBS process can provide a way to study in depth the electroweak symmetry breaking and energies higher than 1 TeV, and it will be the main object of study in this thesis.

2.2.2 Vector Boson Scattering at Hadron Colliders

As the gauge bosons are not stable, the entire process of producing the initial bosons and their subsequent decay must be taken into account when considering the hard process. At hadron colliders like the LHC (Section 3.1), initial bosons may be emitted by partons. The Feynman diagrams for the complete process from the partons to the boson decay products are shown in Figure 2.6.

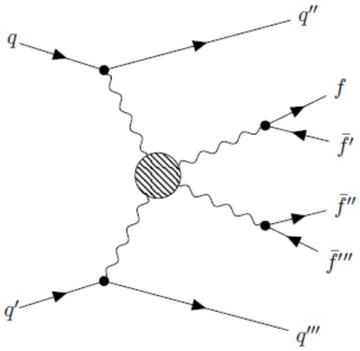

FIGURE 2.6: Feynman diagram for the VBS electroweak process. In the place of the dashed circle can be any of the possible boson scattering diagrams shown in Figure 2.5.

Initial state with gluons cannot initiate such a process. Only quark-initiated diagrams occur at leading order. Since the initial quarks undergo only an electroweak interaction, they are lightly deflected from the beam axis. This leads to the characteristic signature of two tagging jets, with a significant seperation in rapidity and high invariant mass. This rapidity separation is depicted graphically in Figure 2.7. The final state includes the decay products of the vector bosons as well as the tagging jets, and it is usually labeled $VVjj$, while also including diagrams with non-resonant bosons.

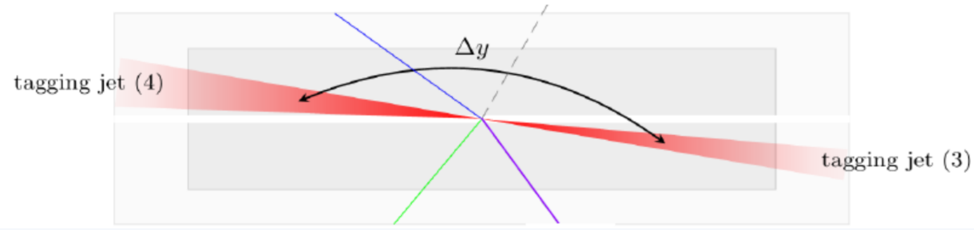

FIGURE 2.7: The rapidity separation of the two tagging jets.

According to Figure 2.6, all couplings are related to the electroweak interaction. The coupling structure for the squared matrix element for these diagrams is given by $|\mathcal{M}^2| \propto \alpha_{EW}^6$ (α_{EW}^5 if a photon exists in the final state, as the photon does not decay) at leading order, where α_{EW} is a generalization of the electromagnetic and weak coupling constants combined, and characterizes the order of a process. The same final state can also be produced with a different coupling structure, $|\mathcal{M}^2| \propto \alpha_{EW}^4\alpha_S^2$, which has larger cross-sections due to the larger value of α_S at typical hard scales. However, since only the $|\mathcal{M}^2| \propto \alpha_{EW}^6$ coupling structure has contributions from vector boson scattering, the definition of the signal process includes this requirement. The signal is the $VVjj$ final state for specific bosons and decay product combination. Diagrams with less than six electroweak interaction vertices are considered as background and vetoed. This signal process is referred to as $VVjj - EW6$. On the other hand, interference contributions of order $\alpha_{EW}^5\alpha_S$ may also be included in the signal process definition. It should be noted that the $VVjj - EW6$ signal definition includes diagrams that do not involve vector boson scattering but have the same coupling structure, as illustrated in Figure 2.8.

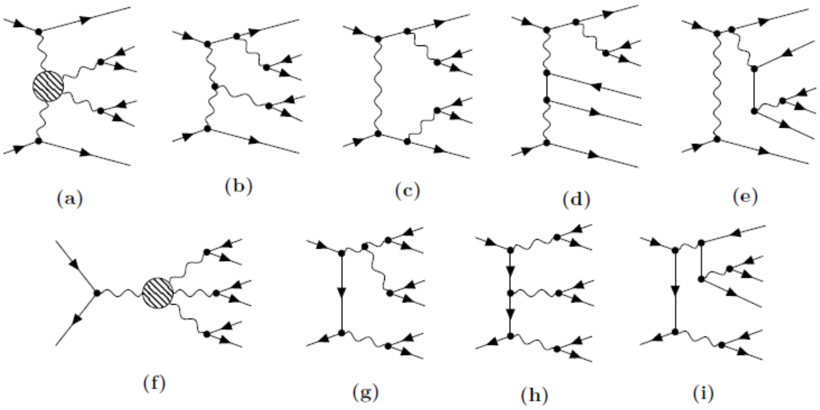

FIGURE 2.8: Feynman diagrams for the $VVjj - EW6$ process at LO. In the place of the dashed circle can be any of the possible boson scattering diagrams shown in Figure 2.5. On the top row, there are diagrams in the t- or u-channel, while on the bottom row, the s-channel diagrams are shown.

The contributions to vector boson scattering can be classified into three categories: t-, u- or s-channels, based on the connection of the initial and final state quark lines. In the s-channel diagrams, the initial quarks are connected by a continuous fermion line, while in the t- or u-channel contributions, each initial quark line is connected to a final state quark.

These different connections have significant impacts on the observed kinematics of jets. In s-channel diagrams, the final state quarks may come from the decay of one of the electroweak gauge boson, resulting in a peak in the invariant mass of the two jets at around $80 - 90\,GeV$ and increased with contributions at lower (off-shell) invariant masses. This is different from the typical high invariant mass behavior observed in vector boson scattering. Some s-channel diagrams have similar couplings to the pure vector boson scattering topology $V\,V \rightarrow V\,V$, which is realized in a $V \rightarrow VVV$ topology as indicated by the blob in Figure 2.8f. In vector boson scattering diagrams, final state fermions other than the tagging jets are usually found in pairs that originate from a common electroweak gauge boson decay. The invariant mass of these pairs can be used as a selection criterion to suppress backgrounds. However, in non-resonant diagrams such as those shown in Figures 2.8d, 2.8e, and 2.8i, at least one fermion pair does not come from a common gauge boson decay.

The VBS signal process is typically defined without considering terms of order $\mathcal{O}(\alpha_{EW}^4 a_S^2)$ which is often referred to as QCD initiated background because of the presence of α_S in comparison to the VBS process that is purely electroweak at LO. The label used for the QCD background is $VVjj - EW4$ and the corresponding feynman diagrams are shown in Figure 2.9.

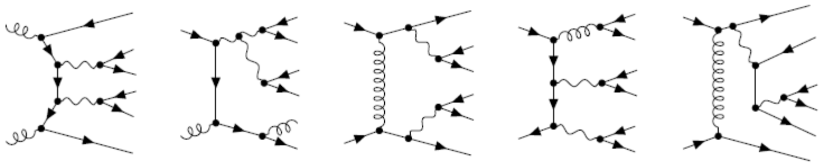

FIGURE 2.9: Feynman diagrams for the $VVjj - EW4$ process at LO.

Experimentally, it is difficult to differentiate between a jet that originates from a hard process, shower or pile up. Therefore, the two jets required in the final state can also be seen as radiative corrections to the diboson production of order $\mathcal{O}(a_{EW}^4)$. To fully define this background, diagrams with fewer jets in the final state should be included. The coupling order in α_{EW} is usually four for this process.

Figure 2.9 shows that the $VVjj - EW4$ process includes gluon-induced diagrams, which are typically PDF-enhanced, meaning that at low parton momenta, the likelihood of finding a gluon is much higher than finding a quark. Since α_S is typically larger than α_{EW} at higher energies, the $VVjj - EW4$ process has larger cross-sections and is less suppressed by couplings.

To suppress contamination from $VVjj - EW4$, it is important to identify kinematic differences between $VVjj - EW6$ and $VVjj - EW4$. The final state jets in $VVjj - EW4$ are always color-connected, making additional QCD radiation more likely. Also, the high invariant mass and significant rapidity separation signature of $VVjj - EW6$ are not expected in $VVjj - EW4$.

Finally, at leading order, the $VVjj$ final state also includes interference effects between $VVjj - EW4$ and $VVjj - EW6$ processes, which have the same initial and final state and can give negative contributions. These interference effects have a coupling order of $\mathcal{O}(\alpha_{EW}^5)$ and are suppressed if one of the processes is suppressed.

2.2.3 Comparison of different final states

There are many boson combinations that can participate to the VBS process, including the $W^\pm W^\pm$, $W^\pm W^\mp$, $W^\pm Z$, ZZ, $Z\gamma$ and $\gamma\gamma$. The scattering of massive gauge bosons is of special theoretical interest because of the couplings to the Higgs boson and the connection to the electroweak symmetry breaking mechanism. However, these channels have additional complexity in experimental observations due to the instability of massive $W^\pm$ and Z bosons. On the other hand, photons from the hard process can be recognized directly or through electrons after conversion.

The decay of gauge bosons into hadronic final states has high branching ratios, but it suffers from additional backgrounds due to the same resulting final state. Additionally, identifying and measuring jets accurately is more difficult than identifying leptons. In comparison, final states with charged leptons are easier to identify and provide cleaner signatures. However, the disadvantage is that they have lower signal cross-sections due to reduced branching ratios. Experimentally, the fully-leptonic one offers the best sensitivity. Table 2.2 shows a summary of available experimental measurements of electroweak gauge boson scattering at 13 TeV in different final state.

The fully leptonic $W^{\pm}W^{\pm}$ channel in the $l^{\pm}l^{\pm}\nu_l\nu_l jj$ final state has significantly less contamination from the $VVjj - EW4$ background process. However, the analysis of this process suffers by two types of experimental backgrounds. One comes from the misidentification of other signals as prompt leptons, and the other comes from the misidentification of the charge of a lepton. Despite these experimental backgrounds, this final state shows the largest expected significances.

The $W^{\pm}W^{\mp}$ channel in the fully leptonic $l^{\pm}l^{\mp}l^{\pm}\nu_l\nu_l jj$ final state is affected by higher background contamination not only from the $VVjj - EW4$ process but also from other processes such as $t\bar{t}$ and $Z + jets$ production.

The ZZ channel in the $l^{\pm}l^{\mp}l^{\pm}l^{\mp}jj$ final state has a very clear signature with minimal background contamination, but the cross-section is reduced due to the lower branching fraction of the leptons.

The $W^{\pm}Z$ channel in the $l^{\pm}l^{\mp}l^{\pm}\nu_l jj$ is a very important channel due to its high cross-section among the other processes. This channel differs from other boson channels in VBS as it include irreducible background from a single t quark produced in association with a Z boson. Figure 2.10 shows the corresponding Feynamn diagram. The final state and coupling structure of this subprocess match those of the $WZjj - EW6$ signal process, and it contributes significantly to the $lll'\nu jj$ final state due to the enhancement of the t resonance. The contributions are separated based on the quark flavors in the hard process. In order to eliminate the tZj contribution, the $WZjj - EW6$ VBS signal process is restricted to events without any b quark in the matrix element of either the initial or final state, while the tZj process always has a b quark in the matrix element of the final and the initial state. This has the advantage of avoiding interference between these two processes. However, the tZj process has still contributions of VBS topologies, where the incoming Z boson is radiated off a b quark.

In this thesis, the $W^{\pm}Z$ channel in the fully leptonic final state is studied in depth.

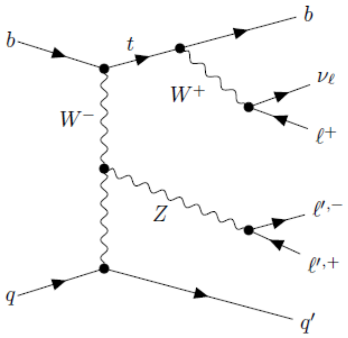

FIGURE 2.10: Example Feynman diagram for the tZj process at LO. The upper quark line contains a top-quark resonance, motivating the definition of these contributions as a background process.

final state	observed $\$sigma(VVjj-EWK)[fb]$	predicted $\sigma(VVjj-EWK)[fb]$	Reference
$l^{\pm}l^{\pm}\nu_l\nu_l jj$			
-ATLAS	$2.89^{+0.59}_{-0.56}$	$3.08^{+0.45}_{-0.46}$	[8]
-CMS	$3.83^{+0.75}_{-0.75}$	$4.25^{+0.27}_{-0.27}$	[9]
$l^{\pm}l^{\mp}l^{\pm}\nu_l\nu_l jj$			
-ATLAS	-	-	-
-CMS	$10.2^{+2.0}_{-2.0}$	$9.1^{+0.6}_{-0.6}$	[10]
$l^{\pm}l^{\mp}l^{\pm}l^{\mp}jj$			
-ATLAS	$0.82^{+0.21}_{-0.21}$	$0.61^{+0.03}_{-0.03}$	[11]
-CMS	$0.33^{+0.15}_{-0.13}$	$0.275^{+0.021}_{-0.021}$	[12]
$l^{\pm}l^{\mp}l^{\pm}\nu_l jj$			
-ATLAS	$0.57^{+0.26}_{-0.14}$	$0.321^{+0.028}_{-0.024}$	[13]
-CMS	$1.81^{+0.41}_{-0.41}$	$4.54^{+0.90}_{-0.90}$	[14]

TABLE 2.2: Summary of available experimental measurements of electroweak gauge boson scattering at 13 TeV in different final states is shown.

2.3 Beyond the Standard Model

2.3.1 Introduction

The Standard Model is widely accepted as a valid theory, but it has some internal issues. One of the most significant issues is the hierarchy problem, which arises because, according to quantum field theory calculations, the Higgs boson mass receives quantum corrections that are sensitive to the energy scale at which new physics beyond the standard model should appear. These corrections tend to push the Higgs boson mass towards the Planck scale. As a consequence, all quarks, charged leptons and W, Z masses are raised as well. It is possible to counteract these corrections by selecting the free parameter of the bare Higgs mass appropriately, but this parameter has to be selected very precisely to match the quantum corrections. This need for finely-tuned parameters is considered a conceptual issue, and it may be resolved by the presence of additional particles that can naturally counteract the quantum corrections. The hierarchy problem is a primary motivation for the development of supersymmetry (SUSY).

In addition to the internal theoretical issues, there are certain phenomena that do not align with SM predictions within uncertainties. Among the most significant discrepancies are the magnetic moment of the muons and issues with flavor physics, such as in the study of β-decays. Additionally, the SM does not account for the masses of neutrinos, despite the observation of neutrino oscillations indicating that at least two neutrinos are massive. Neutrino research is an active field, and ongoing studies aim to answer various open questions, such as the mass hierarchy and whether the neutrino is a Majorana particle. Finally, there are other basic phenomena on cosmic scales that cannot be explained from SM and are addressed in extensions of the SM, such as the matter-antimatter asymmetry and the existence of dark matter.

There are many proposed extensions of the Standard Model to explain different subsets of these issues. Some popular extension are, e.g. supersymmetry, extra dimensions, or string theory. An attractive model-independent approach is an extension of the SM Lagrangian by introducing interactions between existing particles via higher dimensional operators. In this thesis, this approach will be studied in depth.

2.3.2 Effective Field Theory

Therefore, one can search for physics beyond the standard model in two ways. The first one is to search directly for new physics, via the production of new particles predicted by various models or theories (e.g. SUSY) and the second one is is to search for new interactions between the known Standard Model particles [15].

Such an approach has two advantages. Firstly, it enables us to explore new physics without being constrained by a specific extension of the standard model. Secondly, if no new physics is discovered, it allows us to measure the precision with which the possibility of new physics can be excluded.

If a model-independent approach is considered, several favorable requirements should be fullfilled

- Any extension of the standard model should satisfy the S-matrix axioms of unitarity, analyticity, etc.
- The symmetries of the SM, as the Lorentz invariance and $SU(3) \times SU(2)_L \times U(1)_Y$ gauge symmetry, should be respected.
- The SM has to be recovered in an appropriate limit.
- The extended theory should have a broad enough scope to encompass any physics beyond the standard model, while also providing guidance on where the effects of new physics are most likely to be observed.

- Radiative corrections at any order should be able to be calculated in the SM interactions in the extended theory.
- Radiative corrections at any order should be able to be calculated in the new interactions of the extended theory.

An effective quantum field theory is the only approach that can encompass all of these requirements. While the first two features on their own suggest a quantum field theory, the remaining features can only be fully incorporated via an effective quantum field theory [16, 17].

To create an effective quantum field theory of the SM, the first step is to begin with the most general theory of quark and lepton fields along with a single Higgs doublet field, which interact via an $SU(3) \times SU(2)_L \times U(1)_Y$ gauge symmetry, which is essentially the SM. In this model, all operators (i.e. products of fields) in the Lagrangian are restricted to have a mass dimension of four or less. To extend the theory beyond the standard model, higher-dimensional operators are added. These operators have coefficients of inverse powers of mass according to dimensional analysis and are suppressed if the mass is much larger than the experimentally accessible energies. The lowest dimensional operators will be the most dominant extensions to the theory.

The mass scale that describes the higher-dimension operators' coefficients is denoted as Λ. This scale represents the scale of new physics, and the assumption is that it is much larger than the experimentally-accessible energies. An effective quantum field theory is a low-energy approximation to this new physics, where "low" means energies less than Λ. The scale Λ could be anywhere from a few TeV up to the Planck scale, and the new physics could include new particles, extra spacetime dimensions, or even physics not described by ordinary quantum field theory, such as string theory.

The effective quantum field theory lagrangian can be expressed as

$$\mathcal{L} = \mathcal{L}_{\text{SM}} + \mathcal{L}_{\text{EFT}} = \mathcal{L}_{\text{SM}} + \sum_i \frac{c_i}{\Lambda_i^2} O_i^{(6)} + \sum_i \frac{f_i}{\Lambda_i^4} O_i^{(8)} + \ldots \tag{2.40}$$

where the first order corresponds to the SM Lagrangian, the second order to the dimension-6 expansion and the third order to the dimension-8 expansion. The $\mathcal{O}_i^{(6)}$ and $\mathcal{O}_i^{(8)}$ are the gauge and Lorentz invariant dimension-6 and dimension-8 operators respectively and the c_i and f_i are the dimension-6 and dimension-8 coefficients, respectively, called Wilson coefficients. These coefficients are dimensionless and parameterize the strength with which the new physics couples to the SM particles. Only even-dimensional operators conserve both lepton and baryon number, therefore the dimension-5 and dimension-7 operators are excluded from the Lagrangian.

Based on the desirable features of a model-independent approach to nonstandard interactions, the SM can be recovered in the limit $\Lambda \to \infty$. Any new physics will resemble a quantum field theory at lower energies. Therefore, an effective field theory can be used to capture the low-energy effects of any physics beyond the standard model, provided that all possible terms, consistent with the symmetries of the theory, are included. Additionally, the extended theory can be used to calculate both tree-level and loop processes.

To employ the effective field theory approach, it is necessary to specify the fields from which the operators $\mathcal{O}_i^{(6)}$ and $\mathcal{O}_i^{(8)}$ are derived. These fields must be present at low energies, that is, energies below Λ. It can be assumed that the fields are the same as those in the standard model, including the Higgs doublet field. The Higgs doublet field is included due to the accurate electroweak data, supporting the existence of a Higgs boson at low energy. If future experiments uncover new particles at low energies, the effective field theory must be revised to incorporate the associated fields, including an extended Higgs sector.

Finally, the effective quantum field theory approach is limited to energies up to a certain scale denoted by Λ. Beyond this energy scale, operators of dimension greater than eight cannot be neglected anymore because they are not suppressed. At very high energies, operators of arbitrarily high dimension become significant and the approach becomes less useful because there are an infinite number of them.

2.3.2.1 Dimension-6 operators

The EFT Lagrangian truncated at the dimension-6 level [18], which is used to explore the existence of anomalous Triple Gauge Couplings ($aTGCs$), is given by:

$$\mathcal{L}_{\mathcal{EFT}} = \mathcal{L}_{\text{SM}} + \mathcal{L}_6 \tag{2.41}$$

where $\mathcal{L}_{\text{SM}}$ is shown in Equation 2.39. All lepton- and baryon-number violating terms, which includes the dimension-5 Weinberg operator that generates a Majorana mass term for neutrinos, are neglected.

The Lagrangian $\mathcal{L}_6$ contains a complete and non-redundant basis of dimension-6 operators Q_α constructed with the SM fields and they are invariant under the $SU(3)_C \times U(2)_L \times U(1)_Y$ gauge symmetry. The study of the dimension-6 operators can be highly difficult due to a large number of parameters in the Effective Field Theory (EFT). For instance, when considering one fermion generation ($n_f = 1$), there are 76 parameters, and when $n_f = 3$, there are 2499 parameters. To tackle this challenge, symmetry assumptions based on flavor, which are supported by experimental constraints at low scales, are employed to reduce the number of operators.

Additionally, a way to reduce the number of operators is to focus on processes that involve nearly on-shell intermediate narrow states of the Standard Model (SM). For these reasons, the Warsaw basis [19], whose operators are grouped into 8 categories, is used. Class 8 is divided into a further 4 groups:

$$\begin{aligned} \mathcal{L}_6 &= \mathcal{L}_6^{(1)} + \mathcal{L}_6^{(2)} + \mathcal{L}_6^{(3)} + \mathcal{L}_6^{(4)} + \mathcal{L}_6^{(7)} + \mathcal{L}_6^{(8)} + \left[\mathcal{L}_6^{(5)} + \mathcal{L}_6^{(6)} + \text{ h.c.}\right] \\ \mathcal{L}_6^{(8)} &= \mathcal{L}_6^{(8a)} + \mathcal{L}_6^{(8b)} + \mathcal{L}_6^{(8c)} + \left[\mathcal{L}_6^{(8d)} + \text{ h.c.}\right] \end{aligned} \tag{2.42}$$

Each of these Lagrangians has the form

$$\mathcal{L}_6^{(n)} = \frac{1}{\Lambda^2}\sum_\alpha C_\alpha Q_\alpha \tag{2.43}$$

with the sum running over the class-n operators Q_α shown in Table 2.3 and C_α referred to the associated Wilson coefficients. In general, both Q_α and C_α have flavor indices, that are implicitly contracted in Equation 2.43. In this basis, explicit CP violation is carried by the real coefficients $C_{\widetilde{G}}, C_{\widetilde{W}}, C_{H\widetilde{G}}, C_{H\widetilde{W}}, C_{H\widetilde{B}}, C_{H\widetilde{W}B}$ and by the imaginary parts of the Wilson coefficients related to non-Hermitian fermionic operators, particularly those in $\mathcal{L}_6^{(5),(6),(8d)}$ and the O_{Hud}. Operators that violate baryon numbers are not included.

The operators definitions use the following notation

$$\begin{aligned} \widetilde{X}^{\mu\nu} &= \frac{1}{2}\varepsilon^{\mu\nu\rho\sigma}X_{\rho\sigma}, & H^\dagger i\overleftrightarrow{D}_\mu H &= H^\dagger\left(iD_\mu H\right) - \left(iD_\mu H^\dagger\right)H \\ \sigma^{\mu\nu} &= \frac{i}{2}\left[\gamma^\mu, \gamma^\nu\right], & H^\dagger i\overleftrightarrow{D}^i_\mu H &= H^\dagger\sigma^i\left(iD_\mu H\right) - \left(iD_\mu H^\dagger\right)\sigma^i H \end{aligned} \tag{2.44}$$

and they are splitted into three categories according to the interacting fields: the bosonic operators, the boson to fermion operators and the four-fermion operators.

2.3.2.2 Dimension-8 operators

The EFT Lagrangian part for the dimension-8 operators [20], which is used to explore the existence of the anomalous Quartic Gauge Couplings ($aQGCs$), is given by:

$$\mathcal{L}_{\mathcal{EFT}} = \mathcal{L}_{\text{SM}} + \mathcal{L}_8. \tag{2.45}$$

In this case, the Lagrangian for the four gauge boson vertices takes the form

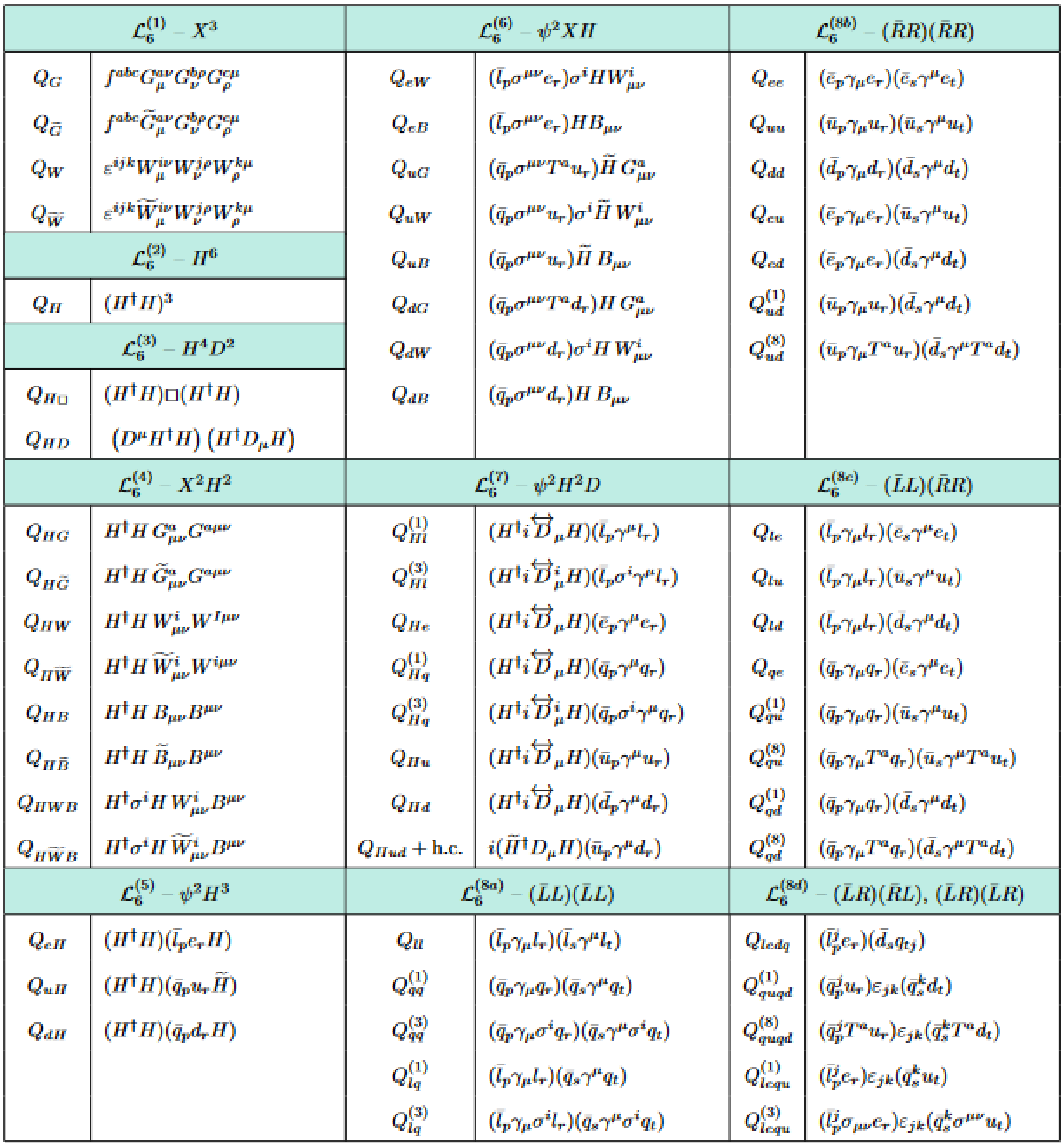

$\mathcal{L}_6^{(1)}$ – X^3		$\mathcal{L}_6^{(6)}$ – $\psi^2 XH$		$\mathcal{L}_6^{(8b)}$ – $(\bar{R}R)(\bar{R}R)$	
Q_G	$f^{abc}G_\mu^{a\nu}G_\nu^{b\rho}G_\rho^{c\mu}$	Q_{eW}	$(\bar{l}_p\sigma^{\mu\nu}e_r)\sigma^i H W_{\mu\nu}^i$	Q_{ee}	$(\bar{e}_p\gamma_\mu e_r)(\bar{e}_s\gamma^\mu e_t)$
$Q_{\widetilde{G}}$	$f^{abc}\widetilde{G}_\mu^{a\nu}G_\nu^{b\rho}G_\rho^{c\mu}$	Q_{eB}	$(\bar{l}_p\sigma^{\mu\nu}e_r)H B_{\mu\nu}$	Q_{uu}	$(\bar{u}_p\gamma_\mu u_r)(\bar{u}_s\gamma^\mu u_t)$
Q_W	$\varepsilon^{ijk}W_\mu^{i\nu}W_\nu^{j\rho}W_\rho^{k\mu}$	Q_{uG}	$(\bar{q}_p\sigma^{\mu\nu}T^a u_r)\widetilde{H}\, G_{\mu\nu}^a$	Q_{dd}	$(\bar{d}_p\gamma_\mu d_r)(\bar{d}_s\gamma^\mu d_t)$
$Q_{\widetilde{W}}$	$\varepsilon^{ijk}\widetilde{W}_\mu^{i\nu}W_\nu^{j\rho}W_\rho^{k\mu}$	Q_{uW}	$(\bar{q}_p\sigma^{\mu\nu}u_r)\sigma^i\widetilde{H}\, W_{\mu\nu}^i$	Q_{eu}	$(\bar{e}_p\gamma_\mu e_r)(\bar{u}_s\gamma^\mu u_t)$
$\mathcal{L}_6^{(2)}$ – H^6		Q_{uB}	$(\bar{q}_p\sigma^{\mu\nu}u_r)\widetilde{H}\, B_{\mu\nu}$	Q_{ed}	$(\bar{e}_p\gamma_\mu e_r)(\bar{d}_s\gamma^\mu d_t)$
Q_H	$(H^\dagger H)^3$	Q_{dG}	$(\bar{q}_p\sigma^{\mu\nu}T^a d_r)H\, G_{\mu\nu}^a$	$Q_{ud}^{(1)}$	$(\bar{u}_p\gamma_\mu u_r)(\bar{d}_s\gamma^\mu d_t)$
$\mathcal{L}_6^{(3)}$ – H^4D^2		Q_{dW}	$(\bar{q}_p\sigma^{\mu\nu}d_r)\sigma^i H\, W_{\mu\nu}^i$	$Q_{ud}^{(8)}$	$(\bar{u}_p\gamma_\mu T^a u_r)(\bar{d}_s\gamma^\mu T^a d_t)$
$Q_{H\Box}$	$(H^\dagger H)\Box(H^\dagger H)$	Q_{dB}	$(\bar{q}_p\sigma^{\mu\nu}d_r)H\, B_{\mu\nu}$		
Q_{HD}	$(D^\mu H^\dagger H)\,(H^\dagger D_\mu H)$				
$\mathcal{L}_6^{(4)}$ – X^2H^2		$\mathcal{L}_6^{(7)}$ – ψ^2H^2D		$\mathcal{L}_6^{(8c)}$ – $(\bar{L}L)(\bar{R}R)$	
Q_{HG}	$H^\dagger H\, G_{\mu\nu}^a G^{a\mu\nu}$	$Q_{Hl}^{(1)}$	$(H^\dagger i\overleftrightarrow{D}_\mu H)(\bar{l}_p\gamma^\mu l_r)$	Q_{le}	$(\bar{l}_p\gamma_\mu l_r)(\bar{e}_s\gamma^\mu e_t)$
$Q_{H\widetilde{G}}$	$H^\dagger H\,\widetilde{G}_{\mu\nu}^a G^{a\mu\nu}$	$Q_{Hl}^{(3)}$	$(H^\dagger i\overleftrightarrow{D}^i_\mu H)(\bar{l}_p\sigma^i\gamma^\mu l_r)$	Q_{lu}	$(\bar{l}_p\gamma_\mu l_r)(\bar{u}_s\gamma^\mu u_t)$
Q_{HW}	$H^\dagger H\, W_{\mu\nu}^i W^{I\mu\nu}$	Q_{He}	$(H^\dagger i\overleftrightarrow{D}_\mu H)(\bar{e}_p\gamma^\mu e_r)$	Q_{ld}	$(\bar{l}_p\gamma_\mu l_r)(\bar{d}_s\gamma^\mu d_t)$
$Q_{H\widetilde{W}}$	$H^\dagger H\,\widetilde{W}_{\mu\nu}^i W^{i\mu\nu}$	$Q_{Hq}^{(1)}$	$(H^\dagger i\overleftrightarrow{D}_\mu H)(\bar{q}_p\gamma^\mu q_r)$	Q_{qe}	$(\bar{q}_p\gamma_\mu q_r)(\bar{e}_s\gamma^\mu e_t)$
Q_{HB}	$H^\dagger H\, B_{\mu\nu}B^{\mu\nu}$	$Q_{Hq}^{(3)}$	$(H^\dagger i\overleftrightarrow{D}^i_\mu H)(\bar{q}_p\sigma^i\gamma^\mu q_r)$	$Q_{qu}^{(1)}$	$(\bar{q}_p\gamma_\mu q_r)(\bar{u}_s\gamma^\mu u_t)$
$Q_{H\widetilde{B}}$	$H^\dagger H\,\widetilde{B}_{\mu\nu}B^{\mu\nu}$	Q_{Hu}	$(H^\dagger i\overleftrightarrow{D}_\mu H)(\bar{u}_p\gamma^\mu u_r)$	$Q_{qu}^{(8)}$	$(\bar{q}_p\gamma_\mu T^a q_r)(\bar{u}_s\gamma^\mu T^a u_t)$
Q_{HWB}	$H^\dagger\sigma^i H\, W_{\mu\nu}^i B^{\mu\nu}$	Q_{Hd}	$(H^\dagger i\overleftrightarrow{D}_\mu H)(\bar{d}_p\gamma^\mu d_r)$	$Q_{qd}^{(1)}$	$(\bar{q}_p\gamma_\mu q_r)(\bar{d}_s\gamma^\mu d_t)$
$Q_{H\widetilde{W}B}$	$H^\dagger\sigma^i H\,\widetilde{W}_{\mu\nu}^i B^{\mu\nu}$	Q_{Hud} + h.c.	$i(\widetilde{H}^\dagger D_\mu H)(\bar{u}_p\gamma^\mu d_r)$	$Q_{qd}^{(8)}$	$(\bar{q}_p\gamma_\mu T^a q_r)(\bar{d}_s\gamma^\mu T^a d_t)$
$\mathcal{L}_6^{(5)}$ – ψ^2H^3		$\mathcal{L}_6^{(8a)}$ – $(\bar{L}L)(\bar{L}L)$		$\mathcal{L}_6^{(8d)}$ – $(\bar{L}R)(\bar{R}L)$, $(\bar{L}R)(\bar{L}R)$	
Q_{eH}	$(H^\dagger H)(\bar{l}_p e_r H)$	Q_{ll}	$(\bar{l}_p\gamma_\mu l_r)(\bar{l}_s\gamma^\mu l_t)$	Q_{ledq}	$(\bar{l}_p^j e_r)(\bar{d}_s q_{tj})$
Q_{uH}	$(H^\dagger H)(\bar{q}_p u_r\widetilde{H})$	$Q_{qq}^{(1)}$	$(\bar{q}_p\gamma_\mu q_r)(\bar{q}_s\gamma^\mu q_t)$	$Q_{quqd}^{(1)}$	$(\bar{q}_p^j u_r)\varepsilon_{jk}(\bar{q}_s^k d_t)$
Q_{dH}	$(H^\dagger H)(\bar{q}_p d_r H)$	$Q_{qq}^{(3)}$	$(\bar{q}_p\gamma_\mu\sigma^i q_r)(\bar{q}_s\gamma^\mu\sigma^i q_t)$	$Q_{quqd}^{(8)}$	$(\bar{q}_p^j T^a u_r)\varepsilon_{jk}(\bar{q}_s^k T^a d_t)$
		$Q_{lq}^{(1)}$	$(\bar{l}_p\gamma_\mu l_r)(\bar{q}_s\gamma^\mu q_t)$	$Q_{lequ}^{(1)}$	$(\bar{l}_p^j e_r)\varepsilon_{jk}(\bar{q}_s^k u_t)$
		$Q_{lq}^{(3)}$	$(\bar{l}_p\gamma_\mu\sigma^i l_r)(\bar{q}_s\gamma^\mu\sigma^i q_t)$	$Q_{lequ}^{(3)}$	$(\bar{l}_p^j\sigma_{\mu\nu}e_r)\varepsilon_{jk}(\bar{q}_s^k\sigma^{\mu\nu}u_t)$

TABLE 2.3: $\mathcal{L}_6$ operators in the Warsaw basis, categorized into eight classes$\mathcal{L}_6^{(n)}$.

$$\mathcal{L}^{VVV'V'} = c_0^{VV'}O_0^{VV'} + c_1^{VV'}O_1^{VV'} \tag{2.46}$$

where the Lorentz invariant structures that are possible, if considering effective interactions that do not contain derivatives of the gauge fields, are

$$\begin{aligned}
O_0^{WW} &= g^{\alpha\beta} g^{\gamma\delta} \left[W_\alpha^+ W_\beta^- W_\gamma^+ W_\delta^-\right] \\
O_1^{WW} &= g^{\alpha\beta} g^{\gamma\delta} \left[W_\alpha^+ W_\beta^+ W_\gamma^- W_\delta^-\right] \\
O_0^{WZ} &= g^{\alpha\beta} g^{\gamma\delta} \left[W_\alpha^+ Z_\beta W_\gamma^- Z_\delta\right] \\
O_1^{WZ} &= g^{\alpha\beta} g^{\gamma\delta} \left[W_\alpha^+ W_\beta^- Z_\gamma Z_\delta\right] \\
O_0^{ZZ} = O_1^{ZZ} &= g^{\alpha\beta} g^{\gamma\delta} \left[Z_\alpha Z_\beta Z_\gamma Z_\delta\right].
\end{aligned} \tag{2.47}$$

Additionally, in the SM, $SU(2)_L$ gauge invariance and renormalizability imply that

$$c_{0,\mathrm{SM}}^{WW} = -c_{1,\mathrm{SM}}^{WW} = \frac{2}{c_W^2} c_{0,\mathrm{SM}}^{WZ} = -\frac{2}{c_W^2} c_{1,\mathrm{SM}}^{WZ} = g^2 \quad c_{\mathrm{SM}}^{ZZ} = 0 \tag{2.48}$$

where c_W is the cosine of the weak mixing angle and g is the $SU(2)_L$ coupling constant.

On the other hand, if the SM is considered to be only valid as an effective theory applicable up to a certain energy scale Λ, one can expect to see deviations from the equation Equation 2.48 even if one still keeps the gauge symmetry group, fermionic spectrum, and the pattern of spontaneous symmetry breaking (EWSB) as valid components to describe physical phenomena at energies $E << \Lambda$. In such a scenario, the Lagrangian for the four gauge boson interactions may still be written as Equation 2.47, but the coefficients c_0 and c_1 will now generally be independent and they can be written as

$$c_i^{VV'} = c_{i,\mathrm{SM}}^{VV'} + g^2 \Delta c_i^{VV'} \tag{2.49}$$

The deviations Δc_i will be generated by higher dimension operators parameterizing the low energy effect of the new physics. The order on the expansion at which these deviations are expected to appear depends on whether the low energy spectrum contains the SM Higgs boson responsible of EWSB or, on the contrary, EWSB is due to a heavy (or not fundamental) Higgs boson (if ever discovered).

The classification of potential dimension-8 operators depends on whether they come from the vector boson field strength terms or the covariant derivative acting on the Higgs field:

$$\begin{aligned}
D_\mu \Phi &= \left(\partial_{\mu|} + i\frac{g'}{2} B_\mu + igW_\mu^i \frac{\tau^i}{2}\right) \Phi \\
\hat{W}_{\mu\nu} &= ig\frac{\tau^i}{2} \left(\partial_\mu W_v^i - \partial_\nu W_\mu^i - g\epsilon_{ijk} W_\mu^j W_v^k\right) \\
\hat{B}_{\mu\nu} &= \frac{i}{2} g' \left(\partial_\mu B_v - \partial_\nu B_\mu\right)
\end{aligned} \tag{2.50}$$

The terms in the first case refer to the gauge bosons' longitudinal modes (originating from the Higgs vacuum expectation value in unitary gauge), while those in the second case refer to the transverse degrees of freedom of the boson fields. Finally, there are also mixed terms that can respect the symmetry. As a result, there are three categories of interaction terms: the longitudinal, the transverse, and the mixed interaction terms.

There are three dimension-8 operators without derivatives of the gauge fields i.e. the longitudinal operators:

$$\begin{aligned}
\mathcal{L}_{S,0} &= \frac{c_{S,0}}{\Lambda^4}\left[\left(D_\mu\Phi\right)^\dagger\left(D_v\Phi\right)\right]\times\left[\left(D^\mu\Phi\right)^\dagger\left(D^v\Phi\right)\right]\\
\mathcal{L}_{S,1} &= \frac{c_{S,1}}{\Lambda^4}\left[\left(D_\mu\Phi\right)^\dagger\left(D^\mu\Phi\right)\right]\times\left[\left(D_v\Phi\right)^\dagger\left(D^v\Phi\right)\right]\\
\mathcal{L}_{S,2} &= \frac{c_{S,2}}{\Lambda^4}\left[\left(D_\mu\Phi\right)^\dagger\left(D_v\Phi\right)\right]\times\left[\left(D^v\Phi\right)^\dagger\left(D^\mu\Phi\right)\right]
\end{aligned}\tag{2.51}$$

The $\mathcal{L}_{S,0}$ and $\mathcal{L}_{S,2}$ operators are not independent and they will be taken into account as one operator, called $\mathcal{L}_{S,02}$

The transverse operators, containing just the field strength tensor, are

$$\begin{aligned}
\mathcal{L}_{T,0} &= \mathrm{Tr}\left[\hat{W}_{\mu\nu}\hat{W}^{\mu\nu}\right]\times\mathrm{Tr}\left[\hat{W}_{\alpha\beta}\hat{W}^{\alpha\beta}\right]\\
\mathcal{L}_{T,1} &= \mathrm{Tr}\left[\hat{W}_{\alpha\nu}\hat{W}^{\mu\beta}\right]\times\mathrm{Tr}\left[\hat{W}_{\mu\beta}\hat{W}^{\alpha\nu}\right]\\
\mathcal{L}_{T,2} &= \mathrm{Tr}\left[\hat{W}_{\alpha\mu}\hat{W}^{\mu\beta}\right]\times\mathrm{Tr}\left[\hat{W}_{\beta\nu}\hat{W}^{\nu\alpha}\right]\\
\mathcal{L}_{T,5} &= \mathrm{Tr}\left[\hat{W}_{\mu\nu}\hat{W}^{\mu\nu}\right]\times B_{\alpha\beta}B^{\alpha\beta}\\
\mathcal{L}_{T,6} &= \mathrm{Tr}\left[\hat{W}_{\alpha\nu}\hat{W}^{\mu\beta}\right]\times B_{\mu\beta}B^{\alpha\nu}\\
\mathcal{L}_{T,7} &= \mathrm{Tr}\left[\hat{W}_{\alpha\mu}\hat{W}^{\mu\beta}\right]\times B_{\beta\nu}B^{\nu\alpha}\\
\mathcal{L}_{T,8} &= B_{\mu\nu}B^{\mu\nu}B_{\alpha\beta}B^{\alpha\beta}\\
\mathcal{L}_{T,9} &= B_{\alpha\mu}B^{\mu\beta}B_{\beta\nu}B^{\nu\alpha}
\end{aligned}\tag{2.52}$$

Finally, the mixed operators are

$$
\begin{aligned}
\mathcal{L}_{M,0} &= \mathrm{Tr}\left[\hat{W}_{\mu\nu}\hat{W}^{\mu\nu}\right] \times \left[(D_\beta\Phi)^\dagger D^\beta\Phi\right] \\
\mathcal{L}_{M,1} &= \mathrm{Tr}\left[\hat{W}_{\mu\nu}\hat{W}^{\nu\beta}\right] \times \left[(D_\beta\Phi)^\dagger D^\mu\Phi\right] \\
\mathcal{L}_{M,2} &= \left[B_{\mu\nu}B^{\mu\nu}\right] \times \left[(D_\beta\Phi)^\dagger D^\beta\Phi\right] \\
\mathcal{L}_{M,3} &= \left[B_{\mu\nu}B^{\nu\beta}\right] \times \left[(D_\beta\Phi)^\dagger D^\mu\Phi\right] \\
\mathcal{L}_{M,4} &= \left[(D_\mu\Phi)^\dagger \hat{W}_{\beta\nu}D^\mu\Phi\right] \times B^{\beta\nu} \\
\mathcal{L}_{M,5} &= \left[(D_\mu\Phi)^\dagger \hat{W}_{\beta\nu}D^\nu\Phi\right] \times B^{\beta\mu} \\
\mathcal{L}_{M,6} &= \left[(D_\mu\Phi)^\dagger \hat{W}_{\beta\nu}\hat{W}^{\beta\nu}D^\mu\Phi\right] \\
\mathcal{L}_{M,7} &= \left[(D_\mu\Phi)^\dagger \hat{W}_{\beta\nu}\hat{W}^{\beta\mu}D^\nu\Phi\right]
\end{aligned}
\tag{2.53}
$$

2.3.2.3 Unitarity bounds

The introduction of aQGC parameters, which modify the quartic gauge boson coupling, disturbs the precise cancellation between different contributions to the scattering amplitude of longitudinally polarised, massive electroweak gauge bosons. As a consequence, the cross section for the scattering of massive electroweak gauge bosons is rising with increasing centre-of-mass energy $\sqrt{s}$. So, one issue that is very important to be examined is what the range of validity can be of a specific EFT model [21]. There is no exact answer to this question unless one starts with a certain theory and derives the EFT Lagrangian 2.40 by decoupling the additional degrees of freedom. However, in order to maintain theoretical consistency, the partial wave amplitudes must satisfy the perturbative unitarity criterion in addition to the obvious restriction that the EFT technique can only be valid for the energy scale $E < \Lambda$ (unfortunately with unknown value of Λ). The condition $E^2 < \Lambda \leq s^U$, where $s^U \equiv s^U(f_i)$ is the perturbative partial wave unitarity bound as a function of the selected operators and the values of the coefficients f_i's, corresponds to the perturbative unitarity criterion. The upper bound on the validity of the EFT based ”model” is therefore given by the value of $\Lambda^2_{max} = s^U$. Since the magnitude of the expected (or observed) experimental effects also depends on the same f_i, one has a frame for a consistent use of the EFT “model” to describe the data. An important consideration for a BSM discovery in the EFT framework is how to use the ”model” correctly. It makes no physical sense to extend the EFT ”model” beyond its range of applicability, set by the condition $E < \Lambda$.

Tables 2.4, 2.5 and 2.6 show the unitarity bounds [22] in the multidimensional parameter space of the Wilson coefficients of the relevant dimension-8 operators in a linear realization of the electroweak symmetry. This study has been done by taking into account just one non-vanishing aQCG Wilson coefficient at a time. In more realistic scenarios where more than one aQGC operator contributes, the partial-wave analyses do not lead to the strongest unitarity bounds for all Wilson-coefficient combinations.

Wilson coefficient	Bound
$\|\frac{f_{S0}}{\Lambda^4}\|$	$32\pi s^{-2}$
$\|\frac{f_{S1}}{\Lambda^4}\|$	$\frac{96}{7}\pi s^{-2}$
$\|\frac{f_{S2}}{\Lambda^4}\|$	$\frac{96}{5}\pi s^{-2}$

Table 2.4: Unitarity constraints on the Wilson coefficients of the $\mathcal{L}_{S,i}$ operators when just one coefficient is nonvanishing.

Wilson coefficient	Bound
$\|\frac{f_{M0}}{\Lambda^4}\|$	$\frac{32}{\sqrt{6}}\pi s^{-2}$
$\|\frac{f_{M1}}{\Lambda^4}\|$	$\frac{128}{\sqrt{6}}\pi s^{-2}$
$\|\frac{f_{M2}}{\Lambda^4}\|$	$\frac{16}{\sqrt{2}}\pi s^{-2}$
$\|\frac{f_{M3}}{\Lambda^4}\|$	$\frac{64}{\sqrt{2}}\pi s^{-2}$
$\|\frac{f_{M4}}{\Lambda^4}\|$	$32\pi s^{-2}$
$\|\frac{f_{M5}}{\Lambda^4}\|$	$64\pi s^{-2}$
$\|\frac{f_{M7}}{\Lambda^4}\|$	$\frac{256}{\sqrt{6}}\pi s^{-2}$

Table 2.5: Unitarity constraints on the Wilson coefficients of the $\mathcal{L}_{M,i}$ operators when just one coefficient is nonvanishing.

Wilson coefficient	Bound
$\|\frac{f_{T0}}{\Lambda^4}\|$	$\frac{12}{5}\pi s^{-2}$
$\|\frac{f_{T1}}{\Lambda^4}\|$	$\frac{24}{5}\pi s^{-2}$
$\|\frac{f_{T2}}{\Lambda^4}\|$	$\frac{96}{13}\pi s^{-2}$
$\|\frac{f_{T5}}{\Lambda^4}\|$	$\frac{8}{\sqrt{3}}\pi s^{-2}$
$\|\frac{f_{T6}}{\Lambda^4}\|$	$\frac{48}{7}\pi s^{-2}$
$\|\frac{f_{T7}}{\Lambda^4}\|$	$\frac{32}{\sqrt{3}}\pi s^{-2}$
$\|\frac{f_{T8}}{\Lambda^4}\|$	$\frac{3}{2}\pi s^{-2}$
$\|\frac{f_{T9}}{\Lambda^4}\|$	$\frac{24}{7}\pi s^{-2}$

Table 2.6: Unitarity constraints on the Wilson coefficients of the $\mathcal{L}_{T,i}$ operators when just one coefficient is nonvanishing.

In the WZ VBS case, the EFT ”model” can be maximally valid up to certain invariant mass $M = \sqrt{s}$ of the WZ system

$$M_{WZ} < \Lambda \leq M^{U}_{WZ}(f_i)$$

where $M^{U}_{WZ}(f_i)$ is fixed by the partial wave perturbative unitarity constraint, $(M^{U}_{WZ}(f_i))^2 = s^{U}(f_i)$.

2.3.2.4 The decomposition procedure

The amplitude of a process described with an EFT Lagrangian can be written as

$$|A_{SM} + \sum_i c_i A_i| \tag{2.54}$$

given that in the EFT approach, the higher than dimension-4 operators are added as extra terms in an expansion around the Standard Model Lagrangian. The A_{SM} is the SM amplitude while the A_i are amplitudes containing the individual higher dimension operators.

The total squared amplitude is then given by

$$|A_{SM} + \sum_i c_i A_i|^2 = |A_{SM}|^2 + \sum_i c_i 2Re(A_{SM} A_i) + \sum_i {c_i}^2 |A_i|^2 + \sum_{ij, i \neq j} c_i c_j 2Re(A_i A_j) \tag{2.55}$$

where $\sum_i c_i 2Re(A_{SM} A_i)$ are the amplitudes of the interference between the SM and the EFT operators, named interference terms, $\sum_i {c_i}^2 |A_i|^2$ are the pure EFT operator contributions, which are called quadratic terms and $\sum_{ij,i \neq j} c_i c_j 2Re(A_i A_j)$ are the amplitudes of the interference between two EFT operators, which are called cross term.

This procedure is called the decomposition method. The outcome is a polynomial in the EFT Wilson coefficients c_i. The decomposition method provides the ability to avoid generating events with different values of the Wilson coefficients for the tested operators, but rather use simple scaling based on the above formula to provide the expected contribution and various values of the Wilson coefficients.

Chapter 3

The Large Hadron Collider and the ATLAS detector

The Large Hadron Collider (LHC) is a circular hadron accelerator. The ATLAS experiment is one of the two multi-purpose experiments installed at the LHC with a wide range of research areas in High-Energy physics. In this chapter the accelerator complex of CERN as well as the main aspects of the ATLAS detector are presented.

3.1 The Large Hadron Collider

The Large Hadron Collider (LHC) is the largest particle accelerator and collider in the world. It was built from 1998 to 2009 by the European Organisation for Nuclear Research ($CERN$). It has a circumference of $26.7\ km$, housed in the tunnel original built for the Large Electron-Positron Collider (LEP). The tunnel lies underground at an average depth of 100 m and crosses the French-Swiss border. The LHC is designed to reach a center of mass energy of $14\,TeV$ ($\sqrt{s} = 14\,TeV$) by accelerating counter-circulating proton beams or Pb ions beams. Although, during the first data-taking period (Run 1 $2009 - 2013$) the provided center-of-mass energy was limited to $8\ TeV$. At the second data-taking period (Run 2 $2015 - 2018$) the center-of-mass energy was pushed to $13\ TeV$. In the ongoing third data-taking period (Run 3), the the center-of-mass energy is $13.6\,TeV$.

The proton beams collide at four intersection points located at fixed areas around the ring, where the related experiments are built. The four main experiments are:

ATLAS ($A\ Toroidal\ LHC\ ApparatuS$) **[23]** the largest, general-purpose particle detector at the LHC, designed to observe phenomena that involve highly massive particles and to search for evidence of theories of particle physics beyond the Standard Model.

CMS $(Compact\ Muon\ Solenoid)$ **[24]** general-purpose particle detector with the same purpose as ATLAS.

Alice $(A\ Large\ Ion\ Collider\ Experiment)$ **[25]** a detector designed to study the properties of quark-gluon plasma in heavy ion collisions

LHC-b $(Large\ Hadron\ Collider\ beauty)$ **[26]** a detector specialized in b-physics in order to measure the parameters of CP-violation in the interactions of b-hadrons

3.1.1 The LHC acceleration complex

Before entering in the LHC, protons have to pass a succession of linear and circular accelerators in order to reach the desirable energy. The LHC acceleration complex is shown in Figure 3.1.

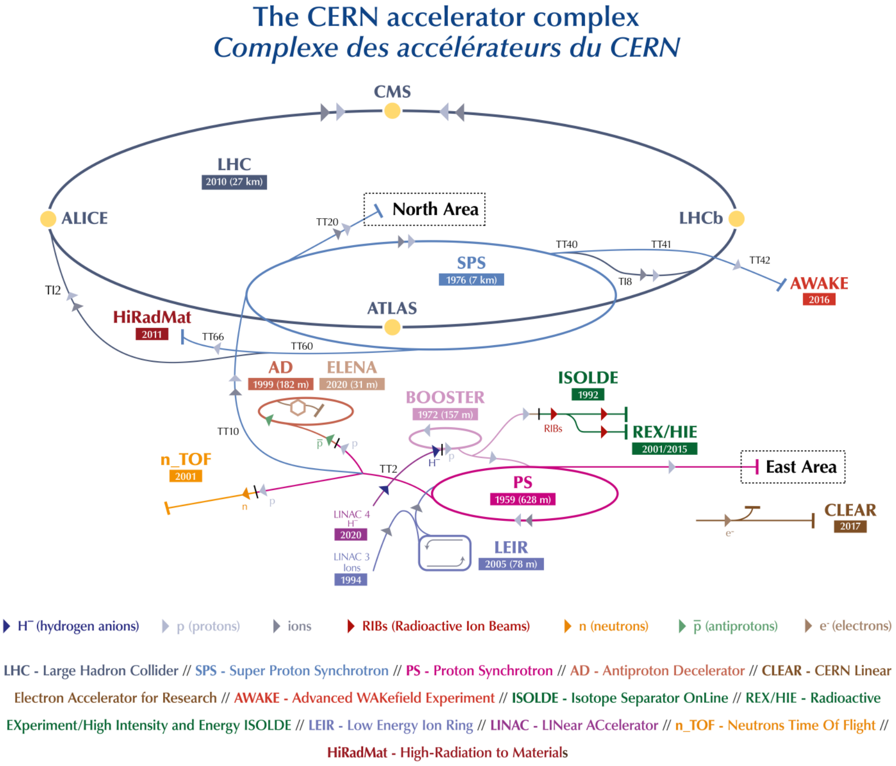

FIGURE 3.1: The LHC accelerator complex.

The first accelerator is the Linear accelerator 4 $(Linac4)$ and it is the source of the proton beams. The negative hydrogen ions H^-, which are consisted of a hydrogen atom with an additional electron, are accelerated to 160 MeV and they are prepared to enter the Proton Synchrotron Booster (PSB). During the injection from Linac4 to PSB, the electrons are separated from the ions, leaving only protons. The protons are accelerated to 2 GeV in order to be injected to the Proton Synchrotron (PS), which pushes the beam up to 26 GeV. After that, the beam is entered to the Super Proton Synchrotron (SPS), where it is accelerated up to 450 GeV. The last step is the LHC, where the proton are split into two beam pipes, where the beam in the one pipe circulates clockwise and the beam in the other pipe circulates anticlockwise. It needs 4 minutes and 20 seconds to fill each LHC ring and 20 minutes for the protons to reach their maximum energy of 6.5 TeV. This energy is reached thanks to radio-frequency cavities, placed along the beam path. At this point, the center-of-mass energy is $\sqrt{s} = 13TeV$ and the protons move at about 99% of the speed of light. At every fill, 2.808 proton bunches with 10^{11} protons in each bunch are injected into the LHC. The interactions between the two beams are happened every 25 ns. The bunch collision rate is 40 MHz.

Thanks to superconducting dipole magnets,which produce a $8T$ magnetic field, the beams keep their circular path. Additionally, some quadrapole magnets keep the beam focused, when stronger quadrapole magnets, located close to interaction points, are used to maximize the chances of interaction where the two beams cross. Finally, magnets of higher multipole orders are used to correct smaller imperfections in the field geometry. The LHC is the largest cryogenic facility in the world at liquid helium temperature, as the superfluid helium-4 is used to keep the magnets at their operating temperatures of 1.9 K.

Protons are not the only particles accelerated in the LHC. Lead ions for the LHC start from a source of vaporised lead and enter Linear accelerator 3 ($Linac3$) before being collected and accelerated in the Low Energy Ion Ring ($LEIR$). Then, they follow the same route to maximum energy as the protons.

3.1.2 Luminosity

One of the most important quantities of the LHC is the instantaneous luminosity $\mathcal{L}$. $\mathcal{L}$ is associated to the proton-proton interaction rate R, with $R = \frac{dN_{pp\to X}}{dt}$, and the cross -section of a proton-proton inelastic interaction by

$$R = \mathcal{L} \times \sigma_{pp\to X} \tag{3.1}$$

$\mathcal{L}$ can be expressed as:

$$\mathcal{L} = \frac{N_b^2 n_b f_{rev} \gamma_r}{4\pi\epsilon_n\beta^*} F \tag{3.2}$$

where the N_b is referred to the number of protons per bunch, when the n_b represents the number of bunches per beam. f_{rev} is the revolution frequency of the LHC, of about 11 kHz, γ_r is the relativistic gamma factor, ϵ_n is the normalized transverse beam emmitance related to the beam size, β^* is the beta function at the collision point related to the beam focusing and F

is a correction factor, referred as the geometric luminosity reduction factor, to account for the non-zero crossing angle of the beams at the interaction point.

Integrating the instantaneous luminosity defined above over time gives the integrated luminosity, which is directly related to the total number of observed events and is therefore commonly used to express the size of a dataset:

$$N_{tot} = \sigma \cdot \int \mathcal{L} dt \tag{3.3}$$

The LHC was designed to reach a luminosity of $\mathcal{L} = 10^{34}\ cm^{-2}\ s^{-1}$. In 2015, the desirable luminosity was not reached but was achieved during 2016 and was exceeded by the end of Run 2 in 2018 with a peak luminosity of $\mathcal{L} = 2.1 \times 10^{34}\ cm^{-2}\ s^{-1}$, as it is shown in Figure 3.2.

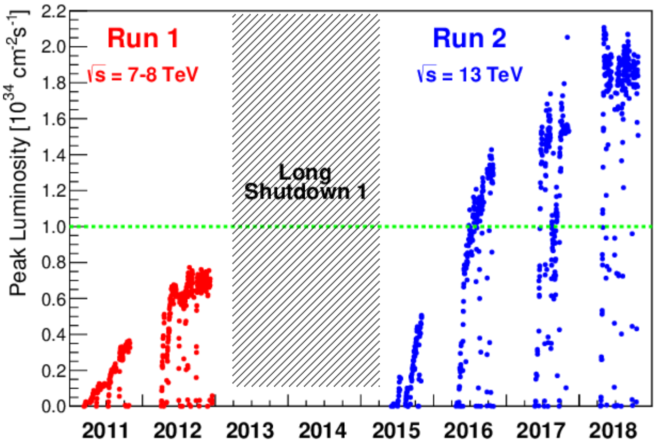

FIGURE 3.2: The integrated luminosity over the years in LHC.

During the Run 2, the LHC delivered an integrated luminosity of $\mathcal{L} = 156\ fb^{-1}$, where the ATLAS experiment recorded an integrated luminosity of $\mathcal{L} = 139\ fb^{-1}$, as it can be seen in Figure 3.3. The recent estimate of the integrated luminosity during the Run 2 is $\mathcal{L} = 140\ fb^{-1}$ [27].

In order to achieve a high luminosity in particle collisions, a large collision frequency and beam density are required. As a result, multiple collisions can occur during a single bunch crossing, a phenomenon referred to as $pileup$. For Run 2, the average number of simultaneous interactions per bunch crossing was found to be $< \mu > = 33.7$, with a peak average of $< \mu > = 37.8$ in 2017, as shown Figure 3.4. Apart from the $in - time$ pileup, which refers to collision events occurring during the same bunch-crossing as the event of interest, $out - of - time$ pileup also needs to be taken into consideration. This is defined as the measured overlayed signals originating from other bunch crossings than the interesting one.

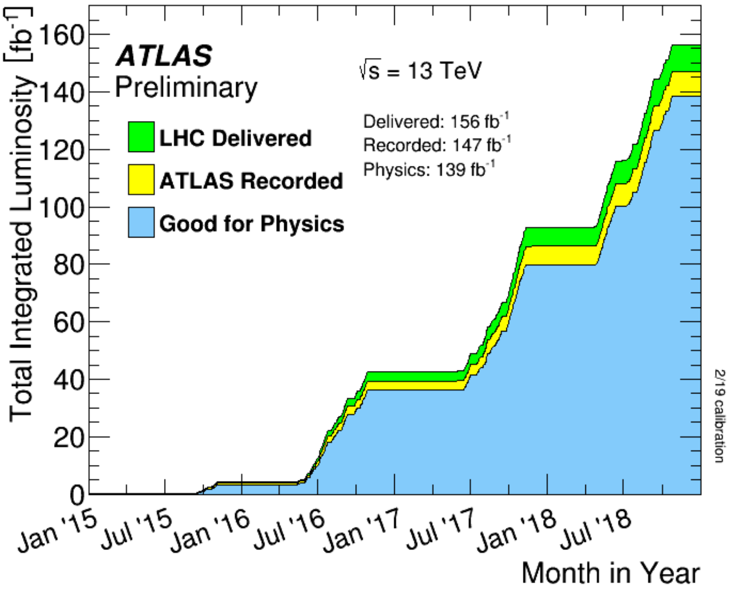

FIGURE 3.3: Integrated luminosity over the years delivered by LHC and recorded by ATLAS during Run 2.

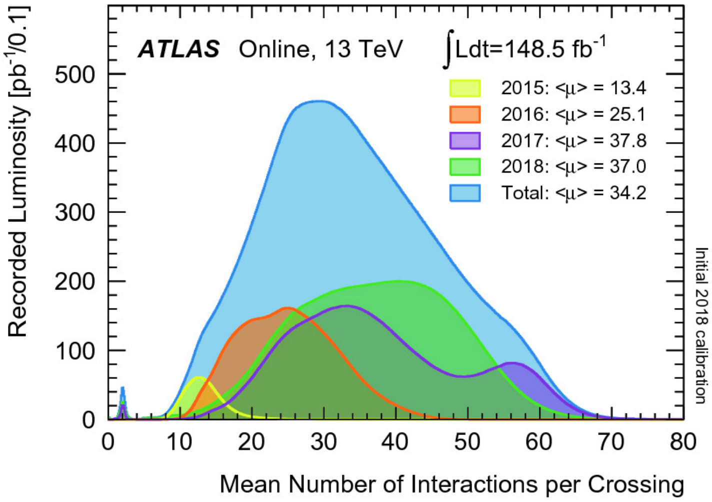

FIGURE 3.4: Average number of simultaneous interactions per bunch crossing for Run 2.

3.2 The ATLAS detector

The ATLAS detector is the largest of the four large-scale experiments at the LHC and it is a general-purpose detector, with close to 4π solid angle coverage, designed to explore a wide range of physical processes. ATLAS dimensions are: $44\ m$ long, $21\ m$ high and $21\ m$ wide and it weights approximately $7000\ tons$. It has a cylindrical shape, with a layered structure of four subsystems around the beam pipe and centered around the nominal interaction point. The overall ATLAS detector layout is shown in Figure 3.5.

The Inner Detector (ID) is the closest subsystem to the nominal interaction point and it measures charged particles whose trajectories are bended by the $2\ T$ solenoidal magnetic

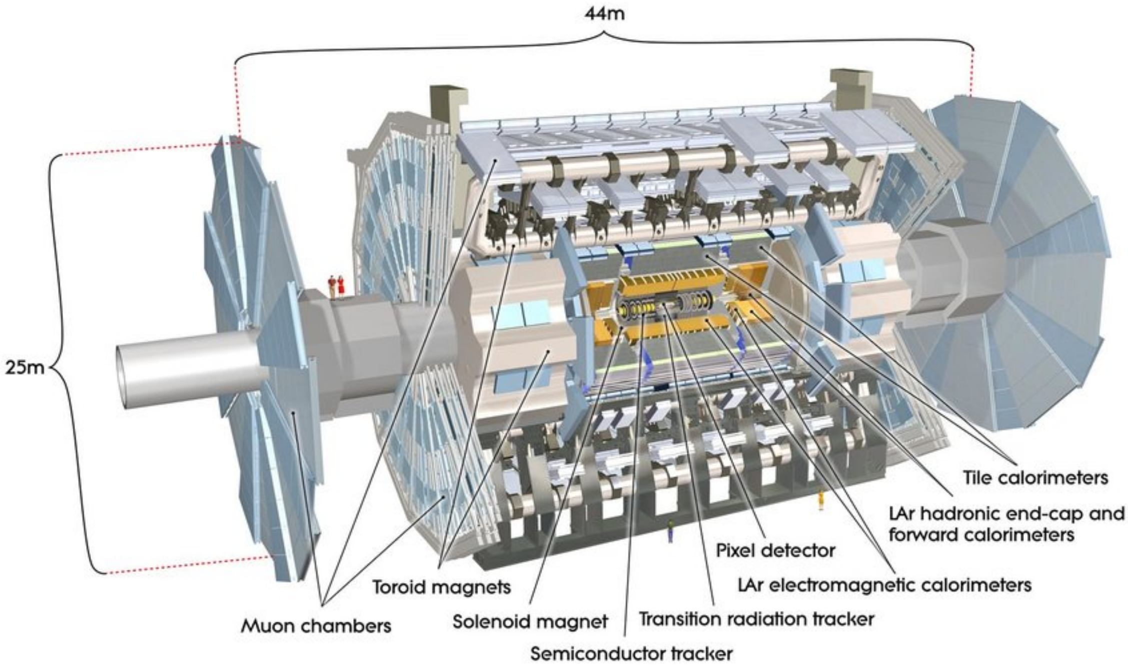

FIGURE 3.5: Cut-away view of the ATLAS detector and its subsystems.

field. The ID is surrounded by the Electromagnetic Calorimeter $(EMCal)$ and by the Hadronic Calorimeter $(HCal)$ where the most particles stop and deposit their energies. The last layer of the ATLAS detector is the Muon Spectrometer (MS) which measures the muon's tracks and momentum with the help of three toroidal magnets which bend their trajectories. All these subsystems are analyzed below.

3.2.1 Coordinate system

A common coordinate system is used throughout ATLAS, as presented in Figure 3.6. The origin of the coordinate system is at the center of the detector. The z-axis runs along the beam line. The $x - y$ plane is perpendicular to the beam line, is referred to as the transverse plane and is often described in terms of $r - \phi$. The positive y-axis points upward to the surface of the earth, while the positive x-axis points from the interaction point to the center of the LHC ring. The azimuthal angle ϕ is measured from the x-axis, around the beam while the polar angle θ is defined as the angle from the positive z-axis. Finally, the radial dimension, r, measures the distance from the beam line.

The polar angle is often reported in terms of pseudorapidity, defined as:

$$\eta = -ln \tan \frac{\theta}{2}. \tag{3.4}$$

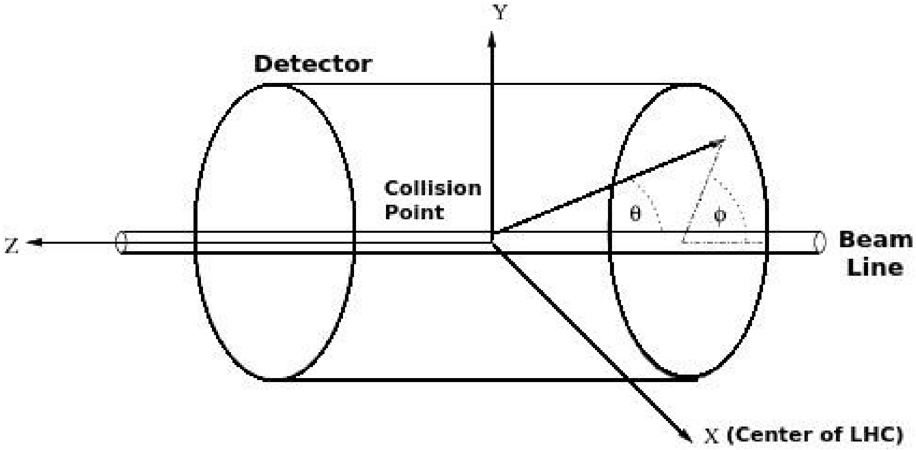

FIGURE 3.6: Coordinate system used in ATLAS.

For massive objects such as jets, the rapidity is used

$$y = \frac{1}{2} \ln \left(\frac{|E| + p_Z}{|E| - p_Z} \right). \tag{3.5}$$

Particle momentum and energy measured in the transverse plane are referred to as the transverse momentum (p_T) and transverse energy (E_T) accordingly and are defined as:

$$p_T = p \sin \theta \tag{3.6}$$

$$E_T = E \sin \theta \tag{3.7}$$

Finally, the relative distance ΔR, which is used in order to define the angular separation between two objects, is written in η-ϕ space as:

$$\Delta R = \sqrt{(\Delta\eta)^2 + (\Delta\phi)^2} \tag{3.8}$$

3.2.2 The Inner Detector

The Inner Detector (ID) [28] provides precise measurement of tracks of charged particles. Using a pattern recognition algorithm, the tracks are efficiently reconstructed and their origin can be extrapolated back to the interaction point. This allows vertex identification for both primary vertices, from the proton-proton interactions and secondary vertices from the decays of long-lived particles. It consists of three different subsystems: the Silicon Pixel Detector, the Semi-Conductor Tracker (SCT) and the Transition Radiation Tracker (TRT). Finally, a superconducting solenoid that generates a uniform axial magnetic field with a strength of $2\,T$, surrounds the three subsystems. The charged particles are bent by the magnetic field and the

ID layers allow a precise measurement of their trajectories. The charge and momentum of the traversing particles are determined, thanks to the high bending power and the granularity. A cut-away view of the ID is shown in Figure 3.7.

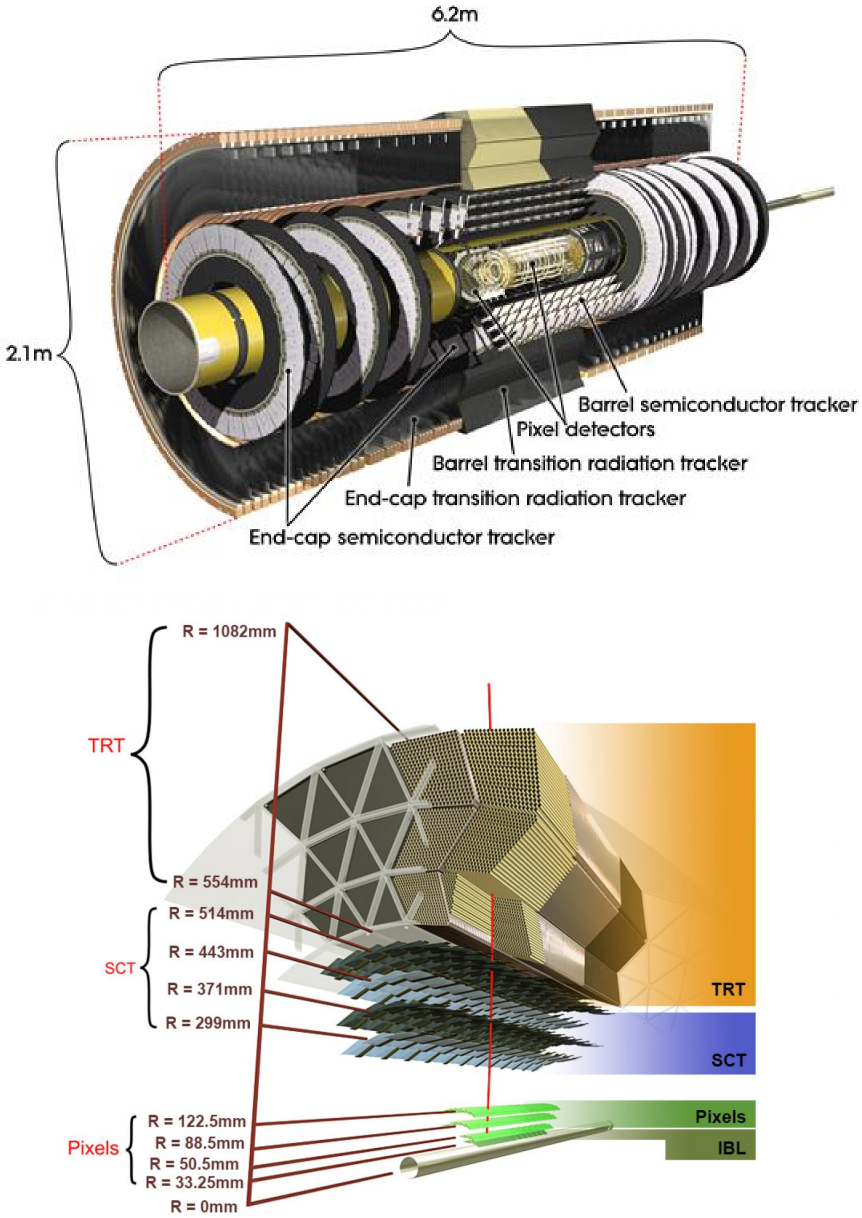

FIGURE 3.7: Cut-away view of the ATLAS ID detector and its subsystems.

The Silicon Pixel Detector [29] is the one that is closest to the interaction point, and it has the most granularity required to deal with the high particle densities around the vertex region. It is composed of four silicon pixel layers wrapped around the z-axis in the barrel, extending from 3.3 cm to 15 cm with respect to the beam, and 3 disk layers in both end-caps, yielding a total of about 80.4 million n^{+}/n silicon sensors, each covering a $400\ \times 50\ \mu m$ surface. The three outermost layers are able to achieve an accuracy of 115 μm along the z direction and up to 10 μm in the $R-\phi$ plane. In Run 2, the innermost layer, the Insertable B-layer (IBL) [30], was also added. Due to its finer resolution of 8 μm in the $R - \phi$ plane, the IBL improved the tracking capability and the vertex reconstruction, especially concerning the secondary vertices used for b-jet identification.

Around the Pixel detector, in the region $R = 30 - 56$ cm, is the Semiconductor Tracker (SCT). Similar in structure, it has 9 disks in both end-caps and 4 detection layers in the barrel. It uses a total of 6.3 million $80\,\mu m \times 16\,cm$ single-sided p/n silicon strips as detecting medium in place of silicon pixels. Two separate layers, with a small 40 $mrad$ angle between them to enable stereo-pairing, make up each barrel layer which enhances the resolution along the z-axis. Due to the significantly lower particle density in its detection range, this layout leads to a resolution of 16 μm in the $R - \phi$ plane and 580 μm along z axis.

The last part of the ID is the Transition Radiation Tracker (TRT) and it is composed of around 350 thousands individual straw tubes. In order to complete ATLAS tracking capability in the range $|\eta| < 2.0$, 72 layers of 144 cm long tubes, with a 4 mm diameter are arranged parallel to the beam axis in the barrel and 160 layers of shorter $36\,cm$ long tubes are orientated radially in the end-caps. A $Xe - CO_2 - O_2$ gas combination is used as an interacting medium. Each tube has a 31 mm thick gold-coated tungsten wire working as an anode, and the tube walls acting as a cathode. A 2.5×10^4 gain is produced by applying a 1.5 kV potential difference between the anodes and cathodes, which enables the detection of the extremely faint signals left by particles interacting with the gas mixture. These layers of straws are separated by polypropylene tubes that produce transition-radiation photons from interacting electrons, which are crucial for identifying electrons and distinguishing them from pions.

3.2.3 The Calorimeters

The ATLAS Calorimeter System [31], which includes the Electromagnetic and the Hadronic calorimeters, is placed after the ID and its schematic view is shown in Figure 3.8. Table 3.1 summarizes the pseudorapidity coverage, granularity, and segmentation of the calorimeters in depth. These calorimeters cover the range $|\eta| < 4.9$, using different techniques suited to the widely varying requirements of the physics processes of interest and of the radiation environment over this large η-range. The fine granularity of the ElectroMagnetic (EM) calorimeter is perfectly suited for accurate measurements of electrons and photons over the η region that matches the inner detector. The rest of the calorimeter's coarser granularity is adequate to satisfy the physics requirements for jet reconstruction and E_T^{miss} measurements.

Calorimeters must limit punch-through into the muon system and must provide good containment for electromagnetic and hadronic showers. Consequently, calorimeter depth is a crucial design factor. The EM calorimeter's overall thickness is more than 24 radiation lengths (X_0) in the end-caps and more than 22 X_0 in the barrel. On the other hand, for the hadronic calorimeter, the approximate 9.7 interaction lengths (λ) of active calorimeter in the barrel $(10\lambda$ in the end-cups) are sufficient to provide good resolution for high- energy jets (Table 3.1). The total thickness, including $1.3\,\lambda$ from the outer support, is $11\,\lambda$ at $\eta = 0$, which is sufficient to reduce punch-through below the irreducible level of prompt or decay muons. This thickness guarantees a good E_T^{miss} measurement in addition to the large η-coverage, which is crucial for various physics signatures and in particular for SUSY particle searches.

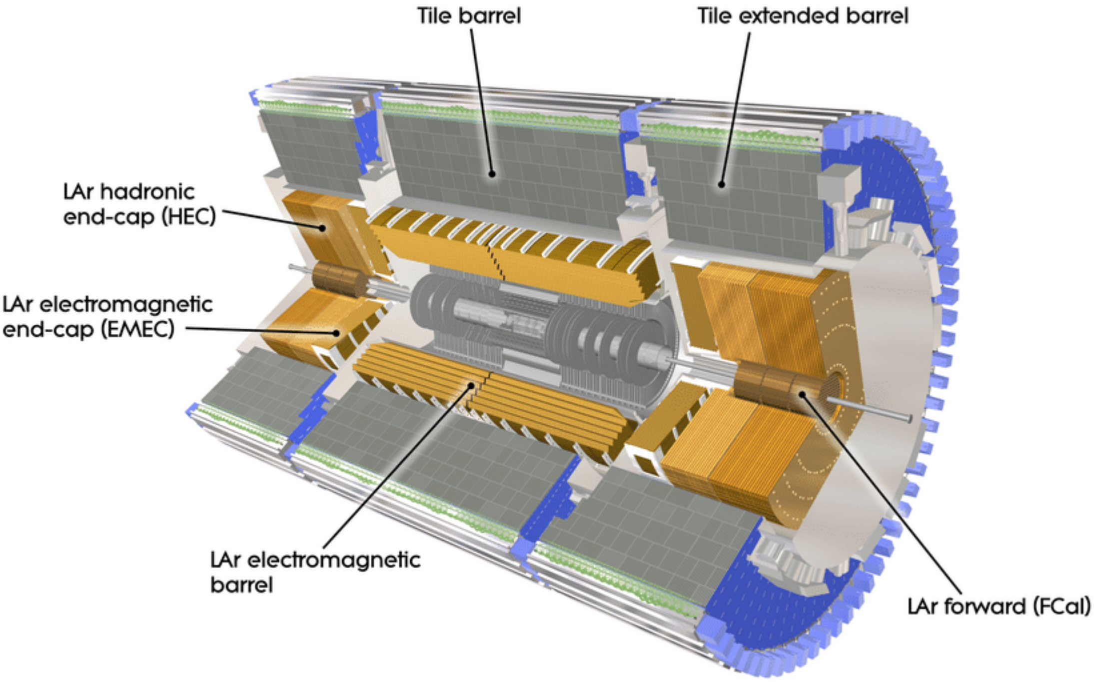

FIGURE 3.8: Schematic view of the ATLAS Calorimeter System.

3.2.3.1 The LAr Electromagnetic Calorimeter

The EM calorimeter is seperated into three parts: the barrel part $(|\eta| < 1.475)$ and two end-cap components $(1.375 < |\eta| < 3.2)$, where each of them is placed in its own cryostat. To achieve the desired calorimeter performance, the material must be optimized due to the location of the central solenoid in front of the EM calorimeter. As a result, then two vacuum walls are removed and the central solenoid and LAr calorimeter share a single vacuum vessel. A slight gap $(4\,mm)$ at $z = 0$ seperates the two identical half-barrels that consist the barrel calorimeter. Each end-cap calorimeter is split into two coaxial wheels: an outer wheel that covers the range $1.375 < |\eta| < 2.5$ and an inner wheel that covers the range $2.5 < |\eta| < 3.2$.

The EM calorimeter is a lead-LAr detector with accordion-shaped kapton electrodes and lead absorber plates over its full coverage, a sketch of which can be found in Figure 3.9. Complete ϕ symmetry, without azimuthal cracks, is provided by the accordion geometry. In order

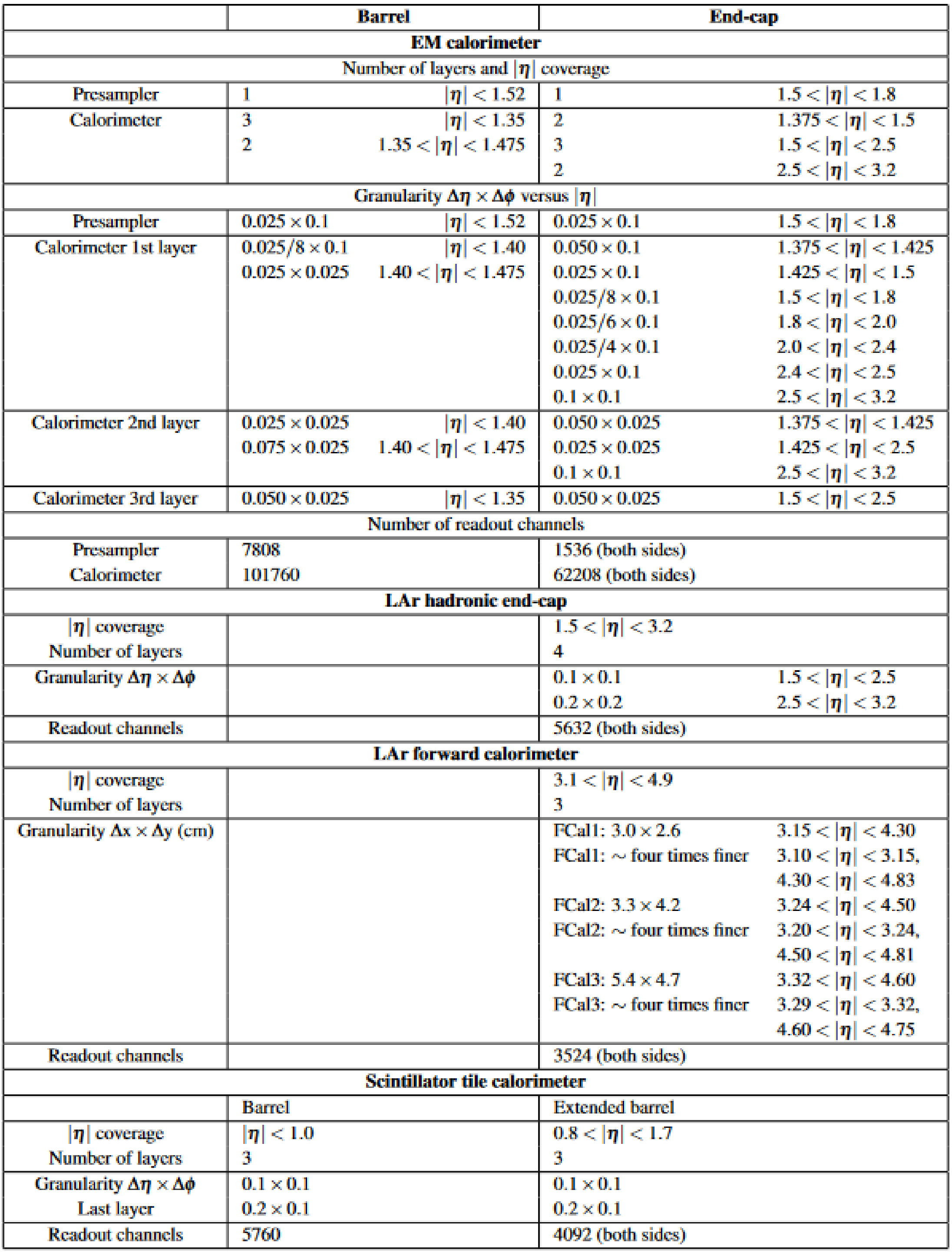

	Barrel		**End-cap**	
EM calorimeter				
Number of layers and $\lvert\eta\rvert$ coverage				
Presampler	1	$\lvert\eta\rvert < 1.52$	1	$1.5 < \lvert\eta\rvert < 1.8$
Calorimeter	3	$\lvert\eta\rvert < 1.35$	2	$1.375 < \lvert\eta\rvert < 1.5$
	2	$1.35 < \lvert\eta\rvert < 1.475$	3	$1.5 < \lvert\eta\rvert < 2.5$
			2	$2.5 < \lvert\eta\rvert < 3.2$
Granularity $\Delta\eta \times \Delta\phi$ versus $\lvert\eta\rvert$				
Presampler	0.025×0.1	$\lvert\eta\rvert < 1.52$	0.025×0.1	$1.5 < \lvert\eta\rvert < 1.8$
Calorimeter 1st layer	$0.025/8 \times 0.1$	$\lvert\eta\rvert < 1.40$	0.050×0.1	$1.375 < \lvert\eta\rvert < 1.425$
	0.025×0.025	$1.40 < \lvert\eta\rvert < 1.475$	0.025×0.1	$1.425 < \lvert\eta\rvert < 1.5$
			$0.025/8 \times 0.1$	$1.5 < \lvert\eta\rvert < 1.8$
			$0.025/6 \times 0.1$	$1.8 < \lvert\eta\rvert < 2.0$
			$0.025/4 \times 0.1$	$2.0 < \lvert\eta\rvert < 2.4$
			0.025×0.1	$2.4 < \lvert\eta\rvert < 2.5$
			0.1×0.1	$2.5 < \lvert\eta\rvert < 3.2$
Calorimeter 2nd layer	0.025×0.025	$\lvert\eta\rvert < 1.40$	0.050×0.025	$1.375 < \lvert\eta\rvert < 1.425$
	0.075×0.025	$1.40 < \lvert\eta\rvert < 1.475$	0.025×0.025	$1.425 < \lvert\eta\rvert < 2.5$
			0.1×0.1	$2.5 < \lvert\eta\rvert < 3.2$
Calorimeter 3rd layer	0.050×0.025	$\lvert\eta\rvert < 1.35$	0.050×0.025	$1.5 < \lvert\eta\rvert < 2.5$
Number of readout channels				
Presampler	7808		1536 (both sides)	
Calorimeter	101760		62208 (both sides)	
LAr hadronic end-cap				
$\lvert\eta\rvert$ coverage			$1.5 < \lvert\eta\rvert < 3.2$	
Number of layers			4	
Granularity $\Delta\eta \times \Delta\phi$			0.1×0.1	$1.5 < \lvert\eta\rvert < 2.5$
			0.2×0.2	$2.5 < \lvert\eta\rvert < 3.2$
Readout channels			5632 (both sides)	
LAr forward calorimeter				
$\lvert\eta\rvert$ coverage			$3.1 < \lvert\eta\rvert < 4.9$	
Number of layers			3	
Granularity $\Delta x \times \Delta y$ (cm)			FCal1: 3.0×2.6	$3.15 < \lvert\eta\rvert < 4.30$
			FCal1: $\sim$ four times finer	$3.10 < \lvert\eta\rvert < 3.15$, $4.30 < \lvert\eta\rvert < 4.83$
			FCal2: 3.3×4.2	$3.24 < \lvert\eta\rvert < 4.50$
			FCal2: $\sim$ four times finer	$3.20 < \lvert\eta\rvert < 3.24$, $4.50 < \lvert\eta\rvert < 4.81$
			FCal3: 5.4×4.7	$3.32 < \lvert\eta\rvert < 4.60$
			FCal3: $\sim$ four times finer	$3.29 < \lvert\eta\rvert < 3.32$, $4.60 < \lvert\eta\rvert < 4.75$
Readout channels			3524 (both sides)	
Scintillator tile calorimeter				
	Barrel		Extended barrel	
$\lvert\eta\rvert$ coverage	$\lvert\eta\rvert < 1.0$		$0.8 < \lvert\eta\rvert < 1.7$	
Number of layers	3		3	
Granularity $\Delta\eta \times \Delta\phi$	0.1×0.1		0.1×0.1	
Last layer	0.2×0.1		0.2×0.1	
Readout channels	5760		4092 (both sides)	

TABLE 3.1: Main parameters of the calorimeter system.

to get the best EM calorimeter performance in terms of energy resolution, the lead thickness in the absorber plates has been optimized as a function of η. The EM calorimeter is divided into three deep sections over the area designated for precision physics ($|\eta| < 2.5$). For the end-cap inner wheel, the calorimeter is split in two sections in depth and has a coarser lateral granularity than for the rest of the acceptance.

Finally, a presampler detector is used to correct for the energy lost by electrons and photons upstream of the calorimeter, in the region of $|\eta| < 1.8$. The barrel (end-cup) area of the presampler contains an active LAr layer that is $1.1\,cm\ (0.5\,cm)$ thick.

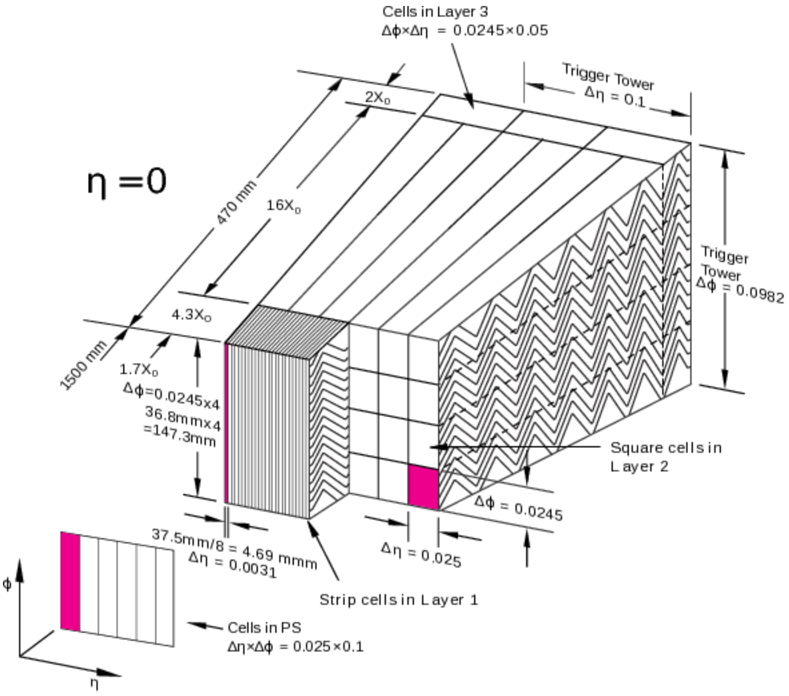

FIGURE 3.9: Sketch of a EM calorimeter barrel module. The cell granularity in η and ϕ for the three layers are shown.

3.2.3.2 The Hadronic Calorimeters

Tile Calorimeter [32] The tile calorimeter is located directly outside the EM calorimeter envelope. Its barrel has a range of $|\eta| < 1.0$, and its two extended barrels have a range of $0.8 < |\eta| < 1.7$. It is a sampling calorimeter using steel as the absorber and scintillating tiles as the active material. The barrel and extended barrels are split azimuthally into 64 modules. The tile calorimeter extends from an inner radius of $2.28\,m$ to an outer radius of $4.25\ m$. For the barrel and the extended barrel, it is split in depth into three layers that are respectively 1.5, 4.1, and 1.8 interaction lengths (λ) thick and 1.5, 2.6, and 3.3 λ, respectively. At $\eta = 0$, the total detector thickness at the outer edge of the tile-instrumented region is $9.7\ \lambda$. Two sides of the scintillating tiles are read out by wavelength shifting fibres into two separate photomultiplier tubes. In η, the readout cells built by grouping fibres into the photomultipliers are pseudo-projective towards the interaction region.

LAr hadronic end-cap calorimeter The Hadronic End-cap Calorimeter (HEC), which shares the same LAr cryostats as the End-cap Electromagnetic Calorimeter and is located exactly behind it, is made up of two independent wheels per end-cap. The HEC extends out to $|\eta| = 3.2$, therefore overlapping with the forward calorimeter, to reduce the drop in material density at the transition between the end-cap and the forward calorimeter (around $|\eta| = 3.1$). Similarly, the HEC η range also slightly overlaps that of the tile calorimeter ($|\eta| < 1.7$) by extending to $|\eta| = 1.5$. 32 identical wedge-shaped modules are used to construct each wheel, assembled with fixtures at the periphery and at the central bore. Each wheel is divided into two segments in depth, for a total of four layers per end-cap. $50\,mm$ parallel copper plates are used for the wheels farther away, whereas $25\,mm$ parallel copper plates are used for the wheels closest to the interaction point (for all wheels the first plate is half-thickness). Except for the area where the copper plates overlap with the forward calorimeter, where the inner radius is 0.372 m, the copper plates have an outside radius of $2.03\,m$ and an inner radius of $0.475\,m$. The active media for this sampling calorimeter is consisted of copper plates that are sandwiched together with 8.5 mm LAr gaps.

LAr forward calorimeter In order to provide uniform calorimetric coverage and lower radiation background levels in the muon spectrometer, the Forward Calorimeter $(FCal)$ is integrated into the end-cap cryostats. To minimize neutron albedo in the inner detector cavity, the front face of the FCal is positioned about 1.2 m back from the front face of the EM calorimeter. This sets a significant restriction on the calorimeter's depth and necessitates a high-density design. The FCal has three modules in each end-cap and it is about 10 interaction lengths deep. The first module is composed of copper and it is optimized for electromagnetic measurements, while the other two are built of tungsten and primarily measure the energy of hadronic interactions. Each module consists of a metal matrix, with regularly spaced longitudinal channels filled with the electrode structure consisting of concentric rods and tubes parallel to the beam axis. The LAr in the gap between the rod and the tube is the sensitive medium. In order to prevent issues brought on by ion buildup, this design enables good control of the gaps, which are as narrow as 0.25 mm in the first segment.

3.2.4 The Muon Spectrometer

The Muon Spectrometer (MS) [33] is the outer part of the ATLAS detector and is designed to detect charged particles exiting the barrel and end-cap calorimeters and to measure their momentum in the pseudorapidity range $|\eta| < 2.7$. The layout of the muon spectrometer is shown in Figure 3.10 and the main parameters of the muon chambers are listed in Table 3.2. Additionally, it is designed to trigger on these particles in the range of $|\eta| < 2.4$. For 1 TeV tracks, the driving performance target is a stand-alone transverse momentum resolution of approximately $10\,\%$, which corresponds to a sagitta along the z $(beam)$ axis of approximately $500\,\mu m$, measured with a precision of ≤ 50 μm. The spectrometer can measure muon momenta as low as a few GeV ($3\,GeV$, due to energy loss in the calorimeters). Finally, the stand-alone measurements still offer a sufficient momentum resolution and satisfactory charge identification at the upper limit of the available range $(3\,TeV)$.

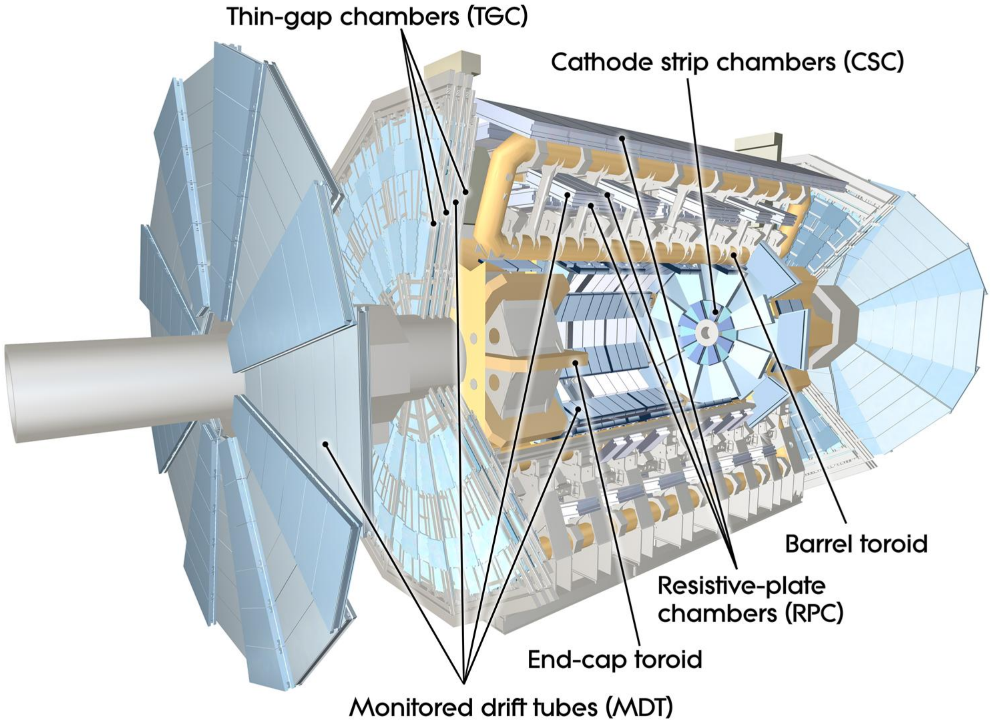

FIGURE 3.10: Cut-away view of the ATLAS muon system.

More specific, the muon spectrometer is based on the magnetic deflection of muon tracks in the large superconducting air-core toroid magnets that are instrumented with separate trigger and highly accurate tracking chambers. The large barrel toroid provides magnetic bending across the range $|\eta| < 1.4$. Two smaller end-cap magnets fitted into both ends of the barrel toroid, bend muon tracks for $1.6 < |\eta| < 2.7$. Over $1.4 < |\eta| < 1.6$, typically referred to as the transition region, magnetic deflection is provided via a combination of barrel and end-cap fields. While minimizing the loss of resolution from multiple scattering, this magnet design provides a field that is primarily orthogonal to the muon trajectories. The selection and design of the spectrometer instruments, as well as the performance factors including rate capability, granularity, ageing properties, and radiation hardness, have all been significantly influenced by the anticipated high amount of particle flux.

The precision-tracking chambers in the barrel region are situated between and on the eight coils of the superconducting barrel toroid magnet, while the end-cap chambers are in front and behind the two end-cap toroid magnets. The muon chamber system, which is made up of eight octants, has a symmetric structure that reflects the ϕ symmetry of the toroids. Each octant is divided into two sectors, a large and a small sector, with slightly different lateral expansions in the azimuthal direction, resulting in a region of overlap in ϕ. By allowing the

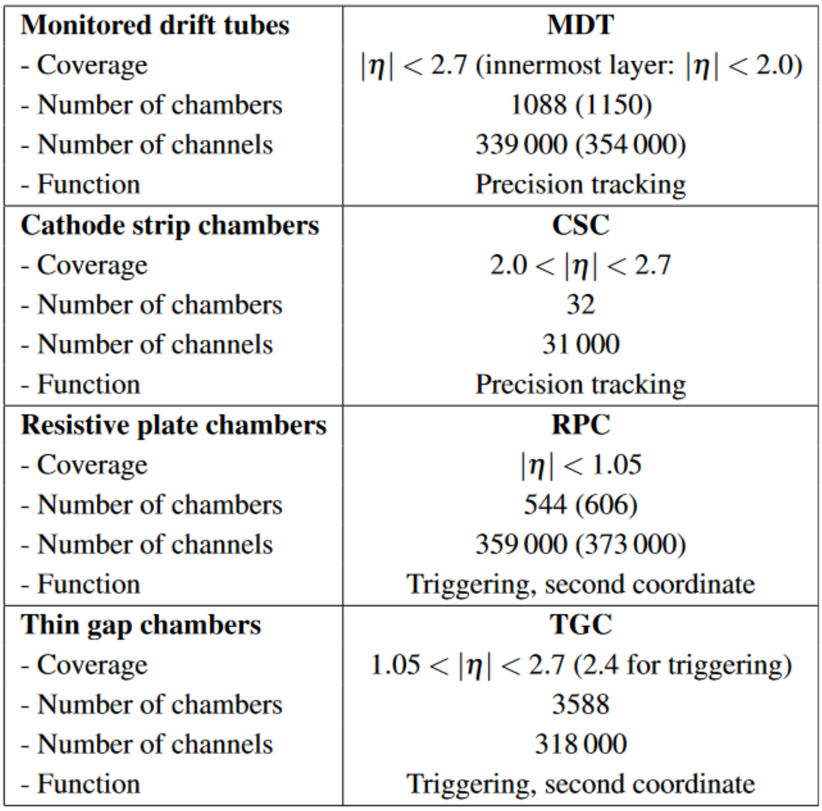

Monitored drift tubes	**MDT**
- Coverage	$\|\eta\| < 2.7$ (innermost layer: $\|\eta\| < 2.0$)
- Number of chambers	1088 (1150)
- Number of channels	339 000 (354 000)
- Function	Precision tracking
Cathode strip chambers	**CSC**
- Coverage	$2.0 < \|\eta\| < 2.7$
- Number of chambers	32
- Number of channels	31 000
- Function	Precision tracking
Resistive plate chambers	**RPC**
- Coverage	$\|\eta\| < 1.05$
- Number of chambers	544 (606)
- Number of channels	359 000 (373 000)
- Function	Triggering, second coordinate
Thin gap chambers	**TGC**
- Coverage	$1.05 < \|\eta\| < 2.7$ (2.4 for triggering)
- Number of chambers	3588
- Number of channels	318 000
- Function	Triggering, second coordinate

Table 3.2: Main parameters of the muon spectrometer. Numbers in brackets for the MDT's and the RPC's refer to the final configuration of the detector in 2009.

chamber boundaries to overlap, gaps in detector coverage are minimized and tracks from both big and small chamber can be used to align neighboring sectors relatively.

Around the beam axis, the chambers in the barrel are positioned in three concentric cylindrical shells with radii of roughly $5\ m$, $7.5\ m$, and $10\ m$. In the two end-cap regions, muon chambers form large wheels, perpendicular to the z-axis and located at distances of $|z| \approx 7.4\ m,\ 10.8\ m,\ 14\ m$, and $21.5\ m$ from the interaction point. Cross-sections in the planes transverse to, and containing, the beam axis, are shown in Figures 3.11 and 3.12, respectively. To facilitate servicing of the solenoid magnet, calorimeters, and inner detector, a gap in chamber coverage has been left open at the center of the detector ($|\eta| \approx 0$). The size of the gap varies based on the service necessities from sector to sector, with the largest gaps of $1-2\,m$ being found in the large sectors. The angular range where a high momentum $straight$ track is not recorded in all three muon layers due to the gaps is around $\pm\,4.8°$ ($|\eta| \leq 0.08$) in the large sectors and $\pm\,2.3°$ ($|\eta| \leq 0.04$) in the small sectors, as seen from the interaction point. Sectors 12 and 14 have additional gaps in acceptance as a result of the detector support structure ($feet$).

The Monitored Drift Tube chambers (MDT's) are used to make precise momentum measurements. They are chosen because they offer a high level of measurement accuracy, are able

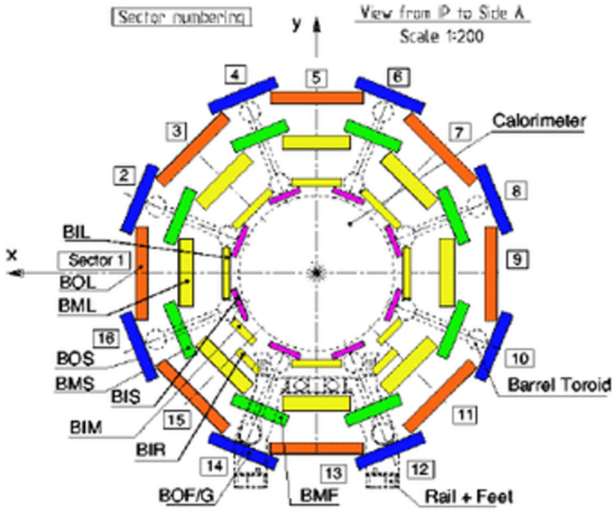

FIGURE 3.11: Cross-section of the barrel muon system perpendicular to the beam axis $(non - bending\,plane)$, showing three concentric cylindrical layers of eight large and eight small chambers. The outer diameter is about 20 m.

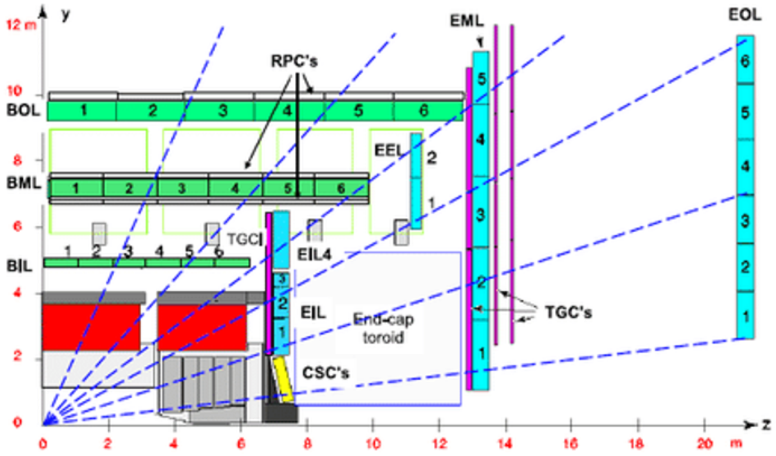

FIGURE 3.12: Cross-section of the muon system in a plane containing the beam axis $(bending\,plane)$. Infinite-momentum muons would propagate along straight trajectories which are illustrated by the dashed lines and typically traverse three muon stations.

to predict mechanical deformations, and are simple to construct. Except for the innermost end-cap layer, where their coverage is restricted to $|\eta| < 2.0$, they cover the pseudorapidity range $|\eta| < 2.7$. These chambers, which have three to eight layers of drift tubes and operate at an absolute pressure of 3 bar, have an average resolution of 80 μm per tube, or roughly 35 μm per chamber.

Cathode-Strip Chambers (CSC) are used in the inner-most tracking layer in the forward area $(2.0 < |\eta| < 2.7)$ because of their better rate capability and time resolution. The CSC's are multiwire proportional chambers with cathode planes segmented into strips in orthogonal directions. This makes it possible to determine both coordinates from the induced-charge distribution. A chamber has a resolution of 40 μm in the bending plane and around 5 mm in the transverse plane. Due to the varied readout pitch and the fact that the azimuthal readout runs parallel to the anode wires, the resolution between the bending and non-bending planes differs.

The positions of MDT wires and CSC strips along a muon trajectory must be known to better than $30\mu m$ in order to obtain the sagitta resolution mentioned above. For this purpose, a high-precision optical alignment system keeps track of the locations and internal deformations of the MDT chambers and finally it is complemented by track-based alignment algorithms.

The muon system's ability to trigger on muon tracks was a key design criterion. As a result, a set of quick trigger chambers that can transmit track information a few tens of nanoseconds after the particle's passage, has been added to supplement the precision-tracking chambers. Resistive Plate Chambers (RPC) were chosen for this purpose in the barrel region $(|\eta| < 1.05)$, whereas Thin Gap Chambers (TGC) were chosen in the end-cap $(1.05 < |\eta| < 2.4)$. Table 3.3 gives the intrinsic time resolution of the detectors, to which contributions from signal propagation and electronics have to be added. The design goal was to keep these contributions low enough for reliable beam-crossing identification with $\geq 99\%$ probability. Both chamber types deliver signals with a spread of 15–25 ns, thus providing the ability to tag the beam-crossing. The trigger chambers take measurements of the track's coordinates in both the bending (η) and non-bending (ϕ) planes.

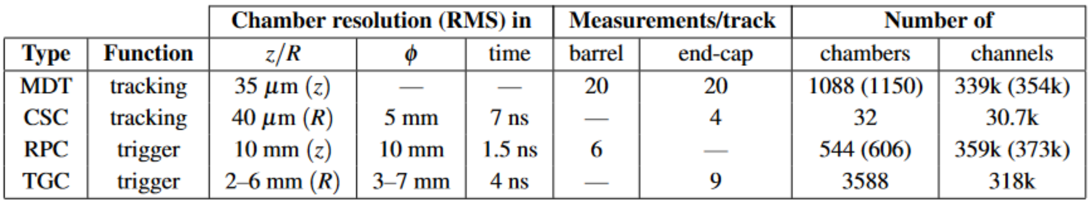

		Chamber resolution (RMS) in			Measurements/track		Number of	
Type	**Function**	z/R	ϕ	time	barrel	end-cap	chambers	channels
MDT	tracking	35 μm (z)	—	—	20	20	1088 (1150)	339k (354k)
CSC	tracking	40 μm (R)	5 mm	7 ns	—	4	32	30.7k
RPC	trigger	10 mm (z)	10 mm	1.5 ns	6	—	544 (606)	359k (373k)
TGC	trigger	2–6 mm (R)	3–7 mm	4 ns	—	9	3588	318k

Table 3.3: Parameters of the four muon detector sub-systems. Uncertainties related to chamber alignment are not included in the quaoted spatial resolution $(columns\ 3,\ 4)$. The intrinsic time resolution of each type of chamber is listed in Column 5, to which the effects of signal propagation and electronics must be added. Numbers in brackets refer to the complete detector configuration as planned for 2009.

The precision-tracking chambers are used to measure the track's coordinate in the bending plane. The MDT and trigger chamber hits are matched in the bending plane, and the trigger chamber's coordinate in the non-bending plane is used as the second coordinate of the MDT measurement. This method assumes that only one track per event is present in any MDT/trigger chamber pair because it is not possible to combine the η and ϕ hits in an unambiguous way with two or more tracks. When this occurs, the ambiguity in η and ϕ -assignment is resolved by matching the muon track candidates with tracks from the inner detector.

3.2.4.1 The New Small Wheel

As previously mentioned, luminosity is a crucial measure of an accelerator's performance, indicating the number of collisions occurring within a specific time period. Higher luminosity translates to increased particle rates, offering more opportunities to observe rare processes. However, the pursuit of higher luminosity necessitates extensive technical upgrades to maintain optimal detector performance, which are carried out during detector shutdown periods.

The goal is to raise the nominal luminosity from $10^{34}\ cm^{-2}s^{-1}$ to $2-3\ 10^{34}\ cm^{-2}s^{-1}$ after the second long shutdown period (LS2) in 2019-2022. This increase will enable the ATLAS detector to collect up to 100 $fb^{-1}/year$ of data. The initial shutdown period, known as Phase-1 upgrade for the ATLAS and CMS detectors, will be followed by the Phase-2 stage in 2026-2028 (LS3). During this phase, the installation of the High-Luminosity LHC (HL-LHC) will take place, with the aim of reaching a luminosity of $5-7\ 10^{34}\ cm^{-2}s^{-1}$. Figure 3.13 provides a timeline illustrating the LHC and HL-LHC run and shutdown periods, along with the corresponding achieved center-of-mass energies and luminosity.

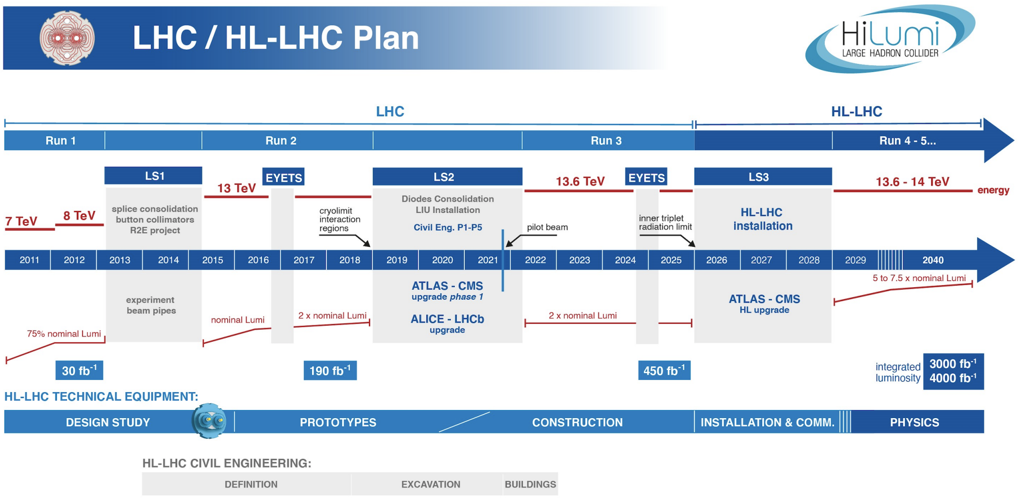

FIGURE 3.13: Timeline for the LHC and HL-LHC run and shutdown periods.

The Small Wheel region, part of the ATLAS Muon Spectrometer, is the region with the highest background rates. The existing system comprises Cathode Strip Chambers (CSCs), Monitored Drift Tubes (MDTs), Thin Gap Chambers (TGCs), and Resistive Plate Chambers (RPCs). However, with the increasing particle rates in Run 3 and the anticipated higher luminosity environment at the HL-LHC, the performance of the current infrastructure, particularly in the first forward station (Small Wheel), would be significantly impacted.

Specifically, following the luminosity increase after LS2, the Small Wheel would be inadequate for muon tracking and efficiency determination. The TGCs, MDTs, and CSCs are not designed to handle the extremely high transverse momentum (p_T) particle flow in the forward region and simultaneously the increased background rate. As a result, the spatial resolution would be limited, and efficiency would decrease. Additionally, in the previous setup, the L1 trigger in the muon end-caps relied on the TGC chambers of the Big Wheel. This trigger rate was dominated by a high number of false events caused by low-energy particles incorrectly attributed to muons with $|\eta| > 1.0$, which were not detected in the Inner Detector.

To address these issues, upgraded detectors were needed. These detectors should exhibit good spatial and fast time resolution, efficient trigger decision capabilities, and maintain high efficiency rates in HL-LHC conditions. They should also be compatible with the existing tracking detectors and end-cap alignment system. The New Small Wheel (NSW) project aims to fulfill these requirements and mitigate the aforementioned problems.

The New Small Wheel (NSW) represents the most important Phase-1 upgrade project within ATLAS. It involved the installation of two large wheels, each with a diameter of $10\,m$, which replace the first muon stations located in the high-rapidity regions of ATLAS ($1.3 < |\eta| < 2.7$). These new wheels incorporate two advanced detector technologies: small-strip Thin Gap Chambers (sTGCs) and Micromegas (MM) detectors [34]. The sTGCs are specifically designed for the L1-trigger, capable of handling background rates of up to $15\,kHz/cm^2$. They offer an angular resolution of approximately $1\,mrad$. On the other hand, the MM detectors are optimized for precise muon tracking. Their small gap of $5mm$ and narrow strip pitch of $450\mu m$ enable a spatial resolution of about $100\,\mu m$ per detector layer. In total, these detectors cover an active area exceeding $1200\,m^2$. Both the sTGCs and MM detectors are gas-filled detectors that measure the effects associated with the drifting of electrons and ions caused by the ionization of gas from passing muons. More details for these two detectors are given below.

Each of the two wheels in the NSW upgrade consists of a total of 16 sectors (wedges): eight large and eight small sectors. These sectors are arranged in a way that they partially overlap each other and are mounted on a metallic circular spacer frame. A single sector has two MM wedges attached on both sides of the spacer frame and sandwiched by two sTGC wedges. Each wedge contains four active detector layers, forming quadruplets. Therefore, in total, the NSW upgrade comprises eight layers of MM detectors and eight layers of sTGC detectors. A schematic view of the NSW is shown in Figure 3.14.

sTGC detectors

The concept of Thin Gap Chambers (TGC) was developed in 1983 and has been successfully used in muon trigger systems such as the ATLAS end-cap muon trigger system. The small-strip TGC (sTGC) is a key component of the New Small Wheel (NSW) upgrade in the

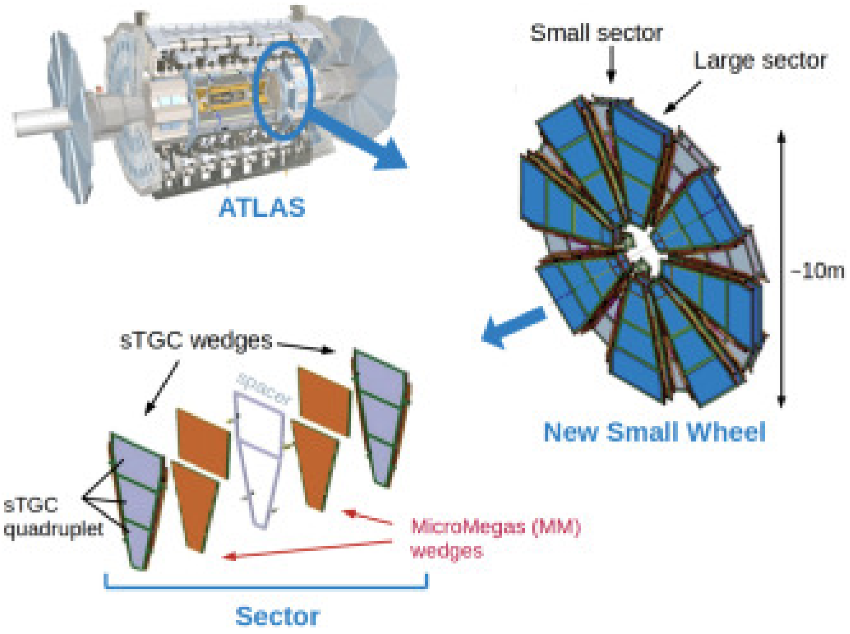

FIGURE 3.14: A schematic view of the NSW.

ATLAS Muon Spectrometer. The basic small-strip TGC (sTGC) structure is shown in Figure 3.15 and it consists of a grid of $50\,\mu m$ gold-plated tungsten wires operating at a potential of $2.9\,kV$, a $1.8\ mm$ pitch and sandwiched between two cathode planes located at a distance of $1.4\ mm$ from the wire plane.

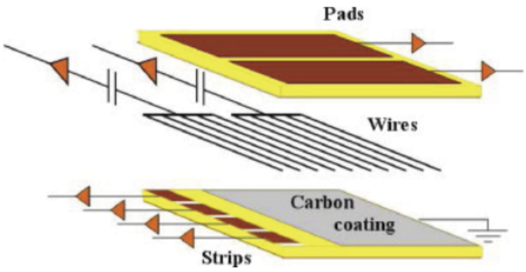

FIGURE 3.15: A schematic view of the basic sTGC structure.

The cathode planes are made of a graphite-epoxy mixture with precision strips on one side and pads on the other, on a $1.6\ mm$ thick printed circuit board (PCB) with the shielding ground on the opposite side. The precision strips, running perpendicular to the wires, have a small pitch of $3.2\ mm$, which is smaller than the strip pitch of the ATLAS TGC. The pads, covering large rectangular surfaces, are used for muon track identification and determining which strips need to be read out for precise measurements in the bending coordinate. The operational gas mixture used in the sTGC detectors is 55% CO_2 and 45% n-pentane.

The production of sTGC detectors for the NSW involves six types of quadruplets, three for the large and small sectors, respectively. The quadruplets have trapezoidal shapes with dimensions ranging from 1 to $2\ m^2$. Production took place at institutions from Canada, Chile, China, Israel, and Russia. A schematic view of the small and large sTGC sectors is shown in Figure 3.16.

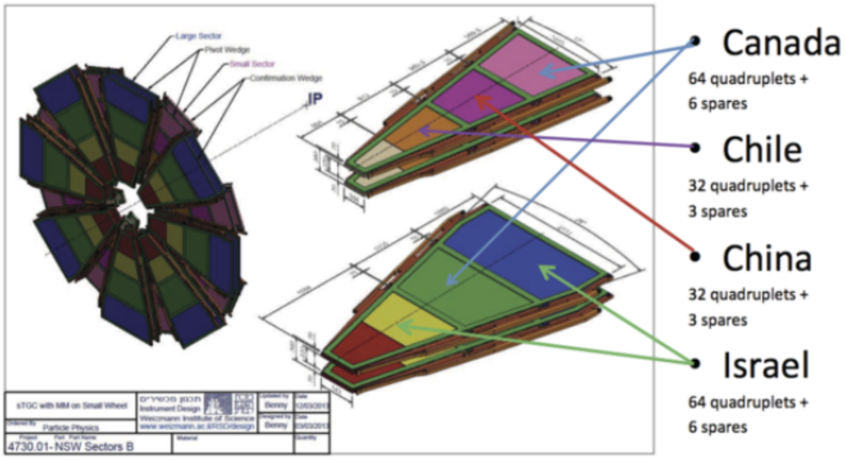

FIGURE 3.16: A schematic view of the small and large sTGC sectors.

Micromegas detector

The Micromegas (MICROMEsh GAseous Structure) technology, developed in the 1990s, is also a very crucial component of the NSW upgrade for the Muon Spectrometer (MS) in the ATLAS experiment. The basic Micromegas structure is shown in Figure 3.17. It consists of a planar drift electrode, a 5 mm gas conversion and drift region, and a thin metallic micromesh located 128 μm away from the readout electrode, creating the amplification region. The readout strips (0.425 mm pitch) are covered by a resistive strip layer to protect against sparking.

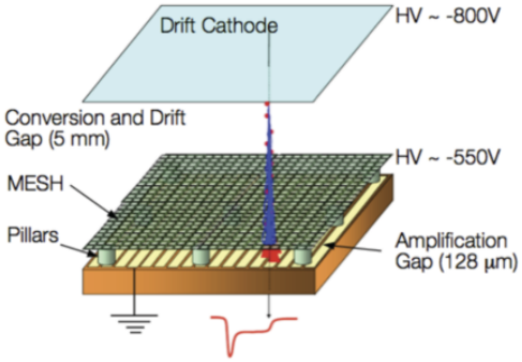

FIGURE 3.17: A schematic view of the basic MM structure.

The Micromegas detectors operate with a high electric field gradient of $40 - 50\ kV/cm^2$ in the amplification region, while the electric field gradient in the drift region is much lower, typically a few hundreds of V/cm. Charged particles passing through the drift space ionize the gas, and the liberated electrons drift towards the micromesh. The micromesh, held at a high electric field, allows more than 95% of the electrons to pass through, resulting in an electron avalanche above the readout electrode. This amplification process occurs rapidly, within a fraction of a nanosecond, producing a fast signal on the readout strips.

The Micromegas technology offers several advantages. Firstly, it has a fast response time due to the rapid amplification process, making it suitable for high particle fluxes. Secondly, it achieves excellent spatial resolution, better than 10 μm, independent of the incident angle of the particle track. This is achieved through a combination of algorithms. For small incident angles, a cluster centroid method is used, while for larger incident angles, the Micromegas is operated in the micro-Time-Projection-Chamber (μTPC) mode. The μTPC method utilizes the measured drift time of charges arriving on individual strips to reconstruct the segment of the track inside the drift gap, providing precise position information.

The production of Micromegas detectors for the NSW involves four types of quadruplets (LM1, LM2, SM1, and SM2) with trapezoidal shapes and dimensions ranging from 2 to 3 m^2. The production is carried out by institutions from France, Germany, Greece, Italy, and Russia. A schematic view of the small and large MM sectors is shown in Figure 3.16.

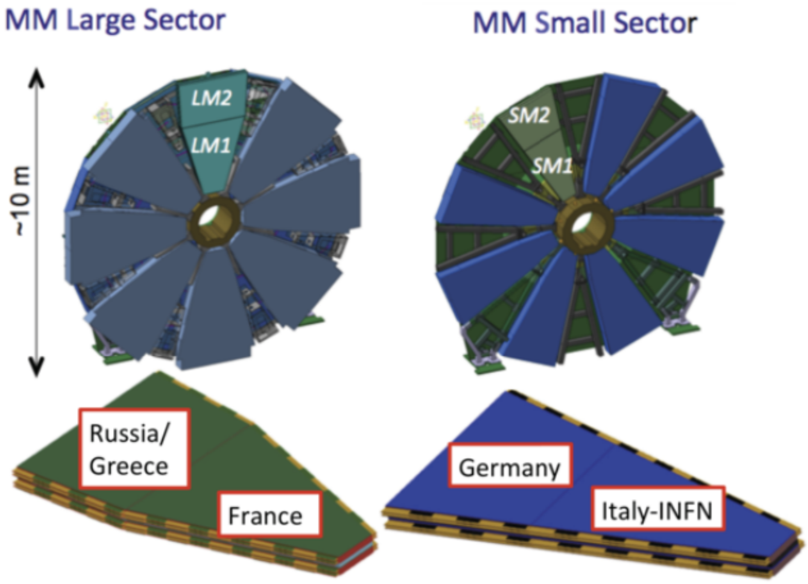

FIGURE 3.18: A schematic view of the small and large MM sectors.

3.2.5 The Forward Detectors

The ATLAS forward region is covered by three smaller detector systems [35]. The main function of the first two systems is to determine the luminosity delivered to ATLAS. LUCID $(LUmi-nosity\ measurement\ using\ Cerenkov\ Integrating\ Detector)$ is located $\pm 17 m$ away from the interaction point. It serves as ATLAS' primary online relative-luminosity monitor and detects inelastic p-p scattering in the forward direction. ALFA ($Absolute\ Luminosity\ For\ ATLAS$) is the second forward detector. It is made up of scintillating fiber trackers housed inside Roman pots that are designed to approach as close as $1mm$ to the beam and is situated at $\pm 240m$ from the interaction point. The Zero-Degree Calorimeter ZDC, the third system, is crucial in establishing the centrality of heavy-ion collisions. It is situated $\pm\ 140\ m$ from the interaction point, just beyond the point where the common straight-section vacuum pipe splits again into two distinct beam pipes. The ZDC modules, which measure neutral particles at pseudorapidities $|\eta|\ \geq\ 8.2$, are layers of alternating quartz rods and tungsten plates.

3.2.6 Trigger, readout, data acquisition, and control systems

The Detector Control System (DCS), the Timing- and Trigger-Control Logic, and the Trigger and Data Acquisition ($TDAQ$) systems are divided into sub-systems that are typically connected to sub-detectors and share the same logical components and building blocks.

Level-1 ($L1$) [36], Level-2 ($L2$), and the event filter are the three distinct level of the trigger system. The L2 and event filter together form the High-Level Trigger (HLT) [37]. Every trigger level improves the choices made at the level before it and, if necessary, adds new selection criteria. At the L1 trigger accept rate, the data acquisition system receives and buffers event data from the detector-specific readout electronics through 1600 point-to-point readout links. The first level uses a limited amount of the total detector information to make a decision in less than 2.5 μs, reducing the rate to about 75 kHz. The two higher levels access more detector information for a final rate of up to 200 Hz with an event size of roughly 1.3 $Mbyte$.

3.2.6.1 The Trigger System

The L1 trigger looks for huge amounts of total and missing transverse energy as well as high transverse-momentum muons, electrons, photons, jets, and τ- leptons decaying into hadrons. Its selection is based on information from a subset of detectors. High transverse-momentum muons are identified using trigger chambers in the barrel and end-cap regions of the spectrometer. Selections for calorimeters are made using reduced-granularity data from each calorimeter. The central trigger processor processes data from the L1 muon and calorimeter triggers and implements a trigger 'menu' made up of combinations of trigger options. It is also possible to pre-scale trigger menu items, which enables the best possible use of the bandwidth as luminosity and background conditions vary. Events that pass the L1 trigger selection are sent on through point-to-point links to the next stages of the detector-specific electronics and then to the data acquisition. A schematic view of the ATLAS trigger and data acquisition system is shown in Figure 3.19

Each time an event occurs, the L1 trigger also specifies one or more Regions-of-Interest $(RoI's)$ of those regions within the detector where the selection process has found interesting features. The RoI data provide details about the kind of feature found and the requirements that were met, such as a threshold. This information is subsequently used by the high-level trigger.

The RoI data, delivered by the L1 trigger across a dedicated data route, is used to seed the L2 selection. The L2 selections utilize all the available detector data within the RoI region, which constitutes around 2% of the total event data, at full precision and granularity. The L2 menu aims to reduce the trigger rate to nearly $3.5\ kHz$, and the processing time per event is approximately $40\ ms$ on average. The final selection stage is performed by the event filter, which reduces the event rate to approximately $200\ Hz$. The event filter uses offline analysis techniques to make its selections, and the average processing time per event is roughly four seconds.

3.2.6.2 The readout architecture and data acquisition

The Readout Drivers $(ROD's)$, which are detector-specific functional elements of the front-end systems, achieve a higher level of data concentration and multiplexing by combining information from several front-end data streams. Despite the fact that each sub-detector employs unique front-end electronics and RODs, these parts are constructed from standardized blocks and are subject to common requirements. Different functional parts are included in the front-end electronics sub-system:

- the front-end analogue or analogue-to-digital processing,
- the L1 buffer, where the data (analog or digital) is stored for a period of time sufficient to account for the L1 trigger latency,
- the derandomizing buffer where data for an L1 trigger accept is kept before being forwarded to the next level. This component is required to support the maximal instantaneous L1 rate without introducing significant deadtime (maximum 1%),
- the dedicated links or buses which are used to transmit the front-end data stream to the next stage.

Once an event is approved by the L1 trigger, the information from the pipelines is moved out of the detector and directed to the ROD's. The digitized signals are organized into a raw data format before being sent to the DAQ system. The RODs follow certain guidelines established by ATLAS, such as defining the data format of the event, outlining error detection and recovery methods to be employed, and specifying the physical interface used for transmitting data to the DAQ system.

The readout system, which is the initial stage of the DAQ, receives and temporarily stores the data in local buffers. The L2 trigger subsequently asks for event data connected to RoI's. The events chosen by the L2 trigger are then sent to the event-building system and subsequently to the event filter for the final selection. The CERN computer center permanently stores the events chosen by the event filter. The data acquisition also enables the configuration, control and monitoring of the hardware and software components that together provide the functionality for data collection.

The DCS acts as a homogeneous interface between all sub-detectors and the technical infrastructure of the experiment and permits the coherent and safe operation of the ATLAS detector hardware. It controls, continuously monitors and archives the operational parameters, signals any unusual behaviour to the operator, and allows automatic or manual corrective actions to be taken. To synchronize the state of the detector with data collection, the DCS also permits bi-directional communication with the data acquisition system. Additionally, it manages communication between the sub-detectors and other independent operated systems, including the ATLAS magnets, the LHC accelerator, the CERN technical services and the detector safety system.

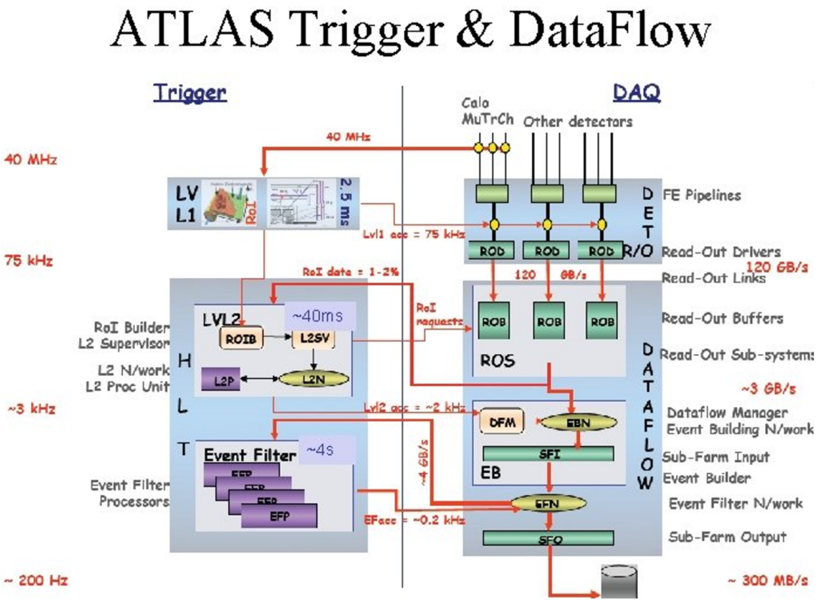

FIGURE 3.19: A schematic view of the ATLAS trigger and data acquisition system.

3.2.7 The Magnet System

ATLAS has a special hybrid system of four sizable superconducting magnets with 22 m diameter and 26 m length [38]. This magnetic system has four superconducting magnets which provide the magnetic field over a volume of approximately $12,000 m^3$, $1.6 GJ$ of stored energy. A schematic view of the ATLAS magnet system is shown in Figure 3.5. The spatial arrangement of the coil windings is shown in Figure 3.20. The ATLAS magnet system, consists of:

- a solenoid, which is aligned on the beam axis and produces a 2 T axial magnetic field for the inner detector, while minimising the radiative thickness in front of the barrel electromagnetic calorimeter,
- a barrel toroid and two end-cap toroids, which provide a toroidal magnetic field of approximately 0.5 T and 1 T for the muon detectors in the central and end-cap regions, respectively.

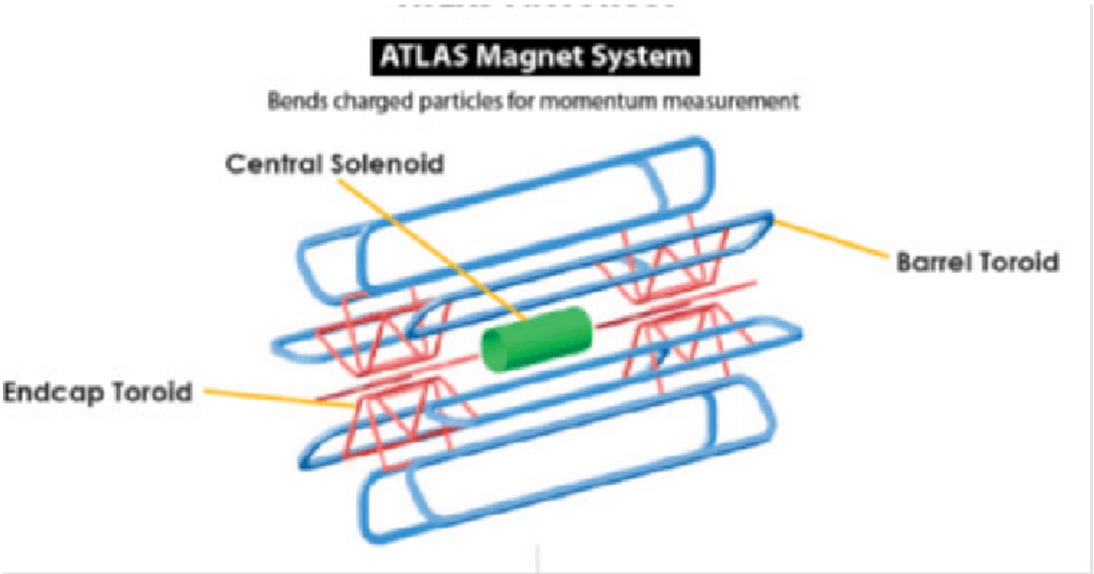

FIGURE 3.20: A schematic view of the ATLAS magnet system.

3.2.7.1 The central solenoid

The central solenoid [39], which is shown in Figure 3.21, is designed to produce a $2T$ axial field (1.998 T at the magnet's centre at the nominal 7.730 kA operational current). The solenoid assembly contributed a total of 0.66 radiation lengths at normal incidence as a consequence of a layout optimization that kept the material thickness in front of the calorimeter as low as possible in order to achieve the targeted calorimeter performance. For this purpose, the solenoid windings and LAr calorimeter share a common vacuum vessel resulting the elimination of the two vacuum walls. Between the solenoid and the inner wall of the cryostat, a second heat shield made of 2 mm thick aluminum panels is installed. In a 12 mm thick Al 5083 support cylinder, the single-layer coil is coiled using a high-strength $NbTi$ conductor that has been specially created to achieve a high field while optimizing thickness. The solenoid has an axial length of 5.8 m with inner and outer diameters of 2.46 m and 2.56 m, respectively, while the coil weighs 5.4 $tonnes$ and 40 MJ of energy is stored in it. In order to achieve a compliance with the design requirement of an extremely light-weight structure, it needs a stored-energy-to-mass ratio of only $7.4\,kJ/kg$ at nominal field. The flux is returned by the steel of the ATLAS hadronic calorimeter and its girder structure. In roughly 30 minutes, the solenoid is charged and discharged. In the case of a quench, the cold mass's enthalpy absorbs the stored energy and increases its temperature to a safe value of 120 K maximum. Within a day, re-cooling to 4.5 K is accomplished.

The coil and warm-to-cold mechanical support, which maintains the concentricity of the windings, work together to counteract the electromagnetic forces. All solenoid services are sent to the appropriate control dewar through an S-shaped chimney at the top of the cryostat.

FIGURE 3.21: Bare central solenoid in the factory after completion of the coil winding.

3.2.7.2 The barrel toroid

Figure 3.22 shows the barrel toroid [40] as installed in the underground cavern. The magnetic field of the barrel toroid, which consists of eight coils enclosed in individual racetrack-shaped, stainless-steel vacuum vessels, fills the cylindrical volume surrounding the calorimeters and both end-cap toroids. There are eight inner and eight outer rings of struts that support the coil assembly. The barrel toroid system's overall length is $25.3\,m$, and its inner and outer diameters are 9.4 m and 20.1 m, respectively.

The barrel and end-cap toroids use essentially the same conductor and coil-winding technology, which is based on winding a pure Al-stabilized Nb/Ti/Cu conductor into pancake-shaped coils, followed by vacuum impregnation.

To counteract the net Lorentz forces of around 1400 tonnes per coil that are directed inward and the self-weight of the toroids, Al-alloy struts are mounted between the eight coils. The barrel toroid structure still deflects significantly under its own weight, but after the temporary support structure is released, and the toroid is loaded with its own weight of 830 tonnes and an additional 400 tonnes of weight from the muon chambers, the final shape of the toroid bore is cylindrical. To allow for structure deflection during load transfer from the temporary support structure, the toroid coils are installed in calculated positions on an oval that is longer by 30 mm in the vertical direction. Since the release and removal of the installation supports, the upper edge of the toroid has moved down by about 26 mm, demonstrating the precise installation of the design values within a few millimeters.

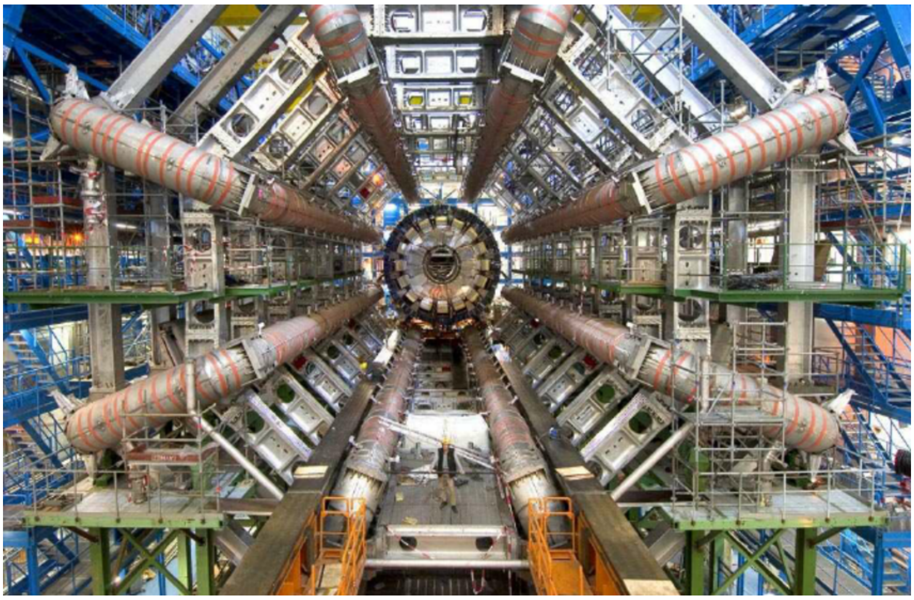

FIGURE 3.22: The barrel toroid as installed in the underground cavern.

3.2.7.3 The end-cap toroids

The two end-cap toroids [41] produce the magnetic field needed to maximize the bending power in the muon spectrometer system's end-cap regions. They can slide along the middle rails and are supported off, making it easier to access and maintain the detector by opening it. Eight flat, square coil units and eight keystone wedges are assembled into a single cold mass for each end-cap toroid, which is then bolted and glued to form a solid structure that can withstand the Lorentz forces.

The cold masses were put together and placed within their cryostats at CERN. Figure 3.23 depicts the interior of the first end-cap toroid right before the vacuum vessel is sealed. The adjustment of the cold mass supports is a vital phase in the integration process. Cold mass and vacuum vessel have respective weights of 140 and 80 tonnes. The whole structure, with the exception of the windings, coil supports and bore tube, is built of aluminum alloy. The end-cap toroids were among the heaviest items lowered into the tunnel, each weighting 240 tonnes. Each of the end-cap toroid cold masses are pushed against the stops mounted on the eight barrel toroid coils by a Lorentz force of 240 tonnes. Therefore, achieving the proper correct sharing of the forces in the axial tie-rods has been a crucial design goal.

FIGURE 3.23: The end-cup toroid interior.

Chapter 4

Data and Monte-Carlo samples

In this chapter, the real data and the Monte-Carlo samples used for this study are presented. The simulations are a very crucial part of the analyses of particle collisions as they include the generation of events for a given process based on an assumed theoretical model. Information of events at this step is referred to as truth-level or particle-level. In order to compare them with the real data, the detector effects and the subsequent reconstruction chain have to be taken into account. This information is referred to as detector-level or reconstruction-level analysis. A detailed description of the procedure following the event generation is presented in [42].

4.1 Data samples

The data samples used for this study, are samples of proton-proton (*pp*) collisions from the LHC, collected by the ATLAS detector during the full Run 2, between 2015 and 2018, at a centre-of-mass energy of $\sqrt{s} = 13\,TeV$. The data were selected using single lepton triggers, as described in Section 6.2.1 and only those with a $25\,ns$ bunch spacing are taken into account. The selected dataset is required to pass quality criteria based on data-quality flags, by means of a good run list (GRL) recommended for all analyses. The GRL ensures that the detector was operating correctly during data was recorded. The dataset corresponds to an integrated luminosity of $140.0\ fb^{-1}$ [43][1]. The uncertainty in the combined 2015-2018 integrated luminosity is $0.83\,\%$, obtained using the LUCID-2 detector [44] for the primary luminosity measurements, complemented by measurements using the inner detector and calorimeters.

---

[1] In this thesis, for both the WZ VBS and diboson analyses, the same dataset is used but the luminosity has been re-estimated from $139.0\ fb^{-1}$, which is used in the WZ dibosn analysis, to $140.0\ fb^{-1}$, which is used in the WZ VBS analysis

4.2 Monte-Carlo simulations

4.2.1 Simulation of hard collisions in LHC

The simulation of a hard collision is a very complex procedure. An example of a collision is shown in Figure 4.1 [45] and it is better to be splitted into multiple phases in order to be studied. In general, the matrix element calculation in perturbation theory produces the most precise predictions but due to the energy-dependent couplings, this method is invalid at low energies. At these energy scales, higher-order terms are not sufficiently suppressed to warrant their neglection. For this reason, the full hadron collision is splitted along the energy scale of the individual interactions.

The simulation of a hard collision is a very complex procedure. Figure 4.1 [45] illustrates the structure of a simulated hadron collision. To simplify the simulation process, the collision must be divided into several phases. The most accurate predictions are typically achieved through matrix element calculation in perturbation theory. However, at low energies, due to the increasing couplings and infra-red logarithms at each order, higher-order terms are not suppressed sufficiently to justify their neglection. To account for these non-perturbative effects, various models have been developed based on previous measurements. As a result, the full hadron collision is split along the energy scale of each individual interaction.

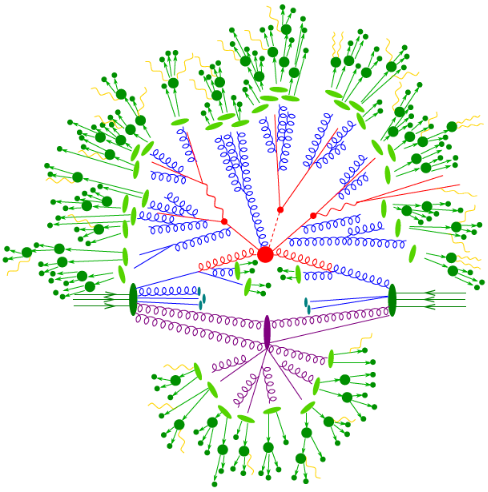

Figure 4.1: Schematic representation of a $t\bar{t}H$ event as produced by an event generator. The hard interaction (big red blob) is followed by the decay of both top quarks and a Higgs boson (small red blobs). Additional hard QCD radiation is produced (red), and a secondary interaction takes place (purple blob) before the final state partons hadronise (light green blobs) and hadrons decay (dark green blobs). Photon radiation occurs at any stage (yellow).

4.2.1.1 Procedure of event generation

Hard Process: The hard process is the part of the interaction that occurs at the largest energy scale and it is computed in fixed-order perturbation theory from the matrix elements of the given scattering process. In proton-proton collisions the cross section can be written as

$$\sigma = \sum_{a,b} \int_0^1 \mathrm{d}x_a \, \mathrm{d}x_b \int \mathrm{d}\Phi_n \, \mathrm{PDF}_a \left(x_a, \mu_\mathrm{F}\right) \cdot \mathrm{PDF}_b \left(x_b, \mu_\mathrm{F}\right) \cdot \frac{1}{2 x_a x_b s} |\mathcal{M}|^2 \left(\Phi_n; \mu_\mathrm{F}, \mu_\mathrm{R}\right) \tag{4.1}$$

where a and b run over the initial partons, x_a and x_b are the momentum fractions of the partons a and b with respect to their parent hadron, μ_F is the factorization scale, μ_R is the renormalization scale, parton distribution function $\mathrm{PDF}_a \left(x_a, \mu_\mathrm{F}\right)$ is the probability to find a parton of type α with a momentum fraction x when a proton is probed at a scale μ_F, $\mathrm{d}\Phi_n$ is the differential phase space element for n-final state particles and $\mathcal{M} \left(\Phi_n; \mu_\mathrm{F}, \mu_\mathrm{R}\right)$ is the matrix element for the transition from the initial to the final state.

This equation holds to all orders in perturbation theory. However, the perturbation theory is unable to provide an accurate description of the low-energetic splittings in the proton, which are taken care of by the PDFs. The scale at which the transition from the hard process to PDFs occurs is determined by the factorization scale.

It is necessary to determine the squared matrix element in order to compute the cross section of the hard process. There are two ways to determine the matrix elements: they can be pre-defined in the event generator or they can be determined dynamically based on specified initial and final states given a set of constraints, such as those on propagators or the coupling order. The pre-defined matrix elements are very efficient but the dynamically generated matrix elements offer a great flexibility to specify the processes to be taken into consideration.

The matrix elements depend on the particle kinematics of the considered phase space as well as on the μ_F and μ_R. These scales are unphysical and there is not an exact way to define what are the ”correct” μ_F and μ_R. These scales can be set to fixed values, but they can also be chosen dynamically based on the kinematics of the event. μ_F and μ_R are mostly set to be equal to typical momentum transfers or resonance masses.

Due to the dimensionality and the complexity of the phase space integrals a Monte-Carlo method is used for the numerical integration of the squared matrix element in the allowed phase space region.This method performs better than other integration methods specifically at high dimensions. The main procedure is to evaluate the integral not on a fixed grid, but at a randomly distributed set of points.

Resonances and even divergencies in the matrix element must be handled carefully in fixed-order calculations. Divergencies can be excluded from the the phase space using a suitable set of selection criteria, such as those based on transverse momenta, invariant masses, or angular distances. Without these additional modifications, resonance calculations would result in significant inefficiencies.

Assigning a weight to each event, which is based on the squared matrix element, is a simple technique to take resonances into consideration. Nevertheless, resonances can result in weights which vary by several orders of magnitude. This large fluctuations of the event weights can be problematic since each event must pass a computationally expensive detector simulation. To overcome this problem, an "unweighting" procedure is followed, and phase space points are rejected based on the probability of the squared matrix element. This, on the other hand, causes inefficiencies during the generation of events. The squared matrix element must either be flat or possible to be turned into a flat distribution in order for this "unweighting" procedure to be most effective. Such transformations are made automatically by phase space integrators in order to decrease the inefficiencies and to improve the phase space sampling performance. Finally, in order to improve the accuracy of the generated cross-section, the event generators optimize these transformations.

Parton Shower: Due to the phase space and the increased complexity of the matrix elements, the hard process is often calculated with no or a few additional QCD emissions. In order to simulate such additional radiations from the particles in the event which can result from partons in their initial and final state, the parton showers are used. The parton shower modelling follows the Markov chain technique [46]. By adding parton emissions, this method evolves the parton ensemble from the scale of the hard process down to a few GeV, where QCD perturbation theory fails. This parton shower method approximates higher-order contributions to all orders.

There are various ways to implement parton showers, which differ in the evolution variable, the kinematic scheme for the distribution of the recoil, or the splitting functions. The $k_\perp$-ordered shower, the angular-ordered shower, and the dipole shower are the most widely used implementations. The treatment of soft emissions for two partons that are near to one another differs between the first two implementations. The splitting functions in the $k_\perp$-ordered shower must be modified to prevent the double counting of such emissions, while in angular-ordered showers, this double-counting is automatically avoided. On the other hand, dipole showers avoid this double counting since the particles are emitted from color dipoles rather than single particles. A color-flow is assigned to the event during each iteration of the shower algorithm, and the shower scale evolution is performed globally for the event.

Finally, particularly for the initial state radiation, the additional splittings during the parton shower simulation cause a momentum recoil on the rest of the event. Momentum conservation must be violated at intermediate phases for the $k_\perp$-ordered and angular-ordered showers in order to allow for the $1 \rightarrow 2$ splittings, while dipole showers do not violate momentum conservation because they use $2 \rightarrow 3$ splittings. Due to the propagation of these recoil effects to the full event, slight necessary momentum boosts and adjustments are applied in order to restore momentum conservation and the overall kinematic [47].

Hadronization: As the parton shower has evolved in an energy scale of a few GeV, where the QCD pertubation theory is not valid, phenomenological models must be used to explain how colorless hadrons are created from unobservable colored partons. For this purpose, two models are implemented in the event generators: the string and the cluster models. These models explain how quark-antiquark pairs are produced after the separation of colour-connected partons according to their momenta.

The string model is based on the confinement property explained in Section 2.1.3 and uses many free parameters in order to match the observed data. The cluster model is based on the so-called pre-confinement property of parton showers. It is shown that the colour structure of the shower at any evolution scale is such that colour singlet combinations of partons (clusters) can be formed with an asymptotically universal invariant mass distribution that is independent of the scale of the hard process or the starting scale of the shower. Compared to the Cluster mode, the string model provides in general better agreement with the observed data, as it has fewer free parameters and more components based on perturbative QCD.

Decay of unstable particles: Following the hadronization phase of event generation a number of unstable hadrons are produced, which must be decayed into particles that are stable within the detector size. For the decay of these particles, it is also important to take into account the effects of the spin correlation and excited unstable particles. Some shower generators simulate these decays using external packages, such as TAUOLA [48] for tau-lepton decays or EvtGen [49] for hadron decays. Newer methods use models based on experimental data along with matrix element calculations.

QED radiation: There are two approaches for the simulation of electromagnetic radiation in the event generators. The most common is to use the same parton shower algorithm that was used for the simulation of QCD radiation considering electromagnetically charged instead of coloured particles. This can cause problems in some processes where there are destructive contributions that would be suppressed by $1/N_c^2$ in QCD, but which are leading in QED. The advantage of this approach is that both QED and QCD radiation can be generated simultaneously and it is the most common approach in Monte Carlo simulations. The Yennie-Frautschi-Suura (YFS) formalism [50] offers an alternate approach. In this approach, the radiation of multiple photons is simulated iteratively and finally corrected to match the event-wide analytical calculation for a specified number of photons. The major advantage of this technique is that allows the exact inclusion of higher-order corrections for the distributions of radiated photons.

Underlying event: In the hadron collisions, there can be effects which are not directly related to the hard interaction - the underlying event. Two distinct partons of a pair of the initial hadrons initiate the hard process but the remaining partons of the hadrons interact softly with each other. On the other hand, there can be more interactions within the same bunch crossing depending on the density of the hadron bunches. These extra interactions are referred to as $multiple parton interactions\ (MPI)$. In these interactions, the high-energy effects can be explained by perturbative QCD, while the low-energy effects are modelled to match data. Finally, the main interaction can be impacted by the particles produced by MPI.

4.2.1.2 Matrix element and NLO matching and merging

To model additional QCD radiation beyond the Born process, which has the lowest coupling order, two approaches are possible: by using the hard process or the parton shower. The hard process is better at describing individual hard and wide-angle gluon emissions, while the parton shower is the only way to model the numerous gluon emissions at low energies and angles. However, due to large logarithms and rapidly increasing dimensionality of phase space with each emission, it is impossible to include these in the hard process calculation. When extending beyond LO calculation of the Born process, combining with the parton shower is complicated, and careful consideration of many details is required. An NLO calculation with a parton shower must avoid double-counting of emissions.

Various methods are accessible for a correct combination of the hard process and the parton shower, depending on how the matrix element calculation is arranged.

Matching Matching algorithms are available and they are used in order to combine a complete NLO matrix element calculation with a parton shower. These algorithms subtract the effects of the parton shower on the Born process to order a_S from the matrix element directly, ensuring that the matrix element calculation is matched to the parton shower.

The parton shower approximates the full calculation to all orders by incorporating leading logarithmic contributions in each order of α_S, which, if naively combined, would be double-counted. Two common formalisms for NLO matching are the MC@NLO-style [51] and the POWHEG-style [52] matching.

The MC@NLO-style calculates leading logarithmic terms explicitly and subtracts them from the full NLO matrix element calculation, avoiding double-counting but introducing the possibility of negative event weights.

In contrast, the POWHEG-style generates the first parton shower emission as part of the matrix element generator, avoiding the need for subtraction terms and negative weights. A method similar to the parton shower can be used to calculate the non-emission probabilities, which are represented by Sudakov form factors [53], directly from the real-emission matrix element instead of using approximations. This approach eliminates the need for negative weights and subtraction terms. The hard process cross-section is therefore identical to that of the complete NLO calculation. However, this approach shifts some of the complexity to the parton shower simulation, which must be adjusted to match the emission pattern of the hard process generation, ensuring that the already generated emission is the hardest in the shower simulation and that the full kinematic region for shower emissions is covered. Truncated and vetoed showers can be used to achieve this.

Merging Merging algorithms are used to combine multiple real emissions included as individual processes at tree level, allowing for the inclusion of additional emissions from the matrix element. These are called LO $multi - leg$ setups. The merging algorithm ensures that parton shower emissions overlapping with the matrix element calculation are vetoed.

Two common merging schemes are the MLM-scheme [54] and the CKKW-scheme [55], which differ in implementation details but are based on similar principles.

MLM-scheme is based on empirical observations and arguments. After the simulation of the parton shower, jets are identified and paired with matrix element partons based on their angular separation. Events where a matrix element parton is not paired with a jet or where a jet is matched with multiple matrix element partons are discarded. This ensures that each matrix-element parton is treated as a separate emission. If an event does not originate from the subprocess with the largest number of additional emissions in the hard-process calculation, it is discarded if an additional jet is identified that is not matched with any of the matrix element partons. The accuracy of this approach is dependent on the specific criteria used for jet clustering and matching, and there is no formal method to assess its accuracy.

On the other hand, CKKW-scheme provides an alternative approach to merge the parton shower and matrix-element calculations. This scheme involves the introduction of a merging scale that divide the phase space available for emissions. If an event has an additional emission below this merging scale compared to the Born process in the matrix-element calculation, it is vetoed. For events with a non-maximal number of considered

> emissions, parton shower emissions above the merging scale are vetoed to avoid double-counting. This veto mechanism ensures that the parton shower calculation dominates for soft emissions while the matrix-element calculation dominates for hard emissions. Non-emission probabilities and different scales for the strong coupling constant are also taken into account, and typical merging scales are around $\mathcal{O}(25\ GeV)$. Finally, the CKKW-scheme initially obtained Sudakov form factors through an analytical approach to correct non-emission probabilities. However, the CKKW-L scheme is an expansion of this method that generates Sudakov form factors through event vetoing rather than emissions, making it more adaptable for new showers.

In recent years, implementations for NLO merging have become available. The procedures are mostly based on combinations of one of the mentioned merging schemes with either MC@NLO or POWHEG-style matching.

4.2.2 Monte-Carlo generators

4.2.2.1 MadGraph5_aMC@NLO

MadGraph5_aMC@NLO [56] combines features of the aMC@NLO and MadGraph5 [57] and it is a general-purpose and fully automated Monte Carlo event generator. Automated calculations at NLO QCD can be performed using this generator. This includes the automatic cancellation of infrared singularities, as well as the evaluation of renormalized one-loop amplitudes and the matching to parton showers.

The MC@NLO approach is used for the matching of the matrix element calculation to the parton showers. This generator does not provide the parton shower simulation and it is necessary to employ external tools to simulate it. Herwig and Pythia are commonly used for the parton shower. At the tree level, the merging to parton showers is based on the MLM-scheme, explained earlier. For NLO calculations the FxFx scheme [58], which combines the MLM merging with MC@NLO-style matching, is available for merging. When Pythia 8 is used for the parton shower simulation also CKKW-L style merging is available.

The automated method of NLO computations also holds for renormalizable extensions of the SM. MadGraph5_aMC@NLO fully supports the FeynRules models [59] which produce events beyond the Standard Model.

On-the-fly calculations can be made for systematic variations of the renormalization and factorization scales, the PDF-set and some of the relevant model parameters, such as particle masses or BSM coupling parameters.

4.2.2.2 $SHERPA$

$SHERPA$ [60] is another general-purpose Monte Carlo event generator for the simulation of particle collisions. The best possible merging of the matrix element calculation and the parton shower was a key consideration in the framework design. This generator accomplishes this automatically by covering the main aspects of the simulation internally without the need to rely on external interfaces. Interfaces to external libraries can be used for collider setups with non-default PDFs or to generate events for BSM physics models.

In $SHERPA$ framework the tree-level matrix elements are generated using two tree-level matrix element generators AMEGIC [61] and COMIX [62] while the external loop-matrix element providers BLACKHAT [63], OPENLOOPS [64], or RECOLA [65] used for the calculation of one-loop matrix elements. Also there are two algorithms available for the parton shower simulation. The CSSHOWER [66], which uses the Catani-Seymour dipole factorization [67], is the default one, while the DIRE [68] shower is an alternative shower that employs a hybrid strategy between a dipole shower and standard collinear shower evolution. Hadronization is based on the cluster fragmentation model.

The MC@NLO-style matching is used for the matching of the NLO matrix elements. The MEPS@NLO merging algorithm, which is based on the CKKW-L scheme and truncated showers, supports and employs LO merging. The MEPS@NLO merging method [69] has been expanded to include MC@NLO-matched processes for the merging of the NLO processes.

QED radiation is implemented with accuracy at leading order in α for some processes. Also there is a decay library for the simulation of hadron decays and τ. Except that, it supports on-the-fly calculations of the systematic variations of the renormalization and factorization scales, and the PDF-set, also supports many output formats, including HepMC [70] and Les Houches (LHE) [71].

Per-process enhancement factors, which allow adjusting the proportions of produced events per subprocess, are supported by $SHERPA$. Events for a subprocess with an enhancement factor $> \ 1$ are produced more frequently when a generation has many subprocesses, such as various jet multiplicities, and the event weights are changed to correct the final distributions. As a result some regions of the phase space can statistically be improved thanks to such enhancement factors.

4.2.2.3 Pythia 8

A particularly popular event generator with a focus on simulating the parton shower and soft QCD effects is PYTHIA 8 [72]. There are two types of showers in PYTHIA 8: the p_T-ordered which is the default and the dipole shower. Hadronization is modelled using the Lund string fragmentation framework [73]. Finally in this generator the basic modelling of particle decays is implemented but the polarization, the spin effects and non-trivial matrix element effects are ignored for many particles.

4.2.2.4 HERWIG 7

HERWIG 7 [74] is a general-purpose event generator that focuses on soft QCD, parton shower, and hadronization effects. It can be used standalone or in shower mode, which simulates the parton shower for events produced from a hard process generator. Both an angular ordered shower and a dipole shower are supported for this generator. The hadronization is based on the cluster hadronization model. Hadron decays are simulated using matrix elements, including spin correlations and off-mass shell effects where possible.

In recent versions, the Matchbox [75] framework, for flexible NLO hard-process calculations combined with parton shower simulation is available when HERWIG 7 is running in standalone mode. Because built-in matrix elements are only available for a small number of SM processes, this framework is dependent on external libraries to provide tree- or loop-level matrix elements. Several external libraries, such as MG5_AMC (tree- and loop-level), OPENLOOPS (loop-level), or VBFNLO (tree- and loop-level, see below), are available.

HERWIG 7 has the capability to simulate the hard process through matrix elements and presents various methods for combining the calculation and the parton shower simulation. For this purpose, both POWHEG and MC@NLO matching approaches are included. Furthermore, HERWIG 7 has implemented NLO merging of multileg processes, which combines CKKW-L style merging with MC@NLO style matching and requires the use of a dipole shower. The shower simulation enables on-the-fly computation of systematic variations of the renormalization and factorization scales, the PDF-set, and some shower parameters.

4.2.2.5 Other Monte-Carlo generators

VBFNLO [76] an event generator that is specialized for the hard process and concentrates on interactions involving electroweak gauge bosons. The matrix elements have been manually optimized and included within the generator, which means that only a limited number of processes are supported. The Standalone VBFNLO provides event generation at the LO level or the calculation of the total cross-section at NLO. The NLO matrix elements can also be used for event generation by employing the HERWIG 7 Matchbox interface.

PowhegBox [77] an event generator that is tailored for a specific process and incorporates the POWHEG matching scheme. Matrix elements for various processes have been manually implemented with varying levels of accuracy. The event generator permits the on-the-fly calculation of systematic variations for the renormalization and factorization scales, as well as for the PDF set.

4.2.3 Monte Carlo samples

Signal and background processes are modelled using Monte Carlo (MC) simulation. The signal and background MC samples used in this study include the simulation of pile-up interactions performed with Pythia 8. Additionally, the $\langle\mu\rangle$ value in data is scaled by $1/1.03$ [78], based on studies of the data/MC agreement for the number of vertices vs $\langle\mu\rangle$. These procedures are performed using the PileupReweightingTool [79]. The full list of Monte Carlo samples is presented in Appendix B.

4.2.3.1 Inclusive signal simulation

The signal MC samples are generated with W and Z gauge bosons decays into muon, electron and τ leptons. τ leptons decay to all known final states.

The primary sample used for $W^{\pm}Z$ simulation is Powheg+Pythia8 with NLO QCD matrix elements matched to parton showers (PS). The CT10NLO PDF set [80] is used for the hard-scattering process, while the CTEQ6L1 PDF set [81] is used for the PS.

A NLO→ NNLO k-factor of 1.18 is derived in the fiducial phase space from the latest calculations of $W^{\pm}Z$ production [82], by comparing the prediction of our Powheg+Pythia MC sample to MATRIX predictions in our fiducial PS [83]. It is used to rescale globally the Powheg+Pythia8 MC prediction.

4.2.3.2 Electroweak $W^{\pm}Zjj$ MC simulation

The $WZjj-$EW process was generated at LO by the MadGraph generator interfaced with Pythia 8 for the modelling of the parton shower, hadronisation and underlying event. The parton distribution function set was `NNPDF3.0NLO` [84]. In the simulation of the parton shower the `NNPDF2.3` [85] PDF set was used. The default dynamic renormalisation and factorisation scale set by MadGraph (option“-1”) is used. It is important to note that for the parton shower, the dipole recoil dipole model is used. This type of parton shower was found to provide a better description of deep-inelastic scattering data [86] in general. It found, for example, to be advantageous for the description of VBS $W^{\pm}W^{\pm}jj$production [87] or $W^{\pm}Zjj$ production [88].

Leptons are required to have $p_T > 4GeV$ and partons are required to have $p_T > 15GeV$. In order to avoid divergences during generation, partons are required to be separated by $\Delta R > 0.4$. Additionally, the separation between lepton-lepton and lepton-parton pairs is required to be $\Delta R > 0.2$.

This sample includes b-quarks as well in the matrix element diagrams. As a consequence, the tZj process is also included, which is an important background to our analysis. Therefore, the sample is split in events with or without a b-quark in the initial state of the matrix element diagrams to separate the $WZjj-\mathrm{EW}$ signal and the tZj background.

Finally, the LO events generated with MadGraph were interfaced with the Herwig parton shower in order to estimate uncertainties related to the parton shower.

4.2.3.3 QCD initiated $W^{\pm}Zjj$ MC simulations

The process $pp \to WZ \to \ell\nu\ell\ell$ was generated at NLO in QCD with MadGraph and Pythia 8, including one or two extra jets: $pp \to WZ + j \to \ell\nu\ell\ell + j$ and $pp \to WZ + 2j \to \ell\nu\ell\ell + 2j$, and merged by the FxFx scheme [56]. The jets had a minimum p_T of 10 GeV and the k_T merging scale was set at 25 GeV. The parton distribution function set was NNPDF3.0NNLO. The default dynamic renormalisation and factorisation scale set by MadGraph (option "-1") is used.

As an alternative generator, Sherpa 2.2.2 is used to model $W^{\pm}Z$ events with up to one parton at NLO and 2 to 3 partons at LO. Generator level cuts require $m_{\ell\ell} > 4\ GeV$, $p_T(\ell_1) > 5\ GeV$, $p_T(\ell_2) > 5\ GeV$. Sherpa generator provides full modelling of the high-energy pp collisions, including hard-scattering, parton shower, hadronization and underlying event. In the generation of this sample diagrams with larger number of partons in the final state are weighted down. This results in a larger number of MC events for higher parton numbers and therefore smaller statistical uncertainties in phase spaces dominated by diagrams with more than 1 parton. This Sherpa sample is generated using the NNPDF3.0NNLO parton distribution function. The default dynamic renormalisation and factorisation scale set internally by Sherpa is also used.

4.2.3.4 Interference between $WZjj-\mathrm{QCD}$ and $WZjj-\mathrm{EW}$

For the simulation of the interference between $WZjj-\mathrm{EW}$ and $WZjj-\mathrm{QCD}$ also the MadGraph generator was used interfaced with Pythia 8, with the same parametrisation and cuts as used for the $WZjj-\mathrm{EW}$ simulation. Since there are only two jets in the final state, at LO only terms of α_S^2 at the matrix element-square level appear. In the phase space of the measurement, the interference represents 6 % of the $WZjj-\mathrm{EW}$ contribution.

4.2.3.5 Other background processes simulation

The background sources in this analysis include processes with two or more electroweak gauge bosons, namely ZZ, WW and VVV ($V = W, Z$); processes with top quarks, such as $t\bar{t}$ and $t\bar{t}V$ and tZ; or processes with gauge bosons associated with jets or photons ($Z + j$ and $Z\gamma$). MC simulation is used to estimate the contribution from background processes with three or more prompt leptons. Background processes with at least one misidentified lepton are evaluated using MC samples, which are estimated using data-driven techniques as described in Section 6.3.

The Sherpa 2.2.2 event generator was used to simulate both gg-initiated ZZ and $q\bar{q}$-initiated ZZ processes using the `NNPDF3.0NNLO` PDF set. It provides a matrix element calculation accurate to NLO in α_s for 0- and 1-jet final states, and LO accuracy for 2- and 3-jet final states.

Both the $t\bar{t}Z$ and $t\bar{t}W$ processes were generated at NLO in QCD with the MadGraph5_aMC@NLO MC generator, using the `NNPDF3.0NLO` PDF set, and interfaced with Pythia 8 for the modelling of the parton shower. k-factors of 1.12 and 1.1 respectively were used for the two samples.

Triboson events were simulated by the Sherpa 2.2.2 event generator at NLO accuracy with 0 additional partons and at LO accuracy with 1 and 2 additional partons.

The $t\bar{t}$ samples are generated at NLO with the Powheg MC generator interfaced to the Pythia 8 parton shower model, using `NNPDF3.0` in the event generation and `NNPDF2.3` in the simulation of the shower. The h_{damp} parameter that controls the emission of the first gluon is set to 1.5 times the top-quark mass. The A14 tune together with `NNPDF2.3LO` PDF set is applied for Pythia 8 showering.

$Z\gamma$ and $W\gamma$ events are generated with Sherpa version 2.2.2 at next-to-leading order NLO accuracy using the `NNPDF3.0NNLO` PDF set.

$Z + j$ processes are generated with the Powheg+Pythia MC generator at NLO using the `CT10` PDF set. The generated cross section is then rescaled to NNLO predictions using a k-factor of 1.026. For the modelling of the parton shower, Pythia 8 is used with the AZNLO tune [89]. In order to simulate the final QED radiation, the samples are interfaced to Photos++ [90].

The tZj sample is simulated using the MadGraph5_aMC@NLO v2.3.3.MC generator at NLO using the `NNPDF3.0`NLO PDF set, and interfaced with Pythia 8.230 for the modelling of the parton shower.

4.2.3.6 EFT MC samples

The Eboli-Garcia Effective Field Theory extension to the Standard Model was simulated using the $pp \rightarrow ll l\nu$ process at LO for the $\mathcal{L}_{S,0}$, $\mathcal{L}_{S,1}$, $\mathcal{L}_{S,2}$ $\mathcal{L}_{T,0}$, $\mathcal{L}_{T,1}$, $\mathcal{L}_{T,2}$, $\mathcal{L}_{M,0}$, $\mathcal{L}_{M,1}$ and $\mathcal{L}_{M,7}$ operators. For the $\mathcal{L}_{S,1}$, $\mathcal{L}_{T,0}$, $\mathcal{L}_{T,1}$, $\mathcal{L}_{T,2}$, $\mathcal{L}_{M,0}$ and $\mathcal{L}_{M,1}$ operators the MadGraph 2.6.5 and Pythia 8 are used, while for the $\mathcal{L}_{S,0}$, $\mathcal{L}_{S,2}$ and $\mathcal{L}_{M,7}$ operators the MadGraph 2.8.1 and Pythia 8 are used. All the samples are produced using the corresponding FeynRules model [91]. In the generation of the samples, the EFT dimension-8 operators were set to three times the existing limit[92][93] in order to create their pure-EFT (quadratic) and SM-EFT interference (linear) contribution terms, based on the decomposition method. For the $\mathcal{L}_{M,7}$ only the MC sample for the quadratic term is available but the effect of the interference term is negligible, as shown in Table 7.13, and it can be ignored. To produce the cross-term for the samples that study the effect of two EFT operators ($T_0 - T_1$, $T_0 - T_2$, $T_1 - T_2$, $M_0 - M_1$), the values for the coefficients in the pair were also taken as three times the existing limits. Finally as the $\mathcal{L}_{S,0}$ and $\mathcal{L}_{S,2}$ are not independent, they are considered as one operator by adding together their quadratic terms and their cross term.

As in the EW signal modeling, the dipole recoil shower option is used, by specifying `"dipoleRecoil=on"` in Pythia 8. For the dynamical scale generation parameter the value 2 is used [94], which corresponds to the following functional form of the factorisation and renormalisation scales μ_F and μ_R

$$HT = \sum_{i=1}^{N} \sqrt{m_i^2 + p_{T,i}^2}. \tag{4.2}$$

The parton distribution function NNPDF3.0 NLO set was used for the hard-scattering model and the NNPDF2.3 set was used for the shower modeling. Finally the A14 tuning was used for the shower modelling.

Furthermore, the generated leptons are required to have $p_{\mathrm{T}}^{l} > 4$ GeV and the partons to have $p_{\mathrm{T}} > 15$ GeV. The dR separation between lepton-lepton, parton-lepton and parton-parton pairs was set to be a minimum of 0.2.

MC generated events are then passed through the full detector simulation, producing a reconstructed dataset.

Chapter 5

Physics objects reconstruction

The ATLAS detector provides information about each pp collision in the form of tracking and energy deposits detected by its sub-systems. Advanced particle reconstruction methods are necessary to interpret this raw data in terms of the particles present in the event and their kinematic properties. This chapter explains these techniques in detail.

5.1 Electrons and photons

Electrons and photons can both be reconstructed [95] within the range of $|\eta| < 2.47$, excluding the $1.37 < |\eta| < 1.52$ barrel-to-end-cap transition region. This is made possible by using their energy deposits in the electromagnetic calorimeter (EMCal). Additionally, the reconstruction of electrons, greatly benefits from tracking information provided by the inner detector (ID).

The reconstruction process for electrons begins by interpreting the information from the EMCal. When electrons and photons pass through the dense medium of the EMCal, they initiate a showering process through cascading bremstrahlung and electron-positron pair production, respectively. This process results in the majority of their energy being deposited in the calorimeter, causing ionization in the liquid argon (LAr) and releasing electrons that are subsequently captured by the nearest electrodes. These extensive particle showers are spread across multiple layers and cells within the calorimeter. Each cell produces a distinct electrical signal that is directly proportional to the energy deposited in it. For reconstruction purpose, a sliding-window algorithm is employed to scan these cells and identify 3×5 cells fixed-size clusters. The algorithm is using a cell size $\Delta\eta \times \Delta\phi = 0.025 \times 0.025$, which corresponds to the granularity of the middle sampling layer. These clusters contain all cells from three sampling layers that are inside the sliding window. The algorithm aims to determine the position of the sliding window that maximizes the measured energy, and if the energy exceeds a threshold of $2.5\ GeV$, the corresponding cluster is designated as a seed cluster.

The clusters obtained from the previous step are then matched with tracks from the inner detector. These tracks are constructed from hits in different layers of the ID. Typically, electron track candidates consist of a total of 12 hits distributed among the IBL, pixel, and silicon strip layers. If a cluster cannot be matched with any tracks, it is identified as an unconverted photon. If the reconstructed seed cluster can be matched with at least one track originating from the hard-scatter (HS) vertex, it can be classified in two ways. Initially, the vertex of origin for the track is determined. If this vertex corresponds to the HS vertex, the cluster is labeled as an electron cluster (in the case where multiple tracks can be matched to the cluster, one track is selected based on the number of silicon hits and its closeness in ΔR to the cluster). If the track cannot be associated with the HS vertex, the cluster is identified as a converted photon. Photon conversion can contribute significantly to background in electron-focused analyses. In order to minimize the photon conversion background and to ensure the reliability of the association with the HS vertex, the tracks are required to fulfill certain conditions: $|d_0/\sigma_{d_0}| < 5\,mm$ and $|z_0 sin(\theta)| < 0.5\,mm$, where d_0 and z_0 are the transverse and longitudinal impact parameters, respectively, and θ is the track's polar angle.

After that, reconstructed electrons undergo identification requirements that vary in strictness or tightness based on different use-cases. These requirements aim to distinguish signal electrons (prompt) from other charged particles exhibiting similar characteristics, such as pions or converted photons. One commonly used identification criterion is the likelihood-based (LH) identification. The LH discriminant is built by combining various quantities related to the quality of reconstruction using a likelihood approach. The complete set of variables utilized to construct the LH discriminant can be found in [95]. This set includes measurements of reconstructed quantities such as electromagnetic shower shape variables, the quality of the associated track, its number of measurements in the silicon detectors (pixel or SCT) and the detection of transition radiation in the TRT. Additionally, variables associated with the quality of hits in the inner detector, such as d_0 and d_0/σ_{d_0}, and variables related to the quality of track-cluster matching, like the E/p ratio (which is the ratio between the cluster energy and corresponding track momentum) are taken into account. Three working points, known as $LooseLH$, $MediumLH$, and $TightLH$, are defined as cuts applying on the LH discriminant. These working points correspond to different electron identification efficiencies, ranging from 95% for the $LooseLH$ working point to 80% for the $TightLH$ working point. The decrease in electron identification efficiency that accompanies the use of a tighter working point is compensated by an improved rejection of background events. This improved background rejection is particularly important for analyses where non-prompt electron backgrounds are significant.

As a final step, the energy of the reconstructed electron candidates is corrected in scale and resolution to account for losses due to detector geometry and operation conditions, as well as deficiencies in the simulations. The electron energy calibration process involves multiple steps, which utilize information from the associated calorimeter cluster [96]. First of all, a correction that is specific to each layer of the calorimeter is applied and it is only performed on data to account for known irregularities in the response behavior of the individual layers. The next stage of the calibration procedure involves an in-situ calibration process to address any remaining differences between the data and the simulation. This is achieved by studying differences observed in $Z \rightarrow ee$ events, where an electron-positron pair is well-identified. Finally, to validate the calibration procedure, the invariant mass distributions of selected events for $J/\psi \rightarrow ee$ decays and radiative Z decays $Z \rightarrow ee$ are examined in both data and simulations.

5.2 Muons

Muons are the only particles that leave traces of their passage in all layers of the ATLAS detector, including the inner detector, calorimeters, and muon spectrometer. Their reconstruction [97] involves combining information from these three systems, depending on their respective acceptance. However, the information provided by the calorimeters is often limited, and therefore tracking information, either from the MS alone or from both the ID and MS, is used for the muon reconstruction.

ID tracks are reconstructed in a similar way to the process described in Section 5.1, and considered as muon track candidates. Independently, in MS, hits from the muon chambers is combined to identify track segments using a linear fit. These segments are required to roughly point towards the interaction point (IP) to reduce non-collision backgrounds like cosmic muons and random hit associations. These segments are then associated between multi-layers to form muon track candidates. This is achieved using a track-finding algorithm that attempts to match segments together into a single track based on angular information and accounting for the track bending caused by the toroidal magnetic field. Generally, at least two compatible segments are needed to reconstruct a muon track, except in the transition region between the barrel and endcap, where a single segment with stricter quality constraints is sufficient. It is not uncommon for a segment to be associated with multiple reconstructed tracks. This can indicate a problematic track. An overlap removal algorithm selects the best assignment to a single track, or allows for the segment to be shared between two tracks. Once the muon track candidate is reconstructed, the hits associated with each track candidate are fitted using a global χ^2 fit. A track candidate is accepted if the χ^2 of the fit satisfies the selection criteria. Hits providing large contributions to the χ^2 are removed and the track fit is repeated. A hit recovery procedure is also performed looking for additional hits consistent with the candidate trajectory. The track candidate is refit if additional hits are found.

At this stage, information from the different subsystems can be combined. Four different combination processes are used, corresponding to four muon types:

Combined muons (CB) track candidates from the ID and MS are paired and a global refit of the associated hits is performed, adding or removing MS hits when needed to improve the fit quality. This category offers the highest quality of muon reconstruction.

Segment-tagged muons (ST) track candidates from the ID and MS are combined but the ID track is required to be associated to at least one segment in the muon system. This category is mainly used to enhance the reconstruction efficiency for muons with low p_T and in regions of limited acceptance such as the barrel-endcap transition region.

Calorimeter-tagged muons (CT) Track candidates from the ID that correspond to energy depositions in the calorimeter consistent with muons are considered and paired. This category has the lowest purity and is mainly used to cover the central crack region in the muon system where $|\eta| < 0.1$.

Extrapolated muons (ME) Track candidates from MS that are approximately matched to the interaction point. The parameters of the muon track are defined at the interaction point, taking into account the estimated energy loss of the muon in the calorimeters. This category is employed to expand the coverage in $|\eta|$ to 2.7, where no ID information is available.

During the reconstruction, if there is an overlap between different types of muons, and the same ID track is shared between two muons, the priority is given with the following order: combined, segment-tagged, and then calorimeter-tagged muons. In the case of overlaps with extrapolated muons, the track that is retained is selected based on the total number of hits and the quality of the fit.

Reconstructed muons undergo an identification process aimed at reducing background contributions primarily from pion and kaon decays. This process evaluates the quality of identification based on three variables. These variables are: the q/p significance, defined as the absolute value of the difference between the ratio of the charge and momentum of the muons measured in the ID and MS divided by the sum in quadrature of the corresponding uncertainties, the $\rho' = \frac{|p_T^{ID} - p_T^{MS}|}{p_T^{track}}$, defined as the absolute value of the difference between the transverse momentum measurements in the ID and MS divided by the pT of the combined track, and the normalized χ^2 of the combined hits-to-track fit.

Similar to the electron identification, three working points, $Loose$, $Medium$, and $Tight$, are defined based on different cuts on the identification variables with different efficiencies. The $Loose$ working point designed to maximise the reconstruction efficiency while providing good-quality muon tracks. It selects all types of muons, only restricting the selection of CT and ST muons to the $|\eta| < 0.1$ region. $Medium$ muons are a subset of $Loose$ muons, where only CB and ME muon tracks within the $2.5 < |\eta| < 2.7$ range are selected. These tracks must satisfy loose requirements for the two of the three identification variables mentioned above, excluding the normalized χ^2. $Tight$ muons are selected to maximise the purity of muons at the cost of some efficiency. Only CB muons with hits in at least two stations of the MS and satisfying the Medium selection criteria are considered. The normalised χ^2 of the combined track fit is required to be $< \ 8$ to remove "bad" tracks. Lastly, a two-dimensional cut in the q/p and ρ' significance variables is performed as a function of the muon p_T to ensure stronger background rejection for momenta below 20 GeV where the misidentification probability is higher.

Finally, muon momentum calibration process uses only combined muons. The process involves a combined weighted average of momentum and resolution corrections of the ID and MS tracks. The correction factors are determined by comparing $Z \ \rightarrow \ \mu\mu$ events in data and Monte Carlo simulations that pass $Medium$ identification. This method is validated using $J/\psi \ \rightarrow \ \mu\mu$ events.

5.3 Lepton isolation

When studying leptons in analyses, their isolation can be used to discriminate between prompt leptons produced by the decay of heavier particles like $W^{\pm}$ and Z, and non-prompt leptons that come from decays of heavy quarks, misidentified hadrons, or converted photons (mostly in the case of electrons). It is a measure to quantify the detector activity in an area in azimuth and pseudorapidity, around the particle candidate of interest. A detailed description of the lepton isolation is given in [95, 97, 98].

The isolation variables used to select an isolated lepton candidate include the calorimeter-based E_T^{coneR} and the track-based p_T^{coneR}. The cone size, denoted by R, is a numeric value that indicates the actual cone size, for example, 0.2 for E_T^{cone20}. For E_T^{coneR}, the energies of all cells within the specified cone size are summed up and corrected to account for the contributions of the lepton candidate, pileup, and underlying event. On the other hand for p_T^{coneR}, the sum of the momenta of all tracks originating from the primary vertex within the cone size around the lepton candidate, excluding the track assigned to the lepton candidate, is used.

Variants with variable cone size labeled "$varconeR$" are created by using a cone size that depends on the transverse momentum or energy of the lepton. This variable is usually defined as the minimum between the ratio of 10 GeV divided by the lepton's transverse momentum or energy, and the baseline cone size denoted by R. An example of this is the $p_T^{varcone20}$ where

$$\Delta R = \min\left(10\mathrm{GeV}/p_{\mathrm{T}}, 0.2\right). \tag{5.1}$$

5.4 Jets

Jets are composite objects that consist of many partons generated from initial quark or gluon hadronisation [99]. These partons create collimated showers in the detector that include charged particles, which produce tracks in the ID and energy deposits in the calorimeterss, as well as neutral particles that interact solely with the calorimeters. While several jet reconstruction algorithms exist for various applications, this work focuses on two approaches. The first approach relies solely on calorimetric data to construct EM topological clusters, which are then used as base components to reconstruct EMTopo jets. The second approach employs both tracking and calorimetric information using a Particle Flow algorithm to create PFlow jets.

These two approaches use the same clustering algorithm, the so-called ”4-2-0” algorithm, for processing calorimetric information. As a first step, individual cells in the calorimeter are identified as potential cluster seeds if their measured energy surpasses a threshold of 4 times the expected noise standard deviation for that cell, $E_{cell} > 4\,\sigma_{noise}$. After that, neighboring cells with energy 2 times above the noise threshold are then recursively added to the cluster until no more cells meeting this criteria are found. In addition, any remaining non-clustered neighbouring cells in the same or adjacent detection layers overlapping in $(\eta\,,\,\phi)$ with the clustered cells are also included in the cluster, regardless of their energy. Finally if the corresponding to a cell energy excess of at least $500\ MeV$ with respect to its direct neighbors,resulting cluster contains multiple local energy maxima, the cluster is split into two clusters with cells assigned to each maximum according to their relative distance from it.

The clusters are called topological clusters and are assigned a 4-vector measured at the electromagnetic energy scale. They are designed to provide good reconstruction of electrons and photons and are assumed to have no mass. To create EMTopo jets, the topoclusters are combined using the $Anti-k_T$ [100, 101] algorithm, which identifies the most energetic cluster and neighboring clusters recursively merged to it in descending transverse momentum order. The topoclusters have to satisfy

$$\min\left(\mathrm{k}_{\mathrm{T},i}^{-2}, \mathrm{k}_{\mathrm{T},j}^{-2}\right)\frac{\Delta R_{ij}}{R^2} < \mathrm{k}_{\mathrm{T},i}^{-2}. \tag{5.2}$$

The $\mathrm{k}_{\mathrm{T},i,j}$ represents the transverse momentum of cluster i and j, with $\mathrm{k}_{\mathrm{T},i} > \mathrm{k}_{\mathrm{T},j}$. ΔR_{ij} is the relative distance between the clusters, and R, which is the jet radius, is a fixed value of 0.4 for all jets used in this study. This algorithm has the advantage over other jet algorithms of producing circular jets, which makes the calibration procedure easier. Additionally, it is colinear safe, meaning it is not affected by the number of particles in the hadronic shower, and infrared-safe, meaning it is not influenced by soft radiations from the initial parton.

The PFlow algorithm takes a different approach by combining the topoclusters with the information from the inner detector to reconstruct the jets before applying the jet algorithm. This method enhances the energy resolution at low jet transverse momentum and makes the jet reconstruction more pile-up robust. Initially, each individual topocluster is matched, when possible, to the ID track that results in a smaller $\Delta R'$ value, which is defined as:

$$\Delta R' = \sqrt{\left(\frac{\Delta\phi}{\sigma_\phi}\right)^2 + \left(\frac{\Delta\eta}{\sigma_\eta}\right)^2} \tag{5.3}$$

where $\Delta\phi$ and $\Delta\eta$ are the angular separations between the track and the topocluster barycenter. The cluster's energy distribution in the corresponding directions around its barycenter is indicated by the Gaussian width represented by σ_ϕ and σ_η. Clusters that cannot be matched to any track are called unmodified neutral clusters and are expected to come from neutral particles. Assuming that the cluster and its corresponding track are coming from a single particle, the expected energy deposit in the calorimeter is expressed as an E/p ratio, where E represents the cluster's energy and p represents the track's momentum. If the measured energy of the cluster is lower than this estimated value, it suggests that the track's energy is shared between multiple topoclusters, and more clusters can be included in the matching.

After matching, the expected energy deposit in the calorimeter is subtracted cell-by-cell from the topoclusters until all cells were covered, or all the energy has been subtracted. If the remaining energy in the topoclusters is consistent with the shower fluctuations of a single particle, the excess energy is removed, and the full particle kinematics are encoded in its corresponding track. If they are not consistent, a modified cluster with no tracks associated to it is formed, assumed to have been initiated by another neutral particle. This procedure results in a set of tracks, unmodified neutral clusters, and modified clusters referred to as Particle Flow Objects (PFO). PFOs whose track can be associated with any vertex other than the primary vertex of interest are removed, and the remaining PFOs are associated into jets using the same Anti-kT procedure as EMTopo jets.

Both EMTopo and PFlow jets undergo similar calibration procedures. Initially, the pileup contamination [102] is corrected by applying a correction factor

$$p_{\mathrm{T}}^{\mathrm{corr}} = p_{\mathrm{T}}^{\mathrm{reco}} - \rho A - \alpha\left(N_{\mathrm{PV}} - 1\right) - \beta\mu \tag{5.4}$$

where ρ is the median transverse energy density, A the jet area, N_{PV} the number of reconstructed primary vertices in the event and μ the number of pp interactions in the event. The coefficients α and β in this correction factor represent the respective fitted slopes of the jet response with respect to N_{PV} and μ.

The jet energy is then corrected to the Jet Energy Scale (JES) using a Monte Carlo-based procedure called MC numerical inversion. In this procedure, the response $R = \frac{E_{reco}}{E_{truth}}$, where E_{reco} and E_{truth} respectively represent the reconstructed and generated jet energies, is evaluated in simulation. These jets are called truth-particle jets and are seeded from generator-level stable particles originating from the hard-scatter vertex. If the energy of the truth-particle jet components associated to the detector-level jet represents more than 50% of the truth-particle jet energy, truth-particle jet are matched to the detector-level jet through a process called jet ghost association [103]. The response R is then fitted in (E_{truth}, η) bins, and a correction factor is extracted for each bin.

The next calibration step is the Global Sequential Correction, which aims to correct for intrinsic jet properties such as the initial parton flavor and the hadron composition resulting from the fragmentation process.

Finally, the Jet Energy Resolution (JER) correction is applied to account for any differences between data and Monte Carlo simulations, which could arise from mismodeled detector effects or from the relative contributions of hard-scatter vertex and any other vertices. This correction is evaluated by comparing the jet p_T to that of well-measured reference objects from $Z + jets$, $W + jets$, and $diijet$ events.

5.5 Missing transverse energy

Certain particles have very weak interactions with matter, which makes them difficult to detect such as neutrinos. Although neutrinos cannot be directly observed like hadrons, electrons, or muons, their kinematics can be partially evaluated based on the principle of momentum conservation. However, since it is not possible to precisely determine the fraction of the initial pp interaction attributed to the initial-state partons in the collision data, the momentum conservation principle is not particularly helpful in the longitudinal direction. Nevertheless, the total transverse momentum is guaranteed to be zero. In the case of neutrino production, the total transverse momentum of the vectorial sum of all final-state particles may be imbalanced. This momentum imbalance is known as missing transverse energy, or E_T^{miss} [104].

The E_T^{miss} can be computed as

$$E_{x(y)}^{\text{miss}} = E_{x,y}^{\text{miss},\gamma} + E_{x,y}^{\text{miss},e} + E_{x,y}^{\text{miss},\mu} + E_{x,y}^{\text{miss},\tau} + E_{x,y}^{\text{miss,jets}} + E_{x,y}^{\text{miss,soft}} \tag{5.5}$$

Each of the terms in the E_T^{miss} corresponds to the signed projection along the x- or y-axis of the sum of momenta for all the hard final state objects, along with a term accounting for soft objects. The soft term is a result of contributions from objects that come from the hard-scatter vertex but cannot be reconstructed as other identified objects. It can be computed using low-p_T tracks, creating a track-based soft term, or by using low energy topological clusters, resulting in a calorimeter-based soft term. Since the tracker can detect particles that cannot reach the calorimeters and is not sensitive to pile-up tracks, the track-based soft term is preferred. Consequently, the soft term can only be calculated in the central region where $|\eta| < 2.5$. The expression for E_T^{miss} can be easily formulated as

$$E_{\mathrm{T}}^{\mathrm{miss}} = \sqrt{\left(E_x^{\mathrm{miss}}\right)^2 + \left(E_y^{\mathrm{miss}}\right)^2}. \tag{5.6}$$

Chapter 6

WZ diboson analysis at $13\,TeV$

6.1 Introduction

The study of the $W^{\pm}Z$ diboson (inclusive) production in proton-proton collisions at a centre-of-mass energy of $13\,TeV$ is very crucial as it tests the electroweak sector predictions of the Standard Model and also it is a very important background process to other searches of new physics at the LHC, as it is described in Section 2.1.5.

The primary way that WZ is produced at the LHC is through quark-antiquark and quark-gluon interactions, which occur at leading order (LO) and at next-to-leading order (NLO) as they are depicted in Figures 6.1 and 6.2, respectively. Figure 6.1 illustrates the feynman diagrams for $W^{\pm}Z$ production at LO, which include a triple electroweak gauge boson interaction vertex in the s-channel. This vertex is a result of the non-abelian structure of the symmetry group that describes electroweak interactions. Presence of anomalous triple gauge couplings (aTGCs) can lead to deviations from SM theoretical predictions, which can be the signature of physics beyond the SM. As example, Figure 6.2 shows one of the feynman diagrams for the $W^{\pm}Z$ production at NLO.

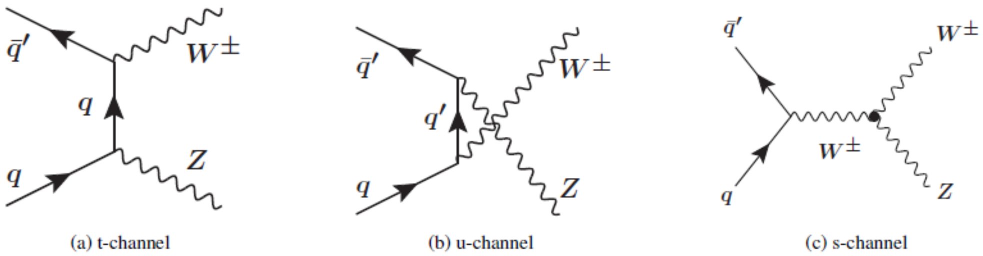

(a) t-channel (b) u-channel (c) s-channel

Figure 6.1: SM tree-level Feynman diagrams for WZ production through quark-antiquark interaction.

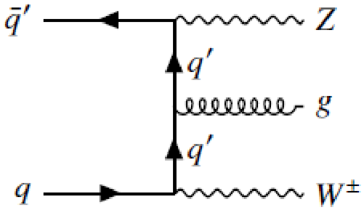

FIGURE 6.2: Example of a feynman diagram for WZ production through quark-gluon interaction.

The gauge bosons can decay hadronically or leptonically. As it is explained in Section 2.2.3, the hadronic decays have a large branching ratio but they have not a clean signature. On the other hand, the leptonic decays have a very clean signature but they have lower branching ratios. Taking into account that experimentally, the fully-leptonic decay mode provide the highest sensitivity, the $WZ \to lll\nu$ is studied in the context of this analysis.

Gauge bosons decay into two same flavour but opposite charge leptons for Z, while W decays into a lepton and a neutrino. In this analysis, leptons can be electrons (e) or muons (μ) as they provide a clean experimental signature in contrast with taus τ which have a short lifetime and decay either hadronically or leptonically, having a much more complex reconstruction than the other two types of leptons. The neutrino cannot be measured at all. Therefore, four flavor channels all with the same branching ratio are considered: $e^{\pm}e^{+}e^{-}$, $\mu^{\pm}e^{+}e^{-}$, $e^{\pm}\mu^{+}\mu^{-}$ and $\mu^{\pm}\mu^{+}\mu^{-}$.

6.2 Object and Event selection

6.2.1 Trigger event selection

Depending on the channel, events in 2015 are required to be recorded by one of the following triggers:

- $WZ \to \mu\nu_{\mu}\mu\mu$ events pass the trigger selection if they are fired by one of two single-muon triggers: HLT_mu20_iloose_L1MU15 or HLT_mu50 [105].
- $WZ \to e\nu_{e}ee$ events are required to be recorded by one of three single-electron triggers: HLT_e24_lhmedium_L1EM20VH, HLT_e60_lhmedium or HLT_e120_lhloose.

The trigger threshold for both leptons was increased to 26 GeV during the 2016-2018 period due to the higher instantaneous luminosity. Consequently, the triggers employed are:

- $WZ \to \mu\nu_{\mu}\mu\mu$ events: HLT_mu26_ivarmedium or HLT_mu50,

- $WZ \rightarrow e\nu_e ee$ events: HLT_e26_lhtight_nod0_ivarloose, HLT_e60_lhmedium_nod0 or HLT_e140_lhloose_nod0.

$WZ \rightarrow e\nu_e\mu\mu$ and $WZ \rightarrow \mu\nu_\mu ee$ events are required to fire one of the five single-lepton triggers from the corresponding trigger menu mentioned above.

6.2.2 Object selection

There are three levels of object selection for electrons and muons: the baseline leptons, the Z leptons, and the W leptons. These selection criteria are applied sequentially, with each level being more stringent and a subset of the previous one. This means that all W leptons also meet the criteria for Z leptons, and both W and Z leptons satisfy the baseline lepton criteria. The baseline lepton selection uses the least restrictive criteria to efficiently veto four-lepton events. Signal leptons must pass the more stringent W and Z lepton selection criteria to suppress any contamination from fake-lepton backgrounds, which are described in details in Section 6.3.

6.2.2.1 Electron object selection

Electrons in ATLAS are reconstructed from clusters of energy deposits in the electromagnetic calorimeter, matched to an ID track. The full procedure of the electrons reconstruction is detailed in Section 5.1 The ElectronPhotonFourMomentumCorrection package [106] is used in order to calibrate the momentum of the raw reconstructed electrons. Also, all electrons must meet the object quality requirements in order to ensure that electrons with clusters which is flagged as problematic due to issues in the electronics, e.g. problems in the high-voltage supply or if a cell in the cluster core is masked, are rejected

Table 6.1 provides a summary of the selection criteria used for electrons which are discussed in detail in the following.

Transverse momentum Electrons must meet certain minimum transverse momentum (p_T) requirements depending on their type: baseline electrons require p_T greater than $5GeV$, Z electrons require p_T greater than 15 GeV, and W electrons require p_T greater than 20 GeV. The p_T of an electron is computed using its calorimetric energy and direction which is determined by the tracker, based on its four-vector.

Pseudorapidity An electron is required to be reconstructed within $|\eta^{\text{cluster}}| < 2.47$, and within the tracking volume $|\eta| < 2.5$. However, for the selection of Z and W electrons, the calorimeter crack region $1.37 < |\eta^{\text{cluster}}| < 1.52$ is excluded in order to improve the rejection of ZZ background, which is explained in detail in Section 6.3.2, using baseline electrons.

Electron object selection			
Selection	Baseline selection	Z selection	W selection
$p_{\mathrm{T}} > 5$ GeV	✓	✓	✓
Electron object quality	✓	✓	✓
$\lvert\eta^{\text{cluster}}\rvert < 2.47$, $\lvert\eta\rvert < 2.5$	✓	✓	✓
`LooseLH+BLayer` identification	✓	✓	✓
$\lvert d_0^{\mathrm{BL}}/\sigma(d_0^{\mathrm{BL}})\rvert < 5$	✓	✓	✓
$\lvert\Delta z_0^{\mathrm{BL}} \sin\theta\rvert < 0.5$ mm	✓	✓	✓
`Loose_VarRad` isolation	✓	✓	✓
e-to-μ and e-to-e overlap removal	✓	✓	✓
e-to-jets overlap removal		✓	✓
$p_T > 15$ GeV		✓	✓
Exclude $1.37 < \lvert\eta^{\text{cluster}}\rvert < 1.52$		✓	✓
`MediumLH` identification		✓	✓
`HighPtCaloOnly` isolation		✓	✓
$p_T > 20$ GeV			✓
`TightLH` identification			✓
`Tight_VarRad` isolation			✓
Unambiguous author			✓
`DFCommonAddAmbiguity` ≤ 0			✓

TABLE 6.1: Electron object selection.

Lepton-vertex assosiation All electrons are required to pass the lepton-vertex association selection [107]. Therefore, the transverse impact parameter significance of the electron tracks relative to the beam line is required to satisfy $|d_0^{\mathrm{BL}}/\sigma(d_0^{\mathrm{BL}})| < 5$ and the longitudinal impact parameter z_0 (the difference between the value of z of the point on the track at which d_0 is defined and the longitudinal position of the primary vertex), is required to satisfy $|z_0^{\mathrm{BL}} \sin\theta| < 0.5\,\text{mm}$.

Identification Electron candidates are evaluated using a likelihood (LH) identification criterion. Baseline electrons are required to pass the LooseLH+BLayer identification, which has a range of efficiencies between 84% to 96% for electrons with p_T between 10 to 80 GeV. MediumLH and TightLH identification criteria are used for the selection of Z and W electrons. The MediumLH ID has efficiencies ranging from 72% to 93%, while the TightLH ID has efficiencies ranging from 68% to 88%, both for electrons with p_T between 10 to 80 GeV.

Isolation Baseline electrons must satisfy the Loose_VarRad isolation requirement. In order to pass Z selection, electrons must meet the HighPtCaloOnly isolation requirement, while for W selection, the Tight_VarRad isolation requirement must be satisfied. Table 6.2 shows the definition of the selected working points.

Nominal WPs	Calo isolation	Track Isolation
$HighPtCaloOnly$	$topoetcone20 < max(0.015 * pt, 3.5GeV)$	-
$Loose\_VarRad$	$topoetcone20/pT < 0.2\,GeV$	$ptvarcone30\_TightTTVALooseCone\_pt1000/p_T < 0.15\,GeV$
$Tight\_VarRad$	$topoetcone20/pT < 0.06\,GeV$	$ptvarcone30\_TightTTVALooseCone\_pt1000/p_T < 0.06\,GeV$

Table 6.2: Definition of the electron isolation working points.

e/γ ambiguity In W selection, the EGammaAmbiguityTool is used to remove ambiguities between electrons and photons. This distinction is made between cases where a candidate passes either the electron reconstruction algorithm alone or both the electron and photon reconstruction algorithms. Electrons are required to fail the photon reconstruction algorithm to veto the $Z\gamma$ background, which is described in Section 6.3.1. This requirement has an inefficiency of approximately 5% on true electrons from the W-boson decay. To further reject converted photons that are misidentified as electrons, the dedicated DFCommonAddAmbiguity tagger [108] is used. All electrons with DFCommonAddAmbiguity greater than 0 are rejected for W selection. This requirement has an inefficiency of around 0.5% on true electrons from W-boson decay, but it further reduces $Z\gamma$ background events by 35% in the inclusive $W^{\pm}Z$ event selection, which is given in detail in Section 6.2.6.

Charge mis-identification To account for the mis-identification of the electron's charge in the Monte Carlo (MC) simulation, a electron charge correction is applied. The EgammaChargeMisIdentificationTool [109] is used to determine the scale factor required to correct the MC and the associated systematic uncertainties. The scale factors are then applied to the electrons that pass the Z and W electron selection.

Overlap removal An overlap removal procedure, which is explained in Section 6.2.5, is implemented specifically for Z and W electrons to distinguish prompt electrons from those arising from the decay of hadrons in a jet. However, no such procedure is applied to baseline electrons.

Finally, it is known that the Monte-Carlo simulation is incomplete and needs corrections to account for known effects in data. The efficiency of the lepton identification, reconstruction, and isolation need to be adjusted to match the corresponding efficiencies in data. To achieve this, scale factors (SFs) in the simulation are used to correct the simulation based on the ratio of data and MC efficiencies

$$\mathrm{SF} = \frac{\varepsilon^{\mathrm{Data}}}{\varepsilon^{\mathrm{MC}}}. \tag{6.1}$$

The lepton SFs and the respective event trigger SF are multiplied together to obtain the total SF. The ElectronEfficiencyCorrection package is used to correct the simulation's electron reconstruction, identification, and isolation, following the Egamma recommendations from September 2018 [110].

6.2.2.2 Muon object selection

The ATLAS experiment uses information from both the inner detector (ID) and muon spectrometer (MS) to reconstruct muons, as described in Section 5.2. Before selecting any objects, the momentum of the muons is calibrated.

Table 6.3 provides a summary of the selection criteria used for muons which are discussed in detail in the following.

Muon object selection			
Selection	Baseline selection	Z selection	W selection
$p_{\mathrm{T}} > 5$ GeV	✓	✓	✓
$\lvert\eta\rvert < 2.7$	✓	✓	✓
`Loose` quality	✓	✓	✓
$\lvert d_0^{\mathrm{BL}}/\sigma(d_0^{\mathrm{BL}})\rvert < 3$ *(for* $\lvert\eta\rvert < 2.5$ *only)*	✓	✓	✓
$\lvert\Delta z_0^{\mathrm{BL}} \sin\theta\rvert < 0.5$ mm *(for* $\lvert\eta\rvert < 2.5$ *only)*	✓	✓	✓
`PflowLoose_FixedRad` isolation	✓	✓	✓
μ-jet Overlap Removal		✓	✓
$p_{\mathrm{T}} > 15$ GeV		✓	✓
$\lvert\eta\rvert < 2.5$		✓	✓
`Medium` quality		✓	✓
$p_T > 20$ GeV			✓
`Tight` quality			✓
`PflowTight_FixedRad` isolation			✓

Table 6.3: Muons object selection.

Transverse momentum Muons must meet certain minimum transverse momentum (p_T) requirements depending on their type: baseline muons require p_T greater than 5 GeV, Z muons require p_T greater than 15 GeV, and W muons require p_T greater than 20 GeV.

Pseudorapidity To ensure that muons are associated with decays of Z and W bosons, they must have $|\eta| < 2.5$. However, for baseline muons, the $|\eta|$ must be less than 2.7 to better reject ZZ background contamination.

Lepton-vertex assosiation All muons are required to pass the lepton-vertex association selection [107]. Therefore, the transverse impact parameter significance of the muon tracks relative to the beam line is required to satisfy $|d_0^{\mathrm{BL}}/\sigma(d_0^{\mathrm{BL}})| < 3$, and the longitudinal impact parameter z_0, is required to satisfy $|z_0^{\mathrm{BL}} \sin\theta| < 0.5$ mm.

Identification MuonSelectionTool [111] sets the quality selection criteria for baseline muons, and they must pass the Loose quality selection. This selection includes calorimeter-tagged muons, which is different from the Medium and Tight working points used for Z and W muons, respectively.

Isolation In the context of this thesis, the isolation criteria are optimized for the baseline, Z and W muons and are presented in Section 6.2.2.3.

Overlap removal An overlap removal procedure, which is explained in Section 6.2.5, is implemented specifically for Z and W muons to distinguish prompt muons from those arising from the decay of hadrons in a jet. However, no such procedure is applied to baseline muons.

Efficiency correction Reconstruction and isolation efficiencies of muons in MC are corrected using the MuonEfficiencyCorrections package with the latest recommendations provided by the MCP group [112].

6.2.2.3 Muon isolation optimization

In the context of this thesis, an muon isolation optimization is performed. The goal of this study is to specify the most optimal baseline, W and Z muon selection, in order to reduce the background contamination, including the non-prompt background, while maintaining the signal efficiency as high as possible. The main contributions to the non-prompt background arise from Z+jets and $t\bar{t}$ events, where a jet is either misidentified as a lepton or a lepton is reconstructed within a jet. Therefore, a well-justified step would be to tighten the isolation criterion for the W muon but also to vary the isolation criterion for the muons from the Z decay.

Signal and background MC samples of `MC16d` period (2017) and $\mathcal{L}= 44.3 fb^{-1}$ were used for this study. Only normalization uncertainties are taken into account (40% for the reducible background, 25% for the VVV contribution, 15% for the $t\bar{t}V$ contribution and 8% for the ZZ contribution).

Tables 6.4 and 6.5 show all the recommended Working Points (WPs) used for this study and their definitions [113].

Baseline muon isolation selection

The first part of this study aims to specify the baseline muon isolation selection. There are two possible WPs: the PflowLoose_FixedRad isolation WP and the PflowLoose_VarRad isolation WP and both are compared to the Loose_FixedRad WP, which is the one used in the previous analysis [114] and it is not recommended anymore.

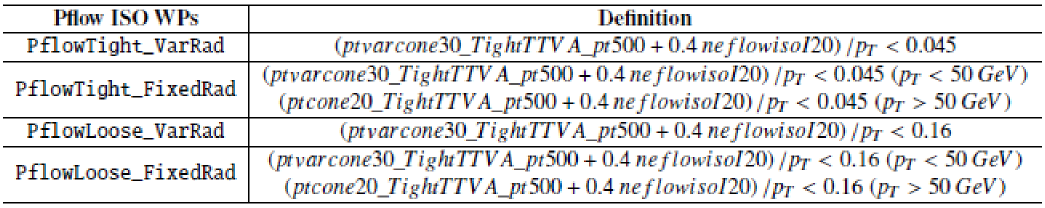

Pflow ISO WPs	Definition
`PflowTight_VarRad`	$(ptvarcone30\_TightTTVA\_pt500 + 0.4\,neflowisol20)\,/p_T < 0.045$
`PflowTight_FixedRad`	$(ptvarcone30\_TightTTVA\_pt500 + 0.4\,neflowisol20)\,/p_T < 0.045\ (p_T < 50\,GeV)$ $(ptcone20\_TightTTVA\_pt500 + 0.4\,neflowisol20)\,/p_T < 0.045\ (p_T > 50\,GeV)$
`PflowLoose_VarRad`	$(ptvarcone30\_TightTTVA\_pt500 + 0.4\,neflowisol20)\,/p_T < 0.16$
`PflowLoose_FixedRad`	$(ptvarcone30\_TightTTVA\_pt500 + 0.4\,neflowisol20)\,/p_T < 0.16\ (p_T < 50\,GeV)$ $(ptcone20\_TightTTVA\_pt500 + 0.4\,neflowisol20)\,/p_T < 0.16\ (p_T > 50\,GeV)$

Table 6.4: The recommended Pflow WPs which are used for this study.

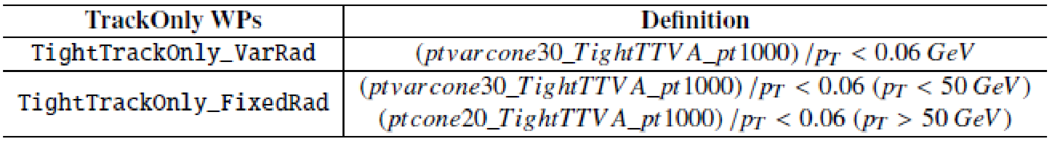

TrackOnly WPs	Definition
`TightTrackOnly_VarRad`	$(ptvarcone30\_TightTTVA\_pt1000)\,/p_T < 0.06\,GeV$
`TightTrackOnly_FixedRad`	$(ptvarcone30\_TightTTVA\_pt1000)\,/p_T < 0.06\ (p_T < 50\,GeV)$ $(ptcone20\_TightTTVA\_pt1000)\,/p_T < 0.06\ (p_T > 50\,GeV)$

Table 6.5: The recommended TrackOnly WPs which are used for this study.

The signal efficiency is measured with respect to Loose_FixedRad isolation WP and it is set to 1 for this WP. In order to estimate the change in background yield, either the signal-to background ratio $\frac{S}{B}$ or the significance $\frac{S}{\sqrt{S+B+\Delta B^2}}$ are employed. S is the signal yield, B is the background yield and ΔB^2 takes into account all the uncertainties from MC statistics, 40% uncertainty for the reducible background, 25% for VVV, 15% for $t\bar{t}$ and 8% for ZZ.

Note that the tZ background is not included in the background yield because of its very signal-like signature.

Figure 6.3 shows the signal efficiency as a function of the signal-to-background ratio (up) and the signal efficiency as a function of the significance (down) for all channels, while Figure 6.4 shows the same quantities for the $\mu\mu\mu$ channel.

The two new WPs have a very similar effect. In both of them, the increase of the signal yield is followed for some increase of the background yield. At the end, the PflowLoose_FixedRad isolation WP is chosen as the baseline muon selection.

Z and W muon isolation selection

The second part of this study is to define the W and Z muon isolation selection. The W muon has to be a subset of the Z muons, which have to be a subset of the baseline muons due to stepwise selection, because otherwise there would be inconsistencies regarding the application of the scale factors. Thus, only the combinations shown in Table 6.6 are possible and only those are tested. The procedure for the comparison of the isolation WPs combinations is that the baseline muon has always the PflowLoose_FixedRad isolation WP, while the W and the Z muon isolation WPs are changed. Also, all the events fullfil the inclusive WZ selection, which is described on Table 6.8 is applied. The "nominal isolation selection", with which all the other WPs combinations are compared, is defined as the PflowLoose_FixedRad isolation WP for the

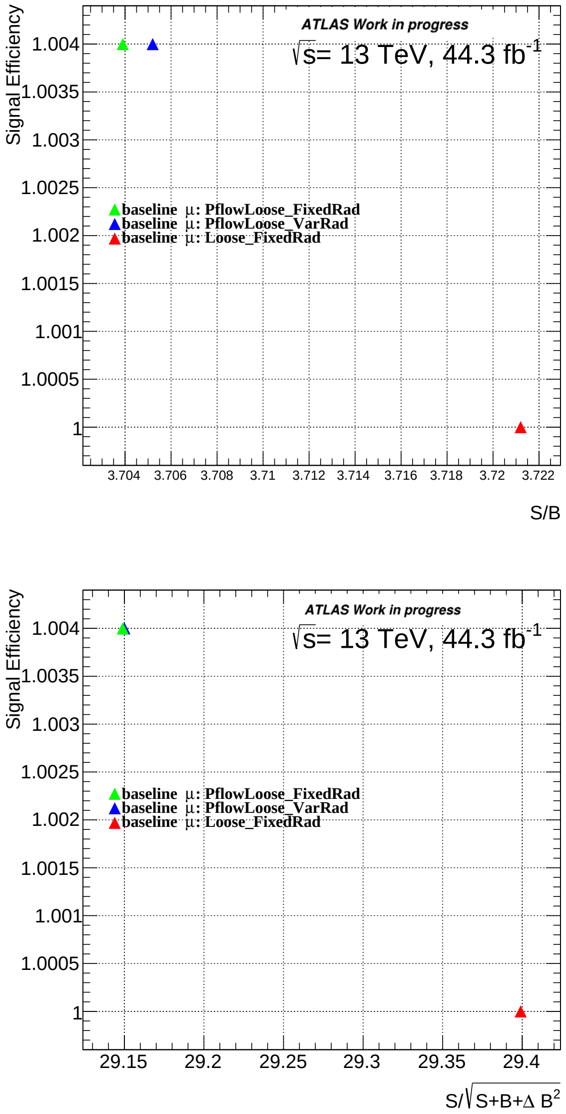

FIGURE 6.3: Signal yield with respect to the `Loose_FixedRad` isolation WP and the $\frac{S}{B}$ ratio(up) and the significance $\frac{S}{\sqrt{S+B+\Delta B^2}}$ (down) for all channels. The uncertainties are not shown in the figure as they are smaller than the size of the mark used.

baseline selection and the TightTrackOnly_FixedRad isolation WP for the W and Z selections. All the isolation WPs combinations tested for this study, are presented on Table 6.6.

The signal efficiency is measured with respect to the ”nominal isolation selection” such that the signal efficiency is set to 1 for the ”nominal isolation selection”. The change in the background yield is estimated as in the baseline selection, by using the signal-to-background ratio and the significance.

The tZ background is not included in the background yield as before.

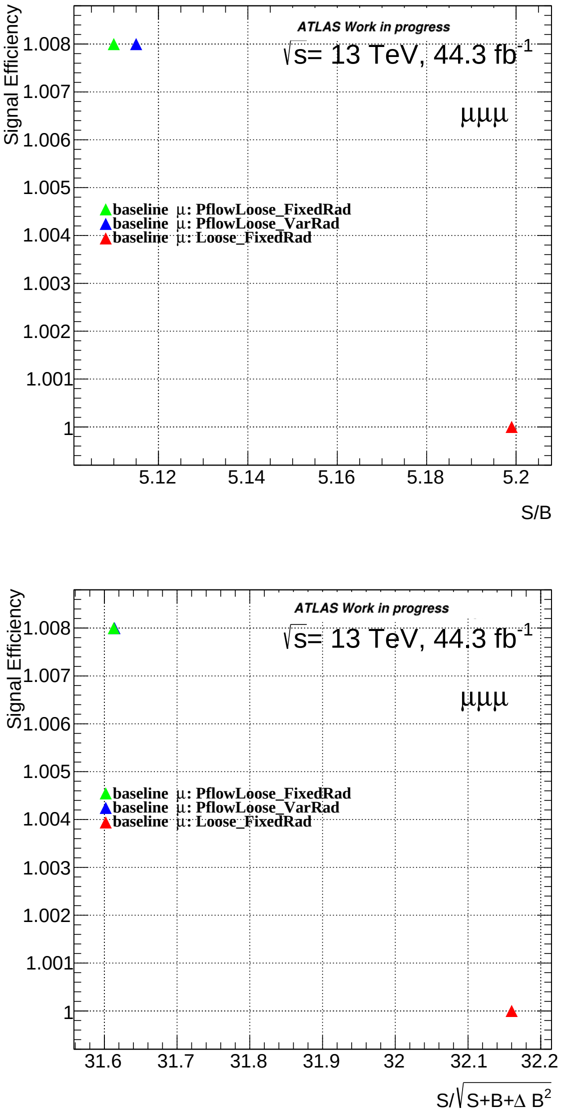

FIGURE 6.4: Signal yield with respect to the `Loose_FixedRad` isolation WP and the $\frac{S}{B}$ ratio(up) and the significance $\frac{S}{\sqrt{S+B+\Delta B^2}}$ (down) for the $\mu\mu\mu$ channel. The uncertainties are not shown in the figure as they are smaller than the size of the mark used.

Some of the isolation WPs combinations give the same results, thus only one combination of them will be taken into account from now on.

Figure 6.5 shows the signal efficiency as a function of the signal-to-background ratio (up), and the signal efficiency as a function of the significance (down), while Figure 6.6 shows the same quantities for the $\mu\mu\mu$ channel.

The combinations which have low signal efficiency are discarded of the possible combinations for the Z and W muon isolation selection. Table 6.7 shows the possible combinations left for the Z and W muon isolation selections.

Z **muons**	W **muons**
`PflowLoose_FixedRad`	`PflowTight_FixedRad`
`PflowLoose_FixedRad`	`PflowTight_VarRad`
`PflowLoose_VarRad`	`PflowTight_FixedRad`
`PflowLoose_VarRad`	`PflowTight_VarRad`
`PflowTight_FixedRad`	`PflowTight_FixedRad`
`PflowTight_FixedRad`	`PflowTight_VarRad`
`PflowTight_VarRad`	`PflowTight_FixedRad`
`PflowTight_VarRad`	`PflowTight_VarRad`
`PflowLoose_FixedRad`	`TightTrackOnly_FixedRad`
`PflowLoose_FixedRad`	`TightTrackOnly_VarRad`
`PflowLoose_VarRad`	`TightTrackOnly_FixedRad`
`PflowLoose_VarRad`	`TightTrackOnly_VarRad`
`TightTrackOnly_FixedRad`	`TightTrackOnly_VarRad`
`TightTrackOnly_VarRad`	`TightTrackOnly_FixedRad`
`TightTrackOnly_VarRad`	`TightTrackOnly_VarRad`
`TightTrackOnly_FixedRad`	`PflowTight_FixedRad`
`TightTrackOnly_FixedRad`	`PflowTight_VarRad`
`TightTrackOnly_VarRad`	`PflowTight_FixedRad`
`TightTrackOnly_VarRad`	`PflowTight_VarRad`

Table 6.6: All the isolation WPs combinations tested for this study

Z **muons**	W **muons**
`PflowLoose_FixedRad`	`PflowTight_FixedRad`
`PflowLoose_FixedRad`	`PflowTight_VarRad`
`PflowLoose_FixedRad`	`TightTrackOnly_FixedRad`
`PflowLoose_FixedRad`	`TightTrackOnly_VarRad`
`TightTrackOnly_FixedRad`	`TightTrackOnly_VarRad`
`TightTrackOnly_VarRad`	`TightTrackOnly_FixedRad`
`TightTrackOnly_VarRad`	`TightTrackOnly_VarRad`

Table 6.7: Possible combinations for the Z and W muon isolation selections.

The preferable option would be to decrease the background events, while keeping the signal yield as high as possible. By choosing the Z isolation WP to be PflowLoose_FixedRad and the W isolation WP to be PflowTight_FixedRad, the background rejection and the relative signal yield are worse with respect to the ”nominal isolation selection”.

On the other hand, by using the PflowLoose_FixedRad for the Z isolation WP and the PflowTight_VarRad for the W isolation WP, the signal loss is less but the background rejection is worse than the previous combination with respect to the ”nominal isolation selection”.

Followingly, by choosing the Z isolation WP to be PflowLoose_FixedRad WP and the W isolation WP to be TightTrackOnly_FixedRad or the TightTrackOnly_VarRad, the signal yield is increased but the background rejection is worse with respect to the two previous options.

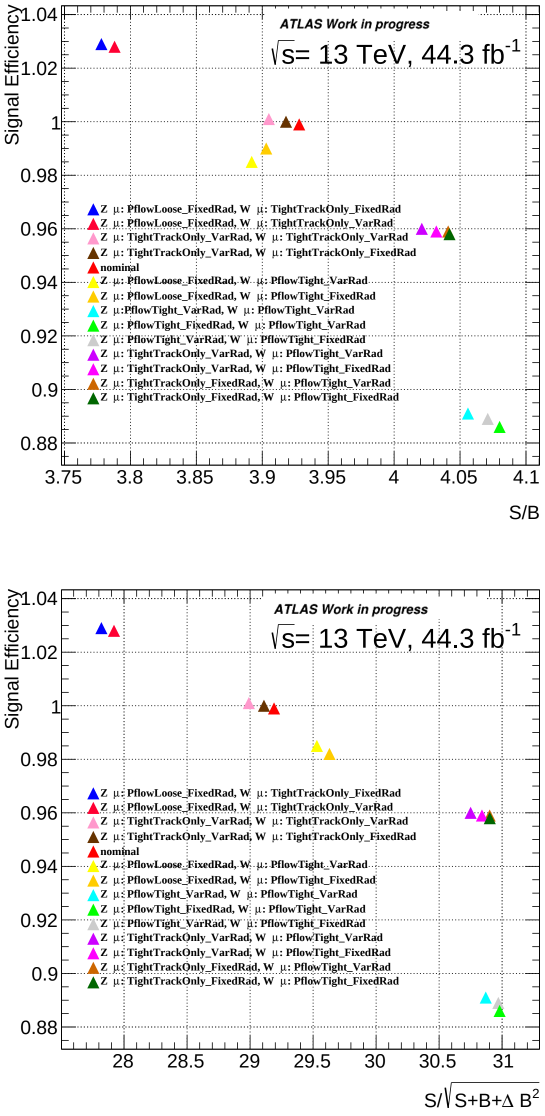

FIGURE 6.5: Signal yield with respect to the "nominal isolation selection" and the $\frac{S}{B}$ ratio(up) and the significance $\frac{S}{\sqrt{S+B+\Delta B^2}}$ (down) for all channels. The uncertainties are not shown in the figure as they are smaller than the size of the mark used.

Finally, for the last three combinations, where the Z and W isolation WPs could be either TightTrackOnly_FixedRad or TightTrackOnly_VarRad, the signal yields are increased but the background rejections are worse with respect to the other combinations.

Concluding on the muon event isolation optimization, the best options to be taken into account are the PflowLoose_FixedRad isolation WP for the Z muon isolation selection and the PflowTight_FixedRad isolation WP for the W muon isolation selection, because it has the best background rejection among all combinations despite a small decrease in the signal yield.

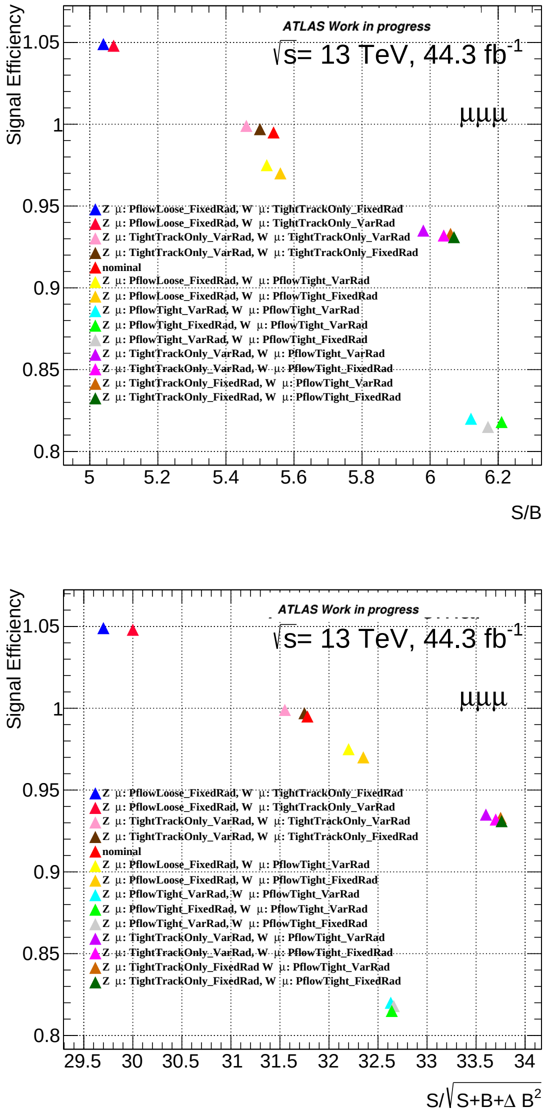

Figure 6.6: Signal yield with respect to the "nominal isolation selection" and the $\frac{S}{B}$ ratio(up) and the significance $\frac{S}{\sqrt{S+B+\Delta B^2}}$ (down) for the $\mu\mu\mu$ channel. The uncertainties are not shown in the figure as they are smaller than the size of the mark used.

6.2.3 Jet object selection

Particle flow objects, which are defined in Section 5.4 are used to reconstruct jets through the anti-kt algorithm with a radius parameter of $\Delta R = 0.4$, corresponding to the EMPFlowJets collection. Only jets with $p_{\mathrm{T}} > 25\ GeV$ and $|\eta| < 4.5$ are considered. The consolidated jet recommendations with the configuration file
JES_MC16Recommendation_Consolidated_PFlow_Apr2019_Rel21.config [115] are applied. Pile-up jets are removed using the JVT tagger for central jets and the fJVT tagger for forward jets [116]. For jets with $p_{\mathrm{T}} < 60\ GeV$ and $|\eta| < 2.4$, a JVT output larger than 0.5 is

required to suppress jets coming from pile-up, following the Tight working point recommendation [116]. For jets with $p_{\mathrm{T}} < 120 GeV$ and $2.5 < |\eta| < 4.5$, the fJVT tagger is applied using the Loose working point. Both taggers' Monte Carlo efficiencies are corrected using data/MC calibrations from May 2020 [116].

As the tZ background is an important background in this analysis and it is characterized by b-jets, the tagging of these jets is mandatory. Jets in the central region ($|\eta| < 2.5$) with $p_{\mathrm{T}} > 25\ GeV$ containing b-hadrons are tagged using the DL1r tagger with the 201903 b-tagging configuration [117]. The 70% b-tagging efficiency working point is applied. Flavour tagging efficiencies are corrected based on data-driven calibration analyses [118].

6.2.4 Missing energy

To determine the imbalance of transverse momentum (Section 5.5) in the detector, the missing transverse momentum E_T^{miss} is computed. This is done by calculating the negative vector sum of the transverse momentum of specifically selected calibrated objects, such as electrons, muons, and jets, along with contributions from the soft events. These soft events are reconstructed from tracks or calorimeter cell clusters that are not associated with the hard objects. In this analysis, E_T^{miss} is calculated using the METMakerTool, from calibrated electrons and muons that have passed the baseline selection, and calibrated jets without any selection. The resolution of the soft term measured through the calorimeter is often degraded due to pile-up. The PFlow E_T^{miss} [119] reconstruction with the track-based measurement of the soft term is used in this analysis.

6.2.5 Overlap

Leptons and jets can both be identified using the same detector information, but sometimes there may overlap. To address this, an overlap removal procedure is used based on the recommendations provided in the Harmonization Document [120]. This procedure involves several steps:

- Jets found within $\Delta R < 0.2$ of a Z-electron are discarded, and jets with fewer than three tracks and a distance $\Delta R < 0.2$ from the direction of Z-muon are also rejected. The selected jets are referred as "overlap-removal-cleaned" jets.
- Baseline electrons sharing an ID track with a baseline muon are ignored, a procedure which removes 0.4% of baseline electrons.
- Electrons passing the Z-selection and overlapping with "overlap-removal-cleaned" jets within $\Delta R < 0.4$ are discarded. This selection has an efficiency $> 99\%$ for Z-electrons.

- Finally, muons passing the Z-selection and found within $\Delta R < 0.4$ of the direction of an "overlap-removal-cleaned" jet with at least three tracks are also discarded. This selection keeps over 98% of muon candidates.

6.2.6 Event selection

The first step of the event selection is to reject events affected by LAr, Tile, or SCT corruption, as well as incomplete events. For this purpose, certain quality conditions are imposed on the recorded data. After that, an event cleaning in both data and simulated events is performed, rejecting any event with at least one misidentified jet of non-collision background or originating from detector problems [121] with respect to the high-efficiency loose working point of selecting jets [122]. Finally, events are required to have a primary vertex with at least two tracks associated with it.

To reduce the background contribution from ZZ processes with four leptons in the final state, a "$ZZ\ veto$" is applied. That means that events with more than three leptons passing the baseline muon or electron selections are rejected. The selection of leptons used for the veto is optimized to identify prompt electron and muon candidates with wide kinematic acceptance. Baseline muons before any overlap removal and baseline electrons that survive overlap removal with muons are used to count the number of leptons for the "$ZZ\ veto$". For a WZ candidate event, exactly three leptons must pass the Z lepton identification selection. A Z boson candidate is formed by requiring two selected leptons of the same flavor that have opposite charges (SFOC). If more than one pair of leptons make a Z candidate, the pair with imvariant mass closest to the Z boson mass is chosen. The W boson candidate is selected by requiring the third remaining lepton to pass the W lepton selection. The leading lepton's transverse momentum threshold is increased to $25\ GeV$ for the 2015 sample and to $27\ GeV$ for 2016–2018 samples to increase the possibility that the lepton firing the trigger is above the trigger efficiency turn-on curve. The SFOC lepton pair must have an invariant mass within $10\ GeV$ of the Z boson mass. Lastly, the transverse mass of the W candidate must be above $30\ GeV$. Table 6.8 summarizes the inclusive event selection.

6.2.7 Reconstruction of kinematic observables

As there is some uncertainty because there is not a complete information about the neutrino four-vector, the reconstuction of the four-vector of the W boson is complicated. The only available information is the missing transverse energy, which is used along with the equation $E^2 = P^2 + M^2$ to calculate the longitudinal momentum p_z of the neutrino four-vector. M represents the world average mass, m_W^{PDG}, and it is reported by the Particle Data Group [123]. This equation is solved using the x and y components of the missing transverse energy, E_T^{miss},

<table>
<tr><th colspan="2">Inclusive event selection</th></tr>
<tr><td>Event cleaning</td><td>Reject LAr, Tile and SCT corrupted events and incomplete events</td></tr>
<tr><td>Primary vertex</td><td>Hard scattering vertex with at least two tracks</td></tr>
<tr><td>Trigger 2015</td><td><code>HLT_e24_lhmedium_L1EM20VH || HLT_e60_lhmedium || HLT_e120_lhloose</code>
<code>HLT_mu20_iloose_L1MU15 || HLT_mu50</code></td></tr>
<tr><td>Trigger 2016–2018</td><td><code>HLT_e26_lhtight_nod0_ivarloose || HLT_e60_lhmedium_nod0 || HLT_e140_lhloose_nod0</code>
<code>HLT_mu26_ivarmedium || HLT_mu50</code></td></tr>
<tr><td>ZZ veto</td><td>Less than 4 baseline leptons</td></tr>
<tr><td>N leptons</td><td>Exactly three leptons passing the Z lepton selection</td></tr>
<tr><td>Leading lepton p_{T}</td><td>$p_{\mathrm{T}}^{\mathrm{lead}} > 25$ GeV (in 2015) or $p_{\mathrm{T}}^{\mathrm{lead}} > 27$ GeV (in 2016)</td></tr>
<tr><td>Z leptons</td><td>Two same flavor oppositely charged leptons passing Z-lepton selection</td></tr>
<tr><td>Mass window</td><td>$|M_{\ell\ell} - M_Z| < 10$ GeV</td></tr>
<tr><td>W lepton</td><td>Remaining lepton passes W-lepton selection</td></tr>
<tr><td>W transverse mass</td><td>$m_{\mathrm{T}}^{W} > 30$ GeV</td></tr>
</table>

Table 6.8: Overview of the inclusive event selection.

and the four-vector of the charged lepton associated with the W boson. If there are two possible solutions for p_z, the one with the smaller magnitude is chosen. On the other hand, if there are no real solutions, the real part of the solution with the smaller magnitude is used. By using this reconstructed neutrino four-vector, the four-vector of the W boson and the invariant mass of the WZ system can be determined.

There are several techniques available to reconstruct the transverse mass of the WZ system [124]. In this analysis, the transverse mass of the WZ system is determined by considering the four-vectors of the final-state leptons associated with the W and Z bosons, and projecting them onto the transverse plane by ignoring their longitudinal component. The M_{T}^{WZ} value is then calculated as the invariant mass of the system formed by combining the projected four-vectors of the three leptons and the missing transverse energy, E_T^{miss}:

$$M_{\mathrm{T}}^{WZ} = \sqrt{\left(\sum_{\ell=1}^{3} p_{\mathrm{T}}^{\ell} + E_{\mathrm{T}}^{\mathrm{miss}}\right)^2 - \left[\left(\sum_{\ell=1}^{3} p_x^{\ell} + E_x^{\mathrm{miss}}\right)^2 + \left(\sum_{\ell=1}^{3} p_y^{\ell} + E_y^{\mathrm{miss}}\right)^2\right]} \tag{6.2}$$

This definition was found to provide the best resolution on M_{T}^{WZ} [124].

6.3 Background estimation

There are several background processes that can mimic the experimental signature of WZ production and contribute to the selected event sample. These processes can be divided into two groups: the reducible backgrounds that have at least one misidentified (”fake”) lepton, and the irreducible backgrounds that have at least three prompt leptons in the final state.

6.3.1 Reducible background

The first group of backgrounds is that of reducible backgrounds (non-prompt), which occur when fake leptons pass the lepton selection criteria. There are different types of fakes, including jets misidentified as leptons, leptons reconstructed within a jet, such as those from the decay of a heavy flavour quark or electrons from photon conversion. These backgrounds mainly consist of $Z + jets$ events, where a jet is misidentified as an electron or muon, $Z\gamma$ events, where a photon is misidentified as an electron, and $t\bar{t}$ events, where a lepton from a b-hadron decay is matched with a W boson lepton to create a fake Z boson. While $W\gamma$ events are also taken into account, they have a negligible contribution and they are combined with the $Z\gamma$ events. Finally, there are contributions from Wt and WW processes. To estimate the reducible background contribution to the event selection, a data-driven method called the Matrix Method is used. This method is described in details in [125, 126]. There are eight identification categories that represent different combinations of $Loose$ or $Tight$ leptons. $Tight$ leptons are those that pass the selection criteria for W or Z leptons, while $Loose$ leptons fail one of the identification criteria. Similarly, there are eight truth-level categories where prompt leptons are categorized as $Real$ leptons and non-prompt leptons categorized as $Fake$ leptons. The yields obtained in each of the eight identification categories can be linked to the truth-level categories using an 8×8 matrix. The matrix elements represent the probabilities of an event belongs to each combination of truth-level and identification categories. The number of events with at least one fake lepton in the analysis selection is then estimated by inverting this matrix.

To validate the estimation of the fake background obtained through the Matrix Method, a MC based fake background estimation method, called Fake Scale Factor method [126], is employed. This method uses control regions, where scale factors are derived to correct the MC predictions for the various sources of fake backgrounds. Dedicated control regions are defined for each type of signal-faking process, $Z + jets$, $t\bar{t}$, and $Z\gamma$. In each of the $Z + jets$, $t\bar{t}$ control regions, four fake scale factors for both fake electrons and muons and separately for W-leptons and Z-leptons are estimated. On the other hand, in the $Z\gamma$ (photon conversion) control region, only two fake scale factors for fake electrons separately for W-electrons and Z-electrons are estimated, as photon conversion processes very rarely occur in case of muons. In the end, this procedure results in a total of 10 distinct fake scale factors that are applied to each truth-matched fake lepton in the analysis region for the relevant samples.

The results obtained from the two methods are very similar overall, and any differences are usually within the uncertainty associated with the Matrix Method estimate, which is of the order of 23% [125].

≥ 2 Z-type leptons, same-flavour and opposite charge (e^+e^- or $\mu^+\mu^-$)	
$\lvert m_{ll} - m_Z^{PDG} < 15 \rvert$ GeV	
fake lepton is highest-p_{T} Matrix Method lepton	
fake electron	**fake muon**
$m_{\mathrm{T}}^{W} < 30$ GeV	$m_{\mathrm{T}}^{W} < 30$ GeV
$E_T^{miss} < 30$ GeV	-
$m_{ll} > 81$ GeV	-

Table 6.9: Selection of the $Z + jets$ control region.

≥ 1 Z-type electron e_Z
≥ 1 Z-type muon μ_Z
$\mathrm{charge}(\mu_Z) \cdot \mathrm{charge}(e_Z) < 0$
remaining highest-p_{T} Matrix Method lepton $\equiv$ fake lepton ℓ_m
lepton with different flavour than fake lepton passes W-lepton requirements: ℓ_W
$\mathrm{charge}(\ell_m) \cdot \mathrm{charge}(\ell_W) > 0$

Table 6.10: Selection of the $t\bar{t}$ control region.

≥ 2 Z-type muons, opposite charge ($\mu^+\mu^-$)
$55 < m_{ll} < 85$ GeV
$m_{3l} < 105$ GeV
fake lepton is highest-p_{T} Matrix Method electron
$m_{\mathrm{T}}^{W} < 30$ GeV
$E_T^{miss} < 30$ GeV

Table 6.11: Selection of the $Z\gamma$ control region.

6.3.2 Irreducible background

The second group of backgrounds are the irreducible (prompt) backgrounds. They have the same final state as the WZ production with correctly identified leptons but they differ from it kinematically. These backgrounds mainly consists of ZZ events, where one lepton fails the lepton identification requirements or the detector kinamatical region and is thus not identified, VVV events, where one of the bosons decays hadronically, $t\bar{t}V$ events and tZ events, where the top quark decays into a W boson and a b-jet. The dominant irreducible background comes from ZZ production.

These backgrounds contributions are estimated using MC events and they are constrained with data in dedicated control regions estimating the corresponding μ factors for each of them. There are two control regions: the ZZ control region and the $t\bar{t}V$ control region.

The ZZ control region is defined based on the final WZ event selection, removing the 4^{th} lepton veto. In this control region, events are selected if they have two leptons of the same flavor and opposite charge with an invariant mass that is consistent with the Z mass, where the difference between the invariant mass and the PDG Z mass should be less than $10\ GeV$. If there are multiple pairs of leptons forming a Z candidate, the one with an invariant mass closest to the PDG Z mass is chosen. The leptons forming the Z candidate must meet the quality criteria specified in Tables 6.1 and 6.3 for Z-leptons. In addition, the event must have two more leptons with transverse momentum greater than 15 and 5 GeV, respectively, and these leptons must meet the quality criteria specified in Tables 6.1 and 6.3 for W-leptons and ”baseline” leptons.

The $t\bar{t}V$ control region is created by imposing the entire WZ event selection and adding a requirement for two b-jets in the events. DL1r tagger [117] is used in order to identify b-jets in the central region ($|\eta| < 2.5$) with p_T greater than $2\,GeV$. The b-jet identification working point corresponds to 85% identification efficiency.

6.4 Fiducial inclusive phase space definition

Both integrated and differential cross-section measurements are carried out within an inclusive fiducial phase space. The inclusive fiducial phase space has been selected to closely match the detector acceptance and the analysis selection, which are explained in Section 6.2. The integrated cross-section is measured within the detector’s fiducial region. This analysis uses a phase space definition that rely on prompt leptons that are associated with the W and Z decay, using the ”resonant shape” algorithm, that is described below. Table 6.12 presents a summary of the phase space definition used in the measurement.

Variable	Fiducial inclusive
Lepton $\|\eta\|$	< 2.5
p_{T} of ℓ_Z, p_{T} of ℓ_W	> 15, > 20 GeV
m_Z range	$\|m_Z - m_Z^{\mathrm{PDG}}\| < 10$ GeV
m_{T}^W	> 30 GeV
$\Delta R(\ell_Z^-, \ell_Z^+)$, $\Delta R(\ell_Z, \ell_W)$	> 0.2, > 0.3

TABLE 6.12: Phase space definition used for the fiducial inclusive cross-section measurements.

η and p_T depict the pseudorapidity and the transverse momentum, respectively, m_Z is the invariant mass of the Z boson and ΔR depicts the distance between two leptons. The W boson’s transverse mass is defined as:

$$m_T^W \;=\; \sqrt{2p_T^l p_T^\nu (1 - cos\Delta\phi)}. \tag{6.3}$$

The phase space definition is based on dressed kinematics of the final-state charged leptons. Dressed leptons are obtained from bare leptons and they are leptons after QED final state radiation (FSR), by summing the momenta of all photons radiated from charged leptons within a cone of $\Delta R < 0.1$ around the bare lepton direction. Dressed leptons are designed to closely mimic the measurement in the electron channel, as the ATLAS cluster reconstruction combines the bare electron energy with that of nearby photons. The use of dressed leptons reduces the

QED FSR correction since the majority of QED FSR photons are collinear and close to the electromagnetic cluster or the bare lepton track. Using dressed leptons enables the combination of channels with leptons radiating differently, such as the electron and muon channels. These dressed lepton with final-state neutrinos not originating from hadrons or τ decays, are appropriately associated with the W and Z boson decay products using an algorithmic approach called "resonant shape" which is based in the value of the estimator

$$P = \left| \frac{1}{m^2_{(\ell^+,\ell^-)} - \left(m_Z^{\mathrm{PDG}}\right)^2 + i\Gamma_Z^{\mathrm{PDG}} m_Z^{\mathrm{PDG}}} \right|^2 \times \left| \frac{1}{m^2_{(\ell',v_{\ell'})} - \left(m_W^{\mathrm{PDG}}\right)^2 + i\Gamma_W^{\mathrm{PDG}} m_W^{\mathrm{PDG}}} \right|^2 . \tag{6.4}$$

The values for m_Z^{PDG} (m_W^{PDG}) (the world average mass) and Γ_Z^{PDG} (Γ_Z^{PDG}) (the total width) of the Z or W bosons are reported by the Particle Data Group [123]. The estimator takes as input the invariant mass, m, of all possible pairs (l^+, l^-) and $(l', v_{l'})$ that satisfy the fiducial selection requirements. The final assignment of leptons to the W or Z bosons is determined by the configuration that yields the highest value of the estimator. By using this particular association algorithm, it becomes possible to calculate the kinematics of the gauge bosons using the kinematics of the associated leptons without relying on any specific details of the internal Monte Carlo generator.

6.5 First measurement of $W^{\pm}Z$ inclusive cross section and future prospects

The first measurement of the $W^{\pm}Z$ inclusive cross section had been done using data which were collected in 2015 and 2016 by the ATLAS experiment at the Large Hadron Collider, and correspond to an integrated luminosity of $36.1 fb^{-1}$ [114]. The measured inclusive cross section in the detector fiducial region for a single leptonic decay mode was $\sigma^{fid}_{W^{\pm}Z \to l'vll} = 63.7 \pm 1.0(stat) \pm 2.3(syst) \pm 1.4(lumi)\ fb$, reproduced by the next-to-next-to-leading-order Standard Model prediction of $61.5^{+1.4}_{-1.3}\ fb$.

The goal is to improve the precision of the measurement of the inclusive cross section using data which were collected from 2015 to 2018 by the ATLAS experiment at the Large Hadron Collider, and correspond to an integrated luminosity of $139\ fb^{-1}$.

6.6 Rivet routine

The Rivet toolkit,(Robust Independent Validation of Experiment and Theory) is a valuable system for validating Monte Carlo event generators. Its collection of experimental analyses is extensive and continuously expanding, making it a helpful resource for MC generator development, validation, and tuning. Rivet is the most widespread way by which analysis code from the LHC and other high-energy collider experiments is preserved for comparison to and development of future theory models. It is used by phenomenologists, MC generator developers, and experimentalists on the LHC and other facilities. The Rivet framework provides a definition of the exact fiducial phase space of an analysis and makes the results exploitable for interpretation studies.

In the context of this thesis, whithin the Rivet framework, the routine for the WZ diboson production is created and tested. The full routine is presented in Appendix C.1. For this purpose, the phase space, that is defined in Table 6.12, is used. In order to validate the routine, a comparison between the Rivet framework and the analysis based on the truth information of the generated signal events, referred below as ”analysis framework”, is done. The kinematical variables that are compared are: the transverse mass of the WZ system, M_T^{WZ}, the difference of ϕ angle of the two bosons, $\Delta\phi_{WZ}$, the transverse momentum of the W boson, p_T^W, the transverse momentum of the Z boson, p_T^Z, the difference of rapidity of the Z boson and the lepton of the W boson, $|y_Z - y_{l,W}|$ and the number of jets, N_{jets}. The signal samples used for the comparison for the $pp \to WZ \to l\nu ll$ process are explained in Sections 4.2.3.1 and 4.2.3.3. These samples are the WZ Powheg+Pythia8 and the WZ Sherpa 2.2.2 samples.

The first step is to compare the integrated cross sections. For the Powheg+Pythia8 sample, the integrated cross section obtained by the Rivet framework is: $61.6165\ fb$ and the one obtained by the analysis framework is: $61.4902\ fb$. The difference between the cross sections given by the analysis and Rivet frameworks is : 0.2%. Accordingly for the Sherpa 2.2.2 sample, the integrated cross section given by the Rivet framework is: $63.5684\ fb$ and the one given by the analysis framework is: $63.6649\ fb$. The difference between the two is: 0.1%.

Finally, the second step is to compare the shapes of the differential distributions of the above mentioned kinematical variables for the two frameworks. The comparison for the Powheg+Pythia8 sample is shown in Figure 6.7 and for the Sherpa 2.2.2 sample in Figure 6.8.

The good agreement between the analysis and Rivet predictions, below 0.5%, allows to validate the Rivet routine.

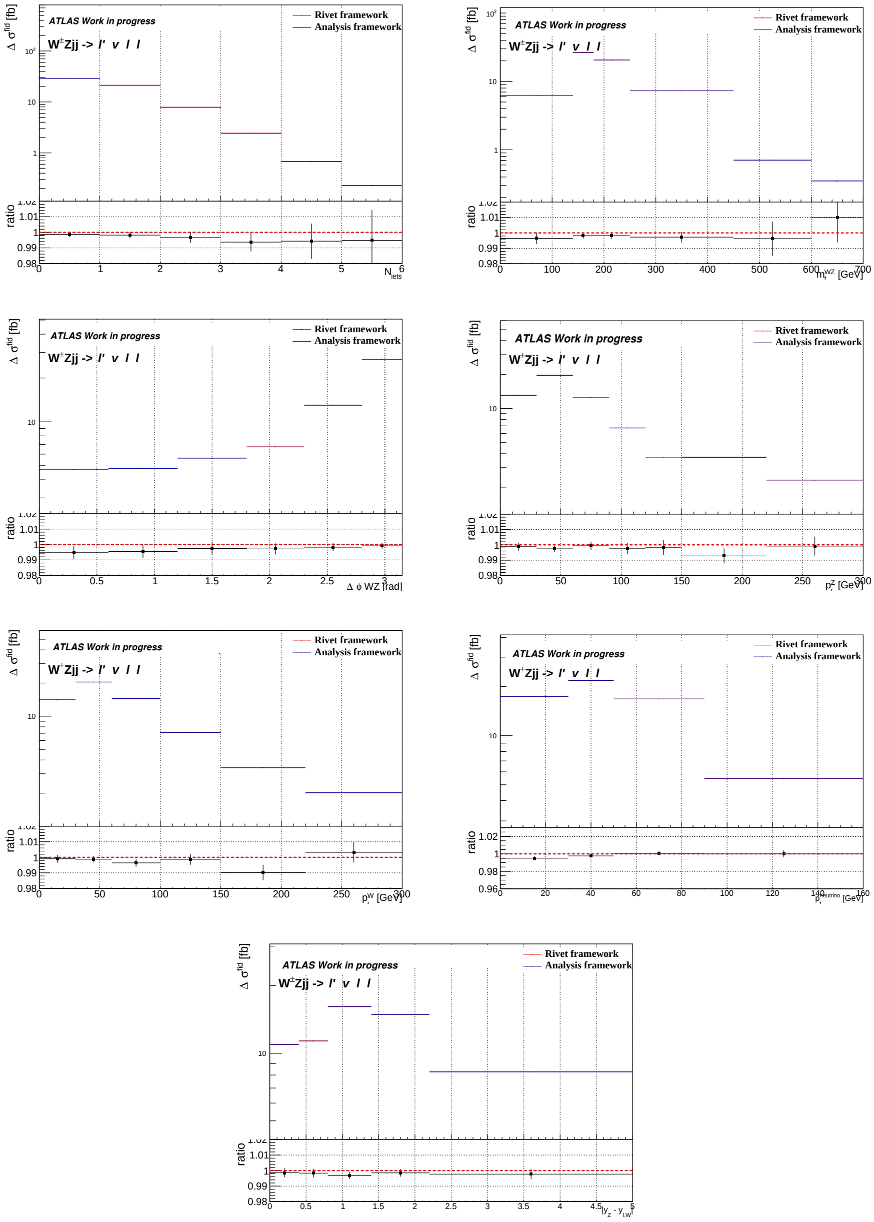

Figure 6.7: Comparison of the shapes of the differential distributions for the Powheg+Pythia8 sample. The error bars in ratio plot depicts the statistical errors of the Powheg+Pythia8 sample.

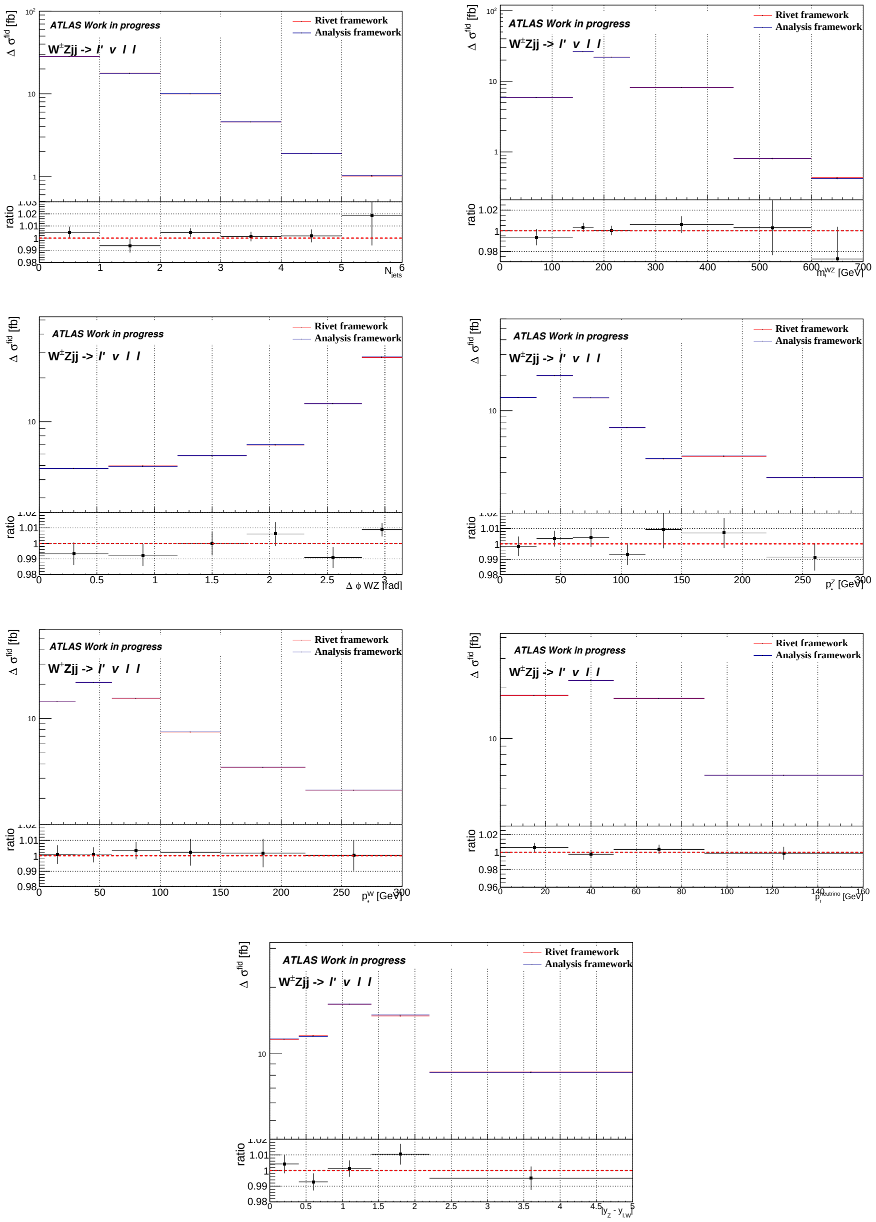

FIGURE 6.8: Comparison of the shapes of the differential distributions for the SHERPA 2.2.2 sample. The error bars in ratio plot depicts the statistical errors of the SHERPA 2.2.2 sample.

6.7 Effective Field Theory re-interpretation of the $W^{\pm}Z$ inclusive cross section

The $W^{\pm}Z$ inclusive production is a very important process as it is very sensitive to new physics effects through anomalous triple gauge couplings ($aTGCs$) that may lead to deviations from SM predictions. As described in Section 2.3.2.1, dimension-6 operators are used to estimate effects of $aTGCs$ both on the cross section measurement and on the shape of the relevant kinematical distributions.

6.7.1 Dimension-6 operators

For the study of the effects of the dimension-6 operators on the $W^{\pm}Z$ inclusive production, parton level MC samples are produced using the MadGraph 2.7.3 generator. The samples for the dimension-6 operators are produced using the $SMEFT@NLO$ FeynRules model [127]. The production of the events in this model can be done profiting from the decomposition method, explained in Section 2.3.2.4. Only CP conserving operators are for the moment included in the model. Furthermore, the model provides NLO QCD corrections but only for the SM and the full samples but not for the decomposed ones. For simplicity, only the WZ fully leptonic inclusive channel $pp \rightarrow \mu^+ \mu^- e^+ \nu_e$ is studied. For every sample, 10k events are produced at parton level and the scale of new physics Λ, explained in Section 2.3.2, is set to $1\,TeV$. The SM cross section in this study is not to be compared with the measured cross section as the event generation is done in LO and does not use the same phase space as in the nominal samples, explained in Section 4.2.

6.7.1.1 Effect of dimension-6 operators on WZ fully leptonic inclusive channel

The WZ inclusive process is affected by the dimension-6 operators. The existence of new physics will then be searched through these operators and if no deviations are found, confidence level (CL) limits will be given in the near future. Previous work on dimension-6 operators for the WZ inclusive channel is presented in [128–130].

As a first step, the effect on the production cross section of the various dimension-6 operators is studied and the ones which affect the measured cross section well above the measured precision of the order of $8-9\%$ (for full Run2 statistics) are kept. For this study, one dimension-6 operator is checked at a time and is set to three times the existing limit [131] [132] (limits from other diboson analyses as there were not any limits for dimension-6 operators for WZ channel at the time period this study took place), while all the other operators are set to the SM value. There are also dimension-6 operators that do not have a limit yet. For those operators, some arbitrary values are chosen in order to study their effect. Finally this part of the study is performed once using no object and event selections and once using a phase space very close to the fiducial one. Table 6.13 shows the object and event selections used for the searching of the sensitive operators.

Figures 6.9 and 6.10 shows the generated cross sections of the full samples for every dimension-6 operator compared to the SM cross section and the percentage difference of these cross sections once without using any selection and once using the fiducial phase space.

As it is depicted in the above figures from the comparison of these two figures, the effect of the dimension-6 operators may differ after applying the fiducial phase space but the sensitive

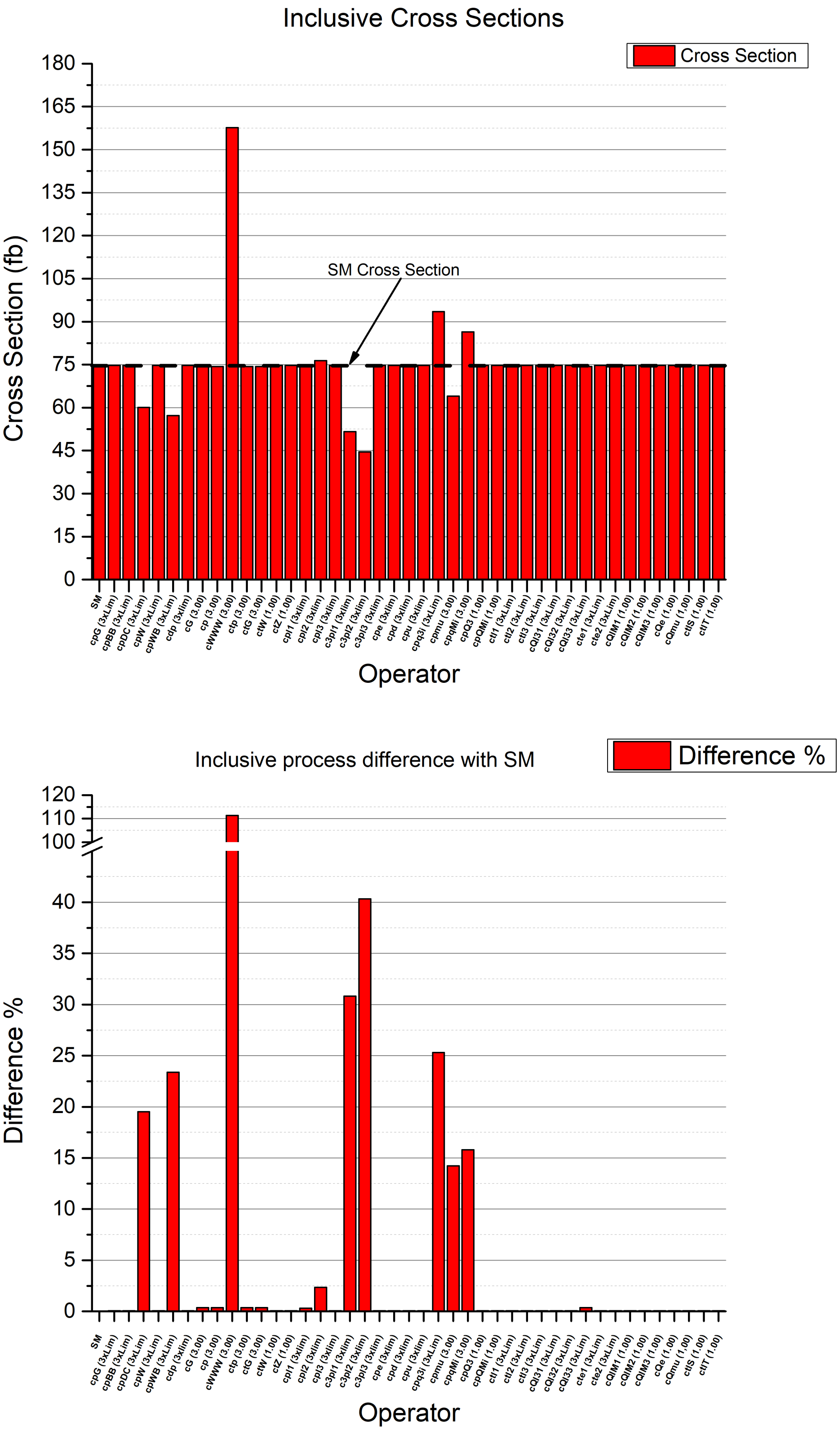

FIGURE 6.9: Comparison of SM cross section with the cross section of the full sample using one dimension-6 operator at a time (up) and the percentage difference between them (down) without applying any selecion.

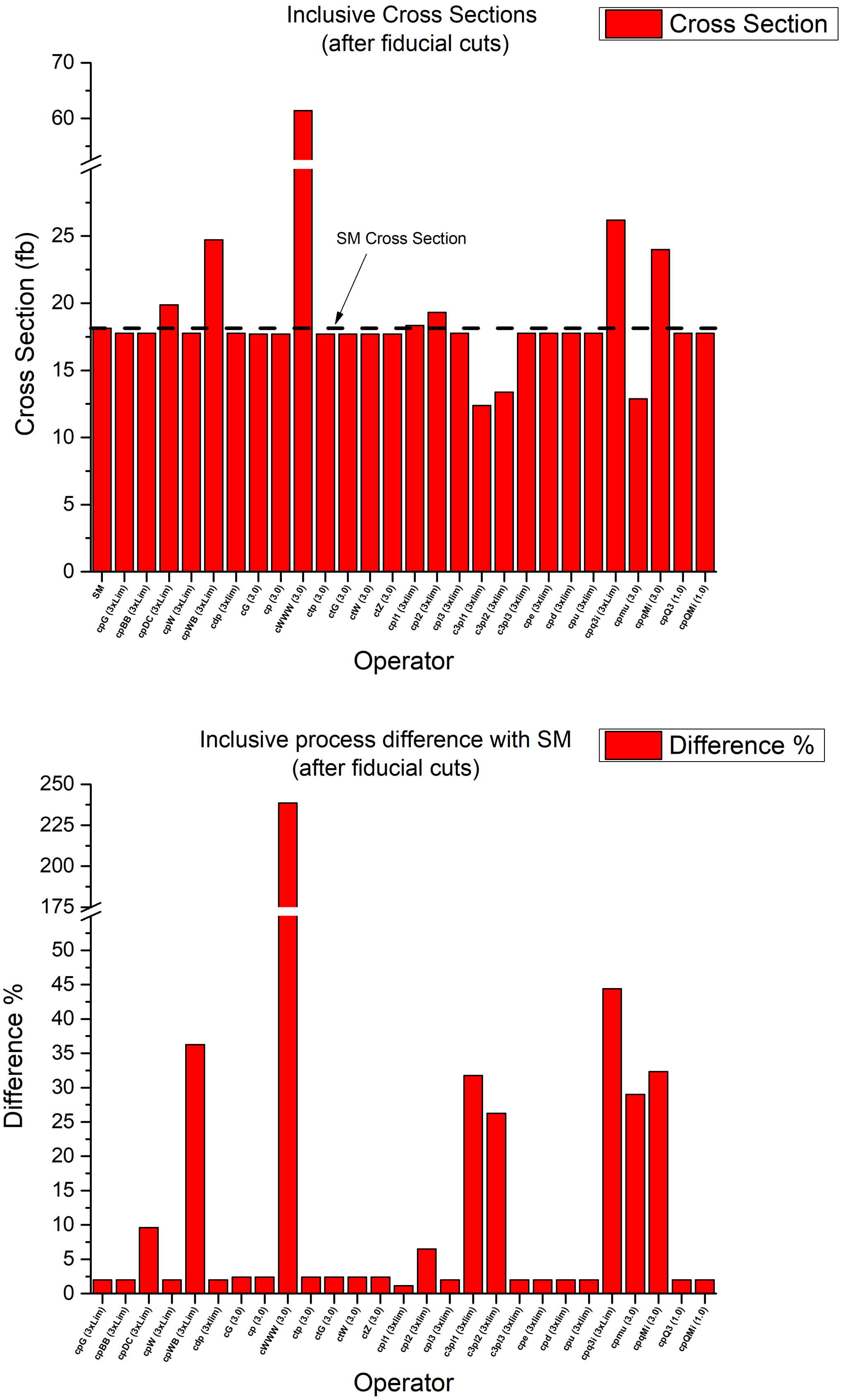

FIGURE 6.10: Comparison of SM cross section with the cross section of the full sample using one dimension-6 operator at a time (up) and the percentage difference between them (down) applying the fiducial phase space.

Fiducial Phase-Space	
p_{T} of Z leptons	> 20 GeV
p_{T} of W leptons	> 30 GeV
$\lvert\eta\rvert$ of leptons	< 2.5
m_Z range	$\lvert m_Z - m_Z^{PDG}\rvert < 10$ GeV
m_T^W	> 30 GeV

Table 6.13: WZ inclusive fiducial phase space definition for the determination of the most sensitive dimension-6 operators.

operators remain the same. So, the most sensitive dimension-6 operators that affect the WZ fully leptonic inclusive channel are the: $cpDC$, $cpWB$, $cWWW$, $c3pl1$, $c3pl2$, $cpmu$ and $cpqMi$ operators. It is necessary to mention here that for the $cWWW$, $cpmu$ and $cpqMi$ operators there were no existing limits at the time of this study and the arbitrary values used may lead to unphysical results, due to violation of unitarity constraints.

Since the most effective operators are determined, a study for the most sensitive kinematical variable for each operator is performed. The goal is to find the kinematical variable most sensitive to shape effects for each operator. In order to find the sensitive kinematical variables, a comparison of the shape of the distributions of some kinematical variables between the SM and the full sample for each dimension-6 operator is done. For this study events in the fiducial phase space are used. 15 different kinematical variables are checked:

Variables related to the kinematics of vector bosons

m_Z, m_W	invariant mass of Z and W bosons
p_T^Z, p_T^W	transverse momentum of Z and W bosons
η_Z, η_W	pseudorapidity of Z and W bosons
m_T^W	transverse mass of W boson
m_{WZ}	invariant mass of WZ system
m_T^{WZ}	transverse mass of WZ system
$m_{3leptons}$, $p_T^{3leptons}$	invariant mass and transverse momentum of the three leptons
$\lvert y_{l,W} - y_Z\rvert$	difference of rapidity of the lepton of W boson and Z boson
$\Delta\phi(l1_Z, l_W)$	difference of ϕ angle of the first lepton of Z boson and the lepton of W boson
$\Delta\phi(l2_Z, l_W)$	difference of ϕ angle of the second lepton of Z boson and the lepton of W boson
$\Delta\phi(Z, l_W)$	difference of ϕ angle of Z boson and the lepton of W boson

The most sensitive kinematical variables of the most effective dimension-6 operators are given in Table 6.14 and some examples of the comparison between the shapes of the distributions of the SM and the full sample for each operator are shown in Figure 6.11. The SM distribution is depicted with the blue line and it is called SM_{dim6}. The $SMEFT@NLO$ model has been used for this production setting all the operators to the SM values. The red line depicts the full sample for every operator and the values for the corresponding Wilson coefficients are shown in the legend.

Sensitive kinematical variables	
$cpDC$	$\Delta\phi(l2_Z, l_W)$
$cpWB$	m_T^{WZ}, $\Delta\phi(l2_Z, l_W)$
$cWWW$	m_T^{WZ}, $m_{3leptons}$
$c3pl1$	$\Delta\phi(l2_Z, l_W)$, $\Delta\phi(Z, l_W)$
$c3pl2$	$\Delta\phi(l2_Z, l_W)$, $\Delta\phi(Z, l_W)$
$cpq3i$	m_T^{WZ}, $\Delta\phi(l2_Z, l_W)$
$cpmu$	$\Delta\phi(l2_Z, l_W)$, $\Delta\phi(Z, l_W)$
$cpqMi$	$\Delta\phi(l2_Z, l_W)$, $\Delta\phi(Z, l_W)$

Table 6.14: Most sensitive kinematical variables of the most effective dimension-6 operators.

As it can be seen in Figure 6.11, there are dimension-6 operators for which the shape of the kinematical variables does not change at all except by an overall factor. That means that these operators have only cross section effects and not shape effects. These operators are the: $c3pl1$, $c3pl2$ and $cpmu$.

Finally, a first study to estimate the effect in the cross section when two dimension-6 operators of the same family are used simultaneously and all the others are set to the SM values is performed. Two pairs of operators are studied: the two bosonic operators $cpDC - cpWB$ and the two fermionic operators $c3pl1 - c3pl2$.

Comparing the cross section of the full samples using these pairs of operators with the SM cross section after the fiducial cuts, the differences from the SM are 56% for the $cpDC - cpWB$ pair and 53% for the $c3pl1 - c3pl2$ pair. The differences from the SM are bigger when using these operators as pairs than using them separately.

The most sensitive kinematical variables for the two pairs are given in Table 6.15 and the comparison of the shapes of the SM and the full sample are shown in Figure 6.12. For this study, events in the fiducial phase space are used.

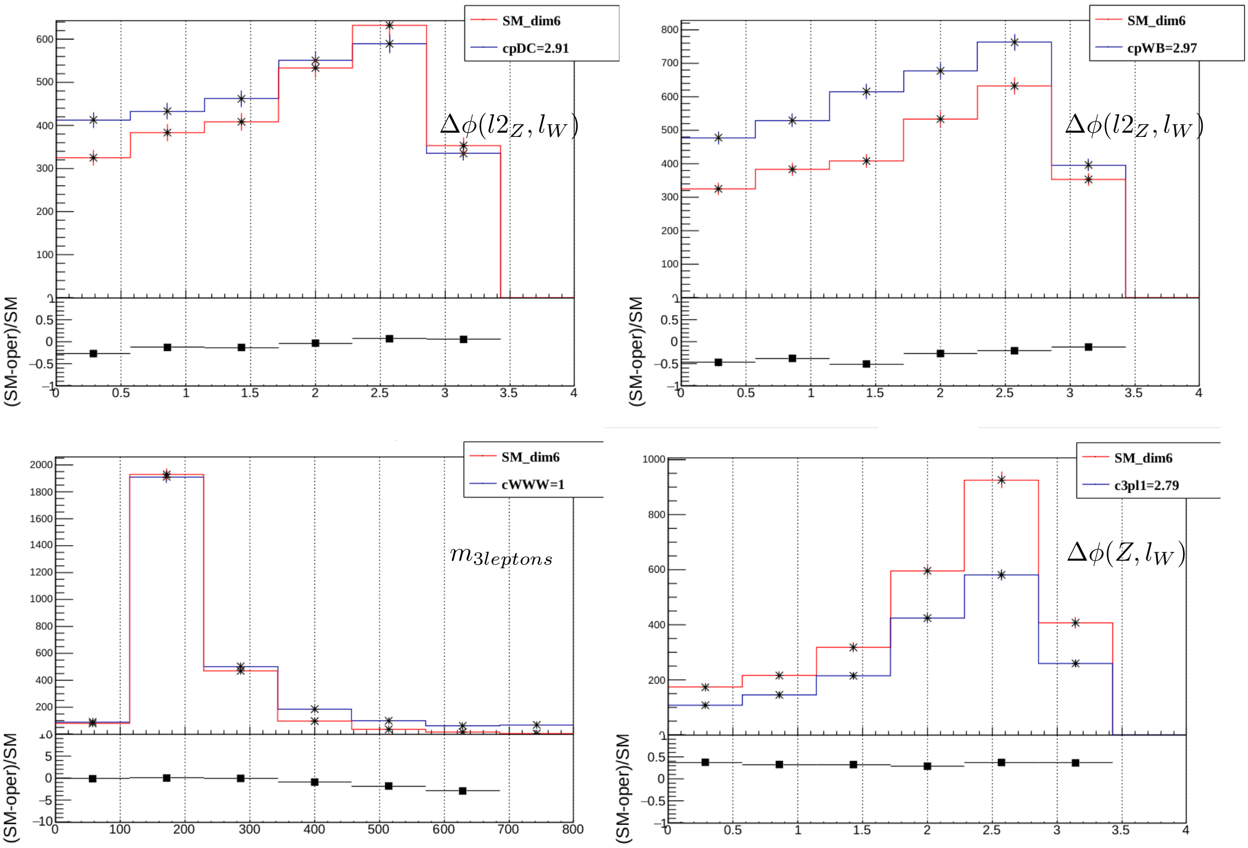

FIGURE 6.11: Examples of the comparison of the shapes of the SM distribution of the most sensitive kinematical variables with the corresponding distributions of the full sample using one dimension-6 operator at a time applying the fiducial phase space.

Sensitive kinematical variables	
$cpDC - cpWB$	$\Delta\phi(l2_Z, l_W)$
$c3pl1 - c3pl2$	$\Delta\phi(l2_Z, l_W)$

TABLE 6.15: Most sensitive kinematical variables for the two pairs of the dimension-6 operators.

6.7.1.2 Comparison of SM production at Leading order (LO) and at Next-to-leading order (NLO)

In order to determine the effect of the NLO QCD corrections to the LO production, a comparison between the shapes of the distributions of some kinematical variables are done and are shown in Figure 6.13. From this comparison, it can be seen that the shape of the LO and NLO distributions does not change at all except by an overall factor. This factor is called k-factor and it could be used in the future for setting a systematic uncertainty for the LO EFT distributions.

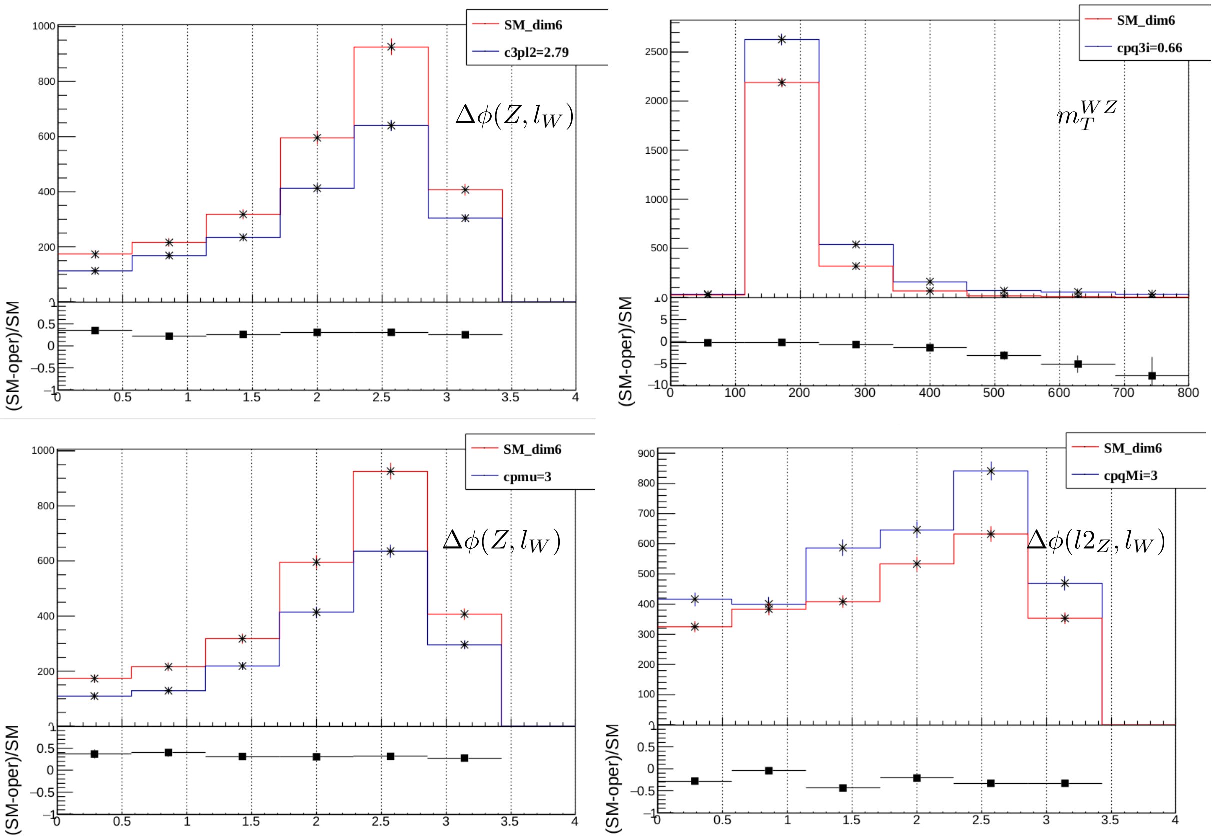

FIGURE 6.11: Examples of the comparison of the shapes of the SM distribution of the most sensitive kinematical variables with the corresponding distributions of the full sample using one dimension-6 operator at a time applying the fiducial phase space.

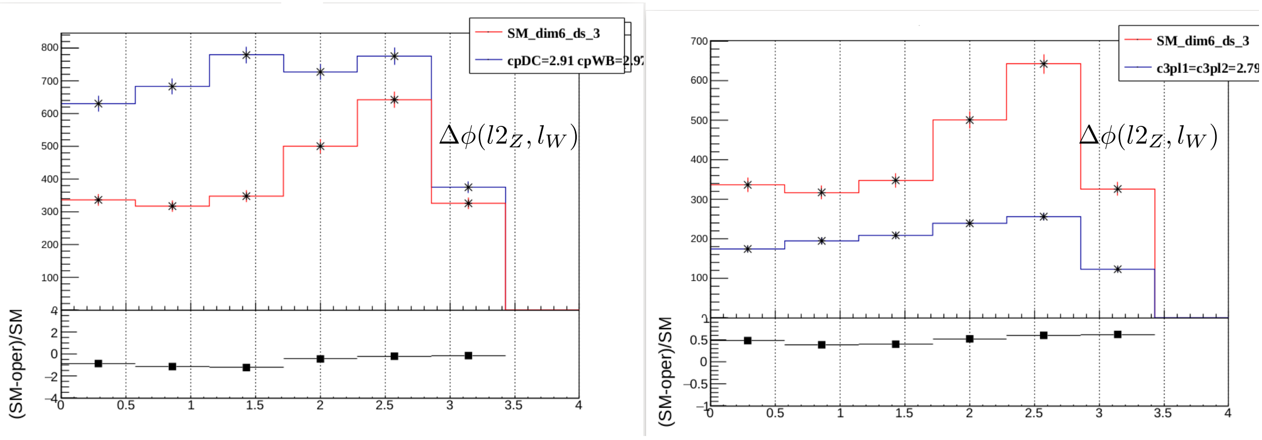

FIGURE 6.12: Comparison of the shapes of the SM distribution of the most sensitive kinematical variables with the corresponding distributions of the full sample using two dimension-6 operator simultaneously applying the fiducial phase space.

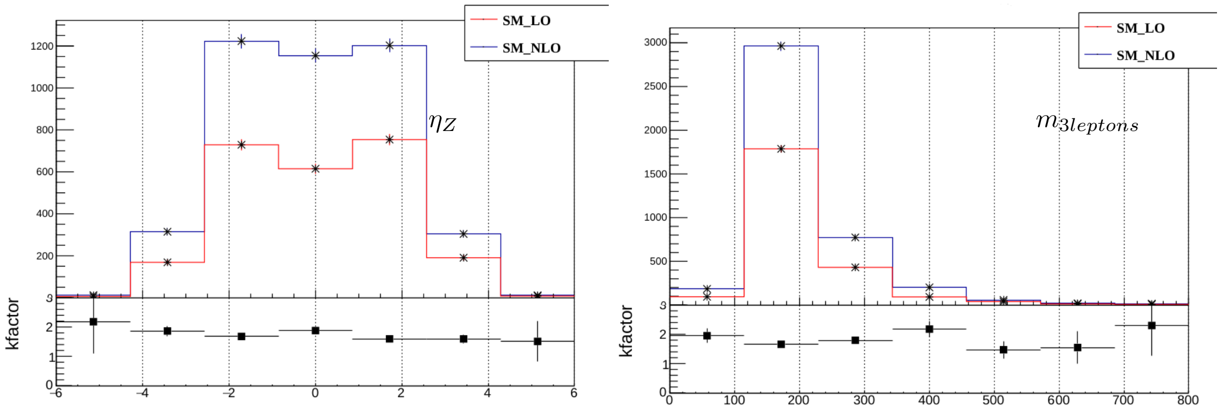

FIGURE 6.13: Examples of the comparison of the shapes of some kinematical variables for the WZ inclusive SM LO production and NLO production applying the fiducial phase space.

6.7.1.3 Validation of the decomposition method

In order to use the decomposition method, described in Section 2.3.2.4, it is necessary to validate it. The validity of the decomposition technique for some individual EFT parameters with arbitary values of the corresponding c_i coefficients has been verified by comparing the full sample with the sum of the decomposed samples. In Table 6.16 it is found that the differences between the $full$ production and the addition of the three terms is always less than 1% and within the MC statistical error for all the EFT parameters under study. More information and results on the validation of the decomposition procedure can be found in [130].

	value	SM xsec(fb)	INT xsec(fb)	QUAD xsec(fb)	FULL xsec(fb)	SUM xsec(fb)	Difference %
$cWWW$	-26.5	74.41	81.44	90330	90340	90490	0.16
$cpDC$	-41.2	74.41	-66.7	6519	5879	2260	0.5

TABLE 6.16: Closure tests

Chapter 7

$WZjj$ VBS analysis at $13\,TeV$

7.1 Introduction

In this thesis the $WZjj$ VBS production in proton-proton collisions at a centre-of-mass energy of $13\,TeV$ is studied as it is a very nice way to investigate the $SU(2)_L \times U(1)_Y$ gauge symmetry of the electroweak theory through the vector bosons self-couplings, as discussed in Section 2.2.2. Any deviations from the predicted couplings of vector bosons in the Standard Model could indicate a sign of existence of new physics. These deviations may result in additional contributions to quartic gauge couplings (QGC) beyond what is predicted by the Standard Model [133].

There are two processes that lead to the same final state. The first category, which includes VBS contributions, involves only weak interactions at Born level of order α_{EW}^6, including boson decays, and is called electroweak production ($WZjj - EW$). α_{EW} is the electroweak coupling constant. The second category involves both strong and electroweak interactions at Born level of order $\alpha_S^2\alpha_{EW}^4$, where α_S is the strong interaction coupling constant. This is known as QCD production ($WZjj - QCD$). The Standard Model predicts a small interference between electroweak and QCD production, which is estimated to be around 6% of the $WZjj - EW$ contribution in the fiducial phase-space, as it will be discussed later. This contribution is included by convension to the $WZjj - QCD$ production as its kinematics is closer to QCD production rather than the electroweak production.

Figure 7.1 shows the Feynman diagrams with VBS topologies for the $W^{\pm}Zjj$ production at the LHC.

There are additional to the Figure 7.1 diagrams that share the same initial and final states as the $WZjj - EW$ process and they are of order six or higher in electroweak coupling constant. The most important contribution comes from the tZj background, where events resulting from

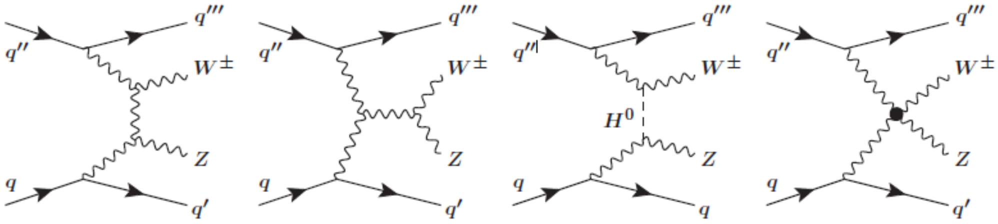

FIGURE 7.1: Feynman diagrams that depict the vector boson scattering process at the LHC and lead to the $WZjj$ final state involve triple and quartic gauge boson vertices, as well as diagrams that include the exchange of the Higgs boson.

an initial state b-quark are mainly dominated by resonant top quark production. Example of a Feynman diagram for this process is shown in Figure 7.2. As it is necessary to exclude this contribution, a veto on b quarks in the initial state of the matrix element is applied.

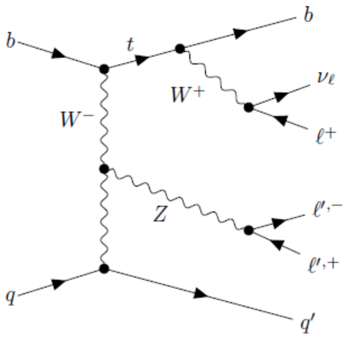

FIGURE 7.2: Example Feynman diagram for the tZj process at LO. The upper quark line contains a top-quark resonance, motivating the definition of these contributions as a background process.

As in Section 6.1, gauge bosons decay into two same flavour but opposite charge leptons for Z, while W decays into a lepton and a neutrino. In the same way, leptons can be electrons (e) or muons (μ) and four flavor channels all with the same branching ratio are considered: $e^{\pm}e^{+}e^{-}$, $\mu^{\pm}e^{+}e^{-}$, $e^{\pm}\mu^{+}\mu^{-}$ and $\mu^{\pm}\mu^{+}\mu^{-}$

7.2 Object and Event selection

7.2.1 Object selection

The object selections used for the study of the electroweak $WZjj$ production are exactly the same as in Section 6.2.2.

7.2.2 Event selection

To enrich the $WZjj$ production in WZ VBS events, a more restrictive selection of events is required compared to the inclusive analysis. This selection, referred to as the "$WZjj$ event selection," is applied on top of the inclusive WZ selection, which is summarized in Table 6.8. The selection is based on the kinematics of the jets associated with the WZ VBS events. The events are required to have exactly two VBS tagging jets with a transverse momentum greater than $40\ GeV$, opposite sign and $|\eta| < 4.5$ pseudorapidity. The leading tagging jet is the one with the highest transverse momentum in the event, regardless of its position, while the second leading jet is the highest transverse momentum jet in the opposite hemisphere among the remaining jets. Events with an invariant mass of the two tagging jets, m_{jj}, smaller than $150\,GeV$ are excluded to reduce the contribution from triboson background, where one of the boson is decaying hadronically.

The "$WZjj$" region is divided into three orthogonal sub-regions. They include the control region for $t\bar{t}V$ and tZj backgrounds (b-CR) with at least one b-jet, the control region for the dominant QCD background ($WZjj - QCD$ CR) with $N_{b-jet} = 0$ and $m_{jj} < 500\,GeV$, and the signal region (SR) with the remaining phase space. Additionally, a separate control region is created for the $ZZjj$ background, as explained in Section 7.3.2. Table 7.1 summarizes the requirements for the $WZjj$ event selection and the aforementioned control and signal regions.

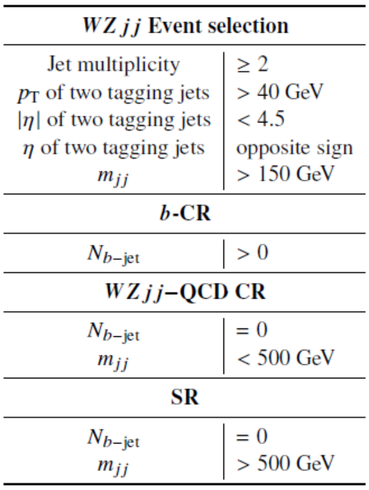

$WZjj$ Event selection	
Jet multiplicity	≥ 2
p_{T} of two tagging jets	> 40 GeV
$\lvert\eta\rvert$ of two tagging jets	< 4.5
η of two tagging jets	opposite sign
m_{jj}	> 150 GeV
***b*-CR**	
$N_{b\text{-jet}}$	> 0
$WZjj$–QCD CR	
$N_{b\text{-jet}}$	= 0
m_{jj}	< 500 GeV
SR	
$N_{b\text{-jet}}$	= 0
m_{jj}	> 500 GeV

Table 7.1: The analysis event selection for the $WZjj - EW$ measurement and the three sub-regions.

7.3 Background estimation

The categories of the background affecting the $WZjj$ are the same as in Section 6.3.

7.3.1 Reducible background

The method for the estimation of the reducible background is the same as described in Section 6.3.1.

7.3.2 Irreducible background

The estimation of the irreducible background follows the same strategy as in Section 6.3.2 but using different control regions. There are two control regions which are orthogonal to the signal region as explained in Section 7.2.2 and as shown schematically in Figure 7.3. The first control region is used for the estimation of the $t\bar{t}V$ and tZj backgrounds, it is referred as $b-CR$ and it contains at least one b-tagged jet. The second control region is the $WZjj-QCD$ CR, which is used in order to study the main background of this analysis, the $WZjj-QCD$ background. In this region, there are no b-tagged jets and the invariant mass of the two tagging jet is $150\,GeV < m_{jj} < 500\,GeV$.

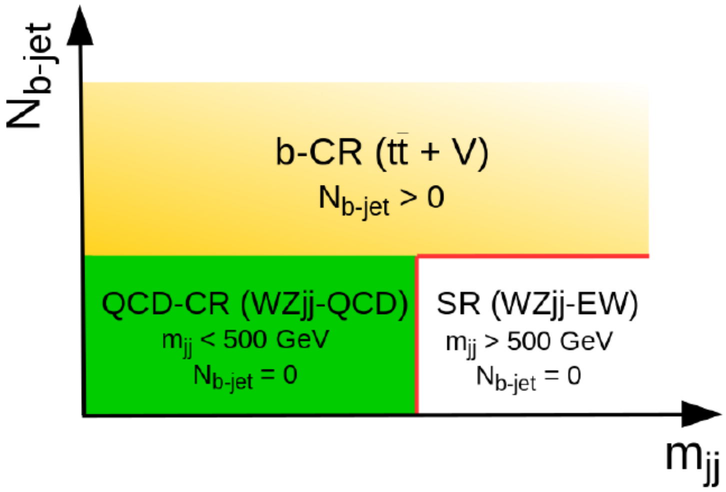

FIGURE 7.3: Schematic view of the signal and control regions definition inside of the VBS selection.

Finally there is a control region in order to estimate the $ZZjj$ background, the so-called $ZZjj - CR$. This is selected as in Section 6.3.2 with the $WZjj$ event selection additionally applied.

7.4 Systematic Uncertainties

In a measurement, systematic uncertainties are uncertainties that arise from biases or errors in the experimental setup, measurement techniques, or analysis procedures, leading to a consistent shift or offset in the results. Systematic uncertainties can affect the accuracy and precision of the measurement, and must be carefully evaluated and accounted for in order to ensure the reliability and validity of the results. The systematic uncertainties are splitted into two categories: the experimental uncertainties and the theoretical uncertainties.

7.4.1 Experimental uncertainties

Experimental uncertainties arise from the detector simulation and reconstruction, and they are not related to any particular process. The following experimental uncertainties are considered:

Muons The primary sources of systematic uncertainties for muons include reconstruction and identification efficiency, transverse momentum resolution and scale, muon isolation, and impact parameter cut efficiency [97]. To account for these uncertainties, various methods are employed. Reconstruction and identification efficiencies are determined through tag-and-probe techniques in $Z \to \mu\mu$ events using both data and simulation. Differences between data and MC are incorporated by applying scale factors (SFs) to the simulation. The SFs are varied within their corresponding systematic uncertainties, resulting to a varied shape of spectrums and ultimately affecting the signal yield. The transverse momentum resolution correction is crucial in these analyses as it impacts the muon selection efficiency, Z boson mass reconstruction, and W lepton p_T determination. To estimate this uncertainty, the di-muon mass resolution is compared between data and MC. Event yields are obtained by independently varying the p_T correction of muons in the Inner Detector and Muon Spectrometer, considering the uncertainties observed in p_T scale and resolution from the data. Finally, regarding muon isolation and impact parameter efficiencies, they are measured by quantifying the differences between data and MC using the Z tag-and-probe method.

Electrons Reconstruction and identification efficiency, electron energy resolution and scale, energy scale and smearing, as well as electron isolation and impact parameters are the main sources of systematic uncertainties for electrons [95]. To address the differences in reconstruction and identification efficiencies between data and MC, scale factors (SFs) are applied to the simulation. These SFs are obtained from auxiliary measurements conducted in different bins. Similar to muons, the uncertainties associated with electron isolation and impact parameters are estimated by comparing data and MC using the Z tag-and-probe method $Z \to ee$. The electron energy resolution is corrected in the MC to match the observed data. Additionally, the electron energy scale is verified and calibrated in both data and MC using $Z \to ee$ events. The dominant uncertainties related to the energy scale arise from the modeling of the ATLAS detector and the calibration of the EM calorimeter pre-sampler energy scale. For both electron resolution and energy scale, all relevant physical effects are combined in quadrature and considered fully correlated in the η region.

Jets The reconstruction and energy calibration of jets introduce systematic uncertainties which arise from uncertainties in the Jet Energy Scale (JES) and Jet Energy Resolution (JER), which are determined using a combination of simulation and in-situ techniques [99]. In addition, for the VBF jets, there are specific requirements such as passing the JVT cut and failing the b-jet existence criterion. Therefore, there are corresponding systematic uncertainties associated with JVT efficiency and b-tagging efficiency.

Missing transverse energy The uncertainties associated with the missing transverse momentum comprise uncertainties related to both the resolution and scale of the track-based soft-term contributions. The uncertainties on the hard-terms are encompassed by variations in the electron, muon, and jet uncertainties.

Pileup This addresses the uncertainties in the pileup used in MC samples, which are generated based on distributions of the number of interactions per bunch crossing that do not accurately reflect the data and thus require correction.

Luminosity Luminosity is used to rescale the simulations to the measured data and a 0.83% uncertainty is incorporated as a modification of the global normalization for each simulation.

Uncertainties in particle reconstruction can be affected by statistical fluctuations due to the limited number of available simulation events. To prevent these fluctuations in the fitting process, a smoothing technique is applied. The first step involves calculating the relative uncertainty for each systematic component and determining its statistical fluctuations via the bootstrap method [134]. Next, the asymmetry and its associated statistical uncertainty between the $\pm 1\sigma$ variations of the systematic are computed. If the mean of the asymmetry across all bins is statistically compatible with zero within a significance level of 2σ, the $\pm 1\sigma$ variations are combined to achieve symmetrical uncertainty variations around the nominal Monte Carlo prediction.

7.4.2 Theoretical uncertainties

Theoretical uncertainties are specific to a dataset of simulated events and represent the level of accuracy of the theory/MC predictions.

PDF and α_S uncertainties for $WZjj-$QCD and $WZjj-$EW The PDF uncertainties are separated into two categories. The first uncertainty relates to the selection of the parton distribution function (PDF) and follows the PDF4LHC recommendations [135]. This uncertainty is determined by computing the standard deviation of 100 Monte Carlo replicas of the NNPDF 3.0 set [84]. The possible variations of the distributions when using other PDF sets, as the MMHT2014 and CT14 sets, are also taken into account. The second uncertainty accounts for changes in the strong coupling constant (α_S) where the nominal value of 0.118 can be varied to 0.117 or 0.119.

QCD scale uncertainty for $WZjj{-}\mathrm{QCD}$ The QCD scale uncertainties are determined by varying the renormalization and factorization scales (denoted as μ_R and μ_F, respectively) separately by a factor of $x = 2$ or $x = \frac{1}{2}$. The envelope of the largest deviations is used to define a QCD scale uncertainty.

QCD scale uncertainty for $WZjj{-}\mathrm{EW}$ For the $WZjj{-}\mathrm{EW}$ process, the QCD scale uncertainties are estimated using alternative definitions for the renormalisation and factorization scales, which are included in the $WZjj{-}\mathrm{EW}$ MadGraph+Pythia MC sample as built-in weights. The definitions $\mu_0 = \sum_{i=1}^{N} \sqrt{m_i^2 + p_{\mathrm{T},i}^2} = HT$, $\mu_0 = HT/2$ and $\mu_0 = \sqrt{p_{\mathrm{T}}^{j_1}\ p_{\mathrm{T}}^{j1_2}}$ have been considered for this study. The uncertainty band on the $WZjj{-}\mathrm{EW}$ MadGraph+Pythia prediction is determined by taking the maximum variations between the various definitions of the scale μ_0 and the scale variations by factors of 2 and $\frac{1}{2}$.

Model uncertainties for $WZjj{-}\mathrm{QCD}$ In order to estimate the model uncertainties for the $WZjj{-}\mathrm{QCD}$, the difference in shape of the distributions obtained by MadGraph+Pythia and Sherpa is used. These are the relevant distributions of the variables used in the control and signal regions for the final fit. The difference between the two predictions is symmetrized and is used to establish an uncertainty band around the MadGraph+Pythia prediction. For the $WZjj{-}\mathrm{EW}$, it is not possible to estimate such an uncertainty as there is no alternate MC sample generated with a different hard-process generator.

Parton shower uncertainty for $WZjj{-}\mathrm{EW}$ To evaluate the uncertainty associated with parton shower in the $WZjj{-}\mathrm{EW}$ MadGraph+Pythia MC simulation, an alternate MC sample is generated using MadGraph and showered with Herwig. The difference between the two predictions is symmetrized and is used to establish an uncertainty band around the MadGraph+Pythia prediction. For the $WZjj{-}\mathrm{QCD}$, it is not possible to estimate such an uncertainty as there is no alternate MC sample generated with a different parton shower generator.

Interference between $WZjj{-}\mathrm{QCD}$ **and** $WZjj{-}\mathrm{EW}$ **processes** The MadGraph+Pythia samples used for analysis contain only purely $WZjj{-}\mathrm{QCD}$ or purely $WZjj{-}\mathrm{EW}$ events. However, since the two processes share the same initial and final states, there is an additional contribution to the $WZjj$ data that arises from the interference between them. This interference contribution can be directly obtained using the MadGraph MC event generator. The ratio of the interference effect on the purely $WZjj-$EW production is determined to be 5.3% at the detector level in the $WZjj$ signal SR. In the fitting process, the interference is added to the QCD prediction as a separate MC contribution using a dedicated template simulated by MadGraph+Pythia. QCD scale and PDF uncertainties are taken into account for this template. Specifically, for the scale uncertainties, the same procedure as described previously for the $WZjj-$QCD MC sample is followed.

Uncertainties on background estimation The uncertainties associated with the reducible background events, that stem from misidentified leptons, are determined using the data-driven matrix method and they are approximately 20% to 25%. On the other hand, the uncertainties related to the irreducible background sources is assessed by propagating the uncertainties associated with their MC cross-sections and they are 25% for VVV and 15% for $ZZjj - EW$ backgrounds. Finally, no normalisation uncertainties are attributed to $t\bar{t}V$, tZj, and $ZZjj - QCD$ backgrounds, as their estimations are based on a data-driven approach in dedicated control regions, as explained in Section 7.3.2.

7.5 Fiducial $WZjj - EW$ phase space definition and theory predictions

The phase space definition of the $WZjj - EW$ measurement is a subset of the inclusive phase space and is used for measuring the cross section of $WZjj - EW$ and total $W^{\pm}Zjj$. It is called fiducial $WZjj - EW$ phase space and its difference with the inclusive phase-space is the addition of jet-based selection criteria.

On top of the selection criteria of the inclusive phase space, which is summarized in Table 6.12, at least two particle-level jets with a transverse momentum greater than $40\,GeV$ and $|\eta_j| < 4.5$ are required. The angular distance between all selected leptons and jets is required to be greater than 0.3 ($\Delta R(j,l) > 0.3$). Jets that do not meet this requirement are discarded. To enhance sensitivity to VBS processes, the invariant mass m_{jj} of the two highest-p_T jets in opposite hemispheres ($\eta_{j1}\,\dot{\eta}_{j2} < 0$) which can be defined as

$$\begin{aligned} m_{jj} &= \sqrt{(E_{j1} + E_{j2})^2 - (\vec{p}_{j1} + \vec{p}_{j2})^2} \\ &= \sqrt{2p_{\mathrm{T}}^{j1} p_{\mathrm{T}}^{j1} (\cosh \Delta\eta(j1, j2) - \cos \Delta\phi(j1, j2))}, \end{aligned} \tag{7.1}$$

assuming massless jets, is required to be greater than $500\,GeV$. These two jets are referred to as tagging jets. Table 7.2 summarizes the definition of the fiducial $WZjj - EW$ phase-space.

Variable	Fiducial inclusive	Fiducial $WZjj-$EW
Lepton $\|\eta\|$	< 2.5	< 2.5
p_{T} of ℓ_Z, p_{T} of ℓ_W [GeV]	$> 15, > 20$	$> 15, > 20$
m_Z range [GeV]	$\|m_Z - m_Z^{\mathrm{PDG}}\| < 10$	$\|m_Z - m_Z^{\mathrm{PDG}}\| < 10$
m_{T}^W [GeV]	> 30	> 30
$\Delta R(\ell_Z^-, \ell_Z^+)$, $\Delta R(\ell_Z, \ell_W)$	$> 0.2, > 0.3$	$> 0.2, > 0.3$
p_{T} two leading jets [GeV]	$-$	> 40
$\|\eta_j\|$ two leading jets	$-$	< 4.5
Jet multiplicity	$-$	≥ 2
$\eta_{j1} \cdot \eta_{j1}$	$-$	< 0
m_{jj} [GeV]	$-$	> 500
$\Delta R(j, \ell)$	$-$	> 0.3
$N_{b-\mathrm{quark}}$	$-$	$= 0$

Table 7.2: Phase space definitions used for the fiducial inclusive and $WZjj - EW$ cross-section measurements.

The cross section for $WZjj-$EW production predicted by MadGraph+Pythia, for a given flavour channel, in the $WZjj-$EW fiducial phase-space is

$$\sigma_{WZjj-\mathrm{EW}}^{\textsc{MadGraph+Pythia}} = 0.370 \pm 0.001\,(\mathrm{stat.})^{+0.006}_{-0.006}\,(\mathrm{PDF})^{+0.030}_{-0.026}\,(\mathrm{scale})\ \mathrm{fb}\,. \tag{7.2}$$

The cross section for $WZjj-$QCD production, for a given flavour channel, can be calculated at the NLO level in QCD and merged to parton shower using MadGraph+Pythia. This cross section in the $WZjj-$EW fiducial phase-space is

$$\sigma_{WZjj-\mathrm{QCD}}^{\textsc{MadGraph+Pythia}} = 1.5145 \pm 0.0086\,(\mathrm{stat.})^{+0.016}_{-0.016}\,(\mathrm{PDF})^{+0.086}_{-0.147}\,(\mathrm{scale})\ \mathrm{fb}\,. \tag{7.3}$$

In the $WZjj-$EW fiducial region the cross section of the interference contribution is calculated at LO using MadGraph+Pythia to be $\sigma^{\mathrm{fid.,\,WZjj-INT\,th.}} = 0.0226 \pm 0.0002\,(\mathrm{stat.})$ fb. It therefore represents 6.1% of the $WZjj-$EW contribution.

7.6 Integrated $WZjj-EW$ and $WZjj-QCD$ cross-section measurements

The first observation of the $WZjj - EW$ production had been done using data which were collected in 2015 and 2016 by the ATLAS experiment at the Large Hadron Collider, and correspond to an integrated luminosity of 36.1 fb^{-1} [136]. The measured fiducial cross-section for electroweak production was

$$\begin{aligned}\sigma_{WZjj-EW} =& 0.57^{+0.14}_{-0.13}\text{ (stat.) }^{+0.05}_{-0.04}\text{ (exp. syst.)}\\ & ^{+0.05}_{-0.04}\text{ (mod. syst.) }^{+0.01}_{-0.01}\text{ (lumi.) fb.}\end{aligned} \tag{7.4}$$

and it was larger than the Sherpa 2.2.2 LO Standard Model prediction of $0.32\ \pm\ 0.03\ fb$.

The goal of the recent analysis is to improve the precision of the measurement of the $WZjj - EW$ cross section and to measure the cross-section of $WZjj - QCD$ production in the same phase space using the entire set of data of the Run 2 period (2015-2018), which were collected by the ATLAS experiment at the Large Hadron Collider, and correspond to an integrated luminosity of $140\ fb^{-1}$.

The analysis method is similar to the one used in the previous analysis, where events in the $WZjj \rightarrow l'\nu lljj$ decay channel are reconstructed and events with exactly three leptons are selected and separated into four channels based on the lepton flavor. Leptons can be electrons or muons. As in the previous analysis, a Boosted-Decision-Tree (BDT) method is used to distinguish between the signal process and background processes on the bases of a BDT score variable, which is built in order to separate background and signal events. The significance of the $WZjj - EW$ cross section observation is extracted using a template fit on the BDT score observable. The fitting procedure comprises a simultaneous fit between the signal and the $b - CR$ and ZZ control regions.

In the current analysis, the $WZjj - QCD$ cross-section is measured simultaneously with $WZjj - EW$ in the signal region. The interference terms between $WZjj - QCD$ and $WZjj - EW$ are included to the $WZjj - QCD$ cross-section, as explained in Section 7.1. Therefore, it is preferred to measure the $WZjj - QCD$ contribution with the $WZjj - EW$ contribution, making the $WZjj - EW$ measurement more robust and less affected by the theory uncertainties of the $WZjj - QCD$ predictions. Thus, the normalization and theory uncertainties of $WZjj - QCD$ measurement depend solely on data in the signal region.

Following this procedure, the integrated $\sigma_{WZjj-EW}$ and $\sigma_{WZjj-QCD}$ cross sections can be measured simultaneously.

7.6.1 Expected results from Asimov fit

In this section the expected sensitivity and the results of the template fit on Asimov data (explained in Section 7.9.2.4) are presented.

Table 7.3 shows the event yields for the signal region and the two background control regions after the first step of background normalization. Statistical, object and theoretical uncertainties are included on the event yields.

	SR	b-CR	ZZ-CR
Data	—	666	210
Total pred.	782 ± 33	660 ± 50	205 ± 11
$WZjj$-EW	125.2 ± 3.4	4.82 ± 0.28	0.725 ± 0.014
$WZjj$-QCD	502 ± 24	77 ± 21	6.2 ± 0.7
$WZjj$-INT	6.5 ± 3.3	0.58 ± 0.29	0.22 ± 0.11
$t\bar{t}+V$	20.9 ± 0.7	289 ± 10	9.89 ± 0.28
tZj	28.5 ± 1.1	134 ± 4	0.432 ± 0.005
ZZ-QCD	41.6 ± 2.8	10.1 ± 0.6	159 ± 9
ZZ-EW	6.7 ± 1.7	0.25 ± 0.06	23 ± 6
VVV	2.4 ± 0.6	0.39 ± 0.10	4.1 ± 1.1
Misid. leptons	49 ± 11	150 ± 40	1.7 ± 0.5

TABLE 7.3: Pre-fit event yields for the electroweak signal and all the backgrounds.

This measurement involves measuring both the $\sigma_{WZjj-EW}$ and $\sigma_{WZjj-QCD}$ cross sections in the signal region, along with the signal strengths μ_{ttV}, μ_{tZ}, and μ_{ZZ} extracted by the fit. Table 7.4 presents the expected uncertainties and precision of the $\sigma_{WZjj-EW}$ and $\sigma_{WZjj-QCD}$ cross-sections. The estimated values of the cross-section match the predictions of each generator as the Asimov data is used. The expected statistical significance for $\sigma_{WZjj-EW}$ is estimated to be $Z_{exp} = 6.57\sigma$.

Region	Parameter	σ [fb]	$\delta\sigma$ [%]	$\frac{\sigma}{\delta\sigma}$	$\frac{\sigma^{\text{meas.}}}{\sigma^{\text{pred.}}}$	Z
Inclusive	$\sigma_{WZjj-EW}$	0.37	18.30	5.46	1.00	6.57
	$\sigma_{WZjj-QCD}$	1.54	8.33	12.01	1.00	> 12
	μ_{ZZ}	1.00	10.63			
	μ_{ttV}	1.00	13.34			
	μ_{tZ}	1.00	21.42			

TABLE 7.4: Expected relative uncertainties on the measured cross sections $\sigma_{WZjj-EW}$ and $\sigma_{WZjj-QCD}$.

The measured values of $\sigma_{WZjj-EW}$ and $\sigma_{WZjj-QCD}$ are displayed in Figure 7.4 along with 68% and 95% confidence level (CL) contours.

Figure 7.5 depicts the pull and the impact of the nuisance parameters, when the Asimov data are used and Figure 7.6 shows the correlation between all parameters of the fit. The parameters corresponding to the modelling of $WZjj-QCD$ are slightly over-constrained from data at low value of the BDT Score in the SR.

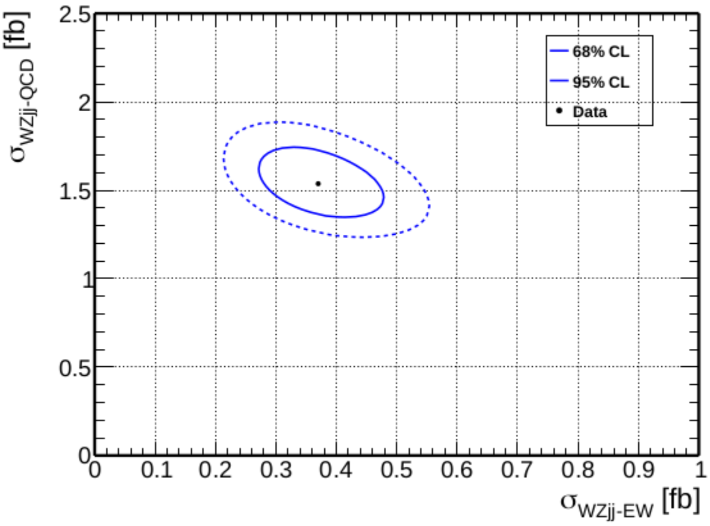

FIGURE 7.4: Values of inclusive $\sigma_{WZjj-EW}$ and $\sigma_{WZjj-QCD}$ cross section from the fit on Asimov data.

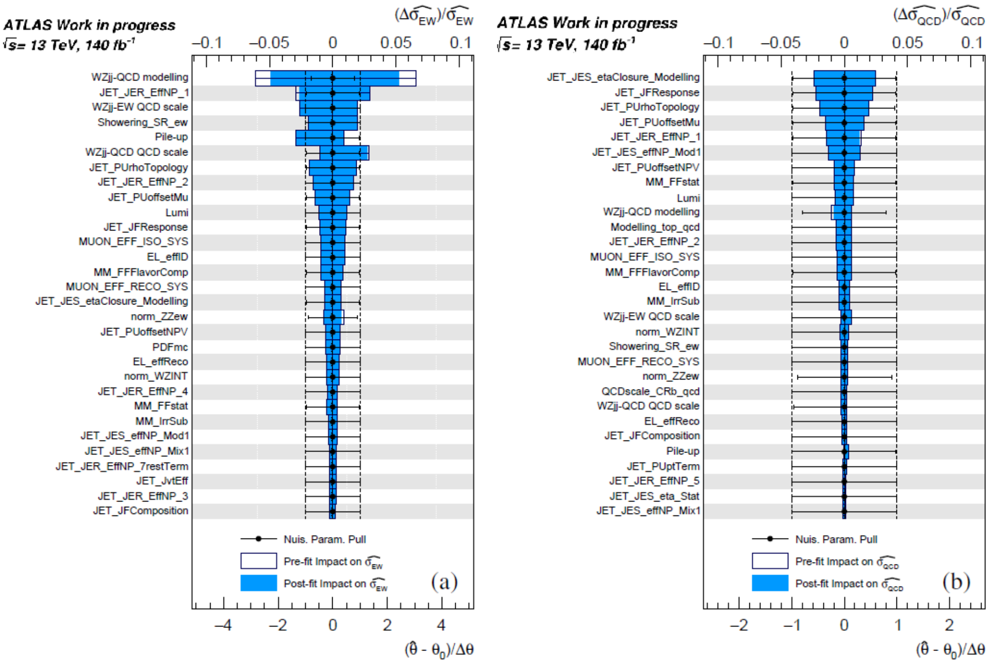

FIGURE 7.5: Pull and ranking by decreasing impact of the main nuisance parameters for the fit on Asimov data, for $\sigma_{WZjj-EW}$ (a) and $\sigma_{WZjj-QCD}$ (b).

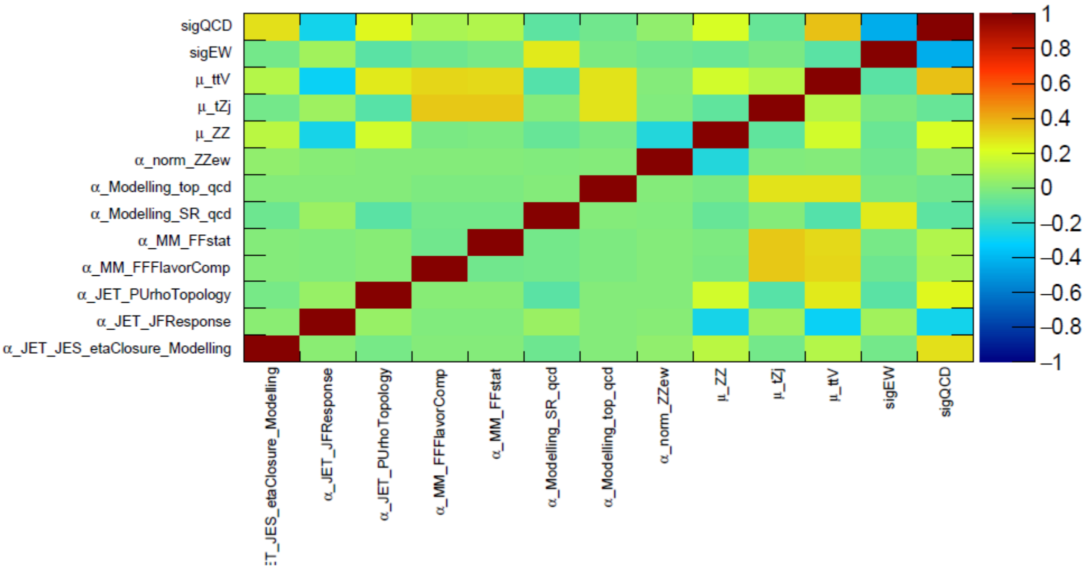

FIGURE 7.6: Correlation of all nuisance parameters and points of interest included in the fit on Asimov data.

Finally, the impact of the main categories of nuisance parameters on the $\sigma_{WZjj-EW}$ and $\sigma_{WZjj-QCD}$ is summarized in Table 7.5. It can be seen that the $WZjj-EW$ and $WZjj-QCD$ theory modelling uncertainties along with the jets uncertainties are the most important uncertainties in the cross sections measurement.

	$\sigma_{WZjj\text{–}EW}$	$\sigma_{WZjj\text{–}QCD}$
Cross section [pb]	0.37	1.54
Source	Relative Uncertainty [%]	
$WZjj$–EW theory modelling	3.4	0.8
$WZjj$–QCD theory modelling	5	1.0
$WZjj$–EW and $WZjj$–QCD interference	0.4	0.6
PDFs	0.7	0.06
Jets	4	5
Pile-up	1.9	0.5
Electrons	0.9	0.8
Muons	0.9	0.9
b-tagging	0.10	0.08
MC statistics	2.8	1.0
Misid. lepton background	1.0	1.3
Other backgrounds	0.9	0.15
Luminosity	0.8	0.9
All systematics	11	6
Statistics	15	5
Total	18	8

TABLE 7.5: Impact of the main categories of nuisance parameters on $\sigma_{WZjj-EW}$ and $\sigma_{WZjj-QCD}$.

7.6.2 Data measurement

In this section the results of the measurement of the integrated $\sigma_{WZjj-EW}$ and $\sigma_{WZjj-QCD}$ cross sections using data are presented.

Table 7.6 shows the event yields for the signal region and the two background control regions after the first step of background normalization. Statistical, object and theoretical uncertainties are included on the event yields.

	SR	b-CR	ZZ-CR
Data	646	666	210
Total pred.	646 ± 25	666 ± 26	213 ± 14
$WZjj$-EW	106 ± 21	4.82 ± 0.27	0.724 ± 0.014
$WZjj$-QCD	378 ± 31	77 ± 21	6.3 ± 0.7
$WZjj$-INT	5.1 ± 2.6	0.57 ± 0.29	0.22 ± 0.11
$t\bar{t}+V$	18.9 ± 2.7	261 ± 35	9.0 ± 1.3
tZj	35 ± 7	164 ± 30	0.53 ± 0.10
ZZ-QCD	45 ± 4	10.1 ± 0.5	171 ± 15
ZZ-EW	5.6 ± 1.3	0.21 ± 0.05	19 ± 5
VVV	2.4 ± 0.6	0.39 ± 0.10	4.1 ± 1.0
Misid. leptons	49 ± 10	148 ± 35	1.7 ± 0.5

TABLE 7.6: Post-fit event yields for the electroweak signal and all the backgrounds.

This measurement involves measuring both the $\sigma_{WZjj-EW}$ and $\sigma_{WZjj-QCD}$ cross sections in the signal region, along with μ_{ttV}, μ_{tZ}, and μ_{ZZ} extracted by the fit. Table 7.7 presents the measured uncertainties and precision of the $\sigma_{WZjj-EW}$ and $\sigma_{WZjj-QCD}$ cross-sections. The measured statistical significance for $\sigma_{WZjj-EW}$ is also shown in Table 7.7.

Region	Parameter	σ [fb]	$\delta\sigma$ [%]	$\frac{\sigma}{\delta\sigma}$	$\frac{\sigma^{\text{meas.}}}{\sigma^{\text{pred.}}}$	Z
Inclusive	$\sigma_{WZjj-EW}$	0.31	20.11	4.97	0.85	5.89
	$\sigma_{WZjj-QCD}$	1.14	9.69	10.32	0.74	> 12
	μ_{ZZ}	1.08	10.11			
	μ_{ttV}	0.90	14.62			
	μ_{tZ}	1.23	18.03			

TABLE 7.7: Relative uncertainties on the measured cross sections $\sigma_{WZjj-EW}$ and $\sigma_{WZjj-QCD}$.

The measured values of $\sigma_{WZjj-EW}$ and $\sigma_{WZjj-QCD}$ are displayed in Figure 7.7 along with 68% and 95% confidence level (CL) contours.

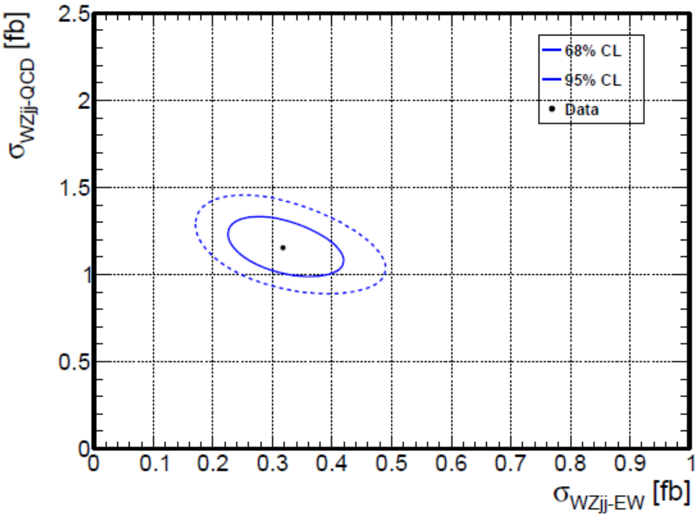

FIGURE 7.7: Values of inclusive $\sigma_{WZjj-EW}$ and $\sigma_{WZjj-QCD}$ cross section from the fit on data.

Figure 7.8 depicts the pull and the impact of the nuisance parameters, when the real data are used and Figure 7.9 shows the correlation between all parameters of the fit.

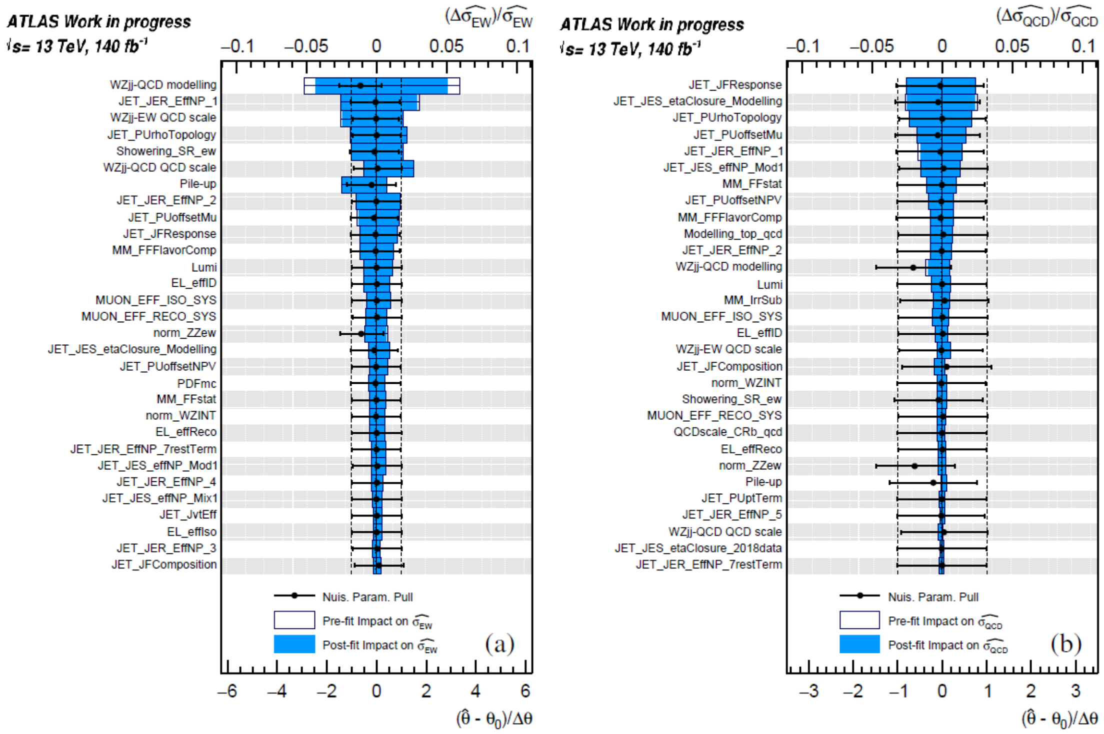

FIGURE 7.8: Pull and ranking by decreasing impact of the main nuisance parameters for the fit on real data, for $\sigma_{WZjj-EW}$ (a) and $\sigma_{WZjj-QCD}$ (b).

Finally, the impact of the main categories of nuisance parameters on the $\sigma_{WZjj-EW}$ and $\sigma_{WZjj-QCD}$ is summarized in Table 7.8. It can be seen that the $WZjj - EW$ and $WZjj -$

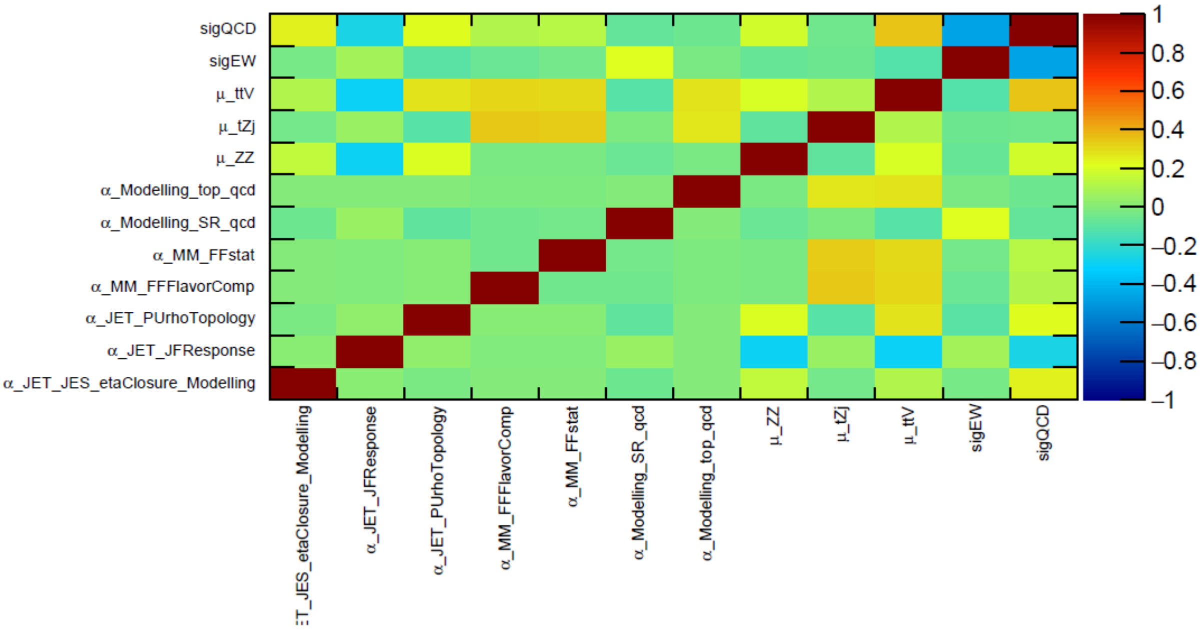

FIGURE 7.9: Correlation of all nuisance parameters and points of interest included in the fit on real data.

QCD theory modelling uncertainties along with the jets uncertainties are the most important uncertainties in the cross sections measurement.

	$\sigma_{WZjj-EW}$	$\sigma_{WZjj-QCD}$
Cross section [pb]	0.31	1.14
Source	Relative Uncertainty [%]	
$WZjj-$EW theory modelling	3.1	0.8
$WZjj-$QCD theory modelling	5	1.0
$WZjj-$EW and $WZjj-$QCD interference	0.33	0.6
PDFs	0.8	0.04
Jets	4	5
Pile-up	1.1	0.4
Electrons	0.8	0.8
Muons	0.9	0.9
b-tagging	0.11	0.11
MC statistics	3.0	1.1
Misid. lepton background	1.4	1.9
Other backgrounds	1.0	0.18
Luminosity	0.8	0.9
All systematics	12	7
Statistics	16	6
Total	20	10

TABLE 7.8: Impact of the main categories of nuisance parameters on $\sigma_{WZjj-EW}$ and $\sigma_{WZjj-QCD}$.

7.7 Differential $W^{\pm}Zjj$ cross-section measurements

The distributions of measured observables can be distorted by detector effects such as finite resolution, limited acceptance, and imperfect efficiency. To obtain the true spectra, x, from the measured ones, y, a response matrix A can be constructed using Monte Carlo simulation. The relation between the true and measured spectra can be expressed as $y = A \cdot x$. To translate the measured distributions to the generated ones, the inverse of A matrix, namely A^{-1}, must be calculated. However, simple algebraic manipulation of the response matrix is usually not feasible. To deal with the problem of unfolding differential distributions, various methods have been developed. In this analysis the Bayesian Iterative method [137] is used. The unfolding procedure involves subtracting the estimated background from data, applying fiducial factors to correct for events falling out of the detector phase-space, inverting the response matrix and applying efficiency factors to account for imperfect detector efficiency. The entire process is illustrated in Figure 7.10.

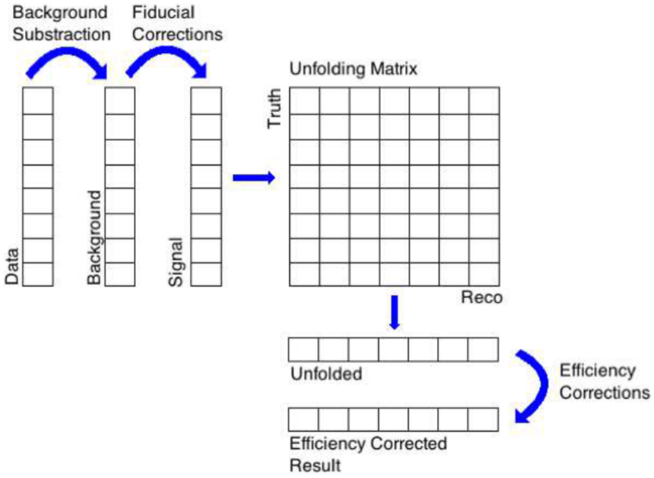

FIGURE 7.10: Schematic view of the unfolding procedure.

All events measured in the $W^{\pm}Zjj$ SR are used and unfolded to the VBS fiducial region defined in Section 7.5. Figure 7.11 shows the measured $W^{\pm}Zjj$ differential cross sections in the VBS fiducial phase space as a function of the transverse mass of the diboson system M_T^{WZ} (a), the sum of the transverse momenta of the three reconstructed leptons $\sum p_T^l$ (b), the absolute difference between the azimuthal angles of the W and Z bosons $\Delta\phi(W, Z)$ (c), the exclusive jet multiplicity N_{jets} of jets with a $p_T > 40 GeV$ (d), the invariant mass of the two jets m_{jj} (e), the absolute difference in rapidity of the two jets Δy_{jj} (f) and the absolute difference in azimuthal angle of the two jets $\Delta\phi_{jj}$ (g). On the other hand, Figure 7.12 depicts the measured $W^{\pm}Zjj$ differential cross sections in the VBS fiducial phase space as a function of the same kinematical variables, when the $WZjj - EWK$ and the $WZjj - QCD$ predictions are rescaled by the post-fit scale factors of Table 7.7 and the measured μ_{EW}^{meas} value.

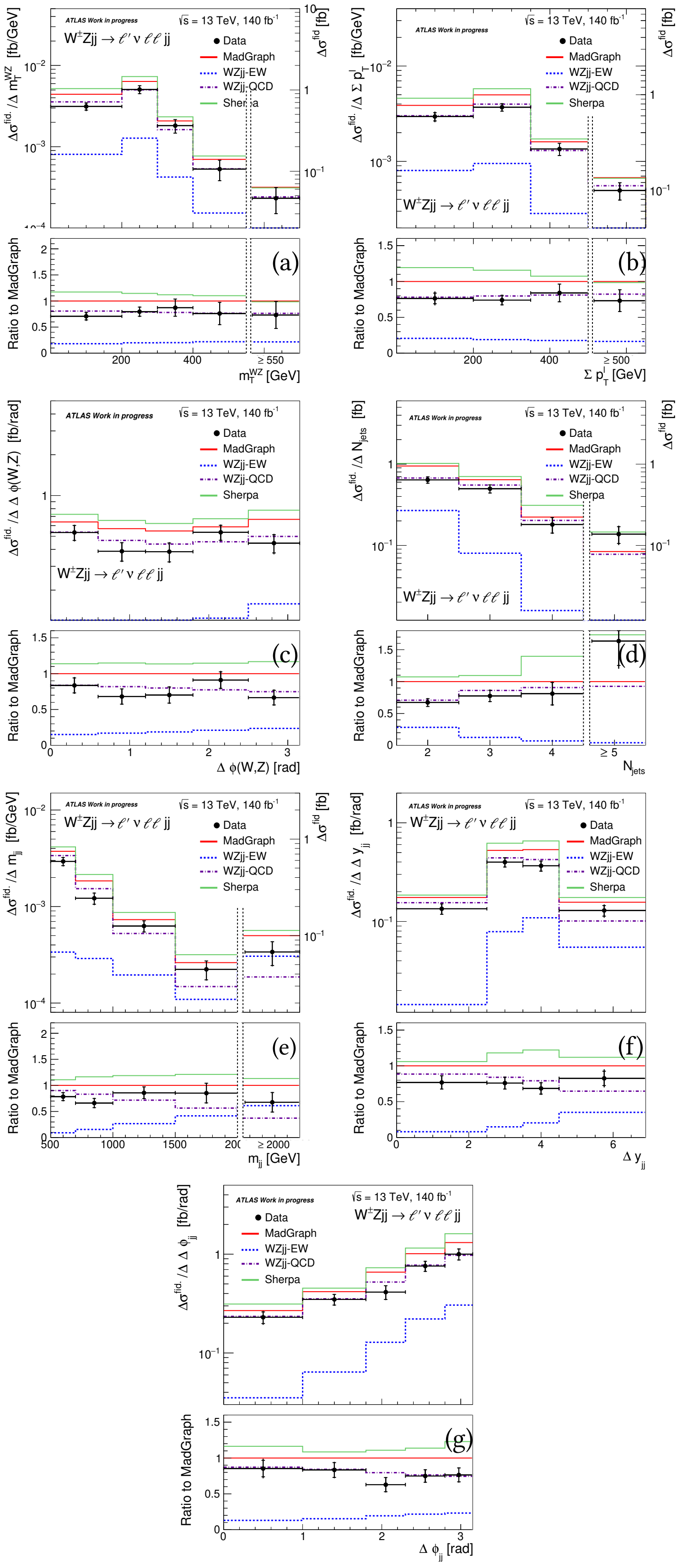

FIGURE 7.11: Measured $W^{\pm}Zjj$ differential cross section in the VBS fiducial phase space as a function of the M_T^{WZ} (a), the $\sum p_T^l$ (b), the $\Delta\phi(W,Z)$ (c), the $p_T > 40\,GeV$ (d), the m_{jj} (e), the Δy_{jj} (f) and the $\Delta\phi_{jj}$ (g).

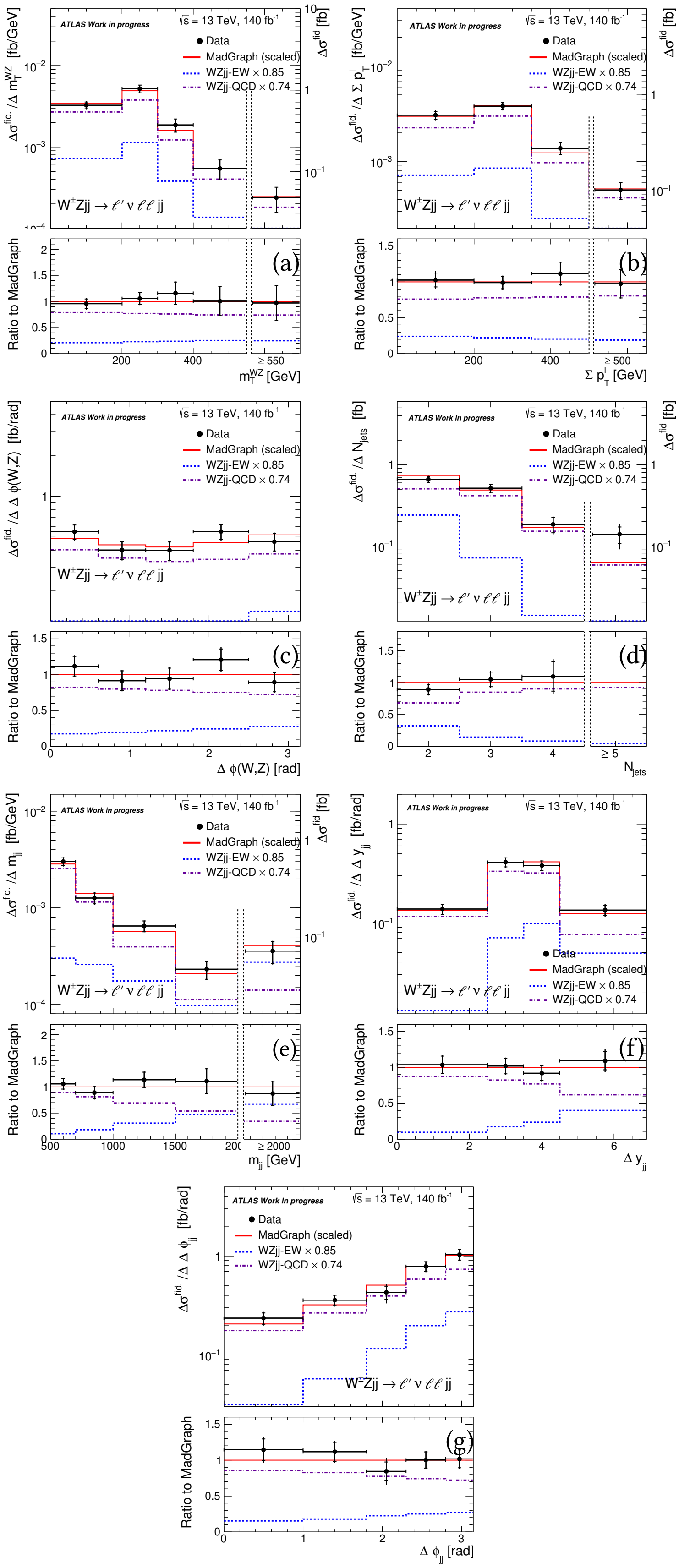

FIGURE 7.12: Measured $W^{\pm}Zjj$ differential cross section in the VBS fiducial phase space as a function of the M_T^{WZ} (a), the $\sum p_T^l$ (b), the $\Delta\phi(W,Z)$ (c), the $p_T > 40\,GeV$ (d), the m_{jj} (e), the Δy_{jj} (f) and the $\Delta\phi_{jj}$ (g), when the $WZjj-EWK$ and the $WZjj-QCD$ predictions are rescaled by the post-fit scale factors of Table 7.7 and the measured μ_{EW}^{meas} value.

7.8 Rivet routine

As in Section 6.6, within the Rivet framework, the routine for the $W^{\pm}Zjj$ VBS production has been created and tested. The full routine is presented in Appendix C.2. For this purpose, the phase space, that is defined in Table 7.2, is used. In order to validate the routine, a comparison between Rivet framework and analysis framework is done. The kinematical variables compared are the: M_T^{WZ}, $\sum P_T^{\mathrm{3lep}}$, $\Delta\phi_{WZ}$, N_{jets}, m_{jj}, Δy_{jj} and $\Delta\phi_{jj}$. The samples used for the comparison for the $WZjj - EW$ process are explained in Section 4.2.3.2 and for the $WZjj - QCD$ process in Section 4.2.3.3.

The first step is to compare the integrated cross sections. For the $WZjj - EW$ process, the integrated cross section obtained by the Rivet framework is: $0.35705\ fb$ and the one obtained by the analysis framework is: $0.35697\ fb$. The difference between the two cross sections is: 0.2%. Accordingly for the $WZjj - QCD$ process, the integrated cross section obtained by the Rivet framework is: $1.5283\ fb$ and the one obtained by the analysis framework is: $1.5145\ fb$. The difference between these two is: 0.9%.

The second step is to compare the shapes of the differential distributions of the above mentioned kinematical variables for the two frameworks. The comparison for the $WZjj - EW$ process is shown in Figure 7.13 and for the $WZjj - QCD$ process in Figure 7.14.

Finally, the third step of the comparison is to do event-by-event comparisons between the two frameworks for some kinematical variables. More details in Appendix C.2.

The good agreement between the analysis and Rivet predictions, below 1.0%, allows to validate the Rivet routine.

7.9 Effective Field Theory re-interpretation of the $W^{\pm}Z$ VBS cross section

The $WZjj$ VBS process is mostly affected by the dimension-8 operators. The $WZjj - EWK$ process, therefore, offers the ideal ground for studying the possible existence of anomalous quartic gauge couplings, $aQGCs$. However, the dimension-6 operators do affect both the $WZjj - EWK$ and the $WZjj - QCD$, so the $WZjj$ production can be used in order to study possible existence of $aTGCs$.

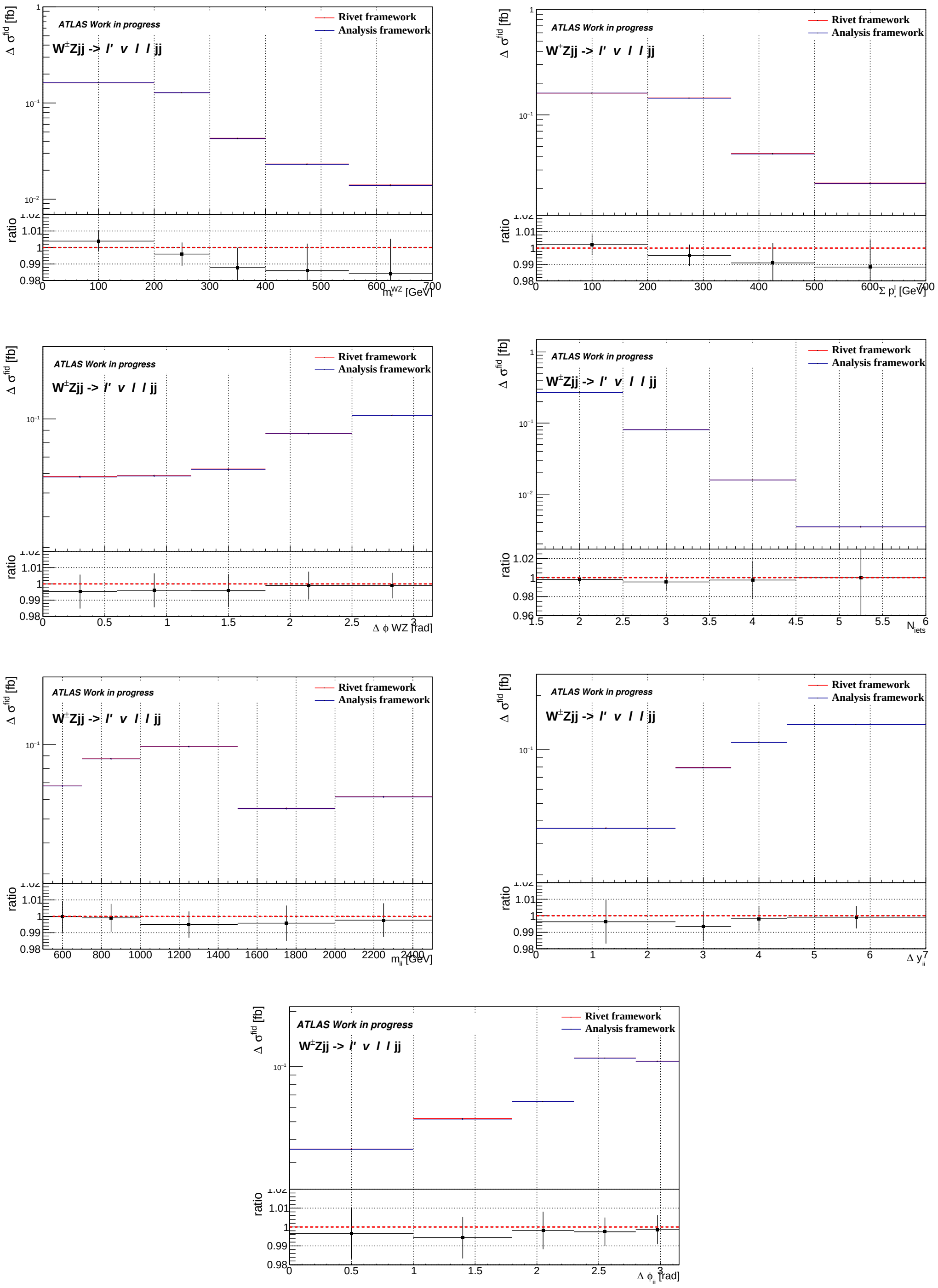

Figure 7.13: Differential distributions for the $WZjj - EW$ process. The error bars in ratio plot depicts the statistical errors of the MC sample used for this study.

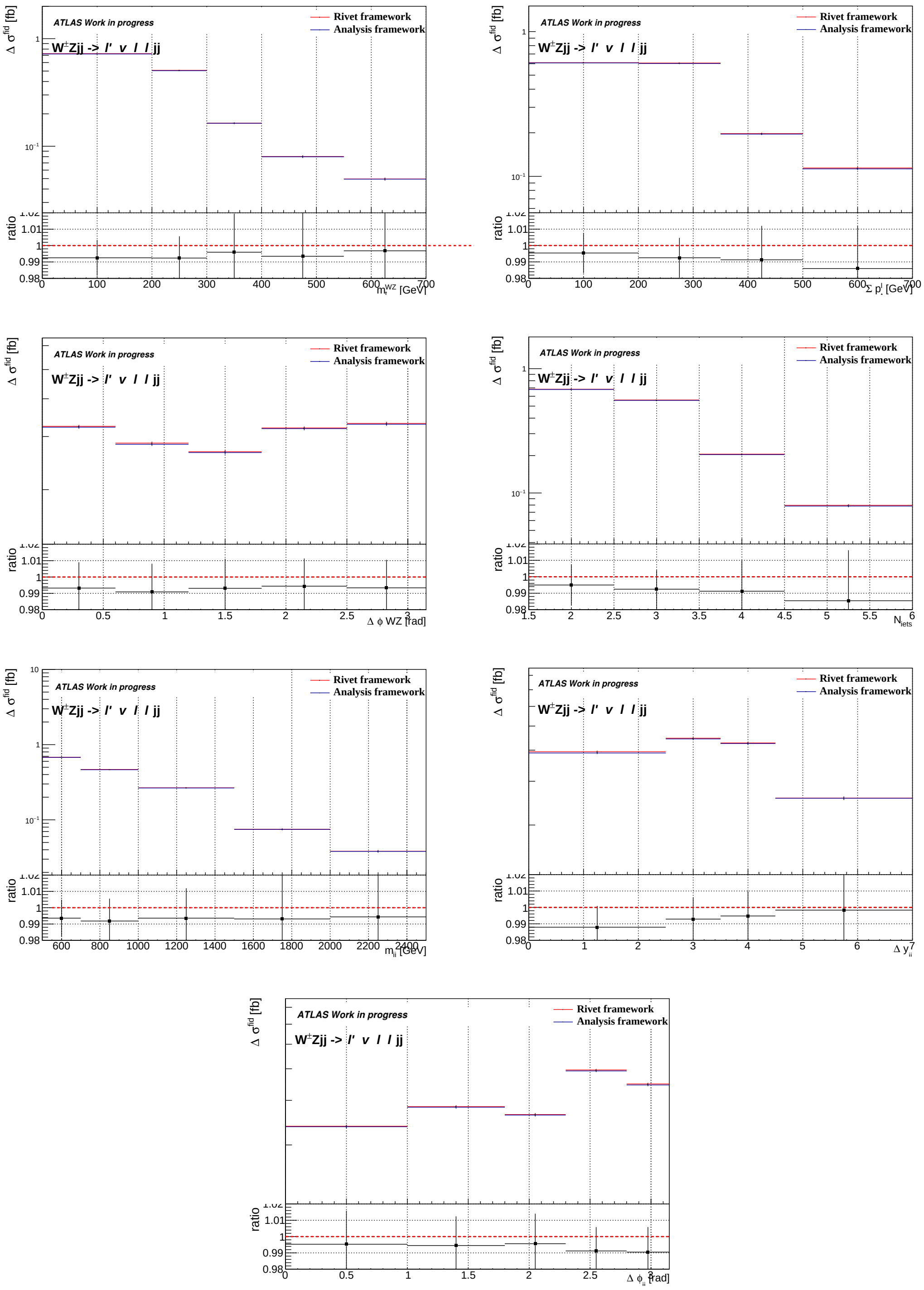

Figure 7.14: Differential distributions for the $WZjj - QCD$ process. The error bars in ratio plot depicts the statistical errors of the MC sample used for this study.

7.9.1 Dimension-6 operators

For the study of the effects dimension-6 operators on the $WZjj$ VBS production, parton level MC samples are produced using the MadGraph 2.7.3 generator, as in Section 6.7.1. The samples for the dimension-6 operators are produced using the $SMEFT@NLO$ FeynRules model. For simplicity, only the $WZjj$ VBS fully leptonic channel $p\,p \;\; \rightarrow \; \mu^+ \; \mu^- \; e^+ \; \nu_e \; j \; j$ is studied. For every sample 10k events are produced at parton level and the scale of new physics Λ is set to $1 \; TeV$. The SM cross section in this study is not to be compared with the measured cross section as the event generation is done in LO and does not use the same phase space as in the nominal samples, explained in Section 4.2.

7.9.1.1 Effect of dimension-6 operators on $WZjj$ VBS fully leptonic channel

As the $WZjj$ VBS process is affected by the dimension-6 operators, it is very important to specify which are the most sensitive operators for this process in order to extract the 95% confidence level (CL) limits in the future.

The procedure followed for the determination of the most sensitive dimension-6 operators is exactly the same as described in Section 6.7.1.1. The only difference is that in the inclusive fiducial phase space, the "WZjj event selection" is added. Table 7.9 shows the WZjj VBS selection.

WZjj VBS Phase Space	
p_{T} of Z leptons	> 20 GeV
p_{T} of W leptons	> 30 GeV
$\lvert\eta\rvert$ of leptons	< 2.5
m_Z range $[GeV]$	$\lvert m_Z - m_Z^{PDG}\rvert < 10$
$m_T^W [GeV]$	> 30
Jet multiplicity	≥ 2
p_{T} of two tagging jets	> 40 GeV
$\lvert\eta\rvert$ of two tagging jets	< 4.5
η of two tagging jets	opposite sign
m_{jj}	> 500 GeV

Table 7.9: WZjj VBS phase space definition for the determination of the most sensitive dimension-6 operators.

Figures 7.15 and 7.16 show the generated cross sections of the full samples for every dimension-6 operator compared to the SM cross section for the $WZjj - EWK$ process and the percentage difference of these cross sections once without using any selection and once using the WZjj VBS phase space.

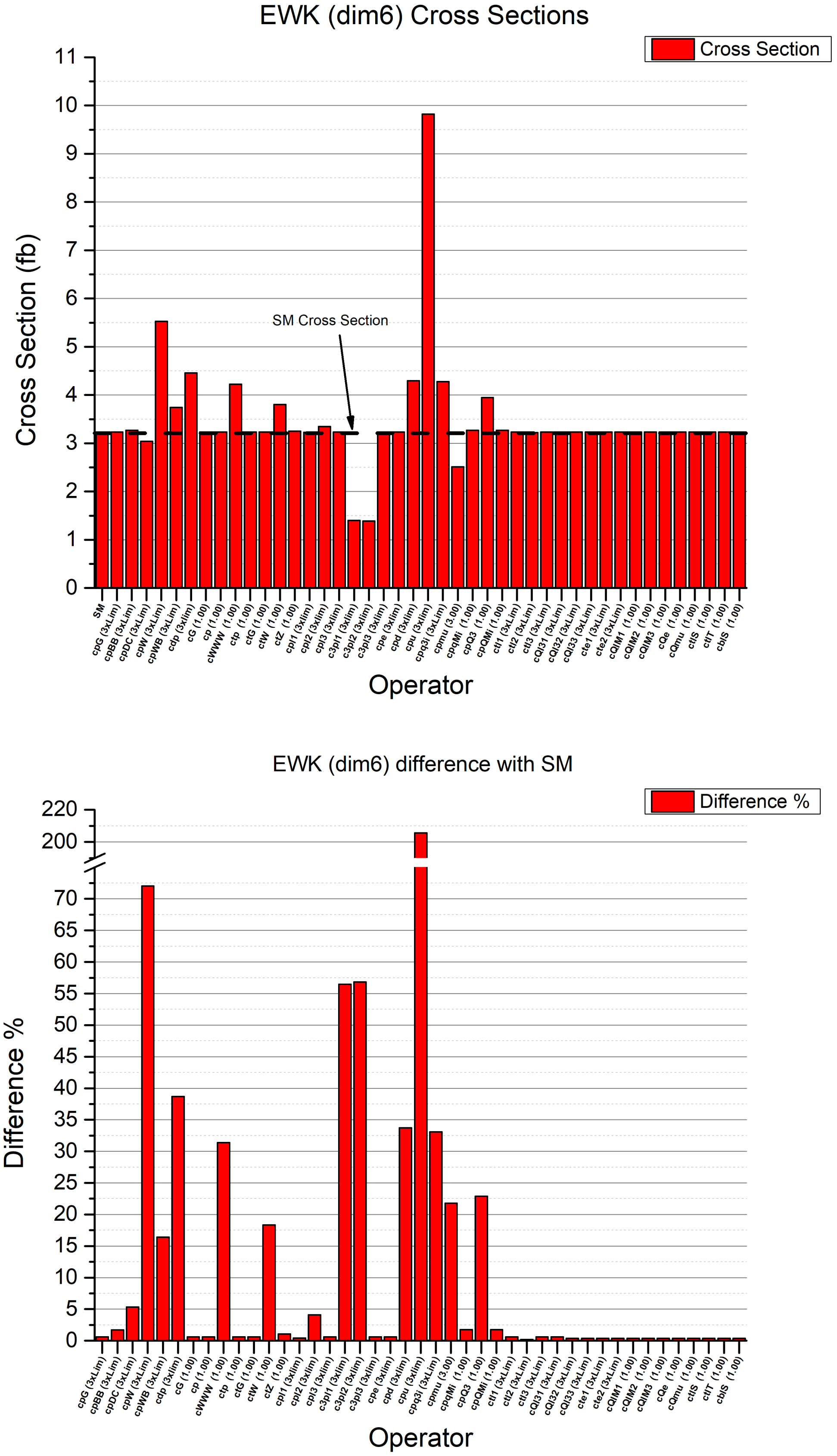

FIGURE 7.15: Comparison of SM cross section with the cross section of the full sample using one dimension-6 operator at a time (up) and the percentage difference between them (down) without applying any selection for the $WZjj - EWK$ process.

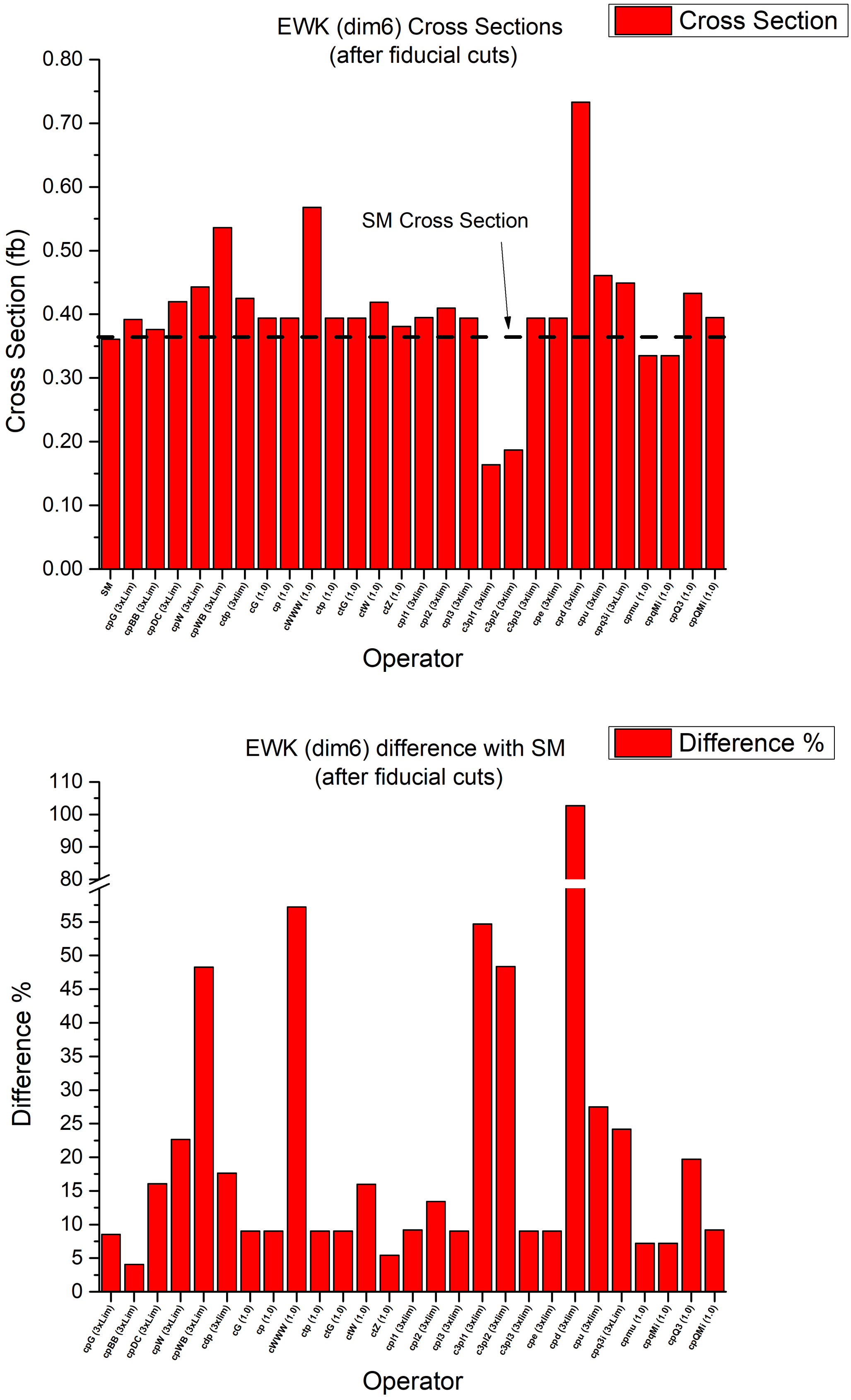

FIGURE 7.16: Comparison of SM cross section with the cross section of the full sample using one dimension-6 operator at a time (up) and the percentage difference between them (down) applying the WZjj VBS phase space for the $WZjj - EWK$ process.

Figures 7.17 and 7.18 shows the generated cross sections of the full samples for every dimension-6 operator compared to the SM cross section for the $WZjj - QCD$ process and the percentage difference of these cross sections once without using any selection and once using the WZjj VBS phase space.

As it is depicted in the above figures, the most sensitive dimension-6 operators that affect the $WZjj - EWK$ process are the: $cpWB$, cpW, cdp, $cWWW$, ctW, $c3pl1$, $c3pl2$, $cpmu$, cpd and $cpQ3$ operators. There are two dimension-6 operators that their effect show after the WZjj VBS selection. These are the: $cpDC$ and $cpl2$ operators.

On the other hand, the most sensitive dimension-6 operators that affect the $WZjj-QCD$ process are the: $cWWW$, $c3pl1$, $c3pl2$, $cpmu$ and $cpq3i$ operators. There are four dimension-6 operators that their effect show after the WZjj VBS selection. These are the: $cpWB$, $cpl1$, cpd and $cpqMi$ operators.

It is necessary to mention here that for the $cWWW$, ctW, $cpmu$ and $cpQ3$ operators there were no existing limits at the time of this study and the arbitrary values used may lead to unphysical results, due to violation of unitarity constraints.

Table 7.10 summarizes the most sensitive dimension-6 operators for the WZ inclusive, $WZjj - EWK$ and $WZjj - QCD$ processes. The results for the most sensitive dimension-6 operators are in agreement with later studies [128, 129, 138], which were published before this thesis.

operator/process	WZ Inclusive	$WZjj - EWK$	$WZjj - QCD$
$cWWW$	✓	✓	✓
$cpDC$	✓	✓	
$cpWB$	✓	✓	✓
cpW		✓	
$cpl1$			✓
$cpl2$		✓	
$c3pl1$	✓	✓	✓
$c3pl2$	✓	✓	✓
$cpmu$	✓	✓	✓
$cpqMi$	✓		✓
cdp		✓	
ctW		✓	
cpd			✓
$cpQ3$		✓	
$cpq3i$			✓

TABLE 7.10: Summary of the most sensitive dimension-6 operators for the WZ inclusive, $WZjj - EWK$ and $WZjj - QCD$ processes.

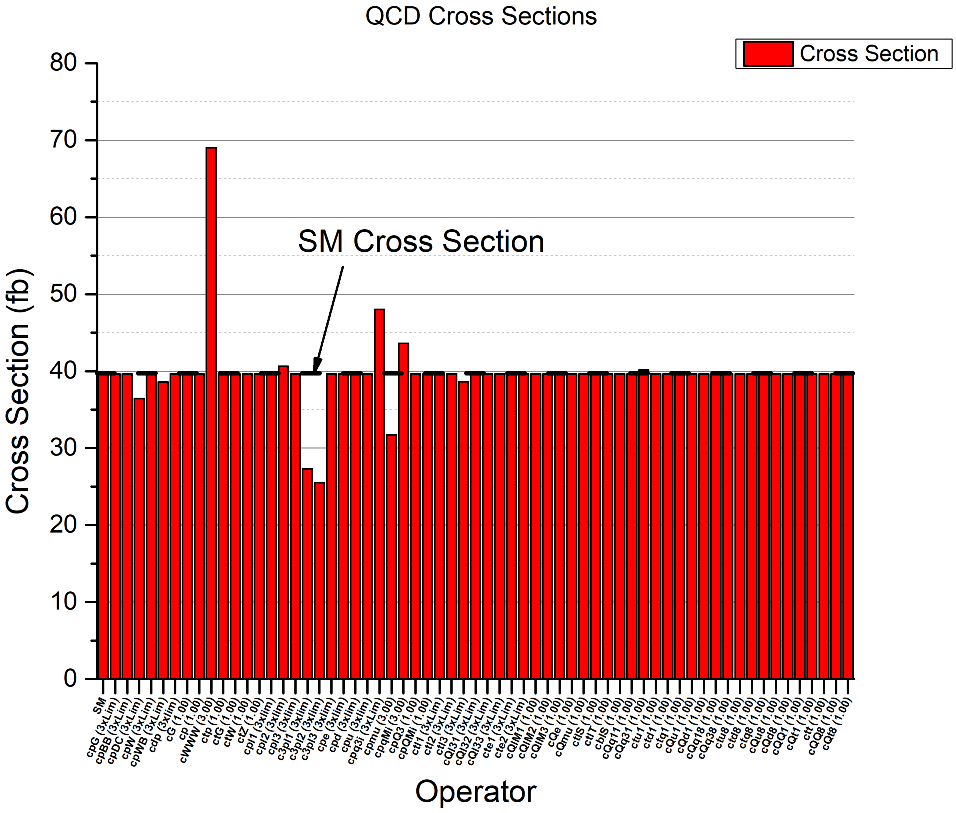

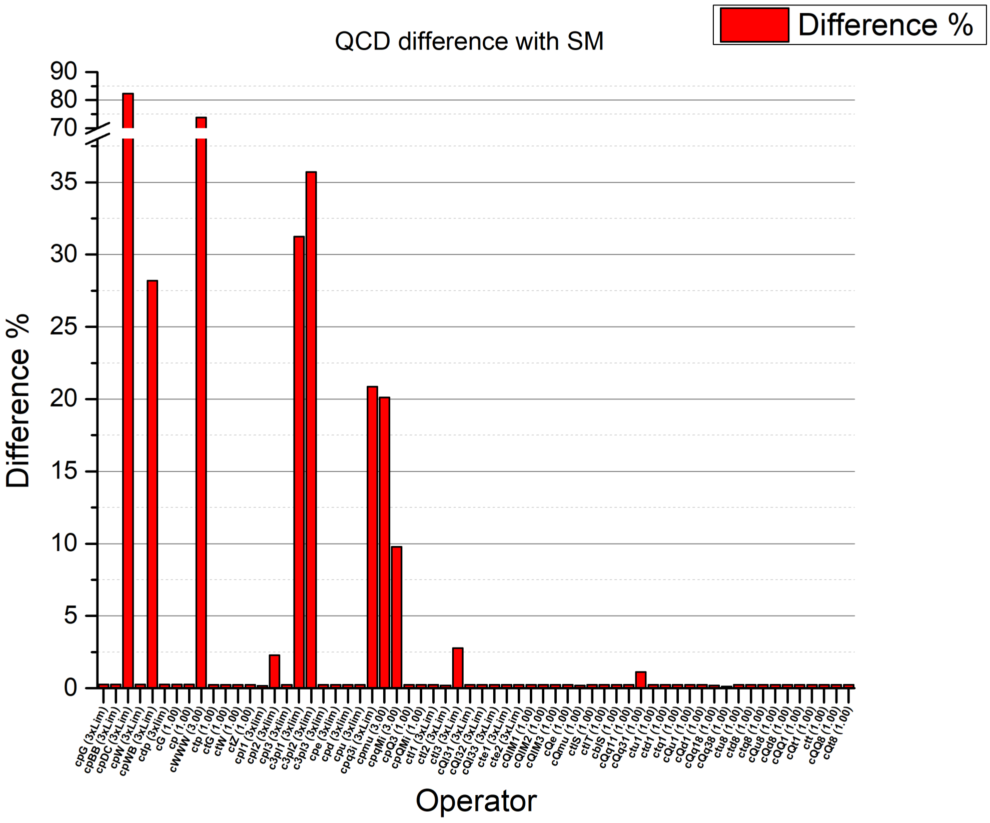

FIGURE 7.17: Comparison of SM cross section with the cross section of the full sample using one dimension-6 operator at a time (up) and the percentage difference between them (down) without applying any selection for the $WZjj - QCD$ process.

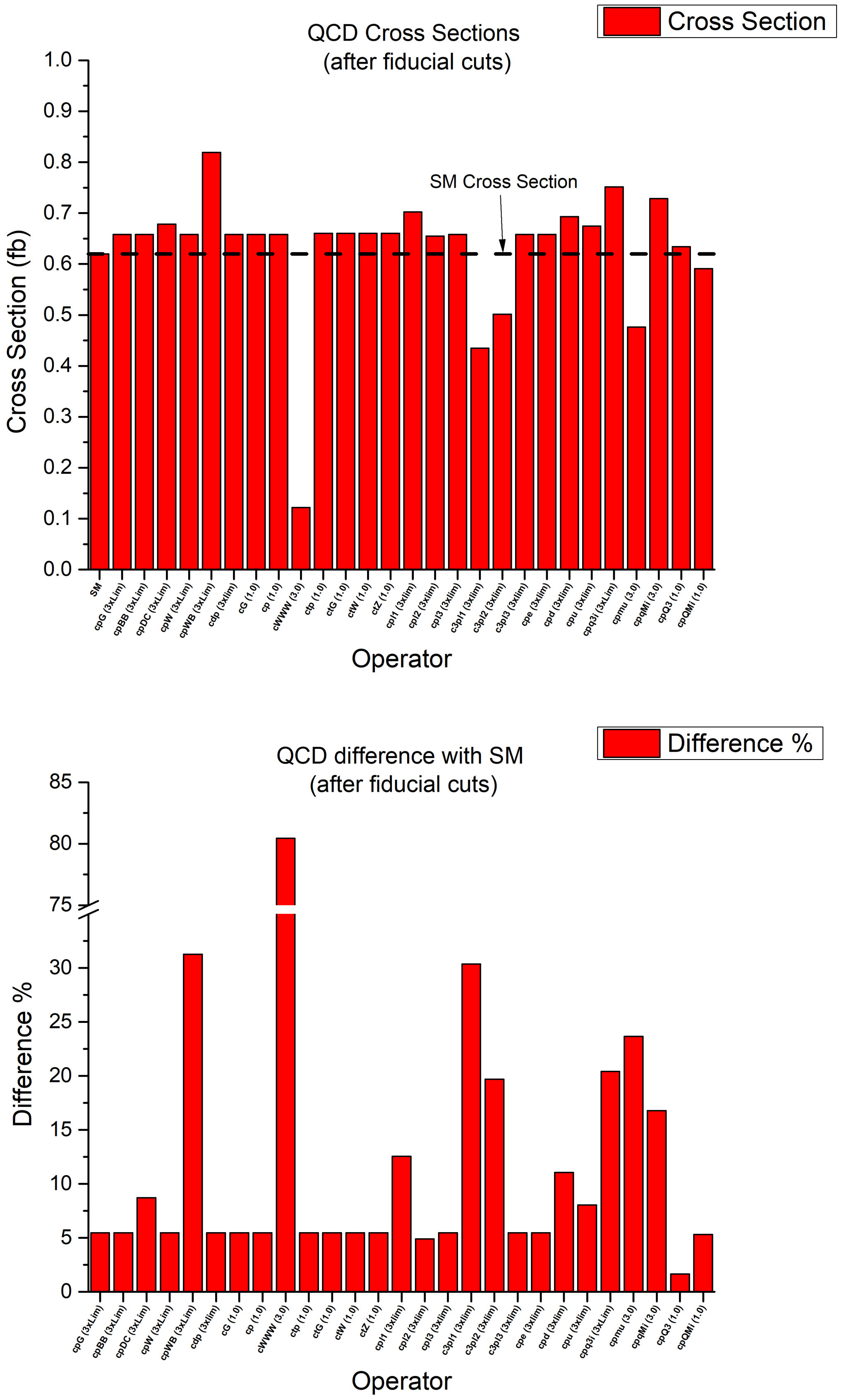

FIGURE 7.18: Comparison of SM cross section with the cross section of the full sample using one dimension-6 operator at a time (up) and the percentage difference between them (down) applying the WZjj VBS phase space for the $WZjj - QCD$ process.

The JobOptions for a future possible official production of samples for the sensitive dimension-6 EFT operators for the above processes are already created and they are presented in Appendix E.

Since the most effective operators are determined, a study for the most sensitive kinematical variable for sensitive operator is performed. The goal is to find the kinematical variable most sensitive to shapes effects for each operator. In order to find the sensitive kinematical variables, a comparison of the shapes of the distributions of some kinematical variables between the SM and the full sample for each dimension-6 operator is done. For this study events in the WZjj VBS phase space are used. 21 different kinematical variables are checked:

Variables related to the kinematics of vector bosons

m_Z, m_W invariant mass of Z and W bosons

p_T^Z, p_T^W transverse momentum of Z and W bosons

η_Z, η_W pseudorapidity of Z and W bosons

m_T^W transverse mass of W boson

m_{WZ} invariant mass of WZ system

m_T^{WZ} transverse mass of WZ system

$m_{3leptons}, p_T^{3leptons}$ invariant mass and transverse momentum of the three leptons

$y_{l,W} - y_Z$ difference of rapidity of the lepton of W boson and Z boson

$\Delta\phi(l1_Z, l_W)$ difference of ϕ angle of the first lepton of Z boson and the lepton of W boson

$\Delta\phi(l2_Z, l_W)$ difference of ϕ angle of the second lepton of Z boson and the lepton of W boson

$\Delta\phi(Z, l_W)$ difference of ϕ angle of Z boson and the lepton of W boson

Variables related to the kinematics of tagging jets

m_{jj} invariant mass of the two tagging jets

$\Delta\eta(j_1, j_2)$ difference of pseudorapidity of the two tagging jets

$\Delta\phi(j_1, j_2)$ difference of ϕ angle of the two tagging jets

Variables related both to jets and leptons kinematics

$\Delta R(j_1, Z)$ distance between of the jet with the highest transverse momentum and Z boson ($\Delta R = \sqrt{\Delta\eta^2 + \Delta\phi^2}$)

$R_{p_T}^{hard}$ transverse component of the vectorial sum of the momentum of the three leptons and the two tagging jets divided by the sum of their transverse momentum $R_{p_T}^{hard} = \frac{\sqrt{(\sum_i p_x^i)^2+(\sum_i p_y^i)^2}}{\sum_i p_T^i}$, where i is: the two leptons of Z boson, the lepton of W boson and the two tagging jets.

ζ_{lep} lepton centrality $\zeta_{lep} = min(\Delta\eta_-, Delta\eta_+)$ where $\Delta\eta_- = min(\eta_l^W, \eta_{l1}^Z, \eta_{l2}^Z) - min(\eta_{j1}, \eta_{j2})$ and $\Delta\eta_+ = max(\eta_{j1}, \eta_{j2}) - max(\eta_l^W, \eta_{l1}^Z, \eta_{l2}^Z)$

The most sensitive kinematical variables for each of the most effective dimension-6 operators for the $WZjj - EWK$ process are given in Table 7.11 and some examples of the comparison between the shapes of the distributions of the SM and the full sample for each operator are shown in Figure 7.19. The SM distribution is depicted with the blue line and it is called EWK_{dim6}. The $SMEFT@NLO$ model has been used for this production setting all the operators to the SM values. The red line depicts the full sample for every operator and the values for the corresponding Wilson coefficients are shown in the legend.

Sensitive kinematical variables	
$cpWB$	$\Delta\phi(l1_Z, l_W)$, $\Delta\phi(l2_Z, l_W)$
cpW	$\Delta\phi(l1_Z, l_W)$, m_T^{WZ}
cdp	m_T^{WZ}, $\Delta\phi(j_1, j_2)$
$cWWW$	m_T^{WZ}, $\Delta\phi(j_1, j_2)$
ctW	$\Delta\phi(l2_Z, l_W)$, m_T^{WZ}
$c3pl1$	$\Delta\phi(j_1, j_2)$
$c3pl2$	$\Delta\phi(j_1, j_2)$
$cpmu$	$\Delta\phi(l2_Z, l_W)$
cpd	$\Delta\phi(l1_Z, l_W)$
$cpQ3$	$\Delta\phi(l1_Z, l_W)$
$cpDC$	$\Delta\phi(l2_Z, l_W)$
$cpl2$	$\Delta\phi(j_1, j_2)$

Table 7.11: Most sensitive kinematical variables of the most effective dimension-6 operators for the $WZjj - EWK$ process.

The most sensitive kinematical variables for each sensitive dimension-6 operator for the $WZjj - QCD$ process are referred in Table 7.12 and some examples of the comparison of the shapes of the distributions of the SM and the full sample for each operator are shown in Figure 7.20. In this case, the SM distribution is called QCD_{dim6}.

As it can be seen in Figures 7.19 and 7.20, there are dimension-6 operators for which the shape of the kinematical variables does not change at all except by an overall factor. That means that these operators have only cross section effects and not shape effects. These operators are for the $WZjj - EWK$ the: $c3pl1$, $c3pl2$, $cpmu$ and cpd and for the $WZjj - QCD$ the: $c3pl1$, $c3pl2$, $cpmu$ and $cpWB$.

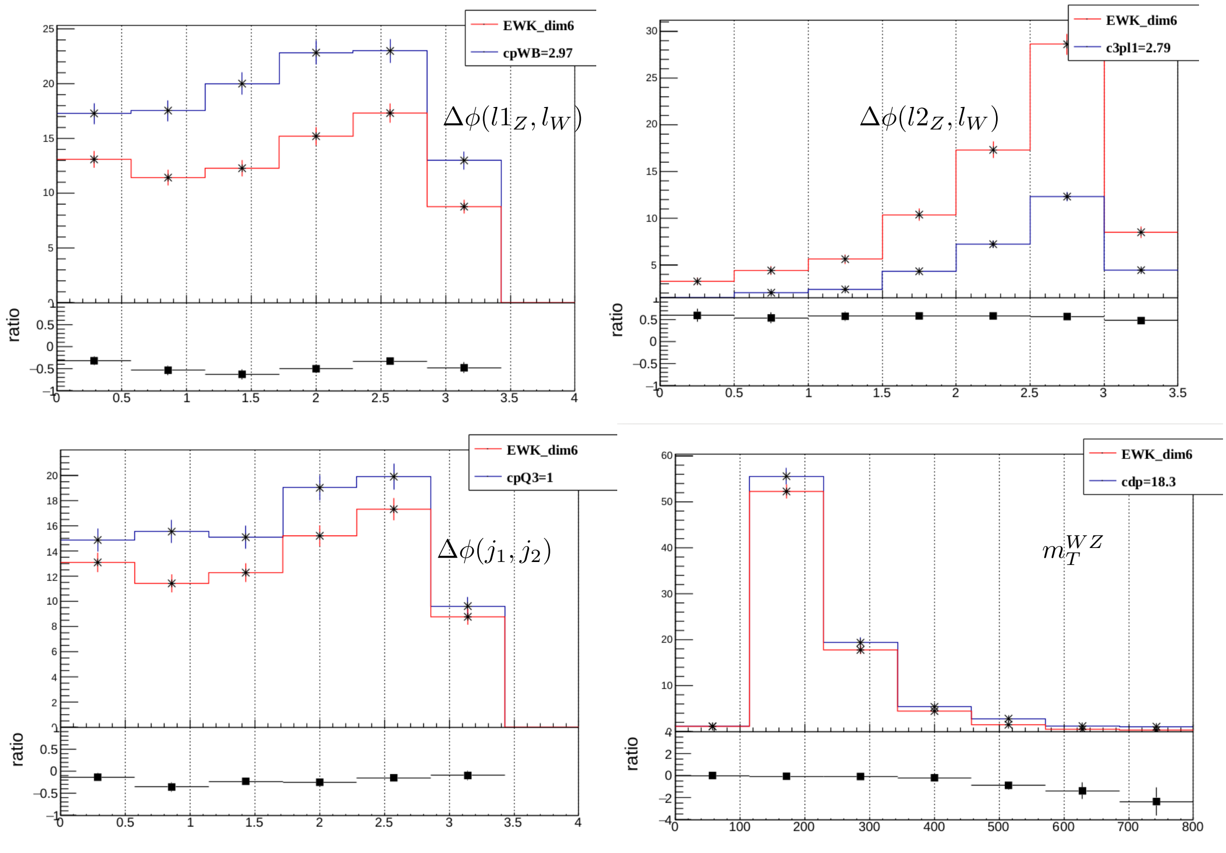

FIGURE 7.19: Examples of the comparison of the shapes of the SM distribution of the most sensitive kinematical variables with the corresponding distributions of the full sample using one dimension-6 operator at a time applying the WZjj VBS phase space for the $WZjj - EW$ process.

Sensitive kinematical variables	
$cWWW$	$\Delta\phi(l2_Z, l_W)$, m_T^{WZ}
$c3pl1$	$\Delta\phi(Z, l_W)$
$c3pl2$	$\Delta\phi(Z, l_W)$
$cpmu$	$\Delta\phi(l1_Z, l_W)$
$cpq3i$	m_T^{WZ}, $m_{3leptons}$, $\Delta\phi(l2_Z, l_W)$
$cpWB$	$\Delta\phi(l1_Z, l_W)$
$cpl1$	$\Delta\phi(j_1, j_2)$, m_T^{WZ}
cpd	$\Delta\phi(l1_Z, l_W)$, $m_{3leptons}$
$cpqMi$	$\Delta\phi(l2_Z, l_W)$

TABLE 7.12: Most sensitive kinematical variables of the most sensitive dimension-6 operators for the $WZjj - QCD$ process.

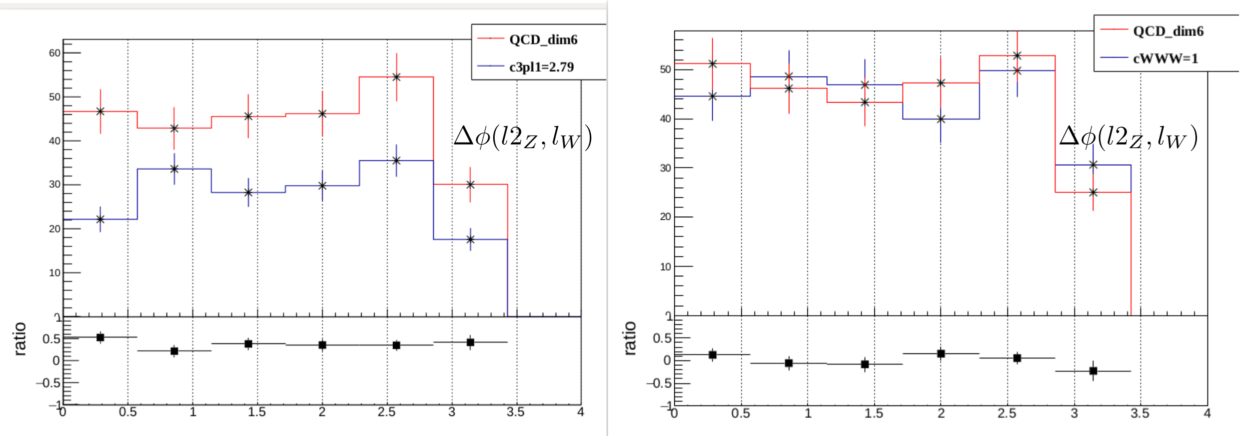

FIGURE 7.20: Examples of the comparison of the shapes of the SM distribution of the most sensitive kinematical variables with the corresponding distributions of the full sample using one dimension-6 operator at a time applying the WZjj VBS phase space for the $WZjj - QCD$ process.

To conclude, the study for the dimension-6 operators can be used in the future in order to set the 95% CL limits for them using the most sensitive kinematical variables. This study reveals that there are operators which do not have shape effects on the distribution of the relevant kinematical variables but they have only cross section effects.

7.9.2 Dimension-8 operators

7.9.2.1 Effect of dimension-8 operators on $WZjj$ VBS fully leptonic channel

For the study of the effect of the dimension-8 operators, parton level MC samples are produced using the MadGraph 2.7.3 generator. The samples for the dimension-8 operators are produced using the $Eboli - Garcia$ FeynRules model [91]. For simplicity, only the $WZjj$ VBS fully leptonic channel $p\,p \;\rightarrow\; \mu^+\,\mu^-\,e^+\,\nu_e\,j\,j$ is studied. For every sample 10k events are produced at parton level and the scale of new physics Λ is set to 1 TeV. The dimension-8 operators are set to three times the existing limits [139]. There are dimension-8 operators that do not have a limit yet. For these operators, some arbitrary values are chosen in order to study their effect. The SM cross section in this study is not to be compared with the measured cross section as the event generation is done in LO and does not use the same phase space as in the nominal samples, explained in Section 4.2.

The effect of the dimension-8 operators in the $WZjj$ VBS process dominates over the effect of the dimension-6 operators and it is thus important to specify the most effective operators for this process. Furthermore, only the $WZjj - EW$ process is affected by the dimension-8 operators.

The procedure followed for the determination of the most sensitive dimension-8 operators is exactly the same as described in Section 7.9.1.1.

Figures 7.21 and 7.22 show the generated cross sections of the full samples for every dimension-8 operator compared to the SM cross section for the $WZjj - EWK$ process and the percentage difference of these cross sections once without using any selection and once using the WZjj VBS phase space.

As it is depicted in the above figures, the most sensitive dimension-8 operators that affect the $WZjj - EWK$ process are the: f_{M0}, f_{M1}, f_{M2}, f_{M3}, f_{M4}, f_{M5}, f_{M7}, f_{T0}, f_{T1}, f_{T2}, f_{T5}, f_{T6} and f_{T7} operators. It is necessary to mention here that for the f_{M2}, f_{M3}, f_{M4}, f_{M5}, f_{T5}, f_{T6} and f_{T7} operators there were no existing limits at the time of this study and the arbitrary values used may lead to unphysical results, due to violation of unitarity constraints.

The most sensitive kinematical variables for the relevant dimension-8 operator of the $WZjj - EWK$ process are the m_T^{WZ} and the $\Delta\phi(j_1, j_2)$. Some examples of the comparison of the shapes of the distributions between the SM and the full sample for each operator are shown in Figure 7.23. In this case he SM distribution is called EWK_{dim8}.

7.9.2.2 Validation of the decomposition method

In order to use the decomposition method, described in Section 2.3.2.4, it is necessary to validate it. The validity of the decomposition technique for some individual EFT parameters with arbitary values of the corresponding f_i coefficients has been verified by comparing the full sample with the sum of the decomposed samples. In Table 7.13 it is found that the differences between the $full$ production and the addition of the three terms is always less than 1% and within the MC statistical error for all the EFT parameters under study. More information and results on the validation of the decomposition procedure can be found in [130, 138].

	value	SM xsec(fb)	INT xsec(fb)	QUAD xsec(fb)	FULL xsec(fb)	SUM xsec(fb)	Difference %
f_{S0}	-26.5	1.049	0.00168	0.02421	1.0750	1.0749	0.09
f_{S1}	-41.2	1.049	0.00167	0.03005	1.0810	1.0804	0.05
f_{M3}	-43.0	1.049	-0.00140	0.12300	1.160	1.1706	0.91
f_{M7}	-13.0	1.049	-0.0004	0.01541	1.061	1.0640	0.28
f_{T2}	-1.2	1.049	0.00476	0.01095	1.070	1.0647	0.50
f_{T6}	3.0	1.049	0.00429	0.06548	1.111	1.1188	0.70

TABLE 7.13: Closure tests

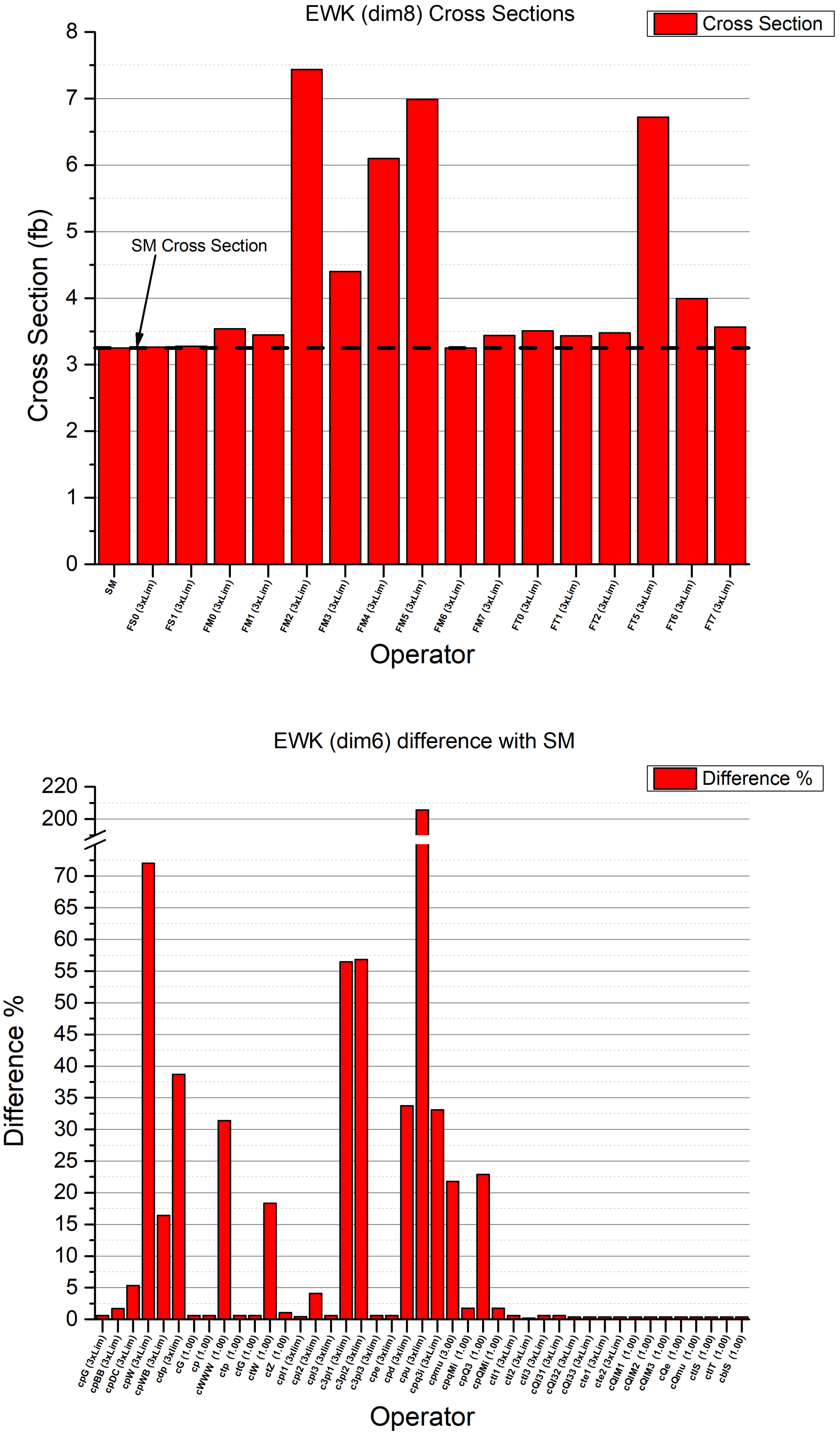

FIGURE 7.21: Comparison of SM cross section with the cross section of the full sample using one dimension-8 operator at a time (up) and the percentage difference between them (down) without applying any selection for the $WZjj - EWK$ process.

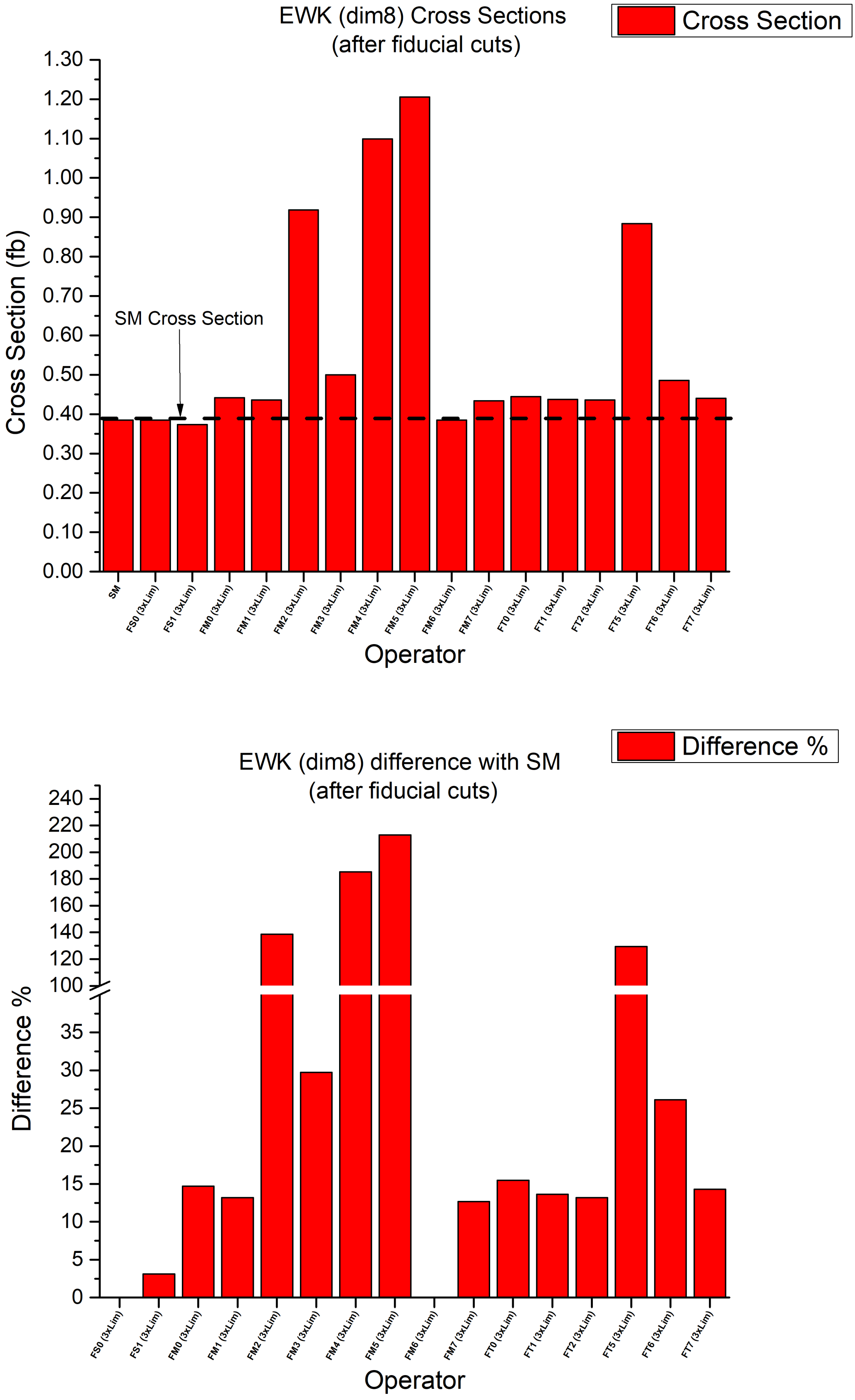

FIGURE 7.22: Comparison of SM cross section with the cross section of the full sample using one dimension-8 operator at a time (up) and the percentage difference between them (down) applying the WZjj VBS phase space for the $WZjj - EWK$ process.

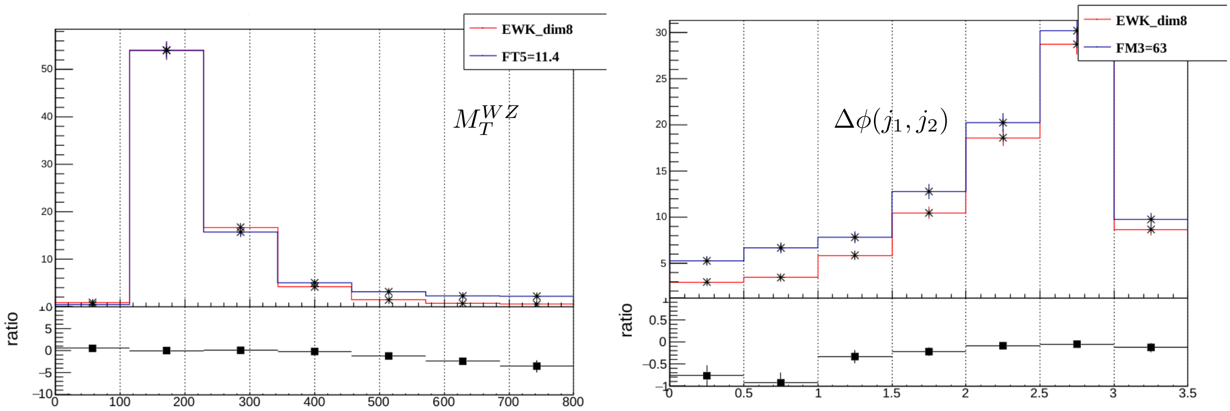

FIGURE 7.23: Examples of the comparison of the shapes between the SM distribution of the most sensitive kinematical variables with the corresponding distributions of the full sample using one dimension-8 operator at a time applying the WZjj VBS phase space for the $WZjj-EWK$ process.

7.9.2.3 Systematic uncertainties used in the limit extraction procedure for the dimension-8 operators

Experimental uncertainties The WZjj measurement is affected by various experimental systematics uncertainties, which are described in detail in Section 7.4.1. A smoothing procedure is applied as described in Section 7.4.1.

Theoretical uncertainties The theoretical uncertainties are computed seperately for the unfolded and reconstructed WZjj measurement.

For the unfolded WZjj measurement, the theoretical uncertainties that are taken into account in the limit extraction procedure are: the PDF and α_S uncertainties and the scale uncertainties, as described in Section 7.4.2. Specifically for the estimation of the scale uncertainty, the procedure followed for the $WZjj-QCD$ is used.

On the other hand, the reconstructed WZjj process is affected by various theoretical uncertainties which are computed as described in Section 7.4.2. Nevertheless, for this part of the analysis also the background estimation uncertainties are taken into account while in the cross section extraction fit, only shape effects were considered for the WZjj-EW and WZjj-QCD processes. The theoretical uncertainties that are taken into account in the limit extraction procedure are: the PDF and α_S uncertainties, the QCD-scale uncertainties, the parton shower uncertainties and the model uncertainties. Particularly for for the estimation of the QCD-scale uncertainties, the procedure followed for the $WZjj-QCD$ is used also for the EFT simulated samples. Finally, for the parton shower uncertainty, it is assumed that the EFT simulated samples are affected in the same way as the WZjj-EW process.

All theoretical uncertainties except the PDF uncertainty are treated as uncorellated for different processes.

Figure 7.24 shows some examples of the effect of the different theory uncertainties on the transverse mass of the two bosons M_T^{WZ} distribution for two different dimension-8 operators.

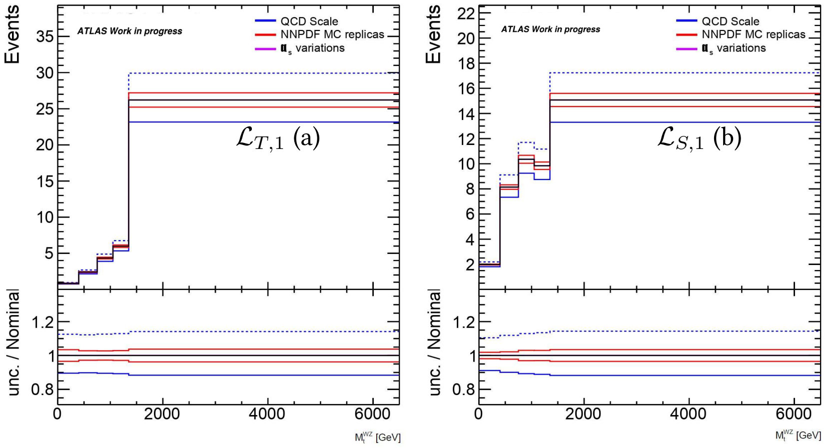

FIGURE 7.24: Effect of the different theory uncertainties, QCD scale variations (blue), PDF MC set variations (red) and α_s variations (violet), on the distributions transverse mass of the two bosons m_T^{WZ} for: the $\mathcal{L}_{T,1}$ operator (a) and the $\mathcal{L}_{S,1}$ (b).

7.9.2.4 Statistical model

General aspects

Profile likelihood method

When analyzing results from experiments in high-energy physics, it is important to take into account the statistical nature of interactions between elementary particles. One commonly used approach for interpreting observations is the profile likelihood method, a test statistic method which incorporates the effect of the nuisance parameters in the likelihood. To explain the profile likelihood method, the example of a simple counting experiment where the background is only known with limited accuracy is used. Although this basic example is sufficient for demonstrating the method, it can also be applied to more complex experiments.

Suppose that there is a need to measure a signal process by counting events. The number of the background events is considered as nuisance parameters in this simplified example. n

represents the total number of events observed in the data, s the number of signal events and b the number of the background events. The number of background events is constrained by an auxiliary measurement, which is for example obtained from simulation or estimated from a control region, with a nominal background yield, b_0. In this example, the probability density function (PDF) $P(b_0|b)$ for this background is taken as a Gaussian distribution, with unknown true value b and standard deviation Δb. Therefore, the PDF for the auxiliary measurement can be expressed as:

$$P\left(b_0 \mid b\right) = \mathrm{G}\left(b_0 \mid b, \Delta b\right) \tag{7.5}$$

The likelihood function for the complete counting experiment is then given by

$$\begin{aligned} \mathcal{L}(n \mid \mu, b) &= \mathrm{Pois}(n \mid \mu s + b) \times \mathrm{G}\left(b_0 \mid b, \Delta b\right), \\ &= \frac{(\mu s + b)^n}{n!} e^{-(\mu s + b)} \times \frac{1}{\sqrt{2\pi \Delta b^2}} e^{-\frac{1}{2}\frac{(b_0 - b)^2}{\Delta b^2}}, \end{aligned} \tag{7.6}$$

where μ is the *signal strength*. This parametrisation is useful because it fixes the number of expected signal events, s, as a constant parameter, while allowing the signal strength to vary. When the parameter μ is set to 0, it represents the background-only hypothesis, while $\mu = 1$ corresponds to the nominal signal hypothesis. It is important to note that b_0 and Δb are fixed parameters of the model, while the floating parameters are the *parameter of interest*, μ, and the *nuisance parameter* , b.

The crucial point of the profile likelihood method is the definition of a test statistic as

$$t_\mu = -2 \log \frac{\mathcal{L}\left(n \mid \mu, \hat{\hat{b}}_\mu\right)}{\mathcal{L}(n \mid \hat{\mu}, \hat{b})} = -2\left[\log \mathcal{L}\left(n \mid \mu, \hat{\hat{b}}_\mu\right) - \log \mathcal{L}(n \mid \hat{\mu}, \hat{b})\right] \equiv -2\Delta \log \mathcal{L}(\mu) \tag{7.7}$$

with $\hat{\mu}$ and $\hat{b}$ being the unconditional maximum likelihood estimators (MLEs) which maximise $\mathcal{L}(n \mid \mu, b)$ globally, while $\hat{\hat{b}}_\mu$ denotes the MLE for each value of μ. This idea can be extended to situations where there are multiple nuisance parameters in a straightforward way. It's important to note the following properties of the test statistic:

- It is valid by definition that $\mathcal{L}\left(n \mid \mu, \hat{b}_\mu\right) \leq \mathcal{L}(n \mid \hat{\mu}, \hat{b})$, so $0 \leq t_\mu < +\infty$.
- If the data agrees with the tested hypothesis ($\hat{\mu} \approx \mu$), the test statistic is close to zero.
- Larger values of the test statistic, t_μ, indicate that the observed data is less compatible with the tested hypothesis for the value of μ.

Resulting from these properties, the p-value, which is defined as the probability of observing data of equal or greater incompatibility with the hypothesis under investigation, is calculated according to

$$p_\mu = \int_{t_{\mu,\mathrm{obs}}}^{+\infty} f\left(t_\mu \mid \mu\right) \mathrm{d}t_\mu \tag{7.8}$$

where μ represents the hypothesis for the true value of the parameter of interest realised in nature and $t_{\mu,\mathrm{obs}}$ is the value of the test statistic observed. Furthermore, $f(t_\mu|\mu')$ denotes the sampling distribution which describes the probability of observing a value of the test statistic of t_μ if μ' is the true value. In certain situations, such as having a large enough sample size, the analytical form of the sampling distribution can be obtained using Wilks' theorem[140]. However, in cases where this approximation is not valid, the sampling distribution can be estimated by using pseudoexperiments, which often require significant computing resources.

Calculating the p-values, significances and confidence intervals can be estimated. The significance, denoted as Z, corresponding to a given p-value is defined such that the probability of finding a normal distributed random variable x with $x \geq Z$ is equal to p. Mathematically, this can be expressed as:

$$Z = \Phi^{-1}(1-p) \tag{7.9}$$

where $\Phi^{-1}(x)$ stands for the inverse of the cumulative normal distribution (quantile function of the normal distribution). The confidence interval for μ for a desired confidence level of $(1 - \alpha)$ is given by the set of all values of μ which satisfy $p_\mu \geq \alpha$

Discovery significance

In the specific scenario of searching for a new phenomenon in high-energy physics, which is indicated by an excess in data, the goal is to reject the background-only hypothesis $\mu = 0$ using the modified test statistic

$$q_0 = \begin{cases} -2\log\frac{\mathcal{L}\left(n|0,\hat{\hat{b}}_0\right)}{\mathcal{L}(n|\hat{\mu},\hat{b})} & \text{for } \hat{\mu} \geq 0 \\ 0 & \text{for } \hat{\mu} < 0 \end{cases} \tag{7.10}$$

By defining $q_0 = 0$ for $\hat{\mu} < 0$, the observation of a deficit in data is not included in the rejection region and, therefore, it is not considered as indication of a signal. Using Wilks theorem, it is found that the distribution of $f(q_0|0)$ follows a half χ^2-distribution $(\frac{1}{2}\chi^2)$ with one degree of freedom. Therefore, the p-value for a non-zero value of the observed $q_{0,obs}$ is equivalent to:

$$p_0 = \int_{q_{0,\mathrm{obs}}}^{+\infty} f\left(q_0 \mid 0\right) \mathrm{d}q_0 = 1 - \Phi\left(\sqrt{q_0}\right) \tag{7.11}$$

which leads with the help of Equation 7.9 to

$$Z = \sqrt{q_0}. \tag{7.12}$$

Confidence Intervals

The profile likelihood method has a wide range of applications, including measuring parameter values and determining their confidence intervals. The parameter of interest is measured using the unconditional maximum likelihood estimator ($\hat{\mu}$), and the confidence interval for a given confidence level ($1 - \alpha$) is given by the set of points μ satisfying $p_\mu \geq \alpha$. For parameters that are bounded on one or both sides by physical constraints, such as cross-sections or Wilson coefficients, different variations of the test statistic (t_μ) are used. In this study, the test statistic t_μ, defined in Equation 7.7, is used for calculating confidence intervals. In the asymptotic regime, where Wilks theorem applies, the sampling distribution follows a χ^2 distribution [141] with one degree of freedom

$$f(t_\mu|\mu) = \chi^2(t_\mu, 1). \tag{7.13}$$

In this approximation, the confidence interval is given by all points μ which satisfy

$$t_\mu = -2\Delta \log \mathcal{L}(\mu) \leq \left(\chi^2\right)^{-1}(1-\alpha, 1) \tag{7.14}$$

where $\left(\chi^2\right)^{-1}(x, 1), 0 \leq x \leq 1$ is the quantile function of the χ^2 distribution with one degree of freedom. By convention, the following numerical values are of special interest
$t_\mu = \left(\chi^2\right)^{-1}(0.950, 1) = 3.84$ (corresponding to a 95% confidence level)
$t_\mu = \left(\chi^2\right)^{-1}(0.683, 1) = 1.00$(corresponding to a 68.3% confidence level).

Definition of Asimov dataset

In order to estimate the ”expected” confidence intervals, the simulated datasets are replaced with an artificial dataset, the ”*Asimov*” dataset [141]. In this dataset all the parameters are fixed to their expected values.

Using the Asimov dataset one can evaluate the “Asimov likelihood” L_A and the corresponding profile likelihood ratio λ_A

$$\lambda_A(\mu) = \frac{L_A(\mu, \hat{\hat{b}})}{L_A(\hat{\mu}, \hat{b})} = \frac{L_A(\mu, \hat{\hat{b}})}{L_A\,(\mu', b)} \tag{7.15}$$

where the estimators for the parameters are equal to their hypothesized values ($\hat{\mu} = \mu'$ and $\hat{b} = b$) when using an Asimov dataset.

The corresponding test-statistic $q_{\mu,A}$ is

$$q_{\mu,A} = -2\ln\lambda_A(\mu) \approx \frac{(\mu - \mu')^2}{\sigma_A^2} \tag{7.16}$$

where the variance σ_A^2 which characterizes the distribution of $\hat{\mu}$ is given by

$$\sigma_A^2 = \frac{(\mu - \mu')^2}{q_{\mu,A}} \tag{7.17}$$

Finally. the median significance of the background-only hypothesis can be written as:

$$med[Z_\mu|0 = \sqrt{q_{\mu,A}}] \tag{7.18}$$

Pull distributions and impact parameters

The pull is a measure that typically describes how much a parameter estimate deviates from its expected value during the Maximum Likelihood Estimator (MLE) estimation process. A ”good” fit would mean that the average pull is zero, and the standard deviation is approximately one. The assumed standard deviation and expected value of a nuisance parameter are often based on auxiliary measurements or Monte Carlo studies.

If a random variable x is generated with a Gaussian distribution of mean μ and width σ, then the pull [142] is given by

$$g = \frac{x - \mu}{\sigma} \tag{7.19}$$

and it is distributed as a standard Gaussian with mean 0 and unit width. Pulls are useful in both hypothesis testing and parameter estimation, as they can help detect potential biases and verify error coverage. In the case of analyzing systematic uncertainties (b), the pulls can be calculated as

$$pull = \frac{\hat{b} - b_0}{\Delta b} \tag{7.20}$$

where $\hat{b}$ is the maximum likelihood estimated value of the systematic uncertainty, b_0 is the nominal systematic value and Δb is the width of the nominal systematic. The corresponding error of the pull is given by

$$pull_{err} = \frac{\Delta \hat{b}}{\Delta b} \tag{7.21}$$

where $\Delta \hat{b}$ is the MLE error.

The impact [143] of a nuisance parameter b for the case of the μ parameter estimation is defined as

$$\text{impact}(b) = \frac{\Delta \mu^{\pm}}{\hat{\mu}} = \frac{\hat{\hat{\mu}}_{b_0 \pm \Delta b} - \hat{\mu}}{\hat{\mu}} \tag{7.22}$$

where $\mu^{\pm} = \hat{\hat{\mu}}_{b_0 \pm \Delta b}$ is the conditional maximum likelihood estimate of the signal strength parameter, where all parameters except for b are profiled and b is set to its expected value plus or minus one standard deviation. The initial MLE of μ is denoted by $\hat{\mu}$. The impact provides a measure of how much the parameter of interest (μ) changes as the nuisance parameter (b) varies. This can help to simplify the fitting procedure by allowing the discarding ("pruning") of nuisance parameters that have a low impact.

Statistical methods used for the EFT interpretation of the $WZjj$ process

For the extraction of the 95% CL expected and observed limits using differential and reconstructed distributions, two different statistical methods are used. For the unfolded measurements of the $WZjj$ process, the asymptotic approximation is used, while for the reconstructed $WZjj$ process, the asymptotic approximation or the profiled Feldman-Cousins method are followed.

Asymptotic method

The probability density function based on a multivariate Gaussian distribution is used in the reinterpretation of the unfolded measurements for the $WZjj$ process. The prediction of the EFT differential cross sections depends on the values of Wilson coefficients f and is also subject to theory systematic uncertainties, which are parametrized by nuisance parameters. Experimental uncertainties are encoded in a covariance matrix. The predicted fiducial cross section x^b_{pred} in a bin b of the unfolded distribution is parametrized as

$$x_b^{\text{pred}}\left(f, \boldsymbol{\theta}_{\text{theo syst}}\right) = x_b^{\text{SM}} \left(1 + \sum_i \frac{f_i x_i^{int}(\theta)}{x_b^{\text{SM}}} + \sum_i \frac{f_i^2 x_i^{quad}(\theta)}{x_b^{\text{SM}}} + \sum_{i \neq j} \frac{f_i f_j x_{ij}^{cross}(\theta)}{x_b^{\text{SM}}}\right) \times \prod_i^{n_{\text{theo syst}}} \left(1 + \theta_j u_j^b\right) \tag{7.23}$$

where f are the Wilson coefficients ,$\theta = (\theta_{1,....,}\theta_{n_{theo\ syst}})$ are nuisance parameters, n_{syst} is the number of theory nuisance parameters affecting the signal prediction, x^b_{SM} is the nominal SM cross prediction, and u^b_j is the relative size of the theory uncertainty j in bin b.

The nominal measured differential cross section of the $WZjj$ process, in n_{bins} bins, are denoted as x. Statistical and systematic uncertainties of the unfolded data are correlated and encoded in a covariance matrix C.

The likelihood function is given by:

$$L\left(\boldsymbol{x}|\boldsymbol{f},\boldsymbol{\theta}\right) = \frac{1}{\sqrt{(2\pi)^{n_{\text{bins}}}\det\left(C\right)}}\exp\left(-\frac{1}{2}\Delta\boldsymbol{x}^T\left(\boldsymbol{f},\boldsymbol{\theta}\right)C^{-1}\Delta\boldsymbol{x}\left(\boldsymbol{f},\boldsymbol{\theta}\right)\right) \quad \times\prod_i^{n_{\text{syst}}} d_i\left(\theta_i\right) \tag{7.24}$$

The d_i correspond to the Gaussian constraints on nuisance parameters, while the vector $\Delta x = (\Delta x_1, ..., \Delta x_{nbins})$ represents the difference between measurement and prediction. The difference between predicted and measured cross section, Δx^b, in a given measurement bin b, is defined as

$$\Delta x^b\left(\boldsymbol{f},\boldsymbol{\theta}\right) = x_b^{\text{meas}} - x^b_{\text{pred}}\left(\boldsymbol{f},\boldsymbol{\theta}\right). \tag{7.25}$$

In order to derive the confidence intervals for the reconstructed WZjj process, the number of expected events N^{pred} is modelled as

$$N^{\text{pred}}(f,\theta) = N^{\text{SM}}(\boldsymbol{\theta})\left(1+\sum_i A_i f_i + \sum_i B_i f_i^2 + \sum_{i<j} C_{ij} f_i f_j\right) + N^{\text{bkg,SM}}(\boldsymbol{\theta}) \tag{7.26}$$

where $N^{\text{SM}}(\boldsymbol{\theta})$ are the number of signal events in the SM, while $N^{\text{bkg,SM}}(\boldsymbol{\theta})$ is the number of expected background events. Both are subject to theoretical and experimental uncertainties which are modelled with nuisance parameters. The EFT parametrization is given by the terms A_i, B_i and C_{ij}.

The measurement likelihood L associated with the observation of $N = (N_0...N_b...N_{nbins}$ signal events in each bin, with a total number of bins equal to n_{bins}, is modelled as a product of Poisson distributions multiplied with constraint terms p_i for each of the in total n_{syst} nuisance parameters

$$L(N \mid \boldsymbol{f},\boldsymbol{\theta}) = \prod_b^{n_{\text{bins}}} \text{Poisson}\left(N_b \mid N_b^{\text{pred}}\left(\boldsymbol{f},\boldsymbol{\theta}\right)\right) \times \prod_i^{n_{\text{syst}}} p_i\left(\theta_i\right). \tag{7.27}$$

In order to estimate the confidence interval for a Wilson coefficient f_i, a profile likelihood ratio test statistics is constructed from the likelihood

$$\lambda\left(f_i\right) = -2\log\frac{L\left(f_i,\hat{\hat{\boldsymbol{\theta}}}\right)}{L\left(\hat{f}_i,\hat{\boldsymbol{\theta}}\right)}. \tag{7.28}$$

where $L\left(f_i,\hat{\hat{\boldsymbol{\theta}}}\right)$ is the maximum of the likelihood for a given f_i and $L\left(\hat{f}_i,\hat{\boldsymbol{\theta}}\right)$ is the value at the absolute maximum of the likelihood. Maximum likelihood fits are performed for individual Wilson coefficients by setting other coefficients to zero and maximizing the likelihood with respect to the nuisance parameters. Additionally, simultaneous fits of multiple Wilson coefficients are performed by also profiling other parameters of interest, i.e. maximizing the likelihood with respect to all relevant nuisance parameters and other Wilson coefficients. Confidence intervals are derived using Wilks' theorem, assuming that $\lambda\left(f_i\right)$ is χ^2 distributed [141].

Profiled Feldman-Cousins method

In order to derive the confidence intervals for the reconstructed WZjj process, a different approach can be followed. In this case the Wilks' theorem is not satisfied as the number of events in every bin of the kinematical variable of interest is very low and the related confidence intervals will not have the appropriate coverage for the reported significance, since the significance of the hypothesis tests cannot be properly evaluated using the χ^2 distribution. However, the likelihood-ratio test itself remains valid and optimal according to the Neyman–Pearson lemma. In such cases another method must be used.

In particle physics, the Original Feldman-Cousins (FC) method [144] is a popular nonparametric method for establishing confidence intervals with accurate coverage. A large number, N, of FC pseudoexperiments are simulated at points sampling the range of parameter values where confidence intervals will be reported. A ”Feldman-Cousins pseudoexperiment” is a hypothetical experimental observation under a certain set of parameters, f, in our case the Wilson coefficients. For each bin of our analysis samples, a Poisson-distributed random number is generated, and the mean of those Poisson distributions is the expected number of events in that bin given f. This process is repeated for each pseudoexperiment.

For each FC pseudoexperiment, x_j , the best fit of the parameter, $\hat{f}_j$, is also found through Maximum Likelihood Estimation. The FC pseudoexperiments are then ordered by the difference in l between the ”true” value used to generate the FC pseudoexperiments and the best fit

$$\lambda_{ij} = l(x_j|f_i) - l(x_j|\hat{f}_j), \tag{7.29}$$

to form a distribution $P(\lambda_i)$ that differs for every f_i. i corresponds to each point in parameter space, while l corresponds to $-2ln\mathcal{L}$.

This approach is referred to as ”nonparametric” since the ordering of the pseudoexperiments produces a distribution for the test statistic, λ_i, without knowing in advance how it should be distributed. The value that is greater than the first αN of the λ_{ij} values is the α-significance-level critical value for this set of true parameters, called $c_a(f_i)$ as specified by the following equation:

$$\int_0^{c_a} P(\lambda_i)d\lambda_i = \alpha. \tag{7.30}$$

The confidence interval at level α is therefore composed of the points where $\lambda_i < c_a(f_i)$, and this process is repeated for each point being tested. Since the critical value $c_a(f_i)$ is empirically determined for each point in parameter space, which will cover α fraction of the pseudoexperiments generated with values f_i, it is obvious that this procedure will give correct coverage, α, if the FC pseudoexperiments are a fair representation of the data.

A crucial issue of the above procedure is the handling of the nuisance parameters. The typical frequentist treatment for the nuisance parameters is to ”profile” over them. In other words, a search is performed over all values of the nuisance parameters at each point in the parameter space, f_i at which the likelihood is to be evaluated, and the combination of nuisance parameters that yields the maximum or minimum likelihood,

$$\hat{\hat{\theta}}_i = \underset{\theta}{\operatorname{argmin}} \ell\left(f_i, \theta\right) \tag{7.31}$$

is adopted. To distinguish it from the globally optimal nuisance parameters, $\hat{\theta}$, which correspond to the best estimate of the parameters of interest, $\hat{f}$, $\hat{\hat{\theta}}$ which relates to point f_i is indicated with two hats. The likelihood ratio is defined as:

$$\lambda_i = l(x|f_i, \hat{\hat{\theta}}_i) - l(x|\hat{f}, \hat{\theta}). \tag{7.32}$$

The coverage guarantees of the Feldman–Cousins procedure rely on our access to a collection of FC pseudoexperiments to inspect, which have been generated at the precise points we wish to include/exclude at a certain significance. When the nuisance parameters are present, it is not possible to have access to such an ensemble since the values of the nuisance parameters are not defined a priori by the point in parameter space being tested. Nevertheless, in order to produce FC pseudoexperiments, some values for the nuisance parameters must be chosen.

For this reason, the Profiled Feldman-Cousins method [145] will be used where at each point in parameter space, f_i, the FC pseudoexperiments is generated assuming the best-fit values of the nuisance parameters, given these parameters and observed data, $\theta_i = \hat{\hat{\theta}}_i$, as defined in Equation 7.31.

Even though the best-fit nuisance parameters are certainly not exactly the true values, they are the best estimate available to us, and the FC pseudoexperiments generated from our best estimate of the true parameters are expected to yield better coverage than experiments not so informed. The Profiled FC method takes the definition of the critical value from

$$\lambda_i = l(x|f_i) - l(x|\hat{f}), \tag{7.33}$$

literally, meaning that the distribution, $P(\lambda_i)$, should be calculated for λ_i with nuisance parameters fixed at $\theta_i = \hat{\hat{\theta}}_i$ as defined in Equation 7.32.

7.9.2.5 Strategy

In this study, the goal is to use the unfolded and reconstructed distibutions of some kinematical variables in order to extract the truth and reconstructed 95% confidence level (CL) limits on the aQGCs dimension-8 parameters for the fully leptonic WZjj process respectively. For the unfolded WZjj measurements the Fiducial WZjj-EW phase space, which is presented to Section 7.5, and is used and a Rivet routine [146], which is discussed in Section 7.8, has been created for this purpose. For the reconstructed measurements the phace space of the WZjj VBS signal region is used and it is presented in Section 7.2.

Eight independent aQGC operators relevant to the WZ VBS process [147, 148] studied are the following: $\mathcal{L}_{S,02}$, $\mathcal{L}_{S,1}$, $\mathcal{L}_{T,0}$, $\mathcal{L}_{T,1}$, $\mathcal{L}_{T,2}$, $\mathcal{L}_{M,0}$, $\mathcal{L}_{M,1}$ and $\mathcal{L}_{M,7}$.

Truth level limits: The asymptotic approximation described in Section 7.9.2.4 is used in order to extract the limits. Limits are extracted using seven different kinematical variables assuming one kinematical variable at a time in order to determine which is the most sensitive to dimension-8 operators. The binning used for each kinematical variable is the one used in the respective differential distribution described in Section 7.7. The observed and expected 95% CL lower and upper limits on the aQGC parameters are derived for two different cases: 1) using one aQGC operator at a time defining all the other anomalous couplings to the SM value and 2) using simultaneously two aQGC operators of the same family and setting all the other anomalous couplings to SM value. The second case is explored in order to study the correlations between various EFT parameters. For the $WZjj - EWK$ and $WZjj - QCD$ contributions, the signal strengths that extracted from the SM simultaneous fit and shown in

Table 7.7 are used. The experimental uncertainties that affect the measurement and the theory uncertainties that affect the $W^{\pm}Zjj$ SM and EFT processes are taken into account and their are described in Section 7.9.2.3. The theoretical uncertainties are calculated using the PMG SystematicTool [149]. Finally, the EFTFun tool [150] constructed based on the decomposition property of the EFT samples, is used for the extraction of the limits.

Reconstructed level limits: The first step in the limit extraction procedure is to optimize the binning of the kinematical variables in contrast to the truth level limits, which are based on the unfolded distibutions of the data where the binning is guided by the minimum required statistics for each bin. After that the asymptotic approximation described in Section 7.9.2.4 is used in order to extract the limits. To maximally profit from the sensitive kinematical variables two variables relatively uncorrelated are selected for the extraction of the reconstructed observed and expected 95% CL lower and upper limits on the aQGC parameters. This template is created by binning two kinematical variables simultaneously. Also a comparison between the limits derived using the two-dimensional fit template and the limits derived using only one kinematical variable is done. As previous the limits are extracted for the two different cases: using one operator at a time and using two operators simultaneously. The limits are also extracted using the unitarity bounds described in Section 2.3.2.3 and they are compared with those without the unitarity bounds. For the $WZjj - EWK$, $WZjj - QCD$, $t\bar{t}V$, tZ and $ZZ - QCD$ contributions, the signal strengths and the μ values that extracted from the SM simultaneous fit and shown in Table 7.7 are used. The experimental and theory uncertainties that affect the $W^{\pm}Zjj$ and EFT processes are taken into account as discussed in Section 7.9.2.3. The tool used for the extraction of the limits are the same as previous.

Finally a comparison between the truth and reconstructed level limits is done.

7.9.2.6 Unfolded-level fits

The procedure described in Section 7.9.2.5 is followed for the extraction of the expected 95% CL lower and upper limits on the aQGC Wilson coefficients of the corresponding dimension-8 operators. Tables 7.14, 7.15 and 7.16 show the individual 95% CL lower and upper expected and observed limits for the Wilson coefficients of the $\mathcal{L}_{S,02}$, $\mathcal{L}_{S,1}$, $\mathcal{L}_{T,0}$, $\mathcal{L}_{T,1}$, $\mathcal{L}_{T,2}$, $\mathcal{L}_{M,0}$, $\mathcal{L}_{M,1}$ and $\mathcal{L}_{M,7}$ operators for each different kinematical variable, which are obtained without using any unitarization procedure. The transverse mass of the diboson system M_T^{WZ} gives the best expected limits for all the operators.

The nuisance parameter pull distributions of the expected fit and the fit to the data using the unfolded transverse mass of the $W^{\pm}Z$ system, M_T^{WZ}, for all the relevant aQGC operators are presented in Figures 7.25 and 7.26, respectively. A constrain is visible on the theory scale

	Variable	Expected (TeV^{-4})	Observed (TeV^{-4})
f_{S02}/Λ^4	M_T^{WZ}	[-23.7, 24.2]	[-23.8, 24.4]
	$\sum P_T^{\text{Lep}}$	[-28.0, 28.3]	[-25.8, 26.1]
	$\Delta\phi_{WZ}$	[-42.4, 43.3]	[-32.5, 33.4]
	m_{jj}	[-40.9, 41.9]	[-37.9, 38.8]
	$\Delta\phi_{jj}$	[-57.7, 58.2]	[-73.7, 74.7]
	Δy_{jj}	[-44.1, 45.4]	[-53.5, 54.8]
	N_{jets}	[-53.5, 55.0]	[-35.8, 37.3]
f_{S1}/Λ^4	M_T^{WZ}	[-68.2, 68.8]	[-68.6, 69.3]
	$\sum P_T^{\text{Lep}}$	[-80.7, 81.0]	[-74.6, 74.9]
	$\Delta\phi_{WZ}$	[-121.7, 123.0]	[-93.8, 95.0]
	m_{jj}	[-115.3, 117.3]	[-106.1, 107.9]
	$\Delta\phi_{jj}$	[-162.5, 161.4]	[-208.2, 209.3]
	Δy_{jj}	[-125.5, 127.9]	[-152.0, 154.6]
	N_{jets}	[-151.2, 154.6]	[-101.4, 104.8]

Table 7.14: Expected and observed lower and upper 95% CL limits on the Wilson coefficients of the $\mathcal{L}_{S,02}$ and $\mathcal{L}_{S,1}$ aQGC operators for each kinematical variable, which are obtained without using any unitarization procedure.

	Variable	Expected (TeV^{-4})	Observed (TeV^{-4})
f_{T0}/Λ^4	M_T^{WZ}	[-1.17, 1.24]	[-1.18, 1.25]
	$\sum P_T^{\text{Lep}}$	[-1.33, 1.37]	[-1.22, 1.25]
	$\Delta\phi_{WZ}$	[-2.46, 2.58]	[-1.98, 2.10]
	m_{jj}	[-2.63, 2.72]	[-2.66, 2.76]
	$\Delta\phi_{jj}$	[-2.92, 2.97]	[-3.71, 3.77]
	Δy_{jj}	[-3.39, 3.43]	[-3.49, 3.51]
	N_{jets}	[-3.28, 3.38]	[-2.43, 2.55]
f_{T1}/Λ^4	M_T^{WZ}	[-0.77, 0.90]	[-0.78, 0.90]
	$\sum P_T^{\text{Lep}}$	[-0.89, 1.00]	[-0.81, 0.91]
	$\Delta\phi_{WZ}$	[-1.56, 1.71]	[-1.22, 1.37]
	m_{jj}	[-1.84, 2.01]	[-1.88, 2.07]
	$\Delta\phi_{jj}$	[-2.06, 2.18]	[-2.59, 2.73]
	Δy_{jj}	[-2.35, 2.50]	[-2.41, 2.55]
	N_{jets}	[-2.24, 2.41]	[-1.62, 1.82]
f_{T2}/Λ^4	M_T^{WZ}	[-2.15, 2.69]	[-2.16, 2.69]
	$\sum P_T^{\text{Lep}}$	[-2.52, 2.97]	[-2.30, 2.73]
	$\Delta\phi_{WZ}$	[-4.47, 5.18]	[-3.51, 4.18]
	m_{jj}	[-5.17, 5.89]	[-5.27, 6.04]
	$\Delta\phi_{jj}$	[-5.86, 6.37]	[-7.41, 8.00]
	Δy_{jj}	[-6.73, 7.30]	[-6.93, 7.45]
	N_{jets}	[-6.36, 7.11]	[-4.55, 5.41]

Table 7.15: Expected and observed lower and upper 95% CL limits on the Wilson coefficients of the $\mathcal{L}_{T,0}$, $\mathcal{L}_{T,1}$ and $\mathcal{L}_{T,2}$ aQGC operators for each kinematical variable, which are obtained without using any unitarization procedure.

	Variable	Expected (TeV^{-4})	Observed (TeV^{-4})
f_{M0}/Λ^4	M_T^{WZ}	[-12.5, 12.4]	[-12.6, 12.5]
	$\sum P_T^{\mathrm{Lep}}$	[-14.1, 14.0]	[-13.0, 12.9]
	$\Delta\phi_{WZ}$	[-25.2, 24.8]	[-20.1, 19.9]
	m_{jj}	[-26.0, 24.9]	[-25.3, 24.2]
	$\Delta\phi_{jj}$	[-29.7, 29.8]	[-38.1, 37.6]
	Δy_{jj}	[-30.6, 29.5]	[-34.6, 33.5]
	N_{jets}	[-32.2, 31.1]	[-22.8, 21.7]
f_{M1}/Λ^4	M_T^{WZ}	[-19.1, 19.5]	[-19.2, 19.5]
	$\sum P_T^{\mathrm{Lep}}$	[-21.9, 22.2]	[-20.1, 20.4]
	$\Delta\phi_{WZ}$	[-37.7, 38.2]	[-30.0, 30.4]
	m_{jj}	[-39.0, 40.2]	[-37.9, 39.1]
	$\Delta\phi_{jj}$	[-46.8, 47.4]	[-59.5, 60.4]
	Δy_{jj}	[-45.3, 46.6]	[-47.8, 49.1]
	N_{jets}	[-48.5, 49.8]	[-33.7, 35.0]
f_{M7}/Λ^4	M_T^{WZ}	[-24.0, 24.0]	[-24.1, 24.1]
	$\sum P_T^{\mathrm{Lep}}$	[-27.2, 27.2]	[-25.0, 25.0]
	$\Delta\phi_{WZ}$	[-49.2, 49.2]	[-39.9, 39.9]
	m_{jj}	[-51.5, 51.5]	[-51.3, 51.3]
	$\Delta\phi_{jj}$	[-55.0, 55.0]	[-71.5, 71.5]
	Δy_{jj}	[-65.7, 65.7]	[-72.3, 72.3]
	N_{jets}	[-63.9, 63.9]	[-45.8, 45.8]

Table 7.16: Expected and observed lower and upper 95% CL limits on the Wilson coefficients of the $\mathcal{L}_{M,0}$, $\mathcal{L}_{M,1}$ and $\mathcal{L}_{M,7}$ aQGC operators for each kinematical variable, which are obtained without using any unitarization procedure.

uncertainty of the SM process which contains the $W^{\pm}Zjj - QCD$ process, $W^{\pm}Zjj - EWK$ process and the interference term between them.

The comparison of the profile likelihood ratio curves on the Wilson coefficients of all the relevant aQGC operators for the expected fit and fit on the data using the unfolded transverse mass of the $W^{\pm}Z$ system, M_T^{WZ} when no nuisance parameters are included and when experimental and theoretical uncertainty nuisance parameters are considered, are presented in Figures 7.27 and 7.28, respectively.

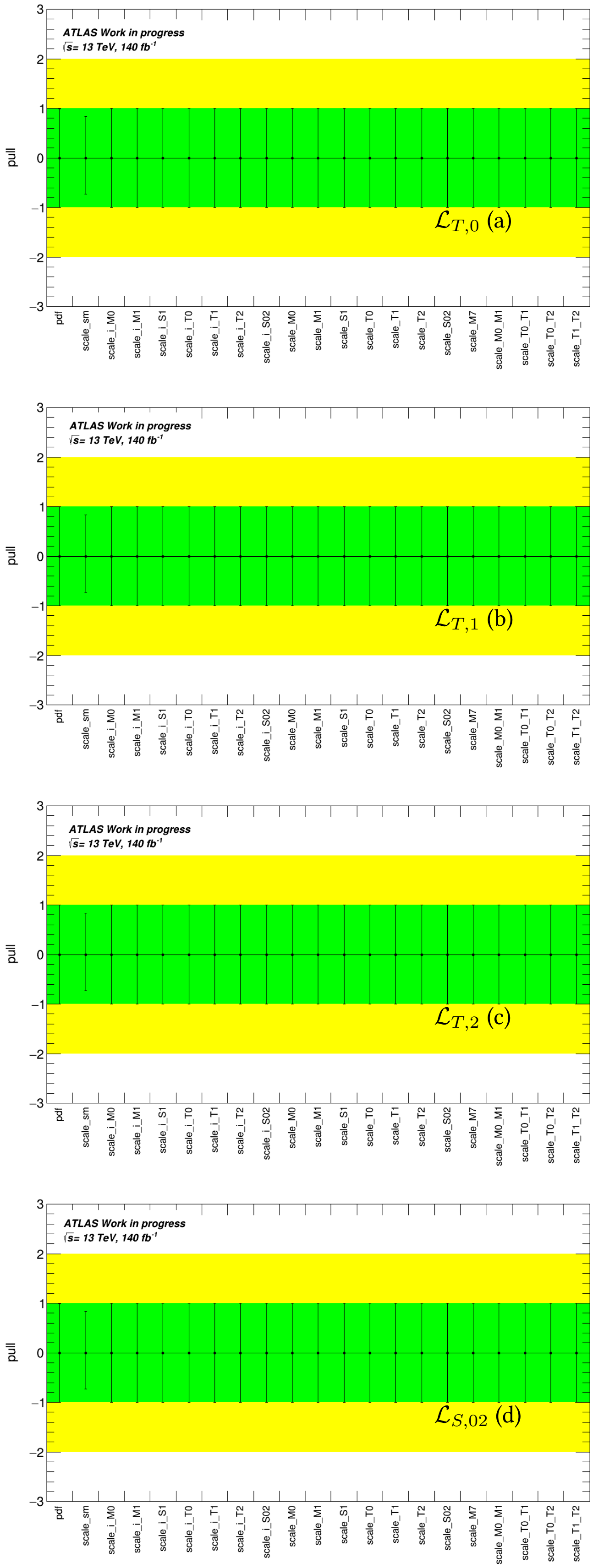

FIGURE 7.25: Nuisance parameter pull distribution of the expected fit to the two dimensional distribution of the M_T^{WZ} for two different aQGC operators, $\mathcal{L}_{T,0}$ (a), $\mathcal{L}_{T,1}$ (b), $\mathcal{L}_{T,2}$ (c), $\mathcal{L}_{S,02}$ (d), $\mathcal{L}_{S,1}$ (e), $\mathcal{L}_{M,0}$ (f), $\mathcal{L}_{M,1}$ (g) and $\mathcal{L}_{M,7}$ (h). (Zero pulls should be ignored as it is concerned operators that are not participating to the fit.)

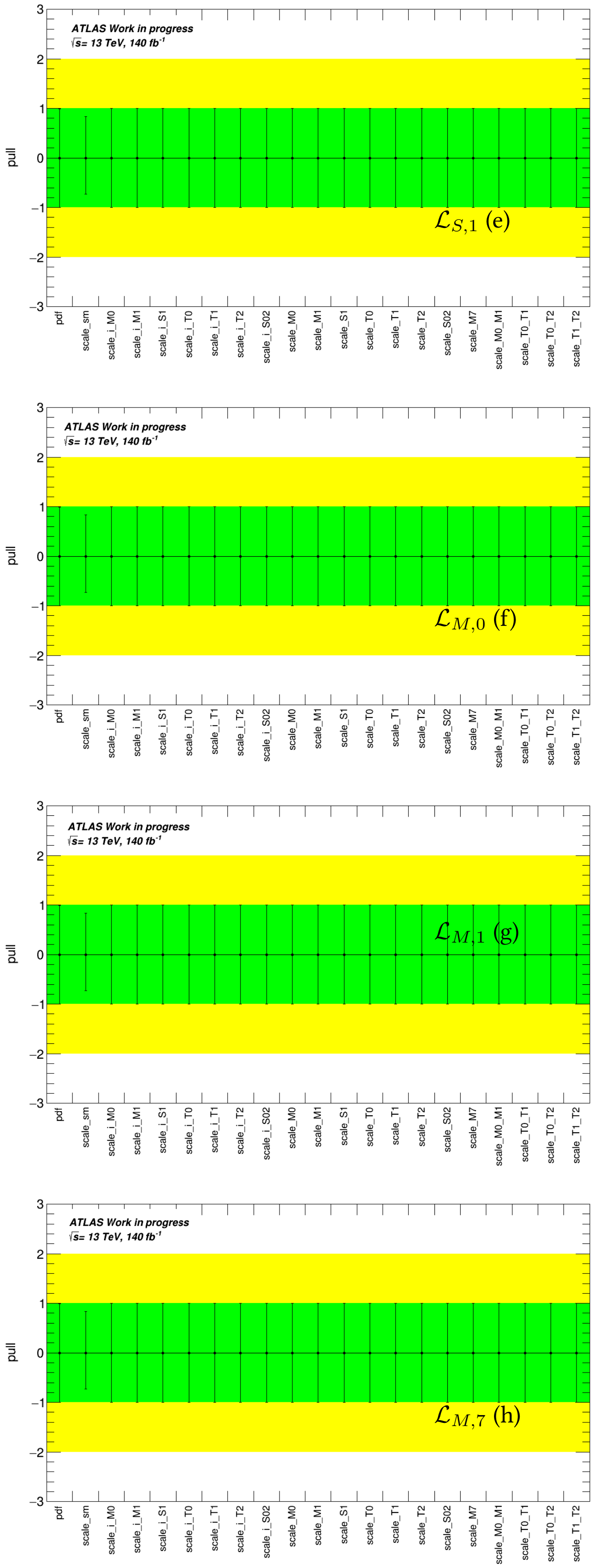

FIGURE 7.25: Nuisance parameter pull distribution of the expected fit to the two dimensional distribution of the M_T^{WZ} for two different aQGC operators, $\mathcal{L}_{T,0}$ (a), $\mathcal{L}_{T,1}$ (b), $\mathcal{L}_{T,2}$ (c), $\mathcal{L}_{S,02}$ (d), $\mathcal{L}_{S,1}$ (e), $\mathcal{L}_{M,0}$ (f), $\mathcal{L}_{M,1}$ (g) and $\mathcal{L}_{M,7}$ (h). (Zero pulls should be ignored as it is concerned operators that are not participating to the fit.)

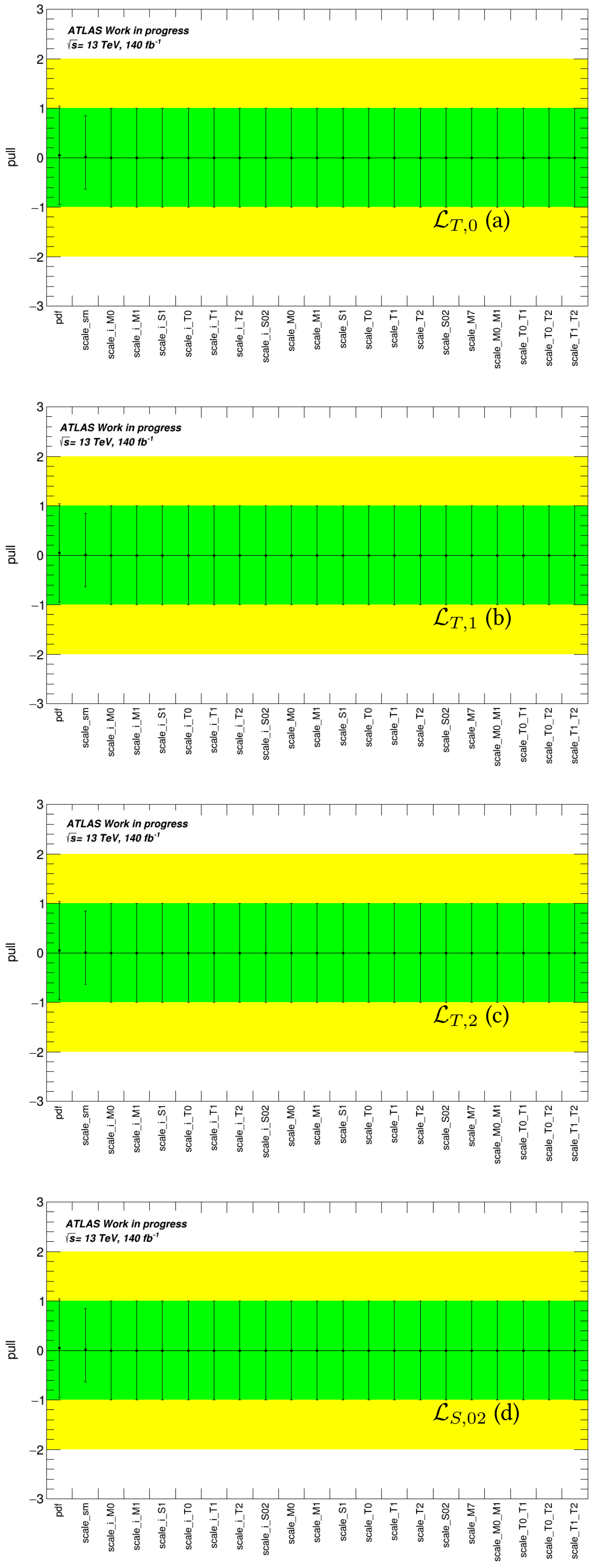

FIGURE 7.26: Nuisance parameter pull distribution of the fit on data using the two dimensional distribution of the M_T^{WZ} for two different aQGC operators, $\mathcal{L}_{T,0}$ (a), $\mathcal{L}_{T,1}$ (b), $\mathcal{L}_{T,2}$ (c), $\mathcal{L}_{S,02}$ (d), $\mathcal{L}_{S,1}$ (e), $\mathcal{L}_{M,0}$ (f), $\mathcal{L}_{M,1}$ (g) and $\mathcal{L}_{M,7}$ (h). (Zero pulls should be ignored as it is concerned operators that are not participating to the fit.)

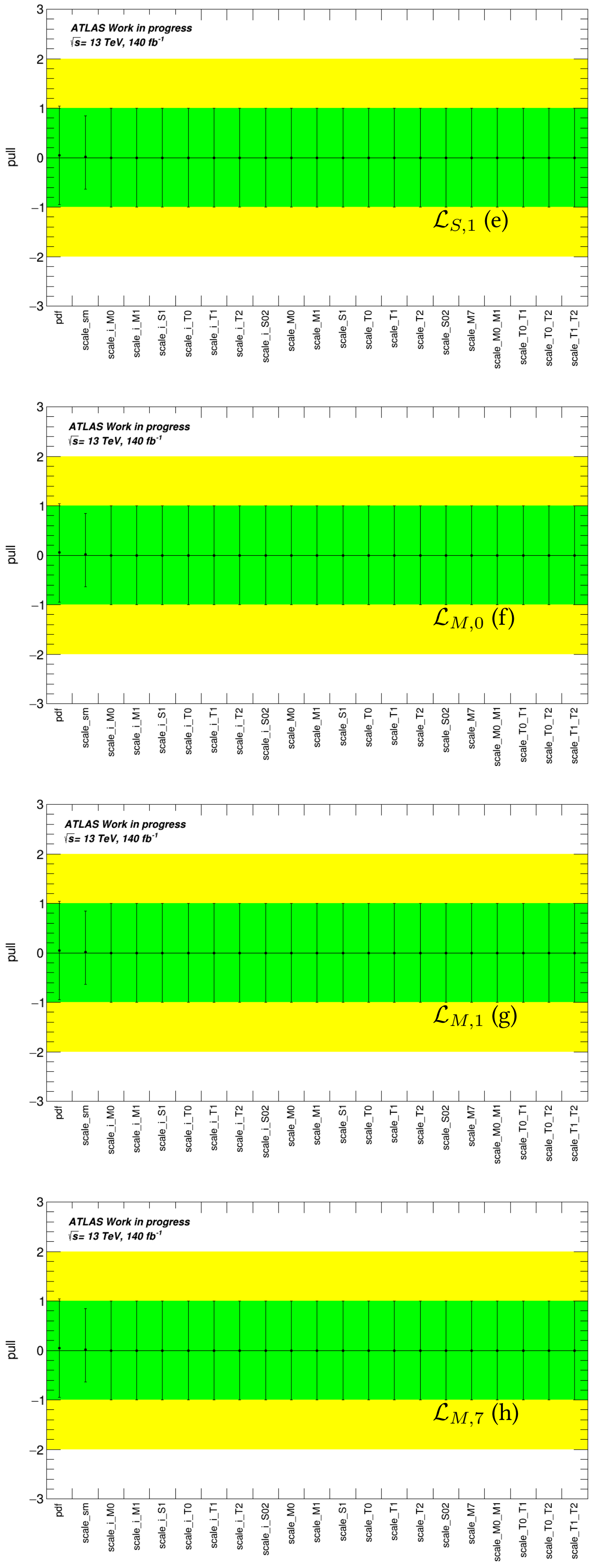

FIGURE 7.26: Nuisance parameter pull distribution of the fit on data using the two dimensional distribution of the M_T^{WZ} for two different aQGC operators, $\mathcal{L}_{T,0}$ (a), $\mathcal{L}_{T,1}$ (b), $\mathcal{L}_{T,2}$ (c), $\mathcal{L}_{S,02}$ (d), $\mathcal{L}_{S,1}$ (e), $\mathcal{L}_{M,0}$ (f), $\mathcal{L}_{M,1}$ (g) and $\mathcal{L}_{M,7}$ (h).(Zero pulls should be ignored as it is concerned operators that are not participating to the fit.)

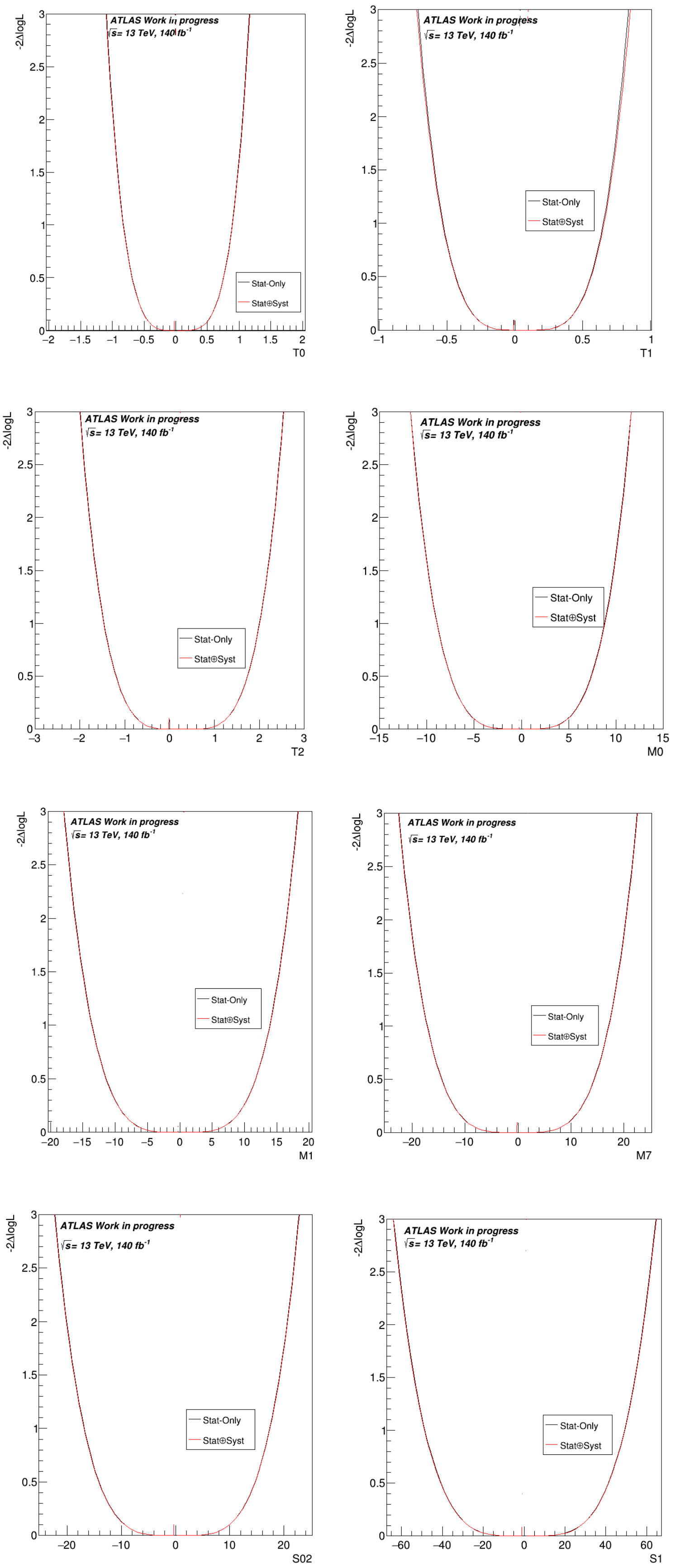

FIGURE 7.27: Comparison of profile likelihood ratio curves on the Wilson coefficients of all the relevant aQGC operators for the expected fit to the two dimensional distributions of the M_T^{WZ} when no nuisance parameters are included (Stat-Only) and when experimental and theoretical uncertainty nuisance parameters are considered (Stat+Syst).

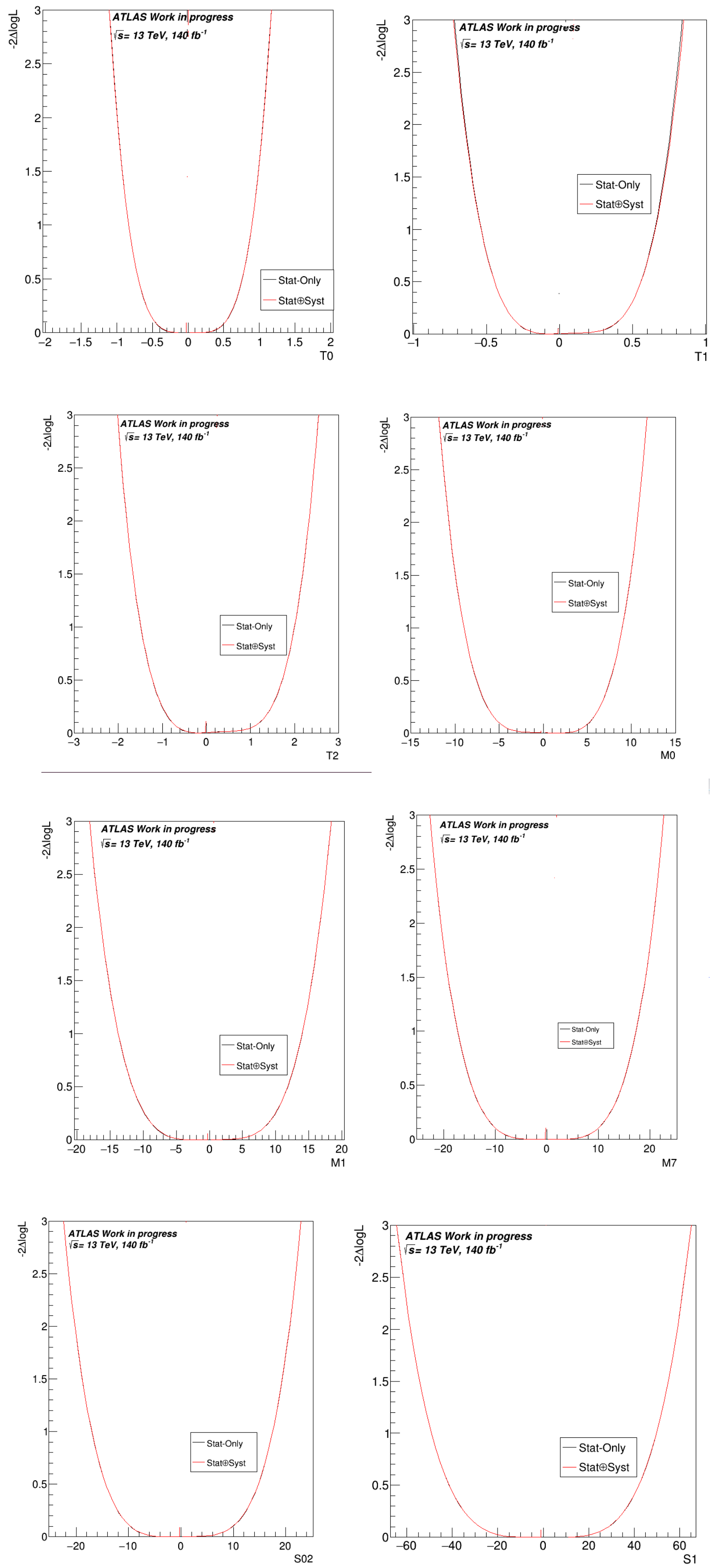

FIGURE 7.28: Comparison of profile likelihood ratio curves on the Wilson coefficients of all the relevant aQGC operators for the fit on data using the two dimensional distributions of the M_T^{WZ} when no nuisance parameters are included (Stat-Only) and when experimental and theoretical uncertainty nuisance parameters are considered (Stat+Syst).

Limits on aQGC Wilson coefficients are also derived using a two-dimensional scan, in order to probe the correlations between various EFT parameters. In this case, two EFT coefficients are included in the fit and the rest of the coefficients is assumed to have zero contribution. The expected and observed 2D 95% CL intervals of the $\mathcal{L}_{M,0}$-$\mathcal{L}_{M,1}$, $\mathcal{L}_{T,0}$-$\mathcal{L}_{T,1}$, $\mathcal{L}_{T,0}$-$\mathcal{L}_{T,2}$ and $\mathcal{L}_{T,1}$-$\mathcal{L}_{T,2}$ combination of operators for the M_T^{WZ} variable are shown in Figures 7.29 and 7.30, respectively. From these Figures, it can be seen that the operators are correlated. The corresponding 2D expected and observed 95% CL lower and upper limits of the Wilson coefficients of the above combination of operators are shown in Tables 7.17, 7.18, 7.19 and 7.20. The transverse mass of the diboson system M_T^{WZ} gives the best expected and observed limits for all the operators but these limits are worse that using only one operator at a time.

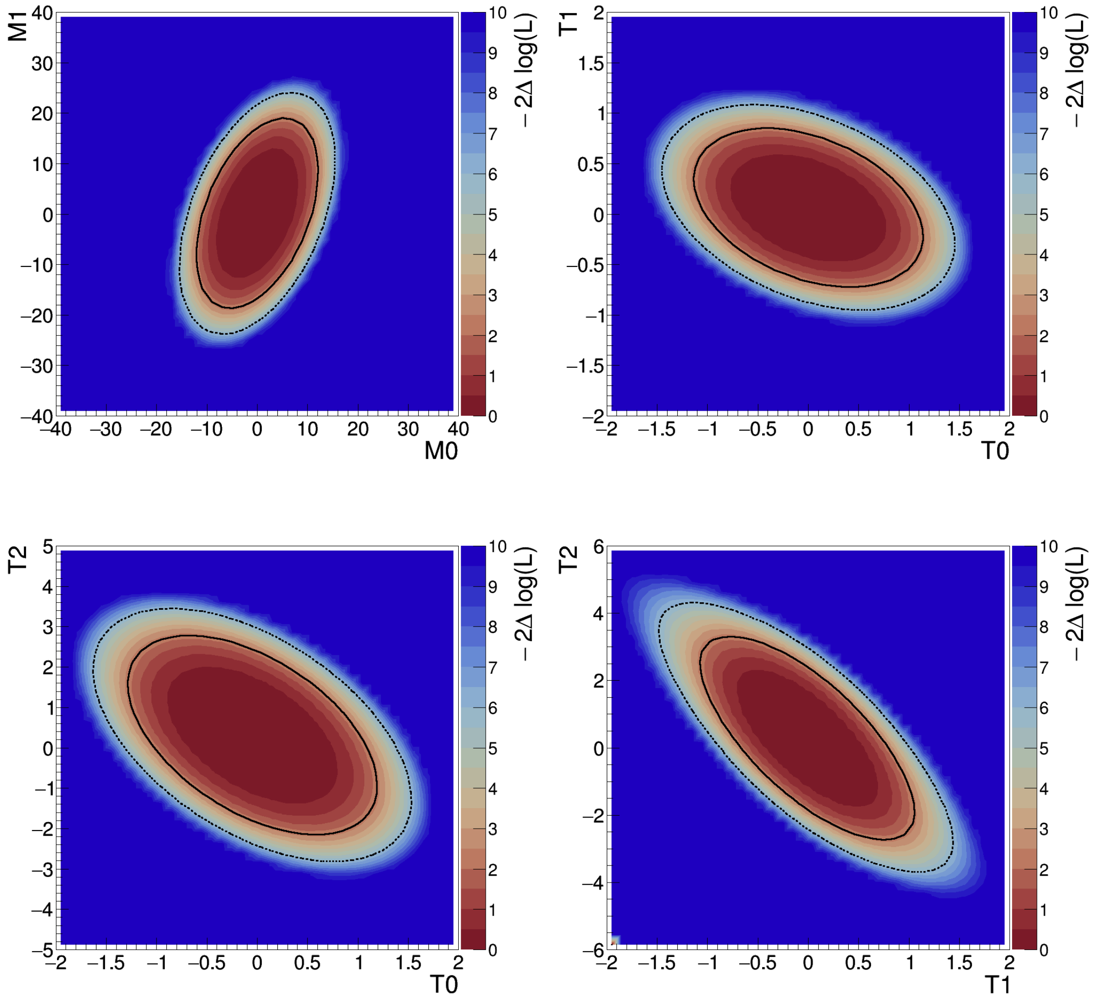

FIGURE 7.29: Two-dimensional expected 95% CL intervals (solid contour) of the $\mathcal{L}_{M,0}$-$\mathcal{L}_{M,1}$, $\mathcal{L}_{T,0}$-$\mathcal{L}_{T,1}$, $\mathcal{L}_{T,0}$-$\mathcal{L}_{T,2}$ and $\mathcal{L}_{T,1}$-$\mathcal{L}_{T,2}$ combination of operators for the M_T^{WZ}.

As a final test, the potential presence of EFT effects in the unfolded data is studied. Pseudodata is generated by combining the contributions from $WZjj-QCD$, $WZjj-EWK$ and $WZjj-INT$ SM processes, and adding an EFT contribution from the $\mathcal{L}_{T,1}$ operator. For

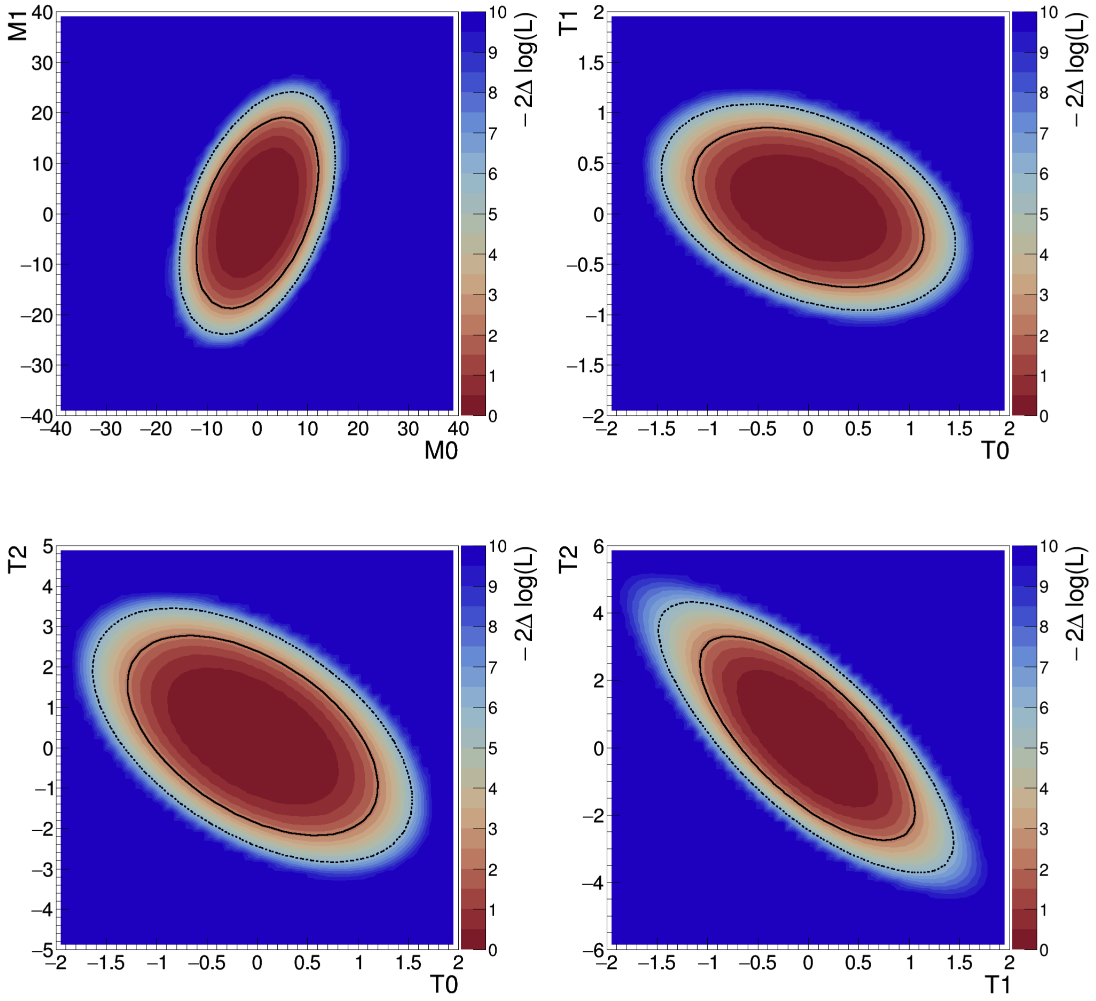

FIGURE 7.30: Two-dimensional observed95% CL intervals (solid contour) of the $\mathcal{L}_{M,0}$-$\mathcal{L}_{M,1}$, $\mathcal{L}_{T,0}$-$\mathcal{L}_{T,1}$, $\mathcal{L}_{T,0}$-$\mathcal{L}_{T,2}$ and $\mathcal{L}_{T,1}$-$\mathcal{L}_{T,2}$ combination of operators for the M_T^{WZ}.

	Variable	Expected (TeV^{-4})	Observed (TeV^{-4})
f_{M0}/Λ^4, f_{M1}/Λ^4	M_T^{WZ}	[-15.5, 15.5], [-23.8, 24.2]	[-15.6, 15.6], [-23.9, 24.2]
	$\sum P_T^{\mathrm{Lep}}$	[-17.6, 17.6], [-27.5, 27.8]	[-16.4, 16.4], [-25.6, 25.8]
	$\Delta\phi_{WZ}$	[-30.6, 30.3], [-46.0, 46.3]	[-25.0, 24.9], [-37.5, 37.8]
	m_{jj}	[-29.0, 27.9], [-43.6, 44.8]	[-28.3, 27.2], [-42.5, 43.7]
	$\Delta\phi_{jj}$	[-37.0, 37.3], [-58.5, 59.2]	[-48.4, 47.9], [-60.1, 61.2]
	Δy_{jj}	[-36.7, 35.9], [-55.0, 55.8]	[-40.9, 39.9], [-61.6, 62.5]
	N_{jets}	[-39.5, 38.6], [-60.3, 61.0]	[-40.9, 39.9], [-44.3, 45.0]

TABLE 7.17: 2D expected and observed lower and upper 95% CL limits on the Wilson coefficients of the $\mathcal{L}_{M,0}$ and $\mathcal{L}_{M,1}$ aQGC operators for each kinematical variable.

	Variable	Expected (TeV^{-4})	Observed (TeV^{-4})
f_{T0}/Λ^4, f_{T1}/Λ^4	M_T^{WZ}	[-1.45, 1.45], [-0.95, 1.09]	[-1.46, 1.46], [-0.96, 1.09]
	$\sum P_T^{\text{Lep}}$	[-1.63, 1.61], [-1.08, 1.19]	[-1.51, 1.49], [-1.00, 1.10]
	$\Delta\phi_{WZ}$	[-3.04, 3.07], [-1.91, 2.06]	[-2.55, 2.58], [-1.57, 1.71]
	m_{jj}	[-3.17, 3.18], [-2.20, 2.37]	[-3.20, 3.21], [-2.24, 2.43]
	$\Delta\phi_{jj}$	[-3.49, 3.48], [-2.45, 2.57]	[-4.30, 4.30], [-3.00, 3.16]
	Δy_{jj}	[-4.07, 4.05], [-2.81, 2.96]	[-4.17, 4.12], [-2.87, 3.01]
	N_{jets}	[-3.98, 3.99], [-2.69, 2.86]	[-3.13, 3.15], [-2.08, 2.26]

Table 7.18: 2D expected and observed lower and upper 95% CL limits on the Wilson coefficients of the $\mathcal{L}_{T,0}$ and $\mathcal{L}_{T,1}$ aQGC operators for each kinematical variable.

	Variable	Expected (TeV^{-4})	Observed (TeV^{-4})
f_{T0}/Λ^4, f_{T2}/Λ^4	M_T^{WZ}	[-1.63, 1.53], [-2.82, 3.46]	[-1.64, 1.54], [-2.84, 3.46]
	$\sum P_T^{\text{Lep}}$	[-1.82, 1.72], [-3.30, 3.86]	[-1.69, 1.59], [-3.05, 3.59]
	$\Delta\phi_{WZ}$	[-3.28, 3.20, [-5.78, 6.56]	[-2.73, 2.66], [-4.70, 5.44]
	m_{jj}	[-3.59, 3.45], [-6.83, 7.69]	[-3.65, 3.51], [-6.98, 7.91]
	$\Delta\phi_{jj}$	[-3.88, 3.77], [-7.66, 8.29]	[-4.75, 4.64], [-9.36, 10.08]
	Δy_{jj}	[-4.53, 4.40], [-8.78, 9.51]	[-4.63, 4.49], [-9.00, 9.69]
	N_{jets}	[-4.39, 4.26], [-8.29, 9.18]	[-3.45, 3.33], [-6.29, 7.27]

Table 7.19: 2D expected and observed lower and upper 95% CL limits on the Wilson coefficients of the $\mathcal{L}_{T,0}$ and $\mathcal{L}_{T,2}$ aQGC operators for each kinematical variable.

	Variable	Expected (TeV^{-4})	Observed (TeV^{-4})
f_{T1}/Λ^4, f_{T2}/Λ^4	M_T^{WZ}	[-1.48, 1.44], [-3.69, 4.32]	[-1.49, 1.44], [-3.72, 4.33]
	$\sum P_T^{\text{Lep}}$	[-1.50, 1.50], [-4.08, 4.54]	[-1.39, 1.38], [-3.77, 4.22]
	$\Delta\phi_{WZ}$	[-2.62, 2.59], [-7.29, 8.06]	[-2.17, 2.14], [-6.00, 6.74]
	m_{jj}	[-2.98, 2.98], [-8.22, 8.93]	[-3.08, 3.08], [-8.42, 9.19]
	$\Delta\phi_{jj}$	[-3.29, 3.26]], [-9.10, 9.68]	[-4.21, 4.16], [-11.48, 12.74]
	Δy_{jj}	[-3.76, 3.77], [-10.67, 11.43]	[-3.83, 3.84], [-11.01, 11.72]
	N_{jets}	[-3.62, 3.61, [-10.08, 10.99]	[-2.82, 2.81], [-11.01, 11.72]

Table 7.20: 2D expected and observed lower and upper 95% CL limits on the Wilson coefficients of the $\mathcal{L}_{M,0}$ and $\mathcal{L}_{M,1}$ aQGC operators for each kinematical variable.

this test, only the quadratic term of the $\mathcal{L}_{T,1}$ contribution is considered, as it dominates the M_T^{WZ} observable used to derive EFT truth-level limits. The value of the Wilson coefficients of the $\mathcal{L}_{T,1}$ operator is conservatively set to 1.0, which is twice the expected sensitivity of reconstructed-level limits, Table 7.23.

The generated pseudo-data is then unfolded to the particle-level using a migration matrix constructed from the sum of $WZjj - QCD$, $WZjj - EWK$ and $WZjj - INT$ SM predictions. The unfolded pseudo-data is compared to the true particle-level distribution, which includes the contributions from $WZjj - QCD$, $WZjj - EWK$, $WZjj - INT$ and the $\mathcal{L}_{T,1}$ EFT effects. This comparison is shown in Figure 7.31.

If the unfolding process is unbiased, the two distributions should perfectly match. Although, a small bias is observed in the last bins of the distribution of the M_T^{WZ}, where the presence of $\mathcal{L}_{T,1}$ EFT effects becomes evident in the pseudo-data. In the iterative Bayesian method, a bias of approximately 10% is observed in the last M_T^{WZ} bin, which can be reduced to around 5% using a bin-by-bin unfolding method. It is noted that this bias is within the range covered by the unfolding uncertainty resulting from the prior definition. The prior uncertainty is determined in a data-driven way, following the approach described in [151, 152].

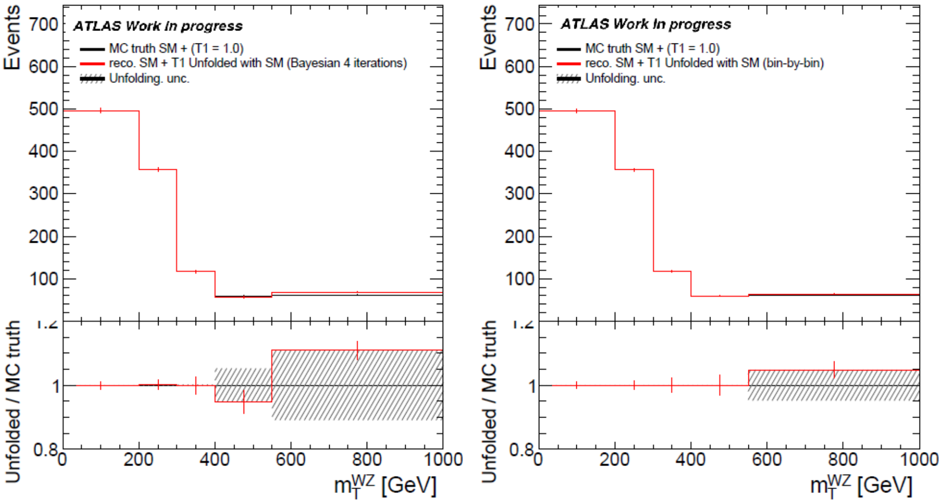

FIGURE 7.31: Comparisons between the true particle-level distribution of the sum of $WZjj-$QCD, $WZjj-$INT, $WZjj-$EW and of the $\mathcal{L}_{T,1}$ effect (black histogram) and the unfolded pseudo-data containing SM and $\mathcal{L}_{T,1}$ EFT effects (red histogram). The comparison is done using the iterative Bayesian unfolding method (left) and the bin-by-bin unfolding method (right). The hatched-grey area represents the unfolding uncertainty due to the prior definition.

7.9.2.7 Reco-level fits

Fit variable binning optimization

Binned Profile-likelihood fits performed using the decomposition method have been shown to be heavily dependent not only on the fit variable, but also on the binning of the histogram that is used in the fit. Thus, an optimization of the binning used for each fit variable is necessary. The procedure to define the optimal binning for the variables used in the Reco-level fits is as follows:

1. For a given number of bins, create a large number of variable binning options for the fit histogram, while requiring ≥ 5 events per-bin in total for all Standard Model processes

(including the estimates from dimension-4 electroweak WZ signal and $WZ-$QCD) and the quadratic term of the $\mathcal{L}_{T,1}$ operator, which is the most sensitive operator to the WZjj process. The $\mathcal{L}_{T,1}$ operator is set to three times the existing limit [139].

2. The binning options are generated by splitting the initial histogram range in steps:
   In the first step, the range is split in n_1+1 bins. In the second step, each one of the n_1+1 bins is split in n_2+1 bins. The process continues for up to n steps, in which case the histogram will have $n+1$ bins.

3. Perform binned profile-likelihood fits for each binning option.
   The 1-operator profile-likehood fits to extract the expected 95% CL value of the Wilson coefficient performed using the quadratic EFT term for the $\mathcal{L}_{T,1}$ operator.

4. The binning choice resulting in the narrowest positive-to-negative 95% C.L. Wilson coefficient width is chosen as the optimized binning.

The results of the optimization procedure are shown in Table 7.21.

M_T^{WZ} (GeV)	[0, 450, 700, 1050, 1550, ∞]
M_{jj} (GeV)	[500, 1050, ∞]
$BDT\ Score$	[-1.0, -0.25, 0.17, 0.72, 1.0]

TABLE 7.21: Results of the optimization procedure for fit variable histogram binning for variables used in Reco-level fits.

Finally, the CMS binning [93] for the M_T^{WZ} and the M_{jj}, which is shown in Table 7.22, will be used for this study for comparison reasons, as the differences in the $95\ \%$ CL limits when using either the optimized binning or this binning are negligible.

M_T^{WZ} (GeV)	[0, 400, 750, 1050, 1350, ∞]
M_{jj} (GeV)	[500, 1200, ∞]

TABLE 7.22: CMS binning for the M_T^{WZ} and the M_{jj}.

Examples of the yields of the EFT contribution for the $\mathcal{L}_{T,1}$ operator are shown in Figure 7.32.

Reconstructed-level fit results

The procedure described in Section 7.9.2.5 is followed for the extraction of the expected and observed 95% CL lower and upper limits on the aQGC Wilson coefficients of the corresponding dimension-8 operators.

The pseudoexperiments (Feldman-Cousins method) are necessary in the extraction of the reco-level expected limits because the optimized binning used contains bins with low statistics. They have been chosen to have at least 5 events each of them. As pseudoexperiments

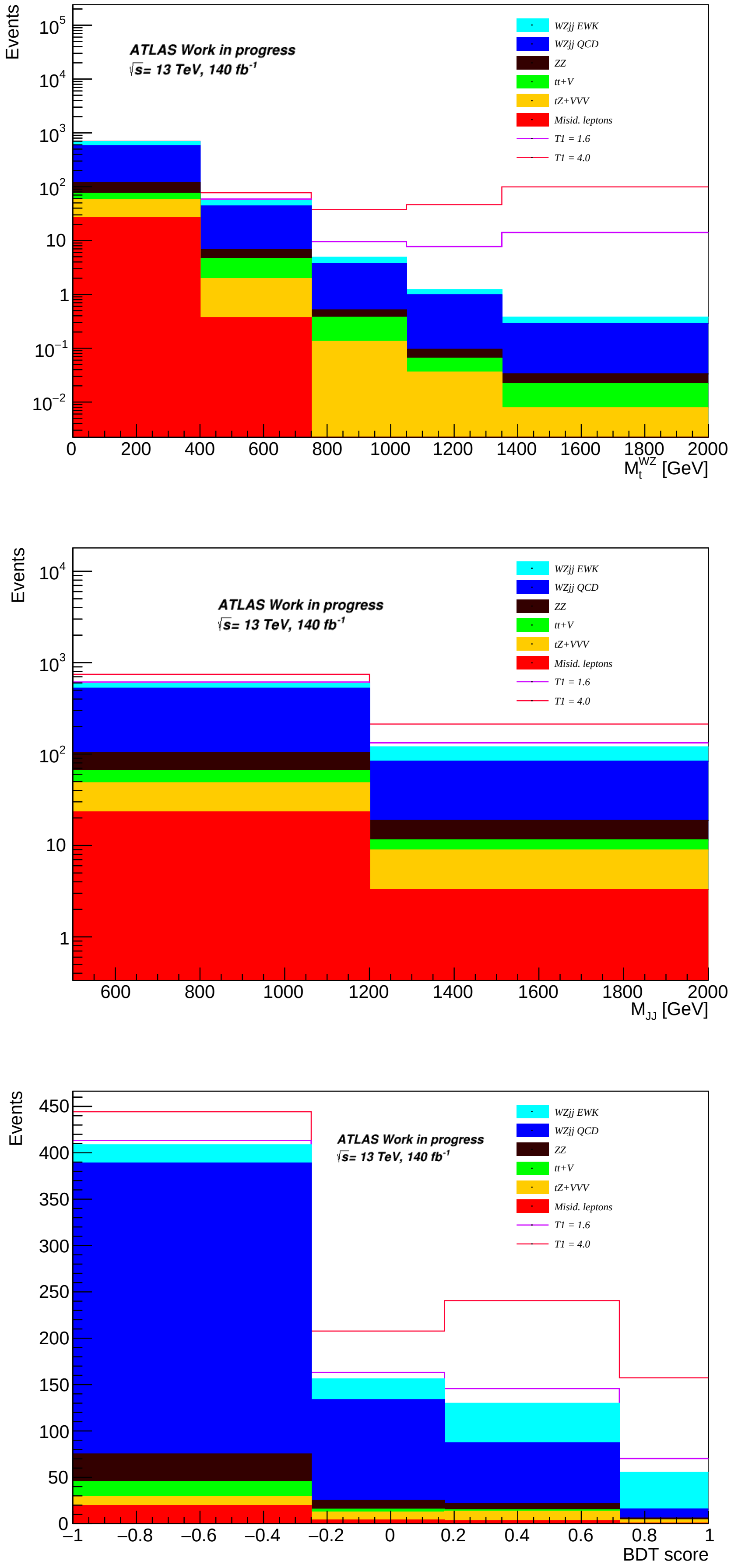

FIGURE 7.32: Reco-level distributions of the $\mathcal{L}_{T,1}$ operator, for the M_T^{WZ}, the M_{jj} and the BDT score.

are very time consuming, the asymptotic method can be used for the extraction of the limits if the results of the two methods are comparable. Figure 7.33 shows the comparison of the probability distribution as a function of the Wilson coefficient of the $\mathcal{L}_{T,1}$ operator for the two methods. For this comparison the M_T^{WZ} distribution is used and no nuisance parameters are applied. Figure 7.34 shows the same comparison using all the nuisance parameters. The blue line corresponds to the Feldman-Cousins method, while the red one corresponds to the asymptotic method. The results of the two methods are comparable, so the asymptotic method can be used for the extraction of the reco-level limits.

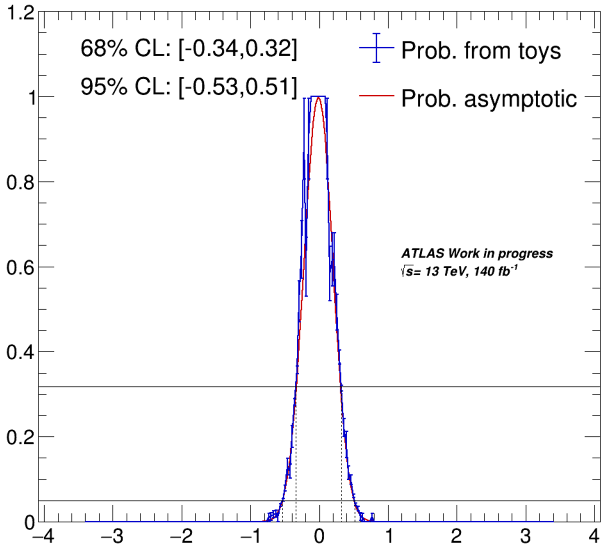

FIGURE 7.33: Comparison of the probability distribution as a function of the value of the Wilson coefficient of the $\mathcal{L}_{T,1}$ operator for the two methods using the M_T^{WZ} and no nuisance parameters.

The limits are extracted using either one dimensional distribution or two-dimensional distribution in the fit. The two-dimensional templates are created by binning two kinematic variables simultaneously and they are transformed to one dimension by 'unrolling' the bin contents, thus allowing them to be inserted as fit templates to the fitting framework. In this study, the one-dimensional distribution used is the M_T^{WZ} and the two-dimensional distributions are the M_T^{WZ} - M_{jj} and the M_T^{WZ} - BDT score. The yields of the EFT contribution for the $\mathcal{L}_{T,1}$ operator for the "unrolled" two dimensional distributions M_T^{WZ} - M_{jj} and M_T^{WZ} - BDT score are shown in Figure 7.35.

As a final step, the contribution of the quadratic term of the two most sensitive aQGC operators, $\mathcal{L}_{T,0}$ and $\mathcal{L}_{T,1}$, of the $ZZjj - EWK$ process, are added as a background to the fitting procedure. The values used for the Wilson coefficients of these two operators are the 95% CL expected upper limit, extracted without the contribution of this background using the

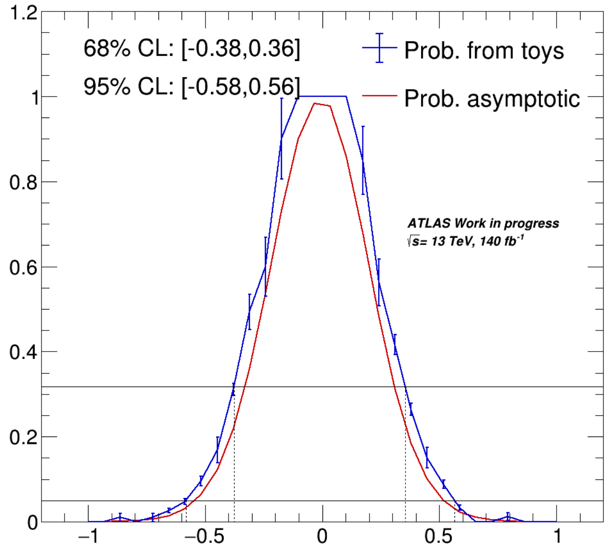

FIGURE 7.34: Comparison of the probability distribution as a function of the value of the Wilson coefficient of the $\mathcal{L}_{T,1}$ operator for the two methods using the M_T^{WZ} and all the nuisance parameters.

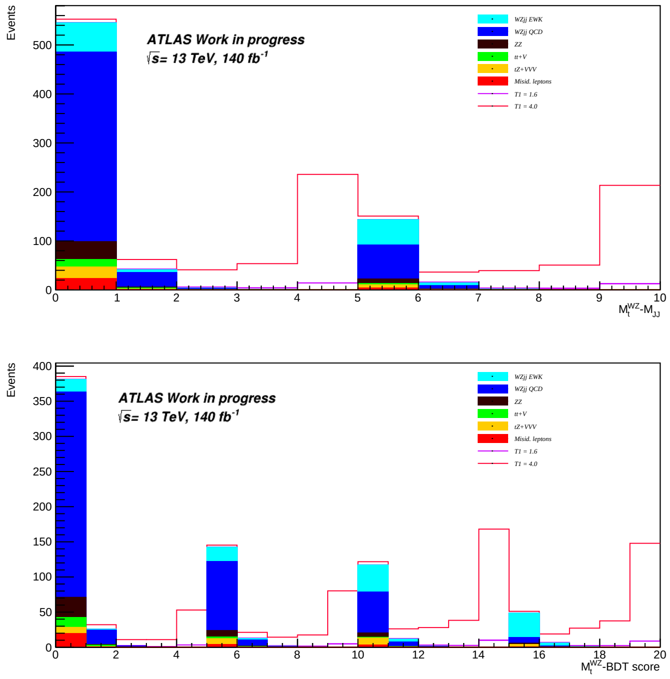

FIGURE 7.35: Reco-level distributions of the $\mathcal{L}_{T,1}$ operator, for the "unrolled" M_T^{WZ} - M_{jj} and M_T^{WZ} - BDT score.

M_T^{WZ} - BDT score. Their effect to the 95% CL expected and observed limits is $\sim\ 1.5\%$ for the Wilson coefficients of all the studied operators.

Table 7.23 shows the individual 95% CL lower and upper expected and observed limits for the Wilson coefficients of the $\mathcal{L}_{S,02}$, $\mathcal{L}_{S,1}$, $\mathcal{L}_{T,0}$, $\mathcal{L}_{T,1}$, $\mathcal{L}_{T,2}$, $\mathcal{L}_{M,0}$, $\mathcal{L}_{M,1}$ and $\mathcal{L}_{M,7}$ operators for the M_T^{WZ}, M_T^{WZ} - M_{jj} and the M_T^{WZ} - BDT score, which are obtained without using any unitarization procedure. The two dimensional template of the M_T^{WZ} with the BDT score gives the best expected limits for all the operators.

	Variable	Expected (TeV^{-4})	Observed (TeV^{-4})
f_{S02}/Λ^4	M_T^{WZ}	[-15.8, 15.8]	[-10.4, 10.4]
	$M_T^{\mathrm{WZ}}vsM_{jj}$	[-15.2, 15.2]	[-10.3, 10.2]
	$M_T^{\mathrm{WZ}}vsBDTscore$	[-13.9, 13.9]	[-10.4, 10.4]
f_{S1}/Λ^4	M_T^{WZ}	[-47.1, 46.8]	[-30.7, 30.3]
	$M_T^{\mathrm{WZ}}vsM_{jj}$	[-45.0, 44.7]	[-30.0, 29.7]
	$M_T^{\mathrm{WZ}}vsBDTscore$	[-40.8, 40.3]	[-30.5, 30.1]
f_{T0}/Λ^4	M_T^{WZ}	[-0.80, 0.80]	[-0.57, 0.55]
	$M_T^{\mathrm{WZ}}vsM_{jj}$	[-0.80, 0.80]	[-0.56, 0.55]
	$M_T^{\mathrm{WZ}}vsBDTscore$	[-0.78, 0.78]	[-0.56, 0.55]
f_{T1}/Λ^4	M_T^{WZ}	[-0.52, 0.49]	[-0.39, 0.35]
	$M_T^{\mathrm{WZ}}vsM_{jj}$	[-0.52, 0.49]	[-0.39, 0.35]
	$M_T^{\mathrm{WZ}}vsBDTscore$	[-0.51, 0.48]	[-0.39, 0.35]
f_{T2}/Λ^4	M_T^{WZ}	[-1.56, 1.43]	[-1.18, 0.99]
	$M_T^{\mathrm{WZ}}vsM_{jj}$	[-1.56, 1.43]	[-1.19, 0.97]
	$M_T^{\mathrm{WZ}}vsBDTscore$	[-1.53, 1.40]	[-1.18, 0.99]
f_{M0}/Λ^4	M_T^{WZ}	[-8.5, 8.5]	[-5.8, 5.6]
	$M_T^{\mathrm{WZ}}vsM_{jj}$	[-8.5, 8.4]	[-5.6, 5.6]
	$M_T^{\mathrm{WZ}}vsBDTscore$	[-8.1, 8.1]	[-5.8, 5.6]
f_{M1}/Λ^4	M_T^{WZ}	[-12.6, 12.5]	[-8.6, 8.5]
	$M_T^{\mathrm{WZ}}vsM_{jj}$	[-12.5, 12.4]	[-8.5, 8.4]
	$M_T^{\mathrm{WZ}}vsBDTscore$	[-12.1, 11.9]	[-8.6, 8.5]
f_{M7}/Λ^4	M_T^{WZ}	[-16.3, 16.3]	[11.0, 11.0]
	$M_T^{\mathrm{WZ}}vsM_{jj}$	[-16.3, 16.3]	[-10.9, 10.9]
	$M_T^{\mathrm{WZ}}vsBDTscore$	[-15.8, 15.8]	[-11.0, 11.0]

TABLE 7.23: Expected and observed lower and upper 95% CL limits on the Wilson coefficients of the $\mathcal{L}_{S,02}$, $\mathcal{L}_{S,1}$, $\mathcal{L}_{T,0}$, $\mathcal{L}_{T,1}$, $\mathcal{L}_{T,2}$, $\mathcal{L}_{M,0}$, $\mathcal{L}_{M,1}$ and $\mathcal{L}_{M,7}$ aQGC operators for the M_T^{WZ}, M_T^{WZ} - M_{jj} and the M_T^{WZ} - BDT score, which are obtained without using any unitarization procedure.

The nuisance parameter pull distributions of the expected fit and the fit on data using the two dimensional distribution of the M_T^{WZ} - BDT score for all the relevant aQGC operators, are presented in Figures 7.36 and 7.37, respectively.

The comparison of the profile likelihood ratio curves on the Wilson coefficients of all the relevant aQGC operators, when no nuisance parameters are included and when experimental and theoretical uncertainty nuisance parameters are considered, are presented in Figures 7.38

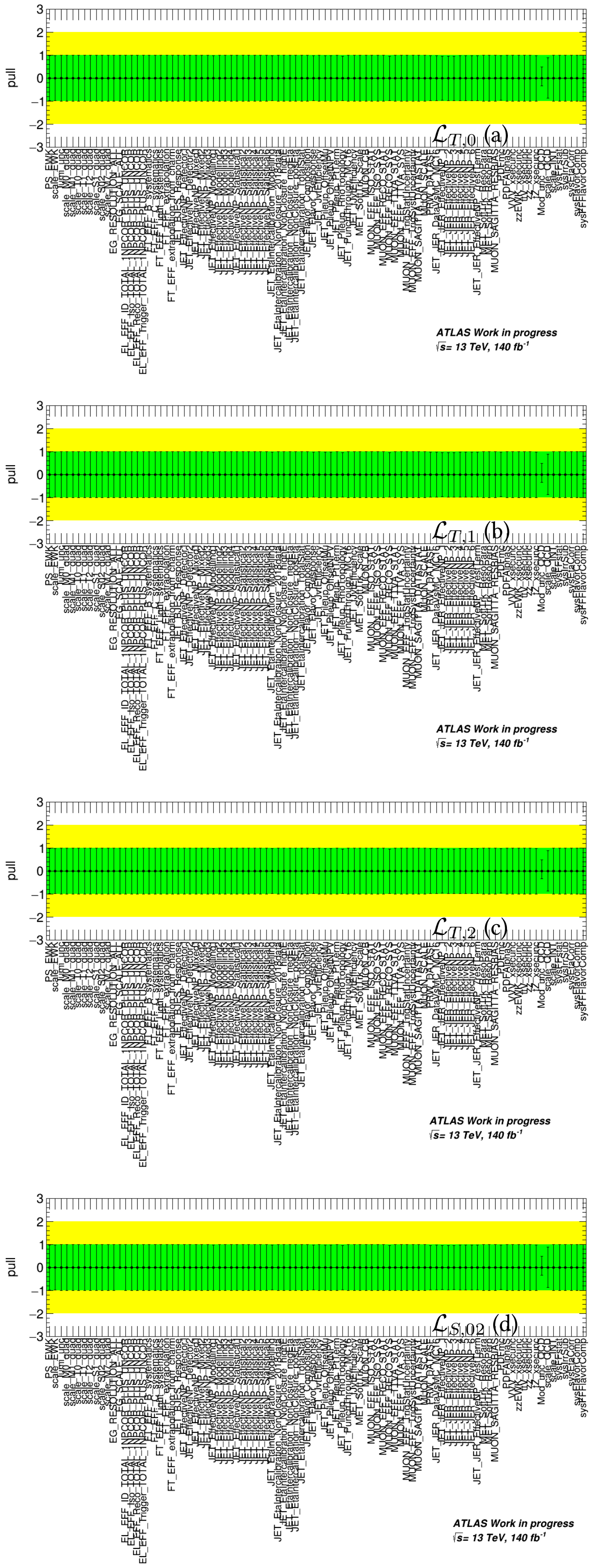

FIGURE 7.36: Nuisance parameter pull distribution of the expected fit to the two dimensional distribution of the M_T^{WZ} - BDT score for two different aQGC operators, $\mathcal{L}_{T,0}$ (a), $\mathcal{L}_{T,1}$ (b), $\mathcal{L}_{T,2}$ (c), $\mathcal{L}_{S,02}$ (d), $\mathcal{L}_{S,1}$ (e), $\mathcal{L}_{M,0}$ (f), $\mathcal{L}_{M,1}$ (g) and $\mathcal{L}_{M,7}$ (h). (Zero pulls should be ignored as it is concerned operators that are not participating to the fit.)

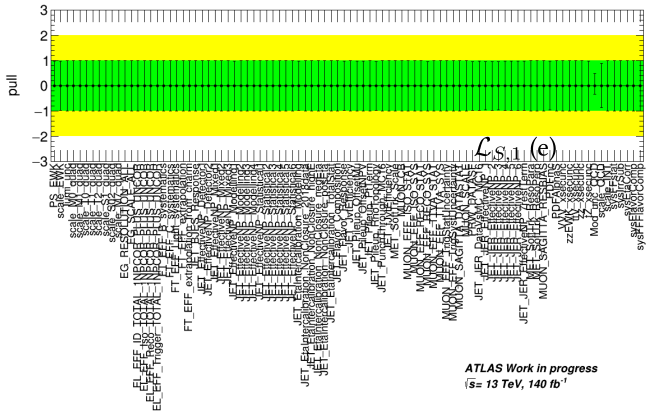

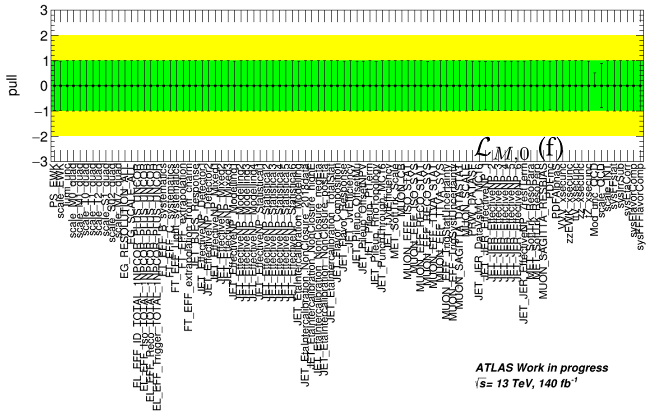

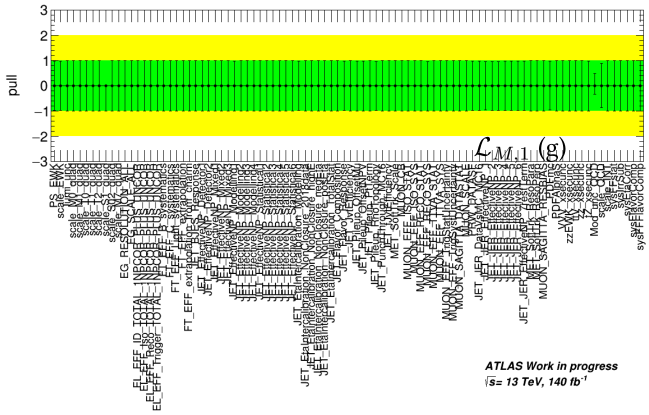

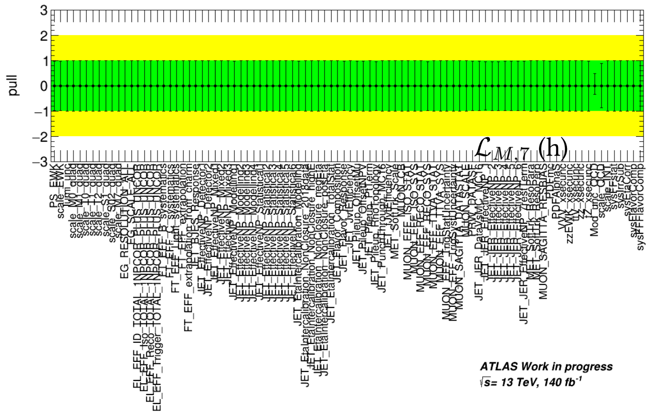

FIGURE 7.36: Nuisance parameter pull distribution of the expected fit to the two dimensional distribution of the M_T^{WZ} - BDT score for two different aQGC operators, $\mathcal{L}_{T,0}$ (a), $\mathcal{L}_{T,1}$ (b), $\mathcal{L}_{T,2}$ (c), $\mathcal{L}_{S,02}$ (d), $\mathcal{L}_{S,1}$ (e), $\mathcal{L}_{M,0}$ (f), $\mathcal{L}_{M,1}$ (g) and $\mathcal{L}_{M,7}$ (h). (Zero pulls should be ignored as it is concerned operators that are not participating to the fit.)

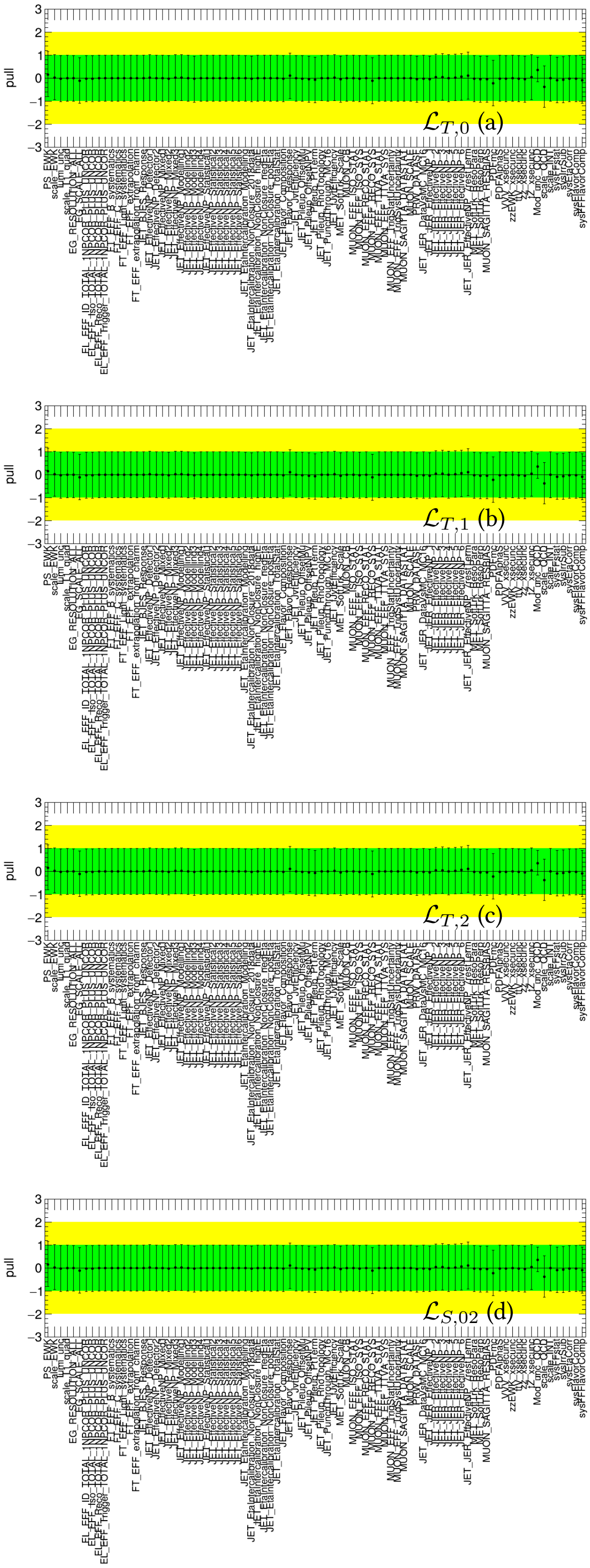

FIGURE 7.37: Nuisance parameter pull distribution of the fit on data using the two dimensional distribution of the M_T^{WZ} - BDT score for two different aQGC operators, $\mathcal{L}_{T,0}$ (a), $\mathcal{L}_{T,1}$ (b), $\mathcal{L}_{T,2}$ (c), $\mathcal{L}_{S,02}$ (d), $\mathcal{L}_{S,1}$ (e), $\mathcal{L}_{M,0}$ (f), $\mathcal{L}_{M,1}$ (g) and $\mathcal{L}_{M,7}$ (h). (Zero pulls should be ignored as it is concerned operators that are not participating to the fit.)

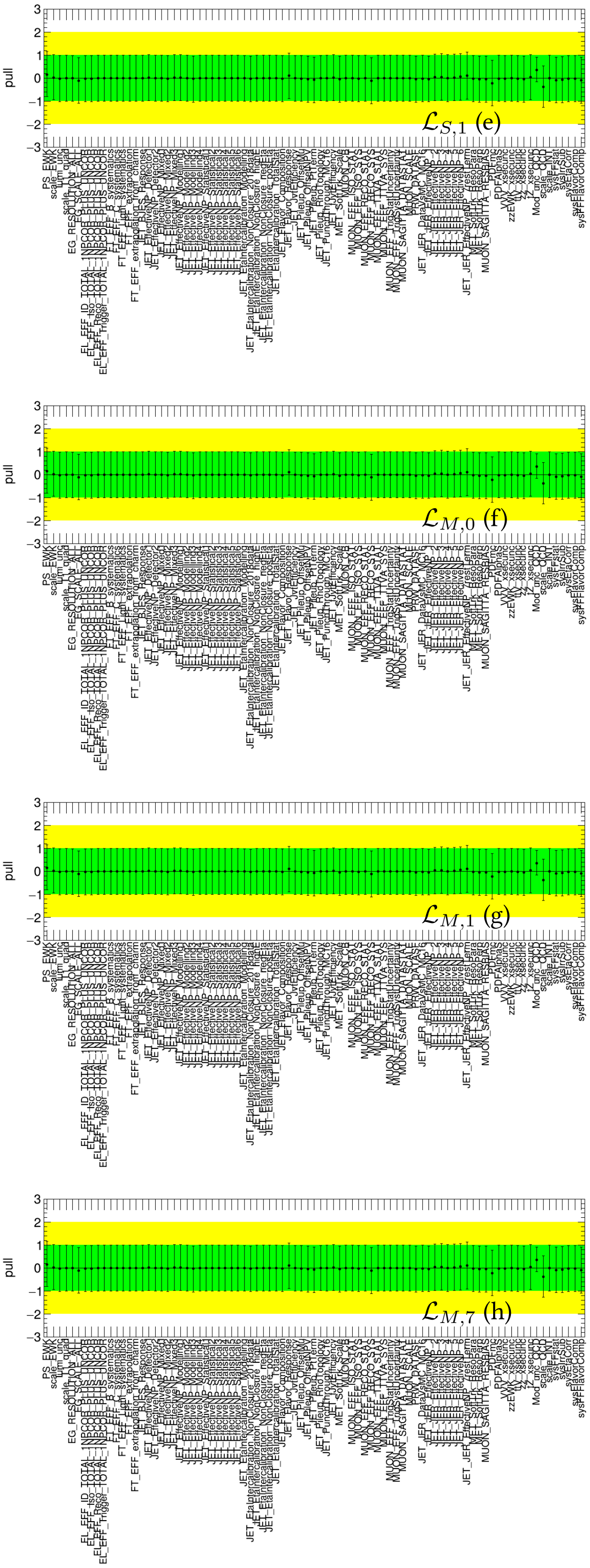

FIGURE 7.37: Nuisance parameter pull distribution of the fit on data using the two dimensional distribution of the M_T^{WZ} - BDT score for two different aQGC operators, $\mathcal{L}_{T,0}$ (a), $\mathcal{L}_{T,1}$ (b), $\mathcal{L}_{T,2}$ (c), $\mathcal{L}_{S,02}$ (d), $\mathcal{L}_{S,1}$ (e), $\mathcal{L}_{M,0}$ (f), $\mathcal{L}_{M,1}$ (g) and $\mathcal{L}_{M,7}$ (h). (Zero pulls should be ignored as it is concerned operators that are not participating to the fit.)

and 7.39 for the expected fit and for the fit in data using the two dimensional distributions of the M_T^{WZ} - BDT score.

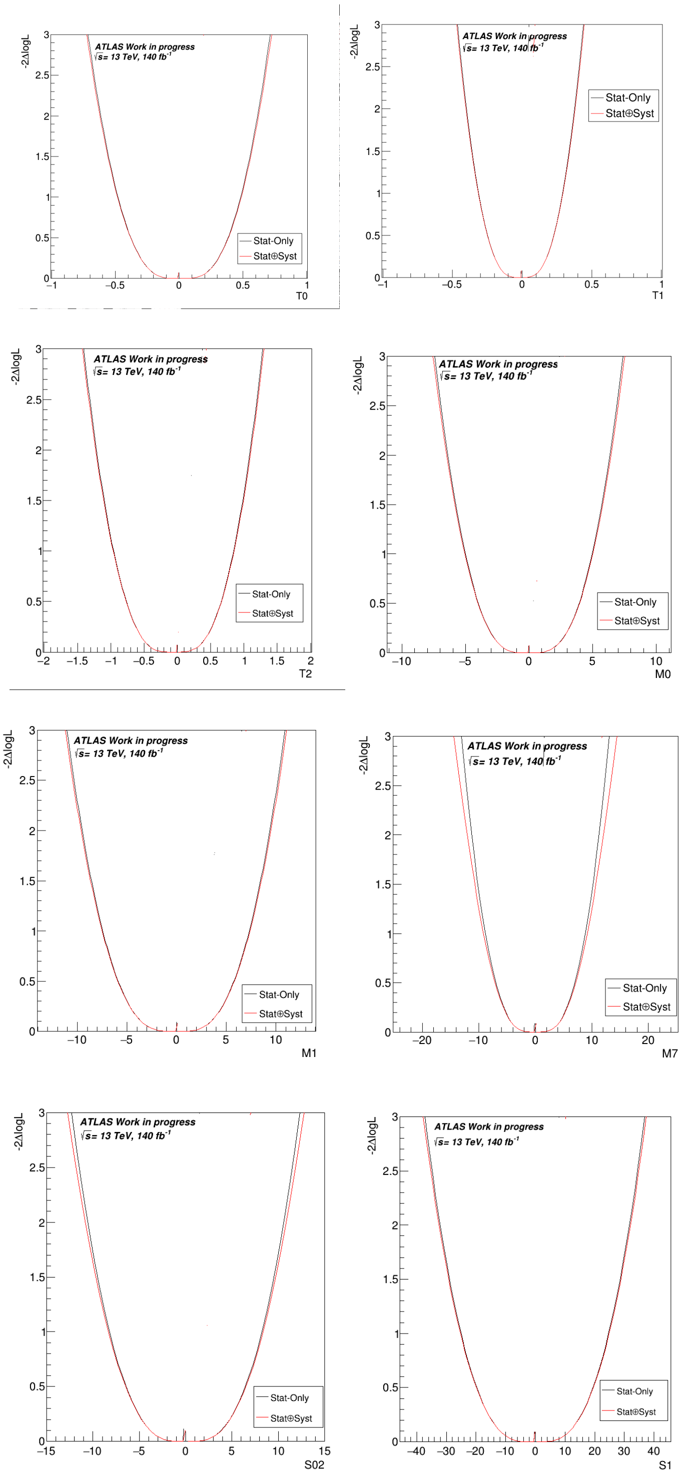

FIGURE 7.38: Comparison of profile likelihood ratio curves on the Wilson coefficients of all the relevant aQGC operators for the expected fit to the two dimensional distributions of the M_T^{WZ} - BDT score when no nuisance parameters are included (Stat-Only) and when experimental and theoretical uncertainty nuisance parameters are considered (Stat+Syst).

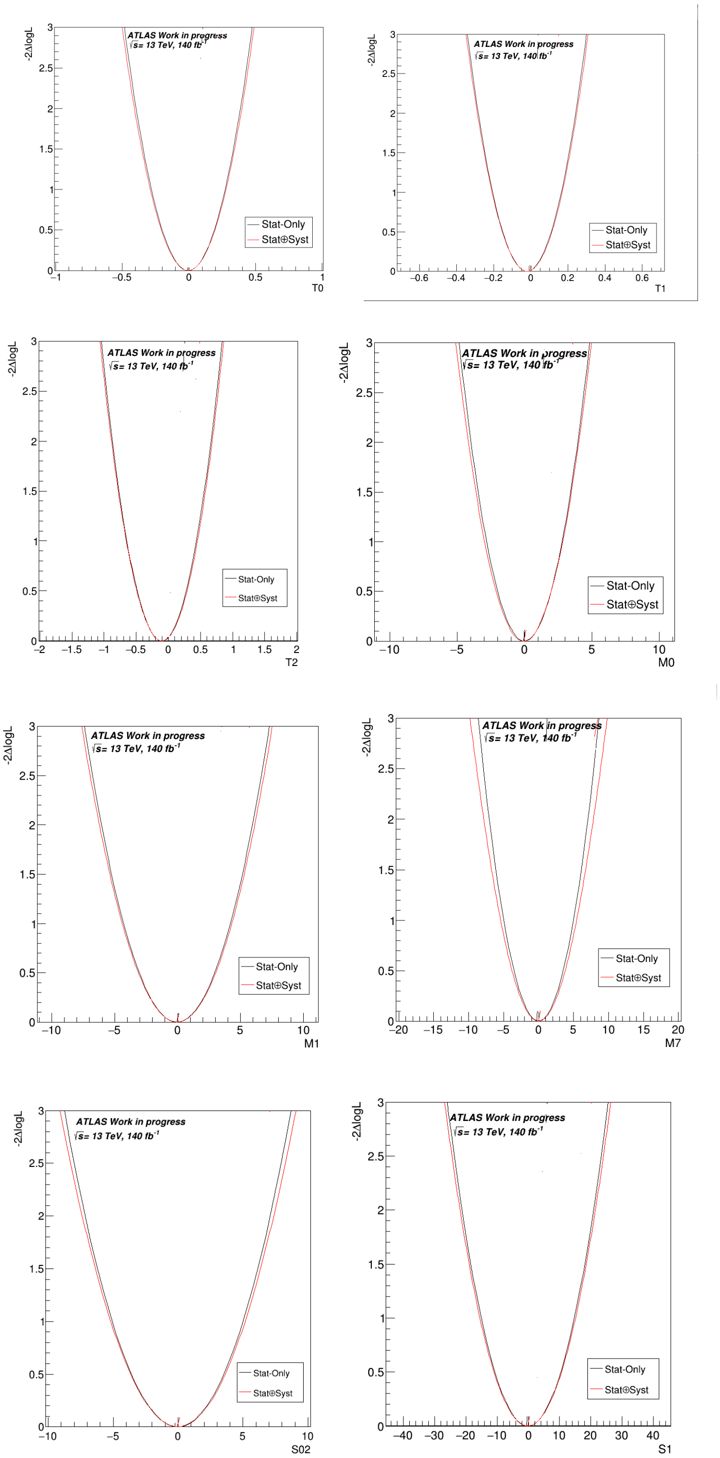

Figure 7.39: Comparison of profile likelihood ratio curves on the Wilson coefficients of all the relevant aQGC operators for the fit on data using the two dimensional distributions of the M_T^{WZ} - BDT score when no nuisance parameters are included (Stat-Only) and when experimental and theoretical uncertainty nuisance parameters are considered (Stat+Syst).

Figure 7.40 illustrates an example of the impact of the nuisance parameters on the 95% CL lower and upper expected and observed limits for the Wilson coefficients of the $\mathcal{L}_{T,1}$ and $\mathcal{L}_{S,1}$ operators.

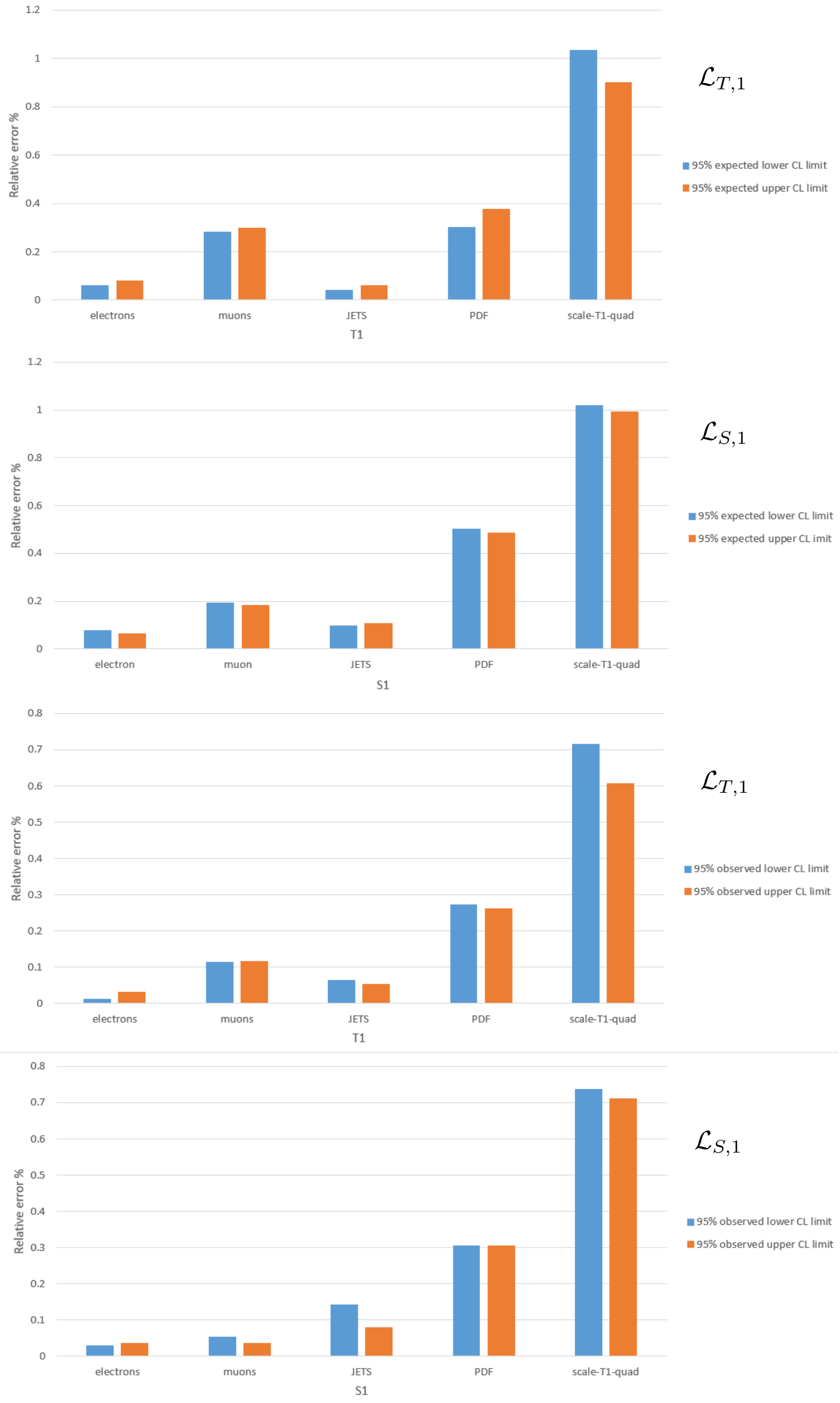

FIGURE 7.40: Examples of the impact of the nuisance parameters on the 95% CL lower and upper expected and observed limits for the Wilson coefficients of the $\mathcal{L}_{T,1}$ and $\mathcal{L}_{S,1}$.

As described in Section 2.3.2.3, the unitarity bounds show the range of validity of the EFT approach, where a contribution of an aQGC operator will not lead to unitarity violation at high energies. Tables 7.24 and 7.25 show the individual 95% CL lower and upper expected and observed limits, respectively, for the Wilson coefficients of the $\mathcal{L}_{S,02}$, $\mathcal{L}_{S,1}$, $\mathcal{L}_{T,0}$, $\mathcal{L}_{T,1}$, $\mathcal{L}_{T,2}$, $\mathcal{L}_{M,0}$, $\mathcal{L}_{M,1}$ and $\mathcal{L}_{M,7}$ operators for the M_T^{WZ} - BDT score, which are obtained using different energy cut-off scales. The evolution of the individual 95%C.L. expected and observed limits of the above operators as a function of the cut-off scale is shown in Figure 7.41. The unitarity bounds (green line) for each operator are also calculated as described in Section 2.3.2.3. The shaded area represents the unitarity allowed region, where the Wilson coefficients of the relevant aQGC operators have physical expected and observed limits.

		Expected Limits (TeV^{-4})			
	Cut-off scale = 500 GeV	Cut-off scale = 1000 GeV	Cut-off scale = 1500 GeV	Cut-off scale = 2000 GeV	No Cut-off
f_{S02}/Λ^4	[-488, 483]	[-68, 67]	[-28, 28]	[-18, 18]	[-14, 14]
f_{S1}/Λ^4	[-1329, 1246]	[-224, 226]	[-94, 93]	[-60, 59]	[-41, 40]
f_{T0}/Λ^4	[-32, 31]	[-7.2, 7.2]	[-2.9, 3.0]	[-1.7, 1.7]	[-0.8, 0.8]
f_{T1}/Λ^4	[-43, 41]	[-6.6, 5.7]	[-2.2, 2.0]	[-1.1, 1.0]	[-0.5, 0.5]
f_{T2}/Λ^4	[-83, 80]	[-18, 14]	[-6.3, 5.3]	[-3.3, 2.9]	[-1.5, 1.4]
f_{M0}/Λ^4	[-167, 168]	[-48, 48]	[-22, 22]	[-14, 14]	[-8, 8]
f_{M1}/Λ^4	[-386, 385]	[-79, 79]	[-32, 32]	[-20, 19]	[-12, 12]
f_{M7}/Λ^4	[-589, 589]	[-105, 105]	[-43, 43]	[-25, 25]	[-16, 16]

Table 7.24: Expected lower and upper 95% CL limits on the Wilson coefficients of the $\mathcal{L}_{S,02}$, $\mathcal{L}_{S,1}$, $\mathcal{L}_{T,0}$, $\mathcal{L}_{T,1}$, $\mathcal{L}_{T,2}$, $\mathcal{L}_{M,0}$, $\mathcal{L}_{M,1}$ and $\mathcal{L}_{M,7}$ aQGC operators for the M_T^{WZ} - BDT score, which are obtained using different energy cut-off scales.

		Observed Limits (TeV^{-4})			
	Cut-off scale = 500 GeV	Cut-off scale = 1000 GeV	Cut-off scale = 1500 GeV	Cut-off scale = 2000 GeV	No Cut-off
f_{S02}/Λ^4	[-278, 260]	[-45, 43]	[-18, 18]	[-12, 12]	[-10, 10]
f_{S1}/Λ^4	[-702, 671]	[-160, 160]	[-60, 60]	[-40, 40]	[-30, 30]
f_{T0}/Λ^4	[-12, 12]	[-3.7, 4.0]	[-1.5, 1.2]	[-1.0, 1.0]	[-0.6, 0.6]
f_{T1}/Λ^4	[-21, 18]	[-3.8, 3.0]	[-1.3, 1.1]	[-0.7, 0.6]	[-0.4, 0.3]
f_{T2}/Λ^4	[-38, 33]	[-10.0, 7.4]	[-3.7, 2.7]	[-2.2, 1.7]	[-1.2, 1.0]
f_{M0}/Λ^4	[-70, 80]	[-25, 27]	[-13, 12]	[-8, 8]	[-6, 6]
f_{M1}/Λ^4	[-181, 178]	[-44, 43]	[-18, 18]	[-12, 12]	[-9, 9]
f_{M7}/Λ^4	[-287, 287]	[-58, 58]	[-24, 24]	[-15, 15]	[-11, 11]

Table 7.25: Observed lower and upper 95% CL limits on the Wilson coefficients of the $\mathcal{L}_{S,02}$, $\mathcal{L}_{S,1}$, $\mathcal{L}_{T,0}$, $\mathcal{L}_{T,1}$, $\mathcal{L}_{T,2}$, $\mathcal{L}_{M,0}$, $\mathcal{L}_{M,1}$ and $\mathcal{L}_{M,7}$ aQGC operators for the M_T^{WZ} - BDT score, which are obtained using different energy cut-off scales.

Limits on aQGC Wilson coefficients are also derived using a two-dimensional scan, in order to probe the correlations between various EFT parameters. In this case, two EFT coefficients are included in the fit and the rest of the coefficients is assumed to have zero contribution. The expected and observed 2D 95% CL intervals of the $\mathcal{L}_{M,0}$-$\mathcal{L}_{M,1}$, $\mathcal{L}_{T,0}$-$\mathcal{L}_{T,1}$, $\mathcal{L}_{T,0}$-$\mathcal{L}_{T,2}$ and $\mathcal{L}_{T,1}$-$\mathcal{L}_{T,2}$ combination of operators for the M_T^{WZ} - BDT score are shown in Figures 7.42 and 7.43. From these Figures, it can be seen that the operators are correlated. The corresponding 2D expected and observed 95% CL lower and upper limits of the Wilson coefficients of the above combination of operators are shown in Tables 7.26, 7.27, 7.28 and 7.29. These limits are worse that using only one operator at a time.

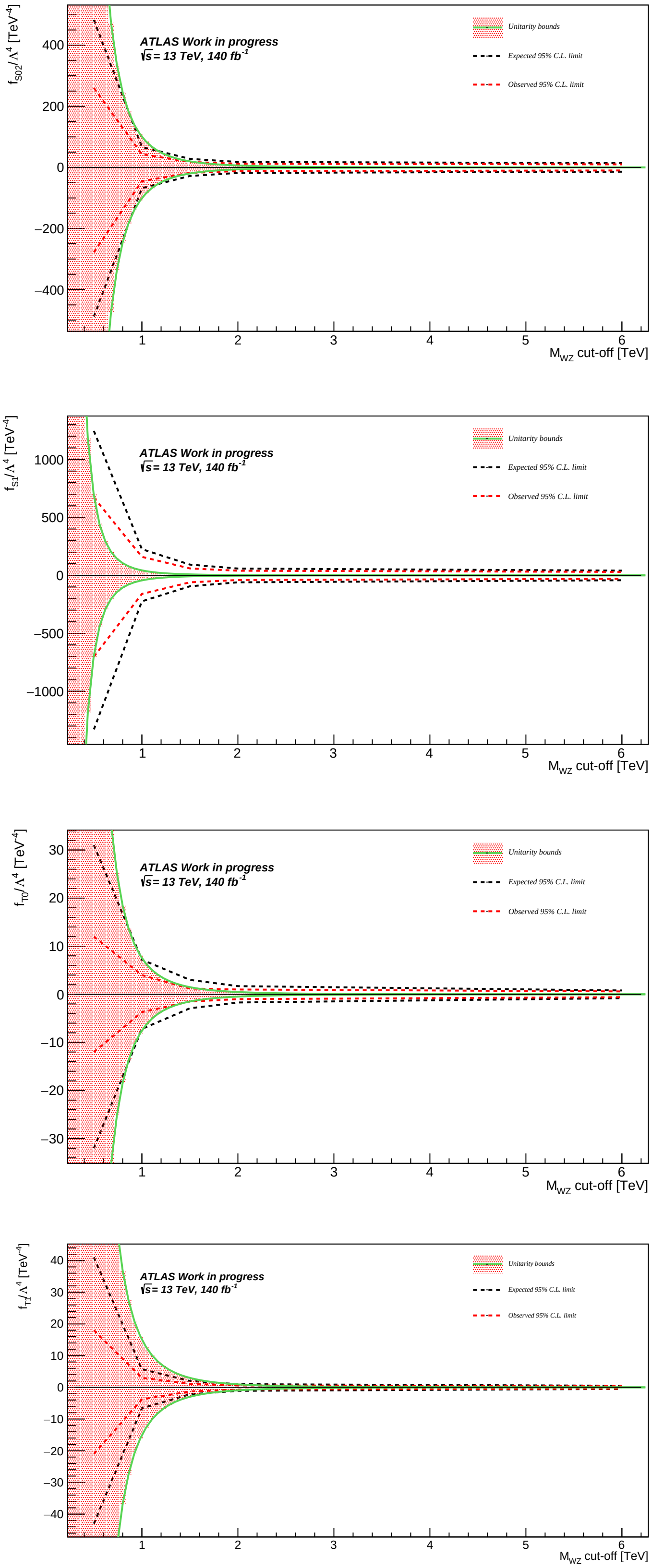

FIGURE 7.41: Evolution of the individual 95%C.L. expected and observed (black dotted line) limits for the Wilson coefficients of the $\mathcal{L}_{S,02}$, $\mathcal{L}_{S,1}$, $\mathcal{L}_{T,0}$, $\mathcal{L}_{T,1}$, $\mathcal{L}_{T,2}$, $\mathcal{L}_{M,0}$, $\mathcal{L}_{M,1}$ and $\mathcal{L}_{M,7}$ operators for the M_T^{WZ} - BDT score as a function of the cut-off scale. The unitarity bounds (green line) for each operator are also calculated as described in Section 2.3.2.3. The shaded area represents the unitarity allowed region.

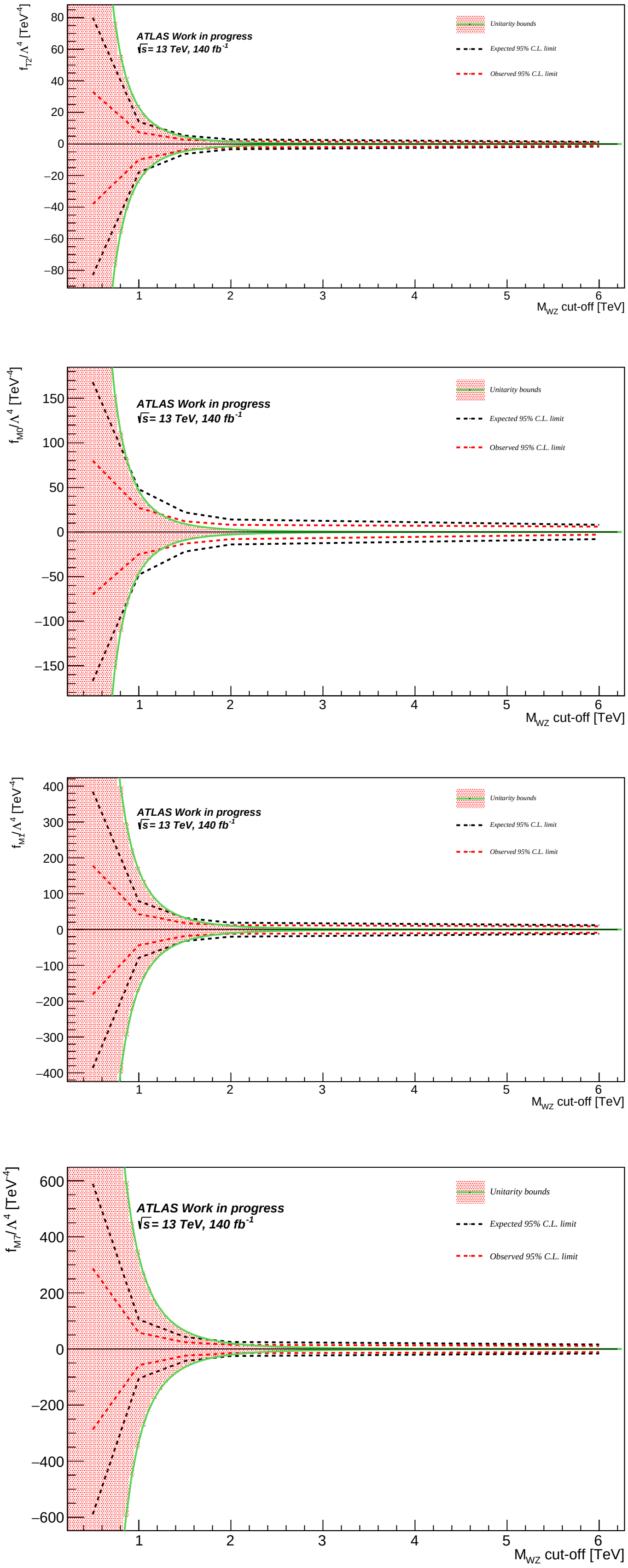

FIGURE 7.41: Evolution of the individual 95%C.L. expected and observed (black dotted line) limits for the Wilson coefficients of the $\mathcal{L}_{S,02}$, $\mathcal{L}_{S,1}$, $\mathcal{L}_{T,0}$, $\mathcal{L}_{T,1}$, $\mathcal{L}_{T,2}$, $\mathcal{L}_{M,0}$, $\mathcal{L}_{M,1}$ and $\mathcal{L}_{M,7}$ operators for the M_T^{WZ} - BDT score as a function of the cut-off scale. The unitarity bounds (green line) for each operator are also calculated as described in Section 2.3.2.3. The shaded area represents the unitarity allowed region.

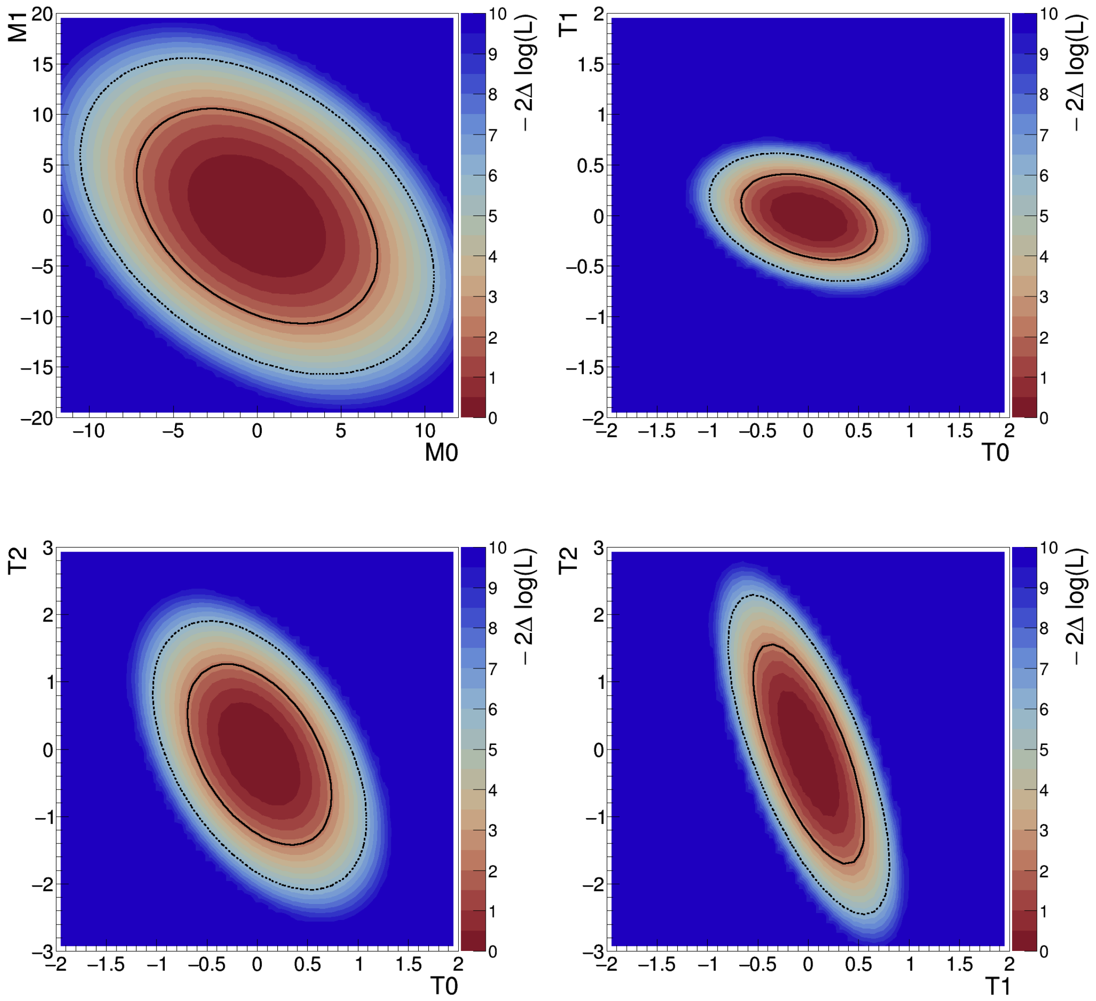

FIGURE 7.42: Two-dimensional expected 95% CL intervals (solid contour) of the $\mathcal{L}_{M,0}$-$\mathcal{L}_{M,1}$, $\mathcal{L}_{T,0}$-$\mathcal{L}_{T,1}$, $\mathcal{L}_{T,0}$-$\mathcal{L}_{T,2}$ and $\mathcal{L}_{T,1}$-$\mathcal{L}_{T,2}$ combination of operators for the M_T^{WZ} - BDT score.

	Variable	Expected (TeV^{-4})	Observed (TeV^{-4})
f_{M0}/Λ^4, f_{M1}/Λ^4	M_T^{WZ}	[-11.1, 11.0], [-16.4, 16.3]	[-8.0, 7.8], [-11.8, 11.8]
	$M_T^{\mathrm{WZ}} vs M_{jj}$	[-11.5, 11.9], [-16.3, 16.2]	[-7.8, 7.7], [-11.7, 11.6]
	$M_T^{\mathrm{WZ}} vs BDTscore$	[-10.5, 10.5], [-15.7, 15.6]	[-8.0, 7.7], [-11.8, 11.8]

TABLE 7.26: 2D expected and observed lower and upper 95% CL limits on the Wilson coefficients of the $\mathcal{L}_{M,0}$ and $\mathcal{L}_{M,1}$ aQGC operators for each kinematical variable.

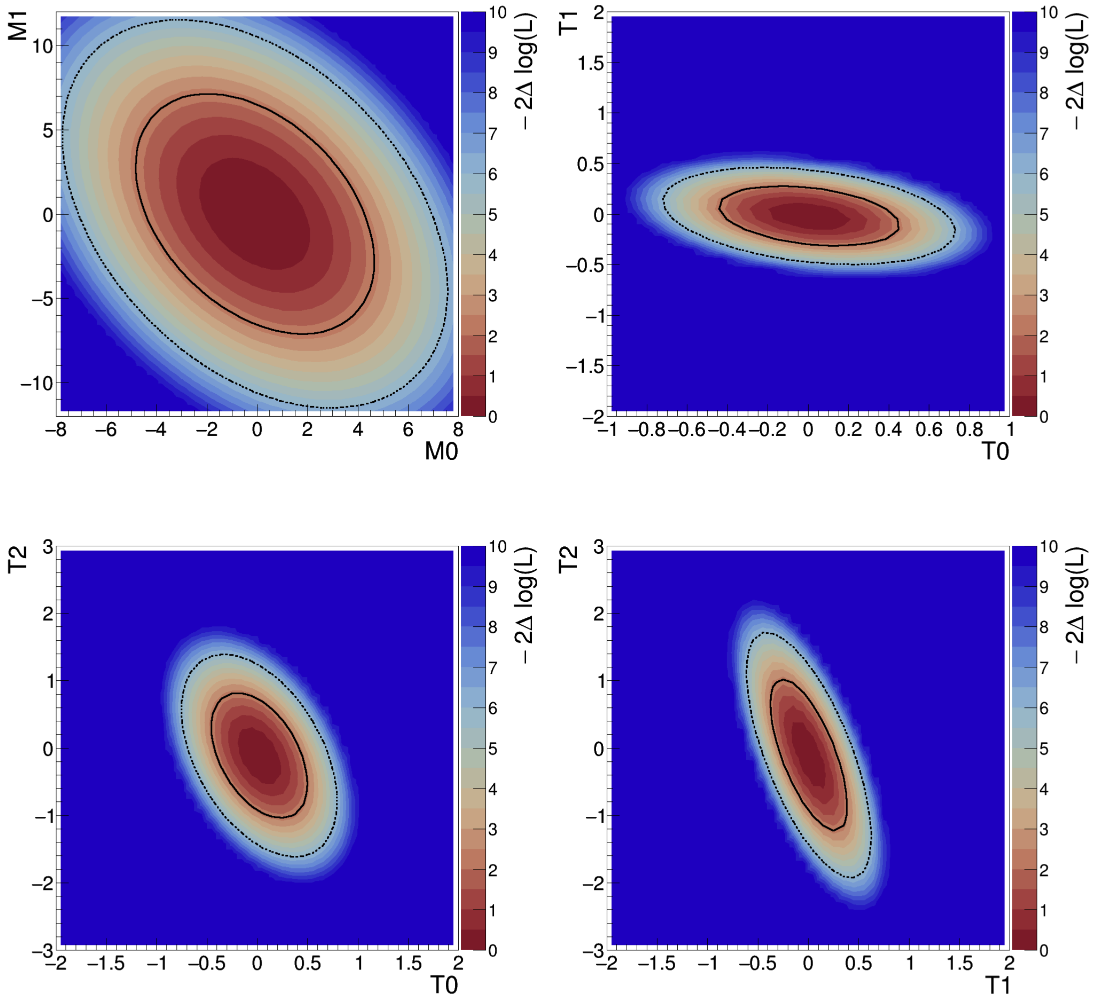

FIGURE 7.43: Two-dimensional observed 95% CL intervals (solid contour) of the $\mathcal{L}_{M,0}$-$\mathcal{L}_{M,1}$, $\mathcal{L}_{T,0}$-$\mathcal{L}_{T,1}$, $\mathcal{L}_{T,0}$-$\mathcal{L}_{T,2}$ and $\mathcal{L}_{T,1}$-$\mathcal{L}_{T,2}$ combination of operators for the M_T^{WZ} - BDT score.

	Variable	Expected (TeV^{-4})	Observed (TeV^{-4})
f_{T0}/Λ^4, f_{T1}/Λ^4	M_T^{WZ}	[-1.00, 1.02], [-0.66, 0.63]	[-0.74, 0.75], [-0.51, 0.47]
	$M_T^{\mathrm{WZ}} vs M_{jj}$	[-1.00, 1.02], [-0.66, 0.63]	[-0.73, 0.73], [-0.51, 0.47]
	$M_T^{\mathrm{WZ}} vs BDTscore$	[-0.99, 1.00], [-0.65, 0.62]	[-0.74, 0.75], [-0.51, 0.47]

TABLE 7.27: 2D expected and observed lower and upper 95% CL limits on the Wilson coefficients of the $\mathcal{L}_{T,0}$ and $\mathcal{L}_{T,1}$ aQGC operators for each kinematical variable.

	Variable	Expected (TeV^{-4})	Observed (TeV^{-4})
f_{T0}/Λ^4, f_{T2}/Λ^4	M_T^{WZ}	[-1.06, 1.10], [-2.11, 1.94]	[-0.77, 0.82], [-1.67, 1.43]
	$M_T^{\mathrm{WZ}} vs M_{jj}$	[-1.06, 1.10], [-2.11, 1.94]	[-0.77, 0.82], [-1.68, 1.41]
	$M_T^{\mathrm{WZ}} vs BDTscore$	[-1.04, 1.09], [-2.09, 1.91]	[-0.77, 0.82], [-1.67, 1.42]

TABLE 7.28: 2D expected and observed lower and upper 95% CL limits on the Wilson coefficients of the $\mathcal{L}_{T,0}$ and $\mathcal{L}_{T,2}$ aQGC operators for each kinematical variable.

	Variable	Expected (TeV^{-4})	Observed (TeV^{-4})
f_{T1}/Λ^4, f_{T2}/Λ^4	M_T^{WZ}	[-0.91, 0.93], [-2.83, 2.62]	[-0.62, 0.63], [-1.93, 1.73]
	$M_T^{\mathrm{WZ}} vs M_{jj}$	[-0.90, 0.93], [-2.81, 2.60]	[-0.61, 0.62], [-1.92, 1.67]
	$M_T^{\mathrm{WZ}} vs BDTscore$	[-0.89, 0.91], [-2.78, 2.56]	[-0.62, 0.63], [-1.93, 1.72]

TABLE 7.29: 2D expected and observed lower and upper 95% CL limits on the Wilson coefficients of the $\mathcal{L}_{T,1}$ and $\mathcal{L}_{T,2}$ aQGC operators for each kinematical variable.

7.9.2.8 Discussion

It is very important to compare the truth and reconstructed level expected and observed 95% CL lower and upper limits on the aQGC Wilson coefficients of the corresponding dimension-8 operators. The kinematical variable used for the comparison is the M_T^{WZ} and in order to compare them the binning has to be the same for the two cases. For this purpose the binning used for the extraction of the truth level limits in Section 7.9.2.6 is used. The full set of uncertainties is used. Table 7.30 shows this comparison. It can be seen that the reconstructed and the truth level limits are comparable.

A comparison for the reconstructed level expected and observed 95% CL lower and upper limits of this study with the CMS limits [93] is also provided. For this purpose the two-dimensional template of M_T^{WZ} - M_{jj} is used. Also, the full set of the systematics uncertainties is used. The comparison is shown in Table 7.31. A direct comparison of the two results cannot be made as the CMS experiment is using an older version of the Eboli-Garcia model.

Lastly, all this study opens the way to a new approach in the question of searches for anomalous vector boson self-couplings. A machine learning approach has already tried using parton level MC samples and it can be found in [153]. The results appear very promising and can be considered for the Run3 analysis.

	Expected Truth (TeV^{-4})	Expected Reconstructed (TeV^{-4})	Observed Truth (TeV^{-4})	Observed Reconstructed (TeV^{-4})
f_{S02}/Λ^4	[-23.7, 24.2]	[-22.4, 22.3]	[-23.8, 24.4]	[-22.0, 21.9]
f_{S1}/Λ^4	[-68.2, 68.8]	[-63.2, 62.8]	[-68.4, 69.3]	[-62.1, 61.8]
f_{T0}/Λ^4	[-1.17, 1.24]	[-1.22, 1.19]	[-1.18, 1.25]	[-1.20, 1.16]
f_{T1}/Λ^4	[-0.77, 0.90]	[-0.84, 0.79]	[-0.78, 0.90]	[-0.82, 0.77]
f_{T2}/Λ^4	[-2.15, 2.69]	[-2.50, 2.25]	[-2.16, 2.69]	[-2.45, 2.21]
f_{M0}/Λ^4	[-12.5, 12.4]	[-12.7, 11.9]	[-12.6, 12.5]	[-11.9, 11.7]
f_{M1}/Λ^4	[-19.1, 19.5]	[-18.3, 18.3]	[19.2, 19.5]	[-18.0, 18.0]
f_{M7}/Λ^4	[-24.0, 24.0]	[-23.9, 23.9]	[24.1, 24.1]	[-23.8, 23.8]

TABLE 7.30: Comparison of truth and reconstructed level expected and observed lower and upper 95% CL limits on the Wilson coefficients of the $\mathcal{L}_{S,02}$, $\mathcal{L}_{S,1}$, $\mathcal{L}_{T,0}$, $\mathcal{L}_{T,1}$, $\mathcal{L}_{T,2}$, $\mathcal{L}_{M,0}$, $\mathcal{L}_{M,1}$ and $\mathcal{L}_{M,7}$ aQGC operators for the M_T^{WZ}, which are obtained without using any unitarization procedure.

	Expected ATLAS (TeV^{-4})	Expected CMS (TeV^{-4})	Observed ATLAS (TeV^{-4})	Observed CMS (TeV^{-4})
f_{S1}/Λ^4	[-45, 45]	[-38, 39]	[-31, 30]	[-30, 30]
f_{T0}/Λ^4	[-0.80, 0.80]	[-0.82, 0.85]	[-0.56, 0.55]	[-0.62, 0.65]
f_{T1}/Λ^4	[-0.52, 0.49]	[-0.49, 0.55]	[-0.39, 0.35]	[-0.37, 0.41]
f_{T2}/Λ^4	[-1.6, 1.4]	[-1.4, 1.7]	[-1.2, 1.0]	[-1.0, 1.3]
f_{M0}/Λ^4	[-8.5, 8.5]	[-7.6, 7.6]	[-5.6, 5.6]	[-5.8, 5.8]
f_{M1}/Λ^4	[-13, 13]	[-11, 11]	[-8.5, 8.4]	[-8.2, 8.3]
f_{M7}/Λ^4	[-16, 16]	[-14, 14]	[-11, 11]	[-10, 10]

TABLE 7.31: Comparison of expected and observed lower and upper 95% CL limits on the Wilson coefficients of the $\mathcal{L}_{S,02}$, $\mathcal{L}_{S,1}$, $\mathcal{L}_{T,0}$, $\mathcal{L}_{T,1}$, $\mathcal{L}_{T,2}$, $\mathcal{L}_{M,0}$, $\mathcal{L}_{M,1}$ and $\mathcal{L}_{M,7}$ aQGC operators for the M_T^{WZ} - M_{jj} between ATLAS and CMS experiments, which are obtained without using any unitarization procedure.

Chapter 8

Conclusion and future plans

The SM has proven to be an incredibly powerful and accurate framework for understanding the behavior of elementary particles and their interactions through the electromagnetic, weak, and strong forces. It has been extensively tested and has successfully predicted numerous phenomena and particles that have been subsequently discovered.

However, despite its impressive track record, the SM is not without its shortcomings. The limitations of the SM become evident when considering certain fundamental questions that remain unanswered. For instance, the SM does not incorporate gravity, nor does it provide an explanation for the observed dark matter and dark energy, which make up a significant portion of the universe. Additionally, the SM does not account for the unequal strengths of the fundamental forces or provide a unifying theory that can reconcile all the forces into a single, consistent framework.

These limitations strongly suggest the existence of physics beyond the SM. Many theoretical frameworks, such as supersymmetry, string theory, and extra dimensions, have been proposed as potential extensions to the SM, aiming to address these unanswered questions and provide a more comprehensive description of the universe.

The pursuit of new physics beyond the SM has been a driving force in experimental research, and the Large Hadron Collider (LHC) and the ATLAS detector have played crucial roles in this endeavor. By colliding particles at unprecedented energies and analyzing the resulting data, these experiments have provided valuable insights into the properties of particles and their interactions, as well as placing stringent constraints on new physics scenarios.

This thesis has focused on the study of $W^{\pm}Z$ inclusive diboson and $W^{\pm}Z$ vector boson scattering (VBS) productions at the Large Hadron Collider (LHC) using data collected by the ATLAS detector from 2015 to 2018 that correspond to an integrated luminosity of 140 fb^{-1} at a center-of-mass energy of 13 TeV. These processes play a crucial role in understanding the electroweak symmetry breaking and provide valuable insights into the nature of the Higgs mechanism and potential new physics beyond the Standard Model (SM).

The author's contribution to this research has been significant, initially in the optimization of the muon isolation criteria used in the event selection. This study has enhanced the accuracy and reliability of the analysis, by improving the signal-to-noise ratio and reducing background mainly from fake muons,

Her main contribution concerns the investigation of triple gauge couplings (TGCs) and quartic gauge couplings (QGCs) in the production of these processes that has provided insights into the interactions between gauge bosons. This study has explored the sensitivity of $W^{\pm}Z$ diboson and VBS productions to anomalous TGCs (aTGCs) and QGCs (aQGCs), which could indicate the presence of new physics effects. An Effective Field Theory (EFT) framework has been utilized to parameterize these anomalous couplings and search for deviations from SM predictions, allowing for systematic exploration of higher-dimensional operators.

The thesis has investigated the potential effects of various dimension-6 and dimension-8 operators on the $W^{\pm}Z$ inclusive diboson and VBS productions, highlighting the most sensitive kinematic variables for each operator. Notably, the 95% Confidence Level (CL) expected and observed limits for the dimension-8 operators that affect the $WZjj$ VBS process have extracted. Nevertheless, no excesses from the SM were observed.

This study opens the way to a new approach in the question of searches for anomalous vector boson self-couplings. In the future a simultaneous study of the effect of the dimension-6 and dimension-8 operators on the $WZjj$ VBS process could be performed, since it is technically possible through a new FeynRules model called $SmeftFR$. Also, a machine learning approach to the EFT re-interpretation of the $W^{\pm}Z$ diboson and VBS productions could be considered for the Run 3, as it has been already tried and its results appear very promising. Finally, the combination of the full Run2 results for the dimension-8 operators from many VBS channels has started and it is expected to provide more stricter 95% CL limits for these operators.

On the other hand, for the $WZjj$ VBS process, it is very important to investigate the effect of the NLO EWK corrections on the shape of the distributions from the relevant kinematical variables. It is necessary to encourage theorist to either provide them for individual kinematical variables, or even better, to incorporate them into the relevant generators. Lastly, the study of the $WZjj$ VBS polarization is on of our most challenging future plans, as it is a very rare process and it is very difficult to measure it with the current or near future amount of data.

In conclusion, the utilization of EFT in global fits, exploiting data from many channels simultaneously, proves invaluable in identifying deviations from the Standard Model within various regions of phase space. This approach allows for the detection of anomalous couplings and provides a compelling case for the existence of new physics. It is crucial to emphasize that global fits are feasible only with the availability of large amounts of data as expected from Run 3 and the HL-LHC. By embracing this methodology and the wealth of data on the horizon, we can uncover and explore exciting frontiers in particle physics beyond the Standard Model.

Appendix A

Conventions and Notations

A.1 Natural Units

Using a system of units that simplifies the notation is beneficial, and the convention most often used is called ”natural units.” This convention sets the values of some common variables to simple representations. Ih this scheme

$$\hbar = c = 1 \tag{A.1}$$

However, the unit for energies is not determined by this convention and is typically measured in electronvolts (eV). Masses and momenta can also be expressed using this unit.

A.2 Einstein’s Summation Convention

The purpose of this convention is to enhance the succinctness of notation by eliminating the need for the ”Σ” operator in specific situations. The convention dictates that the ”Σ” operator should be omitted when an index that is otherwise undefined appears in both the superscript and subscript of a term

$$\sum_{\mu=0}^{3} x_\mu x^\mu =: x_\mu x^\mu \tag{A.2}$$

The range of values that the index variable can take on can be inferred from the letter used.

A.3 Relativistic and Dirac Notation

The usual metric tensor is used

$$g_{\mu\nu} = \begin{pmatrix} 1 & & & \\ & -1 & & \\ & & -1 & \\ & & & -1 \end{pmatrix} \tag{A.3}$$

resulting in the relativistic derivative ∂^μ of

$$\partial^\mu = \left(\frac{\partial}{\partial t}; -\frac{\partial}{\partial x}, -\frac{\partial}{\partial y}, -\frac{\partial}{\partial z} \right) \tag{A.4}$$

Gamma matrices γ^μ are used similar to Weyl basis, with adjusted sign convention

$$\gamma^0 = \begin{pmatrix} 0 & 1 \\ 1 & 0 \end{pmatrix}, \qquad \gamma^i = \begin{pmatrix} 0 & -\sigma_i \\ \sigma_i & 0 \end{pmatrix} \tag{A.5}$$

where σ_i are the Pauli spin matrices

$$\sigma_1 = \begin{pmatrix} 0 & 1 \\ 1 & 0 \end{pmatrix}, \quad \sigma_2 = \begin{pmatrix} 0 & -i \\ i & 0 \end{pmatrix}, \quad \sigma_3 = \begin{pmatrix} 1 & 0 \\ 0 & -1 \end{pmatrix} \tag{A.6}$$

A.4 Group Theory

Generators of $SU(2)$

$$L_i = 2 * \sigma_i \tag{A.7}$$

Generators of $SU(3)$ (Gell-Mann matrices)

$$\begin{aligned}
\lambda_1 &= \begin{pmatrix} & 1 & \\ 1 & & \\ & & \end{pmatrix}, & \lambda_2 &= \begin{pmatrix} & -i & \\ i & & \\ & & \end{pmatrix}, \\
\lambda_3 &= \begin{pmatrix} 1 & & \\ & -1 & \\ & & \end{pmatrix}, & \lambda_4 &= \begin{pmatrix} & & 1 \\ & & \\ 1 & & \end{pmatrix}, \\
\lambda_5 &= \begin{pmatrix} & & -i \\ & & \\ i & & \end{pmatrix}, & \lambda_6 &= \begin{pmatrix} & & \\ & & 1 \\ & 1 & \end{pmatrix}, \\
\lambda_7 &= \begin{pmatrix} & & \\ & & -i \\ & i & \end{pmatrix}, & \lambda_8 &= \frac{1}{\sqrt{3}} \begin{pmatrix} 1 & & \\ & 1 & \\ & & -2 \end{pmatrix}.
\end{aligned}$$

Structure constants of $SU(3)$

$$\begin{aligned}
&f_{123} = 1; \\
&f_{458} = f_{678} = \sqrt{3}/2 \qquad\qquad (A.8)\\
&f_{147} = f_{516} = f_{246} = f_{257} = f_{345} = f_{637} = 1/2; \text{ anti-symmetric}
\end{aligned}$$

Appendix B

List of Signal, Background and EFT samples

DSID	Process	Generators	PDF	Events	Filter eff.	Cross-section [pb]
361601	$WZ \to \ell\nu\ell\ell$	Powheg+Pythia8	NLO CT10	$\sim$30M	1.00	4.51
364253	$WZ \to \ell\nu\ell\ell$	Sherpa 2.2.2	NNLO NNPDF30	$\sim$74M	1.00	4.57
361293	$WZ \to \ell\nu\ell\ell$	MadGraph + McAtNlo + Pythia 8	NNLO NNPDF30	$\sim$3.9M	0.34	1.70
364284	$WZjj \to \ell\nu\ell\ell jj$ EW6	Sherpa 2.2.2	NNLO NNPDF30	5.9M	1.00	0.047
364739	$W^-Zjj \to \ell\nu\ell\ell jj$ EW6 OF	MadGraph + Pythia 8	NLO NNPDF30	$\sim$1.4M	1.00	0.015
364740	$W^+Zjj \to \ell\nu\ell\ell jj$ EW6 OF	MadGraph + Pythia 8	NLO NNPDF30	$\sim$2M	1.00	0.026
364741	$W^-Zjj \to \ell\nu\ell\ell jj$ EW6 SF	MadGraph + Pythia 8	NLO NNPDF30	$\sim$0.7M	1.00	0.0077
364742	$W^+Zjj \to \ell\nu\ell\ell jj$ EW6 SF	MadGraph + Pythia 8	NLO NNPDF30	$\sim$0.9M	1.00	0.013
830000	$W^-Zjj \to \ell\nu\ell\ell jj$ EW6 OF	MadGraph + Herwig	NLO NNPDF30	$\sim$1.4M	1.00	0.015
830001	$W^+Zjj \to \ell\nu\ell\ell jj$ EW6 OF	MadGraph + Herwig	NLO NNPDF30	$\sim$2M	1.00	0.026
830002	$W^-Zjj \to \ell\nu\ell\ell jj$ EW6 SF	MadGraph + Herwig	NLO NNPDF30	$\sim$0.7M	1.00	0.077
830003	$W^+Zjj \to \ell\nu\ell\ell jj$ EW6 SF	MadGraph + Herwig	NLO NNPDF30	$\sim$0.9M	1.00	0.013

Table B.1: Summary of signal MC simulation.

DSID	Process	Generators	PDF	Events	Filter eff.	Cross-section [pb]	k-factor
364250	$q\bar{q} \to ZZ \to \ell\ell\ell\ell$	Sherpa 2.2.2	NNLO NNPDF30	~80M	1.00	1.252	
364254	$q\bar{q} \to ZZ \to \ell\ell\nu\nu$	Sherpa 2.2.2	NNLO NNPDF30	~70M	1.00	12.5	
confirmed 364283	$ZZ \to \ell\ell\ell\ell$ EW6	Sherpa 2.2.2	NNLO NNPDF30	0.98M	1.0	0.011	
345705	$gg \to \ell\ell\ell\ell$ 0M4l130	Sherpa 2.2.2	NNLO NNPDF30	0.7M	1.00	0.0099	
345706	$gg \to \ell\ell\ell\ell$ 130M4l	Sherpa 2.2.2	NNLO NNPDF30	~30M	1.00	0.010	
361106	$Z \to ee$	Powheg+Pythia8	CT10	1209702350	1.00	1901.1	1.026
361107	$Z \to \mu\mu$	Powheg+Pythia8	CT10	1193549900	1.00	1901.1	1.026
361108	$Z \to \tau\tau$	Powheg+Pythia8	CT10	133459000	1.00	1901.1	1.026
364500	$Z\gamma \to ee\gamma\ (7 < p_{\mathrm{T}}^{\gamma} < 15)$	Sherpa 2.2.2	NNLO NNPDF30	5000000	1.00	57.62	1.00
364501	$Z\gamma \to ee\gamma\ (15 < p_{\mathrm{T}}^{\gamma} < 35)$	Sherpa 2.2.2	NNLO NNPDF30	4498000	1.00	34.59	1.00
364502	$Z\gamma \to ee\gamma\ (35 < p_{\mathrm{T}}^{\gamma} < 70)$	Sherpa 2.2.2	NNLO NNPDF30	1494000	1.00	6.29	1.00
364503	$Z\gamma \to ee\gamma\ (70 < p_{\mathrm{T}}^{\gamma} < 140)$	Sherpa 2.2.2	NNLO NNPDF30	1489000	1.00	0.49	1.00
364504	$Z\gamma \to ee\gamma\ (p_{\mathrm{T}}^{\gamma} > 140)$	Sherpa 2.2.2	NNLO NNPDF30	755000	1.00	0.063	1.00
364505	$Z\gamma \to \mu\mu\gamma\ (7 < p_{\mathrm{T}}^{\gamma} < 15)$	Sherpa 2.2.2	NNLO NNPDF30	5000000	1.00	57.7	1.00
364506	$Z\gamma \to \mu\mu\gamma\ (10 < p_{\mathrm{T}}^{\gamma} < 35)$	Sherpa 2.2.2	NNLO NNPDF30	4454000	1.00	34.62	1.00
364507	$Z\gamma \to \mu\mu\gamma\ (35 < p_{\mathrm{T}}^{\gamma} < 70)$	Sherpa 2.2.2	NNLO NNPDF30	1498000	1.00	6.29	1.00
364508	$Z\gamma \to \mu\mu\gamma\ (70 < p_{\mathrm{T}}^{\gamma} < 140)$	Sherpa 2.2.2	NNLO NNPDF30	1505000	1.00	0.49	1.00
364509	$Z\gamma \to \mu\mu\gamma\ (p_{\mathrm{T}}^{\gamma} > 140)$	Sherpa 2.2.2	NNLO NNPDF30	755000	1.00	0.063	1.00
364510	$Z\gamma \to \tau\tau\gamma\ (7 < p_{\mathrm{T}}^{\gamma} < 15)$	Sherpa 2.2.2	NNLO NNPDF30	9000000	1.00	57.58	1.00
364511	$Z\gamma \to \tau\tau\gamma\ (10 < p_{\mathrm{T}}^{\gamma} < 35)$	Sherpa 2.2.2	NNLO NNPDF30	10341000	1.00	34.65	1.00
364512	$Z\gamma \to \tau\tau\gamma\ (35 < p_{\mathrm{T}}^{\gamma} < 70)$	Sherpa 2.2.2	NNLO NNPDF30	2490000	1.00	6.29	1.00
364513	$Z\gamma \to \tau\tau\gamma\ (70 < p_{\mathrm{T}}^{\gamma} < 140)$	Sherpa 2.2.2	NNLO NNPDF30	1239000	1.00	0.49	1.00
364514	$Z\gamma \to \tau\tau\gamma\ (p_{\mathrm{T}}^{\gamma} > 140)$	Sherpa 2.2.2	NNLO NNPDF30	450000	1.00	0.063	1.00
364242	$WWW \to 3\ell 3\nu$	Sherpa 2.2.2	NNLO NNPDF30	220000	1.00	0.0072	1.00
364243	$WWZ \to 4\ell 2\nu$	Sherpa 2.2.2	NNLO NNPDF30	220000	1.00	0.0018	1.00
364244	$WWZ \to 2\ell 4\nu$	Sherpa 2.2.2	NNLO NNPDF30	220000	1.00	0.0035	1.00
364245	$WZZ \to 5\ell 1\nu$	Sherpa 2.2.2	NNLO NNPDF30	190000	1.00	0.00019	1.00
364246	$WZZ \to 3\ell 3\nu$	Sherpa 2.2.2	NNLO NNPDF30	189000	0.45	0.0017	1.00
364247	$ZZZ \to 6\ell 0\nu$	Sherpa 2.2.2	NNLO NNPDF30	139000	1.00	0.000014	1.00
364248	$ZZZ \to 4\ell 2\nu$	Sherpa 2.2.2	NNLO NNPDF30	139000	0.22	0.00038	1.00
364249	$ZZZ \to 2\ell 4\nu$	Sherpa 2.2.2	NNLO NNPDF30	139000	0.44	0.00038	1.00
410470	$t\bar{t}(\geqslant 1\ell)$	Powheg+Pythia8		467952000	0.54	729.7	1.14
410218	$t\bar{t}ee$	aMcAtNlo+Pythia 8		491500	1.0	0.037	1.12
410219	$t\bar{t}\mu\mu$	aMcAtNlo+Pythia 8		4922000	1.0	0.037	1.12
410220	$t\bar{t}\tau\tau$	aMcAtNlo+Pythia 8		27936000	1.0	0.037	1.12
410155	$t\bar{t}W$	aMcAtNlo+Pythia 8		27036000	1.0	0.548	1.1
364739	tZ OF	MadGraph + Pythia 8	NLO NNPDF30	~1.4M	1.00	0.015	
364740	tZ OF	MadGraph + Pythia 8	NLO NNPDF30	~2M	1.00	0.026	
364741	tZ SF	MadGraph + Pythia 8	NLO NNPDF30	~0.7M	1.00	0.0077	
364742	tZ SF	MadGraph + Pythia 8	NLO NNPDF30	~0.9M	1.00	0.013	
410658	t (t-channel)	Powheg+Pythia8		97557400	1.0	37.0	1.19
410659	$\bar{t}$ (t-channel)	Powheg+Pythia8		97121350	1.0	22.17	1.18
410648	$Wt\,(2\ell)$	Powheg+Pythia8		3909400	1.0	3.997	0.94
410649	$W\bar{t}\,(2\ell)$	Powheg+Pythia8		3903900	1.0	3.99	0.95
410646	Wt	Powheg+Pythia8		39035000	1.0	37.93	0.94
410647	$W\bar{t}$	Powheg+Pythia8		39006000	1.0	37.91	0.95
410644	t (s-channel) $(\geqslant 1\ell)$	Powheg+Pythia8		7803000	1.0	2.03	1.02
410025	$\bar{t}$ (s-channel) $(\geqslant 1\ell)$	Powheg+Pythia8		7817000	1.0	1.27	1.02

Table B.2: Summary of background MC simulation.

DSID	Process	Generators	PDF	Events	Filter Eff.	Cross-section [pb]	k-factor
502336	epemepvjj_EW6_LSMT_t1_sm	MadGraph + Pythia8	A14NNPDF23LO	60000	1.0	0.0036447000	1.0
502337	epememvjj_EW6_LSMT_t1_sm	MadGraph + Pythia8	A14NNPDF23LO	50000	1.0	0.0022618000	1.0
502338	epemmupvjj_EW6_LSMT_t1_sm	MadGraph + Pythia8	A14NNPDF23LO	60000	1.0	0.0036497000	1.0
502339	epemmumvjj_EW6_LSMT_t1_sm	MadGraph + Pythia8	A14NNPDF23LO	50000	1.0	0.0022672000	1.0
502340	epemtapvjj_EW6_LSMT_t1_sm	MadGraph + Pythia8	A14NNPDF23LO	60000	1.0	0.0036459000	1.0
502341	epemtamvjj_EW6_LSMT_t1_sm	MadGraph + Pythia8	A14NNPDF23LO	50000	1.0	0.0022638000	1.0
502342	mupmumepvjj_EW6_LSMT_t1_sm	MadGraph + Pythia8	A14NNPDF23LO	60000	1.0	0.0036470000	1.0
502343	mupmumemvjj_EW6_LSMT_t1_sm	MadGraph + Pythia8	A14NNPDF23LO	50000	1.0	0.0022674000	1.0
502344	mupmummupvjj_EW6_LSMT_t1_sm	MadGraph + Pythia8	A14NNPDF23LO	60000	1.0	0.0036445000	1.0
502345	mupmummumvjj_EW6_LSMT_t1_sm	MadGraph + Pythia8	A14NNPDF23LO	50000	1.0	0.0036408000	1.0
502346	mupmumtapvjj_EW6_LSMT_t1_sm	MadGraph + Pythia8	A14NNPDF23LO	50000	1.0	0.0022650000	1.0
502347	mupmumtamvjj_EW6_LSMT_t1_sm	MadGraph + Pythia8	A14NNPDF23LO	50000	1.0	0.0022648000	1.0
502348	taptamepvjj_EW6_LSMT_t1_sm	MadGraph + Pythia8	A14NNPDF23LO	60000	1.0	0.0037325000	1.0
502349	taptamemvjj_EW6_LSMT_t1_sm	MadGraph + Pythia8	A14NNPDF23LO	50000	1.0	0.0036504000	1.0
502350	taptammupvjj_EW6_LSMT_t1_sm	MadGraph + Pythia8	A14NNPDF23LO	60000	1.0	0.0037374000	1.0
502351	taptammumvjj_EW6_LSMT_t1_sm	MadGraph + Pythia8	A14NNPDF23LO	50000	1.0	0.0022928000	1.0
502352	taptamtapvjj_EW6_LSMT_t1_sm	MadGraph + Pythia8	A14NNPDF23LO	60000	1.0	0.0037272000	1.0
502353	taptamtamvjj_EW6_LSMT_t1_sm	MadGraph + Pythia8	A14NNPDF23LO	50000	1.0	0.0022806000	1.0
502207	lllvjj_EW6_LSMT_S1_128_quad	MadGraph + Pythia8	A14NNPDF23LO	700000	1.0	0.0051411000	1.0
502208	lllvjj_EW6_LSMT_T0_2p40_quad	MadGraph + Pythia8	A14NNPDF23LO	700000	1.0	0.0047771000	1.0
502209	lllvjj_EW6_LSMT_T1_1p60_quad	MadGraph + Pythia8	A14NNPDF23LO	700000	1.0	0.0042189000	1.0
502210	lllvjj_EW6_LSMT_T2_5p50_quad	MadGraph + Pythia8	A14NNPDF23LO	700000	1.0	0.0060164000	1.0
502211	lllvjj_EW6_LSMT_M0_27_quad	MadGraph + Pythia8	A14NNPDF23LO	700000	1.0	0.0074700000	1.0
502212	lllvjj_EW6_LSMT_M1_28_quad	MadGraph + Pythia8	A14NNPDF23LO	700000	1.0	0.0031581000	1.0
502214	lllvjj_EW6_LSMT_T0_2p40_T1_1p60_cross	MadGraph + Pythia8	A14NNPDF23LO	700000	1.0	0.0026339000	1.0
502215	lllvjj_EW6_LSMT_T0_2p40_T2_5p50_cross	MadGraph + Pythia8	A14NNPDF23LO	700000	1.0	0.0050934000	1.0
502216	lllvjj_EW6_LSMT_T1_1p60_T2_5p50_cross	MadGraph + Pythia8	A14NNPDF23LO	700000	1.0	0.0067387000	1.0
502217	lllvjj_EW6_LSMT_M0_27_M1_28_cross	MadGraph + Pythia8	A14NNPDF23LO	700000	1.0	0.0047661000	1.0
502318	epemepvjj_EW6_LSMT_s0_S02_82	MadGraph + Pythia8	A14NNPDF23LO	60000	1.0	0.0000027393	1.0
502319	epememvjj_EW6_LSMT_s0_S02_82	MadGraph + Pythia8	A14NNPDF23LO	50000	1.0	0.0000018354	1.0
502320	epemmupvjj_EW6_LSMT_s0_S02_82	MadGraph + Pythia8	A14NNPDF23LO	60000	1.0	0.0000027704	1.0
502321	epemmumvjj_EW6_LSMT_s0_S02_82	MadGraph + Pythia8	A14NNPDF23LO	50000	1.0	0.0000016772	1.0
502322	epemtapvjj_EW6_LSMT_s0_S02_82	MadGraph + Pythia8	A14NNPDF23LO	60000	1.0	0.0000027821	1.0
502323	epemtamvjj_EW6_LSMT_s0_S02_82	MadGraph + Pythia8	A14NNPDF23LO	50000	1.0	0.0000018170	1.0
502324	mupmumepvjj_EW6_LSMT_s0_S02_82	MadGraph + Pythia8	A14NNPDF23LO	60000	1.0	0.0000027586	1.0
502325	mupmumemvjj_EW6_LSMT_s0_S02_82	MadGraph + Pythia8	A14NNPDF23LO	50000	1.0	0.0000016304	1.0
502326	mupmummupvjj_EW6_LSMT_s0_S02_82	MadGraph + Pythia8	A14NNPDF23LO	60000	1.0	0.0000028866	1.0
502327	mupmummumvjj_EW6_LSMT_s0_S02_82	MadGraph + Pythia8	A14NNPDF23LO	50000	1.0	0.0000018129	1.0
502328	mupmumtapvjj_EW6_LSMT_s0_S02_82	MadGraph + Pythia8	A14NNPDF23LO	60000	1.0	0.0000027054	1.0
502329	mupmumtamvjj_EW6_LSMT_s0_S02_82	MadGraph + Pythia8	A14NNPDF23LO	50000	1.0	0.0000017560	1.0
502330	taptamepvjj_EW6_LSMT_s0_S02_82	MadGraph + Pythia8	A14NNPDF23LO	60000	1.0	0.0000021205	1.0
502331	taptamemvjj_EW6_LSMT_s0_S02_82	MadGraph + Pythia8	A14NNPDF23LO	50000	1.0	0.0000027420	1.0
502332	taptammupvjj_EW6_LSMT_s0_S02_82	MadGraph + Pythia8	A14NNPDF23LO	60000	1.0	0.0000019162	1.0
502333	taptammumvjj_EW6_LSMT_s0_S02_82	MadGraph + Pythia8	A14NNPDF23LO	50000	1.0	0.0000013894	1.0
502334	taptamtapvjj_EW6_LSMT_s0_S02_82	MadGraph + Pythia8	A14NNPDF23LO	60000	1.0	0.0000022179	1.0
502335	taptamtamvjj_EW6_LSMT_s0_S02_82	MadGraph + Pythia8	A14NNPDF23LO	50000	1.0	0.0000013596	1.0

TABLE B.3: Summary of EFT samples.

DSID	Process	Generators	PDF	Events	Filter Eff.	Cross-section [pb]	k-factor
502198	epemepvjj_EW6_LSMT_t0_T0_2p40	MadGraph + Pythia8	A14NNPDF23LO	60000	1.0	0.0000009806	1.0
502199	epememvjj_EW6_LSMT_t0_T0_2p40	MadGraph + Pythia8	A14NNPDF23LO	50000	1.0	0.0000002468	1.0
502200	epemmupvjj_EW6_LSMT_t0_T0_2p40	MadGraph + Pythia8	A14NNPDF23LO	60000	1.0	0.0000010101	1.0
502201	epemmumvjj_EW6_LSMT_t0_T0_2p40	MadGraph + Pythia8	A14NNPDF23LO	50000	1.0	0.0000002420	1.0
502202	epemtapvjj_EW6_LSMT_t0_T0_2p40	MadGraph + Pythia8	A14NNPDF23LO	60000	1.0	0.0000010122	1.0
502203	epemtamvjj_EW6_LSMT_t0_T0_2p40	MadGraph + Pythia8	A14NNPDF23LO	50000	1.0	0.0000002877	1.0
502204	mupmumepvjj_EW6_LSMT_t0_T0_2p40	MadGraph + Pythia8	A14NNPDF23LO	60000	1.0	0.0000010150	1.0
502205	mupmumemvjj_EW6_LSMT_t0_T0_2p40	MadGraph + Pythia8	A14NNPDF23LO	50000	1.0	0.0000002469	1.0
502218	mupmummupvjj_EW6_LSMT_t0_T0_2p40	MadGraph + Pythia8	A14NNPDF23LO	60000	1.0	0.0000009125	1.0
502219	mupmummumvjj_EW6_LSMT_t0_T0_2p40	MadGraph + Pythia8	A14NNPDF23LO	50000	1.0	0.0000002606	1.0
502220	mupmumtapvjj_EW6_LSMT_t0_T0_2p40	MadGraph + Pythia8	A14NNPDF23LO	60000	1.0	0.0000009655	1.0
502221	mupmumtamvjj_EW6_LSMT_t0_T0_2p40	MadGraph + Pythia8	A14NNPDF23LO	50000	1.0	0.0000002788	1.0
502222	taptamepvjj_EW6_LSMT_t0_T0_2p40	MadGraph + Pythia8	A14NNPDF23LO	60000	1.0	0.0000009827	1.0
502223	taptamemvjj_EW6_LSMT_t0_T0_2p40	MadGraph + Pythia8	A14NNPDF23LO	50000	1.0	0.0000009821	1.0
502224	taptammupvjj_EW6_LSMT_t0_T0_2p40	MadGraph + Pythia8	A14NNPDF23LO	60000	1.0	0.0000009821	1.0
502225	taptammumvjj_EW6_LSMT_t0_T0_2p40	MadGraph + Pythia8	A14NNPDF23LO	50000	1.0	0.0000002492	1.0
502226	taptamtapvjj_EW6_LSMT_t0_T0_2p40	MadGraph + Pythia8	A14NNPDF23LO	60000	1.0	0.0000009974	1.0
502227	taptamtamvjj_EW6_LSMT_t0_T0_2p40	MadGraph + Pythia8	A14NNPDF23LO	50000	1.0	0.0000002515	1.0
502228	epemepvjj_EW6_LSMT_t1_T1_1p60	MadGraph + Pythia8	A14NNPDF23LO	60000	1.0	0.0000080630	1.0
502229	epememvjj_EW6_LSMT_t1_T1_1p60	MadGraph + Pythia8	A14NNPDF23LO	50000	1.0	0.0000038310	1.0
502230	epemmupvjj_EW6_LSMT_t1_T1_1p60	MadGraph + Pythia8	A14NNPDF23LO	60000	1.0	0.0000081175	1.0
502231	epemmumvjj_EW6_LSMT_t1_T1_1p60	MadGraph + Pythia8	A14NNPDF23LO	50000	1.0	0.0000039040	1.0
502232	epemtapvjj_EW6_LSMT_t1_T1_1p60	MadGraph + Pythia8	A14NNPDF23LO	60000	1.0	0.0000081481	1.0
502233	epemtamvjj_EW6_LSMT_t1_T1_1p60	MadGraph + Pythia8	A14NNPDF23LO	50000	1.0	0.0000039261	1.0
502234	mupmumepvjj_EW6_LSMT_t1_T1_1p60	MadGraph + Pythia8	A14NNPDF23LO	60000	1.0	0.0000082216	1.0
502235	mupmumemvjj_EW6_LSMT_t1_T1_1p60	MadGraph + Pythia8	A14NNPDF23LO	50000	1.0	0.0000038652	1.0
502236	mupmummupvjj_EW6_LSMT_t1_T1_1p60	MadGraph + Pythia8	A14NNPDF23LO	60000	1.0	0.0000080705	1.0
502237	mupmummumvjj_EW6_LSMT_t1_T1_1p60	MadGraph + Pythia8	A14NNPDF23LO	50000	1.0	0.0000038506	1.0
502238	mupmumtapvjj_EW6_LSMT_t1_T1_1p60	MadGraph + Pythia8	A14NNPDF23LO	60000	1.0	0.0000080529	1.0
502239	mupmumtamvjj_EW6_LSMT_t1_T1_1p60	MadGraph + Pythia8	A14NNPDF23LO	50000	1.0	0.0000039061	1.0
502240	taptamepvjj_EW6_LSMT_t1_T1_1p60	MadGraph + Pythia8	A14NNPDF23LO	60000	1.0	0.0000079959	1.0
502241	taptamemvjj_EW6_LSMT_t1_T1_1p60	MadGraph + Pythia8	A14NNPDF23LO	50000	1.0	0.0000079452	1.0
502242	taptammupvjj_EW6_LSMT_t1_T1_1p60	MadGraph + Pythia8	A14NNPDF23LO	60000	1.0	0.0000080017	1.0
502243	taptammumvjj_EW6_LSMT_t1_T1_1p60	MadGraph + Pythia8	A14NNPDF23LO	50000	1.0	0.0000039549	1.0
502244	taptamtapvjj_EW6_LSMT_t1_T1_1p60	MadGraph + Pythia8	A14NNPDF23LO	60000	1.0	0.0000082581	1.0
502245	taptamtamvjj_EW6_LSMT_t1_T1_1p60	MadGraph + Pythia8	A14NNPDF23LO	50000	1.0	0.0000038652	1.0
502246	epemepvjj_EW6_LSMT_t2_T2_5p50	MadGraph + Pythia8	A14NNPDF23LO	60000	1.0	0.0000166490	1.0
502247	epememvjj_EW6_LSMT_t2_T2_5p50	MadGraph + Pythia8	A14NNPDF23LO	50000	1.0	0.0000076051	1.0
502248	epemmupvjj_EW6_LSMT_t2_T2_5p50	MadGraph + Pythia8	A14NNPDF23LO	60000	1.0	0.0000169530	1.0
502249	epemmumvjj_EW6_LSMT_t2_T2_5p50	MadGraph + Pythia8	A14NNPDF23LO	50000	1.0	0.0000074491	1.0
502250	epemtapvjj_EW6_LSMT_t2_T2_5p50	MadGraph + Pythia8	A14NNPDF23LO	60000	1.0	0.0000168760	1.0
502251	epemtamvjj_EW6_LSMT_t2_T2_5p50	MadGraph + Pythia8	A14NNPDF23LO	50000	1.0	0.0000074436	1.0
502252	mupmumepvjj_EW6_LSMT_t2_T2_5p50	MadGraph + Pythia8	A14NNPDF23LO	60000	1.0	0.0000167890	1.0
502253	mupmumemvjj_EW6_LSMT_t2_T2_5p50	MadGraph + Pythia8	A14NNPDF23LO	50000	1.0	0.0000073941	1.0
502254	mupmummupvjj_EW6_LSMT_t2_T2_5p50	MadGraph + Pythia8	A14NNPDF23LO	60000	1.0	0.0000167530	1.0
502255	mupmummumvjj_EW6_LSMT_t2_T2_5p50	MadGraph + Pythia8	A14NNPDF23LO	50000	1.0	0.0000076685	1.0
502256	mupmumtapvjj_EW6_LSMT_t2_T2_5p50	MadGraph + Pythia8	A14NNPDF23LO	60000	1.0	0.0000167180	1.0
502257	mupmumtamvjj_EW6_LSMT_t2_T2_5p50	MadGraph + Pythia8	A14NNPDF23LO	50000	1.0	0.0000075500	1.0
502258	taptamepvjj_EW6_LSMT_t2_T2_5p50	MadGraph + Pythia8	A14NNPDF23LO	60000	1.0	0.0000165330	1.0
502259	taptamemvjj_EW6_LSMT_t2_T2_5p50	MadGraph + Pythia8	A14NNPDF23LO	50000	1.0	0.0000168780	1.0
502260	taptammupvjj_EW6_LSMT_t2_T2_5p50	MadGraph + Pythia8	A14NNPDF23LO	60000	1.0	0.0000164480	1.0
502261	taptammumvjj_EW6_LSMT_t2_T2_5p50	MadGraph + Pythia8	A14NNPDF23LO	50000	1.0	0.0000075492	1.0
502262	taptamtapvjj_EW6_LSMT_t2_T2_5p50	MadGraph + Pythia8	A14NNPDF23LO	60000	1.0	0.0000166490	1.0
502263	taptamtamvjj_EW6_LSMT_t2_T2_5p50	MadGraph + Pythia8	A14NNPDF23LO	50000	1.0	0.0000075688	1.0

Table B.4: Summary of EFT samples.

DSID	Process	Generators	PDF	Events	Filter Eff.	Cross-section [pb]	k-factor
502264	epemepvjj_EW6_LSMT_m0_M0_27	MadGraph + Pythia8	A14NNPDF23LO	60000	1.0	0.0000005011	1.0
502265	epememvjj_EW6_LSMT_m0_M0_27	MadGraph + Pythia8	A14NNPDF23LO	50000	1.0	0.0000003259	1.0
502266	epemmupvjj_EW6_LSMT_m0_M0_27	MadGraph + Pythia8	A14NNPDF23LO	60000	1.0	0.0000005223	1.0
502267	epemmumvjj_EW6_LSMT_m0_M0_27	MadGraph + Pythia8	A14NNPDF23LO	50000	1.0	0.0000003087	1.0
502268	epemtapvjj_EW6_LSMT_m0_M0_27	MadGraph + Pythia8	A14NNPDF23LO	60000	1.0	0.0000005725	1.0
502269	epemtamvjj_EW6_LSMT_m0_M0_27	MadGraph + Pythia8	A14NNPDF23LO	50000	1.0	0.0000003246	1.0
502270	mupmumepvjj_EW6_LSMT_m0_M0_27	MadGraph + Pythia8	A14NNPDF23LO	60000	1.0	0.0000005272	1.0
502271	mupmumemvjj_EW6_LSMT_m0_M0_27	MadGraph + Pythia8	A14NNPDF23LO	50000	1.0	0.0000003080	1.0
502272	mupmummupvjj_EW6_LSMT_m0_M0_27	MadGraph + Pythia8	A14NNPDF23LO	60000	1.0	0.0000005557	1.0
502273	mupmummumvjj_EW6_LSMT_m0_M0_27	MadGraph + Pythia8	A14NNPDF23LO	50000	1.0	0.0000003258	1.0
502274	mupmumtapvjj_EW6_LSMT_m0_M0_27	MadGraph + Pythia8	A14NNPDF23LO	60000	1.0	0.0000005865	1.0
502275	mupmumtamvjj_EW6_LSMT_m0_M0_27	MadGraph + Pythia8	A14NNPDF23LO	50000	1.0	0.0000003268	1.0
502276	taptamepvjj_EW6_LSMT_m0_M0_27	MadGraph + Pythia8	A14NNPDF23LO	60000	1.0	0.0000004955	1.0
502277	taptamemvjj_EW6_LSMT_m0_M0_27	MadGraph + Pythia8	A14NNPDF23LO	50000	1.0	0.0000004657	1.0
502278	taptammupvjj_EW6_LSMT_m0_M0_27	MadGraph + Pythia8	A14NNPDF23LO	60000	1.0	0.0000004545	1.0
502279	taptammumvjj_EW6_LSMT_m0_M0_27	MadGraph + Pythia8	A14NNPDF23LO	50000	1.0	0.0000003083	1.0
502280	taptamtapvjj_EW6_LSMT_m0_M0_27	MadGraph + Pythia8	A14NNPDF23LO	60000	1.0	0.0000005344	1.0
502281	taptamtamvjj_EW6_LSMT_m0_M0_27	MadGraph + Pythia8	A14NNPDF23LO	50000	1.0	0.0000003240	1.0
502282	epemepvjj_EW6_LSMT_m1_M1_28	MadGraph + Pythia8	A14NNPDF23LO	60000	1.0	0.0000001716	1.0
502283	epememvjj_EW6_LSMT_m1_M1_28	MadGraph + Pythia8	A14NNPDF23LO	50000	1.0	0.0000001746	1.0
502284	epemmupvjj_EW6_LSMT_m1_M1_28	MadGraph + Pythia8	A14NNPDF23LO	60000	1.0	0.0000001890	1.0
502285	epemmumvjj_EW6_LSMT_m1_M1_28	MadGraph + Pythia8	A14NNPDF23LO	50000	1.0	0.0000001651	1.0
502286	epemtapvjj_EW6_LSMT_m1_M1_28	MadGraph + Pythia8	A14NNPDF23LO	60000	1.0	0.0000001885	1.0
502287	epemtamvjj_EW6_LSMT_m1_M1_28	MadGraph + Pythia8	A14NNPDF23LO	50000	1.0	0.0000001752	1.0
502288	mupmumepvjj_EW6_LSMT_m1_M1_28	MadGraph + Pythia8	A14NNPDF23LO	60000	1.0	0.0000002077	1.0
502289	mupmumemvjj_EW6_LSMT_m1_M1_28	MadGraph + Pythia8	A14NNPDF23LO	50000	1.0	0.0000001723	1.0
502290	mupmummupvjj_EW6_LSMT_m1_M1_28	MadGraph + Pythia8	A14NNPDF23LO	60000	1.0	0.0000001760	1.0
502291	mupmummumvjj_EW6_LSMT_m1_M1_28	MadGraph + Pythia8	A14NNPDF23LO	50000	1.0	0.0000001644	1.0
502292	mupmumtapvjj_EW6_LSMT_m1_M1_28	MadGraph + Pythia8	A14NNPDF23LO	60000	1.0	0.0000001830	1.0
502293	mupmumtamvjj_EW6_LSMT_m1_M1_28	MadGraph + Pythia8	A14NNPDF23LO	50000	1.0	0.0000001740	1.0
502294	taptamepvjj_EW6_LSMT_m1_M1_28	MadGraph + Pythia8	A14NNPDF23LO	60000	1.0	0.0000001839	1.0
502295	taptamemvjj_EW6_LSMT_m1_M1_28	MadGraph + Pythia8	A14NNPDF23LO	50000	1.0	0.0000001752	1.0
502296	taptammupvjj_EW6_LSMT_m1_M1_28	MadGraph + Pythia8	A14NNPDF23LO	60000	1.0	0.0000001764	1.0
502297	taptammumvjj_EW6_LSMT_m1_M1_28	MadGraph + Pythia8	A14NNPDF23LO	50000	1.0	0.0000001798	1.0
502298	taptamtapvjj_EW6_LSMT_m1_M1_28	MadGraph + Pythia8	A14NNPDF23LO	60000	1.0	0.0000001686	1.0
502299	taptamtamvjj_EW6_LSMT_m1_M1_28	MadGraph + Pythia8	A14NNPDF23LO	50000	1.0	0.0000001924	1.0
502300	epemepvjj_EW6_LSMT_s1_S1_128	MadGraph + Pythia8	A14NNPDF23LO	60000	1.0	0.0000006360	1.0
502301	epememvjj_EW6_LSMT_s1_S1_128	MadGraph + Pythia8	A14NNPDF23LO	50000	1.0	0.0000003689	1.0
502302	epemmupvjj_EW6_LSMT_s1_S1_128	MadGraph + Pythia8	A14NNPDF23LO	60000	1.0	0.0000006301	1.0
502303	epemmumvjj_EW6_LSMT_s1_S1_128	MadGraph + Pythia8	A14NNPDF23LO	50000	1.0	0.0000003996	1.0
502304	epemtapvjj_EW6_LSMT_s1_S1_128	MadGraph + Pythia8	A14NNPDF23LO	60000	1.0	0.0000005979	1.0
502305	epemtamvjj_EW6_LSMT_s1_S1_128	MadGraph + Pythia8	A14NNPDF23LO	50000	1.0	0.0000003903	1.0
502306	mupmumepvjj_EW6_LSMT_s1_S1_128	MadGraph + Pythia8	A14NNPDF23LO	60000	1.0	0.0000006194	1.0
502307	mupmumemvjj_EW6_LSMT_s1_S1_128	MadGraph + Pythia8	A14NNPDF23LO	50000	1.0	0.0000004170	1.0
502308	mupmummupvjj_EW6_LSMT_s1_S1_128	MadGraph + Pythia8	A14NNPDF23LO	60000	1.0	0.0000006296	1.0
502309	mupmummumvjj_EW6_LSMT_s1_S1_128	MadGraph + Pythia8	A14NNPDF23LO	50000	1.0	0.0000003684	1.0
502310	mupmumtapvjj_EW6_LSMT_s1_S1_128	MadGraph + Pythia8	A14NNPDF23LO	60000	1.0	0.0000005858	1.0
502311	mupmumtamvjj_EW6_LSMT_s1_S1_128	MadGraph + Pythia8	A14NNPDF23LO	50000	1.0	0.0000004007	1.0
502312	taptamepvjj_EW6_LSMT_s1_S1_128	MadGraph + Pythia8	A14NNPDF23LO	60000	1.0	0.0000006658	1.0
502313	taptamemvjj_EW6_LSMT_s1_S1_128	MadGraph + Pythia8	A14NNPDF23LO	50000	1.0	0.0000005964	1.0
502314	taptammupvjj_EW6_LSMT_s1_S1_128	MadGraph + Pythia8	A14NNPDF23LO	60000	1.0	0.0000005974	1.0
502315	taptammumvjj_EW6_LSMT_s1_S1_128	MadGraph + Pythia8	A14NNPDF23LO	50000	1.0	0.0000003939	1.0
502316	taptamtapvjj_EW6_LSMT_s1_S1_128	MadGraph + Pythia8	A14NNPDF23LO	60000	1.0	0.0000006474	1.0
502317	taptamtamvjj_EW6_LSMT_s1_S1_128	MadGraph + Pythia8	A14NNPDF23LO	50000	1.0	0.0000004207	1.0
507694	lllvjj_EW6_LSMT_INTRF_82_quad	MadGraph + Pythia8	A14NNPDF23LO	182000	1.0	0.0076500000	1.0
507695	lllvjj_EW6_LSMT_S0_82_quad	MadGraph + Pythia8	A14NNPDF23LO	240000	1.0	0.0050000000	1.0
507696	lllvjj_EW6_LSMT_S2_82_quad	MadGraph + Pythia8	A14NNPDF23LO	240000	1.0	0.0050100000	1.0
512195	lllvjj_EW6_LSMT_M7_30_quad	MadGraph + Pythia8	A14NNPDF23LO	180000	1.0	0.0029400000	1.0

Table B.5: Summary of EFT samples.

Appendix C

Rivet routine for the WZ diboson and $WZjj$ VBS productions

C.1 Rivet routine for the WZ diboson production

Source code: `ATLAS_2019_I1720438.cc`

```
// -*- C++ -*-
#include "Rivet/Analysis.hh"
#include "Rivet/Projections/FinalState.hh"
#include "Rivet/Projections/FastJets.hh"
#include "Rivet/Projections/IdentifiedFinalState.hh"
#include "Rivet/Projections/PromptFinalState.hh"
#include "Rivet/Projections/DressedLeptons.hh"
#include "Rivet/Projections/VetoedFinalState.hh"

namespace Rivet {


  /// @brief WZ production cross-section at 13 TeV
  class ATLAS_2019_I1720438 : public Analysis {
  public:

    /// Constructor
    RIVET_DEFAULT_ANALYSIS_CTOR(ATLAS_2019_I1720438);

    /// @name Analysis methods
    //@{


    /// Book histograms and initialise projections before the run
    void init() {

      PromptFinalState photons(Cuts::abspid == PID::PHOTON);

      // Electrons and muons in Fiducial PS
      PromptFinalState leptons(Cuts::abspid == PID::ELECTRON || Cuts::abspid == PID::MUON);
      leptons.acceptTauDecays(false);
      DressedLeptons dressedleptons(photons, leptons, 0.1, Cuts::open(), true);
      declare(dressedleptons, "DressedLeptons");

      // Prompt neutrinos (yikes!)
      IdentifiedFinalState nu_id;
      nu_id.acceptNeutrinos();
      PromptFinalState neutrinos(nu_id);
      neutrinos.acceptTauDecays(false);
      declare(neutrinos, "Neutrinos");
      MSG_WARNING("\033[91;1mLIMITED VALIDITY - check info file for details!\033[m");

      // Muons
      PromptFinalState bare_mu(Cuts::abspid == PID::MUON, true); // true = use muons from prompt tau decays
      DressedLeptons all_dressed_mu(photons, bare_mu, 0.1, Cuts::abseta < 2.5, true);

      // Electrons
      PromptFinalState bare_el(Cuts::abspid == PID::ELECTRON, true); // true = use electrons from prompt tau decays
      DressedLeptons all_dressed_el(photons, bare_el, 0.1, Cuts::abseta < 2.5, true);

      //Jet forming
      VetoedFinalState vfs(FinalState(Cuts::abseta < 5.0));
      vfs.addVetoOnThisFinalState(all_dressed_el);
      vfs.addVetoOnThisFinalState(all_dressed_mu);

      FastJets jets(vfs, FastJets::ANTIKT, 0.4, JetAlg::Muons::ALL, JetAlg::Invisibles::DECAY);
      declare(jets, "Jets");

      // Book auxiliary histograms
      book(_h["pTZ"],    "_pTZ",    refData( 8, 1, 1));
      book(_h["pTW"],    "_pTW",    refData(10, 1, 1));
      book(_h["mTWZ"],   "_mTWZ",   refData(12, 1, 1));
```

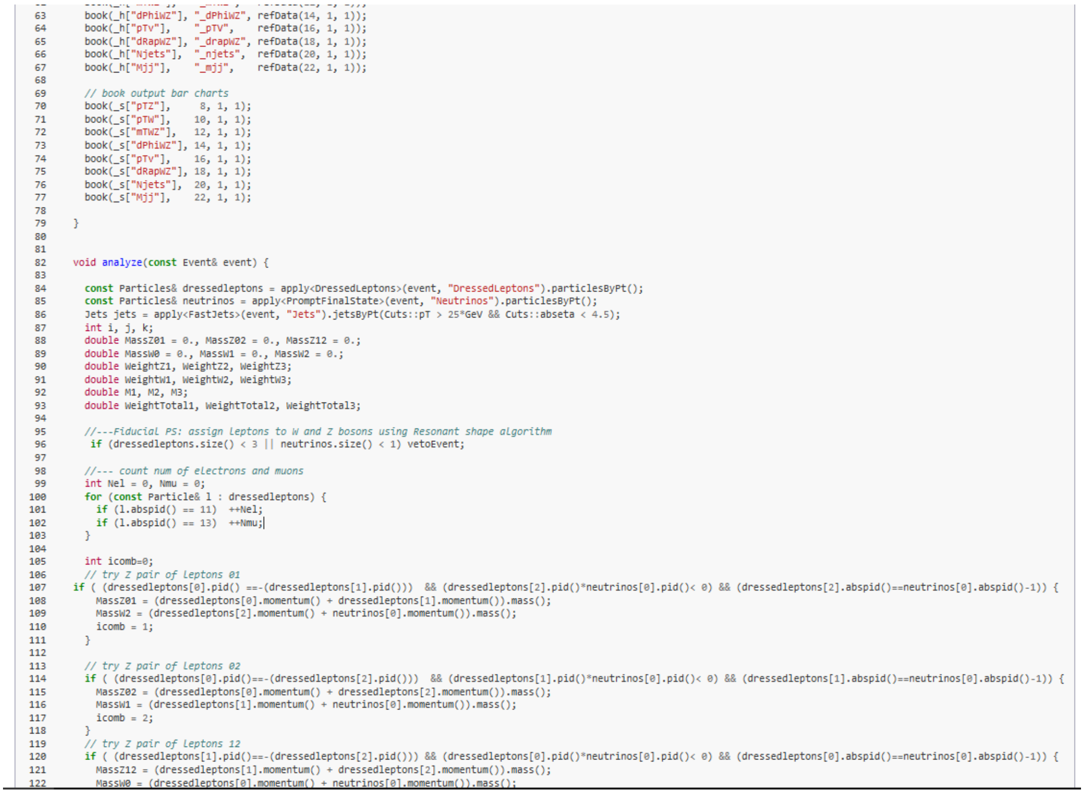

```
      book(_h["dPhiWZ"], "_dPhiWZ", refData(14, 1, 1));
      book(_h["pTv"],    "_pTV",    refData(16, 1, 1));
      book(_h["dRapWZ"], "_drapWZ", refData(18, 1, 1));
      book(_h["Njets"],  "_njets",  refData(20, 1, 1));
      book(_h["Mjj"],    "_mjj",    refData(22, 1, 1));

      // book output bar charts
      book(_s["pTZ"],     8, 1, 1);
      book(_s["pTW"],    10, 1, 1);
      book(_s["mTWZ"],   12, 1, 1);
      book(_s["dPhiWZ"], 14, 1, 1);
      book(_s["pTv"],    16, 1, 1);
      book(_s["dRapWZ"], 18, 1, 1);
      book(_s["Njets"],  20, 1, 1);
      book(_s["Mjj"],    22, 1, 1);

    }


    void analyze(const Event& event) {

      const Particles& dressedleptons = apply<DressedLeptons>(event, "DressedLeptons").particlesByPt();
      const Particles& neutrinos = apply<PromptFinalState>(event, "Neutrinos").particlesByPt();
      Jets jets = apply<FastJets>(event, "Jets").jetsByPt(Cuts::pT > 25*GeV && Cuts::abseta < 4.5);
      int i, j, k;
      double MassZ01 = 0., MassZ02 = 0., MassZ12 = 0.;
      double MassW0 = 0., MassW1 = 0., MassW2 = 0.;
      double WeightZ1, WeightZ2, WeightZ3;
      double WeightW1, WeightW2, WeightW3;
      double M1, M2, M3;
      double WeightTotal1, WeightTotal2, WeightTotal3;

      //---Fiducial PS: assign leptons to W and Z bosons using Resonant shape algorithm
       if (dressedleptons.size() < 3 || neutrinos.size() < 1) vetoEvent;

      //--- count num of electrons and muons
      int Nel = 0, Nmu = 0;
      for (const Particle& l : dressedleptons) {
        if (l.abspid() == 11)  ++Nel;
        if (l.abspid() == 13)  ++Nmu;
      }

      int icomb=0;
      // try Z pair of leptons 01
    if ( (dressedleptons[0].pid() ==-(dressedleptons[1].pid()))  && (dressedleptons[2].pid()*neutrinos[0].pid()< 0) && (dressedleptons[2].abspid()==neutrinos[0].abspid()-1)) {
        MassZ01 = (dressedleptons[0].momentum() + dressedleptons[1].momentum()).mass();
        MassW2 = (dressedleptons[2].momentum() + neutrinos[0].momentum()).mass();
        icomb = 1;
      }

      // try Z pair of leptons 02
      if ( (dressedleptons[0].pid()==-(dressedleptons[2].pid()))  && (dressedleptons[1].pid()*neutrinos[0].pid()< 0) && (dressedleptons[1].abspid()==neutrinos[0].abspid()-1)) {
        MassZ02 = (dressedleptons[0].momentum() + dressedleptons[2].momentum()).mass();
        MassW1 = (dressedleptons[1].momentum() + neutrinos[0].momentum()).mass();
        icomb = 2;
      }
      // try Z pair of leptons 12
      if ( (dressedleptons[1].pid()==-(dressedleptons[2].pid())) && (dressedleptons[0].pid()*neutrinos[0].pid()< 0) && (dressedleptons[0].abspid()==neutrinos[0].abspid()-1)) {
        MassZ12 = (dressedleptons[1].momentum() + dressedleptons[2].momentum()).mass();
        MassW0 = (dressedleptons[0].momentum() + neutrinos[0].momentum()).mass();
```

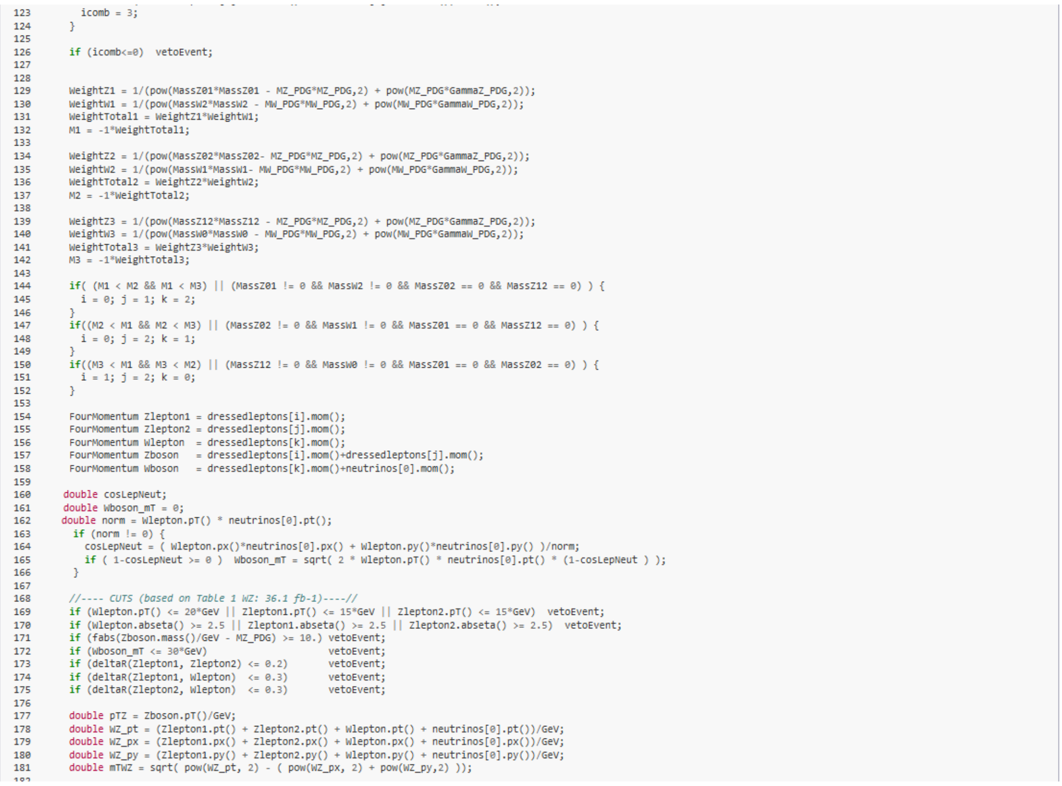

```
        icomb = 3;
      }

      if (icomb<=0)  vetoEvent;


      WeightZ1 = 1/(pow(MassZ01*MassZ01 - MZ_PDG*MZ_PDG,2) + pow(MZ_PDG*GammaZ_PDG,2));
      WeightW1 = 1/(pow(MassW2*MassW2 - MW_PDG*MW_PDG,2) + pow(MW_PDG*GammaW_PDG,2));
      WeightTotal1 = WeightZ1*WeightW1;
      M1 = -1*WeightTotal1;

      WeightZ2 = 1/(pow(MassZ02*MassZ02- MZ_PDG*MZ_PDG,2) + pow(MZ_PDG*GammaZ_PDG,2));
      WeightW2 = 1/(pow(MassW1*MassW1- MW_PDG*MW_PDG,2) + pow(MW_PDG*GammaW_PDG,2));
      WeightTotal2 = WeightZ2*WeightW2;
      M2 = -1*WeightTotal2;

      WeightZ3 = 1/(pow(MassZ12*MassZ12 - MZ_PDG*MZ_PDG,2) + pow(MZ_PDG*GammaZ_PDG,2));
      WeightW3 = 1/(pow(MassW0*MassW0 - MW_PDG*MW_PDG,2) + pow(MW_PDG*GammaW_PDG,2));
      WeightTotal3 = WeightZ3*WeightW3;
      M3 = -1*WeightTotal3;

      if( (M1 < M2 && M1 < M3) || (MassZ01 != 0 && MassW2 != 0 && MassZ02 == 0 && MassZ12 == 0) ) {
        i = 0; j = 1; k = 2;
      }
      if((M2 < M1 && M2 < M3) || (MassZ02 != 0 && MassW1 != 0 && MassZ01 == 0 && MassZ12 == 0) ) {
        i = 0; j = 2; k = 1;
      }
      if((M3 < M1 && M3 < M2) || (MassZ12 != 0 && MassW0 != 0 && MassZ01 == 0 && MassZ02 == 0) ) {
        i = 1; j = 2; k = 0;
      }

      FourMomentum Zlepton1 = dressedleptons[i].mom();
      FourMomentum Zlepton2 = dressedleptons[j].mom();
      FourMomentum Wlepton  = dressedleptons[k].mom();
      FourMomentum Zboson   = dressedleptons[i].mom()+dressedleptons[j].mom();
      FourMomentum Wboson   = dressedleptons[k].mom()+neutrinos[0].mom();

     double cosLepNeut;
     double Wboson_mT = 0;
     double norm = Wlepton.pT() * neutrinos[0].pt();
       if (norm != 0) {
         cosLepNeut = ( Wlepton.px()*neutrinos[0].px() + Wlepton.py()*neutrinos[0].py() )/norm;
         if ( 1-cosLepNeut >= 0 )  Wboson_mT = sqrt( 2 * Wlepton.pT() * neutrinos[0].pt() * (1-cosLepNeut ) );
       }

      //---- CUTS (based on Table 1 WZ: 36.1 fb-1)----//
      if (Wlepton.pT() <= 20*GeV || Zlepton1.pT() <= 15*GeV || Zlepton2.pT() <= 15*GeV)  vetoEvent;
      if (Wlepton.abseta() >= 2.5 || Zlepton1.abseta() >= 2.5 || Zlepton2.abseta() >= 2.5)  vetoEvent;
      if (fabs(Zboson.mass()/GeV - MZ_PDG) >= 10.) vetoEvent;
      if (Wboson_mT <= 30*GeV)                     vetoEvent;
      if (deltaR(Zlepton1, Zlepton2) <= 0.2)       vetoEvent;
      if (deltaR(Zlepton1, Wlepton)  <= 0.3)       vetoEvent;
      if (deltaR(Zlepton2, Wlepton)  <= 0.3)       vetoEvent;

      double pTZ = Zboson.pT()/GeV;
      double WZ_pt = (Zlepton1.pt() + Zlepton2.pt() + Wlepton.pt() + neutrinos[0].pt())/GeV;
      double WZ_px = (Zlepton1.px() + Zlepton2.px() + Wlepton.px() + neutrinos[0].px())/GeV;
      double WZ_py = (Zlepton1.py() + Zlepton2.py() + Wlepton.py() + neutrinos[0].py())/GeV;
      double mTWZ = sqrt( pow(WZ_pt, 2) - ( pow(WZ_px, 2) + pow(WZ_py,2) ));
```

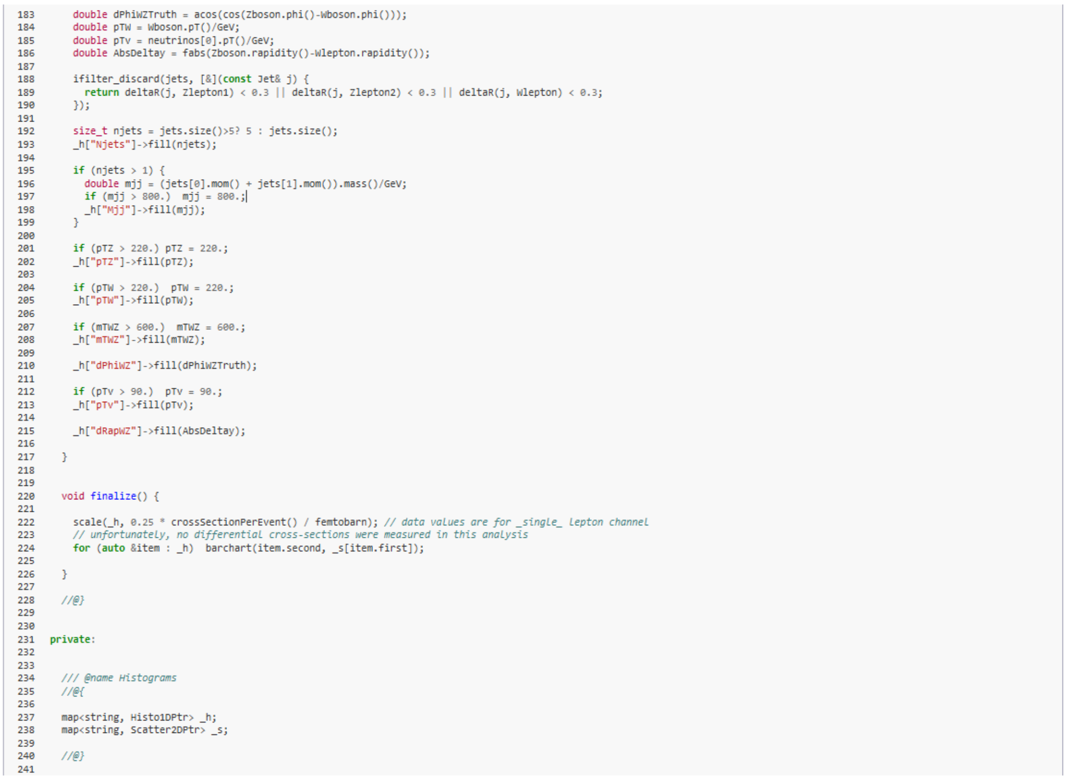

```
      double dPhiWZTruth = acos(cos(Zboson.phi()-Wboson.phi()));
      double pTW = Wboson.pT()/GeV;
      double pTv = neutrinos[0].pT()/GeV;
      double AbsDeltay = fabs(Zboson.rapidity()-Wlepton.rapidity());

      ifilter_discard(jets, [&](const Jet& j) {
        return deltaR(j, Zlepton1) < 0.3 || deltaR(j, Zlepton2) < 0.3 || deltaR(j, Wlepton) < 0.3;
      });

      size_t njets = jets.size()>5? 5 : jets.size();
      _h["Njets"]->fill(njets);

      if (njets > 1) {
        double mjj = (jets[0].mom() + jets[1].mom()).mass()/GeV;
        if (mjj > 800.)  mjj = 800.;
        _h["Mjj"]->fill(mjj);
      }

      if (pTZ > 220.) pTZ = 220.;
      _h["pTZ"]->fill(pTZ);

      if (pTW > 220.)  pTW = 220.;
      _h["pTW"]->fill(pTW);

      if (mTWZ > 600.)  mTWZ = 600.;
      _h["mTWZ"]->fill(mTWZ);

      _h["dPhiWZ"]->fill(dPhiWZTruth);

      if (pTv > 90.)  pTv = 90.;
      _h["pTv"]->fill(pTv);

      _h["dRapWZ"]->fill(AbsDeltay);

    }


    void finalize() {

      scale(_h, 0.25 * crossSectionPerEvent() / femtobarn); // data values are for _single_ lepton channel
      // unfortunately, no differential cross-sections were measured in this analysis
      for (auto &item : _h)  barchart(item.second, _s[item.first]);

    }

    //@}


  private:


    /// @name Histograms
    //@{

    map<string, Histo1DPtr> _h;
    map<string, Scatter2DPtr> _s;

    //@}

```

```
    double MZ_PDG = 91.1876;
    double MW_PDG = 80.385;
    double GammaZ_PDG = 2.4952;
    double GammaW_PDG = 2.085;

  };

  // The hook for the plugin system
  RIVET_DECLARE_PLUGIN(ATLAS_2019_I1720438);
}
```

C.2 Rivet routine for the $WZjj$ VBS productions

Source code: ATLAS_2018_I1711223.cc

```cpp
// -*- C++ -*-
#include "Rivet/Analysis.hh"
#include "Rivet/Projections/FinalState.hh"
#include "Rivet/Projections/FastJets.hh"
#include "Rivet/Projections/IdentifiedFinalState.hh"
#include "Rivet/Projections/PromptFinalState.hh"
#include "Rivet/Projections/DressedLeptons.hh"
#include "Rivet/Projections/VetoedFinalState.hh"


namespace Rivet {


  /// @brief Electroweak WZjj production cross section at 13 TeV
  class ATLAS_2018_I1711223 : public Analysis {
  public:

    /// Constructor
    RIVET_DEFAULT_ANALYSIS_CTOR(ATLAS_2018_I1711223);

    /// @name Analysis methods
    //@{

    /// Book histograms and initialise projections before the run
    void init() {

      // Get photons to dress leptons
      PromptFinalState photons(Cuts::abspid == PID::PHOTON);

      // Electrons and muons in Fiducial PS
      PromptFinalState leptons(Cuts::abspid == PID::ELECTRON || Cuts::abspid == PID::MUON);
      leptons.acceptTauDecays(false);
      DressedLeptons dressedleptons(photons, leptons, 0.1, Cuts::open(), true);                                  // useDecayPhotons=true -- useJetClustering? auto-set to false?
      declare(dressedleptons, "DressedLeptons");

      // Prompt neutrinos (yikes!)
      IdentifiedFinalState nu_id;
      nu_id.acceptNeutrinos();
      PromptFinalState neutrinos(nu_id);
      neutrinos.acceptTauDecays(false);
      declare(neutrinos, "Neutrinos");
      MSG_WARNING("\033[91;1mLIMITED VALIDITY - check info file for details!\033[m");

      //Jets

            // Muons
            PromptFinalState bare_mu(Cuts::abspid == PID::MUON, true); // true = use muons from prompt tau decays
            DressedLeptons all_dressed_mu(photons, bare_mu, 0.1, Cuts::abseta < 5.0, true);

            // Electrons
            PromptFinalState bare_el(Cuts::abspid == PID::ELECTRON, true); // true = use electrons from prompt tau decays
            DressedLeptons all_dressed_el(photons, bare_el, 0.1, Cuts::abseta < 5.0, true);

            //Jet forming
            VetoedFinalState vfs(FinalState(Cuts::abseta < 5));
            vfs.addVetoOnThisFinalState(all_dressed_el);
            vfs.addVetoOnThisFinalState(all_dressed_mu);

            FastJets jets(vfs, FastJets::ANTIKT, 0.4, JetAlg::Muons::ALL, JetAlg::Invisibles::DECAY);
            declare(jets, "Jets");

      // Book auxiliary histograms
```

```cpp
      book(_h["MTWZ"],        "_mTWZ", refData( 6, 1, 1));
      book(_h["sumpt"],       "_sumpT", refData( 8, 1, 1));
      book(_h["dphiWZ"],     "_dphiWZ", refData(10, 1, 1));
      book(_h["Njets_VBS"],   "_njets", refData(12, 1, 1));
      book(_h["mjj"],           "_mjj", refData(14, 1, 1));
      book(_h["dyjj"],       "_dRapjj", refData(16, 1, 1));
      book(_h["dphijj"],     "_dPhijj", refData(18, 1, 1));
      book(_h["Njets_gap"], "_gapJets", refData(20, 1, 1));

      // book output bar charts
      book(_s["MTWZ"],       6, 1, 1);
      book(_s["sumpt"],      8, 1, 1);
      book(_s["dphiWZ"],    10, 1, 1);
      book(_s["Njets_VBS"], 12, 1, 1);
      book(_s["mjj"],       14, 1, 1);
      book(_s["dyjj"],      16, 1, 1);
      book(_s["dphijj"],    18, 1, 1);
      book(_s["Njets_gap"], 20, 1, 1);

    }


    void analyze(const Event& event) {

      const Particles& dressedleptons = apply<DressedLeptons>(event, "DressedLeptons").particlesByPt();
      const Particles& neutrinos = apply<PromptFinalState>(event, "Neutrinos").particlesByPt();
      Jets jets = apply<FastJets>(event, "Jets").jetsByPt(Cuts::pT > 25*GeV && Cuts::abseta < 4.5);

      int i, j, k;
      double MassZ01 = 0., MassZ02 = 0., MassZ12 = 0.;
      double MassW0 = 0., MassW1 = 0., MassW2 = 0.;
      double WeightZ1, WeightZ2, WeightZ3;
      double WeightW1, WeightW2, WeightW3;
      double M1, M2, M3;
      double WeightTotal1, WeightTotal2, WeightTotal3;

      //---Fiducial PS: assign leptons to W and Z bosons using Resonant shape algorithm
      if (dressedleptons.size() < 3 || neutrinos.size() < 1) vetoEvent;

      //--- count num of electrons and muons
      int Nel = 0, Nmu = 0;
      for (const Particle& l : dressedleptons) {
        if (l.abspid() == 11)  ++Nel;
        if (l.abspid() == 13)  ++Nmu;
      }

      int icomb=0;
      // try Z pair of leptons 01
    if ( (dressedleptons[0].pid() ==-(dressedleptons[1].pid()))  && (dressedleptons[2].pid()*neutrinos[0].pid()< 0) && (dressedleptons[2].abspid()==neutrinos[0].abspid()-1)) {
        MassZ01 = (dressedleptons[0].momentum() + dressedleptons[1].momentum()).mass();
        MassW2 = (dressedleptons[2].momentum() + neutrinos[0].momentum()).mass();
        icomb = 1;
      }

      // try Z pair of leptons 02
      if ( (dressedleptons[0].pid()==-(dressedleptons[2].pid()))  && (dressedleptons[1].pid()*neutrinos[0].pid()< 0) && (dressedleptons[1].abspid()==neutrinos[0].abspid()-1)) {
        MassZ02 = (dressedleptons[0].momentum() + dressedleptons[2].momentum()).mass();
        MassW1 = (dressedleptons[1].momentum() + neutrinos[0].momentum()).mass();
        icomb = 2;
```

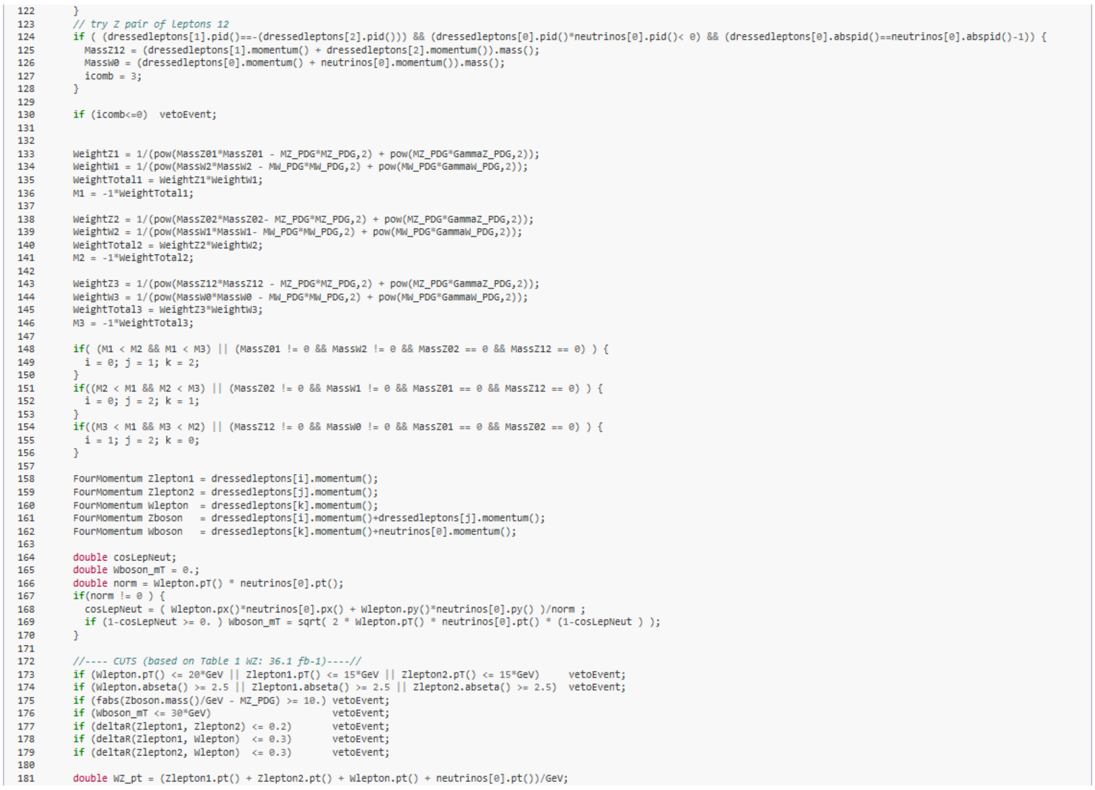

```
    }
    // try Z pair of leptons 12
    if ( (dressedleptons[1].pid()==-(dressedleptons[2].pid())) && (dressedleptons[0].pid()*neutrinos[0].pid()< 0) && (dressedleptons[0].abspid()==neutrinos[0].abspid()-1)) {
      MassZ12 = (dressedleptons[1].momentum() + dressedleptons[2].momentum()).mass();
      MassW0 = (dressedleptons[0].momentum() + neutrinos[0].momentum()).mass();
      icomb = 3;
    }

    if (icomb<=0)  vetoEvent;


    WeightZ1 = 1/(pow(MassZ01*MassZ01 - MZ_PDG*MZ_PDG,2) + pow(MZ_PDG*GammaZ_PDG,2));
    WeightW1 = 1/(pow(MassW2*MassW2 - MW_PDG*MW_PDG,2) + pow(MW_PDG*GammaW_PDG,2));
    WeightTotal1 = WeightZ1*WeightW1;
    M1 = -1*WeightTotal1;

    WeightZ2 = 1/(pow(MassZ02*MassZ02- MZ_PDG*MZ_PDG,2) + pow(MZ_PDG*GammaZ_PDG,2));
    WeightW2 = 1/(pow(MassW1*MassW1- MW_PDG*MW_PDG,2) + pow(MW_PDG*GammaW_PDG,2));
    WeightTotal2 = WeightZ2*WeightW2;
    M2 = -1*WeightTotal2;

    WeightZ3 = 1/(pow(MassZ12*MassZ12 - MZ_PDG*MZ_PDG,2) + pow(MZ_PDG*GammaZ_PDG,2));
    WeightW3 = 1/(pow(MassW0*MassW0 - MW_PDG*MW_PDG,2) + pow(MW_PDG*GammaW_PDG,2));
    WeightTotal3 = WeightZ3*WeightW3;
    M3 = -1*WeightTotal3;

    if( (M1 < M2 && M1 < M3) || (MassZ01 != 0 && MassW2 != 0 && MassZ02 == 0 && MassZ12 == 0) ) {
      i = 0; j = 1; k = 2;
    }
    if((M2 < M1 && M2 < M3) || (MassZ02 != 0 && MassW1 != 0 && MassZ01 == 0 && MassZ12 == 0) ) {
      i = 0; j = 2; k = 1;
    }
    if((M3 < M1 && M3 < M2) || (MassZ12 != 0 && MassW0 != 0 && MassZ01 == 0 && MassZ02 == 0) ) {
      i = 1; j = 2; k = 0;
    }

    FourMomentum Zlepton1 = dressedleptons[i].momentum();
    FourMomentum Zlepton2 = dressedleptons[j].momentum();
    FourMomentum Wlepton  = dressedleptons[k].momentum();
    FourMomentum Zboson   = dressedleptons[i].momentum()+dressedleptons[j].momentum();
    FourMomentum Wboson   = dressedleptons[k].momentum()+neutrinos[0].momentum();

    double cosLepNeut;
    double Wboson_mT = 0.;
    double norm = Wlepton.pT() * neutrinos[0].pt();
    if(norm != 0 ) {
      cosLepNeut = ( Wlepton.px()*neutrinos[0].px() + Wlepton.py()*neutrinos[0].py() )/norm ;
      if (1-cosLepNeut >= 0. ) Wboson_mT = sqrt( 2 * Wlepton.pT() * neutrinos[0].pt() * (1-cosLepNeut ) );
    }

    //---- CUTS (based on Table 1 WZ: 36.1 fb-1)----//
    if (Wlepton.pT() <= 20*GeV || Zlepton1.pT() <= 15*GeV || Zlepton2.pT() <= 15*GeV)     vetoEvent;
    if (Wlepton.abseta() >= 2.5 || Zlepton1.abseta() >= 2.5 || Zlepton2.abseta() >= 2.5)  vetoEvent;
    if (fabs(Zboson.mass()/GeV - MZ_PDG) >= 10.) vetoEvent;
    if (Wboson_mT <= 30*GeV)                     vetoEvent;
    if (deltaR(Zlepton1, Zlepton2) <= 0.2)       vetoEvent;
    if (deltaR(Zlepton1, Wlepton)  <= 0.3)       vetoEvent;
    if (deltaR(Zlepton2, Wlepton)  <= 0.3)       vetoEvent;

    double WZ_pt = (Zlepton1.pt() + Zlepton2.pt() + Wlepton.pt() + neutrinos[0].pt())/GeV;
```

```
    double WZ_px = (Zlepton1.px() + Zlepton2.px() + Wlepton.px() + neutrinos[0].px())/GeV;
    double WZ_py = (Zlepton1.py() + Zlepton2.py() + Wlepton.py() + neutrinos[0].py())/GeV;
    double mTWZ = sqrt( pow(WZ_pt, 2) - ( pow(WZ_px, 2) + pow(WZ_py,2) ) );
    double sumptleptons = (Zlepton1.pt() + Zlepton2.pt() + Wlepton.pt())/GeV;
    double dPhiWZTruth = acos(cos(Zboson.phi()-Wboson.phi()));



    //---- Jet CUTS----//
    ifilter_discard(jets, [&](const Jet& j) {
      return deltaR(j, Zlepton1) < 0.3 || deltaR(j, Zlepton2) < 0.3 || deltaR(j, Wlepton) < 0.3;
    });
    if (jets.size() < 2)  vetoEvent;
    if (jets[0].pT() < 40*GeV)  vetoEvent;

    // Selection of the second jet as the second highest pT jet and in opposite hemisphere with the fisrt jet
    FourMomentum jet_lead = jets[0].mom();
    FourMomentum jet_sublead;
    bool foundVBSJetPair = false;
    for (const Jet& jet : jets) {
      if(jet.pT() > 40*GeV && jet.eta()*jets[0].eta() < 0.) {
        jet_sublead = jet.mom();
        foundVBSJetPair = true;
        break;
      }
    }
    if (!foundVBSJetPair)  vetoEvent;

    const double mJJ = (jet_lead + jet_sublead).mass()/GeV;
    const double dphi_jj = acos(cos(jet_lead.phi() - jet_sublead.phi()));
    const double dyjj = fabs(jet_lead.rap() - jet_sublead.rap());

    //Plots in the SR
    if (mJJ < 500*GeV) vetoEvent;

    const size_t njets40 = filter_select(jets, Cuts::pT > 40*GeV).size();
    fillWithOverflow("Njets_VBS", njets40, 5.1);

    const double y_min = std::min(jet_lead.rap(), jet_sublead.rap());
    const double y_max = std::max(jet_lead.rap(), jet_sublead.rap());
    const size_t njetsGap = count(jets, [&](const Jet& j) {
      return  (j.rap() > y_min && j.rap() < y_max);
    });
    fillWithOverflow("Njets_gap", njetsGap, 3.1);

    fillWithOverflow("MTWZ", mTWZ, 551);
    fillWithOverflow("sumpt", sumptleptons, 501);
    fillWithOverflow("mjj", mJJ, 2001);

    _h["dphiWZ"]->fill(dPhiWZTruth);
    _h["dyjj"]->fill(dyjj);
    _h["dphijj"]->fill(dphi_jj);

  }


  void fillWithOverflow(const string& tag, const double value, const double overflow) {
    if (value < overflow)  _h[tag]->fill(value);
    else                   _h[tag]->fill(overflow);
  }
```

```
    }


    void finalize() {

      scale(_h, crossSectionPerEvent() / femtobarn);
      // unfortunately, no differential cross-sections were measured in this analysis
      for (auto &item : _h)  barchart(item.second, _s[item.first]);

    }


 //@}

  private:


    /// @name Histograms
    //@{

    map<string, Histo1DPtr> _h;
    map<string, Scatter2DPtr> _s;

    //@}

    double MZ_PDG = 91.1876;
    double MW_PDG = 80.385;
    double GammaZ_PDG = 2.4952;
    double GammaW_PDG = 2.085;

  };

  // The hook for the plugin system
  RIVET_DECLARE_PLUGIN(ATLAS_2018_I1711223);
}
```

The third step of the comparison is to do event-by-event comparisons between the two frameworks for some kinematical variables. Figure C.1 and Figure C.2 show the difference between the two frameworks for the compared kinematical variables for the $WZjj - EW$ and $WZjj - QCD$ processes accordingly.

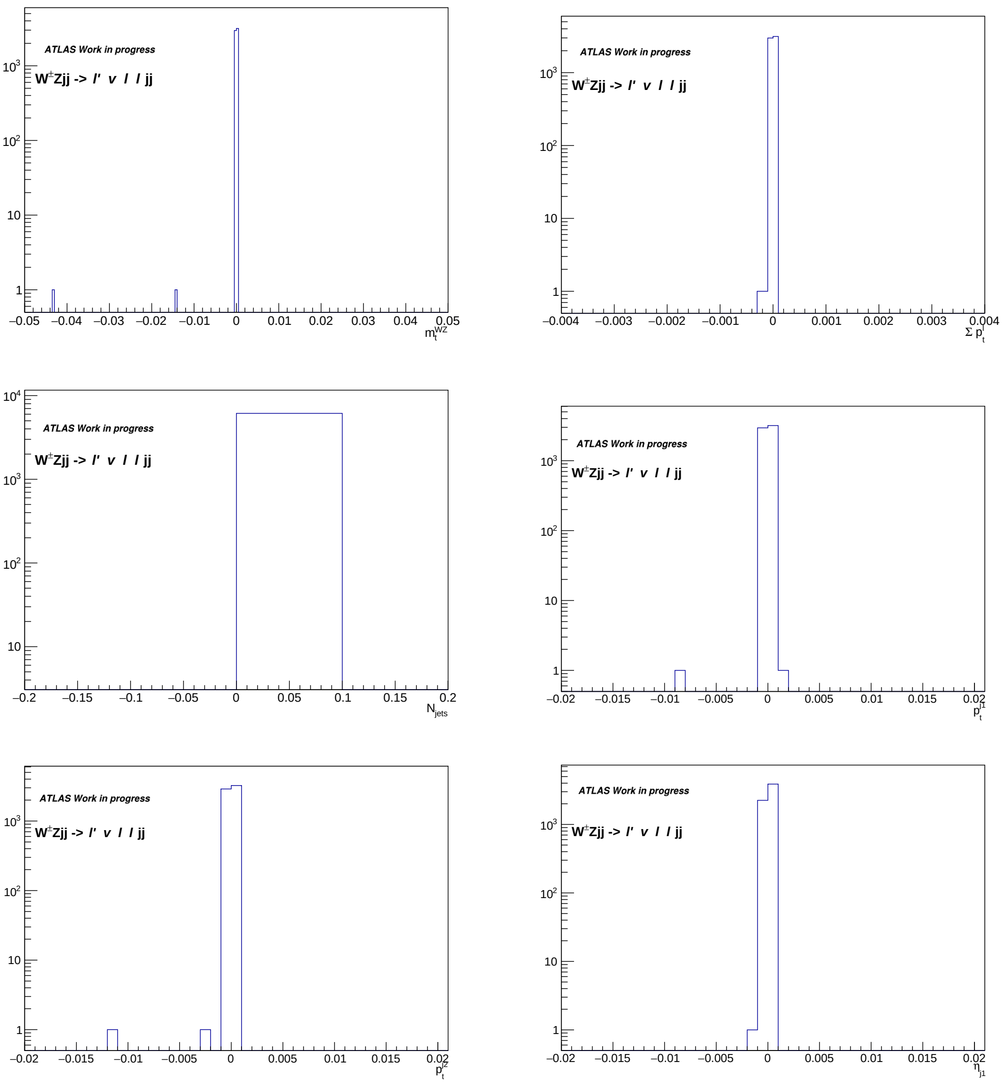

FIGURE C.1: Difference between the two frameworks for the compared kinematical variables for the $WZjj - EW$.

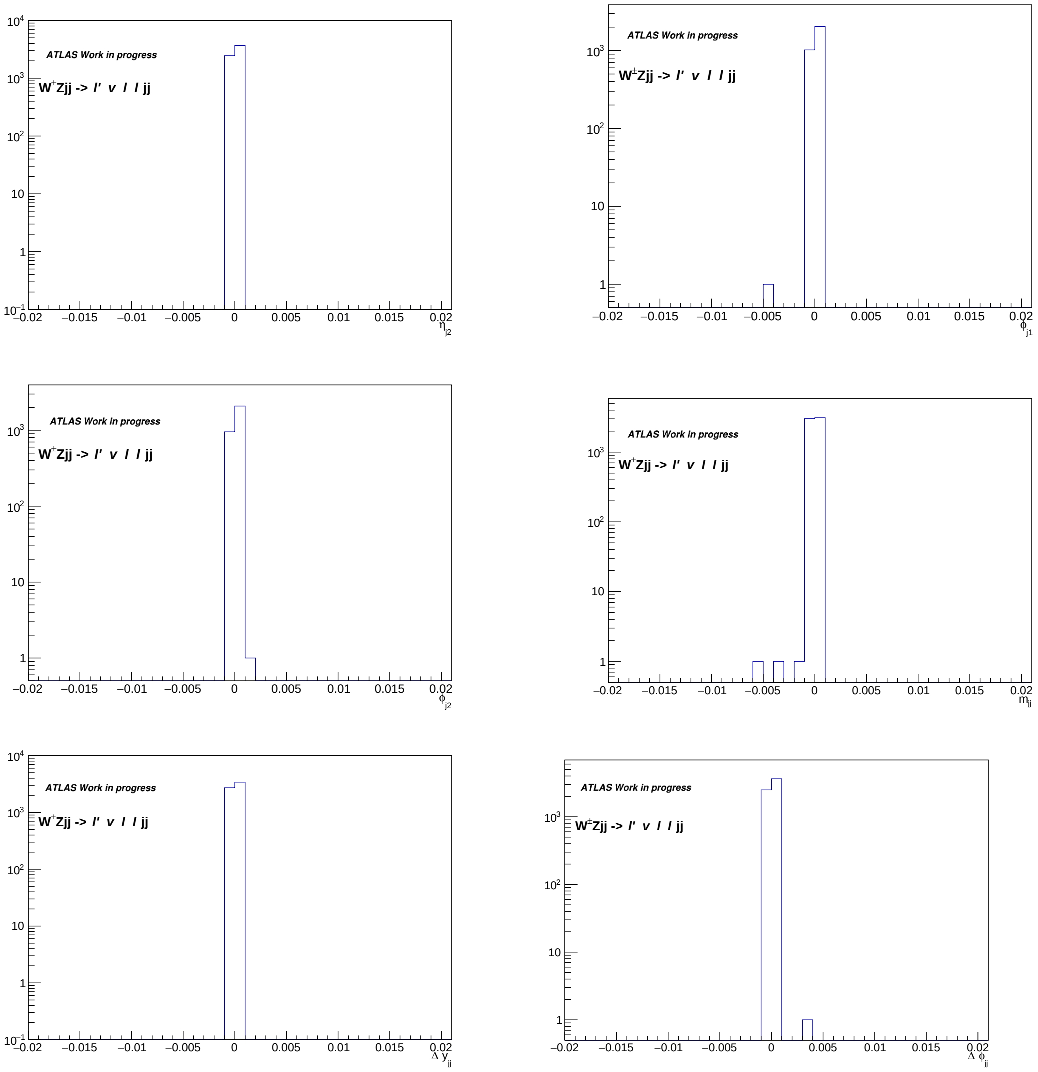

FIGURE C.1: Difference between the two frameworks for the compared kinematical variables for the $WZjj - EW$.

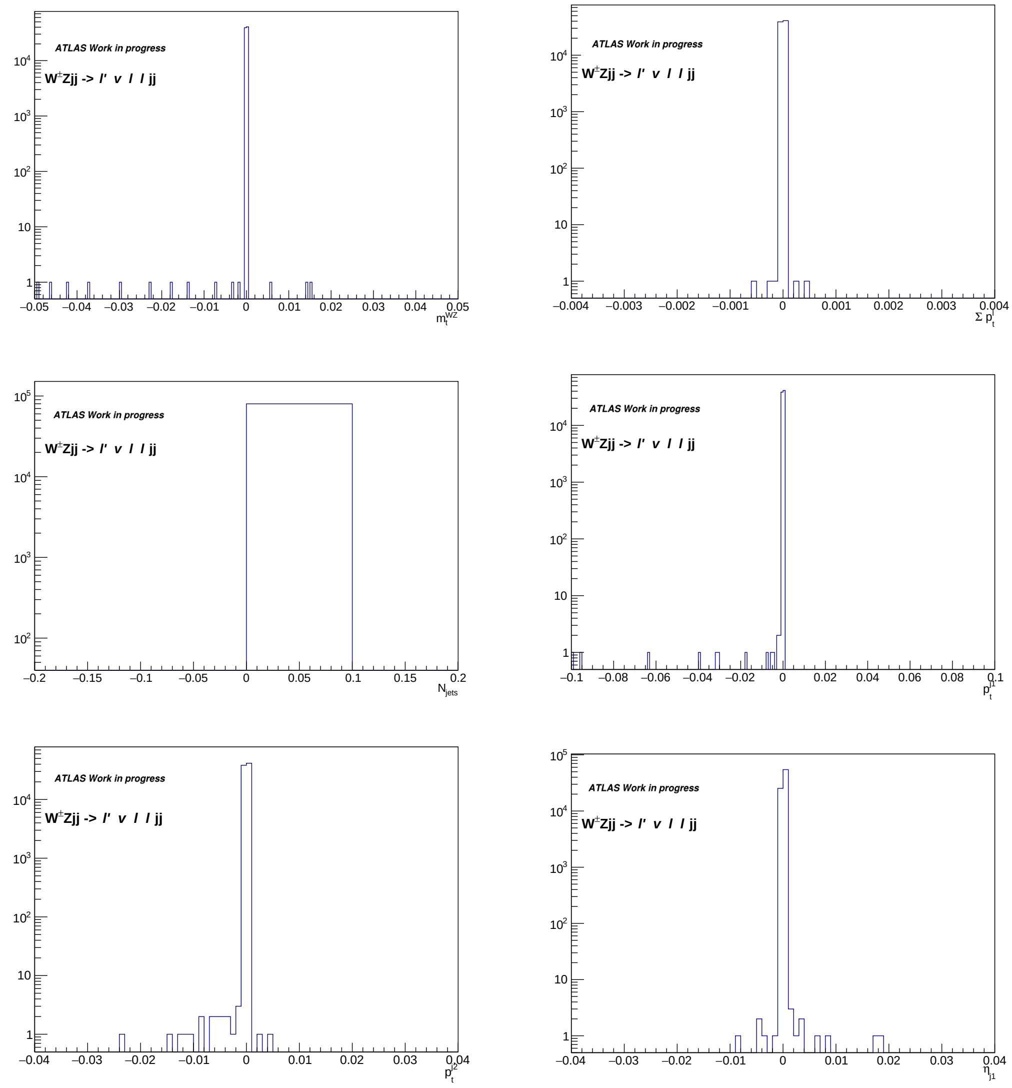

Figure C.2: Difference between the two frameworks for the compared kinematical variables for the $WZjj - QCD$.

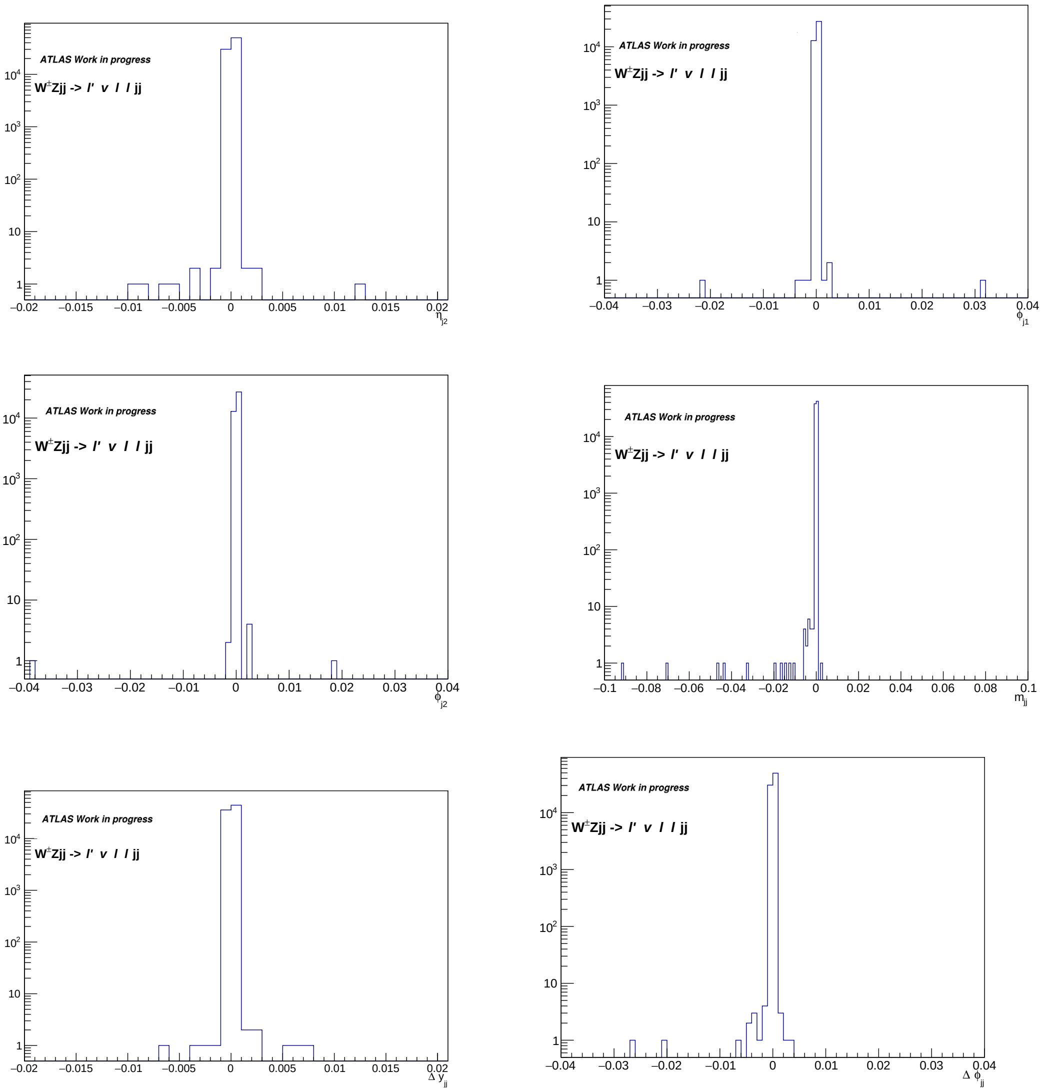

Figure C.2: Difference between the two frameworks for the compared kinematical variables for the $WZjj - QCD$.

Appendix D

Validation of the simulation of the the Micromegas and the sTGC detectors

As discussed in Section 3.2.4.1, a new detector, called New Small Wheel (NSW), was installed in ATLAS experiment at the the second long shutdown period (LS2) in 2019-2022. Since a new detector is installed, the validation of the simulation of the performance of the detector is a very crucial procedure. In the context of my authorship task, I focused to the validation of the digitized, simulated data and the reconstruction of the trajectories in the MicroMegas and sTGCs detectors located on the New Small Wheel (NSW) of the upgraded ATLAS Muon spectrometer.

Two frameworks are created for the validation of the simulation for the two subsystems of the NSW, the Micromegas (MM) and the sTGCs. These frameworks called MMTester [154] and STGCTester [155], respectively, and they are being used until today.

As a first step, some very basic MM-specific quantities were checked. The simulated events used for this study is the:
$group.det - muon.DiMuon10\_100GeV.ESD.rel21\_3\_13.FullATLAS.v001\_EXT1$, which is a di-muon sample with $|\eta| < 2.8$, with flat η and p_T $(10 - 100\ GeV)$ distributions. Firstly, Figure D.1 shows some basic quantities of the clusters belonging to a track (clusters on-track), while Figure D.2 shows the same quantities for clusters that don't belong to a track (clusters not on-track). Also, Figure D.3 depicts the track resolution (left) as well as the track resolution divided by its p_T (right).

After that, some basic variables of the reconstructed muons(ID and MS) were checked. Figure D.4 shows the number of the reconstructed muons, and their p_T, η and ϕ distributions.

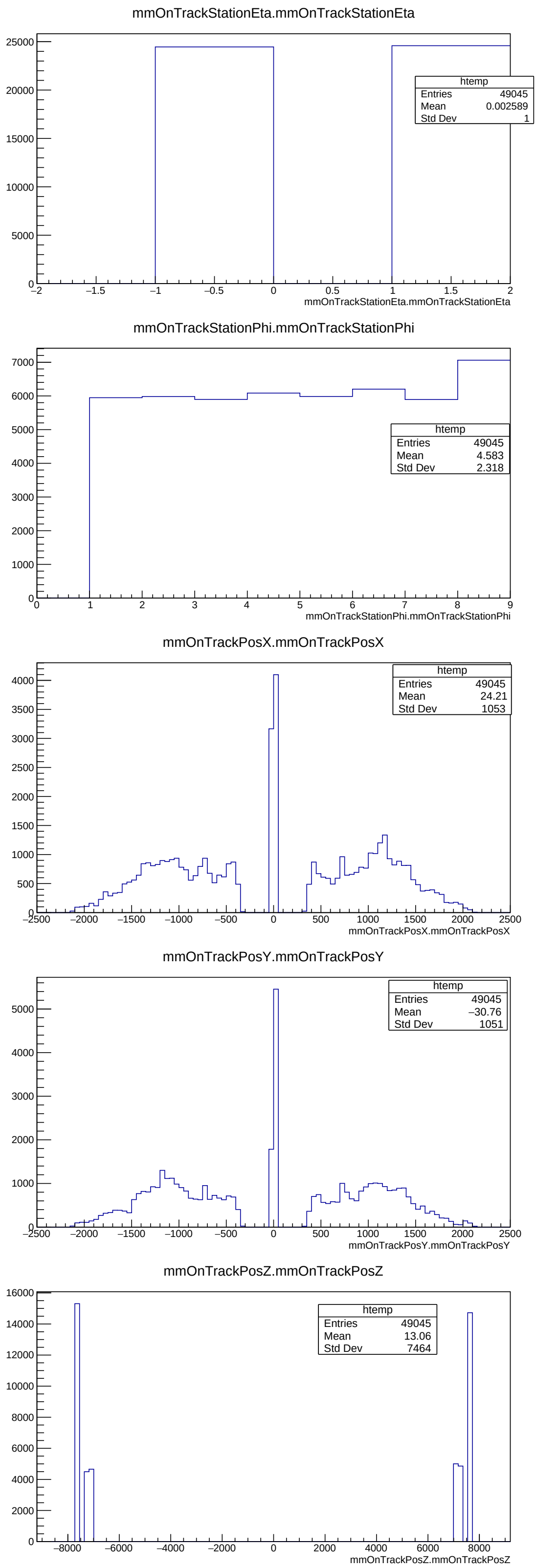

FIGURE D.1: Some very basic MM-specific quantities of the clusters belong to a track, as their η, ϕ, global position on the X axis, global position on the Y axis and global position on the Z axis.

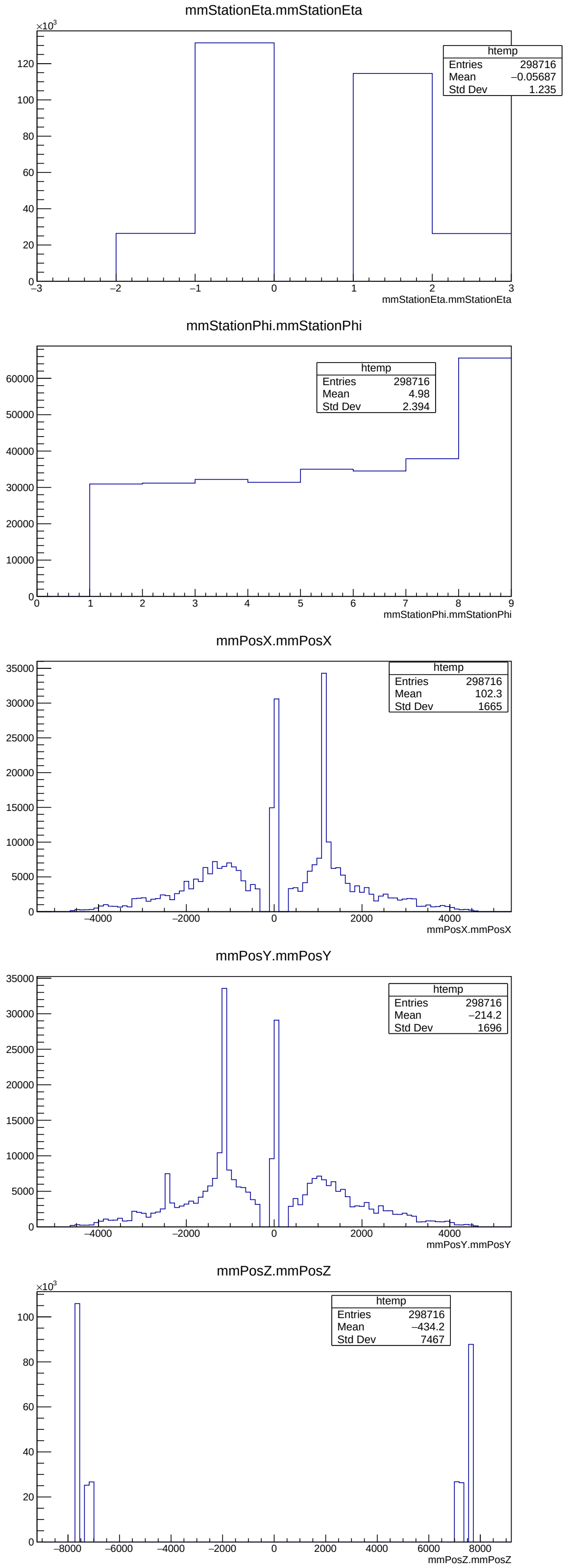

FIGURE D.2: Some very basic MM-specific quantities of the clusters that don't belong to a track, as their η, ϕ, global position on the X axis, global position on the Y axis and global position on the Z axis.

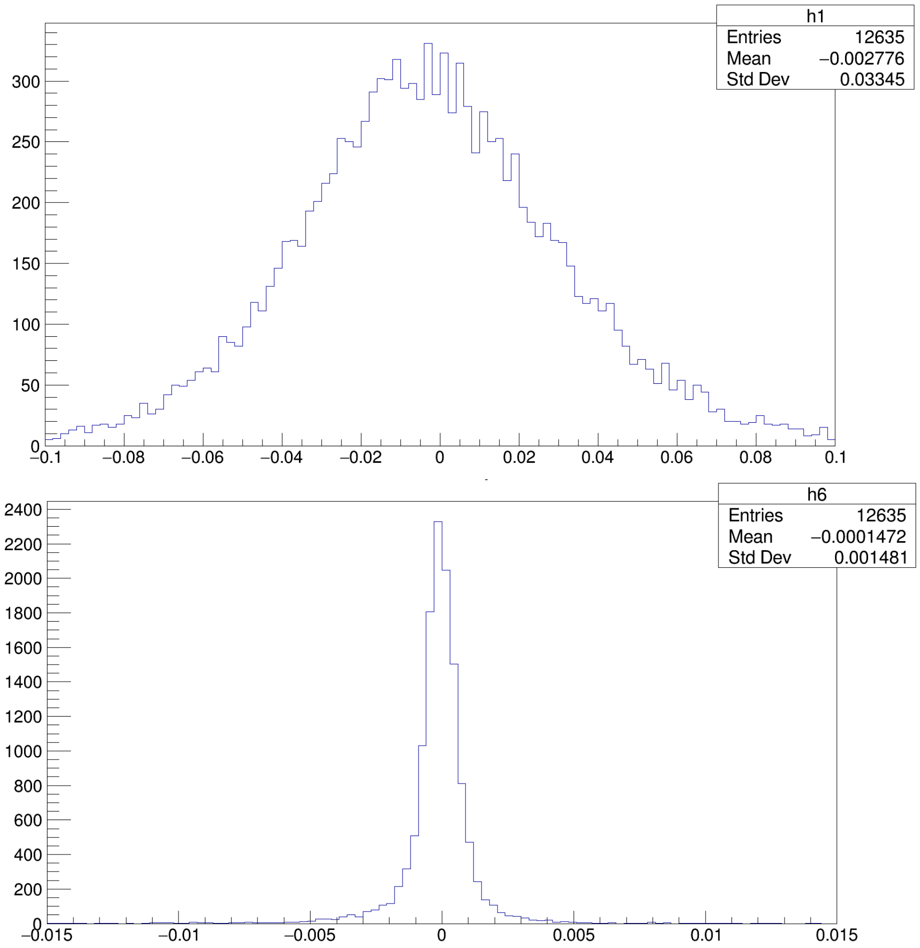

Figure D.3: Track resolution (left) as well as the track resolution divided by its p_T (right).

It is assumed that every reconstructed muon corresponds to a hit in the NSW, as we take into account only the first deposit of energy to the MM and sTGCs. Figure D.5 shows the global (distance from the interaction point) and local (distance from the corresponding detector e.g. MM) positions of the hits of the muons and Figure D.6 the local and global positions of the clusters, that were composed from the hits, on the MM. It can be noticed that not all the hits make a cluster.

As a next step the residual and pull in the X axis were computed. The residual is defined as the subtraction of the position X of the cluster and the position X of the simulated data(hits), while the pull as the residual divided by the error. They are both depicted in Figure D.7.

Figures D.8, D.9 and D.10 show exactly the same quantities for the sTGCs. It can be seen that the sTGCs have even fewer clusters and they are more problematic than MMs.

Moreover, some basic quantities of the primary track particles are studied. Primary particles called the particles which have produced form the primary p-p collision. The track of this particle depicts their course in the detector as simulated by e.g the GEANT generator [156]. Figure D.11 depicts the detector resolution defined as $\frac{p_T\ of\ truth\ particles - p_T\ of\ primary\ track\ particles}{p_T\ of\ truth\ particles}$

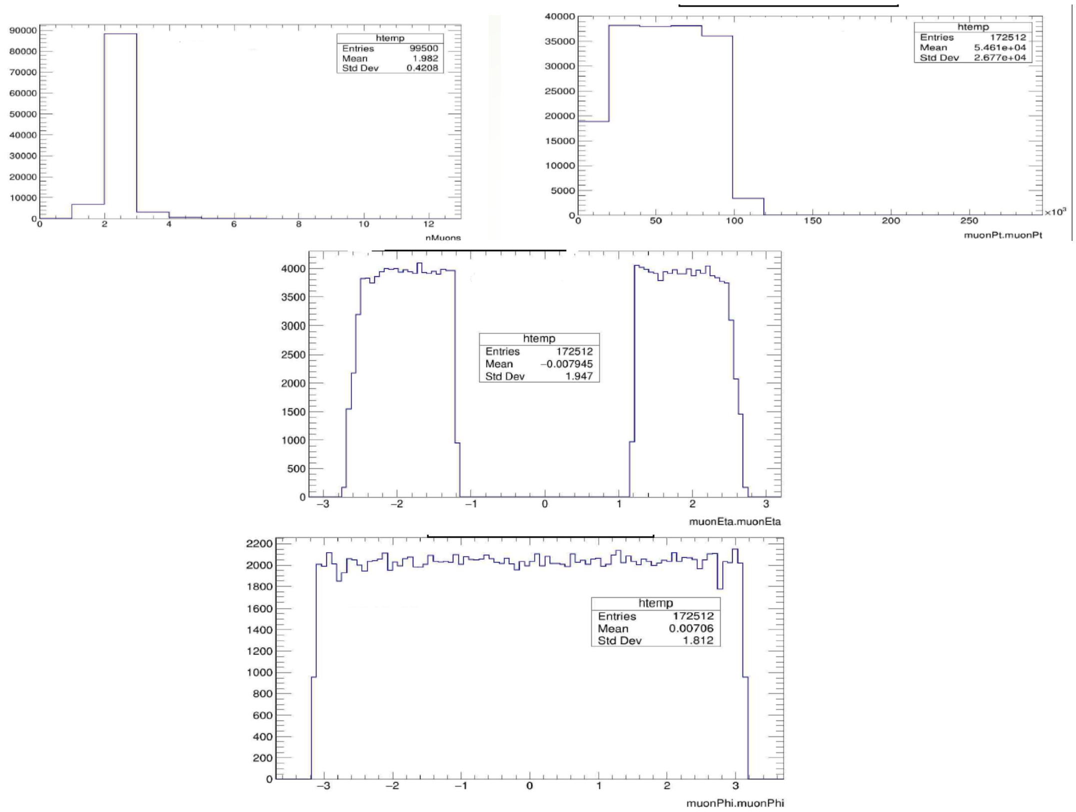

FIGURE D.4: Number of the reconstructed muons, and their p_T, η and ϕ distributions.

p_T, where the truth particles are the simulated particles at the interaction point before travelling across the detector, η and ϕ distributions of these particles.

Some more checks were done using two different samples: $group.detmuon.DiMuon10\_100GeV.ESD.2019-10-25.DigiNominal.v01\_EXT1$ and $group.detmuon.DiMuon10\_100GeV.ESD.2019-10-25.DigiNominal.uTPC.dHalf0p5.v04\_EXT1$. There are di-muon samples with $1.2 < |\eta| < 2.8$, with flat η and p_T $(10-100\,GeV)$ distributions.

First of all, the results for the first sample will be presented.

Firstly, for the MM, Figure D.12 shows the truth and track residuals, which are defined as the subtraction of position X of the cluster and the position X of the simulated data (hits) and the subtraction of position X of the cluster and the position X of the reconstructed track, respectively.

A very interesting variable is the width of the residuals as a function of η, p_T and ϕ of the primary track.

In order to plot the width of the residuals as a function of η, p_T and ϕ of primary track, the following strategy is adopted

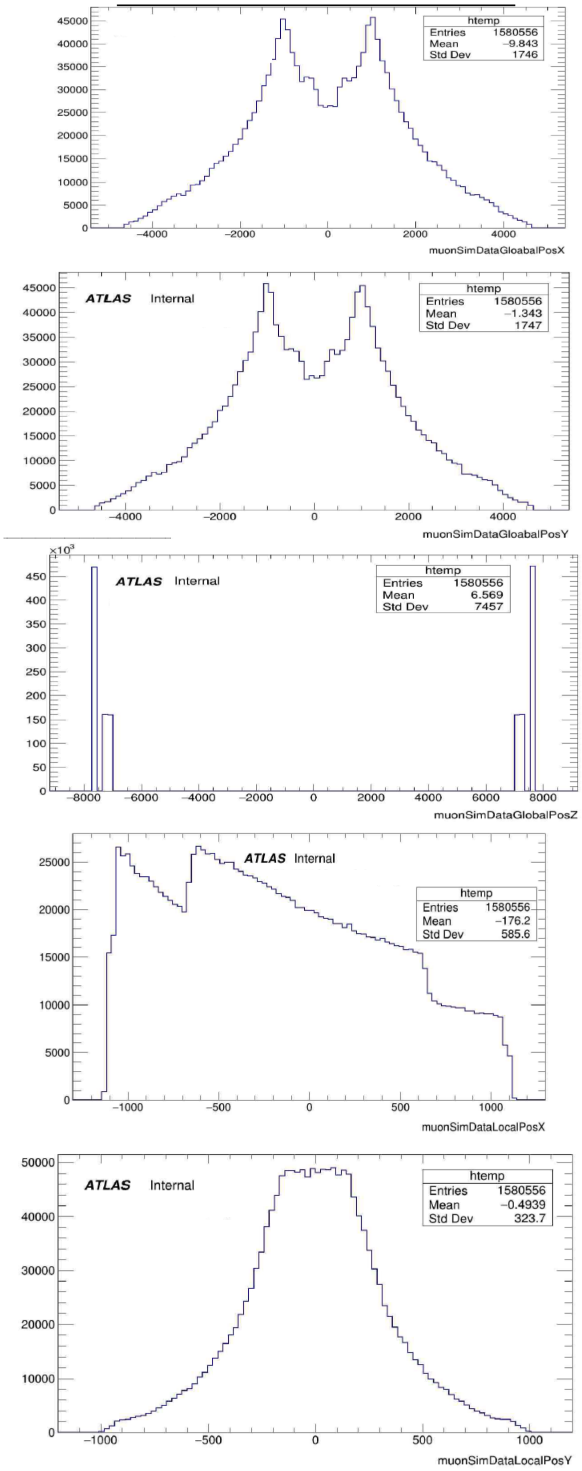

Figure D.5: Global (distance from the interaction point) and local (distance from the corresponding detector e.g. MM) positions of the hits of the muons on the MM.

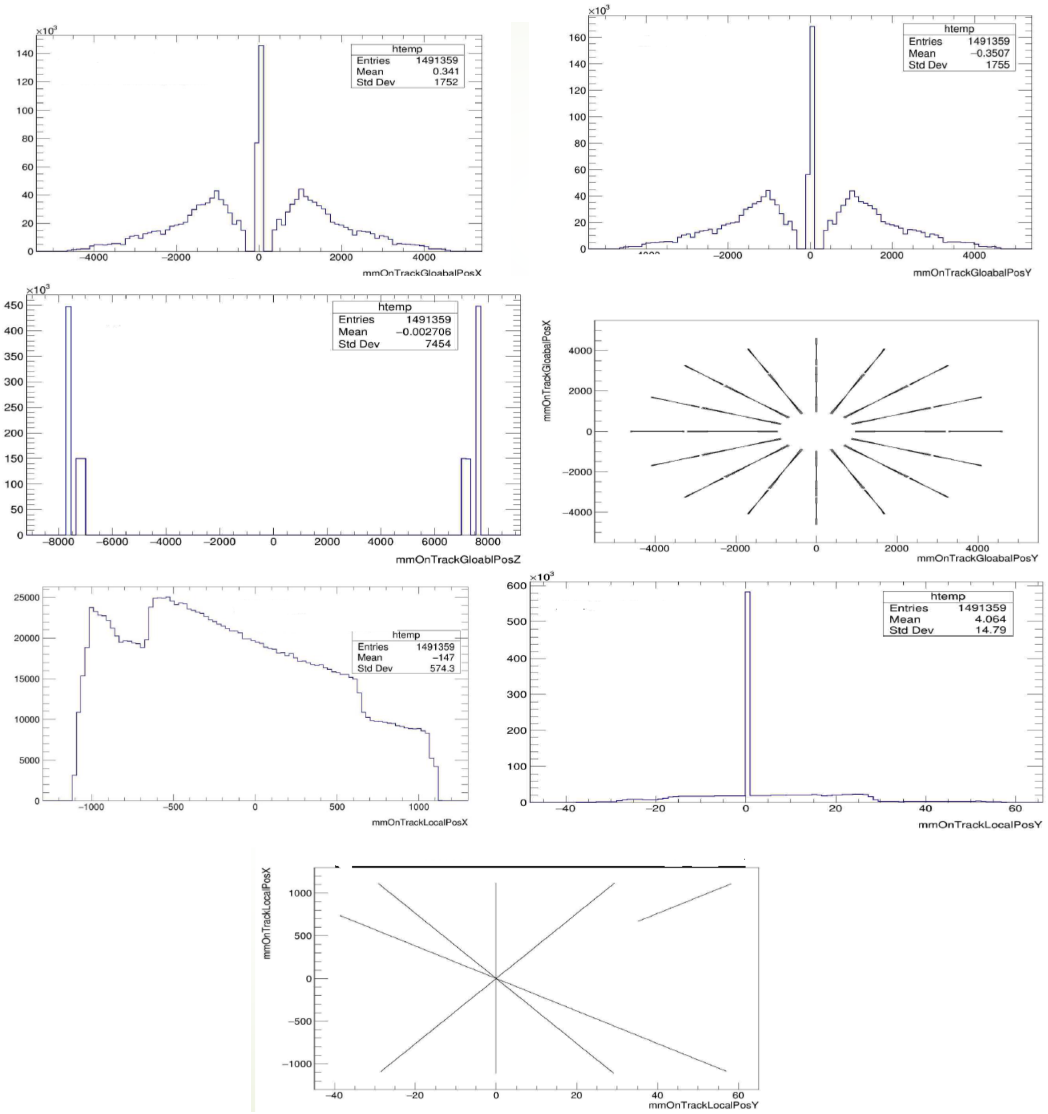

FIGURE D.6: Global (distance from the interaction point) and local (distance from the corresponding detector e.g. MM) positions of clusters, that were composed from the hits, on the MM.

η it is splitted into 8 bins with range $1.2 < |\eta| < 2.8$ and then the residuals as a function of η are plotted.

p_T it is splitted into 7 bins with range $0 < p_T < 105 GeV$ and then the residuals as a function of p_T are plotted.

ϕ t is splitted into 4 bins with range $3.2 < \phi < 3.2$ and then the residuals as a function of ϕ are plotted.

After that, Gaussian fits are applied to the residuals. In some plots, the fit has more narrow range than the total range of the residuals in order to apply a better fit, as it is depicted in the examples of Figure D.13.

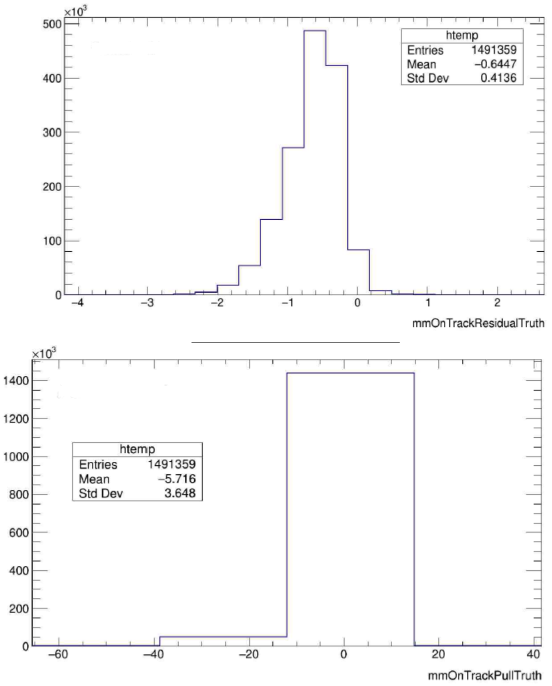

FIGURE D.7: Residual (left) and pull (right) in the X axis were computed (MM). The residual is defined as the subtraction of the position X of the cluster and the position X of the simulated data(hits), while the pull as the residual divided by the error.

Finally, the widths of the Gaussian fits as a function of η, p_T and ϕ are shown in Figure D.14 for the truth residuals and in Figure D.15 for the track residuals. It can be noticed that the width of both of the residuals as a function of eta reduces as the eta increases, while the widths of the residuals as a function ofp_T and ϕ are flat.

Continuing, the same study with the same strategy was performed for the sTGCs. Figure D.16 shows the truth and track residuals, while the widths of the Gaussian fits as a function of η, p_T and ϕ are shown in Figure D.17 for the truth residuals and in Figure D.18 for the track residuals. It can be noted that the peak of the truth residual is not around zero and that the distribution is asymmetric. Also, it can be seen that for the truth residual the last bin of η has a large width value, while the widths of the residuals as a function ofp_T and ϕ are flat.

Finally, the truth and track residuals for the MM and sTGCs for the second sample are shown in Figures D.19 and D.20, respectively. It can be noted that the peak of the truth and track residuals is not around zero.

To conclude, my contribution to the NSW project was the validation of the digitized, simulated data and the reconstruction of the trajectories in the MicroMegas and sTGCs detectors located on the New Small Wheel (NSW) of the upgraded ATLAS Muon spectrometer. As shown, the simulation of the two main subdetectors of NSW, needed some improvement in order to be considered as final.

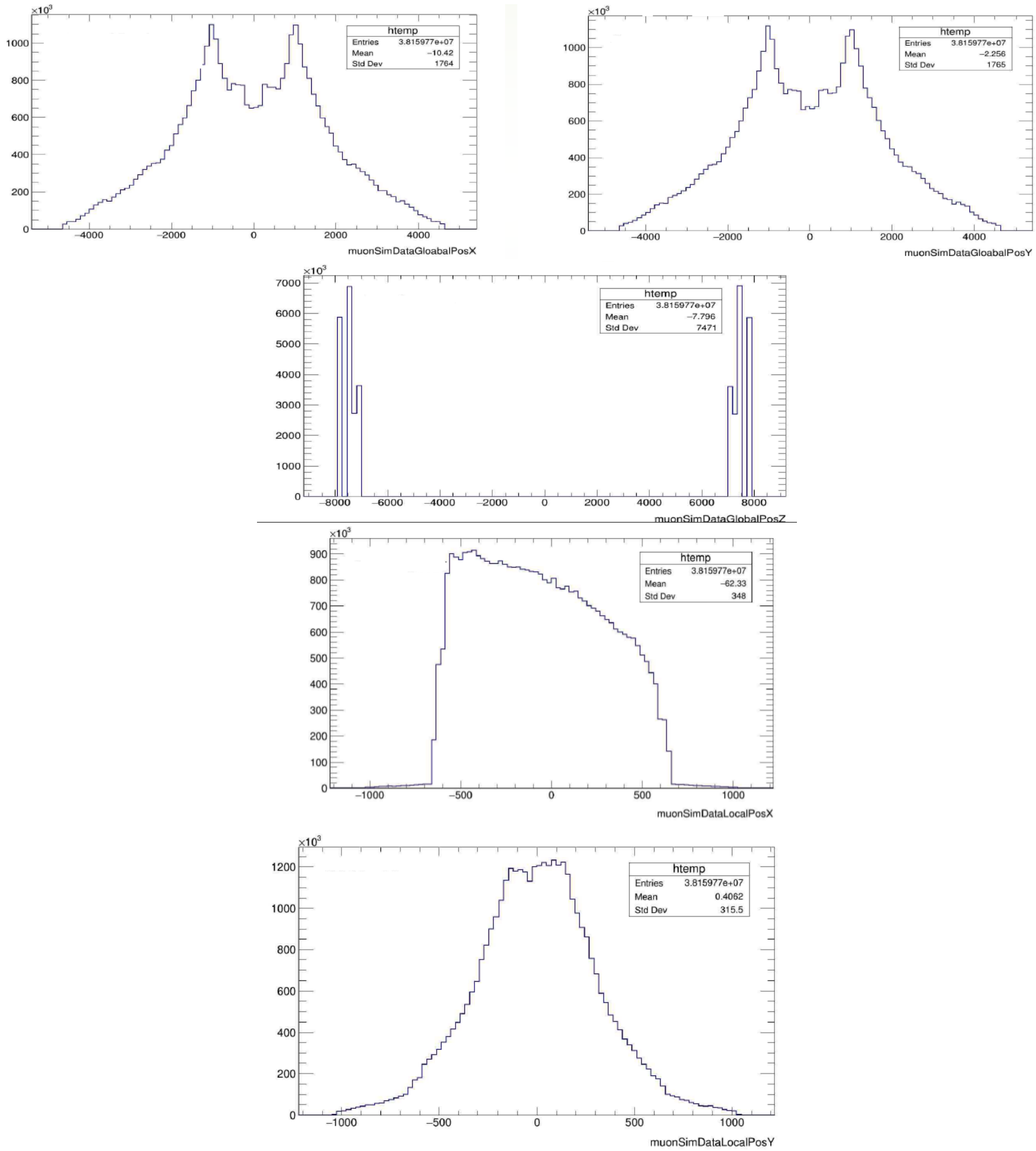

FIGURE D.8: Global (distance from the interaction point) and local (distance from the corresponding detector e.g. MM) positions of the hits of the muons on the sTGCs.

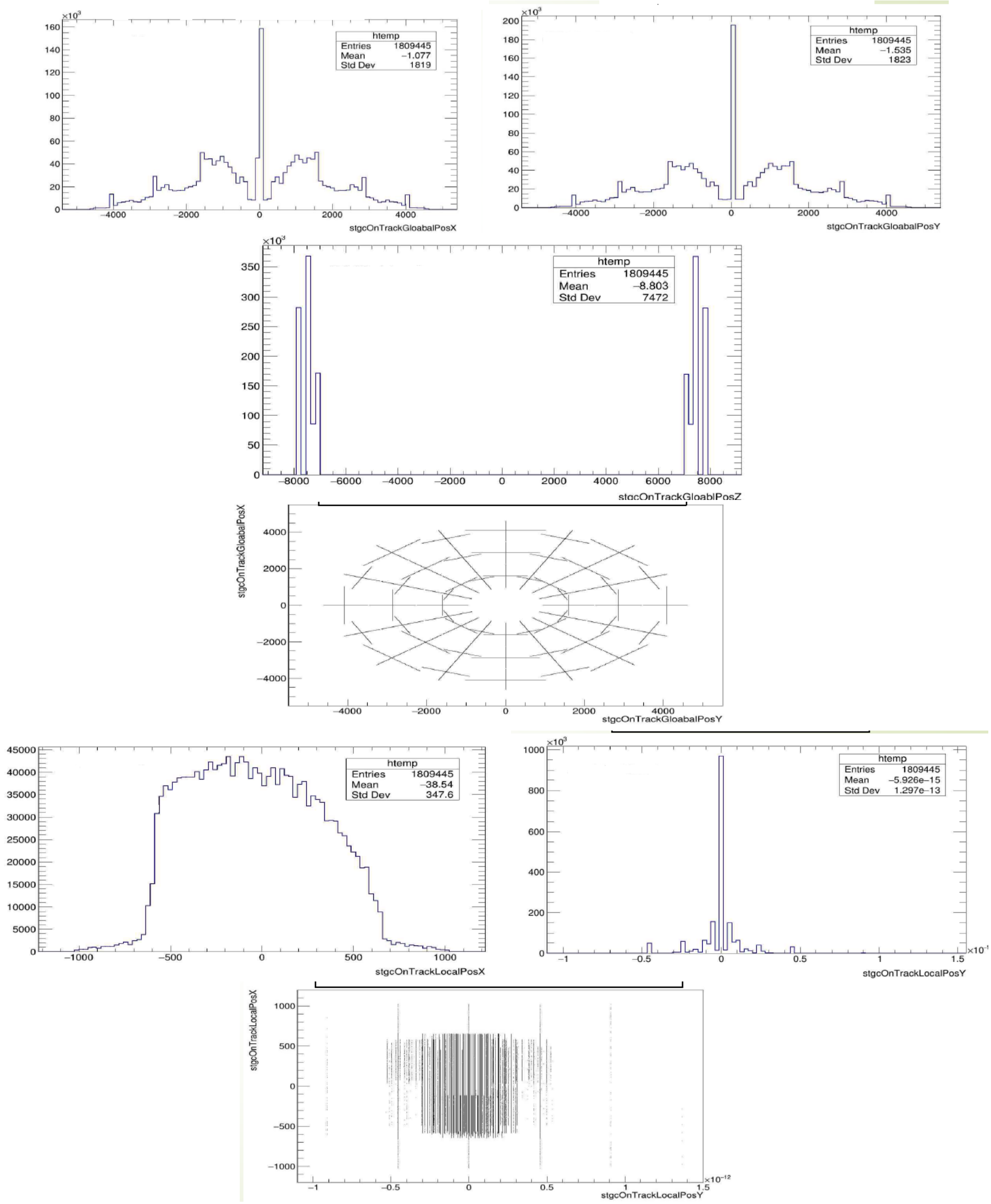

Figure D.9: Global (distance from the interaction point) and local (distance from the corresponding detector e.g. MM) positions of clusters, that were composed from the hits, on the sTGCs.

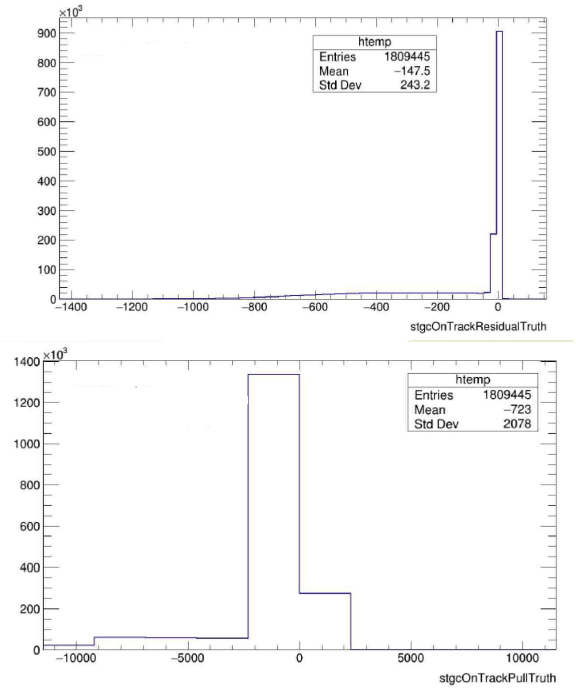

FIGURE D.10: Residual (left) and pull (right) in the X axis were computed sTGCs). The residual is defined as the subtraction of the position X of the cluster and the position X of the simulated data(hits), while the pull as the residual divided by the error.

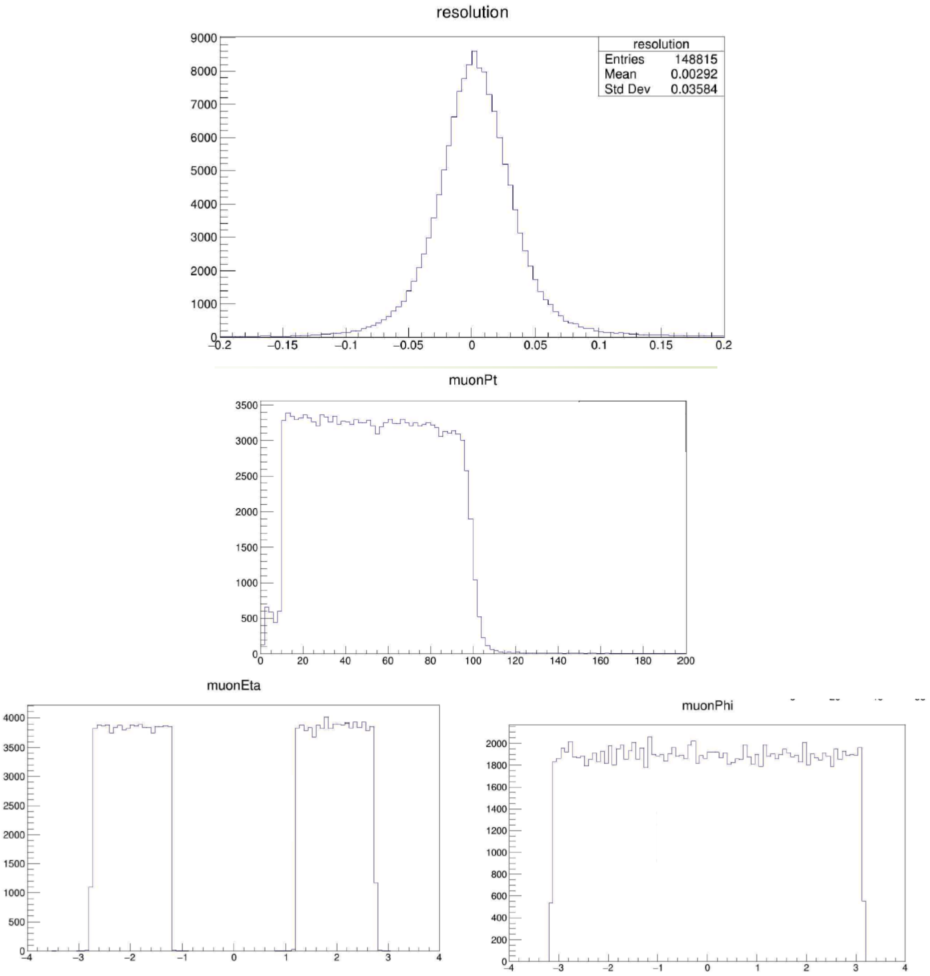

FIGURE D.11: Detector resolution, p_T, η and ϕ distributions of primary track particle.

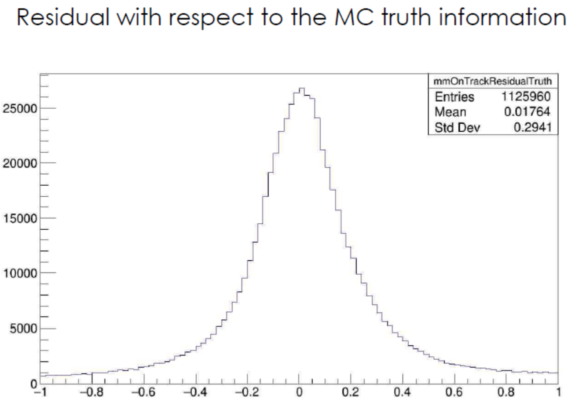
Residual with respect to the MC truth information

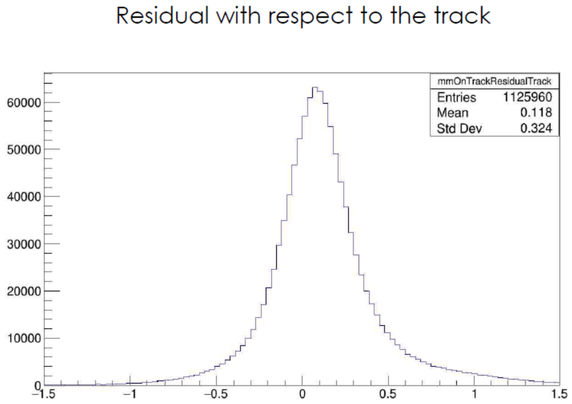
Residual with respect to the track

FIGURE D.12: Truth and track residuals, which are defined as the subtraction of position X of the cluster and the position X of the simulated data (hits) and the subtraction of position X of the cluster and the position X of the reconstructed track (MM).

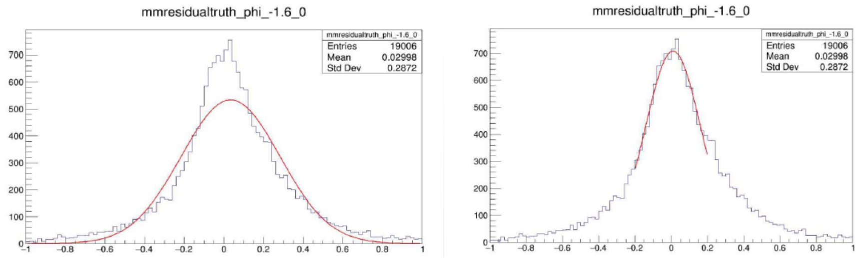
mmresidualtruth_phi_-1.6_0

mmresidualtruth_phi_-1.6_0

FIGURE D.13: Examples of two different Gaussian fits applied to the same bin of the truth residual as a function of ϕ (MM).

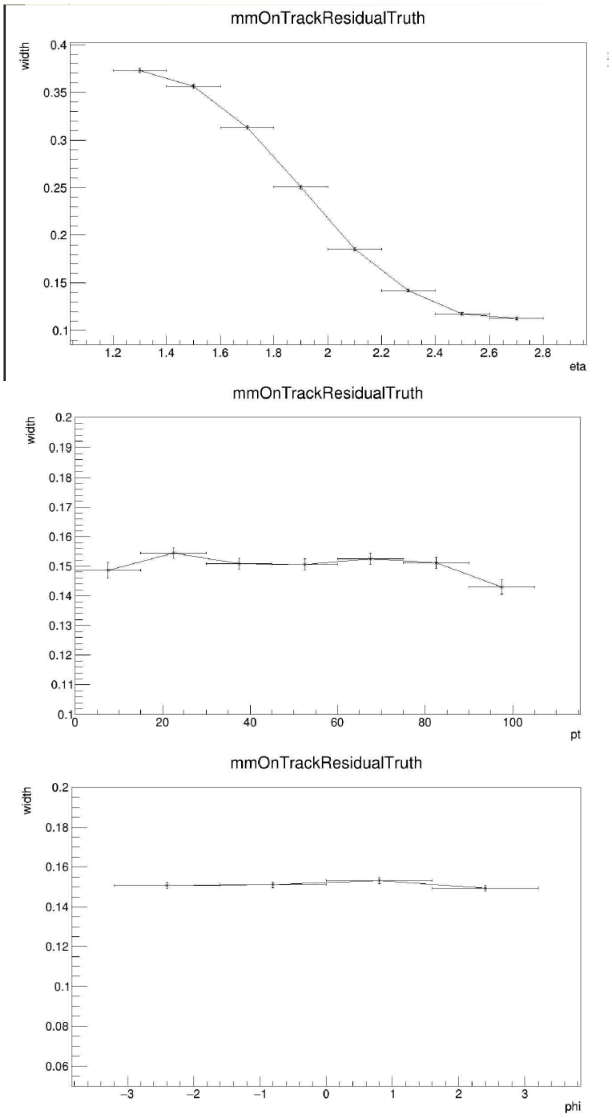

FIGURE D.14: Widths of the Gaussian fits as a function of η, p_T and ϕ for the truth residuals (MM).

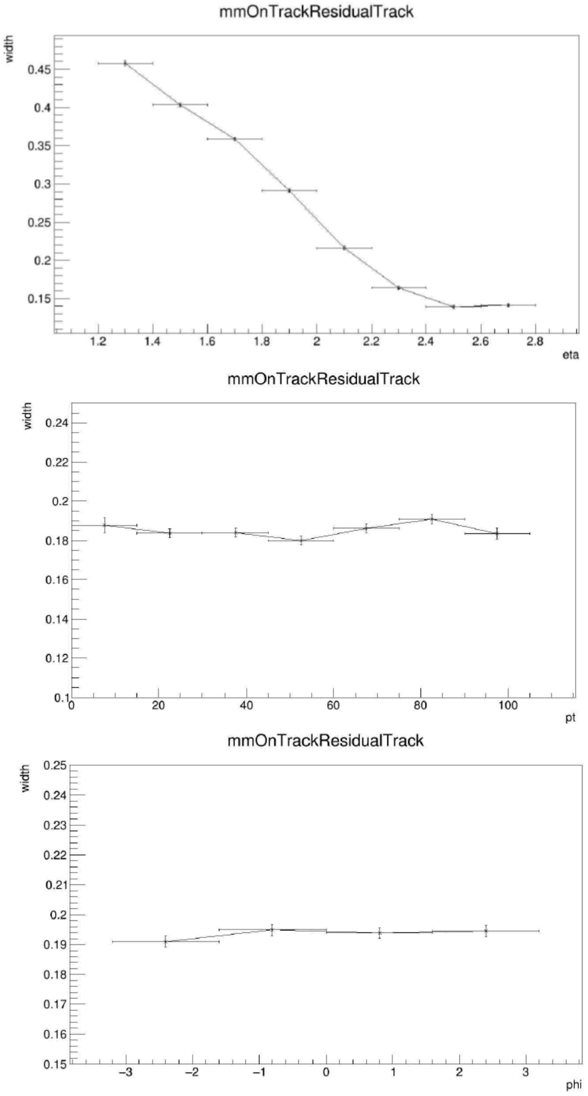

Figure D.15: Widths of the Gaussian fits as a function of η, p_T and ϕ for the track residuals (MM).

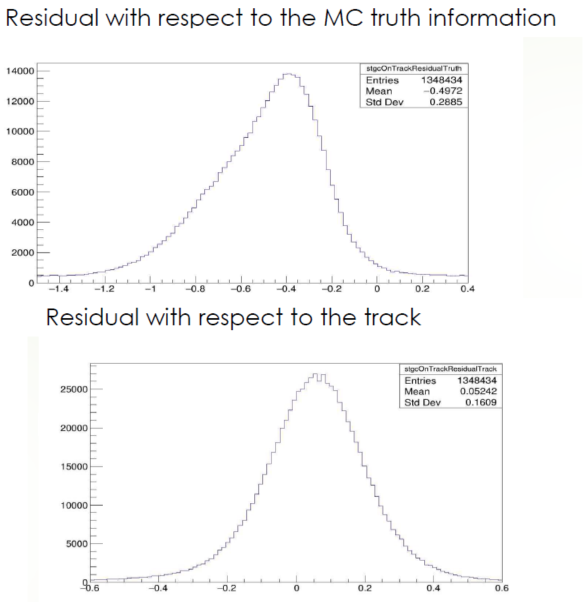

Figure D.16: Truth and track residuals , which are defined as the subtraction of position X of the cluster and the position X of the simulated data (hits) and the subtraction of position X of the cluster and the position X of the reconstructed track (sTGCs).

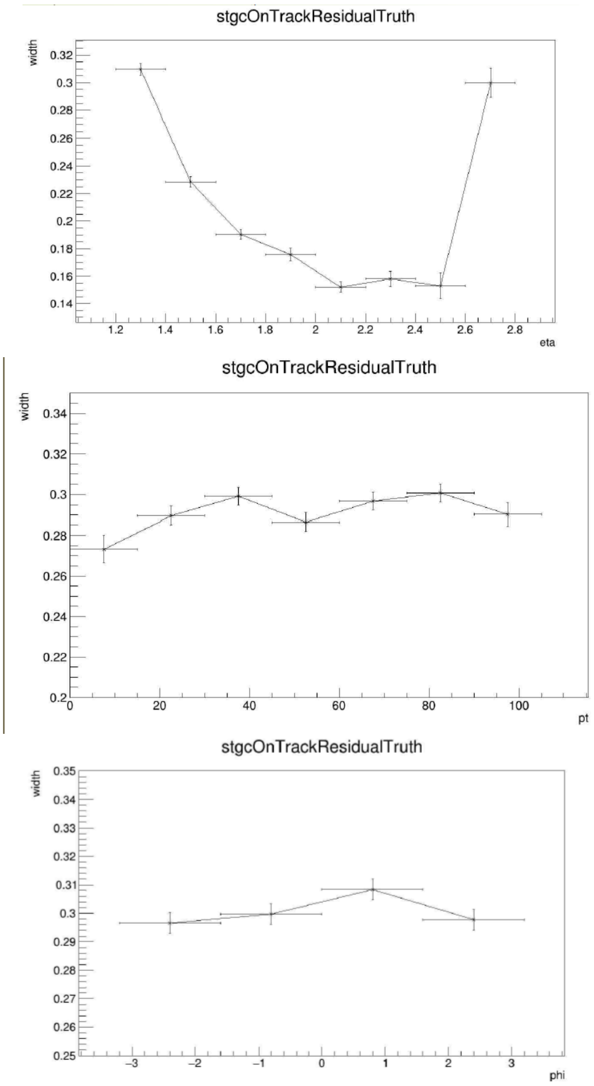

FIGURE D.17: Widths of the Gaussian fits as a function of η, p_T and ϕ for the truth residuals (sTGCs).

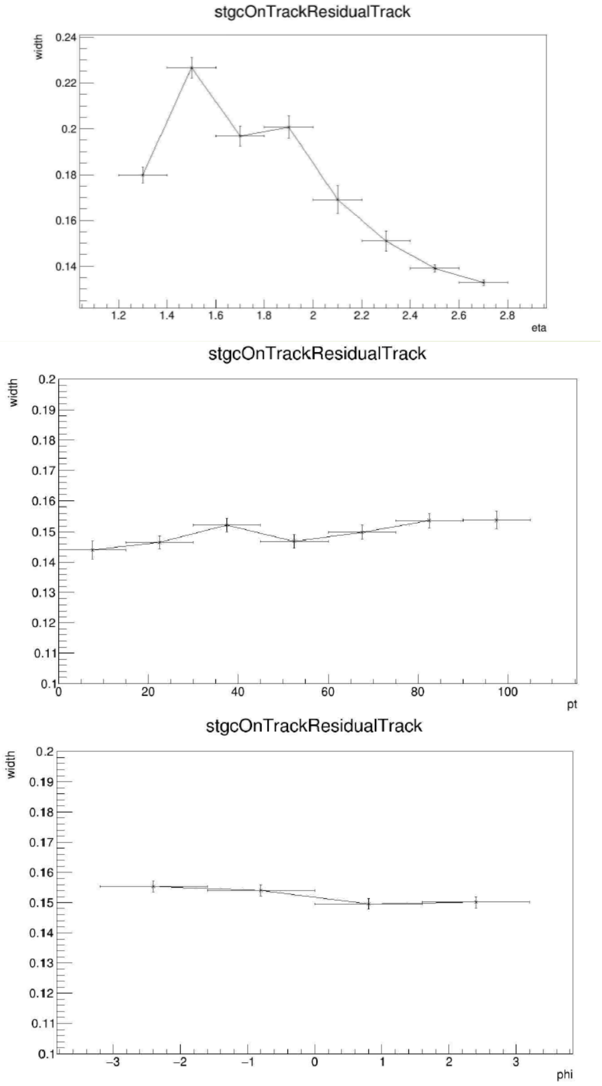

FIGURE D.18: Widths of the Gaussian fits as a function of η, p_T and ϕ for the track residuals (sTGCs).

Residual with respect to the MC truth information

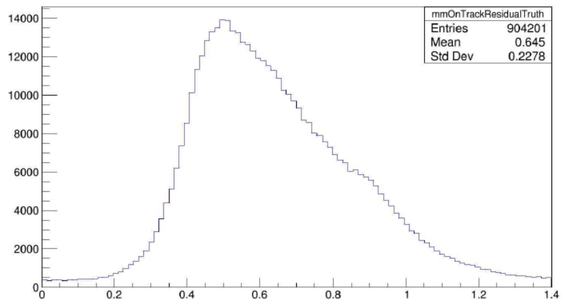

Residual with respect to the track

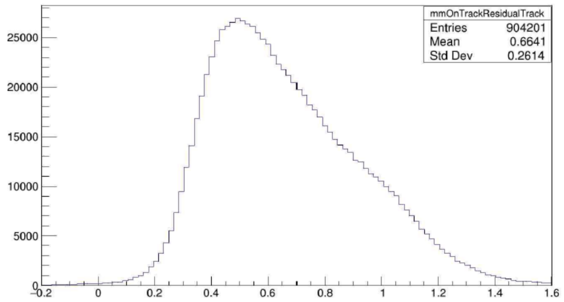

Figure D.19: Truth and track residuals , which are defined as the subtraction of position X of the cluster and the position X of the simulated data (hits) and the subtraction of position X of the cluster and the position X of the reconstructed track (MM).

Residual with respect to the MC truth information

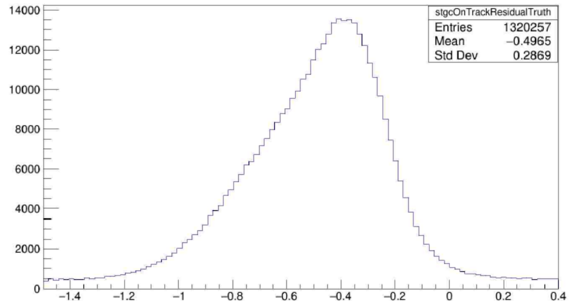

Residual with respect to the track

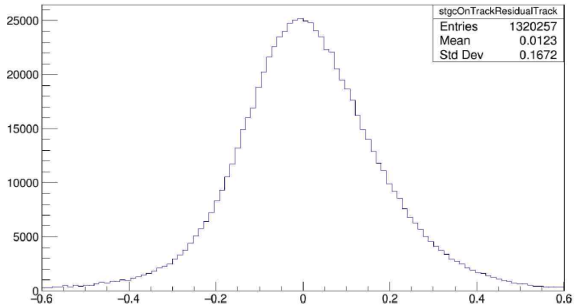

Figure D.20: Truth and track residuals , which are defined as the subtraction of position X of the cluster and the position X of the simulated data (hits) and the subtraction of position X of the cluster and the position X of the reconstructed track (sTGCs).

Appendix E

JobOptions for samples production using dimension-6 EFT operators

E.1 WZ inclusive dimension-6 EFT production

```
import MadGraphControl.MadGraphUtils

MadGraphControl.MadGraphUtils.MADGRAPH_PDFSETTING={
    'central_pdf': 260000, # the lhapf id of the central pdf, see https://lhapdf.hepforge.org/pdfsets
    'pdf_variations':[260000,90400,13100,25200], # pdfs for which all variations (error sets) will be included as weights
    'alternative_pdfs':[266000,265000], # pdfs for which only the central set will be included as weights
    'scale_variations':[0.5,1.,2.], # variations of muR and muF wrt the central scale, all combinations of muF and muR will be evaluated
    'alternative_dynamic_scales' : [1,2,3,4],
}
from MadGraphControl.MadGraphUtils import *

evgenConfig.generators = ["MadGraph", "Pythia8", "EvtGen"]

evgenConfig.keywords = ['SM', 'diboson', 'WZ', '3lepton','dim6','SMEFTatNLO']
evgenConfig.contact = ['eirini.kasimi@cern.ch']

if eft_order == "interference":
    runName = 'lllv_SMEFTatNLO_int'
    description = 'MadGraph_lllv_SMEFTatNLO_int'
    mgproc = """
generate p p > mu+ mu- mu+ vm QCD=0 QED=4 NP^2==2 @0
add process p p > mu+ mu- mu- vm~ QCD=0 QED=4 NP^2==2 @0
add process p p > mu+ mu- e+ ve QCD=0 QED=4 NP^2==2 @0
add process p p > mu+ mu- e- ve~ QCD=0 QED=4 NP^2==2 @0
add process p p > mu+ mu- ta+ vt QCD=0 QED=4 NP^2==2 @0
add process p p > mu+ mu- ta- vt~ QCD=0 QED=4 NP^2==2 @0
add process p p > e+ e- e+ ve QCD=0 QED=4 NP^2==2 @0
add process p p > e+ e- e- ve~ QCD=0 QED=4 NP^2==2 @0
add process p p > e+ e- mu+ vm QCD=0 QED=4 NP^2==2 @0
add process p p > e+ e- mu- vm~ QCD=0 QED=4 NP^2==2 @0
add process p p > e+ e- ta+ vt QCD=0 QED=4 NP^2==2 @0
add process p p > e+ e- ta- vt~ QCD=0 QED=4 NP^2==2 @0
add process p p > ta+ ta- ta+ vt QCD=0 QED=4 NP^2==2 @0
add process p p > ta+ ta- ta- vt~ QCD=0 QED=4 NP^2==2 @0
add process p p > ta+ ta- mu+ vm QCD=0 QED=4 NP^2==2 @0
add process p p > ta+ ta- mu- vm~ QCD=0 QED=4 NP^2==2 @0
add process p p > ta+ ta- e+ ve QCD=0 QED=4 NP^2==2 @0
add process p p > ta+ ta- e- ve~ QCD=0 QED=4 NP^2==2 @0"""
elif eft_order == "quadratic_cross":
    runName = 'lllv_SMEFTatNLO_quad'
    description = 'MadGraph_lllv_SMEFTatNLO_quad'
    mgproc = """
generate p p > mu+ mu- mu+ vm QCD=0 QED=4 NP^2==4 @0
add process p p > mu+ mu- mu- vm~ QCD=0 QED=4 NP^2==4 @0
add process p p > mu+ mu- e+ ve QCD=0 QED=4 NP^2==4 @0
add process p p > mu+ mu- e- ve~ QCD=0 QED=4 NP^2==4 @0
add process p p > mu+ mu- ta+ vt QCD=0 QED=4 NP^2==4 @0
add process p p > mu+ mu- ta- vt~ QCD=0 QED=4 NP^2==4 @0
add process p p > e+ e- e+ ve QCD=0 QED=4 NP^2==4 @0
add process p p > e+ e- e- ve~ QCD=0 QED=4 NP^2==4 @0
add process p p > e+ e- mu+ vm QCD=0 QED=4 NP^2==4 @0
add process p p > e+ e- mu- vm~ QCD=0 QED=4 NP^2==4 @0
add process p p > e+ e- ta+ vt QCD=0 QED=4 NP^2==4 @0
add process p p > e+ e- ta- vt~ QCD=0 QED=4 NP^2==4 @0
add process p p > ta+ ta- ta+ vt QCD=0 QED=4 NP^2==4 @0
add process p p > ta+ ta- ta- vt~ QCD=0 QED=4 NP^2==4 @0
add process p p > ta+ ta- mu+ vm QCD=0 QED=4 NP^2==4 @0
add process p p > ta+ ta- mu- vm~ QCD=0 QED=4 NP^2==4 @0
add process p p > ta+ ta- e+ ve QCD=0 QED=4 NP^2==4 @0
add process p p > ta+ ta- e- ve~ QCD=0 QED=4 NP^2==4 @0"""
    pass
else:
```

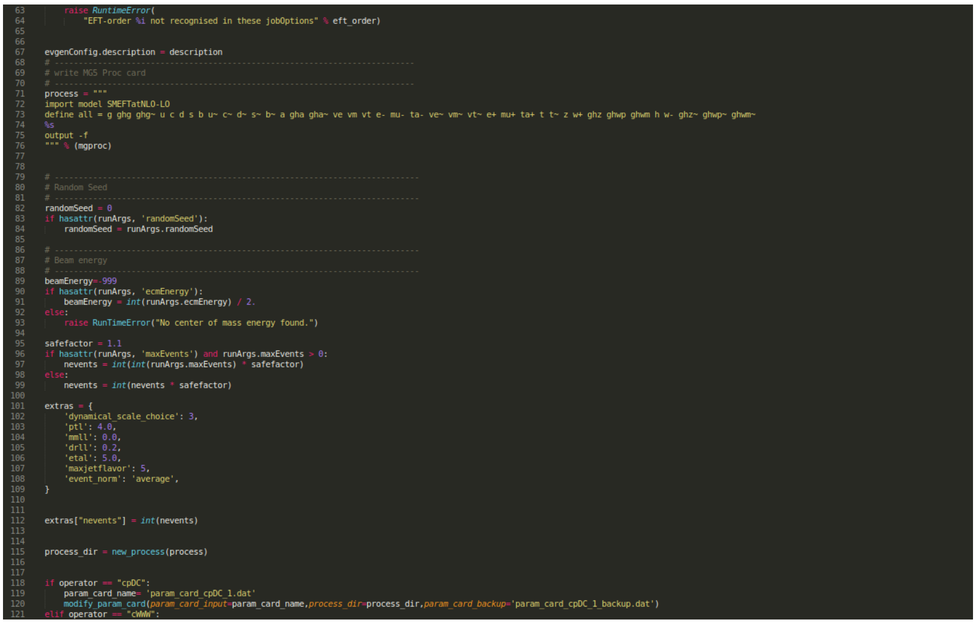

```
    raise RuntimeError(
        "EFT-order %i not recognised in these jobOptions" % eft_order)


evgenConfig.description = description
# ---------------------------------------------------------------------------
# write MG5 Proc card
# ---------------------------------------------------------------------------
process = """
import model SMEFTatNLO-LO
define all = g ghg ghg~ u c d s b u~ c~ d~ s~ b~ a gha gha~ ve vm vt e- mu- ta- ve~ vm~ vt~ e+ mu+ ta+ t t~ z w+ ghz ghwp ghwm h w- ghz~ ghwp~ ghwm~
%s
output -f
""" % (mgproc)


# ---------------------------------------------------------------------------
# Random Seed
# ---------------------------------------------------------------------------
randomSeed = 0
if hasattr(runArgs, 'randomSeed'):
    randomSeed = runArgs.randomSeed

# ---------------------------------------------------------------------------
# Beam energy
# ---------------------------------------------------------------------------
beamEnergy=-999
if hasattr(runArgs, 'ecmEnergy'):
    beamEnergy = int(runArgs.ecmEnergy) / 2.
else:
    raise RunTimeError("No center of mass energy found.")

safefactor = 1.1
if hasattr(runArgs, 'maxEvents') and runArgs.maxEvents > 0:
    nevents = int(int(runArgs.maxEvents) * safefactor)
else:
    nevents = int(nevents * safefactor)

extras = {
    'dynamical_scale_choice': 3,
    'ptl': 4.0,
    'mmll': 0.0,
    'drll': 0.2,
    'etal': 5.0,
    'maxjetflavor': 5,
    'event_norm': 'average',
}


extras["nevents"] = int(nevents)


process_dir = new_process(process)


if operator == "cpDC":
    param_card_name= 'param_card_cpDC_1.dat'
    modify_param_card(param_card_input=param_card_name,process_dir=process_dir,param_card_backup='param_card_cpDC_1_backup.dat')
elif operator == "cWWW":
```

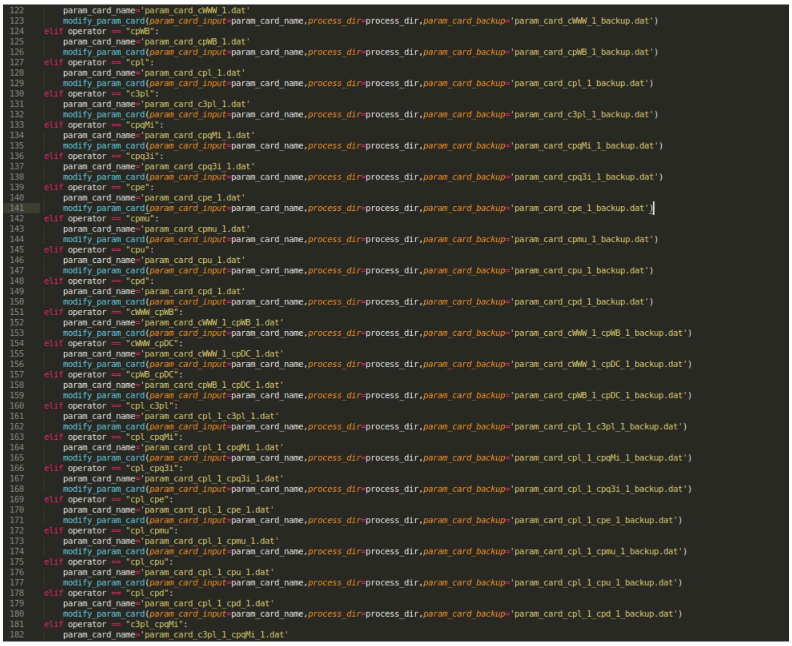

```
    param_card_name='param_card_cWWW_1.dat'
    modify_param_card(param_card_input=param_card_name,process_dir=process_dir,param_card_backup='param_card_cWWW_1_backup.dat')
elif operator == "cpWB":
    param_card_name='param_card_cpWB_1.dat'
    modify_param_card(param_card_input=param_card_name,process_dir=process_dir,param_card_backup='param_card_cpWB_1_backup.dat')
elif operator == "cpl":
    param_card_name='param_card_cpl_1.dat'
    modify_param_card(param_card_input=param_card_name,process_dir=process_dir,param_card_backup='param_card_cpl_1_backup.dat')
elif operator == "c3pl":
    param_card_name='param_card_c3pl_1.dat'
    modify_param_card(param_card_input=param_card_name,process_dir=process_dir,param_card_backup='param_card_c3pl_1_backup.dat')
elif operator == "cpqMi":
    param_card_name='param_card_cpqMi_1.dat'
    modify_param_card(param_card_input=param_card_name,process_dir=process_dir,param_card_backup='param_card_cpqMi_1_backup.dat')
elif operator == "cpq3i":
    param_card_name='param_card_cpq3i_1.dat'
    modify_param_card(param_card_input=param_card_name,process_dir=process_dir,param_card_backup='param_card_cpq3i_1_backup.dat')
elif operator == "cpe":
    param_card_name='param_card_cpe_1.dat'
    modify_param_card(param_card_input=param_card_name,process_dir=process_dir,param_card_backup='param_card_cpe_1_backup.dat')
elif operator == "cpmu":
    param_card_name='param_card_cpmu_1.dat'
    modify_param_card(param_card_input=param_card_name,process_dir=process_dir,param_card_backup='param_card_cpmu_1_backup.dat')
elif operator == "cpu":
    param_card_name='param_card_cpu_1.dat'
    modify_param_card(param_card_input=param_card_name,process_dir=process_dir,param_card_backup='param_card_cpu_1_backup.dat')
elif operator == "cpd":
    param_card_name='param_card_cpd_1.dat'
    modify_param_card(param_card_input=param_card_name,process_dir=process_dir,param_card_backup='param_card_cpd_1_backup.dat')
elif operator == "cWWW_cpWB":
    param_card_name='param_card_cWWW_1_cpWB_1.dat'
    modify_param_card(param_card_input=param_card_name,process_dir=process_dir,param_card_backup='param_card_cWWW_1_cpWB_1_backup.dat')
elif operator == "cWWW_cpDC":
    param_card_name='param_card_cWWW_1_cpDC_1.dat'
    modify_param_card(param_card_input=param_card_name,process_dir=process_dir,param_card_backup='param_card_cWWW_1_cpDC_1_backup.dat')
elif operator == "cpWB_cpDC":
    param_card_name='param_card_cpWB_1_cpDC_1.dat'
    modify_param_card(param_card_input=param_card_name,process_dir=process_dir,param_card_backup='param_card_cpWB_1_cpDC_1_backup.dat')
elif operator == "cpl_c3pl":
    param_card_name='param_card_cpl_1_c3pl_1.dat'
    modify_param_card(param_card_input=param_card_name,process_dir=process_dir,param_card_backup='param_card_cpl_1_c3pl_1_backup.dat')
elif operator == "cpl_cpqMi":
    param_card_name='param_card_cpl_1_cpqMi_1.dat'
    modify_param_card(param_card_input=param_card_name,process_dir=process_dir,param_card_backup='param_card_cpl_1_cpqMi_1_backup.dat')
elif operator == "cpl_cpq3i":
    param_card_name='param_card_cpl_1_cpq3i_1.dat'
    modify_param_card(param_card_input=param_card_name,process_dir=process_dir,param_card_backup='param_card_cpl_1_cpq3i_1_backup.dat')
elif operator == "cpl_cpe":
    param_card_name='param_card_cpl_1_cpe_1.dat'
    modify_param_card(param_card_input=param_card_name,process_dir=process_dir,param_card_backup='param_card_cpl_1_cpe_1_backup.dat')
elif operator == "cpl_cpmu":
    param_card_name='param_card_cpl_1_cpmu_1.dat'
    modify_param_card(param_card_input=param_card_name,process_dir=process_dir,param_card_backup='param_card_cpl_1_cpmu_1_backup.dat')
elif operator == "cpl_cpu":
    param_card_name='param_card_cpl_1_cpu_1.dat'
    modify_param_card(param_card_input=param_card_name,process_dir=process_dir,param_card_backup='param_card_cpl_1_cpu_1_backup.dat')
elif operator == "cpl_cpd":
    param_card_name='param_card_cpl_1_cpd_1.dat'
    modify_param_card(param_card_input=param_card_name,process_dir=process_dir,param_card_backup='param_card_cpl_1_cpd_1_backup.dat')
elif operator == "c3pl_cpqMi":
    param_card_name='param_card_c3pl_1_cpqMi_1.dat'
```

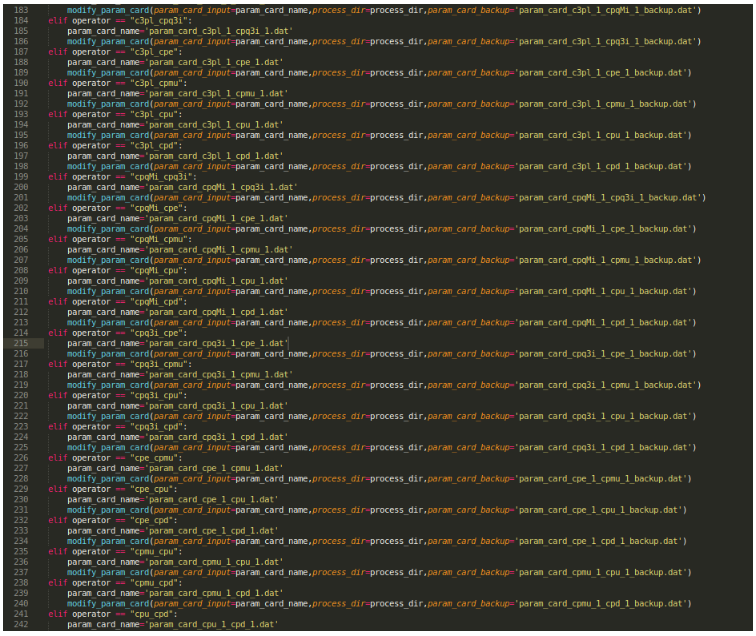

```
    modify_param_card(param_card_input=param_card_name,process_dir=process_dir,param_card_backup='param_card_c3pl_1_cpqMi_1_backup.dat')
elif operator == "c3pl_cpq3i":
    param_card_name='param_card_c3pl_1_cpq3i_1.dat'
    modify_param_card(param_card_input=param_card_name,process_dir=process_dir,param_card_backup='param_card_c3pl_1_cpq3i_1_backup.dat')
elif operator == "c3pl_cpe":
    param_card_name='param_card_c3pl_1_cpe_1.dat'
    modify_param_card(param_card_input=param_card_name,process_dir=process_dir,param_card_backup='param_card_c3pl_1_cpe_1_backup.dat')
elif operator == "c3pl_cpmu":
    param_card_name='param_card_c3pl_1_cpmu_1.dat'
    modify_param_card(param_card_input=param_card_name,process_dir=process_dir,param_card_backup='param_card_c3pl_1_cpmu_1_backup.dat')
elif operator == "c3pl_cpu":
    param_card_name='param_card_c3pl_1_cpu_1.dat'
    modify_param_card(param_card_input=param_card_name,process_dir=process_dir,param_card_backup='param_card_c3pl_1_cpu_1_backup.dat')
elif operator == "c3pl_cpd":
    param_card_name='param_card_c3pl_1_cpd_1.dat'
    modify_param_card(param_card_input=param_card_name,process_dir=process_dir,param_card_backup='param_card_c3pl_1_cpd_1_backup.dat')
elif operator == "cpqMi_cpq3i":
    param_card_name='param_card_cpqMi_1_cpq3i_1.dat'
    modify_param_card(param_card_input=param_card_name,process_dir=process_dir,param_card_backup='param_card_cpqMi_1_cpq3i_1_backup.dat')
elif operator == "cpqMi_cpe":
    param_card_name='param_card_cpqMi_1_cpe_1.dat'
    modify_param_card(param_card_input=param_card_name,process_dir=process_dir,param_card_backup='param_card_cpqMi_1_cpe_1_backup.dat')
elif operator == "cpqMi_cpmu":
    param_card_name='param_card_cpqMi_1_cpmu_1.dat'
    modify_param_card(param_card_input=param_card_name,process_dir=process_dir,param_card_backup='param_card_cpqMi_1_cpmu_1_backup.dat')
elif operator == "cpqMi_cpu":
    param_card_name='param_card_cpqMi_1_cpu_1.dat'
    modify_param_card(param_card_input=param_card_name,process_dir=process_dir,param_card_backup='param_card_cpqMi_1_cpu_1_backup.dat')
elif operator == "cpqMi_cpd":
    param_card_name='param_card_cpqMi_1_cpd_1.dat'
    modify_param_card(param_card_input=param_card_name,process_dir=process_dir,param_card_backup='param_card_cpqMi_1_cpd_1_backup.dat')
elif operator == "cpq3i_cpe":
    param_card_name='param_card_cpq3i_1_cpe_1.dat'
    modify_param_card(param_card_input=param_card_name,process_dir=process_dir,param_card_backup='param_card_cpq3i_1_cpe_1_backup.dat')
elif operator == "cpq3i_cpmu":
    param_card_name='param_card_cpq3i_1_cpmu_1.dat'
    modify_param_card(param_card_input=param_card_name,process_dir=process_dir,param_card_backup='param_card_cpq3i_1_cpmu_1_backup.dat')
elif operator == "cpq3i_cpu":
    param_card_name='param_card_cpq3i_1_cpu_1.dat'
    modify_param_card(param_card_input=param_card_name,process_dir=process_dir,param_card_backup='param_card_cpq3i_1_cpu_1_backup.dat')
elif operator == "cpq3i_cpd":
    param_card_name='param_card_cpq3i_1_cpd_1.dat'
    modify_param_card(param_card_input=param_card_name,process_dir=process_dir,param_card_backup='param_card_cpq3i_1_cpd_1_backup.dat')
elif operator == "cpe_cpmu":
    param_card_name='param_card_cpe_1_cpmu_1.dat'
    modify_param_card(param_card_input=param_card_name,process_dir=process_dir,param_card_backup='param_card_cpe_1_cpmu_1_backup.dat')
elif operator == "cpe_cpu":
    param_card_name='param_card_cpe_1_cpu_1.dat'
    modify_param_card(param_card_input=param_card_name,process_dir=process_dir,param_card_backup='param_card_cpe_1_cpu_1_backup.dat')
elif operator == "cpe_cpd":
    param_card_name='param_card_cpe_1_cpd_1.dat'
    modify_param_card(param_card_input=param_card_name,process_dir=process_dir,param_card_backup='param_card_cpe_1_cpd_1_backup.dat')
elif operator == "cpmu_cpu":
    param_card_name='param_card_cpmu_1_cpu_1.dat'
    modify_param_card(param_card_input=param_card_name,process_dir=process_dir,param_card_backup='param_card_cpmu_1_cpu_1_backup.dat')
elif operator == "cpmu_cpd":
    param_card_name='param_card_cpmu_1_cpd_1.dat'
    modify_param_card(param_card_input=param_card_name,process_dir=process_dir,param_card_backup='param_card_cpmu_1_cpd_1_backup.dat')
elif operator == "cpu_cpd":
    param_card_name='param_card_cpu_1_cpd_1.dat'
```

```
    modify_param_card(param_card_input=param_card_name,process_dir=process_dir,param_card_backup='param_card_cpu_1_cpd_1_backup.dat')
    pass


else:
    raise RuntimeError(
        "Param_card %i not recognised in this jobOption " % operator)

modify_run_card(process_dir=process_dir, run_card_backup='run_card_backup.dat',
                settings=extras)


print_cards()

generate(required_accuracy=0.001,process_dir=process_dir,runArgs=runArgs)


outputDS=arrange_output(process_dir=process_dir,lhe_version=3,saveProcDir=True,runArgs=runArgs)
runArgs.inputGeneratorFile=outputDS

include("Pythia8_i/Pythia8_A14_NNPDF23LO_EvtGen_Common.py")
genSeq.Pythia8.Commands += ["SpaceShower:dipoleRecoil=on"]
include("Pythia8_i/Pythia8_MadGraph.py")
include("Pythia8_i/Pythia8_ShowerWeights.py")

```

E.2 $WZjj - EWK$ inclusive dimension-6 EFT production

```
import MadGraphControl.MadGraphUtils

MadGraphControl.MadGraphUtils.MADGRAPH_PDFSETTING={
    'central_pdf': 260000, # the lhapf id of the central pdf, see https://lhapdf.hepforge.org/pdfsets
    'pdf_variations':[260000,90400,13100,25200], # pdfs for which all variations (error sets) will be included as weights
    'alternative_pdfs':[266000,265000], # pdfs for which only the central set will be included as weights
    'scale_variations':[0.5,1.,2.], # variations of muR and muF wrt the central scale, all combinations of muF and muR will be evaluated
    'alternative_dynamic_scales' : [1,2,3,4],
}
from MadGraphControl.MadGraphUtils import *

evgenConfig.generators = ["MadGraph", "Pythia8", "EvtGen"]

evgenConfig.keywords = ['SM', 'diboson', 'WZ', '3lepton','dim6','SMEFTatNLO']
evgenConfig.contact = ['eirini.kasimi@cern.ch']
if eft_order == "interference":
    if flavorcharge == "OFM":
        runName = 'lllvjj_SMEFTatNLO_int'
        description = 'MadGraph_lllvjj_SMEFTatNLO_int'
        mgproc = """
    generate p p > mu+ mu- e- ve~ j j QCD=0 QED=99 NP^2==2 @0
    add process p p > mu+ mu- ta- vt~ j j QCD=0 QED=99 NP^2==2 @0
    add process p p > e+ e- mu- vm~ j j QCD=0 QED=99 NP^2==2 @0
    add process p p > e+ e- ta- vt~ j j QCD=0 QED=99 NP^2==2 @0
    add process p p > ta+ ta- mu- vm~ j j QCD=0 QED=99 NP^2==2 @0
    add process p p > ta+ ta- e- ve~ j j QCD=0 QED=99 NP^2==2 @0"""
    elif flavorcharge == "OFP":
        runName = 'lllvjj_SMEFTatNLO_int'
        description = 'MadGraph_lllvjj_SMEFTatNLO_int'
        mgproc = """
    generate p p > mu+ mu- e+ ve j j QCD=0 QED=99 NP^2==2 @0
    add process p p > ta+ ta- e+ ve j j QCD=0 QED=99 NP^2==2 @0
    add process p p > e+ e- mu+ vm j j QCD=0 QED=99 NP^2==2 @0
    add process p p > ta+ ta- mu+ vm j j QCD=0 QED=99 NP^2==2 @0
    add process p p > e+ e- ta+ vt j j QCD=0 QED=99 NP^2==2 @0
    add process p p > mu+ mu- ta+ vt j j QCD=0 QED=99 NP^2==2 @0"""
    elif flavorcharge == "SFM":
        runName = 'lllvjj_SMEFTatNLO_int'
        description = 'MadGraph_lllvjj_SMEFTatNLO_int'
        mgproc = """
    generate p p > e+ e- e- ve~ j j QCD=0 QED=99 NP^2==2 @0
    add process p p > mu+ mu- mu- vm~ j j QCD=0 QED=99 NP^2==2 @0
    add process p p > ta+ ta- ta- vt~ j j QCD=0 QED=99 NP^2==2 @0"""
    elif flavorcharge == "SFP":
        runName = 'lllvjj_SMEFTatNLO_int'
        description = 'MadGraph_lllvjj_SMEFTatNLO_int'
        mgproc = """
    generate p p > mu+ mu- mu+ vm j j QCD=0 QED=99 NP^2==2 @0
    add process p p > e+ e- e+ ve j j QCD=0 QED=99 NP^2==2 @0
    add process p p > ta+ ta- ta+ vt j j QCD=0 QED=99 NP^2==2 @0"""
    else:
        raise RuntimeError("Flavor-charge combination %i not recognised in these jobOptions. Has to be one of SFM,SFP,OFM,OFP!" % flavorcharge)
elif eft_order == "quadratic_cross":
    runName = 'lllvjj_SMEFTatNLO_quad'
    description = 'MadGraph_lllvjj_SMEFTatNLO_quad'
    mgproc = """
generate p p > mu+ mu- mu+ vm j j QCD=0 QED=99 NP^2==4 @0
add process p p > mu+ mu- mu- vm~ j j QCD=0 QED=99 NP^2==4 @0
add process p p > mu+ mu- e+ ve j j QCD=0 QED=99 NP^2==4 @0
add process p p > mu+ mu- e- ve~ j j QCD=0 QED=99 NP^2==4 @0
add process p p > mu+ mu- ta+ vt j j QCD=0 QED=99 NP^2==4 @0
add process p p > mu+ mu- ta- vt~ j j QCD=0 QED=99 NP^2==4 @0
```

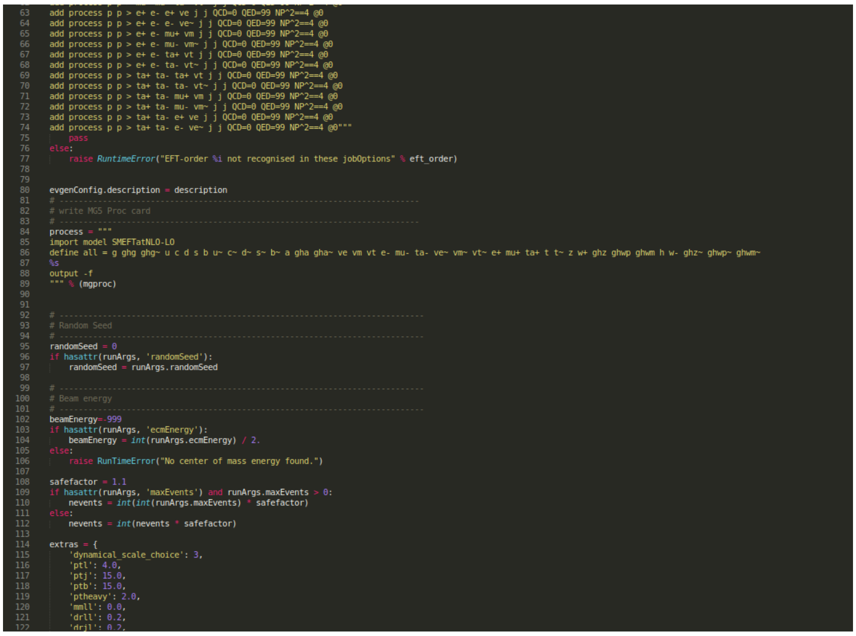

```
add process p p > e+ e- e+ ve j j QCD=0 QED=99 NP^2==4 @0
add process p p > e+ e- e- ve~ j j QCD=0 QED=99 NP^2==4 @0
add process p p > e+ e- mu+ vm j j QCD=0 QED=99 NP^2==4 @0
add process p p > e+ e- mu- vm~ j j QCD=0 QED=99 NP^2==4 @0
add process p p > e+ e- ta+ vt j j QCD=0 QED=99 NP^2==4 @0
add process p p > e+ e- ta- vt~ j j QCD=0 QED=99 NP^2==4 @0
add process p p > ta+ ta- ta+ vt j j QCD=0 QED=99 NP^2==4 @0
add process p p > ta+ ta- ta- vt~ j j QCD=0 QED=99 NP^2==4 @0
add process p p > ta+ ta- mu+ vm j j QCD=0 QED=99 NP^2==4 @0
add process p p > ta+ ta- mu- vm~ j j QCD=0 QED=99 NP^2==4 @0
add process p p > ta+ ta- e+ ve j j QCD=0 QED=99 NP^2==4 @0
add process p p > ta+ ta- e- ve~ j j QCD=0 QED=99 NP^2==4 @0"""
    pass
else:
    raise RuntimeError("EFT-order %i not recognised in these jobOptions" % eft_order)


evgenConfig.description = description
# ---------------------------------------------------------------------------
# write MG5 Proc card
# ---------------------------------------------------------------------------
process = """
import model SMEFTatNLO-LO
define all = g ghg ghg~ u c d s b u~ c~ d~ s~ b~ a gha gha~ ve vm vt e- mu- ta- ve~ vm~ vt~ e+ mu+ ta+ t t~ z w+ ghz ghwp ghwm h w- ghz~ ghwp~ ghwm~
%s
output -f
""" % (mgproc)


# ---------------------------------------------------------------------------
# Random Seed
# ---------------------------------------------------------------------------
randomSeed = 0
if hasattr(runArgs, 'randomSeed'):
    randomSeed = runArgs.randomSeed

# ---------------------------------------------------------------------------
# Beam energy
# ---------------------------------------------------------------------------
beamEnergy=-999
if hasattr(runArgs, 'ecmEnergy'):
    beamEnergy = int(runArgs.ecmEnergy) / 2.
else:
    raise RunTimeError("No center of mass energy found.")

safefactor = 1.1
if hasattr(runArgs, 'maxEvents') and runArgs.maxEvents > 0:
    nevents = int(int(runArgs.maxEvents) * safefactor)
else:
    nevents = int(nevents * safefactor)

extras = {
    'dynamical_scale_choice': 3,
    'ptl': 4.0,
    'ptj': 15.0,
    'ptb': 15.0,
    'ptheavy': 2.0,
    'mmll': 0.0,
    'drll': 0.2,
    'drjl': 0.2,
```

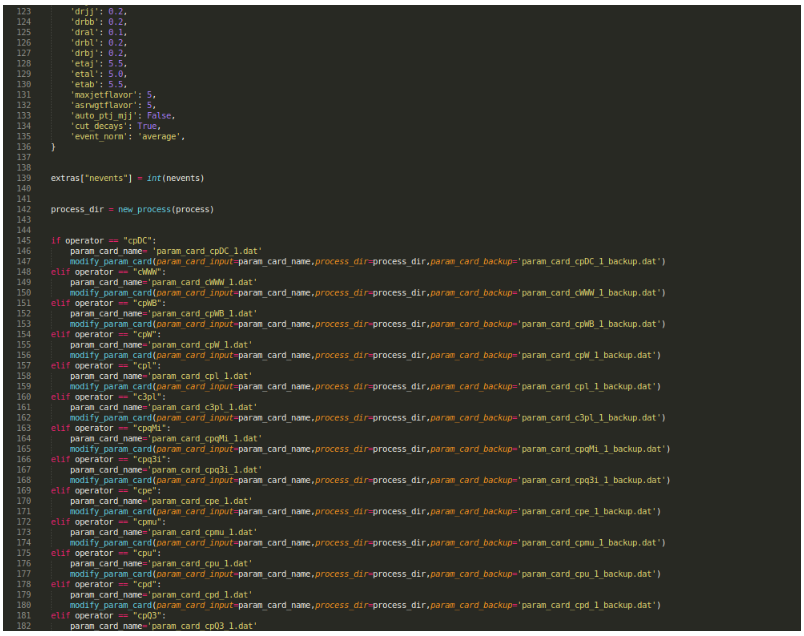

```
    'drjj': 0.2,
    'drbb': 0.2,
    'dral': 0.1,
    'drbl': 0.2,
    'drbj': 0.2,
    'etaj': 5.5,
    'etal': 5.0,
    'etab': 5.5,
    'maxjetflavor': 5,
    'asrwgtflavor': 5,
    'auto_ptj_mjj': False,
    'cut_decays': True,
    'event_norm': 'average',
}


extras["nevents"] = int(nevents)


process_dir = new_process(process)


if operator == "cpDC":
    param_card_name= 'param_card_cpDC_1.dat'
    modify_param_card(param_card_input=param_card_name,process_dir=process_dir,param_card_backup='param_card_cpDC_1_backup.dat')
elif operator == "cWWW":
    param_card_name='param_card_cWWW_1.dat'
    modify_param_card(param_card_input=param_card_name,process_dir=process_dir,param_card_backup='param_card_cWWW_1_backup.dat')
elif operator == "cpWB":
    param_card_name='param_card_cpWB_1.dat'
    modify_param_card(param_card_input=param_card_name,process_dir=process_dir,param_card_backup='param_card_cpWB_1_backup.dat')
elif operator == "cpW":
    param_card_name='param_card_cpW_1.dat'
    modify_param_card(param_card_input=param_card_name,process_dir=process_dir,param_card_backup='param_card_cpW_1_backup.dat')
elif operator == "cpl":
    param_card_name='param_card_cpl_1.dat'
    modify_param_card(param_card_input=param_card_name,process_dir=process_dir,param_card_backup='param_card_cpl_1_backup.dat')
elif operator == "c3pl":
    param_card_name='param_card_c3pl_1.dat'
    modify_param_card(param_card_input=param_card_name,process_dir=process_dir,param_card_backup='param_card_c3pl_1_backup.dat')
elif operator == "cpqMi":
    param_card_name='param_card_cpqMi_1.dat'
    modify_param_card(param_card_input=param_card_name,process_dir=process_dir,param_card_backup='param_card_cpqMi_1_backup.dat')
elif operator == "cpq3i":
    param_card_name='param_card_cpq3i_1.dat'
    modify_param_card(param_card_input=param_card_name,process_dir=process_dir,param_card_backup='param_card_cpq3i_1_backup.dat')
elif operator == "cpe":
    param_card_name='param_card_cpe_1.dat'
    modify_param_card(param_card_input=param_card_name,process_dir=process_dir,param_card_backup='param_card_cpe_1_backup.dat')
elif operator == "cpmu":
    param_card_name='param_card_cpmu_1.dat'
    modify_param_card(param_card_input=param_card_name,process_dir=process_dir,param_card_backup='param_card_cpmu_1_backup.dat')
elif operator == "cpu":
    param_card_name='param_card_cpu_1.dat'
    modify_param_card(param_card_input=param_card_name,process_dir=process_dir,param_card_backup='param_card_cpu_1_backup.dat')
elif operator == "cpd":
    param_card_name='param_card_cpd_1.dat'
    modify_param_card(param_card_input=param_card_name,process_dir=process_dir,param_card_backup='param_card_cpd_1_backup.dat')
elif operator == "cpQ3":
    param_card_name='param_card_cpQ3_1.dat'
```

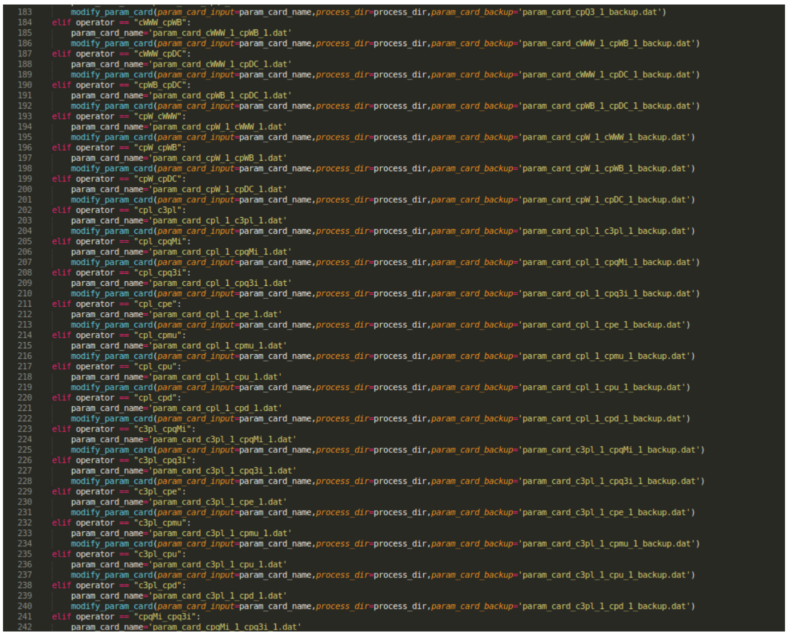

```
    modify_param_card(param_card_input=param_card_name,process_dir=process_dir,param_card_backup='param_card_cpQ3_1_backup.dat')
elif operator == "cWWW_cpWB":
    param_card_name='param_card_cWWW_1_cpWB_1.dat'
    modify_param_card(param_card_input=param_card_name,process_dir=process_dir,param_card_backup='param_card_cWWW_1_cpWB_1_backup.dat')
elif operator == "cWWW_cpDC":
    param_card_name='param_card_cWWW_1_cpDC_1.dat'
    modify_param_card(param_card_input=param_card_name,process_dir=process_dir,param_card_backup='param_card_cWWW_1_cpDC_1_backup.dat')
elif operator == "cpWB_cpDC":
    param_card_name='param_card_cpWB_1_cpDC_1.dat'
    modify_param_card(param_card_input=param_card_name,process_dir=process_dir,param_card_backup='param_card_cpWB_1_cpDC_1_backup.dat')
elif operator == "cpW_cWWW":
    param_card_name='param_card_cpW_1_cWWW_1.dat'
    modify_param_card(param_card_input=param_card_name,process_dir=process_dir,param_card_backup='param_card_cpW_1_cWWW_1_backup.dat')
elif operator == "cpW_cpWB":
    param_card_name='param_card_cpW_1_cpWB_1.dat'
    modify_param_card(param_card_input=param_card_name,process_dir=process_dir,param_card_backup='param_card_cpW_1_cpWB_1_backup.dat')
elif operator == "cpW_cpDC":
    param_card_name='param_card_cpW_1_cpDC_1.dat'
    modify_param_card(param_card_input=param_card_name,process_dir=process_dir,param_card_backup='param_card_cpW_1_cpDC_1_backup.dat')
elif operator == "cpl_c3pl":
    param_card_name='param_card_cpl_1_c3pl_1.dat'
    modify_param_card(param_card_input=param_card_name,process_dir=process_dir,param_card_backup='param_card_cpl_1_c3pl_1_backup.dat')
elif operator == "cpl_cpqMi":
    param_card_name='param_card_cpl_1_cpqMi_1.dat'
    modify_param_card(param_card_input=param_card_name,process_dir=process_dir,param_card_backup='param_card_cpl_1_cpqMi_1_backup.dat')
elif operator == "cpl_cpq3i":
    param_card_name='param_card_cpl_1_cpq3i_1.dat'
    modify_param_card(param_card_input=param_card_name,process_dir=process_dir,param_card_backup='param_card_cpl_1_cpq3i_1_backup.dat')
elif operator == "cpl_cpe":
    param_card_name='param_card_cpl_1_cpe_1.dat'
    modify_param_card(param_card_input=param_card_name,process_dir=process_dir,param_card_backup='param_card_cpl_1_cpe_1_backup.dat')
elif operator == "cpl_cpmu":
    param_card_name='param_card_cpl_1_cpmu_1.dat'
    modify_param_card(param_card_input=param_card_name,process_dir=process_dir,param_card_backup='param_card_cpl_1_cpmu_1_backup.dat')
elif operator == "cpl_cpu":
    param_card_name='param_card_cpl_1_cpu_1.dat'
    modify_param_card(param_card_input=param_card_name,process_dir=process_dir,param_card_backup='param_card_cpl_1_cpu_1_backup.dat')
elif operator == "cpl_cpd":
    param_card_name='param_card_cpl_1_cpd_1.dat'
    modify_param_card(param_card_input=param_card_name,process_dir=process_dir,param_card_backup='param_card_cpl_1_cpd_1_backup.dat')
elif operator == "c3pl_cpqMi":
    param_card_name='param_card_c3pl_1_cpqMi_1.dat'
    modify_param_card(param_card_input=param_card_name,process_dir=process_dir,param_card_backup='param_card_c3pl_1_cpqMi_1_backup.dat')
elif operator == "c3pl_cpq3i":
    param_card_name='param_card_c3pl_1_cpq3i_1.dat'
    modify_param_card(param_card_input=param_card_name,process_dir=process_dir,param_card_backup='param_card_c3pl_1_cpq3i_1_backup.dat')
elif operator == "c3pl_cpe":
    param_card_name='param_card_c3pl_1_cpe_1.dat'
    modify_param_card(param_card_input=param_card_name,process_dir=process_dir,param_card_backup='param_card_c3pl_1_cpe_1_backup.dat')
elif operator == "c3pl_cpmu":
    param_card_name='param_card_c3pl_1_cpmu_1.dat'
    modify_param_card(param_card_input=param_card_name,process_dir=process_dir,param_card_backup='param_card_c3pl_1_cpmu_1_backup.dat')
elif operator == "c3pl_cpu":
    param_card_name='param_card_c3pl_1_cpu_1.dat'
    modify_param_card(param_card_input=param_card_name,process_dir=process_dir,param_card_backup='param_card_c3pl_1_cpu_1_backup.dat')
elif operator == "c3pl_cpd":
    param_card_name='param_card_c3pl_1_cpd_1.dat'
    modify_param_card(param_card_input=param_card_name,process_dir=process_dir,param_card_backup='param_card_c3pl_1_cpd_1_backup.dat')
elif operator == "cpqMi_cpq3i":
    param_card_name='param_card_cpqMi_1_cpq3i_1.dat'
```

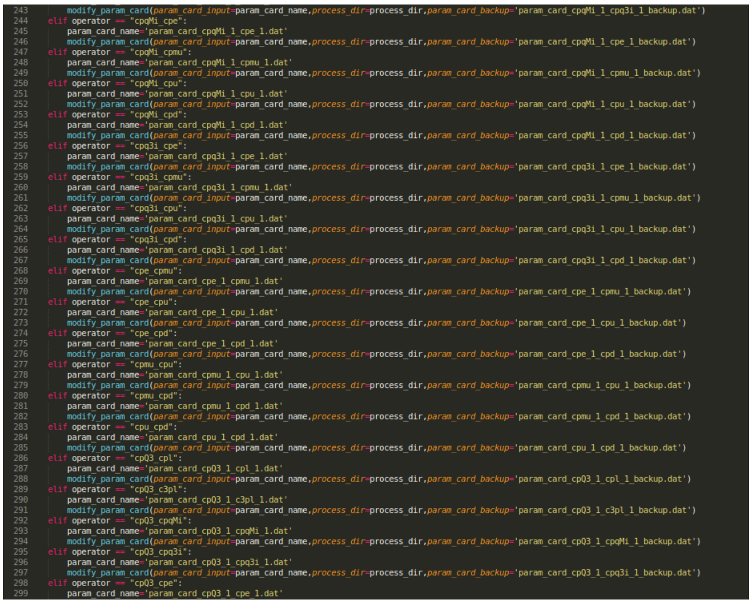

```
    modify_param_card(param_card_input=param_card_name,process_dir=process_dir,param_card_backup='param_card_cpqMi_1_cpq3i_1_backup.dat')
elif operator == "cpqMi_cpe":
    param_card_name='param_card_cpqMi_1_cpe_1.dat'
    modify_param_card(param_card_input=param_card_name,process_dir=process_dir,param_card_backup='param_card_cpqMi_1_cpe_1_backup.dat')
elif operator == "cpqMi_cpmu":
    param_card_name='param_card_cpqMi_1_cpmu_1.dat'
    modify_param_card(param_card_input=param_card_name,process_dir=process_dir,param_card_backup='param_card_cpqMi_1_cpmu_1_backup.dat')
elif operator == "cpqMi_cpu":
    param_card_name='param_card_cpqMi_1_cpu_1.dat'
    modify_param_card(param_card_input=param_card_name,process_dir=process_dir,param_card_backup='param_card_cpqMi_1_cpu_1_backup.dat')
elif operator == "cpqMi_cpd":
    param_card_name='param_card_cpqMi_1_cpd_1.dat'
    modify_param_card(param_card_input=param_card_name,process_dir=process_dir,param_card_backup='param_card_cpqMi_1_cpd_1_backup.dat')
elif operator == "cpq3i_cpe":
    param_card_name='param_card_cpq3i_1_cpe_1.dat'
    modify_param_card(param_card_input=param_card_name,process_dir=process_dir,param_card_backup='param_card_cpq3i_1_cpe_1_backup.dat')
elif operator == "cpq3i_cpmu":
    param_card_name='param_card_cpq3i_1_cpmu_1.dat'
    modify_param_card(param_card_input=param_card_name,process_dir=process_dir,param_card_backup='param_card_cpq3i_1_cpmu_1_backup.dat')
elif operator == "cpq3i_cpu":
    param_card_name='param_card_cpq3i_1_cpu_1.dat'
    modify_param_card(param_card_input=param_card_name,process_dir=process_dir,param_card_backup='param_card_cpq3i_1_cpu_1_backup.dat')
elif operator == "cpq3i_cpd":
    param_card_name='param_card_cpq3i_1_cpd_1.dat'
    modify_param_card(param_card_input=param_card_name,process_dir=process_dir,param_card_backup='param_card_cpq3i_1_cpd_1_backup.dat')
elif operator == "cpe_cpmu":
    param_card_name='param_card_cpe_1_cpmu_1.dat'
    modify_param_card(param_card_input=param_card_name,process_dir=process_dir,param_card_backup='param_card_cpe_1_cpmu_1_backup.dat')
elif operator == "cpe_cpu":
    param_card_name='param_card_cpe_1_cpu_1.dat'
    modify_param_card(param_card_input=param_card_name,process_dir=process_dir,param_card_backup='param_card_cpe_1_cpu_1_backup.dat')
elif operator == "cpe_cpd":
    param_card_name='param_card_cpe_1_cpd_1.dat'
    modify_param_card(param_card_input=param_card_name,process_dir=process_dir,param_card_backup='param_card_cpe_1_cpd_1_backup.dat')
elif operator == "cpmu_cpu":
    param_card_name='param_card_cpmu_1_cpu_1.dat'
    modify_param_card(param_card_input=param_card_name,process_dir=process_dir,param_card_backup='param_card_cpmu_1_cpu_1_backup.dat')
elif operator == "cpmu_cpd":
    param_card_name='param_card_cpmu_1_cpd_1.dat'
    modify_param_card(param_card_input=param_card_name,process_dir=process_dir,param_card_backup='param_card_cpmu_1_cpd_1_backup.dat')
elif operator == "cpu_cpd":
    param_card_name='param_card_cpu_1_cpd_1.dat'
    modify_param_card(param_card_input=param_card_name,process_dir=process_dir,param_card_backup='param_card_cpu_1_cpd_1_backup.dat')
elif operator == "cpQ3_cpl":
    param_card_name='param_card_cpQ3_1_cpl_1.dat'
    modify_param_card(param_card_input=param_card_name,process_dir=process_dir,param_card_backup='param_card_cpQ3_1_cpl_1_backup.dat')
elif operator == "cpQ3_c3pl":
    param_card_name='param_card_cpQ3_1_c3pl_1.dat'
    modify_param_card(param_card_input=param_card_name,process_dir=process_dir,param_card_backup='param_card_cpQ3_1_c3pl_1_backup.dat')
elif operator == "cpQ3_cpqMi":
    param_card_name='param_card_cpQ3_1_cpqMi_1.dat'
    modify_param_card(param_card_input=param_card_name,process_dir=process_dir,param_card_backup='param_card_cpQ3_1_cpqMi_1_backup.dat')
elif operator == "cpQ3_cpq3i":
    param_card_name='param_card_cpQ3_1_cpq3i_1.dat'
    modify_param_card(param_card_input=param_card_name,process_dir=process_dir,param_card_backup='param_card_cpQ3_1_cpq3i_1_backup.dat')
elif operator == "cpQ3_cpe":
    param_card_name='param_card_cpQ3_1_cpe_1.dat'
```

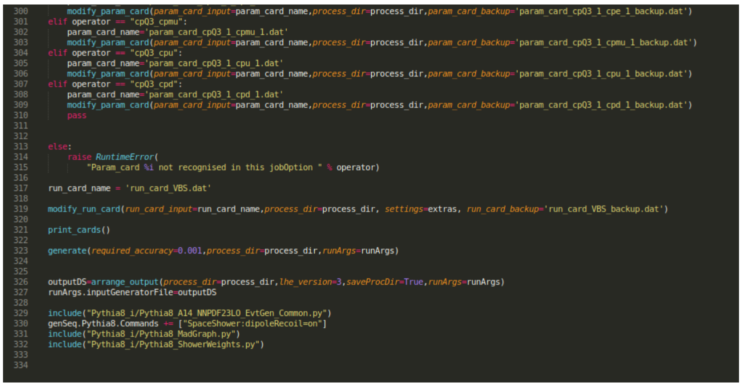

```
    modify_param_card(param_card_input=param_card_name,process_dir=process_dir,param_card_backup='param_card_cpQ3_1_cpe_1_backup.dat')
elif operator == "cpQ3_cpmu":
    param_card_name='param_card_cpQ3_1_cpmu_1.dat'
    modify_param_card(param_card_input=param_card_name,process_dir=process_dir,param_card_backup='param_card_cpQ3_1_cpmu_1_backup.dat')
elif operator == "cpQ3_cpu":
    param_card_name='param_card_cpQ3_1_cpu_1.dat'
    modify_param_card(param_card_input=param_card_name,process_dir=process_dir,param_card_backup='param_card_cpQ3_1_cpu_1_backup.dat')
elif operator == "cpQ3_cpd":
    param_card_name='param_card_cpQ3_1_cpd_1.dat'
    modify_param_card(param_card_input=param_card_name,process_dir=process_dir,param_card_backup='param_card_cpQ3_1_cpd_1_backup.dat')
    pass


else:
    raise RuntimeError(
        "Param_card %i not recognised in this jobOption " % operator)

run_card_name = 'run_card_VBS.dat'

modify_run_card(run_card_input=run_card_name,process_dir=process_dir, settings=extras, run_card_backup='run_card_VBS_backup.dat')

print_cards()

generate(required_accuracy=0.001,process_dir=process_dir,runArgs=runArgs)


outputDS=arrange_output(process_dir=process_dir,lhe_version=3,saveProcDir=True,runArgs=runArgs)
runArgs.inputGeneratorFile=outputDS

include("Pythia8_i/Pythia8_A14_NNPDF23LO_EvtGen_Common.py")
genSeq.Pythia8.Commands += ["SpaceShower:dipoleRecoil=on"]
include("Pythia8_i/Pythia8_MadGraph.py")
include("Pythia8_i/Pythia8_ShowerWeights.py")


```

E.3 $WZjj - QCD$ inclusive dimension-6 EFT production

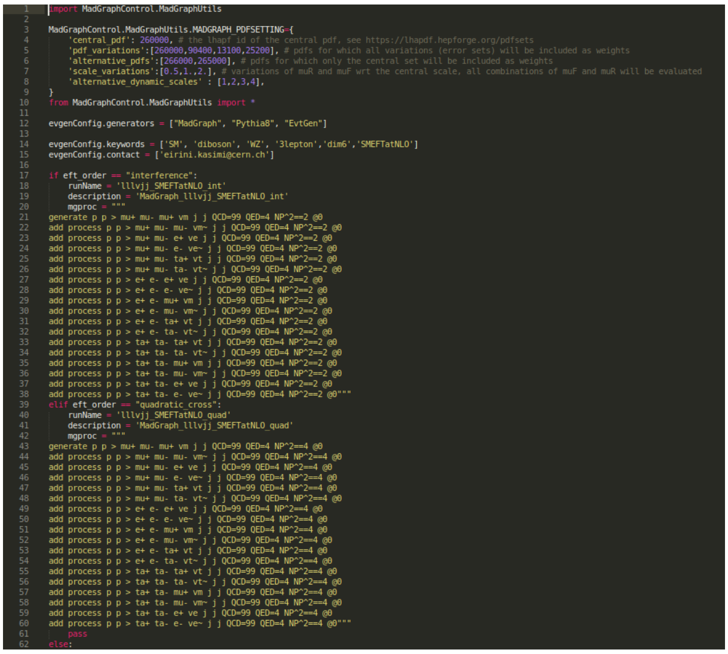

```python
import MadGraphControl.MadGraphUtils

MadGraphControl.MadGraphUtils.MADGRAPH_PDFSETTING={
    'central_pdf': 260000, # the lhapf id of the central pdf, see https://lhapdf.hepforge.org/pdfsets
    'pdf_variations':[260000,90400,13100,25200], # pdfs for which all variations (error sets) will be included as weights
    'alternative_pdfs':[266000,265000], # pdfs for which only the central set will be included as weights
    'scale_variations':[0.5,1.,2.], # variations of muR and muF wrt the central scale, all combinations of muF and muR will be evaluated
    'alternative_dynamic_scales' : [1,2,3,4],
}
from MadGraphControl.MadGraphUtils import *

evgenConfig.generators = ["MadGraph", "Pythia8", "EvtGen"]

evgenConfig.keywords = ['SM', 'diboson', 'WZ', '3lepton','dim6','SMEFTatNLO']
evgenConfig.contact = ['eirini.kasimi@cern.ch']

if eft_order == "interference":
    runName = 'lllvjj_SMEFTatNLO_int'
    description = 'MadGraph_lllvjj_SMEFTatNLO_int'
    mgproc = """
generate p p > mu+ mu- mu+ vm j j QCD=99 QED=4 NP^2==2 @0
add process p p > mu+ mu- mu- vm~ j j QCD=99 QED=4 NP^2==2 @0
add process p p > mu+ mu- e+ ve j j QCD=99 QED=4 NP^2==2 @0
add process p p > mu+ mu- e- ve~ j j QCD=99 QED=4 NP^2==2 @0
add process p p > mu+ mu- ta+ vt j j QCD=99 QED=4 NP^2==2 @0
add process p p > mu+ mu- ta- vt~ j j QCD=99 QED=4 NP^2==2 @0
add process p p > e+ e- e+ ve j j QCD=99 QED=4 NP^2==2 @0
add process p p > e+ e- e- ve~ j j QCD=99 QED=4 NP^2==2 @0
add process p p > e+ e- mu+ vm j j QCD=99 QED=4 NP^2==2 @0
add process p p > e+ e- mu- vm~ j j QCD=99 QED=4 NP^2==2 @0
add process p p > e+ e- ta+ vt j j QCD=99 QED=4 NP^2==2 @0
add process p p > e+ e- ta- vt~ j j QCD=99 QED=4 NP^2==2 @0
add process p p > ta+ ta- ta+ vt j j QCD=99 QED=4 NP^2==2 @0
add process p p > ta+ ta- ta- vt~ j j QCD=99 QED=4 NP^2==2 @0
add process p p > ta+ ta- mu+ vm j j QCD=99 QED=4 NP^2==2 @0
add process p p > ta+ ta- mu- vm~ j j QCD=99 QED=4 NP^2==2 @0
add process p p > ta+ ta- e+ ve j j QCD=99 QED=4 NP^2==2 @0
add process p p > ta+ ta- e- ve~ j j QCD=99 QED=4 NP^2==2 @0"""
elif eft_order == "quadratic_cross":
    runName = 'lllvjj_SMEFTatNLO_quad'
    description = 'MadGraph_lllvjj_SMEFTatNLO_quad'
    mgproc = """
generate p p > mu+ mu- mu+ vm j j QCD=99 QED=4 NP^2==4 @0
add process p p > mu+ mu- mu- vm~ j j QCD=99 QED=4 NP^2==4 @0
add process p p > mu+ mu- e+ ve j j QCD=99 QED=4 NP^2==4 @0
add process p p > mu+ mu- e- ve~ j j QCD=99 QED=4 NP^2==4 @0
add process p p > mu+ mu- ta+ vt j j QCD=99 QED=4 NP^2==4 @0
add process p p > mu+ mu- ta- vt~ j j QCD=99 QED=4 NP^2==4 @0
add process p p > e+ e- e+ ve j j QCD=99 QED=4 NP^2==4 @0
add process p p > e+ e- e- ve~ j j QCD=99 QED=4 NP^2==4 @0
add process p p > e+ e- mu+ vm j j QCD=99 QED=4 NP^2==4 @0
add process p p > e+ e- mu- vm~ j j QCD=99 QED=4 NP^2==4 @0
add process p p > e+ e- ta+ vt j j QCD=99 QED=4 NP^2==4 @0
add process p p > e+ e- ta- vt~ j j QCD=99 QED=4 NP^2==4 @0
add process p p > ta+ ta- ta+ vt j j QCD=99 QED=4 NP^2==4 @0
add process p p > ta+ ta- ta- vt~ j j QCD=99 QED=4 NP^2==4 @0
add process p p > ta+ ta- mu+ vm j j QCD=99 QED=4 NP^2==4 @0
add process p p > ta+ ta- mu- vm~ j j QCD=99 QED=4 NP^2==4 @0
add process p p > ta+ ta- e+ ve j j QCD=99 QED=4 NP^2==4 @0
add process p p > ta+ ta- e- ve~ j j QCD=99 QED=4 NP^2==4 @0"""
    pass
else:
```

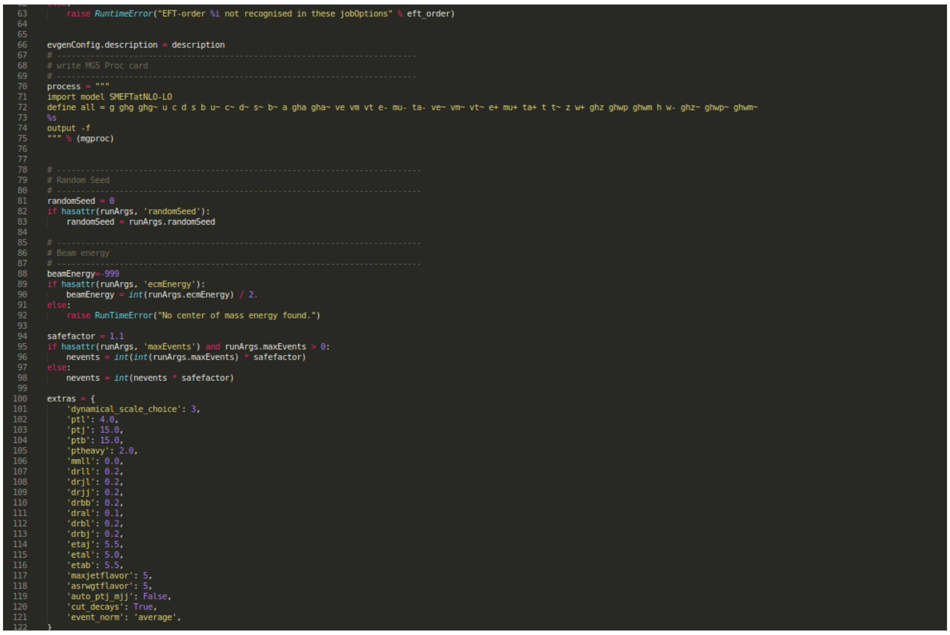

```python
    raise RuntimeError("EFT-order %i not recognised in these jobOptions" % eft_order)


evgenConfig.description = description
# ---------------------------------------------------------------------------
# write MG5 Proc card
# ---------------------------------------------------------------------------
process = """
import model SMEFTatNLO-LO
define all = g ghg ghg~ u c d s b u~ c~ d~ s~ b~ a gha gha~ ve vm vt e- mu- ta- ve~ vm~ vt~ e+ mu+ ta+ t t~ z w+ ghz ghwp ghwm h w- ghz~ ghwp~ ghwm~
%s
output -f
""" % (mgproc)


# ----------------------------------------------------------------------------
# Random Seed
# ----------------------------------------------------------------------------
randomSeed = 0
if hasattr(runArgs, 'randomSeed'):
    randomSeed = runArgs.randomSeed

# ----------------------------------------------------------------------------
# Beam energy
# ----------------------------------------------------------------------------
beamEnergy=-999
if hasattr(runArgs, 'ecmEnergy'):
    beamEnergy = int(runArgs.ecmEnergy) / 2.
else:
    raise RunTimeError("No center of mass energy found.")

safefactor = 1.1
if hasattr(runArgs, 'maxEvents') and runArgs.maxEvents > 0:
    nevents = int(int(runArgs.maxEvents) * safefactor)
else:
    nevents = int(nevents * safefactor)

extras = {
    'dynamical_scale_choice': 3,
    'ptl': 4.0,
    'ptj': 15.0,
    'ptb': 15.0,
    'ptheavy': 2.0,
    'mmll': 0.0,
    'drll': 0.2,
    'drjl': 0.2,
    'drjj': 0.2,
    'drbb': 0.2,
    'dral': 0.1,
    'drbl': 0.2,
    'drbj': 0.2,
    'etaj': 5.5,
    'etal': 5.0,
    'etab': 5.5,
    'maxjetflavor': 5,
    'asrwgtflavor': 5,
    'auto_ptj_mjj': False,
    'cut_decays': True,
    'event_norm': 'average',
}
```

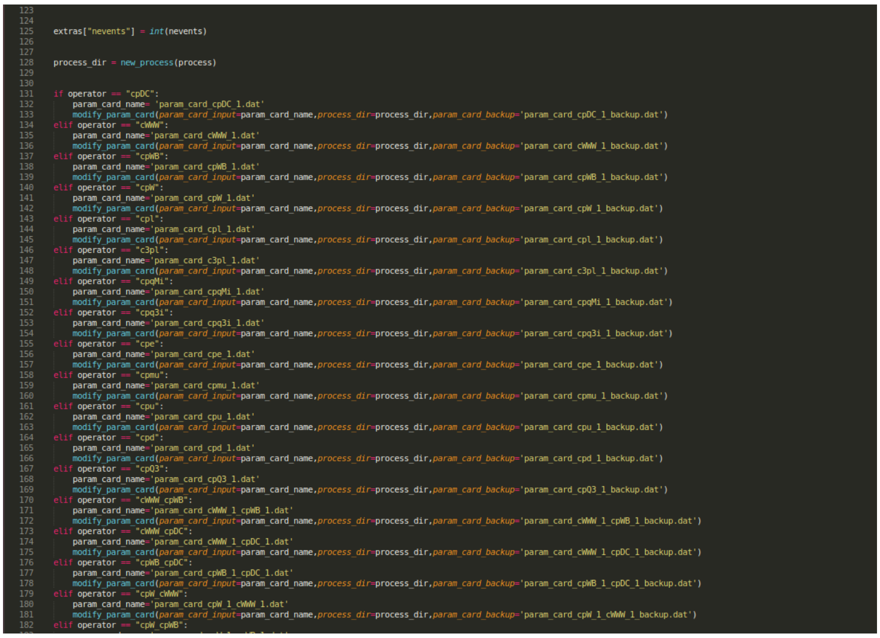

```python
extras["nevents"] = int(nevents)


process_dir = new_process(process)


if operator == "cpDC":
    param_card_name= 'param_card_cpDC_1.dat'
    modify_param_card(param_card_input=param_card_name,process_dir=process_dir,param_card_backup='param_card_cpDC_1_backup.dat')
elif operator == "cWWW":
    param_card_name='param_card_cWWW_1.dat'
    modify_param_card(param_card_input=param_card_name,process_dir=process_dir,param_card_backup='param_card_cWWW_1_backup.dat')
elif operator == "cpWB":
    param_card_name='param_card_cpWB_1.dat'
    modify_param_card(param_card_input=param_card_name,process_dir=process_dir,param_card_backup='param_card_cpWB_1_backup.dat')
elif operator == "cpW":
    param_card_name='param_card_cpW_1.dat'
    modify_param_card(param_card_input=param_card_name,process_dir=process_dir,param_card_backup='param_card_cpW_1_backup.dat')
elif operator == "cpl":
    param_card_name='param_card_cpl_1.dat'
    modify_param_card(param_card_input=param_card_name,process_dir=process_dir,param_card_backup='param_card_cpl_1_backup.dat')
elif operator == "c3pl":
    param_card_name='param_card_c3pl_1.dat'
    modify_param_card(param_card_input=param_card_name,process_dir=process_dir,param_card_backup='param_card_c3pl_1_backup.dat')
elif operator == "cpqMi":
    param_card_name='param_card_cpqMi_1.dat'
    modify_param_card(param_card_input=param_card_name,process_dir=process_dir,param_card_backup='param_card_cpqMi_1_backup.dat')
elif operator == "cpq3i":
    param_card_name='param_card_cpq3i_1.dat'
    modify_param_card(param_card_input=param_card_name,process_dir=process_dir,param_card_backup='param_card_cpq3i_1_backup.dat')
elif operator == "cpe":
    param_card_name='param_card_cpe_1.dat'
    modify_param_card(param_card_input=param_card_name,process_dir=process_dir,param_card_backup='param_card_cpe_1_backup.dat')
elif operator == "cpmu":
    param_card_name='param_card_cpmu_1.dat'
    modify_param_card(param_card_input=param_card_name,process_dir=process_dir,param_card_backup='param_card_cpmu_1_backup.dat')
elif operator == "cpu":
    param_card_name='param_card_cpu_1.dat'
    modify_param_card(param_card_input=param_card_name,process_dir=process_dir,param_card_backup='param_card_cpu_1_backup.dat')
elif operator == "cpd":
    param_card_name='param_card_cpd_1.dat'
    modify_param_card(param_card_input=param_card_name,process_dir=process_dir,param_card_backup='param_card_cpd_1_backup.dat')
elif operator == "cpQ3":
    param_card_name='param_card_cpQ3_1.dat'
    modify_param_card(param_card_input=param_card_name,process_dir=process_dir,param_card_backup='param_card_cpQ3_1_backup.dat')
elif operator == "cWWW_cpWB":
    param_card_name='param_card_cWWW_1_cpWB_1.dat'
    modify_param_card(param_card_input=param_card_name,process_dir=process_dir,param_card_backup='param_card_cWWW_1_cpWB_1_backup.dat')
elif operator == "cWWW_cpDC":
    param_card_name='param_card_cWWW_1_cpDC_1.dat'
    modify_param_card(param_card_input=param_card_name,process_dir=process_dir,param_card_backup='param_card_cWWW_1_cpDC_1_backup.dat')
elif operator == "cpWB_cpDC":
    param_card_name='param_card_cpWB_1_cpDC_1.dat'
    modify_param_card(param_card_input=param_card_name,process_dir=process_dir,param_card_backup='param_card_cpWB_1_cpDC_1_backup.dat')
elif operator == "cpW_cWWW":
    param_card_name='param_card_cpW_1_cWWW_1.dat'
    modify_param_card(param_card_input=param_card_name,process_dir=process_dir,param_card_backup='param_card_cpW_1_cWWW_1_backup.dat')
elif operator == "cpW_cpWB":
```

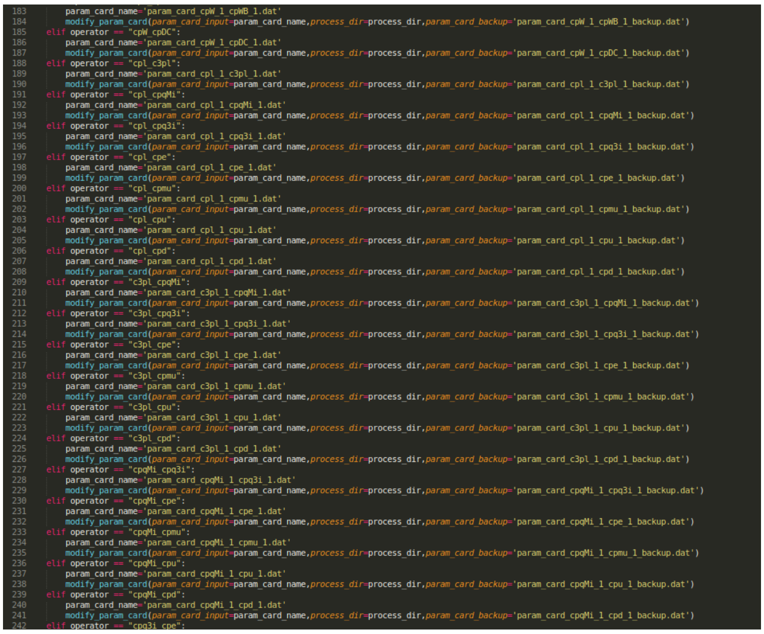

```python
    param_card_name='param_card_cpW_1_cpWB_1.dat'
    modify_param_card(param_card_input=param_card_name,process_dir=process_dir,param_card_backup='param_card_cpW_1_cpWB_1_backup.dat')
elif operator == "cpW_cpDC":
    param_card_name='param_card_cpW_1_cpDC_1.dat'
    modify_param_card(param_card_input=param_card_name,process_dir=process_dir,param_card_backup='param_card_cpW_1_cpDC_1_backup.dat')
elif operator == "cpl_c3pl":
    param_card_name='param_card_cpl_1_c3pl_1.dat'
    modify_param_card(param_card_input=param_card_name,process_dir=process_dir,param_card_backup='param_card_cpl_1_c3pl_1_backup.dat')
elif operator == "cpl_cpqMi":
    param_card_name='param_card_cpl_1_cpqMi_1.dat'
    modify_param_card(param_card_input=param_card_name,process_dir=process_dir,param_card_backup='param_card_cpl_1_cpqMi_1_backup.dat')
elif operator == "cpl_cpq3i":
    param_card_name='param_card_cpl_1_cpq3i_1.dat'
    modify_param_card(param_card_input=param_card_name,process_dir=process_dir,param_card_backup='param_card_cpl_1_cpq3i_1_backup.dat')
elif operator == "cpl_cpe":
    param_card_name='param_card_cpl_1_cpe_1.dat'
    modify_param_card(param_card_input=param_card_name,process_dir=process_dir,param_card_backup='param_card_cpl_1_cpe_1_backup.dat')
elif operator == "cpl_cpmu":
    param_card_name='param_card_cpl_1_cpmu_1.dat'
    modify_param_card(param_card_input=param_card_name,process_dir=process_dir,param_card_backup='param_card_cpl_1_cpmu_1_backup.dat')
elif operator == "cpl_cpu":
    param_card_name='param_card_cpl_1_cpu_1.dat'
    modify_param_card(param_card_input=param_card_name,process_dir=process_dir,param_card_backup='param_card_cpl_1_cpu_1_backup.dat')
elif operator == "cpl_cpd":
    param_card_name='param_card_cpl_1_cpd_1.dat'
    modify_param_card(param_card_input=param_card_name,process_dir=process_dir,param_card_backup='param_card_cpl_1_cpd_1_backup.dat')
elif operator == "c3pl_cpqMi":
    param_card_name='param_card_c3pl_1_cpqMi_1.dat'
    modify_param_card(param_card_input=param_card_name,process_dir=process_dir,param_card_backup='param_card_c3pl_1_cpqMi_1_backup.dat')
elif operator == "c3pl_cpq3i":
    param_card_name='param_card_c3pl_1_cpq3i_1.dat'
    modify_param_card(param_card_input=param_card_name,process_dir=process_dir,param_card_backup='param_card_c3pl_1_cpq3i_1_backup.dat')
elif operator == "c3pl_cpe":
    param_card_name='param_card_c3pl_1_cpe_1.dat'
    modify_param_card(param_card_input=param_card_name,process_dir=process_dir,param_card_backup='param_card_c3pl_1_cpe_1_backup.dat')
elif operator == "c3pl_cpmu":
    param_card_name='param_card_c3pl_1_cpmu_1.dat'
    modify_param_card(param_card_input=param_card_name,process_dir=process_dir,param_card_backup='param_card_c3pl_1_cpmu_1_backup.dat')
elif operator == "c3pl_cpu":
    param_card_name='param_card_c3pl_1_cpu_1.dat'
    modify_param_card(param_card_input=param_card_name,process_dir=process_dir,param_card_backup='param_card_c3pl_1_cpu_1_backup.dat')
elif operator == "c3pl_cpd":
    param_card_name='param_card_c3pl_1_cpd_1.dat'
    modify_param_card(param_card_input=param_card_name,process_dir=process_dir,param_card_backup='param_card_c3pl_1_cpd_1_backup.dat')
elif operator == "cpqMi_cpq3i":
    param_card_name='param_card_cpqMi_1_cpq3i_1.dat'
    modify_param_card(param_card_input=param_card_name,process_dir=process_dir,param_card_backup='param_card_cpqMi_1_cpq3i_1_backup.dat')
elif operator == "cpqMi_cpe":
    param_card_name='param_card_cpqMi_1_cpe_1.dat'
    modify_param_card(param_card_input=param_card_name,process_dir=process_dir,param_card_backup='param_card_cpqMi_1_cpe_1_backup.dat')
elif operator == "cpqMi_cpmu":
    param_card_name='param_card_cpqMi_1_cpmu_1.dat'
    modify_param_card(param_card_input=param_card_name,process_dir=process_dir,param_card_backup='param_card_cpqMi_1_cpmu_1_backup.dat')
elif operator == "cpqMi_cpu":
    param_card_name='param_card_cpqMi_1_cpu_1.dat'
    modify_param_card(param_card_input=param_card_name,process_dir=process_dir,param_card_backup='param_card_cpqMi_1_cpu_1_backup.dat')
elif operator == "cpqMi_cpd":
    param_card_name='param_card_cpqMi_1_cpd_1.dat'
    modify_param_card(param_card_input=param_card_name,process_dir=process_dir,param_card_backup='param_card_cpqMi_1_cpd_1_backup.dat')
elif operator == "cpq3i_cpe":
```

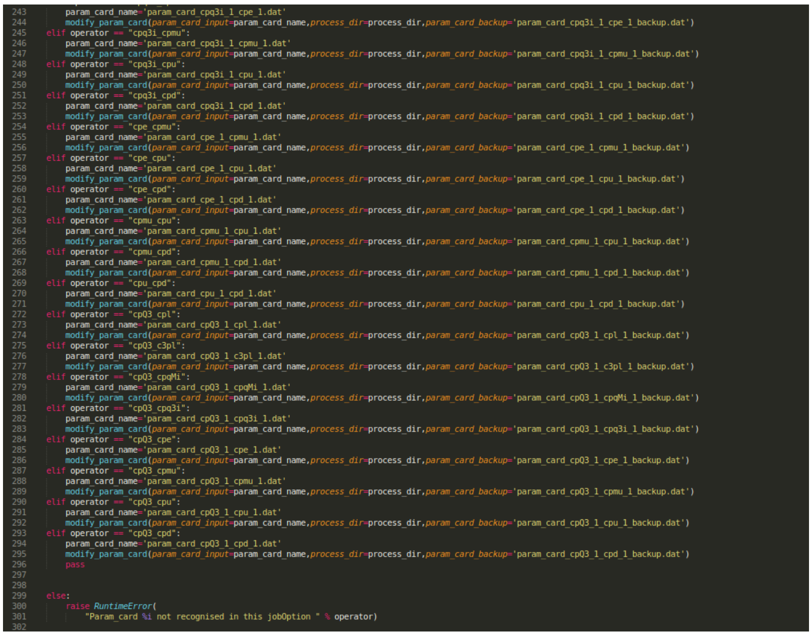

```python
    param_card_name='param_card_cpq3i_1_cpe_1.dat'
    modify_param_card(param_card_input=param_card_name,process_dir=process_dir,param_card_backup='param_card_cpq3i_1_cpe_1_backup.dat')
elif operator == "cpq3i_cpmu":
    param_card_name='param_card_cpq3i_1_cpmu_1.dat'
    modify_param_card(param_card_input=param_card_name,process_dir=process_dir,param_card_backup='param_card_cpq3i_1_cpmu_1_backup.dat')
elif operator == "cpq3i_cpu":
    param_card_name='param_card_cpq3i_1_cpu_1.dat'
    modify_param_card(param_card_input=param_card_name,process_dir=process_dir,param_card_backup='param_card_cpq3i_1_cpu_1_backup.dat')
elif operator == "cpq3i_cpd":
    param_card_name='param_card_cpq3i_1_cpd_1.dat'
    modify_param_card(param_card_input=param_card_name,process_dir=process_dir,param_card_backup='param_card_cpq3i_1_cpd_1_backup.dat')
elif operator == "cpe_cpmu":
    param_card_name='param_card_cpe_1_cpmu_1.dat'
    modify_param_card(param_card_input=param_card_name,process_dir=process_dir,param_card_backup='param_card_cpe_1_cpmu_1_backup.dat')
elif operator == "cpe_cpu":
    param_card_name='param_card_cpe_1_cpu_1.dat'
    modify_param_card(param_card_input=param_card_name,process_dir=process_dir,param_card_backup='param_card_cpe_1_cpu_1_backup.dat')
elif operator == "cpe_cpd":
    param_card_name='param_card_cpe_1_cpd_1.dat'
    modify_param_card(param_card_input=param_card_name,process_dir=process_dir,param_card_backup='param_card_cpe_1_cpd_1_backup.dat')
elif operator == "cpmu_cpu":
    param_card_name='param_card_cpmu_1_cpu_1.dat'
    modify_param_card(param_card_input=param_card_name,process_dir=process_dir,param_card_backup='param_card_cpmu_1_cpu_1_backup.dat')
elif operator == "cpmu_cpd":
    param_card_name='param_card_cpmu_1_cpd_1.dat'
    modify_param_card(param_card_input=param_card_name,process_dir=process_dir,param_card_backup='param_card_cpmu_1_cpd_1_backup.dat')
elif operator == "cpu_cpd":
    param_card_name='param_card_cpu_1_cpd_1.dat'
    modify_param_card(param_card_input=param_card_name,process_dir=process_dir,param_card_backup='param_card_cpu_1_cpd_1_backup.dat')
elif operator == "cpQ3_cpl":
    param_card_name='param_card_cpQ3_1_cpl_1.dat'
    modify_param_card(param_card_input=param_card_name,process_dir=process_dir,param_card_backup='param_card_cpQ3_1_cpl_1_backup.dat')
elif operator == "cpQ3_c3pl":
    param_card_name='param_card_cpQ3_1_c3pl_1.dat'
    modify_param_card(param_card_input=param_card_name,process_dir=process_dir,param_card_backup='param_card_cpQ3_1_c3pl_1_backup.dat')
elif operator == "cpQ3_cpqMi":
    param_card_name='param_card_cpQ3_1_cpqMi_1.dat'
    modify_param_card(param_card_input=param_card_name,process_dir=process_dir,param_card_backup='param_card_cpQ3_1_cpqMi_1_backup.dat')
elif operator == "cpQ3_cpq3i":
    param_card_name='param_card_cpQ3_1_cpq3i_1.dat'
    modify_param_card(param_card_input=param_card_name,process_dir=process_dir,param_card_backup='param_card_cpQ3_1_cpq3i_1_backup.dat')
elif operator == "cpQ3_cpe":
    param_card_name='param_card_cpQ3_1_cpe_1.dat'
    modify_param_card(param_card_input=param_card_name,process_dir=process_dir,param_card_backup='param_card_cpQ3_1_cpe_1_backup.dat')
elif operator == "cpQ3_cpmu":
    param_card_name='param_card_cpQ3_1_cpmu_1.dat'
    modify_param_card(param_card_input=param_card_name,process_dir=process_dir,param_card_backup='param_card_cpQ3_1_cpmu_1_backup.dat')
elif operator == "cpQ3_cpu":
    param_card_name='param_card_cpQ3_1_cpu_1.dat'
    modify_param_card(param_card_input=param_card_name,process_dir=process_dir,param_card_backup='param_card_cpQ3_1_cpu_1_backup.dat')
elif operator == "cpQ3_cpd":
    param_card_name='param_card_cpQ3_1_cpd_1.dat'
    modify_param_card(param_card_input=param_card_name,process_dir=process_dir,param_card_backup='param_card_cpQ3_1_cpd_1_backup.dat')
    pass


else:
    raise RuntimeError(
        "Param_card %i not recognised in this jobOption " % operator)

```

```python

run_card_name = 'run_card_VBS.dat'

modify_run_card(run_card_input=run_card_name,process_dir=process_dir, settings=extras, run_card_backup='run_card_VBS_backup.dat')

print_cards()

generate(required_accuracy=0.001,process_dir=process_dir,runArgs=runArgs)


outputDS=arrange_output(process_dir=process_dir,lhe_version=3,saveProcDir=True,runArgs=runArgs)
runArgs.inputGeneratorFile=outputDS

include("Pythia8_i/Pythia8_A14_NNPDF23LO_EvtGen_Common.py")
genSeq.Pythia8.Commands += ["SpaceShower:dipoleRecoil=on"]
include("Pythia8_i/Pythia8_MadGraph.py")
include("Pythia8_i/Pythia8_ShowerWeights.py")

```

Bibliography

[1] Georges Aad et al. Observation of a new particle in the search for the Standard Model Higgs boson with the ATLAS detector at the LHC. *Phys. Lett. B*, 716:1–29, 2012. doi: 10.1016/j.physletb.2012.08.020.

[2] David J Griffiths. *Introduction to elementary particles; 2nd rev. version*. Physics textbook. Wiley, New York, NY, 2008. URL `https://cds.cern.ch/record/111880`.

[3] Gordon L. Kane. *MODERN ELEMENTARY PARTICLE PHYSICS*. Cambridge University Press, 2 2017. ISBN 978-0-201-62460-1, 978-1-316-73080-5, 978-1-107-16508-3.

[4] E. Noether. Invariante variationsprobleme. *Nachrichten von der Gesellschaft der Wissenschaften zu Göttingen, Mathematisch-Physikalische Klasse*, 1918:235–257, 1918. URL `http://eudml.org/doc/59024`.

[5] Peter W. Higgs. Spontaneous symmetry breakdown without massless bosons. *Phys. Rev.*, 145:1156–1163, May 1966. doi: 10.1103/PhysRev.145.1156. URL `https://link.aps.org/doi/10.1103/PhysRev.145.1156`.

[6] Yoichiro Nambu. Quasi-particles and gauge invariance in the theory of superconductivity. *Phys. Rev.*, 117:648–663, Feb 1960. doi: 10.1103/PhysRev.117.648. URL `https://link.aps.org/doi/10.1103/PhysRev.117.648`.

[7] Jeffrey Goldstone, Abdus Salam, and Steven Weinberg. Broken symmetries. *Phys. Rev.*, 127:965–970, Aug 1962. doi: 10.1103/PhysRev.127.965. URL `https://link.aps.org/doi/10.1103/PhysRev.127.965`.

[8] Morad Aaboud et al. Observation of electroweak production of a same-sign W boson pair in association with two jets in pp collisions at $\sqrt{s} = 13$ TeV with the ATLAS detector. *Phys. Rev. Lett.*, 123(16):161801, 2019. doi: 10.1103/PhysRevLett.123.161801.

[9] Albert M Sirunyan et al. Observation of electroweak production of same-sign W boson pairs in the two jet and two same-sign lepton final state in proton-proton collisions at $\sqrt{s} = 13$ TeV. *Phys. Rev. Lett.*, 120(8):081801, 2018. doi: 10.1103/PhysRevLett.120.081801.

[10] Armen Tumasyan et al. Observation of electroweak W+W− pair production in association with two jets in proton-proton collisions at s=13TeV. *Phys. Lett. B*, 841:137495, 2023. doi: 10.1016/j.physletb.2022.137495.

[11] Georges Aad et al. Observation of electroweak production of two jets and a Z-boson pair. *Nature Phys.*, 19(2):237–253, 2023. doi: 10.1038/s41567-022-01757-y.

[12] Albert M Sirunyan et al. Evidence for electroweak production of four charged leptons and two jets in proton-proton collisions at $\sqrt{s}$ = 13 TeV. *Phys. Lett. B*, 812:135992, 2021. doi: 10.1016/j.physletb.2020.135992.

[13] Morad Aaboud et al. Observation of electroweak $W^{\pm}Z$ boson pair production in association with two jets in pp collisions at $\sqrt{s} = 13$ TeV with the ATLAS detector. *Phys. Lett. B*, 793:469–492, 2019. doi: 10.1016/j.physletb.2019.05.012.

[14] Albert M Sirunyan et al. Measurements of production cross sections of WZ and same-sign WW boson pairs in association with two jets in proton-proton collisions at $\sqrt{s} =$ 13 TeV. *Phys. Lett. B*, 809:135710, 2020. doi: 10.1016/j.physletb.2020.135710.

[15] Celine Degrande, Nicolas Greiner, Wolfgang Kilian, Olivier Mattelaer, Harrison Mebane, Tim Stelzer, Scott Willenbrock, and Cen Zhang. Effective Field Theory: A Modern Approach to Anomalous Couplings. *Annals Phys.*, 335:21, 2013. doi: 10.1016/j.aop.2013.04.016.

[16] Steven Weinberg. Phenomenological Lagrangians. *Physica A*, 96(1-2):327–340, 1979. doi: 10.1016/0378-4371(79)90223-1.

[17] Steven Weinberg. Conceptual Foundations of the Unified Theory of Weak and Electromagnetic Interactions. *Rev. Mod. Phys.*, 52:515–523, 1980. doi: 10.1103/RevModPhys.52.515.

[18] Ilaria Brivio. SMEFTsim 3.0 — a practical guide. *JHEP*, 04:073, 2021. doi: 10.1007/JHEP04(2021)073.

[19] B. Grzadkowski, M. Iskrzynski, M. Misiak, and J. Rosiek. Dimension-Six Terms in the Standard Model Lagrangian. *JHEP*, 10:085, 2010. doi: 10.1007/JHEP10(2010)085.

[20] O.J.P. Eboli, M.C. Gonzalez-Garcia, and J.K. Mizukoshi. $pp \to jje^{\pm}\mu^{\pm}\nu\nu$ and $jje^{\pm}\mu^{\pm}\nu\nu$ at $O(\alpha_{em}^6)$ and $O(\alpha_{em}^4\alpha_s^2)$ for the study of the quartic electroweak gauge boson vertex at CERN LHC. *Phys. Rev. D*, 74:073005, 2006. doi: 10.1103/PhysRevD.74.073005.

[21] Jan Kalinowski, Paweł Kozów, Stefan Pokorski, Janusz Rosiek, Michał Szleper, and Sławomir Tkaczyk. Same-sign WW scattering at the LHC: can we discover BSM effects before discovering new states?. Same-sign WW scattering at the LHC: can we discover

BSM effects before discovering new states? *Eur. Phys. J. C*, 78:403. 24 p, May 2018. doi: 10.1140/epjc/s10052-018-5885-y. URL `https://cds.cern.ch/record/2303677`. 24 pages.

[22] Eduardo da Silva Almeida, O. J. P. Éboli, and M. C. Gonzalez-Garcia. Unitarity constraints on anomalous quartic couplings. *Phys. Rev. D*, 101:113003, Jun 2020. doi: 10.1103/PhysRevD.101.113003. URL `https://link.aps.org/doi/10.1103/PhysRevD.101.113003`.

[23] The ATLAS Collaboration and G Aad. The ATLAS experiment at the CERN large hadron collider. *Journal of Instrumentation*, 3(08):S08003–S08003, August 2008. doi: 10.1088/1748-0221/3/08/s08003. URL `https://doi.org/10.1088/1748-0221/3/08/s08003`.

[24] The CMS Collaboration and S Chatrchyan. The CMS experiment at the CERN LHC. *Journal of Instrumentation*, 3(08):S08004–S08004, August 2008. doi: 10.1088/1748-0221/3/08/s08004. URL `https://doi.org/10.1088/1748-0221/3/08/s08004`.

[25] The ALICE Collaboration and K Aamodt. The ALICE experiment at the CERN LHC. *Journal of Instrumentation*, 3(08):S08002–S08002, August 2008. doi: 10.1088/1748-0221/3/08/s08002. URL `https://doi.org/10.1088/1748-0221/3/08/s08002`.

[26] The LHCb Collaboration and A Augusto Alves. The LHCb detector at the LHC. *Journal of Instrumentation*, 3(08):S08005–S08005, August 2008. doi: 10.1088/1748-0221/3/08/s08005. URL `https://doi.org/10.1088/1748-0221/3/08/s08005`.

[27] Luminosity recommendations, `https://twiki.cern.ch/twiki/bin/viewauth/Atlas/LuminosityForPhysics#2015201813TeVprotonprotonf`.

[28] ATLAS Collaboration. ATLAS Inner Detector: Technical Design Report, 2. ATLAS-TDR-05, 1997. URL `https://cds.cern.ch/record/331064`.

[29] ATLAS Collaboration. ATLAS Pixel Detector: Technical Design Report, 1998. URL `https://cds.cern.ch/record/381263`.

[30] ATLAS Collaboration. ATLAS Insertable B-Layer: Technical Design Report, 2010. URL `https://cds.cern.ch/record/1291633`.

[31] ATLAS Collaboration. ATLAS Liquid Argon Calorimeter: Technical Design Report, 1996. URL `https://cds.cern.ch/record/331061`.

[32] ATLAS Collaboration. ATLAS Tile Calorimeter: Technical Design Report, 1996. URL `https://cds.cern.ch/record/331062`.

[33] ATLAS Collaboration. ATLAS Muon Spectrometer: Technical Design Report. ATLAS-TDR-10, 1997. URL `https://cds.cern.ch/record/331068`.

[34] Nicolas Viaux Maira. The ATLAS New Small Wheel new Muon Stations Ready for LHC Run3. Technical report, CERN, Geneva, 2022. URL `https://cds.cern.ch/record/2812136`.

[35] ATLAS Collaboration. ATLAS Forward Detectors for Measurement of Elastic Scattering and Luminosity: Technical Design Report, 2008. URL `https://cds.cern.ch/record/1095847`.

[36] ATLAS Collaboration. ATLAS Level-1 Trigger: Technical Design Report, 1998. URL `https://cds.cern.ch/record/381429`.

[37] ATLAS Collaboration. ATLAS High-Level Trigger, Data Acquisition and Controls: Technical Design Report, 2003. URL `https://cds.cern.ch/record/616089`.

[38] ATLAS Collaboration. ATLAS Magnet System: Magnet Project Technical Design Report, Volume 1, 1997. URL `https://cds.cern.ch/record/338080`.

[39] ATLAS Collaboration. ATLAS Central Solenoid: Magnet Project Technical Design Report, Volume 4, 1997. URL `https://cds.cern.ch/record/331067`.

[40] ATLAS Collaboration. ATLAS Barrel Toroid: Magnet Project Technical Design Report, Volume 2, 1997. URL `https://cds.cern.ch/record/331065`.

[41] ATLAS Collaboration. ATLAS End-Cap Toroids: Magnet Project Technical Design Report, Volume 3, 1997. URL `https://cds.cern.ch/record/331066`.

[42] Andy Buckley, Jonathan Butterworth, Stefan Gieseke, David Grellscheid, Stefan Höche, Hendrik Hoeth, Frank Krauss, Leif Lönnblad, Emily Nurse, Peter Richardson, Steffen Schumann, Michael H. Seymour, Torbjörn Sjöstrand, Peter Skands, and Bryan Webber. General-purpose event generators for lhc physics. *Physics Reports*, 504 (5):145–233, 2011. ISSN 0370-1573. doi: https://doi.org/10.1016/j.physrep.2011.03.005. URL `https://www.sciencedirect.com/science/article/pii/S0370157311000846`.

[43] Luminosity for physics, `https://twiki.cern.ch/twiki/bin/viewauth/Atlas/LuminosityForPhysics`.

[44] G. Avoni, M. Bruschi, G. Cabras, D. Caforio, N. Dehghanian, A. Floderus, B. Giacobbe, F. Giannuzzi, F. Giorgi, P. Grafström, V. Hedberg, F. Lasagni Manghi, S. Meneghini, J. Pinfold, E. Richards, C. Sbarra, N. Semprini Cesari, A. Sbrizzi, R. Soluk, G. Ucchielli, S. Valentinetti, O. Viazlo, M. Villa, C. Vittori, R. Vuillermet, and A. Zoccoli. The new

lucid-2 detector for luminosity measurement and monitoring in atlas. *Journal of Instrumentation*, 13(07):P07017, jul 2018. doi: 10.1088/1748-0221/13/07/P07017. URL `https://dx.doi.org/10.1088/1748-0221/13/07/P07017`.

[45] T. Gleisberg, S. Höche, F. Krauss, M. Schönherr, S. Schumann, F. Siegert, and J. Winter. Event generation with sherpa 1.1. *Journal of High Energy Physics*, 2009(02):007, feb 2009. doi: 10.1088/1126-6708/2009/02/007. URL `https://dx.doi.org/10.1088/1126-6708/2009/02/007`.

[46] Anosh Joseph. Markov Chain Monte Carlo Methods in Quantum Field Theories: A Modern Primer. SpringerBriefs in Physics. Springer, 12 2019. doi: 10.1007/978-3-030-46044-0.

[47] Stefan Höche. Introduction to parton-shower event generators, 2014. URL `https://arxiv.org/abs/1411.4085`.

[48] S. Jadach, Z. Was, R. Decker, and Johann H. Kuhn. The tau decay library TAUOLA: Version 2.4. *Comput. Phys. Commun.*, 76:361–380, 1993. doi: 10.1016/0010-4655(93)90061-G.

[49] David J. Lange. The evtgen particle decay simulation package. *Nuclear Instruments and Methods in Physics Research Section A: Accelerators, Spectrometers, Detectors and Associated Equipment*, 462(1):152–155, 2001. ISSN 0168-9002. doi: https://doi.org/10.1016/S0168-9002(01)00089-4. URL `https://www.sciencedirect.com/science/article/pii/S0168900201000894`. BEAUTY2000, Proceedings of the 7th Int. Conf. on B-Physics at Hadron Machines.

[50] Keith Hamilton and Peter Richardson. Simulation of QED radiation in particle decays using the YFS formalism. *JHEP*, 07:010, 2006. doi: 10.1088/1126-6708/2006/07/010.

[51] Stefano Frixione and Bryan R. Webber. Matching NLO QCD computations and parton shower simulations. *JHEP*, 06:029, 2002.

[52] Stefano Frixione, Paolo Nason, and Carlo Oleari. Matching NLO QCD computations with parton shower simulations: the POWHEG method. *JHEP*, 11:070, 2007. doi: 10.1088/1126-6708/2007/11/070.

[53] John C. Collins. Sudakov form-factors. *Adv. Ser. Direct. High Energy Phys.*, 5:573–614, 1989. doi: 10.1142/9789814503266_0006.

[54] Johan Alwall et al. Comparative study of various algorithms for the merging of parton showers and matrix elements in hadronic collisions. *Eur. Phys. J. C*, 53:473–500, 2008. doi: 10.1140/epjc/s10052-007-0490-5.

[55] Leif Lonnblad. Correcting the color dipole cascade model with fixed order matrix elements. *JHEP*, 05:046, 2002. doi: 10.1088/1126-6708/2002/05/046.

[56] J. Alwall, R. Frederix, S. Frixione, V. Hirschi, F. Maltoni, O. Mattelaer, H. S. Shao, T. Stelzer, P. Torrielli, and M. Zaro. The automated computation of tree-level and next-to-leading order differential cross sections, and their matching to parton shower simulations. *JHEP*, 07:079, 2014. doi: 10.1007/JHEP07(2014)079.

[57] Johan Alwall, Michel Herquet, Fabio Maltoni, Olivier Mattelaer, and Tim Stelzer. Madgraph 5: going beyond. *Journal of High Energy Physics*, 2011(6), Jun 2011. ISSN 1029-8479. doi: 10.1007/jhep06(2011)128. URL `http://dx.doi.org/10.1007/JHEP06(2011)128`.

[58] Rikkert Frederix and Stefano Frixione. Merging meets matching in MC@NLO. *JHEP*, 12:061, 2012. doi: 10.1007/JHEP12(2012)061.

[59] Adam Alloul, Neil D. Christensen, Céline Degrande, Claude Duhr, and Benjamin Fuks. Feynrules 2.0 — a complete toolbox for tree-level phenomenology. *Computer Physics Communications*, 185(8):2250–2300, 2014. ISSN 0010-4655. doi: https://doi.org/10.1016/j.cpc.2014.04.012. URL `https://www.sciencedirect.com/science/article/pii/S0010465514001350`.

[60] T. Gleisberg, S. Höche, F. Krauss, M. Schönherr, S. Schumann, et al. Event generation with SHERPA 1.1. *JHEP*, 02:007, 2009. doi: 10.1088/1126-6708/2009/02/007.

[61] F. Krauss, R. Kuhn, and G. Soff. AMEGIC++ 1.0: A Matrix element generator in C++. *JHEP*, 02:044, 2002. doi: 10.1088/1126-6708/2002/02/044.

[62] Tanju Gleisberg and Stefan Höche. Comix, a new matrix element generator. *JHEP*, 12:039, 2008. doi: 10.1088/1126-6708/2008/12/039.

[63] C. F. Berger, Z. Bern, L. J. Dixon, F. Febres Cordero, D. Forde, H. Ita, D. A. Kosower, and D. Maitre. An Automated Implementation of On-Shell Methods for One-Loop Amplitudes. *Phys. Rev. D*, 78:036003, 2008. doi: 10.1103/PhysRevD.78.036003.

[64] Fabio Cascioli, Philipp Maierhofer, and Stefano Pozzorini. Scattering Amplitudes with Open Loops. *Phys. Rev. Lett.*, 108:111601, 2012. doi: 10.1103/PhysRevLett.108.111601.

[65] Benedikt Biedermann, Stephan Bräuer, Ansgar Denner, Mathieu Pellen, Steffen Schumann, and Jennifer M. Thompson. Automation of NLO QCD and EW corrections with Sherpa and Recola. *Eur. Phys. J. C*, 77:492, 2017. doi: 10.1140/epjc/s10052-017-5054-8.

[66] S. Schumann and F. Krauss. A parton shower algorithm based on catani-seymour dipole factorisation. *Journal of High Energy Physics*, 2008(03):038, mar 2008. doi: 10.1088/1126-6708/2008/03/038. URL `https://dx.doi.org/10.1088/1126-6708/2008/03/038`.

[67] Steffen Schumann and Frank Krauss. A parton shower algorithm based on Catani–Seymour dipole factorisation. *JHEP*, 03:038, 2008. doi: 10.1088/1126-6708/2008/03/038.

[68] Stefan Höche and Stefan Prestel. The midpoint between dipole and parton showers. *Eur. Phys. J. C*, 75(9):461, 2015. doi: 10.1140/epjc/s10052-015-3684-2.

[69] Stefan Höche, Frank Krauss, Marek Schönherr, and Frank Siegert. QCD matrix elements + parton showers: The NLO case. *JHEP*, 04:027, 2013. doi: 10.1007/JHEP04(2013)027.

[70] Matt Dobbs and Jorgen Beck Hansen. The HepMC C++ Monte Carlo event record for High Energy Physics. *Comput. Phys. Commun.*, 134:41–46, 2001. doi: 10.1016/S0010-4655(00)00189-2.

[71] Johan Alwall et al. A Standard format for Les Houches event files. *Comput. Phys. Commun.*, 176:300–304, 2007. doi: 10.1016/j.cpc.2006.11.010.

[72] Christian Bierlich et al. A comprehensive guide to the physics and usage of PYTHIA 8.3. 3 2022. doi: 10.21468/SciPostPhysCodeb.8.

[73] B. Andersson, G. Gustafson, G. Ingelman, and T. Sjöstrand. Parton fragmentation and string dynamics. *Physics Reports*, 97(2):31–145, 1983. ISSN 0370-1573. doi: https://doi.org/10.1016/0370-1573(83)90080-7. URL `https://www.sciencedirect.com/science/article/pii/0370157383900807`.

[74] M. Bahr et al. Herwig++ physics and manual. *Eur. Phys. J. C*, 58:639, 2008. doi: 10.1140/epjc/s10052-008-0798-9.

[75] Johannes Bellm, Stefan Gieseke, and Simon Plätzer. Merging NLO Multi-jet Calculations with Improved Unitarization. *Eur. Phys. J. C*, 78(3):244, 2018. doi: 10.1140/epjc/s10052-018-5723-2.

[76] J. Baglio et al. Release Note - VBFNLO 2.7.0. 4 2014.

[77] Simone Alioli, Paolo Nason, Carlo Oleari, and Emanuele Re. A general framework for implementing NLO calculations in shower Monte Carlo programs: the POWHEG BOX. *JHEP*, 06:043, 2010. doi: 10.1007/JHEP06(2010)043.

[78] Pileup recommendations, `https://twiki.cern.ch/twiki/bin/viewauth/AtlasProtected/ExtendedPileupReweighting`.

[79] Pileup reweighting, `https://twiki.cern.ch/twiki/bin/view/AtlasProtected/ExtendedPileupReweighting`.

[80] Marco Guzzi, Pavel Nadolsky, Edmond Berger, Hung-Liang Lai, Fredrick Olness, and C. P. Yuan. CT10 parton distributions and other developments in the global QCD analysis. 1 2011.

[81] J. Pumplin et al. New Generation of Parton Distributions with Uncertainties from Global QCD Analysis. *JHEP*, 07:012, 2002. doi: 10.1088/1126-6708/2002/07/012.

[82] Massimiliano Grazzini, Stefan Kallweit, Dirk Rathlev, and Marius Wiesemann. $W^{\pm}Z$ production at the LHC: fiducial cross sections and distributions in NNLO QCD. 2017.

[83] ATLAS Collaboration. Measurement of $W^{\pm}Z$ production cross sections and gauge boson polarisation in pp collisions at $\sqrt{s} = 13$ TeV with the ATLAS detector. *Eur. Phys. J.*, C79(6):535, 2019. doi: 10.1140/epjc/s10052-019-7027-6.

[84] Richard D. Ball et al. Parton distributions for the LHC Run II. *JHEP*, 04:040, 2015. doi: 10.1007/JHEP04(2015)040.

[85] Richard D. Ball, Valerio Bertone, Stefano Carrazza, Luigi Del Debbio, Stefano Forte, Alberto Guffanti, Nathan P. Hartland, and Juan Rojo. Parton distributions with QED corrections. *Nucl. Phys. B*, 877:290–320, 2013. doi: 10.1016/j.nuclphysb.2013.10.010.

[86] Baptiste Cabouat and Torbjörn Sjöstrand. Some Dipole Shower Studies. *Eur. Phys. J.*, C78(3):226, 2018. doi: 10.1140/epjc/s10052-018-5645-z.

[87] Michael Rauch and Simon Plätzer. Parton Shower Matching Systematics in Vector-Boson-Fusion WW Production. *Eur. Phys. J. C*, 77(5):293, 2017. doi: 10.1140/epjc/s10052-017-4860-3.

[88] Barbara Jager, Alexander Karlberg, and Johannes Scheller. Parton-shower effects in electroweak $WZjj$ production at the next-to-leading order of QCD. *Eur. Phys. J.*, C79(3):226, 2019. doi: 10.1140/epjc/s10052-019-6736-1.

[89] ATLAS Collaboration. Measurement of the Z/$\gamma*$ boson transverse momentum distribution in pp collisions at $\sqrt{s} = 7$ TeV with the ATLAS detector. *JHEP*, 09:145, 2014. doi: 10.1007/JHEP09(2014)145.

[90] P. Golonka and Z. Was. PHOTOS Monte Carlo: A Precision tool for QED corrections in Z and W decays. *Eur. Phys. J.*, C45:97–107, 2006. doi: 10.1140/epjc/s2005-02396-4.

[91] Anomalous quartic electroweak gauge-boson interactions, Eboli model, `http://feynrules.irmp.ucl.ac.be/wiki/AnomalousGaugeCoupling`.

[92] Measurement of electroweak WZ production and search for new physics in pp collisions at sqrt(s) = 13 TeV. 2018.

[93] Measurements of production cross sections of same-sign WW and WZ boson pairs in association with two jets in proton-proton collisions at $\sqrt{s}$ = 13 TeV. 2020.

[94] Valentin Hirschi and Olivier Mattelaer. Automated event generation for loop-induced processes, 2015. URL `https://arxiv.org/abs/1507.00020`.

[95] Morad Aaboud et al. Electron reconstruction and identification in the ATLAS experiment using the 2015 and 2016 LHC proton-proton collision data at $\sqrt{s}$ = 13 TeV. *Eur. Phys. J. C*, 79(8):639, 2019. doi: 10.1140/epjc/s10052-019-7140-6.

[96] Georges Aad et al. Electron and photon energy calibration with the ATLAS detector using LHC Run 1 data. *Eur. Phys. J. C*, 74(10):3071, 2014. doi: 10.1140/epjc/s10052-014-3071-4.

[97] Georges Aad et al. Muon reconstruction performance of the ATLAS detector in proton–proton collision data at $\sqrt{s}$ =13 TeV. *Eur. Phys. J. C*, 76(5):292, 2016. doi: 10.1140/epjc/s10052-016-4120-y.

[98] Jean-Baptiste De Vivie De Regie, Jun Guo, Nataliia Kondrashova, Sandrine Laplace, Graham Richard Lee, Arthur Lesage, Jianbei Liu, Simone Michele Mazza, John Morris, Rosy Nicolaidou, Joaquin Poveda, Nadezda Proklova, Yu-Ting Shen, Jared Gregory Vasquez, Zirui Wang, Haijun Yang, Miha Zgubic, Dongliang Zhang, and Liqing Zhang. ATLAS electron, photon and muon isolation in Run 2. Technical report, CERN, Geneva, 2017. URL `https://cds.cern.ch/record/2256658`. This note contains the Moriond 2017 recommendations. It will be updated when new recommendations become available.

[99] Morad Aaboud et al. Jet reconstruction and performance using particle flow with the ATLAS Detector. *Eur. Phys. J. C*, 77(7):466, 2017. doi: 10.1140/epjc/s10052-017-5031-2.

[100] Matteo Cacciari, Gavin P. Salam, and Gregory Soyez. The anti-k_t jet clustering algorithm. *JHEP*, 04:063, 2008. doi: 10.1088/1126-6708/2008/04/063.

[101] Matteo Cacciari, Gavin P. Salam, and Gregory Soyez. FastJet User Manual. *Eur. Phys. J. C*, 72:1896, 2012. doi: 10.1140/epjc/s10052-012-1896-2.

[102] Matteo Cacciari and Gavin P. Salam. Pileup subtraction using jet areas. *Phys. Lett. B*, 659:119–126, 2008. doi: 10.1016/j.physletb.2007.09.077.

[103] Georges Aad et al. New techniques for jet calibration with the ATLAS detector. 3 2023.

[104] ATLAS Collaboration. Performance of Missing Transverse Momentum Reconstruction in ATLAS studied in Proton–Proton Collisions recorded in 2012 at $\sqrt{s} = 8$ TeV. ATLAS-CONF-2013-082, 2013. URL `https://cds.cern.ch/record/1570993`.

[105] . MuonTriggerPhysicsTriggerRecommendations2015, `https://twiki.cern.ch/twiki/bin/view/Atlas/MuonTriggerPhysicsTriggerRecommendations2015`.

[106] . Electron four momentum correction, `https://twiki.cern.ch/twiki/bin/view/AtlasProtected/ElectronPhotonFourMomentumCorrection`.

[107] Tracking CP recomendations, `https://twiki.cern.ch/twiki/bin/view/AtlasProtected/TrackingCPEOYE2015`.

[108] Additional γ^* and material conversion veto, `https://indico.cern.ch/event/862748/contributions/3635039/attachments/1946503/3235131/conversionsIFF2019.11.18.pdf`.

[109] Electron charge efficiency correction tool, `https://twiki.cern.ch/twiki/bin/viewauth/AtlasProtected/EgammaChargeMisIdentificationTool`.

[110] . Electron efficiency corrections, `https://twiki.cern.ch/twiki/bin/view/AtlasProtected/ElectronEfficiencyRun2`.

[111] . Latest MCP recommendation for muon selection, `https://twiki.cern.ch/twiki/bin/view/Atlas/MuonSelectionTool`.

[112] . Muon efficiency corrections, `https://twiki.cern.ch/twiki/bin/view/AtlasProtected/MCPAnalysisGuidelinesMC15`.

[113] Recommended isolation working points for Release 21, `https://twiki.cern.ch/twiki/bin/view/AtlasProtected/RecommendedIsolationWPs`.

[114] ATLAS Collaboration. Measurement of $W^{\pm}Z$ production cross sections and gauge boson polarisation in *pp* collisions at $\sqrt{s} = 13$ TeV with the ATLAS detector. ATLAS-CONF-2018-034, 2018. URL `https://cds.cern.ch/record/2630187`.

[115] . JetEtMiss Recommendations for Release 21 MC16 (2015-2018), `https://twiki.cern.ch/twiki/bin/view/AtlasProtected/JetEtmissRecommendationsR21`.

[116] . Pileup jet recommendations, `https://twiki.cern.ch/twiki/bin/view/AtlasProtected/PileupJetRecommendations`.

[117] . *b*-tagger Recommendations for Release 21, `https://twiki.cern.ch/twiki/bin/view/AtlasProtected/BTagTaggerRecommendationsRelease21`.

[118] . *b*-tagger Calibration Recommendations for Release 21, `https://twiki.cern.ch/twiki/bin/view/AtlasProtected/BTagCalibrationRecommendationsRelease2`.

[119] . Etmiss Recommendations for Full Run2, `https://twiki.cern.ch/twiki/bin/viewauth/AtlasProtected/EtmissRecommendationsFullRun2`.

[120] Recommendations of the Physics Objects and Analysis Harmonisation Study Groups 2014, 2014,ATL-COM-PHYS-2014-451.

[121] ATLAS Collaboration. Selection of jets produced in 13TeV proton-proton collisions with the ATLAS detector. Technical Report ATLAS-COM-CONF-2015-024, CERN, Geneva, May 2015. URL `https://cds.cern.ch/record/2016323`.

[122] . Jet cleaning recommendadtions, `https://twiki.cern.ch/twiki/bin/view/AtlasProtected/HowToCleanJets2015`.

[123] K. A. Olive et al. Review of Particle Physics. *Chin. Phys.*, C38:090001, 2014. doi: 10.1088/1674-1137/38/9/090001.

[124] Houry Keoshkerian and Emmanuel Sauvan. *Mesure de la production de di-bosons WZ aupres du LHC avec l'experience ATLAS.* PhD thesis, Joseph Fourier U., 2014. URL `https://cds.cern.ch/record/1980681`. Presented 08 Sep 2014.

[125] Observation of gauge boson joint-polarisation states in $W^{\pm}Z$ production from pp collisions at $\sqrt{s} = 13$ TeV with the ATLAS detector. 11 2022.

[126] Ioannis Karkanias. *Application of statistical methods with emphasis on Machine Learning for the analysis of experimental data from the ATLAS experiment at the LHC at CERN.* PhD thesis, Ioannina U., 2022.

[127] SMEFT@NLO model, `http://feynrules.irmp.ucl.ac.be/wiki/SMEFTatNLO`.

[128] Jacob J. Ethier, Raquel Gomez-Ambrosio, Giacomo Magni, and Juan Rojo. SMEFT analysis of vector boson scattering and diboson data from the LHC Run II. *Eur. Phys. J. C*, 81 (6):560, 2021. doi: 10.1140/epjc/s10052-021-09347-7.

[129] Combined effective field theory interpretation of Higgs boson and weak boson production and decay with ATLAS data and electroweak precision observables. Technical report, CERN, Geneva, 2022. URL `https://cds.cern.ch/record/2816369`. All figures including auxiliary figures are available at https://atlas.web.cern.ch/Atlas/GROUPS/PHYSICS/PUBNOTES/ATL-PHYS-PUB-2022-037.

[130] Despoina Sampsonidou. *The upgraded ATLAS detector for the search of new physics with diboson final states.* PhD thesis, Aristotle U., Thessaloniki, 2020.

[131] Georges Aad et al. Measurements of differential cross-sections in four-lepton events in 13 TeV proton-proton collisions with the ATLAS detector. *JHEP*, 07:005, 2021. doi: 10.1007/JHEP07(2021)005.

[132] Georges Aad et al. Higgs boson production cross-section measurements and their EFT interpretation in the 4ℓ decay channel at $\sqrt{s}$ =13 TeV with the ATLAS detector. *Eur. Phys. J. C*, 80(10):957, 2020. doi: 10.1140/epjc/s10052-020-8227-9. [Erratum: Eur.Phys.J.C 81, 29 (2021), Erratum: Eur.Phys.J.C 81, 398 (2021)].

[133] Céline Degrande, Nicolas Greiner, Wolfgang Kilian, Olivier Mattelaer, Harrison Mebane, Tim Stelzer, Scott Willenbrock, and Cen Zhang. Effective field theory: A modern approach to anomalous couplings. *Annals of Physics*, 335:21–32, 2013. ISSN 0003-4916. doi: https://doi.org/10.1016/j.aop.2013.04.016. URL `https://www.sciencedirect.com/science/article/pii/S0003491613000894`.

[134] Evaluating statistical uncertainties and correlations using the bootstrap method. Technical report, CERN, Geneva, Apr 2021. URL `http://cds.cern.ch/record/2759945`. All figures including auxiliary figures are available at https://atlas.web.cern.ch/Atlas/GROUPS/PHYSICS/PUBNOTES/ATL-PHYS-PUB-2021-011.

[135] Jon Butterworth et al. PDF4LHC recommendations for LHC Run II. *J. Phys. G*, 43:023001, 2016. doi: 10.1088/0954-3899/43/2/023001.

[136] ATLAS Collaboration. Observation of electroweak $W^{\pm}Z$ boson pair production in association with two jets in pp collisions at $\sqrt{s} = 13$ TeV with the ATLAS detector. *Phys. Lett. B*, 793:469, 2019. doi: 10.1016/j.physletb.2019.05.012.

[137] G. D'Agostini. A multidimensional unfolding method based on Bayes' theorem. *Nucl. Instrum. Meth. A*, 362:487, 1995. doi: 10.1016/0168-9002(95)00274-X.

[138] Despoina Sampsonidou, Joany Manjarres, Tim Herrmann, Stefanie Todt, Chariclia Petridou, Michael Kobel, Hannes Mildner, and Eirini Kasimi. aQGC re-interpretation of ssWW and WZjj. Technical report, CERN, Geneva, 2021. URL `https://cds.cern.ch/record/2791985`.

[139] aQGCs recent limits, `https://twiki.cern.ch/twiki/bin/view/CMSPublic/PhysicsResultsSMPaTGC#aQGCResults`.

[140] S. S. Wilks. The large-sample distribution of the likelihood ratio for testing composite hypotheses. *Ann. Math.Stat.*, 9:60–62, 1938. doi: 10.1214/aoms/1177732360.

[141] Glen Cowan, Kyle Cranmer, Eilam Gross, and Ofer Vitells. Asymptotic formulae for likelihood-based tests of new physics. *The European Physical Journal C*, 71(2), Feb 2011.

ISSN 1434-6052. doi: 10.1140/epjc/s10052-011-1554-0. URL `http://dx.doi.org/10.1140/epjc/s10052-011-1554-0`.

[142] L. Demortier and L. Lyons. Everything you always wanted to know about pulls.

[143] Luca Lista. Practical Statistics for Particle Physicists. In *2016 European School of High-Energy Physics*, pages 213–258, 2017. doi: 10.23730/CYRSP-2017-005.213.

[144] Gary J. Feldman and Robert D. Cousins. Unified approach to the classical statistical analysis of small signals. *Phys. Rev. D*, 57:3873–3889, Apr 1998. doi: 10.1103/PhysRevD.57.3873. URL `https://link.aps.org/doi/10.1103/PhysRevD.57.3873`.

[145] M. A. Acero et al. The Profiled Feldman-Cousins technique for confidence interval construction in the presence of nuisance parameters. 7 2022.

[146] Rivet Routine of the WZjj production, `https://rivet.hepforge.org/analyses/ATLAS2018I1711223.html`.

[147] O. J. P. Éboli, M. C. Gonzalez-Garcia, and J. K. Mizukoshi. $pp \to jje^{\pm}\mu^{\pm}\nu\nu$ and $jje^{\pm}\mu^{\mp}\nu\nu$ at $\mathcal{O}(\alpha_{\rm em}^6)$ and $\mathcal{O}(\alpha_{\rm em}^4\alpha_s^2)$ for the study of the quartic electroweak gauge boson vertex at cern lhc. *Phys. Rev. D*, 74:073005, Oct 2006. doi: 10.1103/PhysRevD.74.073005. URL `https://link.aps.org/doi/10.1103/PhysRevD.74.073005`.

[148] Genessis Perez, Marco Sekulla, and Dieter Zeppenfeld. Anomalous quartic gauge couplings and unitarization for the vector boson scattering process $pp \to W^+W^+jjX \to \ell^+\nu_\ell\ell^+\nu_\ell jjX$. *Eur. Phys. J. C*, 78(9):759, 2018. doi: 10.1140/epjc/s10052-018-6230-1.

[149] PMG SystematicTool, `https://twiki.cern.ch/twiki/bin/viewauth/AtlasProtected/PMGSystematicsTool`.

[150] EFTFun Tool, `https://gitlab.cern.ch/eft-tools/eft-fun`.

[151] Standard Model Unfolding, `https://twiki.cern.ch/twiki/bin/view/AtlasProtected/StandardModelUnfoldingNew`.

[152] Bogdan Malaescu. An Iterative, Dynamically Stabilized(IDS) Method of Data Unfolding. *Proceedings of the PHYSTAT 2011 Workshop, CERN, Geneva, Switzerland*, page 271, 2011.

[153] Konstantinos Bachas, Ioannis Karkanias, Eirini Kasimi, Christos Leonidis, Chara Petridou, Despina Sampsonidou, and Katerina Zachariadou. A machine learning approach to the eft re-interpretation of the wzjj fully leptonic electroweak production. *Journal of Physics: Conference Series*, 2105(1):012011, nov 2021. doi: 10.1088/1742-6596/2105/1/012011. URL `https://dx.doi.org/10.1088/1742-6596/2105/1/012011`.

[154] MMTester, `https://gitlab.cern.ch/atlas-mcp/MuonTester/-/blob/master/MuonTester/Root/MMTester.cxx`.

[155] STGCTester, `https://gitlab.cern.ch/atlas-mcp/MuonTester/-/blob/master/MuonTester/Root/STGCTester.cxx`.

[156] René Brun, F Bruyant, Federico Carminati, Simone Giani, M Maire, A McPherson, G Patrick, and L Urban. *GEANT: Detector Description and Simulation Tool; Oct 1994*. CERN Program Library. CERN, Geneva, 1993. doi: 10.17181/CERN.MUHF.DMJ1. URL `https://cds.cern.ch/record/1082634`. Long Writeup W5013.